

PACIFIC EARTHQUAKE ENGINEERING RESEARCH CENTER

The Second U.S.-Japan Workshop on Performance-Based Earthquake Engineering Methodology for Reinforced Concrete Building Structures

**11–13 September 2000
Sapporo, Hokkaido, Japan**

Sponsors

**Japan Ministry of Education, Science, Sports and Culture
Pacific Earthquake Engineering Research Center
U.S. National Science Foundation**

The Second U.S.-Japan Workshop on Performance-Based Earthquake Engineering Methodology for Reinforced Concrete Building Structures

**11–13 September 2000
Sapporo, Hokkaido, Japan**

Organizers

Toshimi Kabeyasawa
Earthquake Research Institute
University of Tokyo

Jack P. Moehle
Pacific Earthquake Engineering Research Center
University of California, Berkeley

Sponsors

Japan Ministry of Education, Science, Sports and Culture
Pacific Earthquake Engineering Research Center
U.S. National Science Foundation

Research Report
Grant-in-Aid for Scientific Research on Priority Area (Category B)
(Grant No. 11209203)

PEER Report 2000/10
Pacific Earthquake Engineering Research Center
College of Engineering
University of California, Berkeley
March 2000

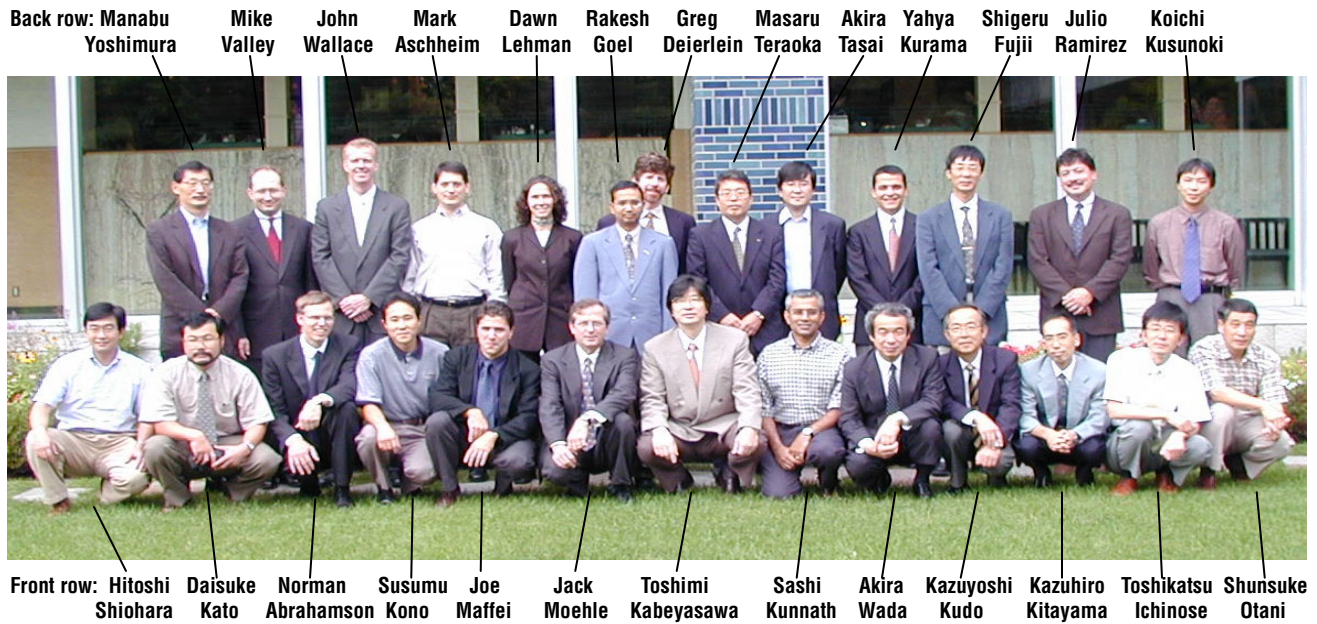
PREFACE

Considerable research is under way throughout the world to establish performance-based assessment and design methodology for buildings. Japan and the United States are at the forefront of this research effort, as well as efforts to implement the research results. The U.S.-Japan Cooperative Research in Urban Earthquake Disaster Mitigation, sponsored in Japan by the Ministry of Education, Science, Sports and Culture, and in the U.S. by the National Science Foundation, is funding collaborative research in Japan and the U.S. The Pacific Earthquake Engineering Research Center in the U.S. has established the development of performance-based earthquake engineering methodology as its primary mission. Because of the importance of this topic, it is timely for researchers and practitioners from the U.S. and Japan to meet to exchange technical data and ideas as well as to identify issues of mutual concern and opportunities for cooperative study.

The Second Workshop on Performance-Based Earthquake Engineering Methodology for Reinforced Concrete Building Structures was organized to meet the needs and opportunities for research and practice in performance-based engineering. The objectives of the workshop were threefold: (1) to discuss different perspectives on performance-based engineering as it is applied to new and existing concrete buildings in Japan and the United States; (2) to exchange the latest findings related to the same subject; and (3) to enhance communications and promote opportunities for new and continuing collaboration.

The Second Workshop was held 11 to 13 September 2000 in Sapporo, Hokkaido. It was attended by 16 Japanese and 13 U.S. participants. The participants are identified on the following page.

JAPAN SIDE	U.S. SIDE
Shunsuke Otani, U Tokyo Toshimi Kabeyasawa, ERI, U Tokyo Kazuyoshi Kudo, ERI, U Tokyo Masaomi Teshigawara, BRI Toshikatsu Ichinose, Nagoya IT Hiroshi Kuramoto, BRI Koichi Kusunoki, IIS, U Tokyo Akira Wada, Tokyo IT Susumu Kono, Kyoto Univ. Akira Tasai, Yokohama N Univ. Daisuke Kato, Niigata Univ. Manabu Yoshimura, Tokyo Metro Univ. Shigeru Fujii, Kyoto Univ. Kazuhiro Kitayama, Tokyo Metro Univ. Masaru Teraoka, Fujita Corp. Hitoshi Shiohara, U Tokyo	Jack Moehle, UC Berkeley Julio Ramirez, Purdue Univ. Norman Abrahamson, Pacific Gas & Electric, Co. Rakesh Goel, California Polytechnic Univ. Sashi Kunnath, U Central Florida Yahya Kurama, Notre Dame Univ. Mark Aschheim, U Illinois Greg Deierlein, Stanford Univ. Joe Maffei, Rutherford & Chekene John Wallace, UCLA Khalid Mosalam, UC Berkeley Dawn Lehman, U Washington Mike Valley, Skilling, Ward & Magnusson



HOST ORGANIZATIONS AND SPONSORS

The workshop was organized under the auspices of the U.S.-Japan Cooperative Research in Earthquake Disaster Mitigation, with funding by the Ministry of Education, Science, Sports and Culture in Japan (Grant No. 11209203), the National Science Foundation in the U.S., the Pacific Earthquake Engineering Research Center, and the State of California.

The technical program was developed by Professor Toshimi Kabeyasawa, Division of Disaster Mitigation Science, Earthquake Research Institute, University of Tokyo, and Professor Jack P. Moehle, Director of the Pacific Earthquake Engineering Research Center, University of California, Berkeley.

ACKNOWLEDGMENTS

This work was supported in part by the Pacific Earthquake Engineering Research Center through the Earthquake Engineering Research Centers Program of the National Science Foundation under Award number EEC-9701568.

CONTENTS

PREFACE	iii
ACKNOWLEDGMENTS	vi
TABLE OF CONTENTS	vii
SESSION I-1: KEYNOTE REPORTS ON PBD ♦ Chaired by Gregory Deierlein and Toshikatsu Ichinose	
New Seismic Design Provisions in Japan ♦ SHUNSUKE OTANI	3
State of Performance-Based Engineering in the United States — ♦ RONALD O. HAMBURGER AND JACK P. MOEHLE	15
SESSION I-2: RECENT TOPICS ON EXPERIMENTAL AND FIELD INVESTIGATIONS ♦ Chaired by Sashi Kunnath and Manabu Yoshimura	
Design and Analysis of a Six-Story Reinforced Concrete Frame-Wall System with Soft First Story for Shaking Table Test ♦ TOSHIMI KABEYASAWA, YASUSHI SANADA, AND HIROSHI KURAMOTO.....	31
SESSION A-1: DESIGN MOTIONS AND SDF RESPONSES ♦ Chaired by Mark Aschheim and Akira Wada	
Site Specific Strong Ground Motion during the Kocaeli, Turkey Earthquake of August 17, 1999, as Inferred from Array Observations of Microtremors ♦ KAZUYOSHI KUDO, TATSUO KANNO, HIROSHI OKADA, OGUZ OZEL, MUSTAFA ERDIK, TSUTOMU SASATANI, SADANORI HIGASHI, MASAYOSHI TAKAHASHI, AND KUNIKAZU YOSHIDA	47
Treatment of Variability and Uncertainty in Numerical and Empirical Methods for Ground Motion Estimation ♦ NORMAN ABRAHAMSON.....	63
Deviation of Plastic Deformation and Equivalent Damping Ratio on Single-Degree-of-Freedom System ♦ MASAOMI TESHIGAWARA, HIROSHI ISODA, AND NOBUYUKI IZUMI	75
Direct Displacement-Based Design Use of Inelastic Design Spectra versus Elastic Design Spectra ♦ RAKESH K. GOEL AND ANIL K. CHOPRA	89
SESSION A-2: INELASTIC RESPONSE OF STRUCTURES ♦ Chaired by Yahya Kurama and Hiroshi Kuramoto	
Displacement Responses of Reinforced Concrete Structures with Flexible Foundation ♦ TOSHIMI KABEYASAWA, CHOON-SOOK YOO, YOU-SOK KIM, AND KAZUYOSHI KUDO	103
Validity of Deformation Demand Estimates Using Nonlinear Static Procedures ♦ SASHI K. KUNNATH AND BALRAM GUPTA.....	117
Inelastic Seismic Response of Existing Reinforced Concrete Buildings ♦ T. ICHINOSE, DINH V. THUAT, H. KAGOHASHI, AND H. UMEMURA.....	129

SESSION A-3: RESPONSE BEHAVIOR OF FRAMES ♦ Chaired by

Rakesh Goel and Masaomi Teshigawara

Performance-Based Seismic Design of Non-Emulative Precast Concrete Walls with Friction Dampers ♦ YAHYA C. KURAMA	143
Sub-Structure Pseudo Dynamic Testing on 6-Story Reinforced Concrete Frame with Soft First Story ♦ HIROSHI KURAMOTO AND TOSHIMI KABEYASAWA	155
The Primacy of the Yield Displacement in Seismic Design ♦ M. A. ASCHHEIM AND E. F. BLACK	167

SESSION A-4: SEISMIC RESPONSE AND DESIGN OF STRUCTURES ♦ Chaired by

Norman Abrahamson and Kazuyoshi Kudo

The Effect of Vertical Excitation on Structural Response Characteristics ♦ KOICHI KUSUNOKI, YOSHIAKI NAKANO, AND TSUNEO OKADA	181
Development of a Two-Parameter Seismic Intensity Measure and Probabilistic Assessment Procedure ♦ PAUL P. CORDOVA, GREGORY G. DEIERLEIN, SAMEH S. F. MEHANNY, AND C. A. CORNELL	195
Suggested Improvements to Performance-Based Seismic Design Guidelines ♦ JOE MAFFEI	215

SESSION B-1: COLUMNS ♦ Chaired by Julio Ramirez and Hitoshi Shiohara

Damage Evaluation of Reinforced Concrete Columns under Multiaxial Cyclic Loadings ♦ SUSUMU KONO AND FUMIO WATANABE	229
Shear Failure and Axial Load Collapse of Existing Reinforced Concrete Columns ♦ J. P. MOEHLE, K. J. ELWOOD, AND H. SEZEN	241
Residual Axial Capacity of Reinforced Concrete Columns during Shear Deterioration ♦ AKIRA TASAL	257
Column Splices: Observed Earthquake Damage, Modeling Approaches, and the PEER/UCLA Research Program ♦ JOHN W. WALLACE AND MURAT MELEK	269

**SESSION B-2: COLUMNS AND SLABS ♦ Chaired by Dawn Lehman and
Shigeru Fujii**

Evaluation of Performance of R/C Columns ♦ DAISUKE KATO AND KOICHI OHNISHI	287
Seismic Evaluation of Waffle Slab Systems for Industrial Facility ♦ KHALID M. MOSALAM, CLAY J. NAITO, AND ERIK KUNKEL	301
Ultimate Limit State of RC Columns ♦ MANABU YOSHIMURA AND NORIYUKI YAMANAKA	313

**SESSION B-3: COLUMNS AND BEAM-COLUMN JOINTS ♦ Chaired by
Michael Valley and Susumu Kono**

Database Study on Capacities of R/C Columns Strengthened with FRP Sheets ♦ SHIGERU FUJII, YASUHIRO MATSUZAKI, KATSUHIKO NAKANO, AND HIROSHI FUKUYAMA	329
---	-----

On the Deformation Capacity of Reinforced Concrete Columns Subjected to Lateral Shear Reversals into the Nonlinear Range ♦ JULIO A. RAMIREZ AND TUREL GUR	341
Influences of Beam and Column Bar Bond on Failure Mechanism in Reinforced Concrete Interior Beam-Column Joints ♦ KAZUHIRO KITAYAMA, YUJI TAJIMA, MAKOTO OKUDA, AND SHINJI KISHIDA	357
Seismic Performance of Reinforced Concrete Beam-Column Joints ♦ DAWN E. LEHMAN, W. GREG MOSIER, AND JOHN F. STANTON	365
SESSION B-4: BEAM-COLUMN JOINTS AND EXISTING BUILDINGS ♦ Chaired by John Wallace and Daisuke Kato	
Seismic Damage and Performance Evaluation of R/C Beam-Column Joints ♦ MASARU TERAOKA AND SHIGERU FUJII	379
Developing Standards for the Evaluation and Rehabilitation of Existing Concrete Buildings ♦ MICHAEL VALLEY	391
Effects of Interaction between Joint Shear and Bond Strength on the Elast-Plastic Behavior of R/C Beam-Column Joints ♦ HITOSHI SHIOHARA	401
Test of an Innovative Reinforcing Detail for High Performance R/C Interior Beam-Column Connections Subjected to Seismic Action ♦ HITOSHI SHIOHARA, SAFAA ZAID, AND SHUNSUKE OTANI	415
RESOLUTIONS.....	425

SESSION I-1: KEYNOTE REPORTS ON PBD

Chaired by

◆ Gregory Deierlein and Tochikatsu Ichinose ◆

NEW SEISMIC DESIGN PROVISIONS IN JAPAN

Shunsuke OTANI

ABSTRACT

The seismic design requirements in the Building Standard Law of Japan were revised in June 2000 toward a performance-based design framework. The performance objectives are (a) life safety and (b) damage control of a building at two corresponding levels of earthquake motions. The design earthquake motion is defined in terms of acceleration response spectrum at engineering bedrock. The amplification of ground motion by surface geology and the soil-structure interaction must be taken into consideration. The response is examined by so-called "capacity spectrum method" by comparing the linearly elastic demand spectrum of design earthquake motions and the capacity curve of an equivalent single-degree-of-freedom (ESDF) system. The structure as designed is reduced to an ESDF system using a nonlinear static analysis under monotonically increasing horizontal forces. Equivalent damping is used to modify the demand spectrum taking into account the energy dissipation capacity of a structure at the prescribed limit states.

1. INTRODUCTION

The objectives of the Building Standard Law, proclaimed in May 1950, are "to safeguard the life, health, and properties of people by providing minimum standards concerning the site, structure, equipment, and use of buildings." The law outlines the basic requirements, and the technical details are specified in the Building Standard Law Enforcement Order (Cabinet Order) and in a series of Notifications by Minister of Construction.

The seismic design provisions of the Building Standard Law Enforcement Order were significantly revised in 1981; major revisions in seismic design were listed below:

- (1) Structural calculation is required to examine (a) maximum story drift under design earthquake forces, (b) lateral stiffness distribution along the height, (c) eccentricity of mass and stiffness in plan, and (d) story shear resisting capacity at the formation of a collapse mechanism,
- (2) Earthquake resistance is specified (a) in terms of story shear rather than horizontal floor forces, (b) as a function of fundamental period of a building and soil type, and (c) separately for the allowable stress design and the examination of story shear resisting capacity, and
- (3) Required story shear resisting capacity is varied for construction materials and with the deformation capacity of hinging members under earthquake forces.

Department of Architecture, Graduate School of engineering, University of Tokyo, Japan
Email: otani@sake.t.u-tokyo.ac.jp

The framework of the law was also significantly revised in 1998, (a) introducing performance-based regulations wherever feasible, (b) allowing private agencies to execute the building confirmation and construction inspection works, (c) deregulating urban land use, and (d) allowing public survey of design and inspection documents. New technical specifications in the form of the Law Enforcement Order and a series of Notifications of Minister of Construction were issued in June 2000, including the definition of performance objectives at design limit states and the specifications for verification methods. This paper introduces briefly the concept and framework of new provisions with emphasis on earthquake resistant building design.

2. PERFORMANCE-BASED REQUIREMENTS

The performance-based regulation is intended (a) to specify the requirements by performance, and (b) to relax and remove administrative control. The performance-based provisions were believed (a) to expand freedom in architectural, structural and mechanical design, (b) to encourage technical development in materials, design, and construction, (c) to enable the use of foreign goods and technologies in Japanese construction, and (d) to activate construction activities. The law requires that design documents and drawings should be submitted to a municipal government for the confirmation of the design documents to satisfy the legal provisions (Building Confirmation). This requirement makes the provisions to be prescriptive because building officials must be able to judge the conformity.

The new framework, introduced in the Building Standard Law, deals with the evaluation and verification of performance (response) at a given set of limit states under the combined loading of (a) dead loads, (b) live loads, (c) snow loads, (d) wind forces, and (e) earthquake forces. The structural specifications include (a) method of structural calculation, (b) quality control of construction and materials, (c) durability of buildings, and (d) performance of nonstructural elements. For continuity, the design loads and forces were maintained at the same levels as the existing provisions. However, a new format of seismic design forces was introduced; i.e., the response acceleration spectrum of the earthquake motion is specified at engineering bedrock, having shear wave velocity in the range of several hundred meters per second. The amplification of ground motion by surface geology above the engineering bedrock must be duly taken into account in defining the design ground motion at the free surface.

Two limit states are considered as the minimum standards for building structures to safeguard the life and property of the inhabitants; i.e., (a) life safety and (b) damage initiation. Two sets of design loadings are considered, each having a different probability of occurrence. The structural damage should be prevented in events that may occur more than once in the lifetime of the building for the protection of properties; i.e., the damage must be prevented in structural frames, members, interior and exterior finishing materials. A return period for such events may be 30 to 50 years. For the protection of human life, no story of the building should collapse under extraordinary loading conditions. The maximum possible earthquake motion level is determined on the basis of historical earthquake data, recorded strong ground motions, seismic and geologic tectonic structures and identified activities of active faults. A return period of several hundred years is assumed in defining the design earthquake motions.

3. DEFINITION OF DESIGN EARTHQUAKE MOTIONS

The acceleration response spectrum $S_A(T)$ of free surface ground motion at a 5% damping factor is represented as follows;

$$S_A(T) = Z \cdot G_s(T) \cdot S_0(T) \quad (1)$$

where Z is the seismic zone factor, $G_s(T)$ is the amplification factor by surface geology, $S_0(T)$ is the response spectral acceleration ordinate of ground motion at exposed engineering bedrock, and T is the period of a building in sec at the damaged state. The engineering bedrock is defined as a thick soil stratum whose shear wave velocity is on the order of 400 m/s or higher. The exposed engineering bedrock is used in the definition to eliminate the effect of the surface geology on the ground motion.

The design spectrum $S_0(T)$ (m/sec²) at exposed engineering bedrock is shown in Fig. 1 or given by Eq. (2) for the life-safety limit state:

$$\begin{aligned} S_0(T) &= (3.2 + 30T) & \text{for } T < 0.16 \\ S_0(T) &= 8.0 & \text{for } 0.16 \leq T < 0.64 \\ S_0(T) &= \frac{5.12}{T} & \text{for } 0.64 \leq T \end{aligned} \quad (2)$$

where T is the period (sec) of the building at the life-safety limit state. For the sake of continuity in seismic design provisions, the intensity of ground motion at the engineering bedrock was established to yield design seismic forces that are comparable to those for intermediate soil condition before the revision of the Building Standard Law. The design spectrum for the damage-initiation limit state is to be reduced to one-fifth of the spectrum for the life-safety limit state.

The amplification $G_s(T)$ of ground motion by surface geology is evaluated using the geological data at the site. The nonlinear amplification of ground motion by surface soil deposits is estimated using the equivalent linearization technique. A lumped-mass shear-spring model (Fig. 2) was used to represent a layer of soil deposits; the stiffness of soil layers was represented by secant shear modulus at maximum response shear strain under the first mode oscillation. The shear modulus reduction factors and damping factors are specified for cohesive and sandy soils at various shear strain levels in the 2000 Minister of Construction Notification No. 1457 (Fig. 3).

The following expressions are given for the amplification function $G_s(T)$ by surface geology (the 2000 Minister of Construction Notification No. 1457);

$$\begin{aligned}
 G_s &= G_{s2} \frac{T}{0.8T_2} && \text{for } T \leq 0.8T_2 \\
 G_s &= G_{s2} + \frac{G_{s1} - G_{s2}}{0.8(T_1 - T_2)} \cdot (T - 0.8T_2) && \text{for } 0.8T_2 < T \leq 0.8T_1 \\
 G_s &= G_{s1} && \text{for } 0.8T_1 < T \leq 1.2T_1 \\
 G_s &= G_{s1} + \frac{G_{s1} - 1.0}{\frac{1}{1.2T_1} - 0.1} \cdot \left(\frac{1}{T} - \frac{1}{1.2T_1} \right) && \text{for } 1.2T_1 < T
 \end{aligned} \tag{3}$$

where T_1 and $T_2 = (T_1/3)$ are the dominant periods of surface soil deposits, G_{s1} and G_{s2} are the amplification factors of the soil deposits in the first and second modes. The first-mode period is estimated on the basis of the depths, shear moduli at strain amplitude and mass density of the soil layers. Empirical formulae are provided to determine the first- and second-mode amplification factors G_{s1} and G_{s2} considering the hysteretic energy dissipation and impedance ratios.

If the detailed analysis is not used, the following simple expression can be used;

1) For soil type I (soil layer consisting of rock, stiff sand gravel, and pre-Tertiary deposits);

$$\begin{aligned} G_s &= 1.5 & \text{for } T < 0.576 \\ G_s &= \frac{0.864}{T} & \text{for } 0.576 \leq T < 0.64 \\ G_s &= 1.35 & \text{for } 0.64 \leq T \end{aligned} \quad (4)$$

where T is the period of a structure (sec).

2) For soil type II (soil layer other than types I and III) and type III (alluvium layer mainly consisting of humus and mud whose depth is more than 30 m, or filled land of more than 3 m deep and worked within 30 years);

$$\begin{aligned} G_s &= 1.5 & \text{for } T < 0.64 \\ G_s &= 1.5 \left(\frac{T}{0.64} \right) & \text{for } 0.64 \leq T < 0.64 \left(\frac{g_v}{1.5} \right) \\ G_s &= g_v & \text{for } 0.64 \left(\frac{g_v}{1.5} \right) \leq T \end{aligned} \quad (5)$$

where $g_v = 2.03$ for type II soil and 2.7 for type III soil.

The seismic zone factor Z evaluates (a) relative difference in expected ground motion parameters, such as peak ground acceleration or peak ground velocity for strong and intermediate intensity earthquake motions, and (b) frequency content for acceleration and velocity waveforms. Two levels of ground motion are defined; i.e., a) Large earthquake: largest annual maximum in 500 years, and b) Intermediate earthquake: 10th largest annual maximum in 500 years. The historical earthquake data over the last 500 years in Japan and fault parameters identified for major earthquakes were used in the study. The expected intensity levels estimated for the 500-year return period are comparable with or slightly larger than the level of seismic force currently in use for type-II soil. Therefore, the seismic zone factors, varying from 0.7 to 1.0, in the previous Building Standard Law Enforcement Order are maintained in the revised design requirements.

4. VERIFICATION OF STRUCTURAL PERFORMANCE

The performance of a building is examined at the two limit states under the two levels of design earthquake motions; i.e., (a) damage-initiation limit state and (b) life-safety limit state. The

damage-initiation limit state is attained when the allowable stress of materials has been reached in any member or when the story drift reaches 0.5 percent of the story height at any story. The initial elastic period is used for a structure. The life-safety limit state is attained when the structure cannot sustain the design gravity loads in any story under additional horizontal deformation; i.e., a structural member has reached its ultimate deformation capacity. The ultimate deformation of a member must be calculated as the sum of flexure and shear deformations of the member and deformation resulting from the deformation in the connection to adjacent members. The ultimate flexural deformation θ_{fu} may be estimated as

$$\theta_{fu} = \frac{\phi_y}{3} a + (\phi_u - \phi_y) \ell_p \left(1 - \frac{\ell_p}{2a}\right) \quad (6)$$

where ϕ_y is the curvature when allowable stress is first reached in the member, ϕ_u is the curvature at the maximum resistance, ℓ_p is the length of plastic region, a is the shear-span or one-half of clear member length.

A multi-story building structure is reduced to an equivalent single-degree-of-freedom (ESDF) system using a “pushover analysis”. The distribution of story shear coefficients (design story shear divided by the weight supported by the story) is defined by the following expression, consistent with the previous Building Standard Law;

$$A_i = 1 + \left(\frac{1}{\sqrt{\alpha_i}} - \alpha_i\right) \cdot \frac{2T}{1 + 3T} \quad (7)$$

$$\alpha_i = \frac{\sum_{j=1}^n W_j}{\sum_{j=1}^n W_j} \quad (8)$$

where W_i is the sum of dead and live loads at i -th floor, and T is the fundamental period of the structure. Horizontal force acting at a floor level is calculated as the difference of story shears immediately above and below. The deflected shape of the pushover analysis is assumed to represent the first-mode shape of oscillation. The deflected shape does not change appreciably with the distribution of horizontal forces along the structural height; therefore, the constant force distribution is used during the pushover analysis.

The modal participation factor Γ_1 is necessary to relate the SDF response and modal response of a structure under horizontal ground motion; i.e.,

$$\Gamma_1 = \frac{\{\phi\}_1^T [m] \{1\}}{\{\phi\}_1^T [m] \{\phi\}_1} \quad (9)$$

where $\{\phi\}_1$ is the first-mode shape vector (normalized to the roof-level displacement), $[m]$ is the lumped floor mass matrix (diagonal matrix), and $\{1\}$ is a vector whose elements are unity.

For a spectral response acceleration $S_A(T)$ and displacement $S_D(T)$ at the first-mode period and damping, the first-mode inertia force vector $\{f\}_1$ and displacement vector $\{d\}_1$ are defined as follows;

$$\begin{aligned} \{f\}_1 &= [m] \{\phi\}_1 \Gamma_1 S_A(T) \\ \{d\}_1 &= \{\phi\}_1 \Gamma_1 S_D(T) \end{aligned} \quad (10)$$

For the mode shape vector normalized to the roof-level displacement, the roof displacement D_{R1} is equal to $\Gamma_1 S_D(T)$. The first-mode base shear V_{B1} is the sum of inertia forces at each floor level. For the lumped floor masses, the base shear is calculated as follows;

$$\begin{aligned} V_{B1} &= \{1\}^T \{f\}_1 \\ &= \{1\}^T [m] \{\phi\}_1 \Gamma_1 S_A(T) \\ &= M_1^* S_A(T) \end{aligned} \quad (11)$$

where M_1^* is the effective modal mass as given below;

$$M_1^* = \Gamma_1 \{\phi\}_1^T [m] \{1\} \quad (12)$$

The effective mass must be not less than 0.75 times the total mass of the structure.

In general, the roof-level displacement D_R and the base shear V_B are governed by the first-mode response. Therefore, the base shear V_B divided by the effective modal mass M_1^* and the roof displacement D_R divided by the participation factor Γ_1 represent the response spectral acceleration $S_A(T)$ and displacement $S_D(T)$;

$$\begin{aligned} S_A(T) &= \frac{V_B}{M_1^*} \\ S_D(T) &= \frac{D_R}{\Gamma_1} \end{aligned} \quad (13)$$

Spectral acceleration $S_A(T)$ and displacement $S_D(T)$ can be defined at each loading stage of a structure. A continuous relation between $S_D(T)$ and $S_A(T)$ may be plotted for a structure under monotonically increasing horizontal forces. The relation is called the “capacity curve (spectrum)” of the structure (Fig. 4). The effective first-mode period T_e of a structure at a loading stage is approximated by the following relation;

$$T_e = 2\pi \sqrt{\frac{S_D(T)}{S_A(T)}} \quad (14)$$

It should be noted that the effective period changes with the amplitude of horizontal forces and displacements. The effective period may be modified taking into account the effect of soil-structure interaction.

Equivalent damping ratio for the first mode is prescribed to be 0.05 for the damage-initiation limit state because the state of a structure remains elastic at this stage. Equivalent viscous damping ratio h_{eq} at the life-safety limit state is defined after a series of nonlinear SDF response studies. The equivalent damping ratio ${}_m h_{eqi}$ of a structural member i is estimated by the following expression;

$${}_m h_{eqi} = \frac{1}{4} \left(1 - \frac{1}{\sqrt{\mu}}\right) \quad (15)$$

where μ is the ductility factor of the member attained at the life-safety limit state of the structure.

If the hysteresis shape of a member exhibits a slip-type characteristic, Eq. (16) must be used;

$${}_m h_{eqi} = \frac{1}{5} \left(1 - \frac{1}{\sqrt{\mu}}\right) \quad (16)$$

The equivalent damping ratio of an SDF system is estimated as the weighted average with respect to strain energy;

$$h_{eq} = \frac{\sum {}_m h_{eqi} {}_m W_i}{\sum {}_m W_i} + 0.05 \quad (17)$$

where ${}_m W_i$ is the strain energy stored in member i at the life-safety limit state. The equivalent damping ratio may be modified considering the soil-structure interaction effect.

The demand spectrum of an earthquake motion is constructed by plotting an SDF response acceleration in the vertical axis and corresponding displacement in the horizontal axis along a straight line with slope equal to the square of a circular frequency. Demand spectra are prepared for a damping ratio of 0.05 at the damage-initiation limit state, and for an equivalent damping ratio at the life-safety limit state. For the life-safety limit state, the response spectral acceleration and displacement are reduced by the following factor F_h ;

$$F_h = \frac{1.5}{1 + 10h_{eq}} \quad (18)$$

The performance of a structure under a given design earthquake motion is examined by comparing the capacity diagram of the structure and the demand spectrum of design earthquake motions. The intersection (called performance point) of the demand spectrum for an appropriate equivalent damping ratio and the capacity curve represents the maximum response under the design earthquake motion if the damping ratio of the demand spectrum is equal to an equivalent damping ratio of the SDF system evaluated at the deformation at the performance point. A continuous capacity curve is not necessary in design, but two points on the capacity curve must be evaluated corresponding to the two limit states.

The Building Standard Law Enforcement Order requires that spectral acceleration of a structure at a limit state should be higher than the corresponding acceleration of the demand spectrum using the equivalent damping ratio at the same limit state. The Building Standard Law Enforcement Order further requires that the exterior finishing and curtain walls should not fail under the design loads and displacements at the life-safety limit state. This requirement is intended to limit the story drift of the structure to a reasonable range.

5. SUMMARY

This paper presented an evaluation procedure of structural seismic performance under major earthquake motions introduced in June 2000 in the revised Building Standard Law and associated regulations. Life safety and damage control of a building are two performance objectives in the seismic provisions. The earthquake motions are defined by acceleration response spectrum that is specified at engineering bedrock in order to consider the soil condition and soil-structure

interaction effect. The return periods of the earthquake motion of approximately 500 years and approximately 50 years are considered for life-safety and damage-initiation limit states, respectively. The capacity spectrum method is used to examine the damage initiation and life-safety of a building. A structure as designed is reduced to an equivalent SDF system by the use of a pushover analysis. A linearly elastic capacity spectrum at a 0.05 damping ratio is modified for an equivalent damping corresponding to the displacement of the nonlinear SDF system at the two limit states.

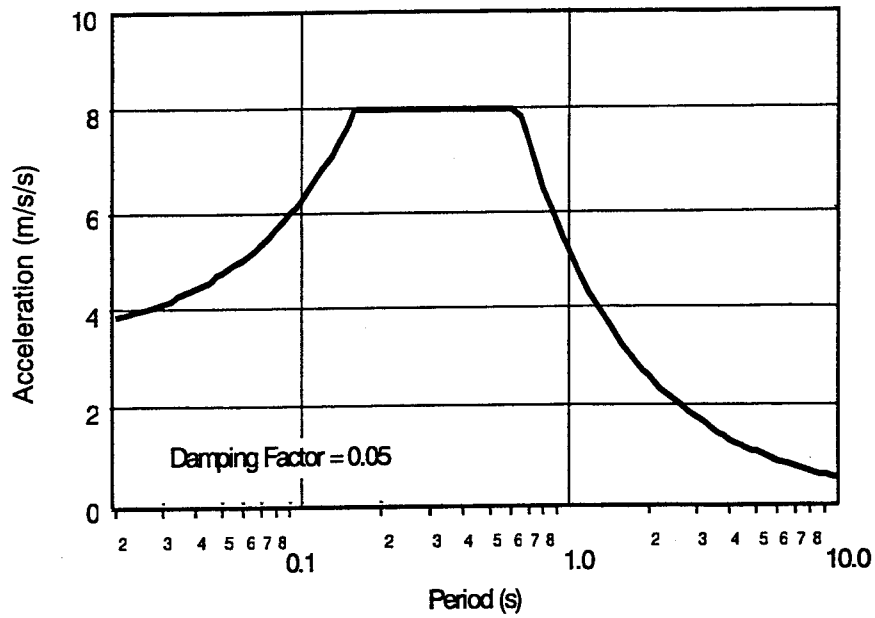


Fig. 1: Design earthquake acceleration response spectrum for life-safety limit state on exposed engineering bedrock

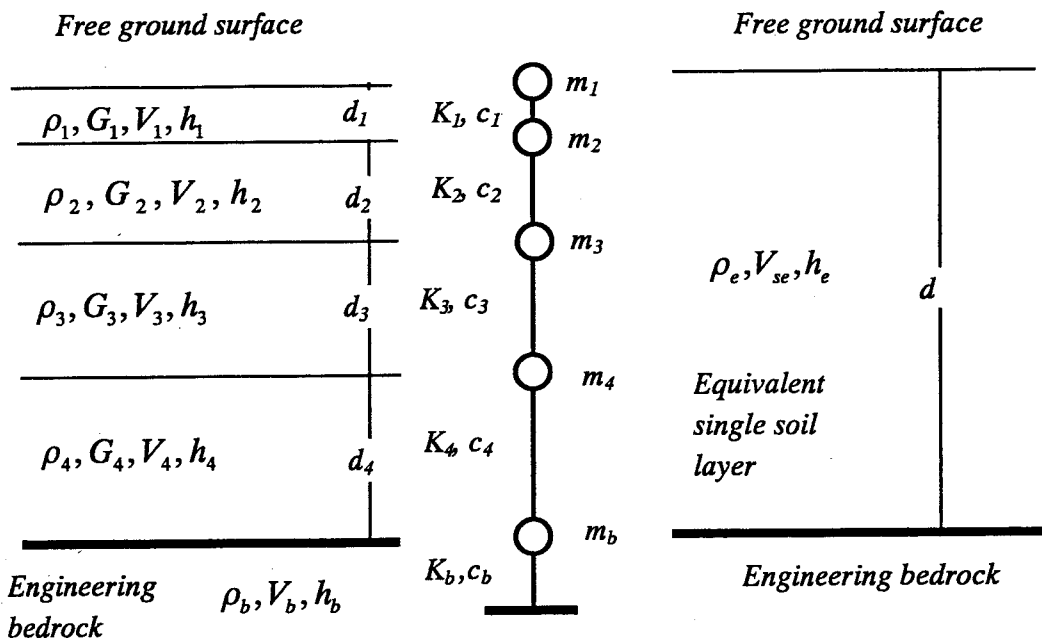


Fig. 2: Equivalent single-layer soil model (ρ : mass density, G : shear modulus, V : shear wave velocity, h : damping factor, d : layer depth, m : mass, K : stiffness, and c : damping coefficient)

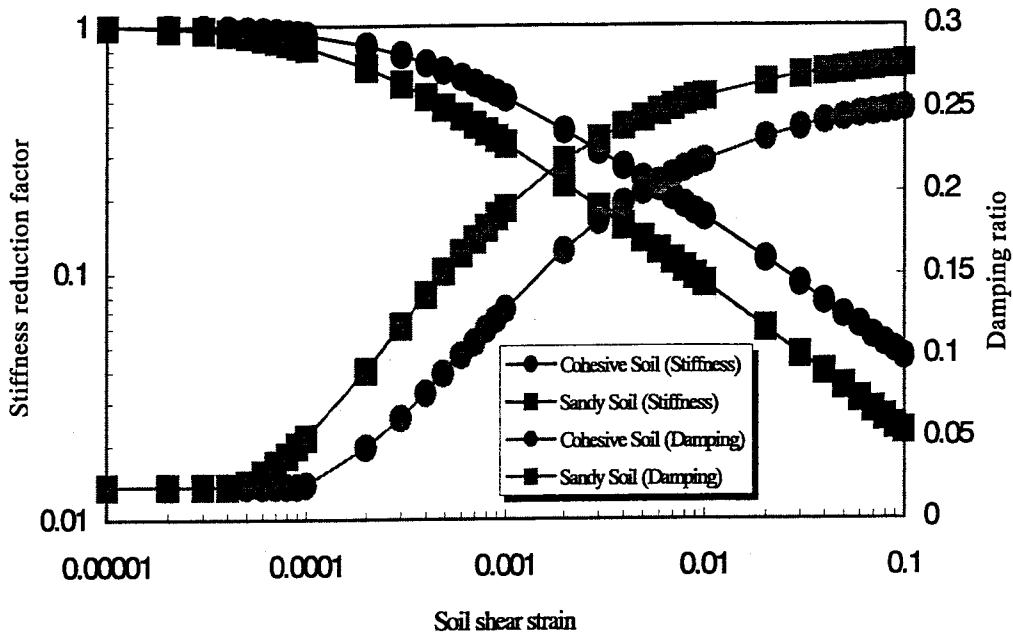


Fig. 3 Soil stiffness reduction factor and damping with shear strain

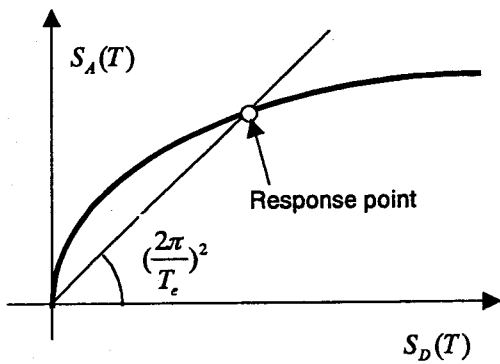


Fig. 4: Capacity curve of a structure in terms of spectral acceleration $S_A(T)$ and displacement $S_D(T)$

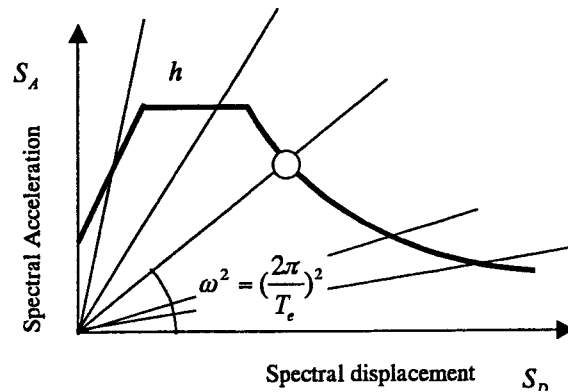


Fig. 5: Formulation of demand spectrum of design earthquake motion

STATE OF PERFORMANCE BASED-ENGINEERING IN THE UNITED STATES

Ronald O. Hamburger, SE
EQE International, Inc.
San Francisco, California/USA

Jack P. Moehle, PE
Pacific Earthquake Engineering Research Center
University of California, Berkeley/USA

Abstract

Performance-based engineering has been a goal of U.S. design practice since the publication of the first U.S. building code (PCBO, 1927) with earthquake provisions. Initially, the intent was to permit structures to withstand earthquakes without collapse or endangerment of life safety. In the 1970s this was extended to include enhanced damage control for structures important to earthquake recovery and response. Although the building codes had this intent, they were not reliably capable of doing this. Within the last ten years, the *ATC-40* (ATC, 1996) and *FEMA-273* (ATC, 1997) reports provided engineering guidelines for more reliable attainment of performance-based seismic upgrade of existing buildings while the *Vision 2000* (SEAOC, 1995) report extended these concepts to new construction. To date, U.S. building codes have not incorporated these performance-based approaches. However, the *1997 NEHRP Provisions* (BSSC, 1998), which is the basis for seismic provisions in the *International Building Code 2000* (ICC, 2000) does adopt, within its commentary, the performance objectives from the *Vision 2000* report. Today, when requested by Owners to do performance-based designs, engineers design to the building code and then verify anticipated building performance using the *ATC-40* and *FEMA-273* methodologies. Furthermore, standards of the American Concrete Institute have introduced notions of performance-based earthquake engineering for conventional and precast structural systems. However, many engineers remain concerned that performance-based design approaches increase their professional liability should structures not perform as anticipated. In response, the SAC Joint Venture has extended these concepts to include a structural reliability framework that permits estimation of a confidence level associated with a building's ability to meet performance expectations. The SAC framework is presently applicable only to steel moment-frame buildings; however, proposals have been developed to extend these reliability concepts to other systems.

Introduction

As defined in SEAOC's *Vision 2000* report, performance-based earthquake engineering consists of those actions, including site selection; development of conceptual, preliminary and final structural designs; construction; and maintenance of a building, over its life, to ensure that it is capable of predictable and reliable seismic performance. Each of the above actions can have significant impact on the ability of a structure to reliably withstand earthquake effects while sustaining desired limited levels of damage. However, in the United States today, among all the participants in the development process, including the developers themselves, the architect, the geotechnical engineer, the structural engineer, the contractor and the building official, only the structural engineer is knowledgeable in the important considerations of performance-based seismic engineering. Unfortunately, this one individual who is knowledgeable in the essential actions inherent in performance-based engineering, often has relatively little ability to significantly effect many of these actions.

Consider, for example, the selection of a project site. Except in rare cases, site selection is performed independent of considerations of seismic risk, and typically before the structural engineer is ever retained for a project. Typically, a site is selected for a project, not because it is free of potential liquefaction or landslide hazards, or because it will produce favorable ground motion spectra, but rather because the developer or owner of the project happens to own the specific piece of land, or because it is located close

to a population center or other resources. Typically, early in the project, a geotechnical engineer will be retained to perform preliminary site analysis and to determine if a site is suitable for the intended project. However, regardless of the seismic hazards that may be present at a site, the geotechnical engineer almost always finds that a selected site is suitable, provided that adequate engineering precautions are taken in the design of structures and foundations. To find otherwise, would be to make the geotechnical engineer appear, to the developer, to be a deal-killer. Deal-killers are not retained by developers for additional services, and so, sites are routinely found to be suitable, whether they are or not, and the structural engineer is left to design a structure that will accommodate those hazards that are present.

Conceptual design is the next step in the performance-based engineering process. Conceptual design consists of preparing the basic design concept, including the building layout and configuration, and also, selection of the structural system. Selection of the building layout and configuration typically is the responsibility of the design architect, an individual who rarely has an understanding of structures and little knowledge of earthquakes. At best, the structural engineer may participate in this process to the extent of consulting on the selection of a structural system. However, even this critically important task may be beyond the structural engineer's control. It is not uncommon that the structural materials and system for a project will be pre-selected, prior to retention of a structural engineer, based on considerations of occupancy and the preferences of the general contractor, who is often brought into a project at the conceptual stage, to provide pre-construction consulting services. Neither of these considerations is particularly relevant to the selection of damage-resistant structural systems.

Once a site has been selected, and a conceptual design has been developed, the structural engineer does generally have good ability to affect the preliminary and final design, and in particular the design of the structure and the building's seismic-force-resisting system. However, the structural engineer typically has little influence over the design of electrical and mechanical systems, or of architectural elements, even though the seismic performance of these elements is critical to the ability of the building to provide desired seismic performance. The result is that the design and installation of these non-structural features often results in buildings with damage-resistant structures, but with highly damageable finishes, cladding, and utilities.

Theoretically, the structural engineer can exercise significant control over the extent that construction conforms to the design expectations, by specifying appropriate levels of quality control and quality assurance, and also by personally visiting the site during construction, to assure that it is constructed appropriately. In fact, the construction quality-assurance process, as required by the building codes, and as contained in typical project specifications, results in significant cost premiums on projects, but fails to provide for adequate construction quality. Typically, the fee paid to construction inspectors on a building project in the United States exceeds that paid the structural engineer. Yet, many inspectors do not do an adequate job of assuring appropriate construction either because they are unaware of the appropriate standards, are improperly trained to determine if the construction conforms to the applicable standards, or are afraid that if they are excessively diligent in the exercise of their responsibilities, they will be confronted by the contractor and perhaps, ultimately removed from their position. Structural engineers, typically do not observe the construction often enough and typically do not have the training to understand if the work they are observing is adequately constructed, unless gross deficiencies are present. The result is that most building construction only marginally conforms to the applicable quality standards and as a result of systemic problems with the construction quality assurance process, it is unlikely that specification of greater quality-assurance activity, by itself, would be sufficient to correct this.

Finally there is the action of building maintenance. Building maintenance includes those activities necessary to ensure that the occupants of the building, over its life, take no action that would compromise the building's performance, for example by adding excessive weight to floors, or installing unanchored

equipment and utilities. Unfortunately, there is even less control of the construction and modification of buildings made on behalf of tenants than there is of the original construction.

Given the above, this paper focuses on that part of the performance-based engineering process, over which the structural engineer can and typically does exercise significant control, that is, the structural design process. In the following sections, we report on the development of performance-based structural design, as opposed to performance-based engineering, in the United States, and its current state of implementation.

Performance-Based Design and Prescription

As used in the United States, the terminology “performance-based design” applies to the general process in which a series of design performance objectives are selected at the initiation of a project, and then serve as the basis for the design. In essence, under this approach, the design process becomes one of demonstrating through rational means, which may consist of calculations, prototype testing, or a combination of these, that the completed design will be capable of providing the desired performance. Although the concept of performance-based design has perhaps made greatest strides in the area of earthquake engineering, it is not limited exclusively to this area of practice. In fact, the International Code Council (ICC), developer of the *International Building Code 2000*, has in place a standing performance-based code committee with the charge of developing a complete performance-based set of code provisions. These performance-based code provisions are intended to cover all aspects of the building design process including fire/life safety, structural safety, mechanical, and electrical systems.

Figure 1- illustrates the process of performance-based design as envisaged by the ICC committee. In addition to verification that a design will be capable of meeting the selected performance objectives, through analysis and calculation, or through prototype testing, the ICC approach also permits verification by demonstrated conformance with deemed-to-comply standards. As an illustration of this process, let us consider that is desired to construct a small residential structure, with overall dimensions of 15 meters by 10 meters. The first step in the process will be the selection of performance objectives. Note that the ICC committee has not yet reached consensus on performance objectives, but will eventually prescribe minimum performance goals for various classes of construction. Let us presume that for single family, residential construction, the prescribed performance objective will be one of providing collapse resistance, for maximum considered earthquake ground shaking, having a 2% probability of exceedance in 50 years, and a slight damage performance, permitting immediate reoccupancy of the structure for more likely earthquake ground motions, perhaps having a 50% probability of exceedance in 50 years. These will be the design objectives, that the designer must demonstrate the completed design is capable of achieving.

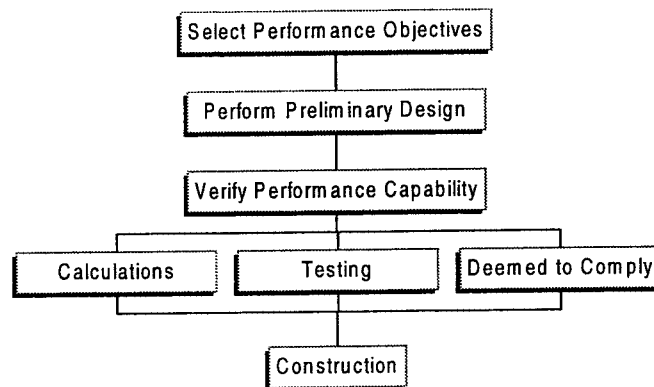


Figure 1 – Performance-based Design Process

The next step is the preliminary design. For our example, let us assume that the designer decides that this is a rectangular structure, and that the exterior walls are to be completely sheathed with plywood, as is the roof, creating a box structure. Openings for doors and windows are postulated and to complete the preliminary design process, a plywood thickness and nailing pattern are selected. Now the designer must demonstrate that such a structure will be capable of meeting the dual performance objectives cited above. The designer will have three alternative ways to do this. One way would be to perform calculations and to demonstrate that the building has adequate strength, stiffness, and ductility to withstand the specified ground shaking levels with acceptable levels of damage. The permissible limiting values of strength, stiffness, and ductility would have to be prescribed by the building code, or alternatively, demonstrated by the designer to be appropriate. Alternatively, if this design was to be used many times for a number of buildings, the designer could construct a prototype building, mount it on a shake table, and subject it to ground motions representative of the design events, to demonstrate that the design is capable of meeting the intended performance. Finally, the designer may only need to demonstrate that the building complies with prescriptive, deemed-to-comply standards. For example, the code may specify that 3/8-inch plywood with 8d nails at 6 inches on center is deemed by the code to comply with these performance objectives, for buildings not exceeding a certain size. As long as the designer complies with or exceeds that detailing, the building would be “deemed to comply” even though specific demonstration of performance-capability was not provided.

Many U.S. engineers view performance-based design as being the antithesis of code-based approaches. That is, rather than having to comply with prescriptive requirements, the designer need only demonstrate through his own selected means, that the design will be capable of achieving the desired performance goals. However, as illustrated by the above discussion, this is not the case. Performance-based codes when they are adopted in the United States, are likely to have substantial prescription, including prescription of the minimum acceptable performance, prescription of allowable limits on design parameters, such as strength, stiffness, and ductility that are appropriate to various performance states, and, potentially, complete prescription of the characteristics of deemed-to-comply standards.

Rather than being an alternative to prescriptive-based codes, performance-based design is in reality, an approach that includes prescription, but that is rationally tied to the achievement of performance objectives, and one that is capable of reliably providing achievement of these objectives. The performance-based code described above, currently under development by the ICC does not yet exist, and for the time being, is something that can be anticipated but not used. However, performance-based design is regularly being performed in the United States today. The balance of this paper focuses on performance-based design as it currently exists in practice and how it has developed to this state.

Historic Development

In reality, all design is in some respect, performance-based, even though the engineers performing the design may not recognize it as such. For example, when an engineer designs for dead and live load resistance, the intent of the design procedure being used is to provide a low probability of failure, under loads that could credibly be applied and a low probability of damage or loss of serviceability under loads that are likely to be applied. This performance-basis is implicit in the load and resistance factor design (LRFD) and Ultimate Strength Design (USD) methods inherent in the design provisions for both steel (AISC, 1993) and concrete (ACI, 1999). In these methodologies, a low probability of failure is obtained by assuring that factored loads are less than factored capacities while serviceability is obtained by evaluating deflections under anticipated (unfactored) design loads. These same procedures are followed for most loading condition including those relating to snow, wind, earth pressure, and similar loads.

Design for earthquake resistance is unique in two key aspects. First, until relatively recently, the design codes have not considered a need to design for serviceability under anticipated earthquake loads and,

second, that design anticipates the potential for localized failure of elements under credible loading, while seeking to avoid global collapse. From the time that the first U.S. code with non-mandatory provisions for earthquake design was published, in 1927, until the publication of the *1976 Uniform Building Code* (ICBO, 1976) earthquake design was conducted with a single performance objective – the avoidance of structural collapse and, thereby, protection of life safety for the largest earthquakes that could credibly be anticipated to affect a building.

The code provisions adopted to achieve this performance objective have, until very recently, largely been developed on an empirical basis. In the earliest of these codes, it was judged that structures capable of resisting a lateral force equal to 10% of their supported weight, would be able to achieve the intended performance. This judgment was made without a good understanding of the actual strength and character of ground motion that could affect buildings, and certainly without any clear understanding either of structural dynamics or nonlinear structural behavior. Later, as buildings designed to these rather crude provisions were affected by actual earthquakes, it was possible to make adjustments to this basic approach, and also to develop new provisions specifically intended to preclude design and construction features that have been seen to result in unacceptable performance. Over a period of 50 years of development, the code was refined still further, as understanding of structural dynamics, nonlinear behavior, and the types of detailing that could provide adequate toughness was developed. Yet, the basic approach, of designing a structure for approximately 10% of its supported weight, remained as a fundamental part of the design approach, regardless of the fact that it was not rationally tied to the understood behavior of structures in earthquakes. Surprisingly, despite this lack of a rational tie between the design approach and physical behavior, the code procedures have seemed to provide reasonably reliable performance with regard to protection against collapse, though not without exceptions.

In the 1960s, despite the fact that the seismic design procedures used in the code continued to be devoid of a specific serviceability evaluation, the Structural Engineers Association of California (SEAOC, 1968) determined that buildings designed in accordance with the code should be capable of meeting an expanded set of performance objectives. This expanded set of objectives included an ability to resist minor levels of earthquake ground motion without damage, and moderate levels of ground motion without structural damage, but perhaps with nonstructural damage. The modifiers “minor” and “moderate” were not clearly defined, but the concept was satisfying.

In 1971, a strong earthquake struck Sylmar, California and affected a number of modern buildings constructed to recent editions of the building code. A number of these buildings experienced partial or total collapse, including several hospitals, one of which, the Olive View Hospital, was a newly constructed facility. Investigation of the damage to modern buildings in this earthquake led to substantial revision of the building code. One of the most significant changes, adopted in the 1976 edition of the *Uniform Building Code*, was the realization that hospitals and other facilities with non-ambulatory occupants, or that are required to assist with disaster recovery operations, should be designed to provide performance superior to ordinary commercial and residential structures. This led to an additional performance-based design objective for these facilities - that they be capable of resisting design earthquake ground shaking with so little damage that they would rapidly be available for occupancy and service following such an event. At the time that this performance objective was adopted, concepts of nonlinear structural analysis, and even linear dynamic analysis, were not yet developed to a point that would permit practical application on a routine basis. As a result, this performance objective was targeted using the very indirect approach of increasing the design base shear forces by 50%.

The code provisions adopted following the 1971 San Fernando earthquake have remained in effect, with moderate adjustment, to the present time, and remain as the basis for the new *International Building Code 2000*. There has been increased emphasis on the use of methods of dynamic analysis, the definition of design ground motion has been refined and improved, design base shear levels have been modified, and

detailing requirements have changed to accommodate new construction systems and to account for observed building performance in recent earthquakes. Although these design provisions have been empirically adjusted and calibrated to provide the intended performance with regard to collapse avoidance, no rational procedure or empirical benchmarking has been included in the code to address performance objectives relating to serviceability and rapid re-occupancy. It should not have been a surprise, therefore, that when a series of moderately large earthquakes affected California in the 1980s and 1990s, the code was found to be incapable of reliably meeting these other performance objectives.

Modern Development

In 1989, a magnitude 7.1 earthquake occurred near Santa Cruz California, located some 100 kilometers to the south of San Francisco. This earthquake produced moderate levels of ground motion throughout the San Francisco Bay area, but resulted in large economic losses, estimated at \$7 million in property damage alone. As a result of this event, engineers, government agencies, and private industry began to question whether current design procedures were adequate to control losses under moderate levels of ground shaking, as suggested by the performance objectives stated in the SEAOC Commentary to the code (SEAOC, 1968). Also, and perhaps more importantly, as a result of the Loma Prieta earthquake, many building owners and corporate tenants in older buildings began to become concerned that their buildings were not adequate to protect their financial interests in the event of future earthquakes. These owners and tenants began to request that these buildings be upgraded. However, rather than asking that the buildings be upgraded to conform to the building code, these owners and tenants began to ask engineers to design upgrades to meet very specific performance objectives related to the amount of business interruption and repair cost that may be incurred in a building for different levels of earthquake ground motion.

A few years after the Loma Prieta earthquake, an association of the Applied Technology Council (ATC), the American Society of Civil Engineers (ASCE) and the Building Seismic Safety Council (BSSC) began work on the development of the *FEMA-273, NEHRP Rehabilitation Guidelines*. This publication was specifically developed to provide performance-based design criteria and procedures for the seismic upgrade of existing buildings, and upon its completion, was the first set of complete, rationally-based procedures for this purpose. In parallel with the development of *FEMA-273*, the Applied Technology Council on behalf of the California Seismic Safety Commission began to develop a parallel document, *ATC-40*, to address the evaluation and upgrade of concrete buildings. These documents were very similar and incorporated nearly identical definitions of performance and procedures for verifying performance. Both *FEMA-273* and *ATC-40* defined performance in terms of performance levels. Three separate performance levels were defined: an Immediate Occupancy level, in which relatively little damage or impairment of the structure occurs; a Collapse Prevention level, in which near complete damage of the structure occurs; and a Life Safety level, defined as a condition of severe damage, but a state in which margin remains against collapse. The basis for design by these documents consisted in the selection of a specific ground motion (upon which the design was to be based) and a performance level (selected from the three levels described previously) that was to be achieved given that this ground motion was experienced.

FEMA-273 and *ATC-40* adopted an approach to performance evaluation based on the nonlinear static analysis, known colloquially as pushover analysis. Under this concept, illustrated in Figure 2, the performance state that a structure experiences is related to the amount of lateral drift induced in the structure by the ground motion. The amount of global drift induced in the structure by the design ground motion is calculated by structural analysis. In *ATC-40*, the capacity-spectrum approach to pushover analysis appears as the preferred method for this purpose. In *FEMA-273*, lateral drift may be calculated by pushover analysis, or any of several other alternative methods including linear static or dynamic analysis or nonlinear dynamic analysis. Although the *FEMA-273* and *ATC-40* methodologies base performance on global lateral deformation demand, actual evaluation of the ability of a structure to meet

the various performance levels is based on evaluation of local, or element level, deformation demands and capacities. (The one exception appears in ATC 40, which limits the global strength degradation to twenty percent of the peak capacity.) This would appear to be a major area of conservatism in these methodologies, as the evaluated performance of a structure is often controlled by a few weak elements. The result is that redundant structures with substantial residual capacity could be evaluated as being near collapse on the basis of the evaluated performance of a few weak or brittle elements.

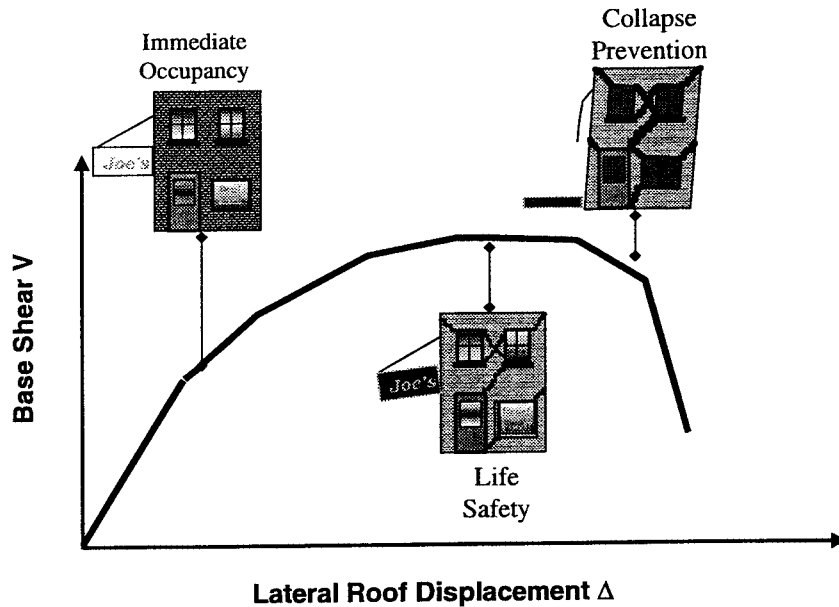


Figure 2 Performance Concept in *FEMA-273* and *ATC-40*

Currently, ASCE is engaged in a project to convert the *FEMA-273* document, which is written in the form of voluntary guidelines, into a formal consensus standard, so that building codes may directly incorporate it by reference. A pre-standard version of this document, which will bear the designation *FEMA-355*, should be published in either late 2000, or early 2001.

In 1994, the magnitude 6.7 Northridge earthquake struck the same region that had been strongly shaken twenty years earlier by the 1971 Sylmar earthquake. With a few noteworthy exceptions, modern buildings meeting recent code criteria again fulfilled the performance objective relating to avoidance of collapse and life safety endangerment. However, financial losses in this earthquake were double those experienced in the 1989 Loma Prieta earthquake, and included extensive damage to modern buildings. Concerned about the extent of these losses, the State of California, Office of Emergency Services, funded SEAOC to develop recommendations for implementation of performance-based design in new building practice. SEAOC turned to the technology then being developed in the *FEMA-273* project for definition of performance and performance objectives, and formalized this into a series of recommended design criteria for new building design, together with a recommended conceptual framework for implementing performance-based design for new buildings. The framework itself was highly conceptual and could not be directly used in the design of buildings, without extensive additional research and development. However, the performance matrix, which contained recommendations for suitable minimum performance objectives for the design of new buildings, was adopted into the commentary to the *1997 NEHRP Recommended Provisions, FEMA-303*, in the form presented in Figure 3, below. In this figure, Seismic Use Group III includes emergency response facilities, such as hospitals, fire stations, and communications centers. Seismic Use Group II includes buildings occupied by a large number of persons, including high rises and assembly halls. Seismic Use Group I includes ordinary occupancy buildings. This performance

matrix, and these Seismic Use Groups serve as the basis for design provisions contained in the *International Building Code 2000 (IBC)*. In order to achieve these performance objectives, the *IBC* specifies different strength levels, different permissible drift ratios, and different permissible structural systems for buildings in each Seismic Use Group. However, as with previous editions of the building code, even though several tiers of performance objectives are targeted, for different levels of earthquake ground shaking, an actual evaluation of performance is performed only for a single ground motion level, indicated as “rare” in the performance matrix. Also, as with previous editions of the building code, the performance evaluation consists of a calculation of building drifts and element forces obtained from a somewhat arbitrarily reduced, elastic response-spectrum analysis.

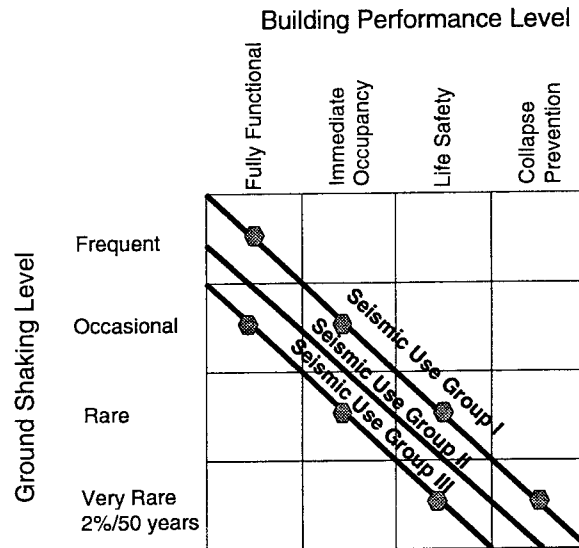


Figure 3 – Performance Matrix in FEMA 303

At this time, the *FEMA-273* and *ATC-40* documents are experiencing widespread use by engineers in zones of high seismicity for the design of seismic upgrades for existing buildings, and to a lesser extent, as a method of verifying the performance capabilities of new buildings designed to conform to the current building code. Now that engineers have tools available to them that will permit them to undertake a rational performance-based design, many have expressed concerns, sometimes seemingly contradictory, with the use of these procedures. One is that the *FEMA-273/ATC-40* procedures seem to be very conservative relative to the standard code procedures they are accustomed to implementing in their designs. Given that judgment has been made in recent earthquakes that the standard code procedures do not seem to be providing adequate performance in moderate levels of ground shaking, it seems reasonable that the new procedures should produce somewhat more conservative designs. Although engineers express concern that the new procedures appear excessively conservative, they simultaneously express concern that, by agreeing to implement a performance-based design approach, they potentially are incurring substantial additional professional liability compared with liability under past methods of practice. These engineers argue that if they design to the building code, and an earthquake causes excessive damage to the building, they need only demonstrate that their design conformed to the code. However, if they design to a client’s request for specific performance, and the building experiences more damage than the client requested as a design basis, they fear they will have no defense.

This concern with regard to liability is a potentially valid one, although it could be argued that as long as the design conforms to an applicable standard, such as the *FEMA-273* or *ATC-40* documents, the engineer could demonstrate that he/she conformed to an appropriate standard of care. However, it is clear that the

analyses used to predict structural demands and capacities used to judge building performance incorporate significant uncertainty. Further uncertainty is introduced by the variation in construction quality that inevitably occurs as a design is translated into a real structure. Finally, there is very large uncertainty inherent in the prediction of the character and strength of ground shaking that will affect a building in the future. Given these uncertainties, it is not possible to design a building for specific performance objectives with complete assurance that it will actually be able to provide the desired performance.

Introduction of Reliability Methods

As previously discussed, the 1994 Northridge earthquake caused unanticipated severe levels of damage to certain types of modern code-conforming buildings, at ground-motion levels that were less severe than the design level. One of the building types that experienced such unanticipated damage was welded steel moment-resisting frames. Contrary to the intended ductile behavior of these frames, it was discovered that many buildings of this type had experienced brittle fractures of their welded beam-to-column connections. In response to the discovery of these unanticipated brittle failures, the Federal Emergency Management Agency entered into a cooperative agreement with a consortium of SEAOC, ATC, and the California Universities for Research in Earthquake Engineering (CUREe), known as the SAC joint venture. In a five-year program, the SAC joint venture performed problem-focused research into the causes of this damage and developed engineering guidelines and design criteria for the evaluation and repair of earthquake-damaged buildings, performance evaluation of existing buildings that have not yet been affected by earthquakes, and for performance-based design of new buildings capable of more reliable performance in the future. The recommended performance-based design and evaluation criteria developed by SAC are presented in a series of three publications (SAC, 2000a, b, and c).

The research conducted by the SAC project included thousands of nonlinear analyses of steel moment-frame buildings for a variety of design and ground motion conditions, as well as nearly two hundred laboratory tests of connection assemblies. This provided a broad statistical database on the behavior of moment-resisting frames and the components used to construct these frames. The challenge to the SAC project was to develop performance-based design and evaluation criteria that incorporated the information available from this statistical database. In order to accomplish this, the SAC project built upon and extended the performance evaluation procedures contained in *FEMA-273* by modifying them to include a structural reliability basis. This structural reliability basis incorporates direct consideration of the uncertainties and variabilities inherent in estimation of structural demands and capacities, and thereby allows calculation of a level of confidence associated with the ability of a building to meet the intended performance objectives. This approach directly responds to engineers' concerns that designs may not actually provide the expected performance, in that it allows them to tell clients exactly how certain they are that a design will be able to accomplish this.

In order to accommodate this reliability approach, a subtle but important change was made to the concept of performance objectives, as contained in *FEMA-273* and *ATC-40*. As described previously, in these documents a performance objective consists of the specification of a desired limiting level of damage, termed a performance level, given that earthquake hazards of specified intensity are experienced. Hazards are typically expressed in terms of the probability that shaking of given, or more severe, intensity is experienced. In the SAC approach to performance evaluation, performance objectives are expressed as the total probability that earthquake induced damage to a structure will exceed a desired level. For example, under *FEMA-273*, a performance objective would be expressed in the form: the building will meet collapse prevention performance given that earthquake shaking with a 2% probability of exceedance in 50 years are experienced. Under the SAC approach, this same performance objective would be expressed as a 2% probability in 50 years of more severe damage than the collapse prevention level.

The difference in the two approaches is that the SAC approach recognizes that there is some probability that ground shaking that is more likely than the specified hazard level could cause damage exceeding the collapse prevention level and also that there is some probability that ground shaking hazards that are less likely than the specified level would cause less damage. In the SAC approach, the total probability that damage more severe than the desired level can occur is obtained by integrating over the hazard curve the probability that demands more severe than the applicable capacities will be experienced, recognizing the uncertainties and variabilities inherent in the prediction of demands and capacities.

Demands that are evaluated in this approach include maximum interstory drift, column axial compression, and column axial tension. Demands may be predicted using any of the four analytical procedures permitted in *FEMA-273*. Once demands are determined by structural analysis, a factored demand-capacity ratio is computed from the equation:

$$\lambda = \frac{\gamma_a D}{\phi C}$$

where γ is a demand variability factor that is derived from the integration of the computed demand over the hazard curve, considering the variability in response due to differences in ground motion; γ_a is a demand uncertainty factor, that accounts for bias and uncertainty inherent in the calculation of demand; D is the calculated demand; ϕ is a resistance factor, that accounts for variability and uncertainty in the estimation of capacity; and C is the estimated capacity.

The factored demand-capacity ratio, λ , is used as an index to determine the level of confidence associated with the probability that demand will be less than capacity. A computed value of λ of unity, indicates a mean level of confidence, on the order of 60 to 70%, that demands will be less than capacities and that the desired performance will be attained. Values of λ less than unity indicate higher levels of confidence and values of λ greater than unity indicate lower levels of confidence. The value of λ is indexed to confidence through determination of the number of logarithmic standard deviations relating to uncertainty above or below the mean the computed value of factored demand-capacity ratio lies. The SAC design criteria provide tables that provide a ready solution of this relationship.

For new buildings, the SAC criteria recommend that designs be proportioned such that there is a 90% level of confidence that there is less than a 2% probability in 50 years of damage more severe than the Collapse Prevention level, as determined by global behaviors, such as development of P-delta instability or buckling of columns; and that a 50% level of confidence be attained for this performance on the basis of local connection behavior. For existing buildings, the user may select any probabilities and confidence levels desired as acceptable behavior. For the evaluation of existing damaged buildings, this reliability approach is used to determine a level of confidence with regard to the ability of a building to resist collapse, given that there is an assumed repeat of the original damaging ground motion, within a period of one year following the earthquake. If greater than a 50% confidence level is calculated, the post-earthquake criteria recommend that the building be permitted to be occupied while it is repaired. If less than a 25% confidence level is determined, it is recommended that the building not be occupied until repaired.

At this time, the various SAC criteria documents have just been published and feedback from the engineering community on the usefulness of this approach has not been obtained. However, AISC has expressed an interest in extending this approach to the design of other steel frame systems, including braced frames.

Methods Specific to Concrete Buildings

In recent years, procedures for performance-based earthquake engineering of concrete buildings have been introduced into codes and other standards. The primary intent of these methods has been to replace traditional detailing requirements by allowing either calculations, testing, or both as means of validating that alternative details are permissible. While these methods are limited in that they apply only to the minimum life-safety performance objectives of current building codes, rather than permitting alternative performance objectives, they represent a practical step in the direction of performance-based earthquake engineering for concrete construction.

The first general procedure is one that permits the reduction of traditional details when calculations indicate that demands are relatively low. The specific application is in design of boundary elements of structural walls. Traditionally, the design of boundary elements was based on calculation of a nominal stress on a gross cross section of the wall. If the nominal stress was less than a prescribed value, confinement of the boundary was not required. Otherwise, the boundary had to be confined by a standard quantity of transverse reinforcement. It was well recognized that this approach did not reflect the actual performance of walls, but it was continued because it was simple to apply and was understood to be conservative. Starting with the 1994 edition of the UBC, and continuing with the 1997 UBC, 1999 ACI, and 2000 IBC, procedures were introduced that related the details more directly to actual behavior – if the compression strain in the boundary zone exceeded a value associated with spalling, confinement was required. The general approach is illustrated in Figure 4.

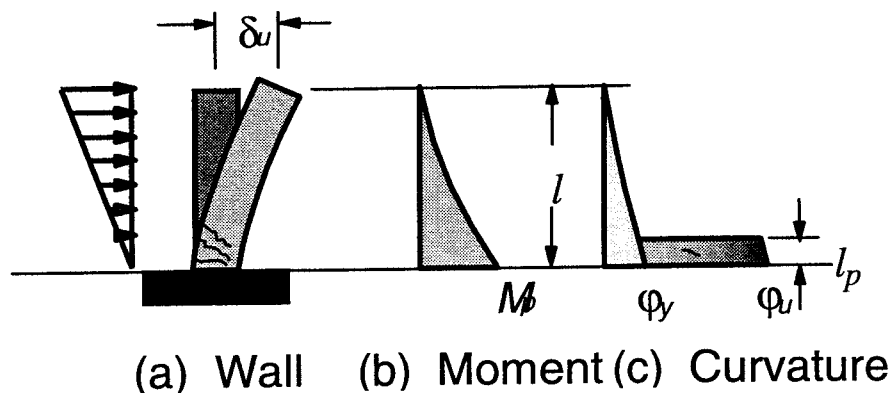


Figure 4 – Procedure for determining wall boundary element confinement requirements

The second procedure is one that permits acceptance of precast moment frames on the basis of structural testing. The procedure is specified in ACI ITG-T1.1-99. According to the procedure, the engineer must identify the characteristic components of the building that deviate from standard detailing practice. Examples of typical connections that might be required to be tested are shown in Figure 5. The standard requires that the specimens be designed by a rational procedure, and be configured to test critical connection details. Only one test per standard connection is required if the general concept under consideration has been tested by a more extensive development program. Specific performance requirements are specified, which, if satisfied, qualify the components as being equivalent to monolithic construction, and enable design force levels to be based on the same values that would be used for monolithic construction. The standard is just now being introduced to practice. Questions remain regarding the number of tests required, specimen scale, and acceptance conditions. Peer review seems inevitable as a requirement until more experience is gained with the use of standards of this nature.

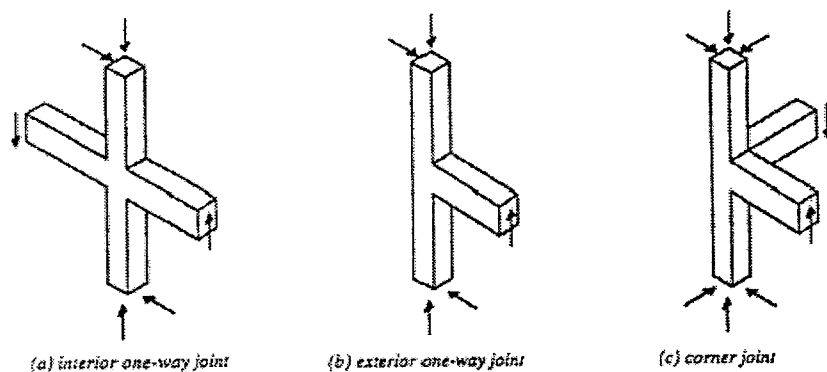


Figure 5 – Test specimen geometries required for typical construction

Summary

Although building codes have always been performance-based, to some extent, the effort to develop rational performance-based procedures, that can reliably predict performance has only occurred within the last ten years. The engineering community in regions of high seismicity in the United States have embraced these procedures, particularly as embodied by the *FEMA-273* and *ATC-40* publications. However, engineers have expressed concern about the potential for performance worse than anticipated and the potential liability that would accrue to designers, should this occur. As part of a program to address the unanticipated fractures in special moment-resisting frames in the 1994 Northridge earthquake, the SAC joint venture extended the methods contained in *FEMA-273* and *ATC-40* to include explicit consideration of the uncertainties and variabilities inherent in performance prediction and design, so that levels of confidence can be determined relative to the ability of a building to actually meet intended performance objectives. It is anticipated that this approach will be extended in the future for application to other structures.

References

- American Concrete Institute (ACI), 1999, *Building Code Requirements for Reinforced Concrete*, Report No. *ACI 318-99*, ACI, Northbrook, IL
- American Concrete Institute, 1999, "Acceptance Criteria for Moment Frames Based on Structural Testing," *ACI ITG/T1.1-99*, ACI, Northbrook, IL.
- American Institute of Steel Construction (AISC), 1993, *Load and Resistance Factor Design Specifications*, AISC, Chicago, IL
- Applied Technology Council (ATC), 1996, *Methodology for Evaluation and Upgrade of Reinforced Concrete Buildings*, Report No. *ATC-40*, California Seismic Safety Commission, Sacramento, California
- Applied Technology Council (ATC), 1997, *NEHRP Guidelines for Seismic Rehabilitation of Buildings*, Report No. *FEMA-273*, Federal Emergency Management Agency, Washington, D.C.

- Building Seismic Safety Council (BSSC), 1998, *NEHRP Recommended Provisions for Seismic Regulation of New Buildings and Other Structures, Report No. FEMA 302*, Federal Emergency Management Agency, Washington, D.C.
- International Code Council (ICC), 2000, *International Building Code 2000*
- International Conference of Building Officials (ICBO), 1976, *Uniform Building Code, 1976 edition*, ICBO, Whittier, California
- Pacific Coast Building Officials (PCBO), 1927, *Uniform Building Code*, Whittier, California
- SAC Joint Venture. 2000, *Recommended Seismic Design Criteria for New Steel Moment-Frame Buildings, Report No. FEMA-350*, Federal Emergency Management Agency, Washington, D.C.
- SAC Joint Venture. 2000, *Recommended Seismic Evaluation and Upgrade Criteria for Existing Welded Steel Moment-Frame Buildings, Report No. FEMA-351*, Federal Emergency Management Agency, Washington, D.C.
- SAC Joint Venture. 2000, *Recommended Postearthquake Evaluation and Repair Criteria for Welded Steel Moment-Frame Buildings, Report No. FEMA-352*, Federal Emergency Management Agency, Washington, D.C.
- Structural Engineers Association of California (SEAOC), 1968, *Recommended Lateral Force Requirements and Commentary*, San Francisco, California
- Structural Engineers Association of California (SEAOC), 1995, *Vision 2000 a Framework for Performance-Based Engineering*, Structural Engineers Association of California, Sacramento, California

**SESSION I-2: RECENT TOPICS ON EXPERIMENTAL AND
FIELD INVESTIGATIONS**

Chaired by

◆ Sashi Kunnath and Manabu Yoshimura ◆

DESIGN AND ANALYSIS OF A SIX-STORY REINFORCED CONCRETE FRAME-WALL SYSTEM WITH SOFT FIRST STORY FOR SHAKING TABLE TEST

Toshimi KABEYASAWA¹,

Yasushi SANADA² and Hiroshi KURAMOTO³

ABSTRACT

Three-dimensional pushover analysis of a reinforced concrete frame-wall system with soft first story was carried out to propose a seismic design method for this system. A scaled model of a structure designed for a shaking table test was analyzed to predict the response behavior of the model. Because of the effect of three-dimensional wall-frame interaction on the ultimate mechanism, the maximum base shear of the frame was much higher than calculated by neglecting the shear transfer of slab. The shear wall in the soft first story carried most of the base shear. A theoretical method for estimating the wall shear in the frame was presented. The plan and the results of the shaking table were also outlined.

1. INTRODUCTION

It was pointed out by an inventory damage survey on reinforced concrete building structures after the 1995 Hyogo-ken Nanbu Earthquake(AIJ, 1997) that the ratios of severe damages were apparently higher in the buildings with soft first story (pilotis-type building structures) than in other regular buildings. Response properties of the pilotis-type buildings, such as displacement concentration in the soft first story, have been investigated analytically and experimentally(Komuro et al, 1996)(Ma et al, 1998). However, responses of members in the soft first story, especially shear and axial forces of columns and walls, have not been evaluated quantitatively in a simple design formula.

In this study, response properties of a frame-wall system with soft first story were investigated through a pushover analysis. A one-third scale model was designed for a

¹ Earthquake Research Institute, The University of Tokyo
Email: kabe@eri.u-tokyo.ac.jp

² Department of Architecture, Graduate School of Engineering, The University of Tokyo
Email: sanada@eri.u-tokyo.ac.jp

³ Building Research Institute, Ministry of Construction
Email: kura@kenken.go.jp

shaking table test based on a proto-type of six-story building. The analysis of the scaled model was conducted to investigate the collapse mechanism, the base shear and the distribution of the floor displacements of this system and the ratios of the column shear and the wall shear in the soft first story. A simple method for estimating the wall shear in the soft first story based on the collapse mechanism of this system was presented.

2. DESIGN OF ANALYZED FRAME

A reinforced concrete structure consisting of only columns in the soft first story (Building-A) was designed, tested and analyzed(Nakatsuka et al, 2000). The arrangements of columns in the first story and walls in the upper stories are shown in Fig. 1. In this study, a frame-wall structure with soft first story (Building-B) was designed based on Building-A. Building-B was supposed to have one wall for every three spans as shown in Fig. 2.

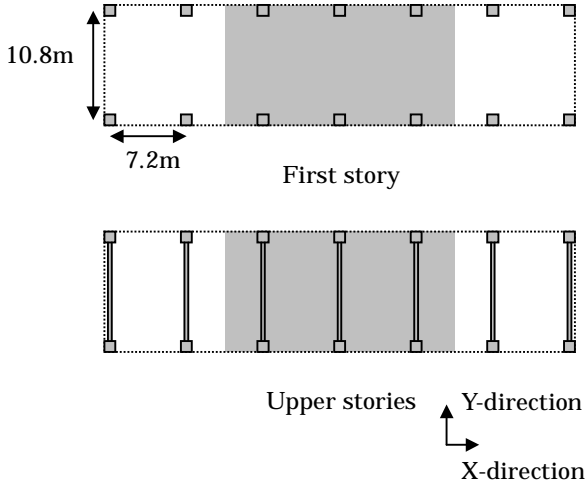


Fig. 1 Plan of Building-A

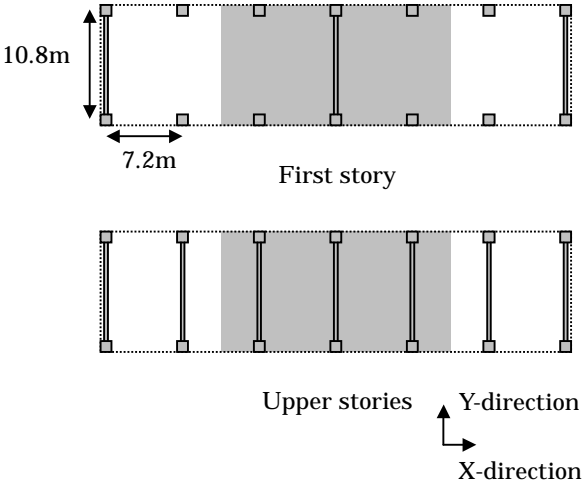


Fig. 2 Plan of Building-B

The member strength of Building-B was designed so that the ultimate base shear coefficient of the building is equal to that of Building-A. The strength of Building-A was calculated through the pushover analysis using the fiber model for the columns in the first story and the elastic model for the walls in the upper stories. The strength of Building-B was approximately calculated as sum of each frame strength neglecting shear transfer of the slabs, which was used as a simple method in practical design. Specifically, the strength of

the plane frame with the soft first story referred to as the pilotis-type frame below was calculated using the same model used in the analysis of Building-A, while the width and the depth of the columns were assumed to be $750 \times 750\text{mm}$, the bar arrangement in the columns was 16-D25 and the weight per floor area was 11.8kN/m^2 . The required strength of the plane frame with the shear wall in the first story referred to as the wall-type frame was evaluated based on the concept mentioned above. However, these columns and walls were assumed to fail not in shear but in bending, the compressive strength of concrete was 23.5MPa and the tensile strength of steel was 343.2MPa . The column and wall sections are shown in Table 1.

The analyzed frame is a one-third scaled model representing the interior 3-span of the Building-B as shown with mesh in Fig. 2. The model is designed as a specimen for a shaking table test planned to be conducted in July of 2000. This study was conducted as a part of the preliminary analysis of the experiment. Figure 3 shows the plan of the first and the upper floors and Figure 4 shows the elevations of the analyzed model. Table 2 gives the column and wall sections.

Table 1 Member sections of Building-A

Story	Column		Wall	
	X × Y	750 × 750	Width	250
2 ~ 6	Main bar	16-D25	Wall bar	D10@100 double
	X × Y	750 × 750	Width	300
1	Main bar	16-D25	Wall bar	D10@100 double

Unit : mm

Table 2 Member sections of 1/3 scale

Story	Column		Wall	
	X × Y	250 × 250	Width	80
2 ~ 6	Main bar	12-D10	Wall bar	D6@75
	X × Y	250 × 250	Width	300
1	Main bar	12-D10	Wall bar	D6@75

Unit : mm

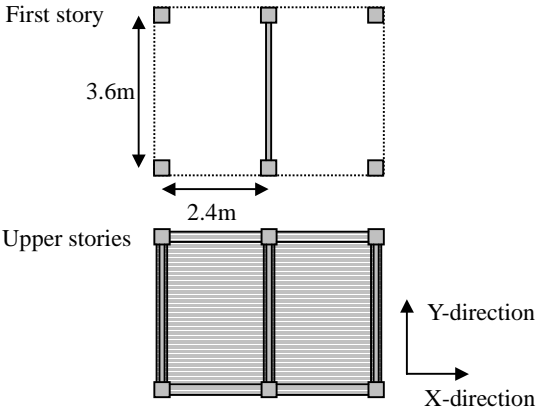


Fig. 3 Plans of the analyzed frame

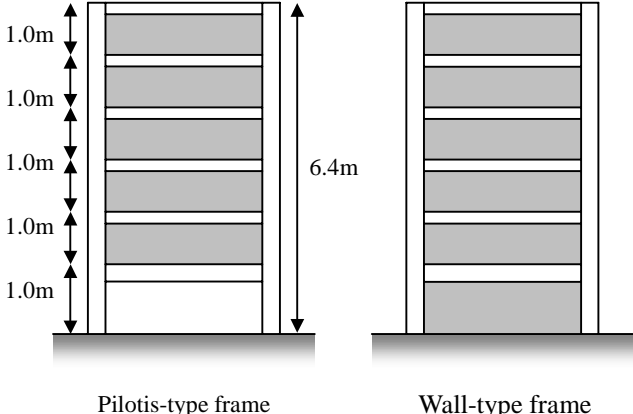


Fig. 4 Elevations of the analyzed frame

3. PUSHOVER ANALYSIS METHOD

The columns in the soft first story were subjected to large fluctuating axial forces due to overturning moment at the second floor level. The fiber model was used for the columns to consider the interaction between bending moment and axial force. The flexibility distributions for bending and axial deformation of the columns were assumed to be parabolic from the end of the member to the inflection point. The fiber slices at the ends of the columns consisted of steel elements and five concrete elements divided along the Y-axis. The detail of the fiber model is described with the verification of accuracy elsewhere (Sanada and Kabeyasawa, 1998)(Sanada and Kabeyasawa, 1999).

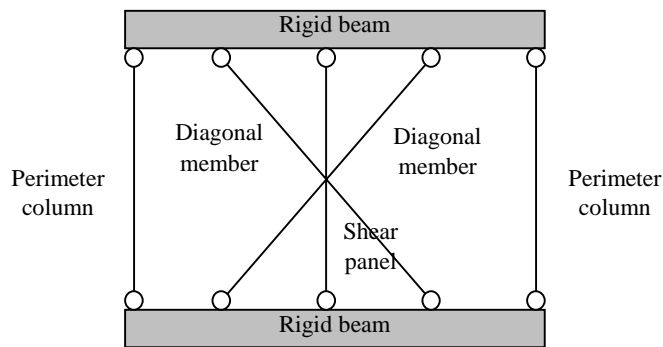
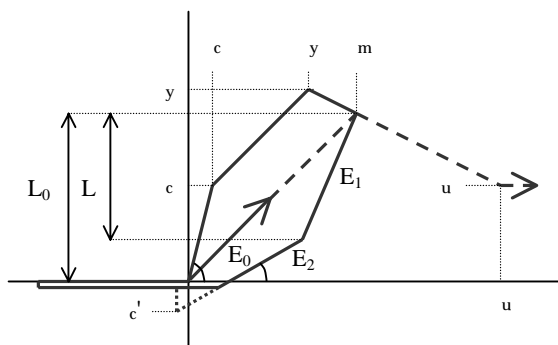
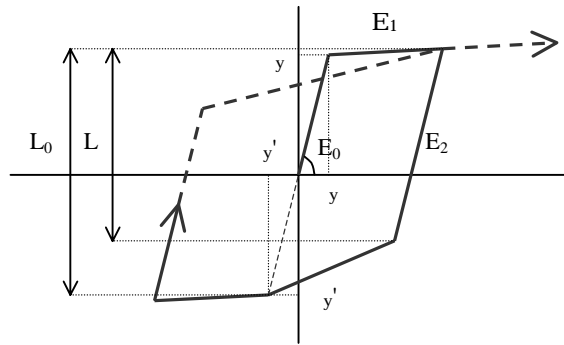


Fig. 5 Truss model for shear wall



$$L = 3/4 \times L_0, E_1 = E_0 \times (y / m)^{1/2}, E_2 = E_1 / 4$$

Fig. 6 Hysteresis model of concrete



$$L = 0.75 \times L_0, E_1 = 0.01 \times E_0, E_2 = E_1$$

Fig. 7 Hysteresis model of steel

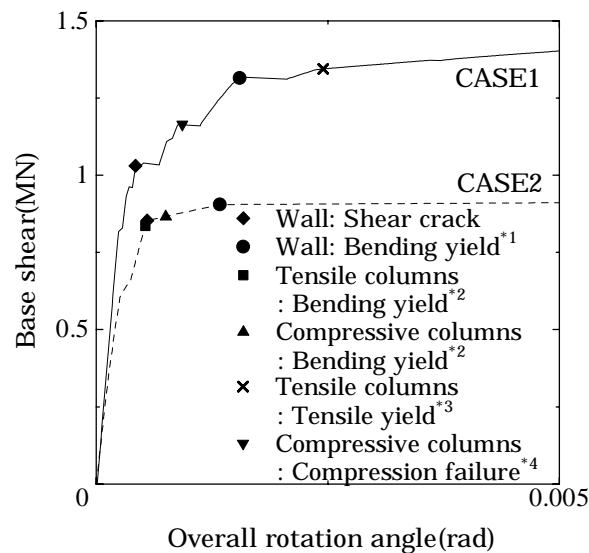
The truss model based on the material properties of concrete and steel (Matsumoto and Kabeyasawa, et al 1993) was used for the shear walls. This model consists of three vertical

members to resist bending moment, two diagonal members to resist shear force, and upper and lower rigid beams to join these members as shown in Fig. 5. The hysteresis models of the stress-strain relationships for concrete and steel used for the fiber model and the truss model are shown in Fig. 6 and Fig. 7, respectively.

The slabs were assumed to be in-plane rigid while the vertical forces were to be transferred only by the beams between the adjacent frames. The frames were subjected to static loading of an inverted triangular distribution in Y-direction in the pushover analysis.

4. RESULTS OF PUSHOVER ANALYSES

Two cases of analyses were carried out and compared in this study: CASE1 was the analysis of the frame considering the shear transfer of the slabs, and the other CASE2 was the analysis of the frame neglecting shear transfer, in other words, the analyses of three plane frames. Figure 8 shows the relation of the base shear and the overall rotation angle with the base shear from CASE2 equal to the total base shear of the three plane frames.



- *1: When whole vertical bars yielded
- *2: When whole main bars on tensile side yielded
- *3: When whole main bars yielded
- *4: When concrete on compressive edge failed

Fig. 8 Base shear vs. overall rotation angle

This figure also shows the process of failure in both cases. The base shear in CASE1 exceeded that in CASE2, because the collapse mechanism of the pilotis-type frame in CASE1 was different from that in CASE2 as illustrated in Fig. 9. In the center frame of a continuous wall, the overall collapse mechanism formed in both cases. However, in the pilotis-type frames, the overall collapse mechanism due to the yielding of tensile columns formed in CASE1, while the story collapse mechanism formed in CASE2. Therefore, both columns in the soft first story in CASE1 resisted higher overturning moment than those in CASE2.

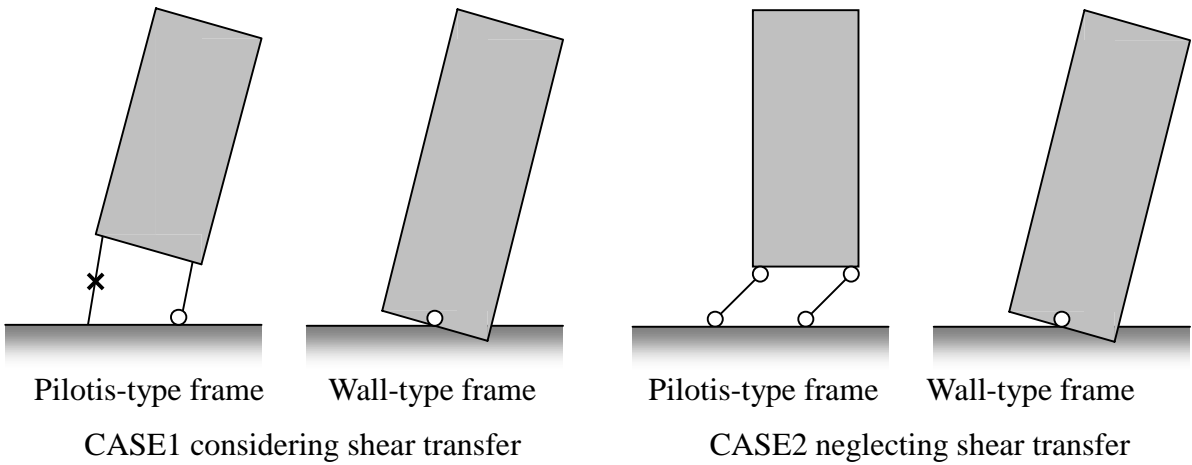


Fig. 9 Collapse mechanisms

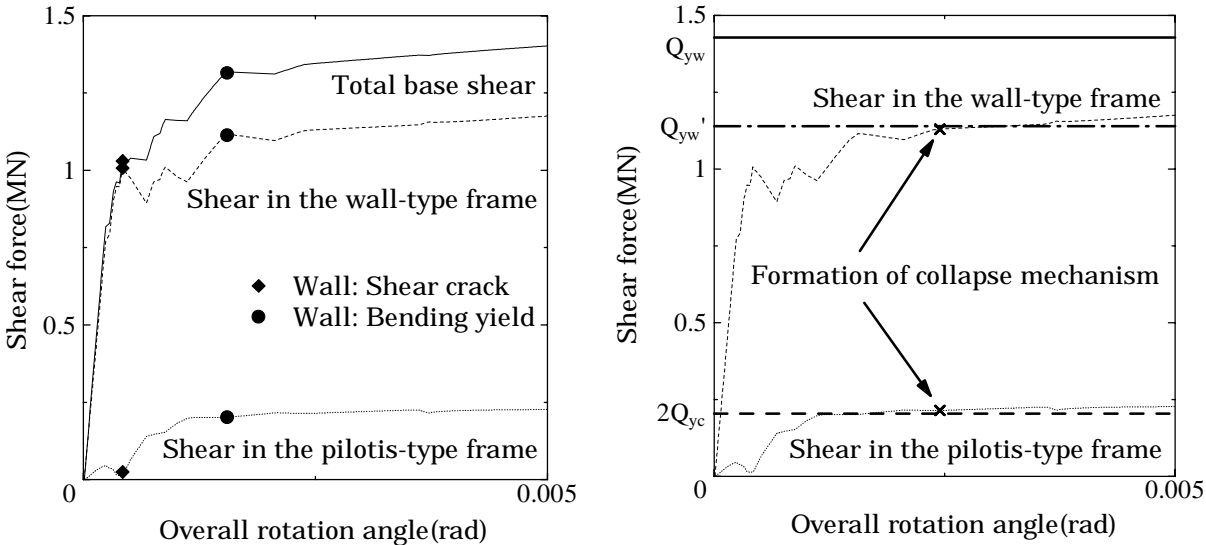


Figure 10 shows the relations between the shear forces carried by the pilotis-type frame (columns) and the wall-type frame (wall) and the overall rotation angle in the CASE1 analysis. The solid line in the figure is the same as the total base shear shown in Fig. 8. The wall-type frame was subjected to 98 percent of the total base shear in the elastic region. Most of the base shear force was carried by the wall-type frame until the wall cracked in shear. As the shear stiffness of the wall degraded because of the shear crack, the shear forces of the columns in the pilotis-type frame increased. However, 85 percent of the total base shear was kept in the wall-type frame even after yielding of the frame. This shows that the shear wall in the soft first story resisted not only the external forces in the wall-type frame but also those in the pilotis-type frame transferred by the slab.

5. WALL SHEAR FOR SEISMIC DESIGN

The wall shear force in the soft first story for seismic design was investigated based on the results from CASE1. When the collapse mechanism formed, bending yield hinges were formed at both ends of the columns on the compressive side in the pilotis-type frames and all the main bars in the columns on the tensile side had yielded. Therefore, the shear force of the column on the compressive side Q_{yc} is calculated as follows (AIJ, 1988):

$$\begin{aligned}
 N_c &> 0.4 \cdot b \cdot D \cdot F_c \\
 M_{yc} &= 0.8 \cdot a_t \cdot \sigma_y \cdot D + 0.12 \cdot b \cdot D^2 \cdot F_c \\
 &= 0.064 \text{MN} \cdot \text{m} \\
 Q_{yc} &= M_{yc} / (h_1 / 2) \\
 &= 0.102 \text{MN}
 \end{aligned}$$

where, N_c : axial force of column on the compressive side, M_{yc} : yield moment of column on the compressive side, b : width of column, D : depth of column, F_c : compressive strength of concrete, a_t : sum of section area of tensile bars in column, σ_y : tensile strength of steel, h_1 : height of first story.

Twice of Q_{yc} was compared with the shear force in the pilotis-type frame from the analysis in Fig. 11. The shear force from the analysis was simulated well by the twice of Q_{yc} , which corresponded to the shear approximated only for the two columns on the compression side.

This means that the wall-type frame is subjected to all the external shear force except for the shear carried by the pilotis-type frames. Therefore, the shear force of the wall in the first story for seismic design may be evaluated through estimating the ultimate base shear at the overall yield mechanism.

The overall yield base shear of the pilotis-type frame M_{yp} is calculated using the equation for estimating the bending strengths of walls in AIJ guidelines (AIJ, 1990) as follows

$$\begin{aligned} M_{yp} &= a_t' \cdot \sigma_y \cdot l_w + 0.5 \cdot N \cdot l_w + M_{yc} \\ &= 2.208 \text{MN} \cdot \text{m} \end{aligned}$$

where, a_t' : sum of section area of main bars in the column, l_w : length between centers of both perimeter columns, N : sum of axial forces of members in the plane frames.

The yield moment of the wall-type frame M_{yw} is also estimated in the same way and that of the whole frame M_y is calculated as follows

$$\begin{aligned} M_{yw} &= a_t' \cdot \sigma_y \cdot l_w + 0.5 \cdot a_w \cdot \sigma_y \cdot l_w + 0.5 \cdot N \cdot l_w \\ &= 3.014 \text{MN} \cdot \text{m} \end{aligned}$$

$$\begin{aligned} M_y &= 2 \cdot M_{yp} + M_{yw} \\ &= 7.430 \text{MN} \cdot \text{m} \end{aligned}$$

where, a_w : sum of section area of vertical bars in the wall.

Therefore, the total external force, which is equal to the total base shear, is estimated as follows

$$\begin{aligned} Q_y &= M_y / h \\ &= 1.633 \text{MN} \end{aligned}$$

where, h : height of centroid of external force.

Because the total shear force except for $2Q_{yc}$ is carried by the wall-type frame, the shear force in the wall for the first story Q_{yw} is evaluated as follows

$$\begin{aligned} Q_{yw} &= Q_y - 2 \cdot Q_{yc} \\ &= 1.429 \text{MN} \end{aligned}$$

The thick solid line in Fig. 11 shows Q_{yw} . Q_{yw} exceeded by as much as 1.25 times the shear in the wall from the analysis. This was caused by the difference between the estimated yield moment of the wall-type frame M_{yw} and the result of the analysis: $M_{yw}' = 1.701 \text{MN} \cdot \text{m}$. Q_{yw}' , which is the estimation using M_{yw}' , is shown by the thick dash-dot-dash line in Fig. 11. The result of the analysis was simulated well by Q_{yw}' .

6. OUTLINE OF THE SHAKING TABLE TEST

The shaking table test of the one-third scaled model in Figs. 3 and 4 was planned and conducted in July, 2000, with the following specific objectives: (1) to prove expected seismic performance and 3-D collapse mechanism of frame-wall pilotis buildings, (2) to measure ultimate design shear and axial forces in column and wall to prevent story collapse, (3) to verify analytical tools, such as wall model, and in addition, (4) to develop a method of using seismograph for quick post-earthquake damage and safety evaluation. Based on the simulation of the test, additional analyses and theoretical interpretation, a general performance-based seismic design method in practice for will be proposed.

The total weight of the tested structure is 113.3ton above the base being sum of the self weight of 49.1ton and the steel weight of 64.2ton in addition. The weight of the specimen is 140.5ton including the foundation of 27.2ton. The steel weight should be up to 100ton (150ton in total above the base) to realize ideal scaling from the proto-type, by which the vertical stress due to gravity load and the fundamental period could be equivalent. However, the available weight was limited to 0.61 times of the required, therefore, the real scaling of time and acceleration amplitude was modified considering the reduced weight as shown in Table 3. Consequently, the time scale was made as ($0.61/3$) times and the acceleration amplitude as $1/0.61$ times from the original record.

On the other hand, the calculated ultimate base shear under the inverted triangular lateral load is 1.4MN (140tonf) in CASE1 and 0.9MN (90tonf) in CASE2 as shown in Fig. 8. Calculated shear strength of the wall is 2.0MN (200tonf) as non-yielding member, which will be reduced to 1.5MN (150ton) due to the inelastic deformation with flexural yielding. The ultimate base shear at the overall mechanism (CASE1) under high input acceleration will be over 140ton due to the change of lateral load distribution, in other words, due to the effect of higher mode on the dynamic force. Therefore, the mechanism is expected to be the overall mechanism of flexural yielding at the base of the wall in the first stage but to change story under the higher input acceleration level into the side sway mechanism due to the shear failure of the wall in the first story. As the concrete strength was much higher than the design nominal strength, the shear strength of the wall could be higher than the calculated at the stage of design.

The elastic fundamental frequency identified from the response to white noise was 11.2 Hz,

which is a little lower than calculated. The past accelerograms were used as the input acceleration scaled in terms of time as ($0.61/3$) times from the original record. The intensity of the input motion was selected considering the maximum velocity equivalent to the prototype building. The maximum equivalent velocity levels to the prototype were selected as 12.5, 25, 37, 50, 75 and 135, which were modified to the scaled model considering the scaling as shown in Table 4. After these main tests, TAK were input with three levels of 70, 100, 120 to observe the behavior to collapse.

Table 3 Ideal scaling and real scaling in the test

Dimension	Length	Area	Volume	Horizontal Stress	Vertical Stress	Horizontal Force	Vertical Force
ideal scale	1/3	1/3 ²	1/3 ³	1	1	1/3 ²	1/3 ²
real scale	1/3	1/3 ²	1/3 ³	1	0.61	1/3 ²	1/3 ² × 0.61

Horizontal Acceleration	Vertical Acceleration	Time	Velocity	Weight	Base shear coefficient	Fundamental Period
1	1	1/3	1/3	1/3 ²	1	1/3
1/0.61	1	0.61/3	1/3 × 0.61	1/3 ² × 0.61	1/0.61	0.61/3

Table 4 Plan of the actual and equivalent input accelerations

eVmax (kine)	record	Amax	Vmax	Amp	Ampin	Ain	Vin	eA'max	eV'max
12.5	TOH	258.2	40.9	0.3	0.3/0.61	127.0	9.1	77.5	12.3
25	TOH	258.2	40.9	0.6	0.6/0.61	254.0	18.1	154.9	24.5
37.5	ELC	341.7	34.8	1.1	1.1/0.61	616.2	28.3	375.9	38.3
50	ELC	341.7	34.8	1.4	1.4/0.61	784.2	36.0	478.4	48.7
75	ELC	341.7	34.8	2.2	2.2/0.61	1232.4	56.6	751.7	76.6
75	TOH	258.2	40.9	1.8	1.8/0.61	761.9	54.4	464.8	73.6
75	JMA	820.6	85.4	0.9	0.9/0.61	1210.7	56.8	738.5	76.9
135	TAK	605.5	124.2	1.1	1.1/0.61	1091.9	101.0	666.1	136.6
70	TAK	605.5	124.2	0.6	0.6/0.61	595.6	55.1	363.3	74.5
100	TAK	605.5	124.2	0.8	0.8/0.61	794.1	73.5	484.4	99.4
120	TAK	605.5	124.2	1.0	1.0/0.61	992.6	91.8	605.5	124.2

Note: unit of acceleration in gal, cm/sec/sec, and unit of velocity in kine, cm/sec

eVmax: intended approximate maximum velocity equivalent to the proto-type building

TOH: Tohoku University record (NS) during 1978 Miyagi-ken-oki Earthquake

ELC: El Centro record (NS) during 1940 Imperial Valley Earthquake

JMA: JMA Kobe record (NS) during 1995 Hyogo-ken-nambu Earthquake

TAK: JR Takaori record (NS) during 1995 Hyogo-ken-nambu Earthquake

Amax and Vmax: maximum acceleration and velocity of the original record

Amp: selected amplitude for the original record to the proto-type building

Ampin (=Amp/0.61): modified amplitude considering the scaling of the weight

Ain(=Amax*Ampin): maximum acceleration input to the scaled model on the shaking table

Vin(=Vmax*Ampin*($0.61/3$)): maximum velocity input to the scaled model on the shaking table

eA'max(=Amax*Amp=Ain*0.61): calculated maximum velocity equivalent to the proto-type building

eV'max(=Vmax*Amp=Vin*($0.61*3$)): calculated maximum velocity equivalent to the proto-type building

The shaking tests were successfully conducted in July, 2000. The major findings derived from direct observation on the tests are: (1) Due to 3-D and dynamic effects on the collapse mechanism and lateral strength, the collapse mechanism changed from an overall flexural yielding until run 7 (JMA75) into side-sway mechanism during and after run 8 under the maximum input of (TAK135, Fig.11), (2) Base shear was much higher than the statically computed due to the dynamic effect(Fig.12), (3) shear distribution on the wall, tensile and compressive columns were measured: in inelastic stage the shear was carried as mostly by the wall, and by the compressive columns, but not by the tensile columns, (4) axial loads on the columns were varied up to the full yield strength of main bars in tension and the same reaction in compression.

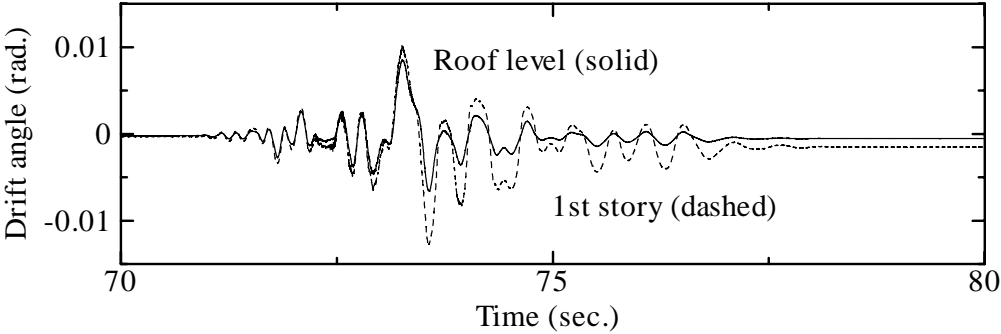


Fig. 11 Overall and 1st story drift angles during TAK135

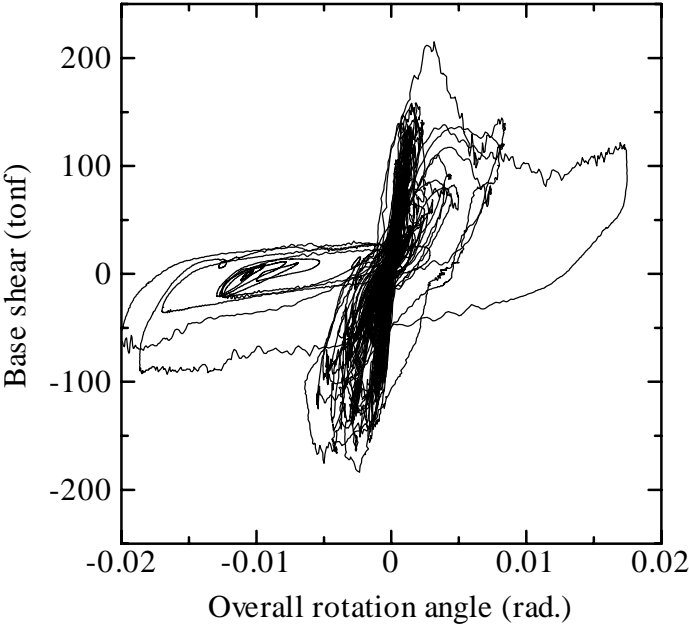


Fig. 12 Base shear vs overall rotation relations during the main tests and collapse tests

Analytical studies are being conducted on: (1) analytical simulation of the test, especially to develop verify practical member models, including inelastic wall and slab model,. (2) method of response and damage evaluation using seismographs, (3) general and practical design procedure for pilotis-type structures: shear design of wall, taking dynamic and three-dimensional behavior into account.

7. CONCLUSIONS

A reinforced concrete frame-wall system with soft first story was analyzed. A scaled model of this system was designed for a shaking table test based on the proto-type building. A preliminary pushover analysis was carried out to predict the seismic behavior. The ultimate base shear of this system was much higher than calculated by neglecting shear transfer of slab, which was caused by the collapse mechanisms of the pilotis-type frames due to the interaction with the wall-type frame. The overall collapse mechanism formed in the pilotis-frame considering shear transfer of slab, while the story collapse mechanism formed in the frame without shear transfer. Therefore, the frame considering shear transfer resisted higher overturning moment. Moreover, it was found that most of the base shear was carried by the shear wall in the soft first story. A practical method of evaluating the wall shear force in the soft first story based was presented on the collapse mechanism of this system. It was confirmed that the shear force estimated theoretically simulated the shear from the pushover analysis. The results of the shaking table test were also summarized.

8. ACKNOWLEDGEMENT

The shaking table test was conducted at the Large Scale Earthquake Simulator, National Research Institute for Earth Science and Disaster Prevention (NIED) under a financial support of Science Technology Agency. Cooperative works of many researchers before and during the test should gratefully be acknowledged, especially those of Dr. Toshihumi Fukuta, BRI, Dr. Nobuyuki Ogawa and Mr Atsushi Kato, NIED, Dr. Kazuyuki Matsumoto, Fujiki Komuten, and Mr. Seiya Naraoka and Mr. Masahiro Hirata with ERI.

9. REFERENCES

- (1)AIJ(1997), "Report on the Hanshin-Awaji Earthquake Disaster Building Series Volume 1 Structural Damage to Reinforced Concrete Building(in Japanese)," AIJ.
- Komuro, T., Kawabata, I. and Otani, S.(1996), "Characteristics of Seismic Response of Piloties-Type Buildings with Multi-Story Structural Wall," Proceedings of the Japan Concrete Institute, JCI, Vol. 18, No. 2, pp. 755-760
- Ma, H., Wen, S., Suzuki, K. and Ohno, Y.(1998), "Simplified Method to Predict Earthquake Response of Reinforced Concrete Building with Soft-First Story," Proceedings of the Japan Concrete Institute, JCI, Vol. 20, No. 3, pp. 25-30
- Nakatsuka, Y., Kuramoto, H., Gu, J. and Kabeyasawa, T.(2000), "Substructure Pseudo Dynamic Test on 6story Reinforced Concrete Building with Soft First Story," Proceedings of the Japan Concrete Institute, JCI, Vol. 22, No. 3, pp. 31-36
- Sanada, Y. and Kabeyasawa, T.(1998), "Responses of Reinforced Concrete Buildings Considering Axial Deformation of Beams," Proceedings of the Japan Concrete Institute, JCI, Vol. 20, No. 3, pp. 37-42
- Sanada, Y. and Kabeyasawa, T.(1999), "Evaluation of Incremental Shear Forces of Columns Based on Axial Deformations of Beams Estimated from Restraining Stiffness," Proceedings of the Japan Concrete Institute, JCI, Vol. 21, No. 3, pp. 49-54
- Matsumoto, K., Kabeyasawa, T. and Kuramoto, H.(1993), "A Member Model for Reinforced Concrete Shear Wall in Non-Linear and Dynamic Structural Analyses," Proceedings of the Japan Concrete Institute, JCI, Vol. 15, No. 2, pp. 1173-1178
- AIJ(1988), "Standard for Structural Calculation of Reinforced Concrete Structures," AIJ.
- AIJ(1990), "Design Guidelines for Earthquake Resistant Reinforced Concrete Buildings Based on Ultimate Strength Concept," AIJ.

10. KEYWORDS

soft first story, frame-wall system, pushover analysis, reinforced concrete, wall, seismic design, shaking table test

SESSION A-1: DESIGN MOTIONS AND SDF RESPONSES

Chaired by

◆ Mark Aschheim and Akira Wada ◆

SITE SPECIFIC STRONG GROUND MOTION DURING THE KOCAELI, TURKEY EARTHQUAKE OF AUGUST 17, 1999, AS INFERRED FROM ARRAY OBSERVATIONS OF MICROTREMORS

Kazuyoshi KUDO¹,
Tatsuo KANNO², Hiroshi OKADA³, Oguz ÖZEL⁴, Mustafa ERDIK⁵, Tsutomu SASATANI⁶,
Sadanori HIGASHI⁷, Masayoshi TAKAHASHI⁸, and Kunikazu YOSHIDA⁹

ABSTRACT

Array observations of microtremors and aftershocks were carried out near permanent strong motion observation sites run by Kandilli Observatory & Earthquake Research Institute as well as Ministry of Public Works and Settlement and the damaged areas after the Kocaeli, Turkey earthquake of August 17, 1999. Major objectives are to determine S-wave velocity structures and to understand the site effects relatively on strong motion or damage. Most strong motion sites near the fault are classified to stiff and/or very hard soil. The records cannot directly be used for interpreting damage of buildings in sedimentary basin.

A large and long duration of strong motion records at ATS, near Avcilar, west of Istanbul are closely related to the low velocity ($V_s \sim 200$ m/sec) of surface layers. The S-wave velocity structure at Avcilar where severely damaged during the mainshock is similar to the lowland (ATS) and it differs significantly from that of CNA where the strong motion record from the mainshock was obtained and it locates 4 km northeast from Avcilar. The strong ground motion at Avcilar during the mainshock is estimated to be similar to that at ATS. The strong motion sites, Sakarya (SKR) is located on very hard soil, while thick and soft sediments covers downtown Adapazari. It is plausible that strong ground motions during the mainshock at damaged area, ADC, were significantly different from those of SKR. A large difference of strong motions between a hillside and Izmit Bay area in and around Golcuk is also indicated by the comparison of aftershock records.

1. INTRODUCTION

The major damage of buildings and loss of lives during the Kocaeli (Izmit), Turkey earthquake of August 17, 1999, were concentrated in a narrow band along the ground surface fault zone. Therefore, the primary reasons of the damage will be attributed to the near earthquake source effects, leaving aside the quality of buildings. However, the following examples will be out of above category. One example is the heavy damage of buildings in Avcilar, west of Istanbul, even

-
1. *Earthquake Research Institute, University of Tokyo, E-mail: kudo@eri.u-tokyo.ac.jp*
 2. *Earthquake Research Institute, University of Tokyo, E-mail: kanno@eri.u-tokyo.ac.jp*
 3. *Hokkaido University, E-mail: hokada@eos.hokudai.ac.jp*
 4. *Kandilli Observatory, Earthquake Engineering Research Institute, Bogagici University, E-mail: ozeoguz@hamlin.cc.boun.edu.tr*
 5. *Kandilli Observatory, Earthquake Engineering Research Institute, Bogagici University, E-mail: erdik@hamlin.cc.boun.edu.tr*
 6. *Faculty of Science, Hokkaido University, E-mail: sasatani@ares.sci.hokudai.ac.jp*
 7. *Central Research Institute of Electric Power Industry, E-mail:*
 8. *Earthquake Research Institute, University of Tokyo, E-mail: taka-m@eri.u-tokyo.ac.jp*
 9. *Faculty of Science, Hokkaido University, E-mail: sasatani@ares.sci.hokudai.ac.jp*

relatively further (~150 km) from the source (e.g., Cranswick et al., 2000). In addition, the strong contrast of damage ratios between the strong motion observation site; Sakarya (SKR), and the downtown Adapazari, and wide variation of the damage ratios even in a relatively narrow area of Golcuk (the Architectural Institute of Japan Reconnaissance Team et al., 2000) are also similar issues. We have to remind poor construction of collapsed buildings, however, site effects on earthquake ground motion were plausibly significant on the damage in these areas.

A strong motion record is a key for understanding the damage and the earthquake source dynamics. The strong motion records from the Kocaeli earthquake were successfully recovered and quickly distributed through the Internet by the Earthquake Research Department, Directorate for Disaster Affairs of the Ministry of Public Works and Settlement (ERD) (1999), and Kandilli Observatory and Earthquake Research Institute (KOERI) (1999). The efforts were very valuable for scientists and engineers, as they could quickly understand the severity of ground motion during the earthquake. However, because of sparse network in Turkey (Celebi et al., 2000), no strong motion record was obtained at severely damaged areas, except Duzce (DZC). The surface geological and/or the geotechnical data near the strong motion observation sites and damaged areas are very limited, therefore, it is very hard to quantitatively interpret the variation of ground motion severity and its relation to earthquake damage.

It has been suggested that an S-wave velocity structure at a site is a most valuable data for understanding the site effects on ground motion. However, the methods for determining S-wave velocity structure for deep sedimentary basin are quite limited and any conventional geophysical exploration are hardly applicable to damaged areas just after a devastating earthquake. We, therefore, carried out array observations of microtremors aiming to determine the S-wave velocity structures beneath the strong motion observation sites and damaged areas.

2. ARRAY OBSERVATION OF MICROTREMORS

2.1 Method

Pioneer works for determining velocity structure by using microtremors or microseisms were carried out by Aki (1957), Toksoz (1964), and Lacoss et al. (1969). The methods are provided for estimating velocity structures by using the phase velocity dispersion of surface waves included in microtremors. Asten and Henstridge (1984), Horike (1985), and Matsushima and Okada (1990) made efforts to increase the resolution of phase velocity determination by using array observation of microtremors, applying the frequency-wavenumber (f-k) analysis (Capon, 1969). Horike (1985)

developed also an inversion method of obtained phase velocity of Rayleigh waves for determining S-wave velocity structure. Aki (1957) gave a theoretical basis of the spatial autocorrelation coefficient defined for microtremors data and developed a method to estimate phase velocity dispersion of surface waves contained in microtremors by using a specially designed circular array. Henstridge (1979) also introduced a licit expression of a relationship between the spatial autocorrelation coefficient and the phase velocity of fundamental-mode Rayleigh waves. The method has been used as an exploration method by Okada et al. (1990), Matsuoka et al. (1996), and Okada (1998), that is currently called SPAC method. The SPAC method has been employed throughout the present study. A flow of observation and analysis in the method is shown in Figure 1.

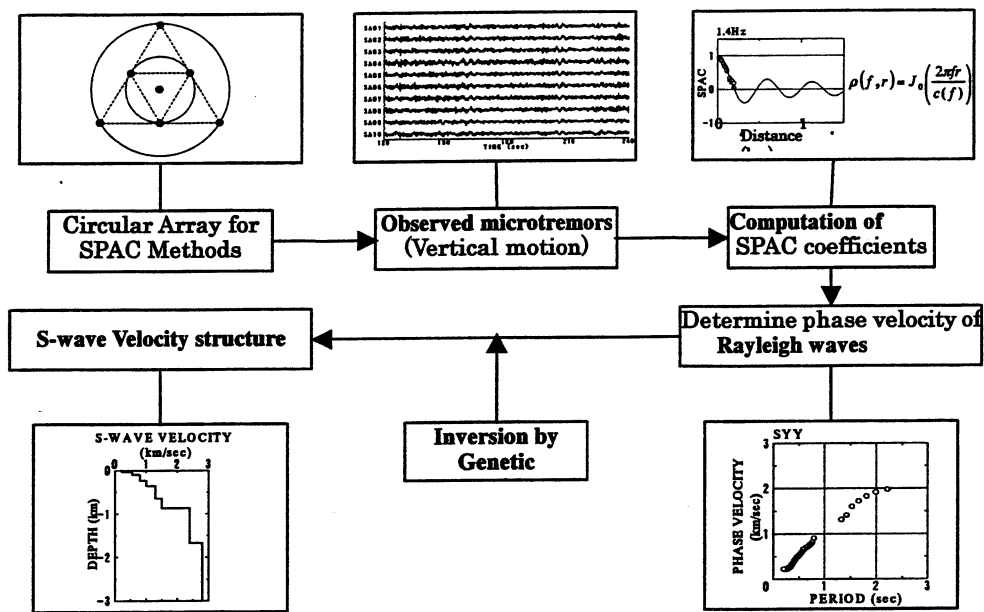


Figure 1. A flow of observation and analysis in the SPAC method for estimating S-wave velocity structures using array observations of microtremors.

We have carried out array microtremors measurements at the strong motion observation sites (ATS, CNA, YPT, SKR, and DZC) and damaged areas at Avclar (ISU and AVC), Adapazari (ADC and ADU), Golcuk (GLF and GLH), and Degirmendere (DMD) during September and December in 1999. Figure 2 shows the location map of the surveyed areas.

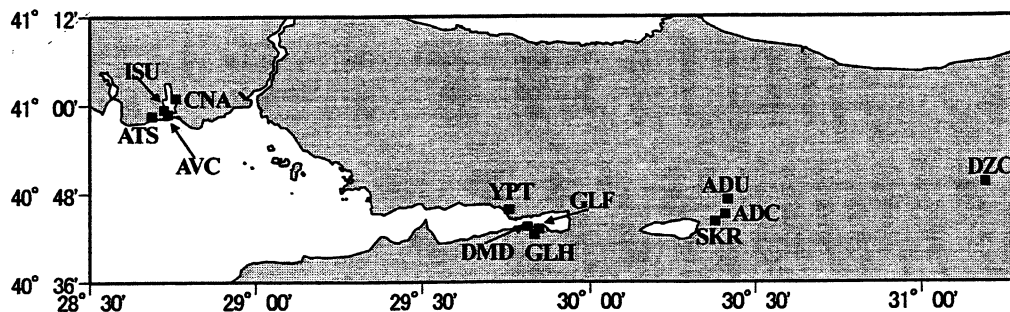


Figure 2. A location map of the sites for array observations of microtremors

Table 1. Sites where the array observations of microtremors were carried out and the array sizes (L: length of one side of a triangle).

Site Name	Code	Latitude	Longitude	Array Size L (m)	
				Sept., 1999	Dec., 1999
Ambarli	ATS	40.976	28.687	25, 100, 200	
Avcilar (Istanbul Univ.)	ISU	40.991	28.723	100, 200	25, 50
Avcilar	AVC	40.981	28.736		25, 100
Cekmece	CNA	41.017	28.759	25, 100, 200	
Yarmca	YPT	40.764	29.762	25, 200, 500	
Degirmendere	DMD	40.726	29.798		25, 100, 200, 346
Glocuk	GLH	40.708	29.834		29, 100, 200
Glocuk (Ford-Otosan)	GLF	40.721	29.849	25, 100, 200	
Adapazari	SKR	40.737	30.381	50	
Adapazari	ADC	40.787	30.419		25, 100, 200
Adapazari	ADU	40.753	30.411	100, 200	25, 400
Duzce	DZC	40.825	31.192		50, 200, 400

A circular array consisting of four (optionally seven) stations was used, which is a regular triangle-shape with a center, as shown in Figure 1. A size of an array was selected associated with the availability of space at a site. As shown in Table 1, plural arrays by changing sizes at different time were deployed, except SKR site, to cover wide wavelength or phase velocity change as a function of frequency. Generally speaking, measurements were restricted with narrow areas of observation rather than we expected, therefore, the resolution of determined phase velocities at low frequencies would be limited. We made measurements in daytime and an observation time duration of microtremors for one measurement was 30 minutes for small ($L < 100$ m) arrays and 45 or 60 minutes for larger ones, respectively.

2.2 Instruments

Five (optionally seven) sets of the portable seismographs (Kudo et al., 1998) were used for array microtremors measurements. The seismograph is originally developed for temporal observation of strong and weak earthquake motions. They are composed of a tri-axial accelerometer (Akashi Co. Ltd.) of highly damped ($h \sim 26$) moving coil type (natural frequency of 3 Hz), signal conditioner (amplifier and filter), and a data logger (24 bits digitizer, 20 megabytes flash memory, and GPS time synchronization; Hakusan-Kogyo Co. Ltd.). A flat response (-3 dB) of ground acceleration is attained from 0.1 Hz to an anti-aliasing frequency. The sensitivity of the sensor is 1 Volt/g and optionally 5 Volt/g; g denotes the gravity. Instruments were also used for aftershock observation without amplifying. The clipping level of sensor is 150 cm/sec; the maximum observable acceleration is 1 g at 1 Hz or 10 g at 10 Hz. The allowable input level of the data logger is selectable for 1 or 5 Volts. Total weight including an inner battery (2 kg) is 7 kg. The low-pass filter of cut-off frequencies at 2, 5, and 30 Hz is provided. We used the filter at cutoff frequency of 2 Hz for large arrays and 5 Hz for small ones in microtremors observation.

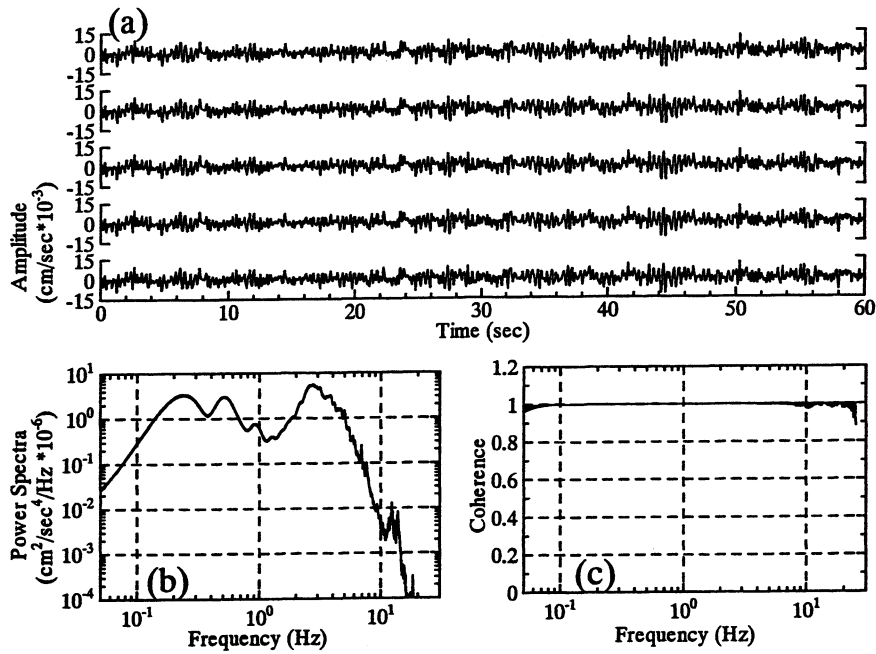


Figure 3. Velocity waveforms of microtremors integrated from simultaneously recorded accelerations at one place (a), power spectra of observed accelerations (b), and the coherence (c).

2.3 Analysis and Results

We use only vertical motion of microtremors for aiming to extract Rayleigh waves. Figure 3 shows an example of the velocity time histories integrated from acceleration of microtremors that were simultaneously recorded at one place, their power spectra, and coherence. It is apparent that there is no use for instrumental correction in the higher frequency range than 0.1 Hz.

The integrated velocity computed from original acceleration was used in the following analysis. The SPAC coefficients at a frequency are calculated for each time blocks divided into every 81.92 seconds. The time block was chosen for over-rapping 21.92 seconds to the next block. Finally the SPAC coefficients were averaged. One example of the results for representative frequencies

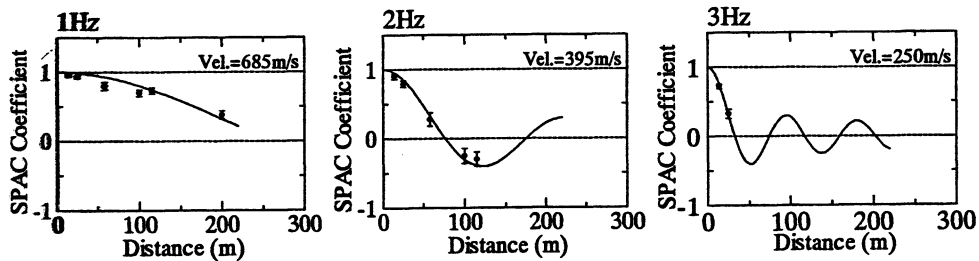


Figure 4. Examples of the Bessel function fitted to the SPAC coefficients at ATS for some representative frequencies. The solid lines show fitted Bessel function and circles and the error bars indicate the SPAC coefficients and their standard deviations, respectively.

obtained at ATS is shown in Figure 4. The error bar in the figure shows the standard deviation of the SPAC coefficients obtained from 20 to 40 blocks. The quality of determined phase velocity is controlled by the degree of matching between the Bessel function and the observed SPAC coefficients against distances. The results are not so excellent, but satisfactory. Next, we will find a dispersion curve or S-wave velocity structure that fits to observed data by using the genetic algorithm (GA) (Yamanaka and Ishida, 1996). Circles as well as triangles in Figure 5 show the phase velocities determined by the SPAC method, while continuous lines show dispersion curves estimated by using the genetic algorithm with some minor manual corrections. P-wave velocities are assumed corresponding to S-waves by using the empirical relation by Ludwig et al. (1970). Thus determined phase velocity dispersions at the sites and the estimated S-wave velocity (V_s) structures are shown in Figure 5 and Table 2. They are summarized as follows:

Table 2. Estimated S-wave velocity structures by array observations of microtremors.

ATS		ISU		AVC		CNA	
V_s (m/s)	Thickness (m)	V_s (m/s)	Thickness (m)	V_s (m/s)	Thickness (m)	V_s (m/s)	Thickness (m)
204	32	225	18	291	46	311	15
364	57	370	75	434	91	613	32
608	164	584	197	584	267	778	42
919	295	919	188	919	inf.	1018	66
1018	100	1018	164			1230	141
1230	inf.	1230	inf.			1500	inf.
YPT		DMD		GLH		GLF	
V_s (m/s)	Thickness (m)	V_s (m/s)	Thickness (m)	V_s (m/s)	Thickness (m)	V_s (m/s)	Thickness (m)
344	42	283	19	303	22	150	14
445	94	512	52	455	60	259	70
591	90	694	97	594	295	531	270
727	290	752	61	950	inf.	950	300
950	200	950	203			1120	inf.
1120	inf.	1120	inf.				
SKR		ADC		ADU		DZC	
V_s (m/s)	Thickness (m)	V_s (m/s)	Thickness (m)	V_s (m/s)	Thickness (m)	V_s (m/s)	Thickness (m)
1050	72	234	38	166	44	257	36
1500	56	441	97	331	88	459	44
2000	inf.	728	242	500	281	514	48
		1500	70	878	63	769	236
		2000	inf.	1050	100	1020	273
				1500	inf.	1268	309
						1500	inf.

West Istanbul

ATS: Strong motion observation site run by the Kandilli Observatory and Earthquake Research Institute (KOERI). No significant damage was found in the building where strong motion instrument has been installed. S-wave velocities of surface layers increase from 200 m/sec to 1200

m/sec with depth (from surface down to 550 m). The high level and relatively long period accelerations from the mainshock can be attributed to those soft surface layers ($V_s < 400$ m/sec).

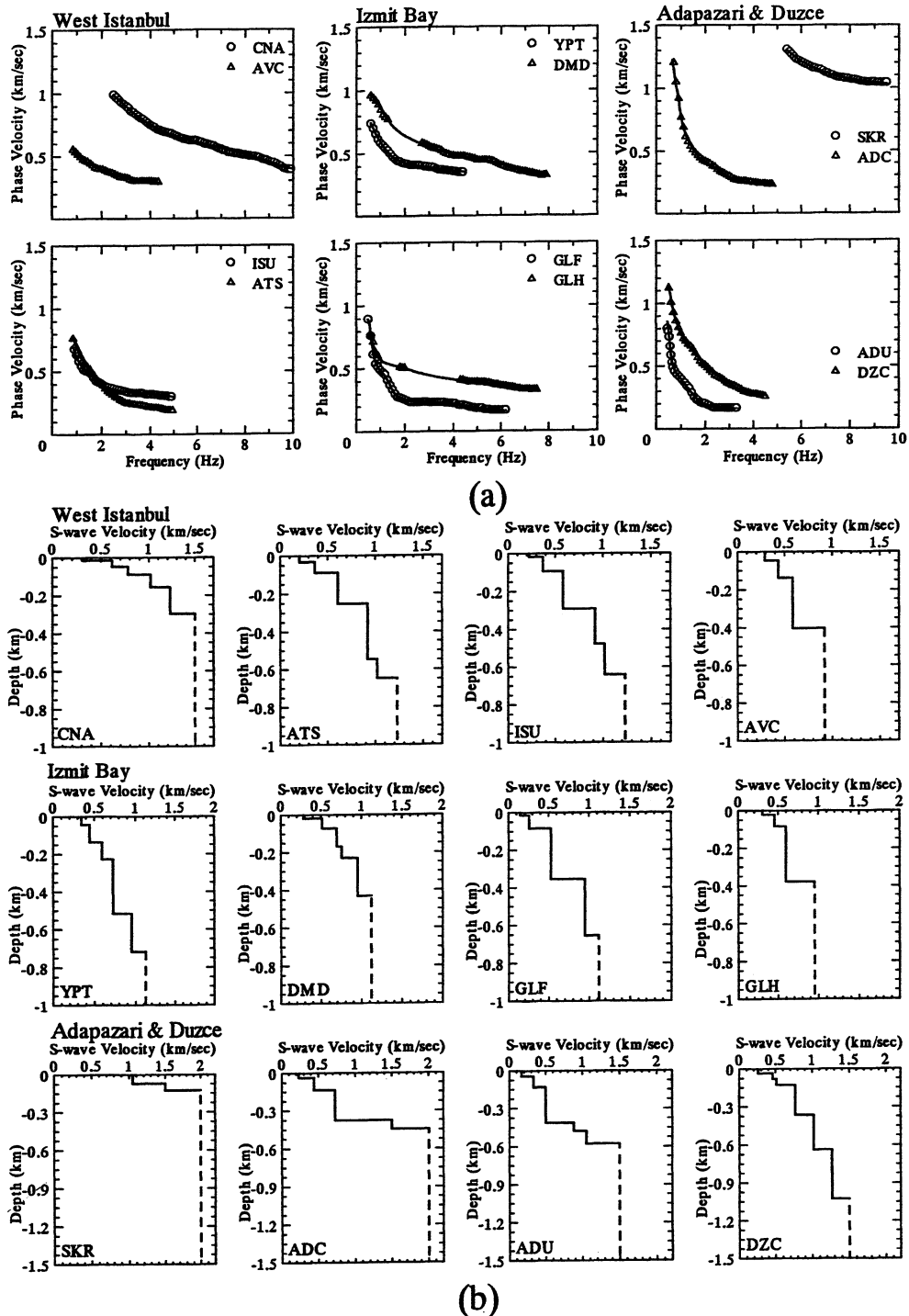


Figure 5. Phase velocity dispersions of Rayleigh waves determined by array observations of microtremors at the surveyed area (a) and the corresponding estimated S-wave velocity structures (b). Circles as well as triangles and continuous lines in (a) show the observations and the computed dispersions obtained by using the genetic algorithm with minor manual modifications.

ISU and AVC: These sites are close to the damaged area of Avcilar and their velocity structures are similar to that of ATS. Therefore, their ground motions during mainshock are supposed to be similar to that of ATS. This will be discussed later with the aftershock data.

CNA: Strong motion observation site run by KOERI. A thin (~15 m) low velocity ($V_s \sim 300$ m/sec) layers exist near the surface, but high velocity ($V_s > 600$ m/sec) layers are underlying at a shallow depth. The reason of high acceleration at CNA can be qualitatively interpreted by the existence of shallow thin surface layers of low S-wave velocity with high velocity contrast.

Izmit Bay area

YPT: Strong motion observation site run by KOERI. There was no distinctive damage in the buildings where the strong motion instrument has been installed. The S-wave velocity of surface layer is estimated to be 340 m/s and it increases with depth. The observed deepest layer having S-wave velocity of 950 m/sec is estimated at a depth of about 500 m.

GLF: The site is located in the eastern part of Golcuk where a big factory is under-construction. The area sank about two meters during or after the mainshock. The site has very thick (~80 m) sedimentary layers of which S-wave velocity of 150 and 260 m/sec. A rather high velocity (950 m/sec) layer is estimated at a depth of about 350 m.

DMD: The site is located near west of the Naval base and close to the west margin of the inland where surface fault was observed. Large number of medium-rise (higher than four stories) buildings were heavily damaged or collapsed near the site. Soft sediments ($V_s < 400$ m/sec) are very thin compared with GLF and YPT.

GLH: The site is located on the hill of the south of damaged area in Golcuk. This area consisting of mostly low-rise buildings had slight damage. The S-wave velocities of layers to a depth of about 100 m are higher than the other sites near Golcuk.

Adapazari City

SKR: Strong motion observation site run by the Earthquake Research Department (ERD). The available area for array observation of microtremors was so narrow that one small array observation could be carried out. Dispersions of phase velocity were slight but the velocity itself was relatively high. The S-wave velocity of near surface is estimated to be approximately 1000 m/sec or higher.

ADC: The site is located on the heavily damaged area in Adapazari City, three kilometers northeast from SKR. A soft layer ($V_s \sim 230$ m/sec) extends to a depth of about 40m. A thick (~100 m) and an intermediately hard layer ($V_s \sim 440$ m/sec) underlie this soft layer.

ADU: The site is located on a few kilometers northeast from the heavily damaged area in downtown Adapazari City. The buildings at the surveyed area were mostly one or two stories and the damage was very light compared with downtown Adapazari. Very soft and thick layers with V_s of 170 and

330 m/sec cover the surface. It is not so definite, but total thickness of sedimentary layers ($V_s < 1000$ m/sec) is estimated to be 470 m.

The strong motion data from the mainshock cannot be directly used for interpretation of damage in the sedimentary basin extending in Adapazari City. This will be discussed later.

Duzce

DZC: Because there was no enough space to carry out the array observation of microtremors at the ERD strong motion site, we moved to one kilometer east from the site. Duzce suffered severe damage from the August earthquake as well as the November 12 earthquake (Mw7.2). The site is a sedimentary basin consists of thick and soft sediments at surface ($V_s \sim 260$ m/sec) and intermediate depths ($V_s \sim 460-510$ m/sec). We may also say that the ground motions during two large events were strongly affected by surface soils.

3. ESTIMATION OF GROUND MOTION AT AVCILAR

One of the significant questions about the present earthquake is why severe damage of buildings in Avcilar, west of Istanbul occurred (Cranswick et al., 2000). One of the possible reasons will be fragility of buildings; however, is that an only reason? The strong ground motion during the mainshock at ATS, near Avcilar, showed large amplification compared with other sites in west of Istanbul, e.g. CNA. Their velocity seismograms and acceleration spectra are compared in Figure 6 and we can identify the large difference between them, nevertheless the epicentral distances are almost same.

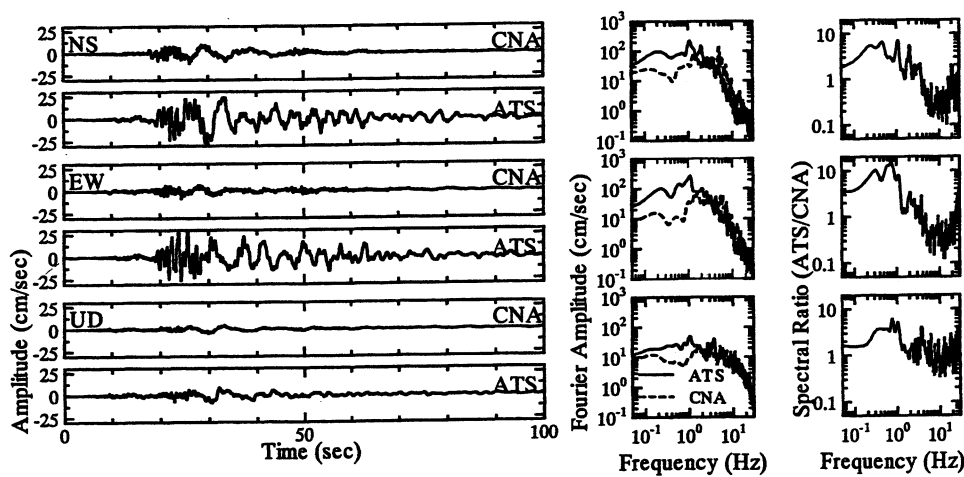


Figure 6. Comparisons of velocity seismograms and spectra at ATS and CNA, west of Istanbul.

We have temporally installed a portable accelerograph without amplifier on a basement of building in the campus of Istanbul University (ISU). The building was moderately damaged during the mainshock. The ground motions from the Marmara Sea earthquake of October 20 (M=4.4, 40.76N, 28.94E, Depth=9.6 km determined by KOERI) were recorded at this site as well as at both CNA and ATS. Figure 7(a) shows the Fourier spectral amplitudes at CNA and ATS during the mainshock on August 17, 1999 along with those at CNA, ATS, and ISU during the event (M 4.4) on October 20, 1999. Figure 7(b) shows the spectral ratios of CNA to ATS for the mainshock and those of CNA and ISU to ATS for the event on October 20, 1999. These figures show that the spectral ratios (CNA/ATS) have no significant difference between the strong motion from the mainshock and the weak motion from the M4.4 event; this implies that the effects of distance, azimuth, and non-linearity of soils are small or negligible at CNA and ATS. Figures 6 and 7(b) indicate that ATS is amplified by a factor of 5-10 compared with CNA at lower frequency than 4 Hz, on the other hand, the relation becomes reverse in the high frequency range. Gray lines in Figure 7(b) indicate that the ground motions at ISU and ATS are comparable. Cranswick et al. (2000) has suggested a large amplification of ground motion in the longer period than 4 sec in Avcilar, however, they obtained similar result with us in shorter periods than 1 sec.

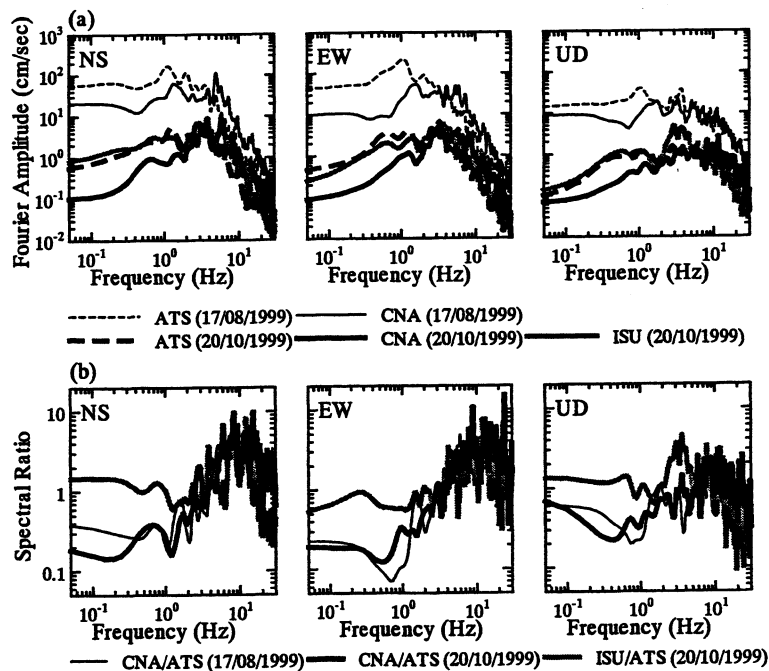


Figure 7. (a): Spectral amplitudes of CNA and ATS during the mainshock of August 17 are shown by thin broken and solid lines, respectively. Thick solid, broken, and gray lines show those of CNA, ATS and ISU from the October 20 event (M4.4), respectively. (b): spectral ratios of CAN and ISU to ATS showing both for the mainshock and the M4.4 earthquake.

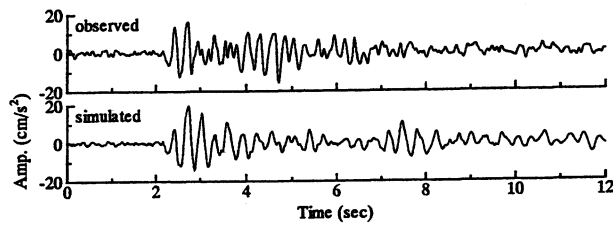


Figure 8. Synthetic transverse ground acceleration at ISU for the Marmara Sea earthquake of October 20 (M4.4) is compared with the observed ones. A good match was obtained at least initial part of S-wave arrival.

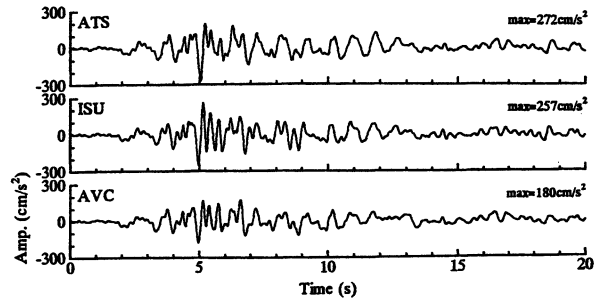


Figure 9. Synthetic transverse accelerations at ISU and AVC are compared with the observed acceleration at ATS

We estimated strong ground motion during the mainshock in damaged area using underground structures determined by array observations of microtremors and earthquake motion observed near the damaged areas. First, we estimated the incident wave at ATS by deconvolving the responses of the surface layers from the record of the M4.4 event based on 1D S-wave propagation theory by using the velocity structure model estimated by microtremors (see Table 2 or Fig. 5). Next, the estimated input motion is convolved with the velocity structure model at ISU, assuming the common input motion at the layer of S-wave velocity of 1230 m/sec. Thus obtained synthetic transverse motion is compared with the observation as shown in Figure 8. Later arrivals are not well simulated, but major early S-wave arrivals are satisfactory. The S-wave velocity models with assuming constant Q are shown in Table 4. As we could not find any significant effects of non-linearity at ATS during mainshock (Fig. 12), a similar approach for the mainshock will be permitted. The estimated transverse motions during the mainshock at ISU and AVC are compared with that of ATS in Figure 14. The ground acceleration at AVC is lowest among them; however, the differences are not so significant.

4. ESTIMATION OF GROUND MOTION IN THE ADAPAZARI BASIN

The strong ground motion at downtown Adapazari is also a matter of our concern, because no strong motion record was obtained in the fast-growing urban/industrial area of the Adapazari basin where buildings were severely damaged (Celebi et al., 2000). Principally, a similar approach to the case of Avcilar may not be suitable for estimating ground motion at Adapazari area, because it plausibly includes near source and non-linear effects of soft soil during strong shaking. First, we

estimated ground motions during the mainshock at ADC and ADU where S-wave velocity structure models have been estimated (Fig. 5 and Table 4) similar to the case of Avcilar. That is, the EW component of the ground motion at SKR deconvolved by the response of the surface layer is used for an input motion at ADC and ADU and the synthetic motions at ADC and ADU are estimated by convolving the sedimentary layers determined by microtremors. The velocity models and Q factors used in the computation are shown in Table 4. Figure 10 shows the synthetic ground accelerations and velocities at ADC and ADU, assuming 1D propagation of S-wave without any corrections of distance and non-linearity. The synthetic motions will only be valuable as an upper band of estimation at the sites. The distances at SKR, ADC, and ADU from the nearest surface fault line were 3.4, 6.4, and 9.6 km, respectively. The peak acceleration (582 cm/sec^2) and velocity (108 cm/sec) at ADC will be reduced to 488 cm/sec^2 and 74 cm/sec , respectively, using the relative distance relation with the help of the empirical formula (Joyner and Boore, 1982). In case of ADU, those will become to 368 cm/sec^2 and 61 cm/sec , respectively.

Table 4. S-wave velocity structure model used for synthetic ground motion.

ATS			ISU			AVC		
Vs (m/s)	Thickness (m)	Q	Vs (m/s)	Thickness (m)	Q	Vs (m/s)	Thickness (m)	Q
204	32	15	225	18	20	291	46	25
364	57	30	370	75	30	434	91	40
608	164	60	584	197	50	584	267	50
919	295	200	919	188	200	919	188	200
1018	100	200	1018	164	200	1018	164	200
1230	inf.	200	1230	inf.	200	1230	inf.	200
SKR			ADC			ADU		
Vs (m/s)	Thickness (m)	Q	Vs (m/s)	Thickness (m)	Q	Vs (m/s)	Thickness (m)	Q
1050	72	200	234	38	20	166	44	15
1500	inf.	200	441	97	40	331	88	30
			728	242	70	500	281	50
			1500	inf.	200	878	63	80
						1050	100	200
						1500	inf.	200

Our next concern is non-linear effects on strong ground motion. Liquefaction was observed in downtown Adapazari; however, it was not evident at ADC and ADU. During the 1995 Hyogo-ken nambu earthquake, nonlinear effects on ground motion were not so significant at least several seconds after S-wave arrival or before the occurrence of liquefaction (Aguirre and Irikura, 1997). In addition, the non-linearity of ground was not an essential effect for the long period ground motions recorded at Niigata City where liquefaction was observed during the 1964 Niigata earthquake (Kudo et al, 2000). The estimated ground motions at ADC and ADU dominate in longer period than

1 second; therefore, we are not necessary to make drastic corrections, at least for long period motions in ADC and ADU. Our discussion is restricted in qualitative due to non-availability of soil dynamic and other necessary data; therefore, we have to despair of further corrections especially for short period motion.

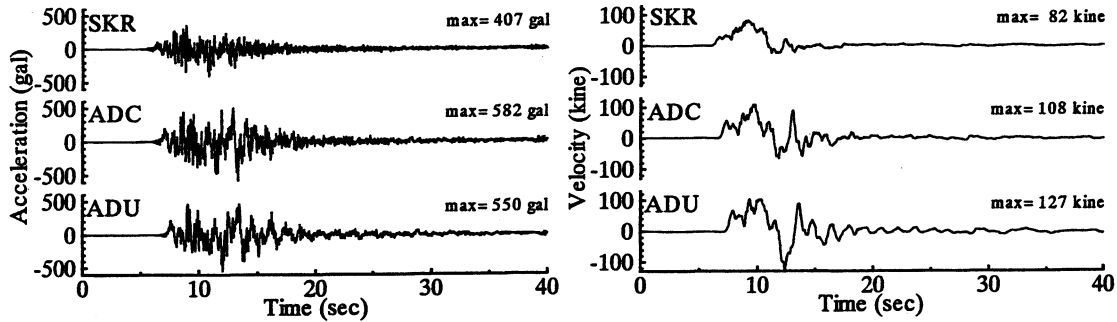


Figure 10. Observed ground accelerations and integrated velocities during the mainshock without any filtering processes at SKR and synthetic ground motions at ADC and ADU, assuming 1D propagation of S-wave without any corrections of distance and non-linearity.

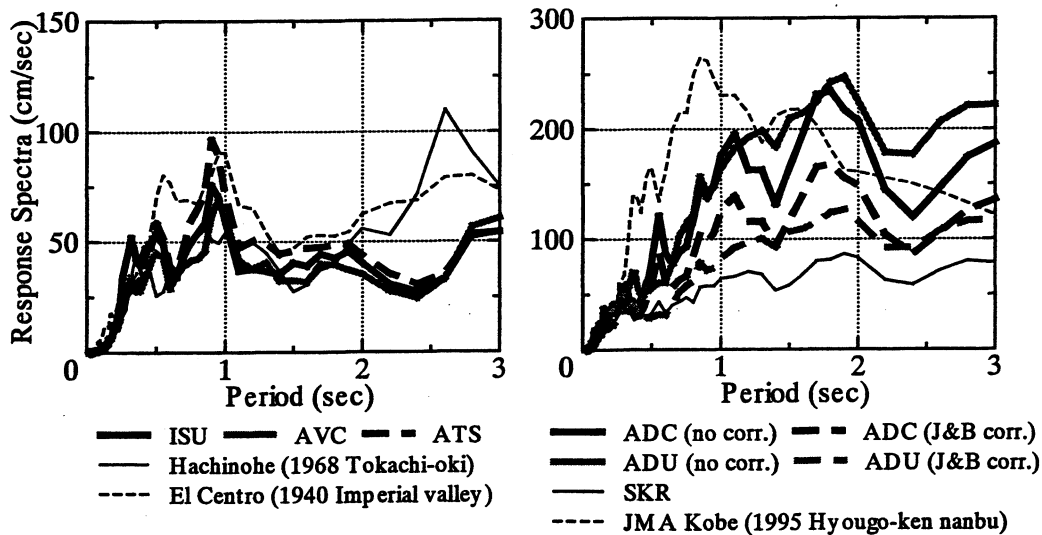


Figure 11. Comparison of the pseudo velocity response spectra ($h=5\%$) of the simulated and the observed strong motions during the mainshock with those of strong motion records that have been used in earthquake engineering. Estimated ground motion at Avclar (AVC, ISU) during the mainshock is similar to those at Hachinohe and El Centro as shown in the left figure. The thick solid and broken lines in the right figure indicate the response spectra at ADC without distance correction and with the correction using the empirical relationship by Joyner and Boore (1983), respectively. Similarly, the gray solid and broken lines also indicate those at ADU with and without distance correction, respectively.

Although the effects of 2D or 3D effects are not taken into account, because of too sparse of geotechnical data in the Adapazari basin, the estimation of ground motions as an upper band will possibly be corrected.

5. DISCUSSION

It is a matter of our concern to understand the severity of the estimated ground motions at Avclar (AVC and ISU) and in Adapazari basin (ADC and ADU) relative to the strong motions that have ever been recorded. Figure 16 compares the pseudo velocity response spectra ($h=5\%$) of simulated motions with those of some records that have been used in earthquake engineering.

The left of Figure 16 shows the response spectra calculated from the simulated motions at ISU and AVC and those obtained from the recorded motions at ATS. They are compared with those of El Centro from the 1940 Imperial Valley earthquake (M_s 7.1) and Hachinohe from the 1968 Tokachi-Oki earthquake (M 7.8). The response spectra of ISU, AVC, and ATS are comparable in amplitude with those of El Centro and Hachinohe at periods shorter than 2 sec. The amplitudes of the response spectra in the period range are most significant for low- and medium- rise buildings. In fact many reinforced concrete buildings near the strong motion site were severely damaged during the Tokachi-oki earthquake. As a result, this earthquake became trigger for the revision of the building code in Japan. The buildings with similar quality are still used in Japan as well as everywhere in the world.

The right of Figure 16 shows the response spectra calculated from the simulated motions at ADC as well as ADU and the recorded motions at SKR together with those of Kobe (JMA) from the 1995 Hyogo-ken Nambu earthquake. The thick broken and solid lines indicate the response spectra at ADC with and without distance correction, respectively. In the distance correction, the empirical relationship by Joyner and Boore (1982) was referred to. Similarly, the gray broken and solid lines also indicate those at ADU with and without distance correction. The simulated velocity responses of ADC after a distance correction are comparable to those of Kobe at a period around 2 sec. Those in the period range from 1 to 1.5 sec. are almost 50 % of Kobe but exceeding 100 cm/sec. Roughly saying, the velocity responses of ADC are two times larger than those of SKR in the frequency range from 0.5 to 3 sec. Such ground motions at ADC would be very serious for medium- and high-rise buildings. A very high contrast of building damage between SKR and ADC or downtown Adapazari could probably be attributed to the difference of the site response.

6. CONCLUSION

We conclude that the array observation of microtremors is very promising method for determining S-wave velocity structures from shallow to intermediate depths, even in damaged areas, while the

aftershock observation allow us to directly compare site responses. A linkage of S-wave velocity structure and aftershock data provides for quantitative evaluation of site responses. A large and long duration of strong motion records at ATS are closely related to the low velocity ($V_s=200$ m/sec) of soft surface layers. The sedimentary layers in Avcilar (ISU and AVC) are similar to those of ATS, so that the ground motion at Avcilar during the mainshock may be similar to that of ATS. Aftershock data prove actually this estimation. The ground motion at a period around 1 sec (response of 60-80 cm/sec) is comparable to those of El Centro (1940) and Hachinohe (1968) that have been used for building design in Japan. At Hachinohe, the damage of RC-building was especially severe during the 1968 Tokachi-oki earthquake.

Through the array observations of microtremors, it becomes evident that SKR is located on very hard soil ($V_s >1000$ m/sec), while thick soft sediments cover the downtown and its extent (ADC and ADU). The ground motion at ADC in downtown Adapazari during the mainshock is estimated to be two or three times larger than that of SKR. Especially large amplifications in the period range from 1 to 2 sec were very severe to medium-rise buildings near ADC.

7. ACKNOWLEDGEMENTS

Strong motion records distributed by ERD and KOERI were used. We wish to express our gratitude to all efforts for acquiring the data. We also express our thanks to all organizations and people in Turkey that permitted and helped us to carry out the microtremors and aftershock observations. A part of this study was conducted as a member of the Architectural Institute of Japan Reconnaissance Team (Leader: Prof. T. Kabeyazawa). The supports from the members were valuable. This work was in part financially supported by the Grant-in-Aid for Scientific Research No.11694134 from Ministry of Education, Science and Culture of Japan and the Kajima Foundation.

8. REFERENCES

- Aguirre, J. and K. Irikura (1997). Nonlinearity, liquefaction, and velocity variation of soft soil layers in Port Island, Kobe, during the Hyogo-ken Nanbu earthquake, *Bull. Seism. Soc. Am.* **87**, 1244-1258.
- Aki, K. (1957). Space and time spectra of stationary stochastic waves, with special reference to microtremors, *Bull. Earthq. Res. Inst.* **35**, 415-456.
- Architectural Institute of Japan Reconnaissance Team with Bogazici University, Istanbul Technical University, and Middle East Technical University (2000). Progress report on damage investigation after Kocaeli earthquake by Architectural Institute of Japan, *International Journal for Housing Science and Its Applications* **24**, 97-126.

- Asten, M. and J. D. Henstridge (1984). Array estimators and the use of microseisms for reconnaissance of sedimentary basins, *Geophysics* **49**, 1828-1837.
- Capon, J. (1969). High-resolution frequency-wavenumber spectrum analysis, *Proc. IEEE* **57**, 1408-1418.
- Celebi, M., S. Toprak, and T. Holzer (2000). Strong-motion, site-effects and Hazard Issues in rebuilding Turkey: in light of the 17 August, 1999 earthquake and its aftershocks, *International Journal for Housing Science and Its Applications*, **24**, 21-38.
- Cranswick, E., O. Ozel, M. Meremonte, M. Erdik, E. Safak, C. Mueller, D. Overturf, and A. Frankel (2000). Earthquake damage, site response, and building response in Avcilar, west of Istanbul, Turkey, *International Journal for Housing Science and Its Applications* **24**, 85-96.
- Earthquake Research Department, Directorate for Disaster Affairs of the Ministry of Public Works and Settlement (ERD) (1999). http://www.deprem.gov.tr/main_e.htm.
- Henstridge, J. D. (1979). A signal processing method for circular array, *Geophysics* **44**, 179-184.
- Horike, M. (1985). Inversion of phase velocity of long-period microtremors to S-wave-velocity structure down to the basement in urbanized areas, *J. Phys. Earth*. **33**, 59-96.
- Joyner, W. B. and D. M. Boore (1982). Prediction of earthquake response spectra, *USGS Open-file rep.*, **82-977**, 1-16.
- Kandilli Observatory and Earthquake Research Institute (KOERI) (1999). <http://kandilli.koc.net/earthquake.htm>.
- Kudo, K., M. Takahashi, M., Sakaue, T., Kanno, H. Kakuma, and D. Tsuboi (1998). A highly over-damped moving coil type accelerometer for mobile strong motion observation and its performance tests, *Report of Grant-in-Aid for Scientific Research-07558056, in Japanese with English abstract*.
- Kudo, K., T. Uetake, and T. Kanno (2000). Re-evaluation nonlinear site response during the Niigata earthquake using the strong motion records at Kawagishi-cho, Niigata city, *Proc. The Twelfth World Conf. Earthq. Eng., CD-ROM*, Paper No. 969/4/ A
- Lacoss, R. T., E. J. Kelly, and M. N. Toksoz (1969). Estimation of seismic noise structure using arrays, *Geophysics* **34**, 21-38.
- Ludwig, W. J., J. E. Nafe, and Drake (1970). Seismic refraction, *The Sea* **4-1**, 53-84.
- Matsuoka, T., N. Umezawa, and H. Makishima (1996). Experimental studies on the applicability of the spatial autocorrelation method for estimation of geological structures using microtremors, *BUTSURI-TANSA* **49**, 26-41, in Japanese with English abstract.
- Mtsushima, T. and H. Okada (1990). Determination of deep geological structures under urban areas, *BUTSURI-TANSA* **43**, 21-33.
- Okada, H., T. Matsushima, T. Moriya, and T. Sasatani (1990). An exploration technique using long-period microtremors for determination of deep geological structures under urbanized areas, *BTSURI-TANSA* **43**, 402-417, in Japanese with English abstract.
- Okada, H. (1998). Microtremors as an exploration method, *Geo-exploration handbook, Soc. Exploration Geophysicists of Japan* **2**, 203-211, in Japanese.
- Toksoz, M. N. (1964). Microseisms and an attempted to exploration, *Geophysics* **29**, 154-177.
- Yamanaka, H. and H. Ishida (1996). Application of genetic algorithms to an inversion of surface-wave dispersion data, *Bull. Seism. Soc. Am.* **86**, 436-444.

TREATMENT OF VARIABILITY AND UNCERTAINTY IN NUMERICAL AND EMPIRICAL METHODS FOR GROUND MOTION ESTIMATION

Norman ABRAHAMSON¹

ABSTRACT

Aleatory variability of ground motion represents randomness, whereas, epistemic uncertainty represents scientific uncertainty as to the probability distribution of the ground motion. The variability and uncertainty need to be treated differently in developing design ground motions. An evaluation of the data from the 1999 Turkey and Taiwan earthquakes indicates that the variability of the ground motion is reasonably well modeled based on existing attenuation relations, but there is large uncertainty in the median ground motion values for large magnitude earthquakes, particularly for near-fault ground motions.

1. INTRODUCTION

Variability and uncertainty are terms that are often used interchangeably in discussions of ground motions. In many cases, the term uncertainty is used for both variability and uncertainty. In developing ground motions for design, random variability and scientific uncertainty in ground motions are treated differently. Variability is the randomness in the ground motions that a model predicts will occur in future earthquakes. For example, variability in ground motion is often quantified by the standard deviation of an attenuation relation. In contrast, uncertainty represents the scientific uncertainty in the ground motion model due to limited data. For example, the uncertainty in attenuation relations is often characterized by alternative attenuation relations. That is, uncertainty is captured by considering alternative models.

In seismic hazard analyses, the terms “aleatory” and “epistemic” are used for variability and uncertainty, respectively. To keep the notation clear, in this paper I will use the terms aleatory variability and epistemic uncertainty.

¹ *Geosciences Department, Pacific Gas and Electric Company, San Francisco, CA, USA*
Email: naa2@pge.com

2.TREATMENT OF ALEATORY VARIABILITY AND EPISTEMIC UNCERTAINTY

The distinction between aleatory variability and epistemic uncertainty is useful for seismic hazard analysis; however, a further subdivision is needed for the practical estimation of these two factors which is shown in Table 1. There are two ways that the variability of ground motion models is evaluated. First the models can be evaluated against recordings from past earthquakes. This is called the “modeling” term. The second way that a model is evaluated is by varying the free parameters of the model. This is called the “parametric” term.

Table 1: Decomposition of Variability and Uncertainty

	Aleatory Variability	Epistemic Uncertainty
Modeling	Variability between model predictions of ground motions and observations of ground motion data.	Select (and weight) alternative ground motion models. Results in differences in both the median ground motion and the variability of the ground motion.
Parametric	Variability of ground motions due to variability of <u>additional</u> earthquake source parameters. “Additional” source parameters are those that are not included in the specification of the design earthquake.	Select (and weight) alternative models for the distributions of the additional parameters. Results in differences in both the median ground motion and the variability of the ground motion.

The modeling component is a measure of the inability of the model to predict ground motions from past earthquakes. In general, the cause of the modeling variability is not understood. It is

assumed to be random. (If the cause of the modeling variability was understood, then the model could be improved to fit the observations.)

The parametric component is a measure of the variability of the ground motion from causes that are understood. That is, there is randomness in the earthquake source process that is understood and its effect on ground motion is part of the model.

In general, both the modeling and parametric terms need to be considered in a ground motion model. As our understanding and modeling of earthquakes improves, there will be a trend of reducing the modeling variability (unexplainable variability) but this will likely be offset by an increase in the parametric variability (explainable variability). While the total variability (combination of the modeling variability and the parametric variability) may not be reduced significantly with improved models, there is an advantage to understanding the causes of the variability, particularly if the model is being extrapolated beyond the empirical data on which it was evaluated.

2.1 Empirical Attenuation Relations

In empirical attenuation models, the standard deviation given for the model is modeling variability. In most attenuation models, there is no parametric variability component to the aleatory variability. As new attenuation models are developed, they may begin to include a parametric variability component. For example, if an attenuation relation used the static stress-drop as an additional source parameter, then the variability of static stress-drop would be treated as parametric variability.

Generally, for empirical attenuation relations, epistemic uncertainty is addressed by considering alternative attenuation relations.

2.2 Numerical simulation models

In numerical simulations, the total aleatory variability is often not presented. Typically, only the parametric variability is presented and the modeling variability is ignored. This occurs because it is straight-forward for modelers to exercise the model in forward predictions varying the input parameters (e.g. parametric variability), but it is much more work to quantify the modeling variability. To accurately represent the total aleatory variability from numerical simulations requires both the modeling variability and the parametric variability (Wong and Stepp, 1998).

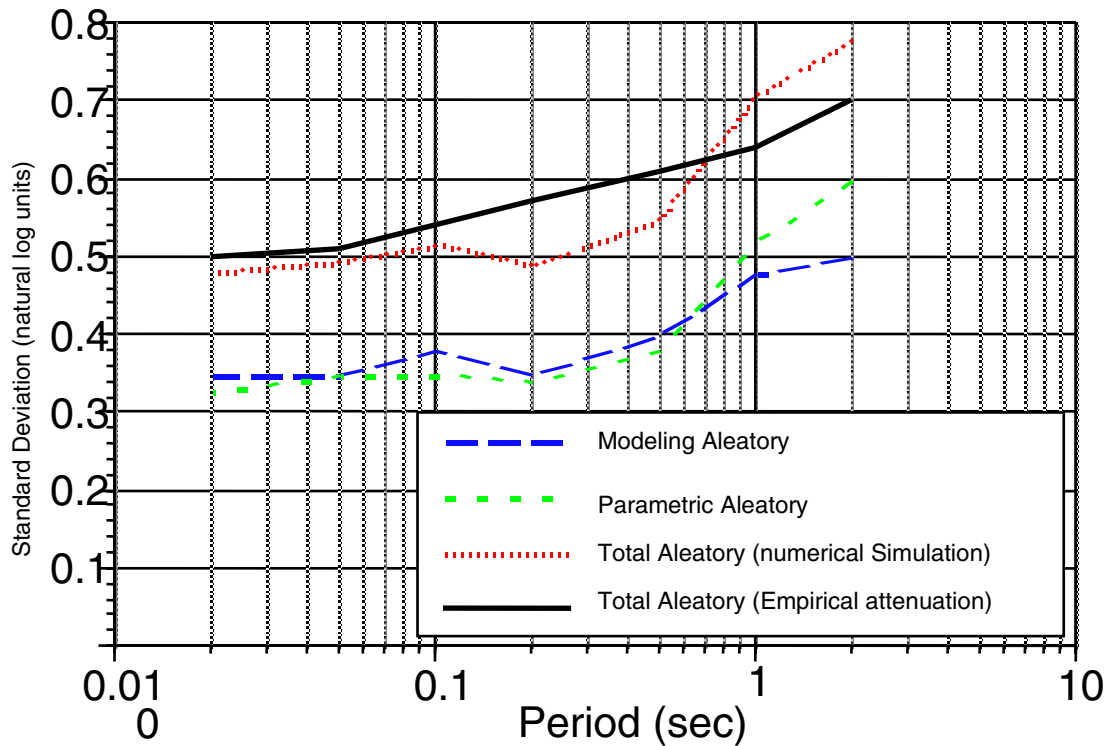


Figure 1. Example of parametric and modeling contribution to the aleatory variability for numerical simulation. This case is for a magnitude 6.5 strike-slip earthquake at a distance of 5 km.

As an example, the modeling variability and parametric variability for a numerical simulation method are shown in Figure 1. This example is for a magnitude 6.5 strike-slip earthquake at a distance of 5 km. In this case, the modeling variability and the parametric variability are about equal at short periods, and the parametric variability is larger than the modeling variability at long periods. This indicates that the long periods are more sensitive to the model parameters

than are the short periods. Also shown on this figure is the standard deviation from the Abrahamson and Silva (1997) empirical attenuation relation. The total variability from the numerical simulation is similar to the standard deviation of the empirical attenuation relation. That is, the aleatory variability has not been reduced by using a numerical simulation instead of an empirical attenuation relation, but about half of the aleatory variability from the numerical simulation can be explained by specific source parameters.

3. EVALUATIONS OF EMPIRICAL MODELS WITH THE 1999 TURKEY AND TAIWAN DATA

The ground motions recorded in the 1999 Kocali and Duzce earthquakes in Turkey and the 1999 Chi-Chi earthquake in Taiwan were compared to the Abrahamson and Silva (1997) attenuation relation for shallow crustal earthquakes. The mean residuals of the 5% damped response spectral accelerations are shown in Figure 2 for stations within 20 km of the fault. The error bars shown in this figure represent the standard error of the mean residual.

The aleatory variability of the response spectral values are compared to the Abrahamson and Silva (1997) model in Figure 3. The aleatory variability computed for the three earthquakes represent only the within event variability. Therefore, the event-to-event variability in the Abrahamson and Silva (1997) attenuation relation was removed before comparing with the observed variability. Figure 3 shows that the estimated standard deviations from the Chi-Chi earthquake do not show the strong period dependence that is in the empirical model.

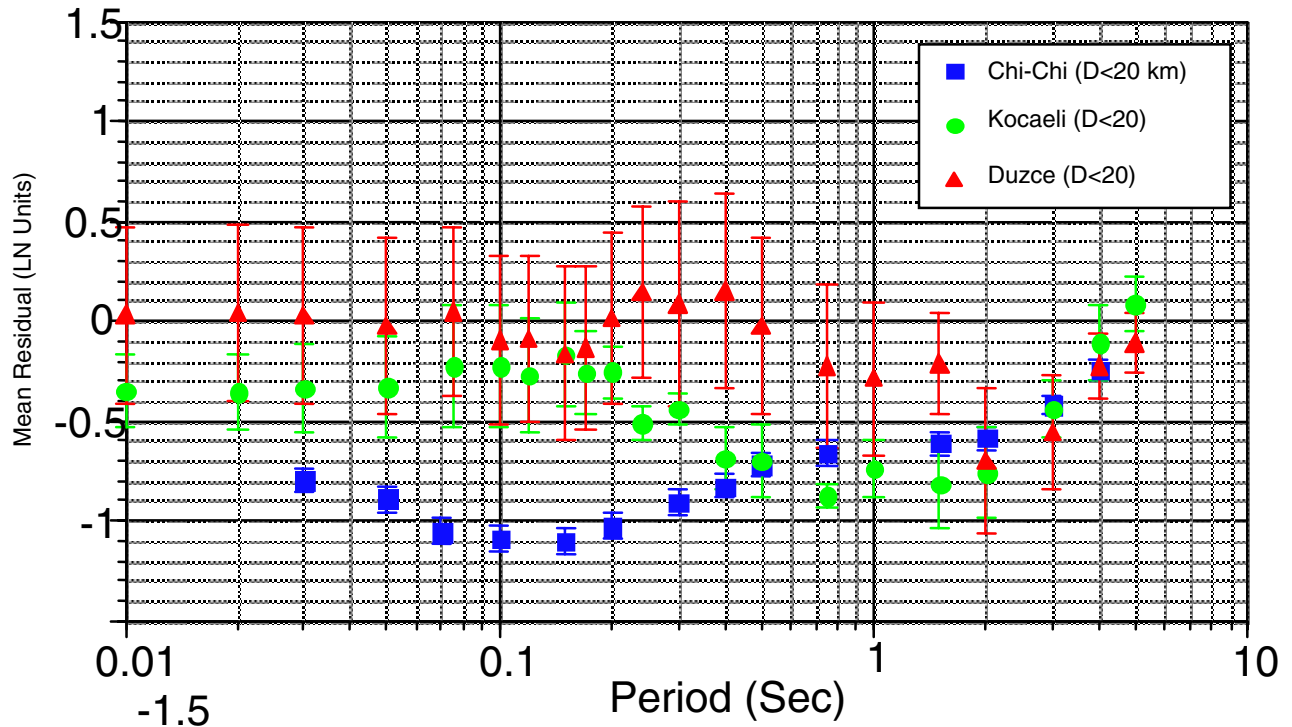


Figure 2. Mean residuals for distances less than 20 km using the Abrahamson and Silva (1997) attenuation relation.

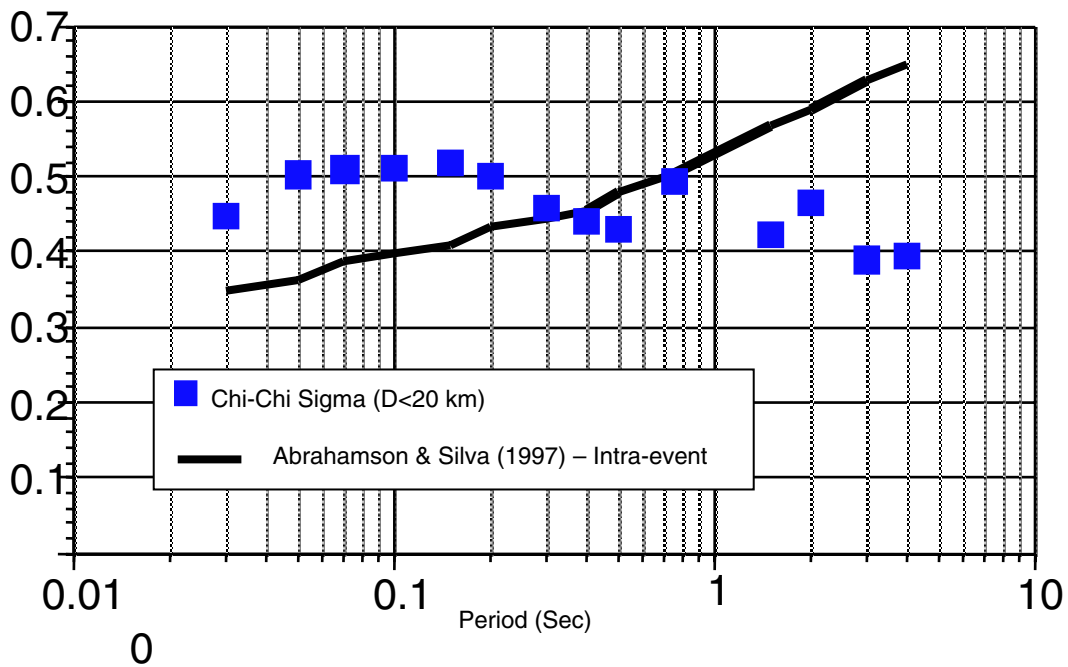


Figure 3. Comparison of the aleatory variability from the Chi-Chi earthquake with the aleatory variability (within event) from the Abrahamson and Silva (1997) attenuation relation.

4. KEY AREAS OF GROUND MOTION UNCERTAINTY

4.1 Magnitude Scaling of Ground Motions for Very Large Magnitude

Earthquakes

The lower than expected near fault ground motions during the 1999 Turkey and Taiwan earthquakes lead to a significant uncertainty in the prediction of median ground motions for large magnitude earthquakes. In particular, these low ground motions may lead to a re-evaluation of the magnitude scaling of ground motions. In current empirical attenuation relations for crustal earthquakes used in the western United States, the magnitude scaling of the median ground motion is reasonably well determined for magnitudes 6.0 to 7.0; however, the scaling above magnitude 7 is not well constrained by data (before the Turkey and Taiwan earthquakes).

Somerville (2000) has compared ground motions from earthquakes with large surface rupture with the ground motions from earthquakes with buried surface rupture and has found that buried ruptures produce much larger ground motions. His interpretation of the lower than expected near-fault ground motions (at periods less than 2 seconds) recorded in the 1999 Turkey and Taiwan earthquakes is that during large surface rupturing events, there is a reduction in the normal stresses on the fault plane due to elevated fluid dynamic pressure. This suggests that surface rupture or buried rupture should be a parameter in a ground motion attenuation relation for crustal earthquakes.

4.2 Long Period Pulses

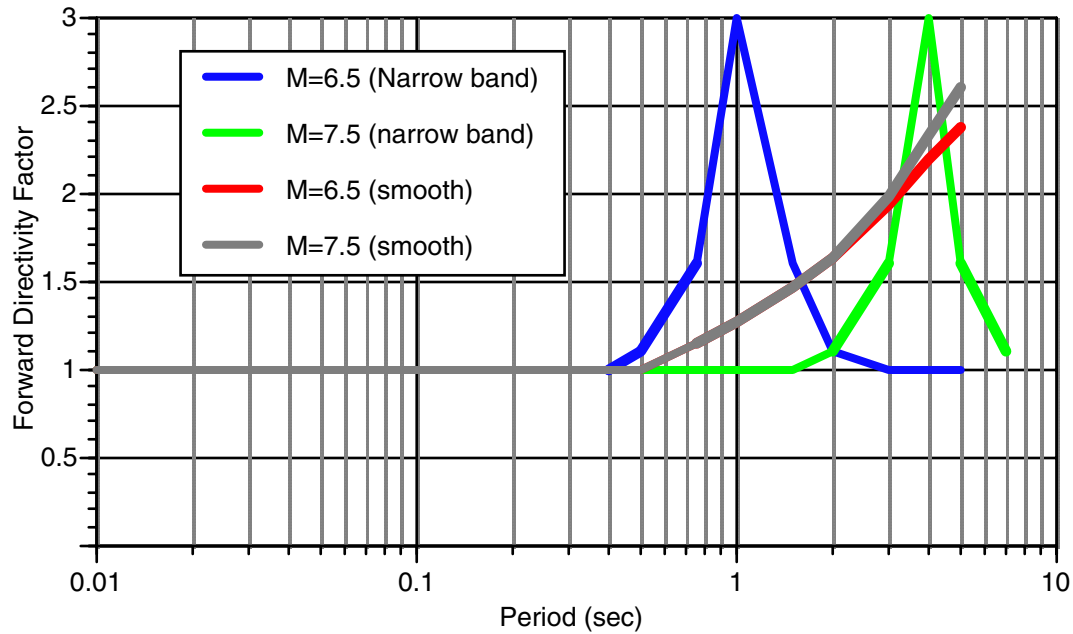
Over the last decade, there has been a lot of discussion of long period pulses observed in near-fault ground motion. These long period pulses have been called “fling”, “directivity” and “killer pulses”. There are two causes of long period pulses in near-fault ground motions. One is due to constructive interference of the dynamic shaking due to rupture directivity effects. The other is due to the permanent offset of the ground close to faults with large amounts of fault offset. These two causes of long period pulses attenuate very differently from one another. To keep these two effects separate, we are using the terms “directivity pulse” and “fling-step” for these two effects.

Rupture directivity effects occur when the rupture is toward the site and the slip direction (on the fault plane) is aligned with the rupture direction. For strike-slip earthquakes, rupture directivity is observed on the fault normal component and static displacement effects are observed on the fault parallel component. Thus, for strike-slip earthquakes, the rupture directivity pulse and the permanent displacement pulse will naturally separate itself on the two horizontal components. For dip-slip earthquakes, it is more complicated. The rupture directivity effect will be strongest on the fault normal component at a location directly updip from the hypocenter. The fling step will also be observed on the component perpendicular to the strike of the fault. Thus for dip-slip faults, directivity-pulse effects and fling-step effects need to be separated from each other.

Prior to the 1999 Turkey and Taiwan earthquakes, nearly all of the observed large long period pulses in near-fault ground motions were caused by rupture directivity effects. So this effect was not a significant problem with the data. With the large amount of data from Turkey and Taiwan that contain these permanent displacements, these different effects need to be addressed.

4.3 Rupture Directivity Models

A preliminary model quantifying effects of the directivity on ground motion was given by Somerville et al (1997). This model used a smooth broad spectrum to describe the directivity in terms of scale factors that are applied to standard attenuation relations without directivity. These smooth factors are shown in Figure 4. As an example, the median spectra for a magnitude 6.5 and 7.5 earthquakes a distance of 10 km developed for forward directivity conditions are compared to standard spectra in Figure 5. In this model, the median spectrum from the larger magnitude ($M=7.5$) earthquake is greater than the spectrum from the smaller magnitude ($M=6.5$) at all periods.



0
 Figure 4. Comparison of smooth vs narrow band adjustment factors for directivity.

Abrahamson (2000) showed that including rupture directivity effects in ground motion models, there can be a significant effect (up to a factor of 1.5) on long period design ground motions. In a probabilistic analysis, if the return period of the design ground motion is greater than about twice the mean recurrence interval of a large earthquake, then directivity effects will significantly increase the probabilistic estimate of the long period ($T > 1$ sec) ground motion; however, if the return period of the design ground motion is less than the earthquake recurrence interval then including directivity does not have a significant effect on the design ground motion. The size of this effect on probabilistic analysis will strongly depend on the use of either broad smooth directivity effects or narrow band directivity effects. This is a large outstanding epistemic uncertainty in the prediction of near fault long period ground motion.

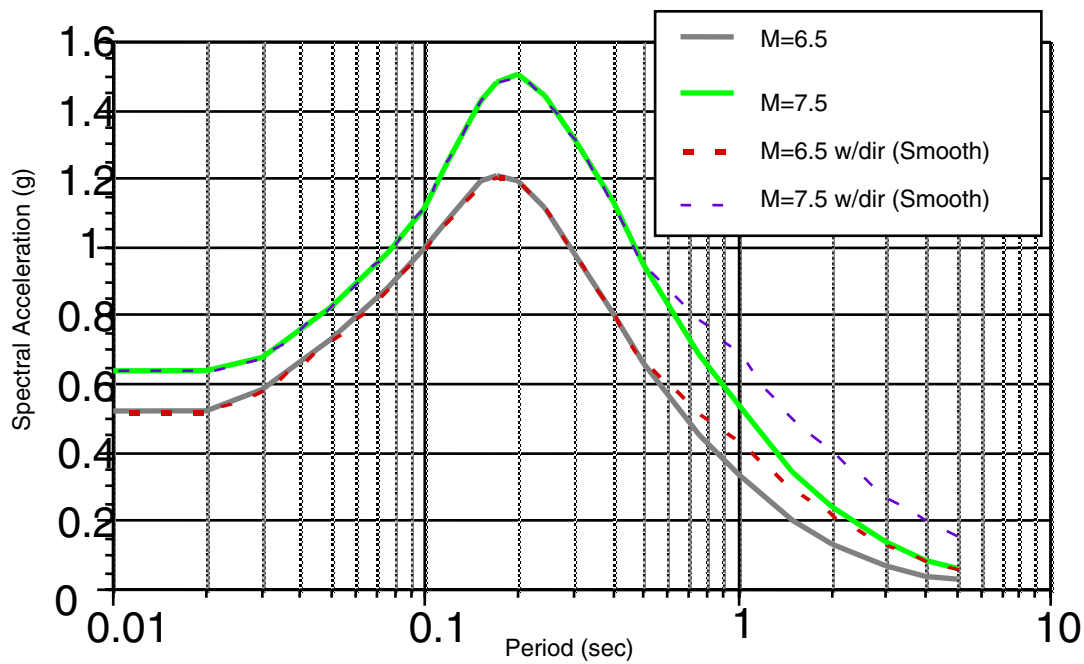


Figure 5. Example of applying a smooth directivity effects model.

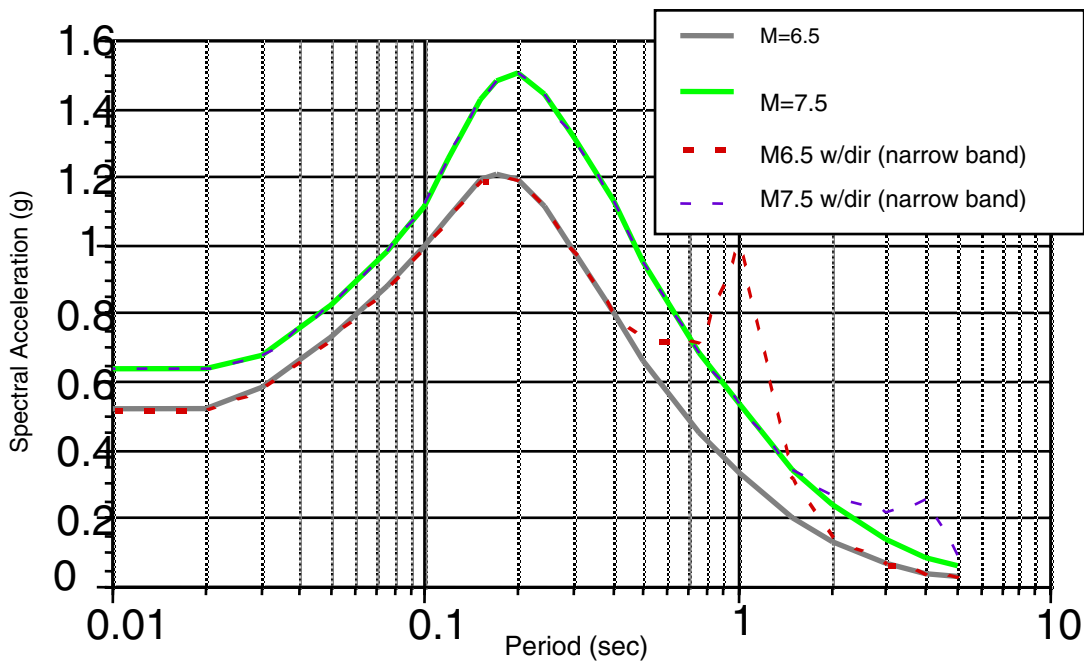


Figure 6. Example of applying a narrow band directivity effects model.

5. References

Abrahamson, N. A. (2000). Effects of rupture directivity on probabilistic seismic hazard analysis, Proc. Sixth International Conference on Seismic Zonation, Nov. 2000, Palm Springs.

Abrahamson, N. A. and W. J. Silva (1997). Empirical response spectral attenuation relations for shallow crustal earthquakes, *Seism. Res. Let.*, **68**, 94-127.

Somerville, P. G. (2000). Magnitude scaling of near fault ground motions, Proceedings of the International Workshop on Annual Commemoration of Chi-Chi Earthquake, September 28-20, 2000, Taipei.

Somerville, P. G., N. F. Smith, R. W. Graves. and N. A. Abrahamson (1997). Modification of empirical strong ground motion attenuation relations to include the amplitude and duration effects of rupture directivity, *Seism. Res. Let.*, Vol. **68**, 199-222.

Wong, I. G. and J. C. Stepp (1998). Probabilistic seismic hazard analyses for fault displacement and vibratory ground motion at Yucca Mountain, Nevada, Report to the U. S. Geological Survey.

DEVIATION OF PLASTIC DEFORMATION AND EQUIVALENT DAMPING RATIO ON SINGLE-DEGREE-OF FREEDOM SYSTEM

Masaomi TESHIGAWARA¹, Hiroshi ISODA¹, Nobuyuki IZUMI²

ABSTRACT

When the applicability of Equivalent Linearizing Method (ELM), which has been understood as one of the techniques to obtain earthquake responses, is examined associated with the deviation of the plastic deformation. In the fundamental study on ELM, responses of Single-Degree-Of-Freedom are compared between by ELM and by Time History Analysis. By the parametric approach, the deviation of plastic deformation is examined. Then the equivalent damping is evaluated. This damping evaluation is applied to the real structure as the following study to totally examine the accuracy of this ELM. Obtained results are (1) the deviation of the plastic deformation of the building in the case of strong earthquake is relatively small within the small ductility range, and (2) the damping constant of $0.25(1-1/\sqrt{\mu})+0.05$ gives the lower bound to estimate the substitute damping by time history response.

1. INTRODUCTION

This paper examined the applicability of equivalent linearizing method (ELM) that is considered as one of the simplified methods to estimate the maximum response in the large earthquake. The ELM was used as a possible hand calculation technique to obtain the earthquake response when the computer was undeveloped. Now that the computer has been extremely developed and it can simply complete time history response (THR) analysis, ELM is positioned as one of the techniques which obtain the earthquake response, when the earthquake was defined as the spectrum in order to give the generality excluding individuality of earthquake waves. However, the ELM is theoretically established in steady-state vibration with harmony of external force. As for the random vibration, equivalent rigidity, equivalent damping (ED) are assumed. Then approximate response is supposed to be obtained. By restoring force characteristics and earthquake waves, there generates the deviation of the plastic deformation, and accordingly the difference with the stationary response may increase. In this paper, parametric earthquake response analysis was carried out, and the deviation of

¹ Department of Structural Engineering, Building Research Institute, Ministry of Construction, Japan
Email: teshi@kenken.go.jp, hisodak@kenken.go.jp

² TODA Corporation, Japan
Email: izumi@toda-jp.com

the plastic deformation of the building, which was related to the applicability of ELM, was examined. Method for calculating appropriate equivalent rigidity, ED, and the accuracy of this method are also reported.

2. FUNDAMENTAL STUDY FOR EQUIVALENT LINEAR METHOD

Fundamental study for ELM is conducted. Responses of the SDOF between by Time history analysis and by ELM are compared. Several artificial waves fit to the standard response spectrum are used for this fundamental study. SDOF hysteresis models are degrading in bilinear (DBL) and normal bilinear shapes (NBL). Used parameters are elastic periods, yield strength, and after yield stiffness. Figure 1 shows the relationship between the ductility factor by the THR and that of the equivalent linear analysis for degrading bilinear restoring force characteristics. In this comparison, damping is calculated by steady-stable hysteresis loop. It is found that estimated response using equivalent linear analysis increases linearly with THR. For the above reason, maximum responses can be traced using equivalent linear analysis if damping constant. is suitably decreased.

Figure 2 is also the comparison of Max. response between by ELM and by THR, in the case that the applied hysteresis rule is NBL. The max. responses obtained by the both methods have linear relation in the range of u is less than about 7. It is because of the fact that ELM is applicable to the stational vibration. In the case of the large deformation range, deviation of deformation is observed as shown in Fig 3. As well known, the is applicable to the response with steady stable vibration. In order to apply the ELM to the random vibration, the ED and the equivalent stiffness under the condition for stable oscillation are investigated. This linear relation suggests the fact that ELM using appropriate ED gives good max. response estimation. It is necessary to consider the effect of $K2/K1$ in the evaluation of ED.

3. STUDY ON THE DEVIATION OF PLASTIC DEFORMATION

When earthquake response analysis was carried out, the deviation of the plastic deformation of the building, which was related to the applicability of ELM, was examined. Using one

mass system with elastoplastic restoring force characteristics, the following parameters were set (refer to Fig.4): Elastic period (3cases), yield strength (0.2,0.4, 2 cases), stiffness ratio (3 cases), etc. in normal TRI type where 18 cases are studied. In addition, 18 cases are studied in degrading TRI type (TAKEDA). In normal TRI type, the reference point of the ductility rate was set at the Q_y point. In TAKEDA type, the reference point of the ductility rate was made to be the second break point Q_y . Internal viscosity damping was to be secant stiffness proportional ($h_1=3\%$) in TAKEDA and stiffness proportional ($h_1=2\%$) in normal TRI type, respectively.

Earthquake motions of EL CENTRO NS, HACHINOHE NS, TOHOKU NS are standardized at 50cm/s of maximum velocity, and JMA NS (Hyogo-ken Nanbu Earthquake and Kobe marine meteorological observatory ^{*1}) was used with the intensity of the original wave. BGJ L2^{*2} was made to be 2 waves (the engineering basis) which changed the phase.

As the index that shows the deviation of the plastic deformation, the deviation ratio (α) defined in Eq. (1), is used. α is valued as the ratio of largest ductility rate (u_{max}) to the average ductility rate (u_{mean}).

$$\alpha = |u_{max}| / |u_{mean}| \quad \text{Eq. (1)}$$

With the large plastic deformation in the initial stage of the vibration, central axis in the hysteresis of the response tends to move in normal TRI type. In TAKEDA, the deviation is comparatively smaller, and it tends to increase a little in the latter half in duration time. Example of response is shown in Fig. 5. The relationship between ductility rate (u_{max}) and α as shown in Fig. 6 are examined on the data of u_{max} which are under 10. The value of α is bigger, as u_{max} is bigger. α_{mean} is about 1.4 within the u_{max} being bigger than 10, α_{mean} is 1.49 in normal TRI and, 1.25 in TAKEDA, and the difference is bigger. α_{mean} is about 1.1 under the range of u_{max} of 5, and the difference between normal TRI and TAKEDA is smaller, and there are some cases in which α exceeds 1.3, in the case that u_{max} is over 5.

4. STUDY ON THE EQUIVALENT DAMPING RATIO

Total input energy is absorbed by equivalent viscous damping in the SDOF with the equivalent stiffness at max. response point. The ED is evaluated by Eq. (2)

$$h_s = \frac{-\int_0^t \ddot{y}_0 \dot{y} dt}{2\omega_e \int_0^t \dot{y}^2 dt} \quad \text{Eq. (2)}$$

\dot{y} : response velocity

\ddot{y}_0 : input ground acceleration

t : duration time

$$\omega_e = \sqrt{\frac{k_{eq}}{m}}$$

k_{eq} : equivalent stiffness, m : mass

Following study is done in the range that the ductility factor is less than 6. Figure seven shows the relation among substitute damping defined by Eq. (2), square marks, and ductility factor obtained by NBL hysteresis rule. Left part in Fig. 7 shows the results of NBL with K2/K1 of 1/1000 and right part with K2/K1 of 2/10. Red line indicates the ED obtained by Eq. (3) and blue line indicates the value by Eq. (4) that is derived from stable steady hysteresis loop.

$$heq = 0.25(1 - 1/\sqrt{\mu}) + 0.05 \quad \text{Eq. (3)}$$

μ : ductility rate

$$heq = \frac{1}{4\pi} \left(\frac{\Delta W_{cyc}}{W} \right) \quad \text{Eq. (4)}$$

ΔW_{cyc} : absorbed energy by hysteresis loop,

W : potential energy

The heq by Eq. (4) in the left part of fig. 7 is larger than that in the right part. Substitute damping obtained by Time History analysis (Eq.(2)) is followed by the Eq. (3). Figure 8 shows the substitute damping obtained by NBL with several K2/K1 ratios. The Eq. (3) covers the lower bound of these substitute damping. Figure 9 also shows the relation between the substitute damping and ductility factor in case of D-tri type. In DBL hysteresis rule, the

damping evaluated by the Eq. (3) also estimate the substitute damping in safety side. Figure 10 plots the all case studies of DBL model. Eq. (3) covers the lower bound of substitute damping.

So far, the study was conducted using artificial EQ. motion. The figure 11 shows the relation between substitute damping and ductility factor in case of NBL type against the recorded EQ. motions. Kobe, Elcentro, are used as the recorded EQ. motions. Deviation is larger compared with the results for artificial EQ. motions. The same results obtained for the hysteresis model of DBL is shown in Fig. 12. Eq. (3), however, covers the lower bound of substitute damping.

5. APPLICATION TO REAL STRUCTURE

Next step is the damping evaluation applied to the real structure. The results of push over analysis of 5, 10, 20 stories steel buildings are converted to SDOF under lateral force distribution based on A_i shear coefficient in Fig. 13. These skeleton curves are modeled into the tri-linear curve. Marks present the first, and second yield points for Tri-Linear model. As the building story becomes higher, the stiffness of after yielding, K_3 , becomes smaller. Therefore, h_{eq} , by eq. (4) is larger in the high rise building. In this study, base shear coefficient (C_b) is varied in order to get the different response level. As for RC building, 6,10, 19 stories RC buildings are also modeled to the SDOF in Fig. 14 by the same way as Steel buildings.

Substitute damping are calculated for each structure against artificial earthquake motions in Fig. 15 and 16. Proposed damping Eq. (3) presents the substitute damping. Red line shows the damping by Eq. (4), and blue line is the damping by Eq. (3). For RC model, Eq. (3) follows the substitute damping in the safety side, where the range of ductility factors is more than 1.

6. CONCLUSIONS

- (1) The deviation of the plastic deformation in strong earthquake of the building is relatively small within the small ductility range.
- (2) The damping constant of Eq. (3) gives the lower bound to estimate the substitute damping by THR.

7. REFERENCES

- Hayashi. M et. al. (1999). Sesimic Evaluation of Buildings by Acceleration Response Spectrum at Engineering Bedrock (Part 3: Study on Deviation of Plastic Deformations). *Proceedings AIJ Annual Conference*.
- Isoda. H et. al. (1999). Sesimic Evaluation of Buildings by Acceleration Response Spectrum at Engineering Bedrock (Part 9: Evaluation of equivalent damping ratio on SDOF). *Proceedings AIJ Annual Conference*.

8. KEYWORDS

equivalent linearizing method, deviation of plastic deformations, equivalent damping ratio, earthquake response

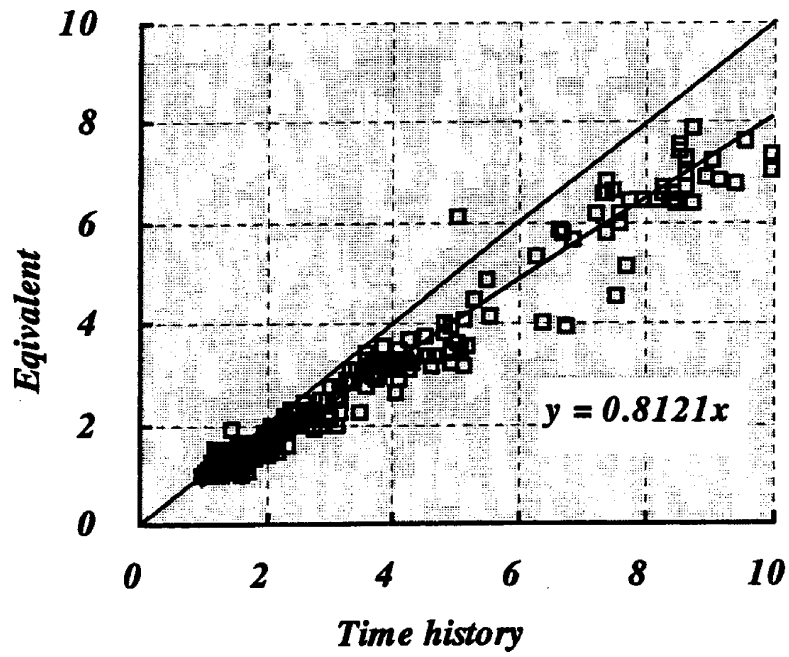
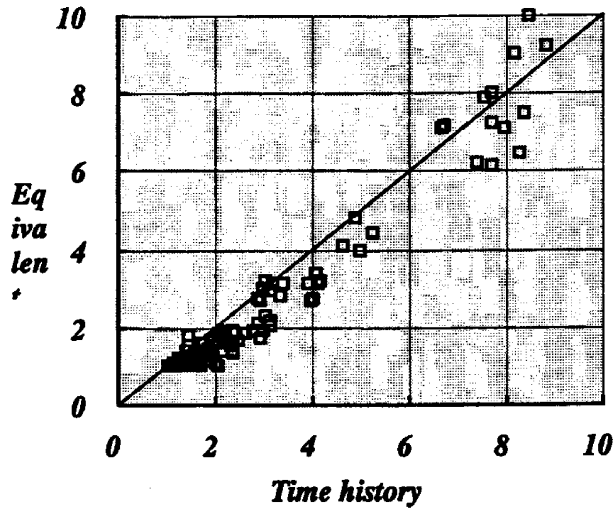
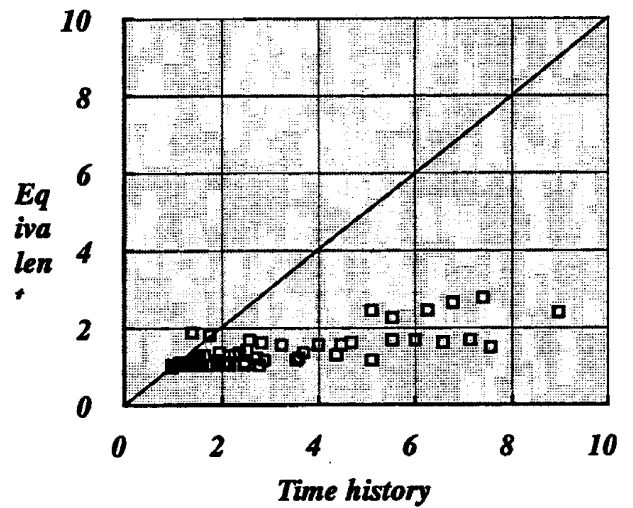


Fig. 1 Comparison of Max. Response (Degrading bi-linear)



$k_2=4/10k_1$



$k_2=1/1000k_1$

Fig. 2 Comparison of Max. response (Normal bi-linear)

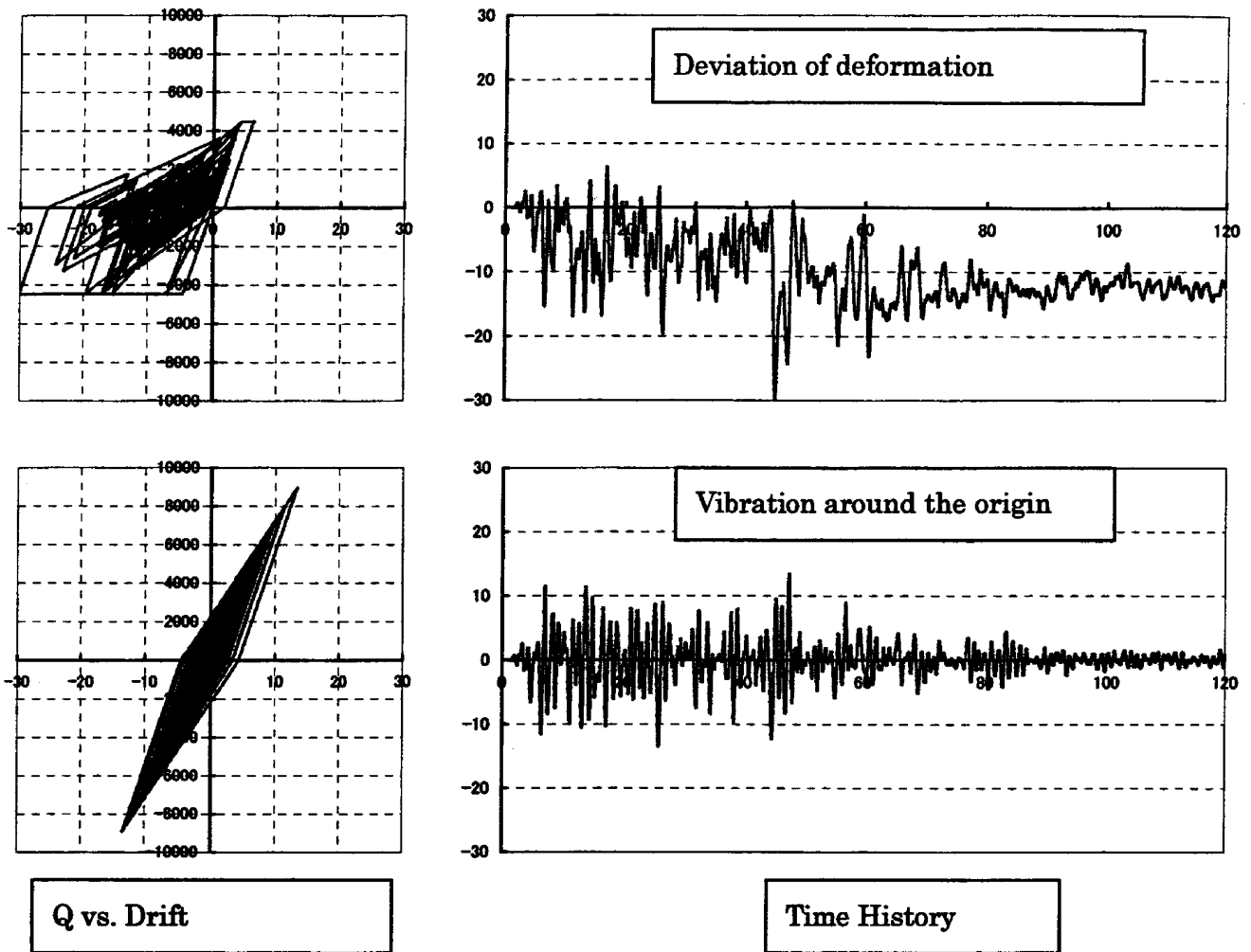
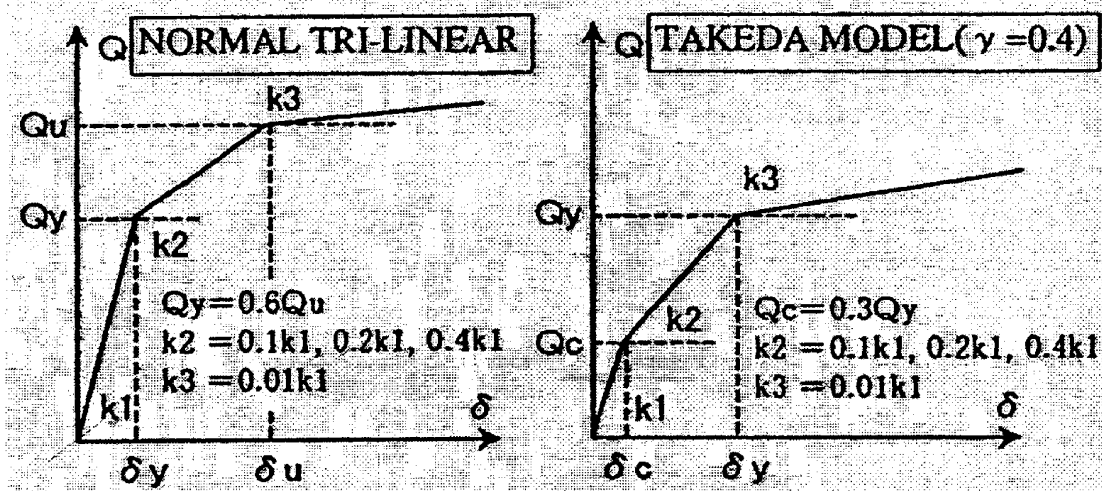


Fig. 3 Difference in Response Estimation



**One mass system with normal TRI type, and degrading TRI type (TAKEDA)
Elastic period: 0.25, 0.5, 1.0 sec.
Yield strength: 0.2, 0.4, Stiffness ratio, etc.**

Fig. 4 Analysis Model for deviation of plastic deformation

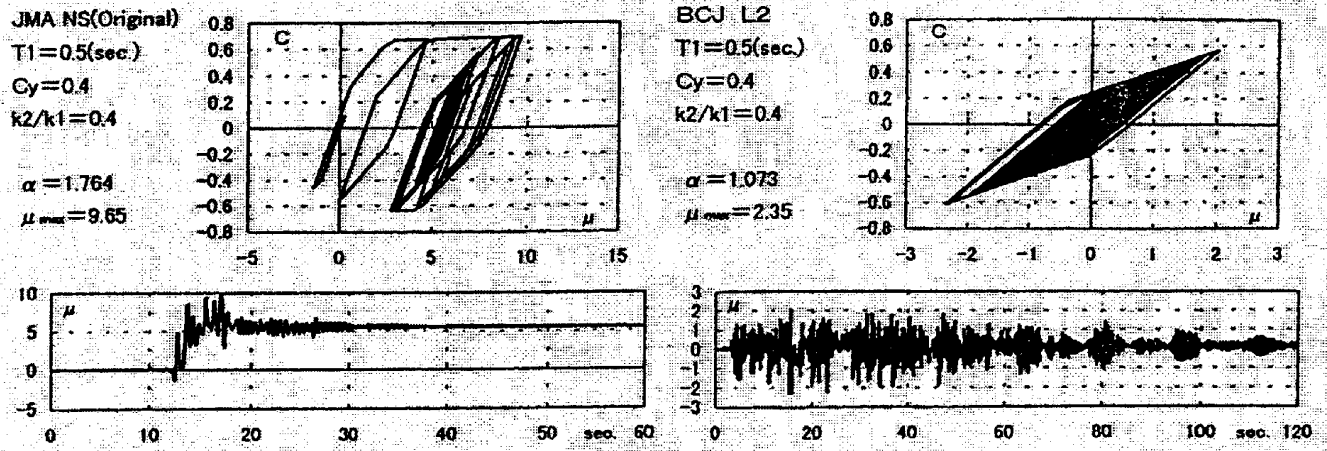


Fig. 5 Example of analysis

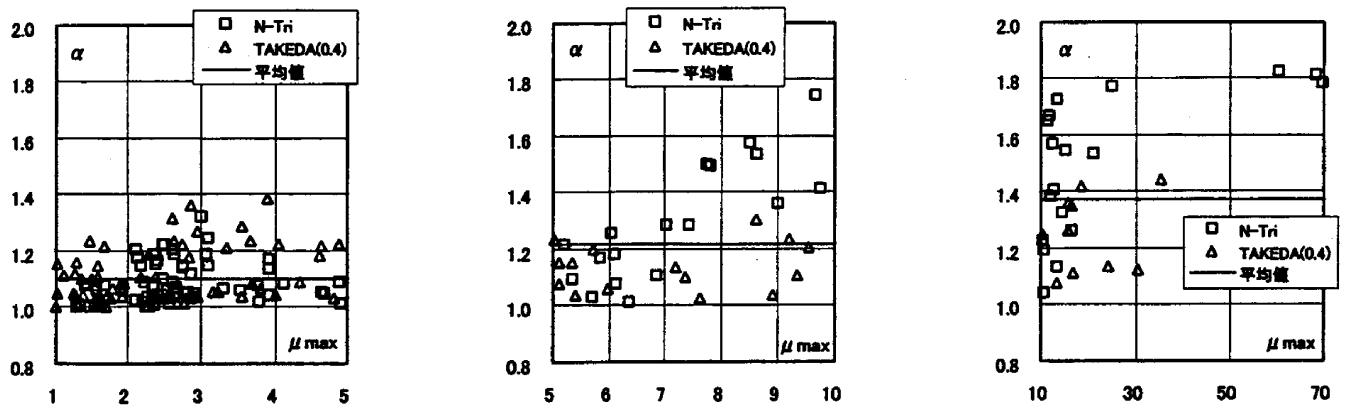


Fig. 6 Relation of ductility rate and the index of deviation of deformation

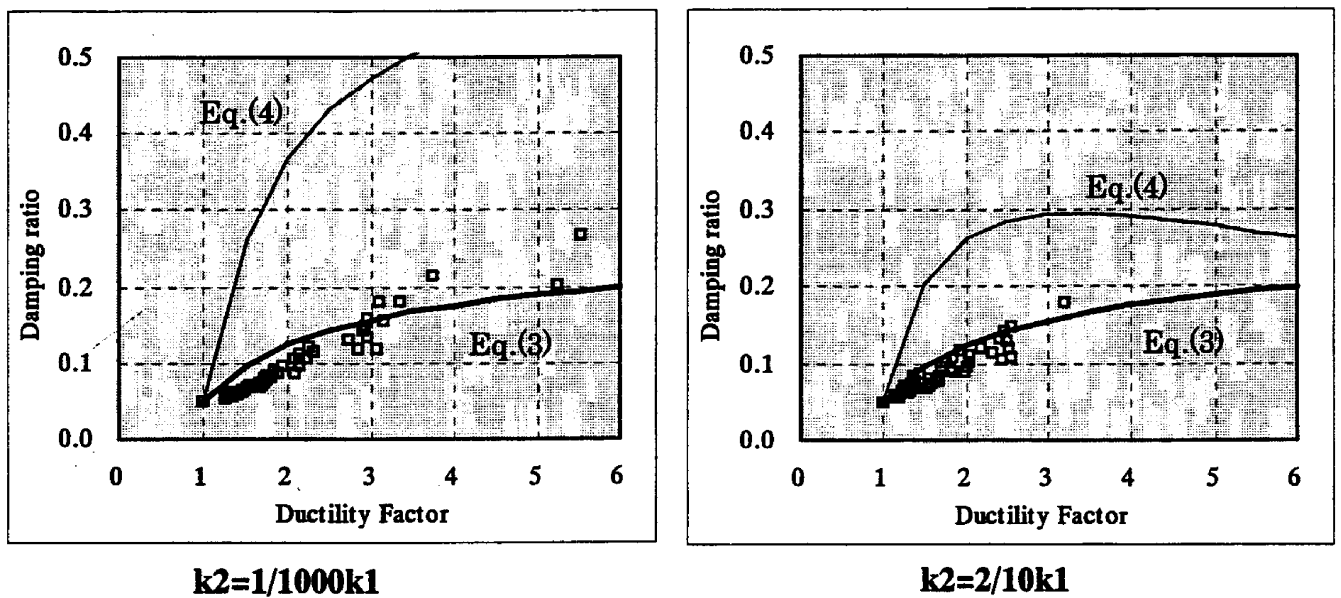


Fig. 7 Substitute damping, equivalent damping, and proposed damping for NBL

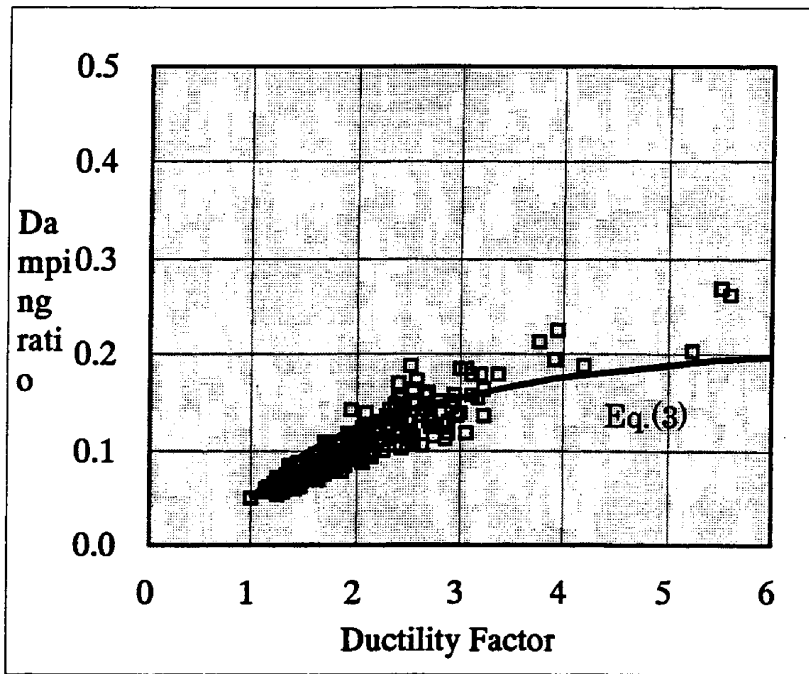
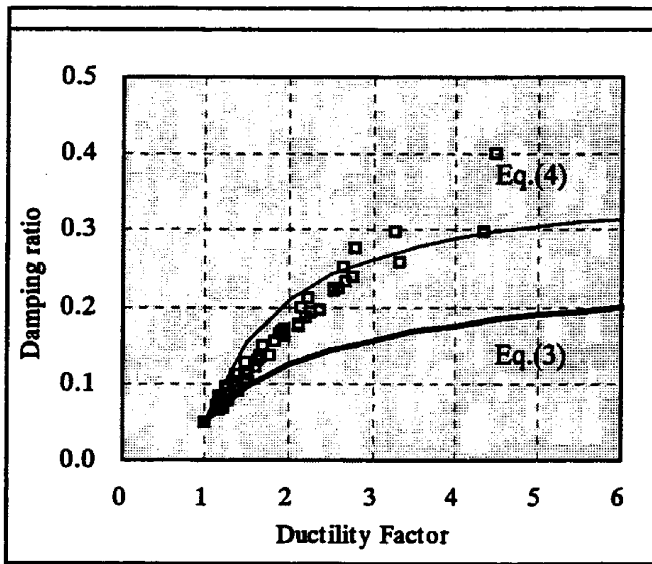
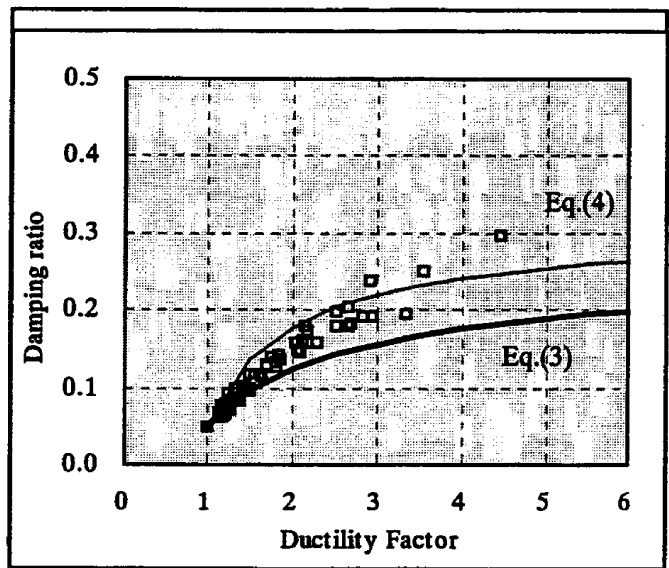


Fig. 8 Substitute damping for NBL type



$k_2 = 1/1000k_1$



$k_2 = 2/10k_1$

Fig. 9 Substitute damping, equivalent damping, and proposed damping for DBL

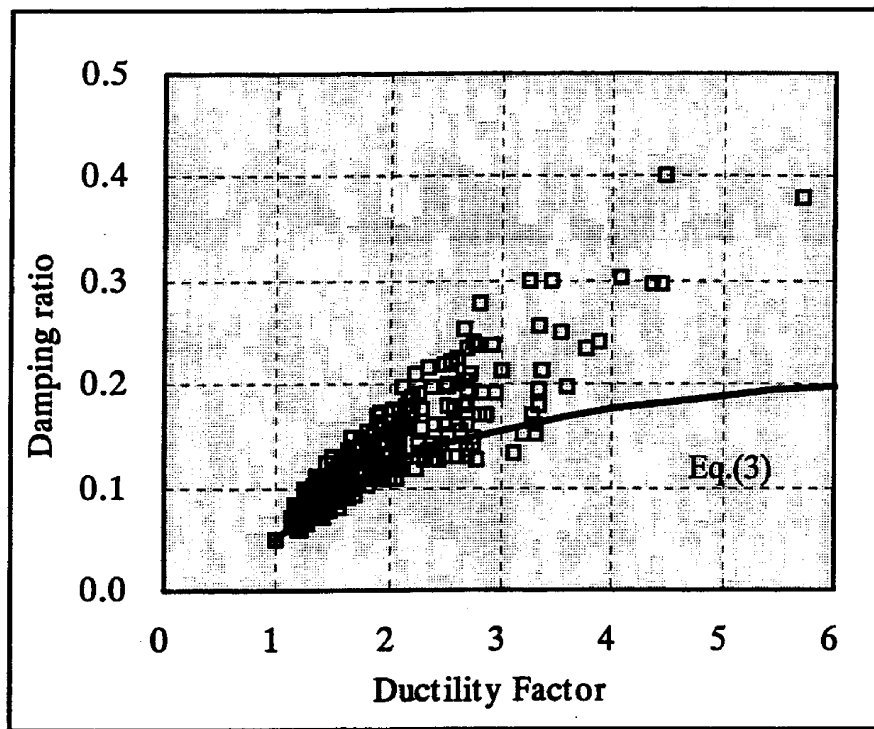


Fig. 10 Substitute damping for DBL type

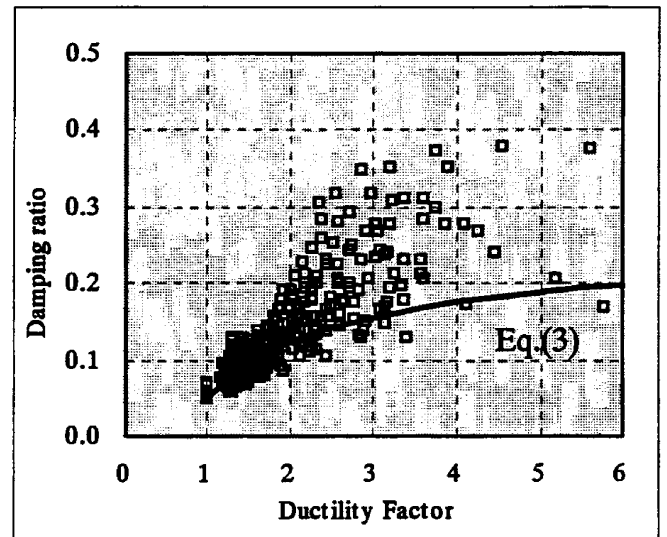
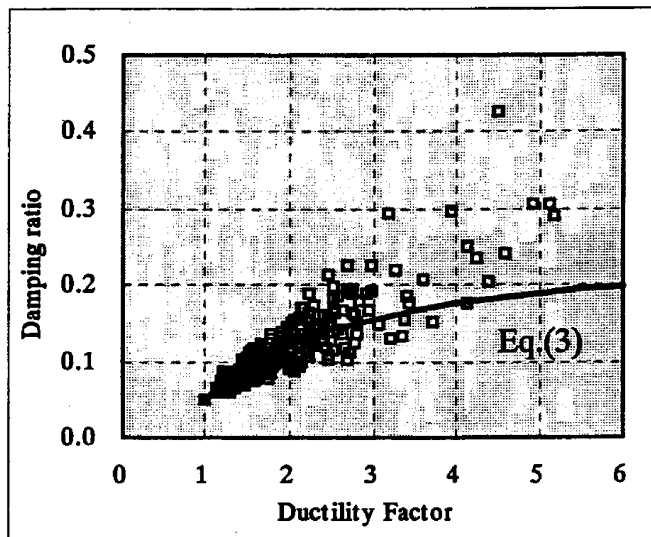


Fig. 11 Substitute damping against recorded earthquake for NBL

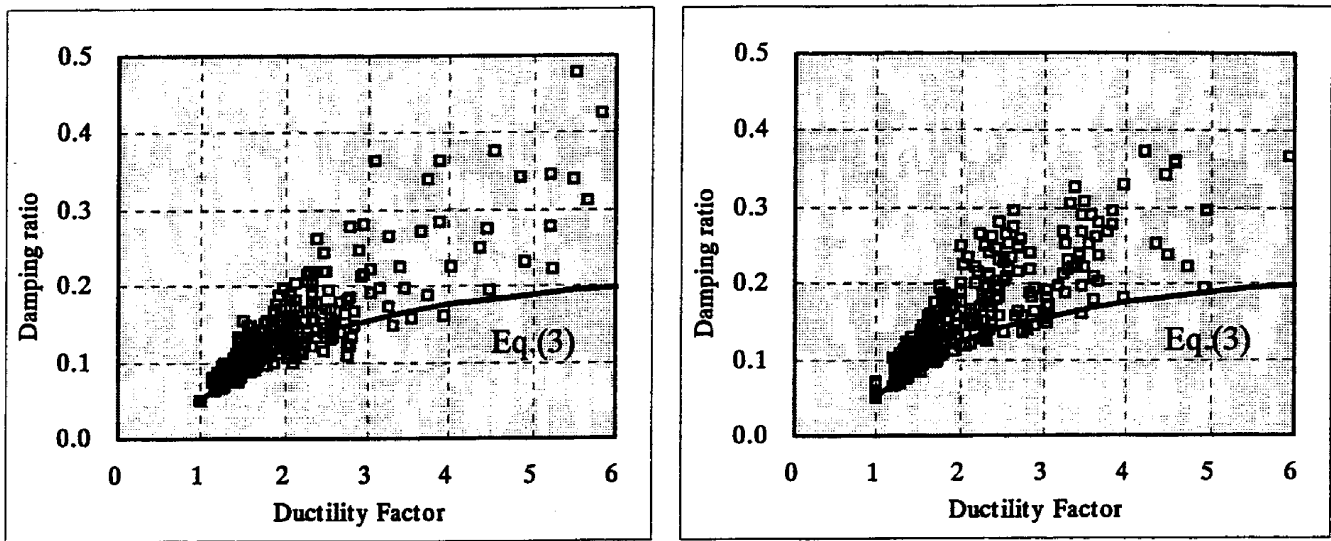


Fig. 12 Substitute damping against recorded earthquake for DBL

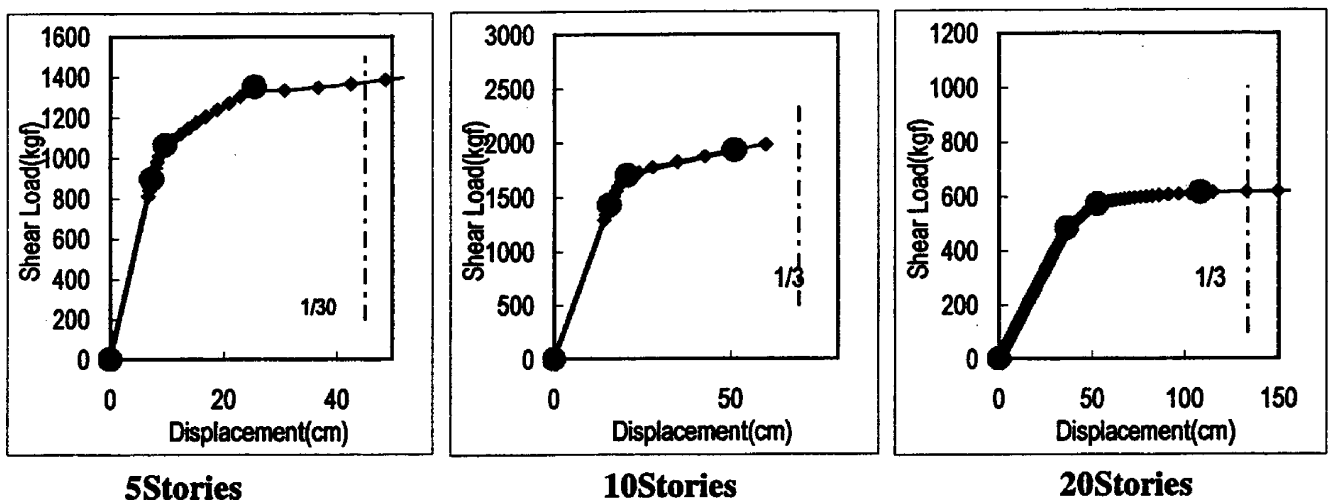


Fig. 13 Push over analysis and Conversion of SDOF for Steel Buildings

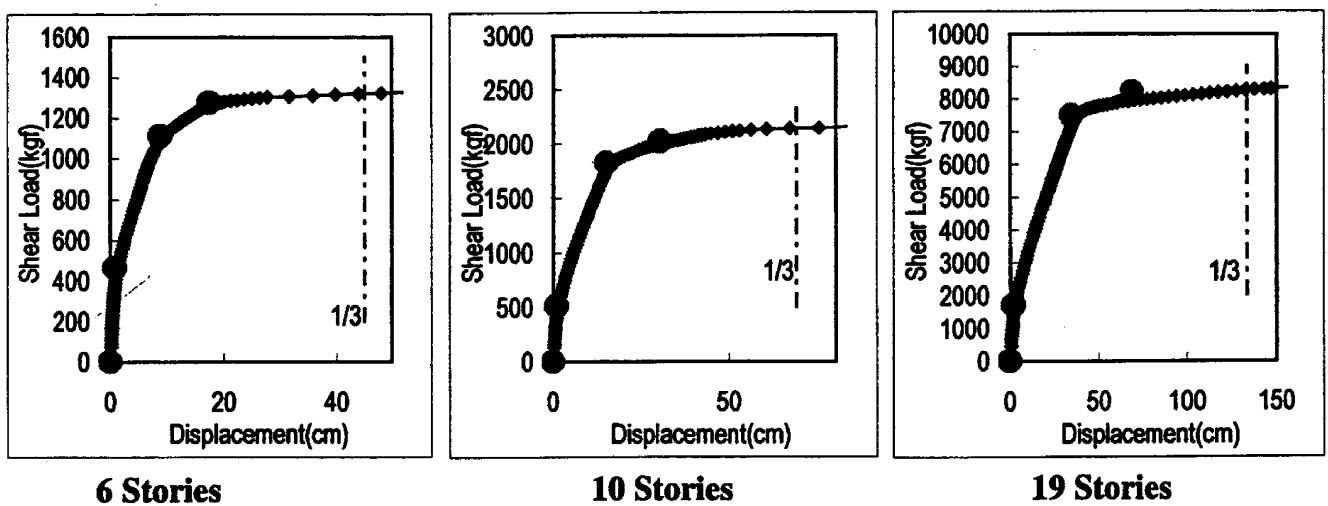
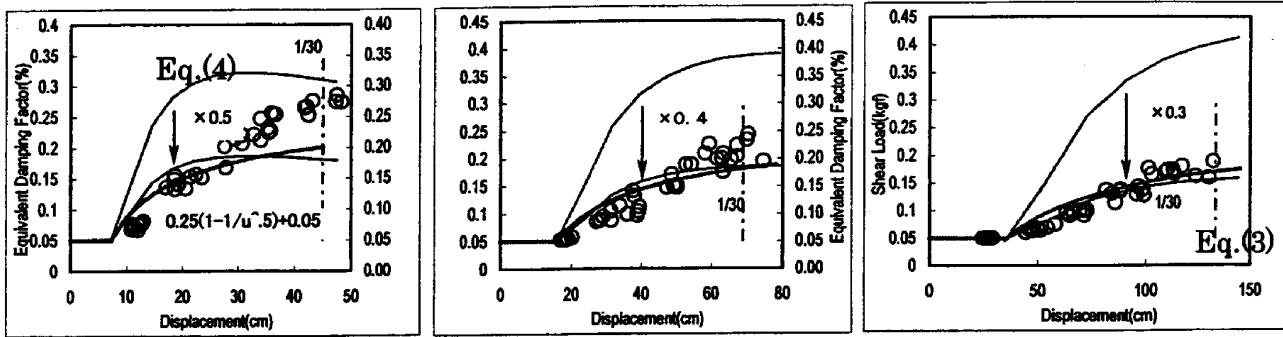


Fig. 14 Push over analysis and Conversion of SDOF for RC Buildings

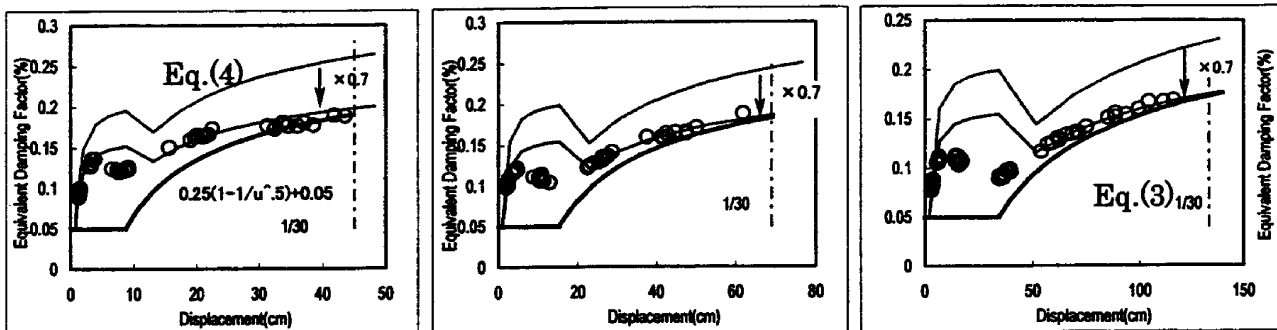


5 Stories

10 Stories

20 Stories

Fig. 15 Normal Tri-linear Model (Steel Structure)



6 Stories

10 Stories

19 Stories

Fig. 16 Takeda model (RC structure)

Direct Displacement-Based Design: Use of Inelastic Design Spectra Versus Elastic Design Spectra

Rakesh K. Goel¹ and Anil K. Chopra²

ABSTRACT

Direct displacement-based design requires a simplified procedure to estimate the seismic deformation of an inelastic SDF system, representing the first (elastic) mode of vibration of the structure. This step is usually accomplished by analysis of an “equivalent” linear system using elastic design spectra. In this paper, an equally simple procedure is developed that is based on the well-known concepts of inelastic design spectra. We demonstrate in this paper that the procedure provides: (1) accurate values of displacement and ductility demands, and (2) a structural design that satisfies the design criteria for allowable plastic rotation. In contrast, the existing procedure using elastic design spectra for equivalent linear systems is shown to underestimate significantly the displacement and ductility demands. The existing procedure is shown to be deficient in yet another sense; the plastic rotation demand on structures designed by this procedure may exceed the acceptable value of the plastic rotation, leaving an erroneous impression that the allowable plastic rotation constraint has been satisfied.

1. INTRODUCTION

Direct displacement-based design is being advocated as a more rational and relevant approach to seismic design of structures compared to traditional strength-based design (Shibata and Sozen, 1976; Moehle, 1992; Kowalsky, Priestley, and MacRae, 1994). Displacement-based design involves several steps (to be described later), one of which is to estimate the seismic deformation of an inelastic SDF system representing the first (elastic) mode of vibration of the MDF system. In some of the present procedures, this step is accomplished by approximate methods in which the nonlinear system is replaced by an “equivalent” linear system (Shibata and Sozen, 1976; Priestley, Seible, and Calvi, 1996). The period and damping of this linear system are determined by the secant stiffness method (Jennings, 1968) or its variants, e.g., the substitute structure method (Shibata and Sozen, 1976).

The purpose of this paper is to demonstrate application of inelastic design spectra to direct displacement-based design of structures. The resulting design procedure is shown to produce a satisfactory structural design. In contrast, it is shown that the design produced by the procedure that uses elastic design spectra and equivalent linear systems does not necessarily satisfy the

¹ Associate Professor, Department of Civil & Environmental Engineering, California Polytechnic State University, San Luis Obispo, CA 93407. Email: rgoel@calpoly.edu

² Johnson Professor, Department of Civil & Environmental Engineering, University of California, Berkeley, CA 94720. Email: chopra@ce.berkeley.edu

design criteria. In particular, it can leave an erroneous impression that the allowable plastic rotation constraint has been satisfied. Note that this paper is a summary of the full-length manuscript recently submitted for publication (Chopra and Goel, 2000).

To focus on this theme, this presentation is intentionally restricted to structures idealized as SDF systems with bilinear force-deformation relations (Figure 1). The distraction of approximations inherent in a one-mode representation of MDF systems and bilinear idealization of a pushover curve are thus avoided.

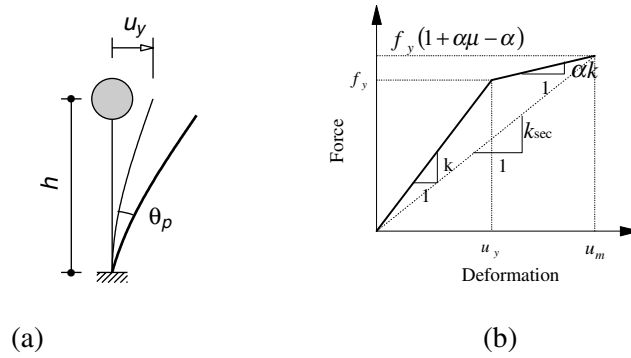


Figure 1. Idealized SDF system with bilinear force-deformation relation.

2. DISPLACEMENT-BASED DESIGN USING ELASTIC DESIGN SPECTRA

2.1 Equivalent Linear System

Needed in existing displacement-based design procedures, the properties of the equivalent linear system are summarized here. Consider an inelastic SDF system with bilinear force-deformation relationship on initial loading (Figure 1b). The stiffness of the elastic branch is k and that of the yielding branch is αk . The yield strength and yield displacement are denoted by f_y and u_y , respectively. If the peak (maximum absolute) deformation of the inelastic system is u_m , the ductility factor $\mu = u_m / u_y$.

For the bilinear system of Figure 1b, the natural vibration period of the equivalent linear system with stiffness equal to k_{sec} , the secant stiffness, is

$$T_{eq} = T_n \sqrt{\frac{\mu}{1 + \alpha\mu - \alpha}} \quad (1)$$

where T_n is the natural vibration period of the system vibrating within its linearly elastic range ($u \leq u_y$).

The most common method for defining equivalent viscous damping is to equate the energy dissipated in a vibration cycle of the inelastic system and of the equivalent linear system. Based on this concept, it can be shown that the equivalent viscous damping ratio is (Chopra and Goel, 1999):

$$\zeta_{eq} = \frac{2(\mu - 1)(1 - \alpha)}{\pi \mu (1 + \alpha \mu - \alpha)} \quad (2)$$

The total viscous damping of the equivalent linear system is

$$\hat{\zeta}_{eq} = \zeta + \zeta_{eq} \quad (3)$$

where ζ is the viscous damping ratio of the bilinear system vibrating within its linearly elastic range ($u \leq u_y$).

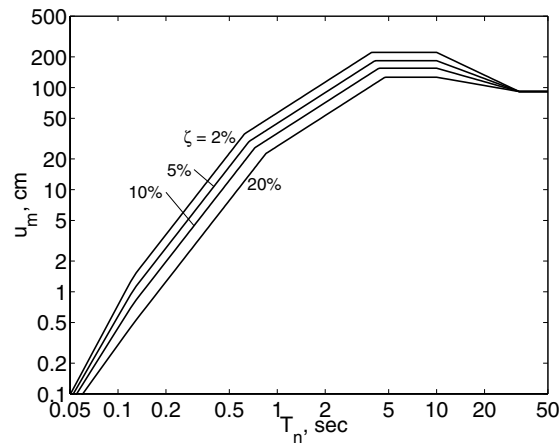


Figure 2. Elastic deformation design spectrum.

2.2 Elastic Design Spectra

To implement the existing displacement-based design procedure, an elastic design spectrum is needed. For this purpose, we have used a median-plus-one-standard-deviation spectrum constructed for peak values of the ground acceleration, velocity, and displacements of $\ddot{u}_{go} = 1g$, $\dot{u}_{go} = 122$ cm/s (48 in/s), and $u_{go} = 91.4$ cm (36 in), respectively, by the procedure of Newmark and Hall (1982). The displacement (or deformation) design spectrum needed in the

displacement-based design is determined from the standard pseudo-acceleration design spectrum, using the well-known relationship between pseudo-acceleration A and deformation D :

$$u_m = D = \left(\frac{T_n}{2\pi} \right)^2 A \quad (5)$$

Figure 2 shows such spectra for several values of the damping ratio.

2.3 Step-By-Step Procedure

Adapted from Priestley and Calvi (1997), a direct displacement-based design procedure for bilinear SDF systems (Figures 1a and 1b) using elastic design spectra is outlined as a sequence of steps:

1. Estimate the yield deformation u_y for the system.
2. Determine acceptable plastic rotation θ_p of the hinge at the base.
3. Determine design displacement u_m

$$u_m = u_y + h\theta_p \quad (6)$$

and design ductility factor $\mu = u_m / u_y$.

4. Estimate the total equivalent viscous damping, $\hat{\zeta}_{eq}$, for the design ductility factor from Equations 2 and 3.
5. Enter the deformation design spectrum for elastic systems with known u_m and $\hat{\zeta}_{eq}$ to read T_{eq} (Figure 2). Determine the secant stiffness

$$k_{sec} = \frac{4\pi^2}{T_{eq}^2} m \quad (7)$$

where m is the mass of the system.

6. Determine the required yield strength f_y from Figure 1b:

$$f_y = \frac{k_{sec} u_m}{1 + \alpha\mu - \alpha} \quad (8)$$

7. Estimate member sizes and detail (reinforcement in R/C structures, connections in steel structures) to provide f_y . Calculate initial elastic stiffness k and $u_y = f_y / k$.
8. Repeat steps 3 to 7 until a satisfactory solution is obtained.

2.4 Example

Consider a portion of a long reinforced-concrete viaduct that is a part of a freeway. The total weight of the superstructure, 190 kN/m, is supported on identical bents 9 m high, uniformly spaced at 39.6 m. Each bent consists of a single circular column 1.5 m in diameter (Figure 3a). Using the design procedure described earlier, we will design the longitudinal reinforcement of the column for the design earthquake defined by Figure 2 scaled to $\ddot{u}_{go} = 0.5g$.

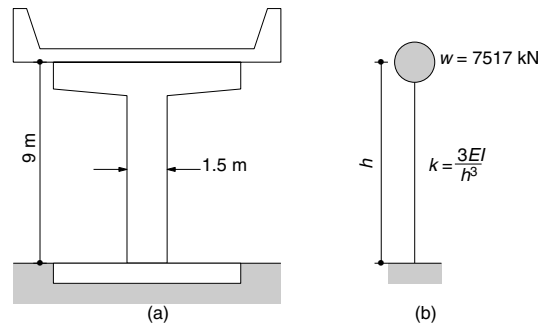


Figure 3. Example single-column bent and idealized SDF system.

For the transverse ground motion, the viaduct can be idealized as an SDF system (Figure 3b) with its lateral stiffness computed from $k = 3EI / h^3$, where E is the elastic modulus of concrete, I is the effective moment of inertia of the reinforced-concrete cross section, and h is the column height. Based on the American Concrete Institute design provisions ACI 318-95, the effective EI for circular columns subjected to lateral load is given by $EI = E_c I_g (0.2 + 2\rho_t \gamma^2 E_s / E_c)$ where I_g is the second moment of inertia of the gross section, E_c and E_s are the elastic moduli of concrete and reinforcing steel, ρ_t is the longitudinal reinforcement ratio, and γ is the ratio of the distances from the center of the column to the center of the outermost reinforcing bars and to the column edge.

The system properties selected are: concrete strength = 27.6 MPa (4 ksi), steel strength = 413 MPa (60 ksi) and $\gamma = 0.9$. The mass of the idealized SDF system is the tributary mass for one bent, i.e., the mass of 39.6 m length of the superstructure, $m = w / g =$

$(7517 \times 1000 \text{ N})/9.8 \text{ m/s}^2 = 767041 \text{ kg}$. The initial elastic vibration period of this system is 1.82 s, which falls in the velocity-sensitive region of the design spectrum.

The step-by-step procedure described earlier in this section is now implemented as follows:

1. An initial estimate of $u_y = 4.5 \text{ cm}$.
2. The plastic rotation acceptable at the base of the column is $\theta_p = 0.02 \text{ radians}$.
3. The design displacement given by Equation 6 is $u_m = u_y + h\theta_p = 4.5 + 900 \times 0.02 = 22.5 \text{ cm}$ and the design ductility factor is $\mu = u_m/u_y = 22.5/4.5 = 5$.
4. For $\alpha = 5\%$ and $\mu = 5$, Equations 2 and 3 give $\hat{\zeta}_{eq} = 45\%$.
5. The deformation design spectrum for elastic systems is constructed for $\hat{\zeta}_{eq} = 45\%$. Corresponding to $u_m = 22.5 \text{ cm}$ this spectrum gives $T_{eq} = 2.81 \text{ s}$ and k_{sec} is computed by Equation 7, $k_{sec} = (2\pi/2.81)^2 \times 767041 = 3.835 \times 10^6 \text{ N/m} = 38.35 \text{ kN/cm}$.
6. The yield strength is given by Equation 8, $f_y = (38.35 \times 22.5)/(1 + 0.05 \times 5 - 0.05) = 719.1 \text{ kN}$.
7. The circular column is then designed using ACI318-95 for axial load due to superstructure weight of 7517 kN plus column self weight of 375 kN and the bending moment due to lateral force = f_y : $M = hf_y = 6472 \text{ kN-m}$. For the resulting column design, $\rho_t = 1.19\%$, flexural strength = 7395 kN-m, and lateral strength = 821.7 kN. For $\rho_t = 1.19\%$, $EI = 2.22 \times 10^6 \text{ kN-m}^2$, $k = 91.3 \text{ kN/cm}$, and $u_y = f_y/k = 821.7/91.3 = 9 \text{ cm}$.
8. Since the yield deformation computed in Step 7 differs significantly from the initial estimate of $u_y = 4.5 \text{ cm}$, iterations are necessary.

The procedure converged after three iterations giving a column design with $\rho_t = 1.3\%$. This column has an initial stiffness, $k = 95.17 \text{ kN/cm}$ and lateral yield strength, $f_y = 839.7 \text{ kN}$. The deformation demand $u_m = 26.8 \text{ cm}$. Due to reason of brevity, results of intermediate iterations are not presented here; they are available in Chopra and Goel (2000).

3. DISPLACEMENT-BASED DESIGN USING INELASTIC DESIGN SPECTRA

Presented next is a direct displacement-based design procedure that uses the well-known constant-ductility design spectra instead of the elastic design spectra for equivalent linear systems.

3.1 Inelastic Design Spectrum

A constant-ductility spectrum for an elastoplastic hysteretic system is a plot of A_y versus the initial elastic period T_n for selected values of μ . The pseudo-acceleration A_y is related to the yield strength f_y by $f_y = (A_y/g)w$ where w is the weight of the system. The yield strength reduction factor is given by $R_y = f_o/f_y = A/A_y$ where $f_o = (A/g)w$ is the minimum yield strength required for the structure to remain elastic during the earthquake; A is the pseudo-acceleration ordinate of the elastic design spectrum at (T_n, ζ) .

A constant-ductility design spectrum is established by dividing the elastic design spectrum by appropriate ductility-dependent factors that depend on T_n ; detailed procedure is described in Chopra (1995, Chapter 7). The Newmark and Hall (1982) recommendations for the reduction factor, R_y , are $\sqrt{2\mu-1}$ in the acceleration-sensitive region, and μ in the velocity- and displacement-sensitive regions. In recent years, several other recommendations for the reduction factor have been developed (Krawinkler and Nassar, 1992; Vidic, Fajfar, and Fischinger, 1994; Miranda and Bertero, 1994).

The peak deformation u_m of the inelastic system is given by:

$$u_m = \mu \left(\frac{T_n}{2\pi} \right)^2 A_y = \mu \frac{1}{R_y} \left(\frac{T_n}{2\pi} \right)^2 A \quad (9)$$

Computed by using Equation 9 and $R_y - \mu$ relations of Newmark and Hall (1982), the deformation design spectrum is shown in Figure 4.

3.2 Step-By-Step Procedure

The first three steps of this procedure are identical to those in the previously-described displacement-based design procedure, and steps 4 to 8 are replaced by the following steps based on the deformation design spectra for inelastic systems (Figure 4).

4. Enter Figure 4 with known u_m and μ to read T_n . Determine the initial elastic stiffness:

$$k = \frac{4\pi^2}{T_n^2} m \quad (10)$$

5. Determine the required yield strength

$$f_y = k u_y \quad (11)$$

6. Estimate member sizes and detail (reinforcement in R/C structures, connections in steel structures, etc.) to provide the strength determined from Equation 11. For the resulting design of the structure, calculate the initial elastic stiffness k and yield deformation $u_y = f_y/k$.

7. Repeat steps 3 to 6 until a satisfactory solution is obtained.

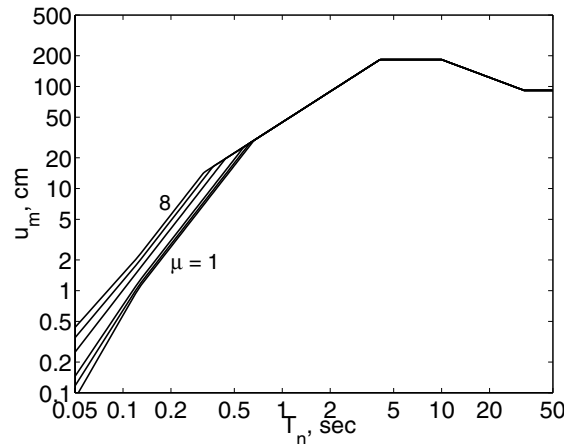


Figure 4. Inelastic deformation design spectra.

The graphical implementation of Step 4 in the modified design procedure may be attractive for its similarity to the previous procedure. However, the graphical feature is not essential and the Step 4 can be implemented numerically; from Equation (9)

$$T_n = 2\pi \sqrt{\frac{u_m R_y}{A \mu}} \quad (12)$$

where R_y and μ are related, for example, by relations of Newmark and Hall (1982). Because this relation depends on T_n , iteration may be necessary to determine T_n from Equation 12.

3.3 Example

The step-by-step procedure described in this section is now implemented for the system designed previously by the displacement-based design procedure using the elastic design spectra.

1. An initial estimate of $u_y = 4.5$ cm.
2. The plastic rotation acceptable at the base of the column is $\theta_p = 0.02$ radians.
3. The design displacement given by Equation 6 is $u_m = u_y + h\theta_p = 4.5 + 900 \times 0.02 = 22.5$ cm and the design ductility factor is $\mu = u_m / u_y = 22.5 / 4.5 = 5$.
4. The deformation design spectrum for inelastic systems is constructed for $\mu = 5$. Corresponding to $u_m = 22.5$ cm, this spectrum gives $T_n = 1.01$ s and k is computed by Equation 10, $k = (2\pi / 1.01)^2 \times 767041 = 29.9 \times 10^6$ N/m = 298.7 kN/cm.
5. The yield strength is given by Equation 11, $f_y = ku_y = 298.7 \times 4.5 = 1344$ kN.
6. The circular column is then designed using ACI318-95 for axial load due to superstructure weight of 7517 kN plus column self weight of 375 kN and the bending moment due to lateral force = f_y : $M = hf_y = 12096$ kN-m. For the resulting column design, $\rho_t = 3.62\%$, flexural strength = 12976 kN-m, and lateral strength = 1441 kN. For $\rho_t = 3.62\%$, $EI = 4.24 \times 10^6$ kN – m², $k = 174.4$ kN/cm, and $u_y = f_y / k = 1441 / 174.4 = 8.27$ cm.
7. Since the yield deformation computed in Step 6 differs significantly from the initial estimate of $u_y = 4.5$ cm, iterations are necessary.

The procedure converged after five iterations giving a column design with $\rho_t = 5.5\%$. This column has an initial stiffness, $k = 238.6$ kN/cm and lateral yield strength, $f_y = 1907$ kN. The deformation demand $u_m = 26.0$ cm. Due to reason of brevity, results of intermediate iterations are not presented here; they are available in Chopra and Goel (2000).

4. EVALUATION OF EXAMPLE DESIGNS

The column design resulting from both procedures is evaluated in this section. Whether a design is satisfactory will be judged by calculating the deformation demand and plastic rotation demand

imposed by the design earthquake. These demands can be computed for a system with known properties (initial elastic stiffness, k , mass, m , and yield-strength f_y) by the following procedure:

1. Calculate the initial elastic period, T_n , from the known mass, m , and the initial elastic stiffness, k .
2. Determine the pseudo-acceleration A from the elastic design spectrum; the elastic design force, $f_o = (A/g)w$.
3. Calculate the yield-strength reduction factor, $R_y = f_o / f_y$, in which f_o is computed in Step 2 and f_y is known yield-strength of the designed system.
4. Determine the ductility demand μ using the $R_y - \mu - T_n$ relations.
5. Calculate u_m from Equation 9, and θ_p from Equation 6, where $u_y = f_y / k$ and f_y is known yield-strength of the system.

The deformation and plastic rotation demands are computed by this procedure for the example system and compared with those estimated by the two afore-mentioned design procedures.

4.1 Structural Design Using Elastic Design Spectra

In designing the structure by using the elastic design spectra for equivalent linear systems, the deformation of the designed structure was estimated to be 26.8 cm. However, when the designed structure is analyzed, the deformation demand is 39.7 cm. Which of the two values is more accurate? Clearly it is the latter value because it comes from inelastic design spectra which are based on nonlinear response history analyses of inelastic systems considering a wide range of system parameters and many ground motions (Krawinkler and Nassar, 1992; Vidic, Fajfar, and Fischinger, 1994). In contrast, the former value comes from an approximate procedure based on equivalent linear systems, a procedure that is known to be inaccurate (Chopra and Goel, 2000). Thus the design procedure has underestimated the deformation demand by 32.6%.

The displacement-based design procedure based on elastic design spectra for equivalent linear systems has additional deficiencies. Although the structure was designed for an acceptable value of the plastic rotation $\theta_p = 0.02$ radians, the plastic rotation demand = 0.0343 radians, 72% more than the acceptable value. Thus the design procedure leaves an erroneous impression that the allowable plastic rotation constraint has been satisfied.

4.2 Structural Design Using Inelastic Design Spectra

In designing the structure by the procedure based on inelastic design spectra, the deformation demand for the designed structure was estimated to be 26.0 cm. When the designed structure is analyzed, the deformation demand is 25.9 cm. Clearly the design procedure has estimated the deformation demand consistent with that predicted by well-established concepts of inelastic design spectra. Furthermore, the plastic rotation demand of 0.0199 radians is essentially identical to the acceptable value of 0.02 radians that was imposed on the design, and the proposed procedure has produced a satisfactory design.

Note that for the examples considered, the displacement-based design procedure using inelastic design spectra leads to a structure with more longitudinal reinforcement and thus higher strength compared to the design based on elastic design spectra for equivalent linear systems. A stronger column is necessary to satisfy the selected design criteria.

5. CONCLUSIONS

Direct displacement-based design requires a simplified procedure to estimate the seismic deformation of an inelastic SDF system, representing the first (elastic) mode of vibration of the structure, an MDF system. A simplified procedure that uses the well-known inelastic design spectra has been presented in this paper. With the aid of examples, it has been demonstrated that the procedure (1) provides displacement estimates consistent with those predicted by the well-established concepts of inelastic design spectra, and (2) produces a structural design that satisfies the design criteria for acceptable plastic rotation.

The displacement-based design procedure proposed by several researchers in recent years uses elastic design spectra for equivalent linear systems based on the secant stiffness method or its variations like the substitute structure method. In this paper, we have demonstrated that the deformation and ductility factor that are estimated in designing the structure by this procedure are much smaller than the deformation and ductility demands determined by nonlinear analysis of the system using inelastic design spectra. Furthermore, it has been shown that the plastic rotation demand on structures designed by this procedure may exceed the acceptable value of the plastic rotation. Thus, the design procedure leaves an erroneous impression that the allowable plastic rotation constraint has been satisfied.

6. ACKNOWLEDGMENTS

This research investigation is supported by the National Science Foundation under Grant CMS-9812531. The authors are grateful for this support.

7. REFERENCES

- Chopra, A. K. (1995). *Dynamics of structures: Theory and applications to earthquake engineering*. Prentice Hall, Upper Saddle River, NJ.
- Chopra, A. K. and Goel, R. K. (2000). Direct displacement-based design: use of inelastic design spectra versus elastic design spectra. Submitted for Publication to *Earthquake Spectra*, EERI.
- Chopra, A. K. and Goel, R. K. (2000). Evaluation of a NSP to estimate seismic deformation: SDF systems. *Journal of Structural Engineering*, ASCE, Vol. 126, No. 4, pp. 482-490.
- Chopra, A. K. and Goel, R. K. (1999). Capacity-demand-diagram methods for estimating seismic deformation of inelastic structures: SDF systems. *Report No. PEER-1999/02*, Pacific Earthquake Engineering Research Center, University of California, Berkeley, April.
- Jennings, P. C. (1968). Equivalent viscous damping for yielding structures. *Journal of the Engineering Mechanics Division*, ASCE, Vol. 94, No. EM1, pp. 103-116.
- Kowalsky, M., Priestley, M. J. N., and MacRae, G. A. (1994). Displacement-based design of RC bridge columns. *Proceedings, 2nd International Workshop on the Seismic Design of Bridges*, Queenstown, New Zealand, Vol. 1, pp. 138-163.
- Krawinkler, H., and Nassar, A. A. (1992). Seismic design based on ductility and cumulative damage demands and capacities. *Nonlinear Seismic Analysis and Design of Reinforced Concrete Buildings*, P. Fajfar and H. Krawinkler, Eds., Elsevier Applied Science, New York, 1992.
- Miranda, E., and Bertero, V. V. (1994). Evaluation of strength reduction factors for earthquake-resistant design. *Earthquake Spectra*, Vol. 10, No. 2, pp. 357-379.
- Moehle, J. P. (1992). Displacement-based design of R/C structures subjected to earthquakes. *Earthquake Spectra*, Vol. 8, No. 3, pp. 403-427.
- Newmark, N. M., and Hall, W. J. (1982). *Earthquake Spectra and Design*. Earthquake Engineering Research Institute, Berkeley, CA.
- Priestley, M. J. N., Seible, F., and Calvi, G. M. (1996). *Seismic design and retrofit of bridges*. John Wiley & Sons, New York, NY.
- Priestley, M. J. N., and Calvi, G. M. (1997). Concepts and procedures for direct displacement-based design. *Seismic Design Methodologies for the Next Generation of Codes*, Fajfar and Krawinkler (eds), Balkema, Rotterdam, pp. 171-181.
- Shibata, A., and Sozen, M. A. (1976). Substitute structure method for seismic design in R/C. *Journal of the Structural Division*, ASCE, Vol. 102, No. ST1, pp. 1-18.
- Vidic, T., Fajfar, P., and Fischinger, M. (1994). Consistent inelastic design spectra: strength and displacement, *Earthquake Engineering and Structural Dynamics*, Vol. 23, No. 5, pp. 507-521.

SESSION A-2: INELASTIC RESPONSE OF STRUCTURES

Chaired by

◆ Yahya Kurama and Hiroshi Kuramoto ◆

DISPLACEMENT RESPONSES OF REINFORCED CONCRETE STRUCTURES WITH FLEXIBLE FOUNDATION

Toshimi KABEYASAWA¹,

YOO Choon-Sook², KIM You-Sok² and Kazuyoshi KUDO³

ABSTRACT

The effects of soil-structure interaction (SSI) on the seismic response demand of the buildings are studied through observation and simulation. Dense observation system of seismographs has been set up in school buildings and shallow soil to identify the effect of SSI on the response of the buildings including inelastic behaviour of soil. The observed response under a moderate earthquake is analysed by the detailed frame model with and without SSI. A better correlation is observed in case of the analysis with SSI. A parametric study on the effects of SSI was conducted using a simple model with elasto-plastic behavior of both structure and soil. The results indicate that SSI effects are higher only in the cases with inelastic behaviour both in structure and soil. The theoretical background based on energy distribution is being studied.

1. INTRODUCTION

Analytical studies on the dynamic response of soil-structure interaction (SSI) systems have been well conducted in the past decades. Theoretical backgrounds in simple cases of elastic behavior and stationary response have been understood with various numeral analyses (Jennings and Bielak, 1973, Veletsos and Meek 1974). In these cases, the response including SSI is generally smaller than that which would occur in the cases if the structures were on the fixed base. This is mainly because of the energy dissipated by radiation and internal friction into the soil. However, the rocking and lateral swaying of the foundation would also increase the response of building due to the resonance of the SSI system to the peculiar frequency of the input motion. The result of numerical analyses where the latter effect is dominant has been reported for nonlinear SSI systems(Bielak, 1978).

On the other hand, the effects of soil-structure interactions have not verified well yet neither through shaking table tests nor through site observations with actual SSI systems. It is very difficult to conduct the dynamic test on SSI system, whereas the observation data available

¹ Earthquake Research Institute, The University of Tokyo
Email: kabe@eri.u-tokyo.ac.jp

² Graduate student, Department of Architecture, The University of Tokyo
Email: ycs@eri.u-tokyo.ac.jp

³ Earthquake Research Institute, The University of Tokyo
Email: kudo@eri.u-tokyo.ac.jp

for the verification of the effect of SSI is very much limited. As for the observation, only the accelerogram observed on the base of the building is not enough for the verification of the SSI effect, although it is the record as a result of SSI response. In that case the motion which would have occurred without SSI system, in other words, recorded in a comparable free field, must be estimated. The records in the structure with those in the soils and on near free field are very few so far.

The purpose of this study is to investigate the effects of soil-structure interaction (SSI) on the seismic response demand of the buildings through observation and simulation. Dense observation system of seismographs on school buildings and shallow soil developed by ERI research group are introduced. The results of the SSI analysis on the observed responses under a moderate earthquake are presented. Collaterally, a parametric study with simple SSI model is conducted taking elasto-plastic behavior in both structure and soil into account.

2. OBSERVATION IN EXISTING BUILDINGS

2.1 Description of the observed buildings

Dense observation system of seismographs on building and soil has been set up at school buildings of Seisho High School in Odawara city. The observation started from August of 1999. Two buildings called as D-building and E-building of the school were selected for the instrumentation. The E-building is a pilotis-type (soft-first story) structure and is observed with other objective than the research on SSI. The observation only for the D-building is reported here.

The D-building of the Seisho High School is a 4-story reinforced concrete frame structure which has a rectangular plan of 48.0m in longitudinal (E-W) direction and 9.6m in transverse (N-S) direction. The total height of the building is 18m. Figure 1 shows a view of this building from south.

The floor plan, which is common from the first to the third floor, is shown in Fig. 2. The structural system is typical as standard school buildings in Japan. Three frames in the longitudinal direction are regular open frames with 4.8m span beams. Seven frames out of the eleven frames in the transverse direction have wall panels. Incidentally, the lateral stiffness or fundamental periods in the two directions were almost identical, 2.5 second, both by calculation and by observation, despite of the different structural types.

The building is supported by the foundation of PC-piles. The soil classification by a boring inspection is shown in Figure 2. The ground is relatively soft soil with silt. P-wave and S-wave velocities were reported as 90m/sec to 200m/sec down to 8m from the ground level and 230m to 1700m below 8m.



Figure 1. A south view of D-building

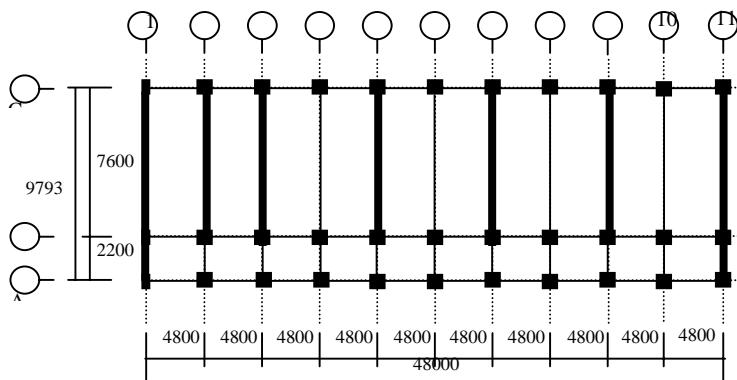


Figure 2. A typical floor plan of D-building

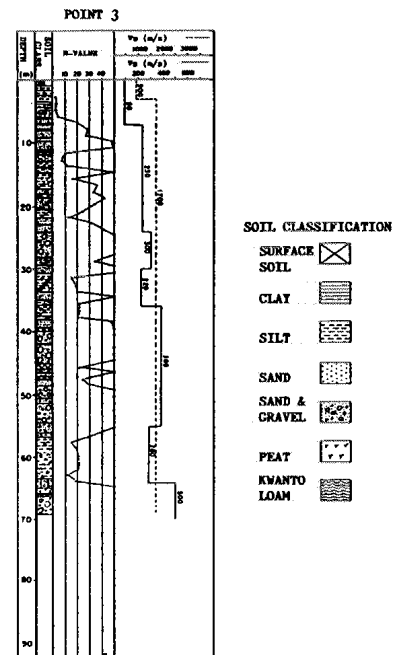


Figure 3. Soil conditions

2.2 Instrumentation of seismometers on the building and soil

The strong-motion instrumentation was implemented as shown in Figure 3. Six triaxial accelerometers (six sensors of 18 channels in total) are located in the building and soil: (1) GL-6m under the nearby free field at 17m east from the building, (2) GL-1m at the nearby free field, (3) GL-6m underneath the building, (4) the south end on the foundation beam at the east side of the building, (5) the north side of the same foundation beam, and (6) roof beam level above the location(5). Data is recorded at a rate of 100 Hz per channel. From these seismographs, differences between motions at the base of the building and at the free field, the response of the structures and rocking of foundation, shear strains of soils, from which SSI model will be verified.

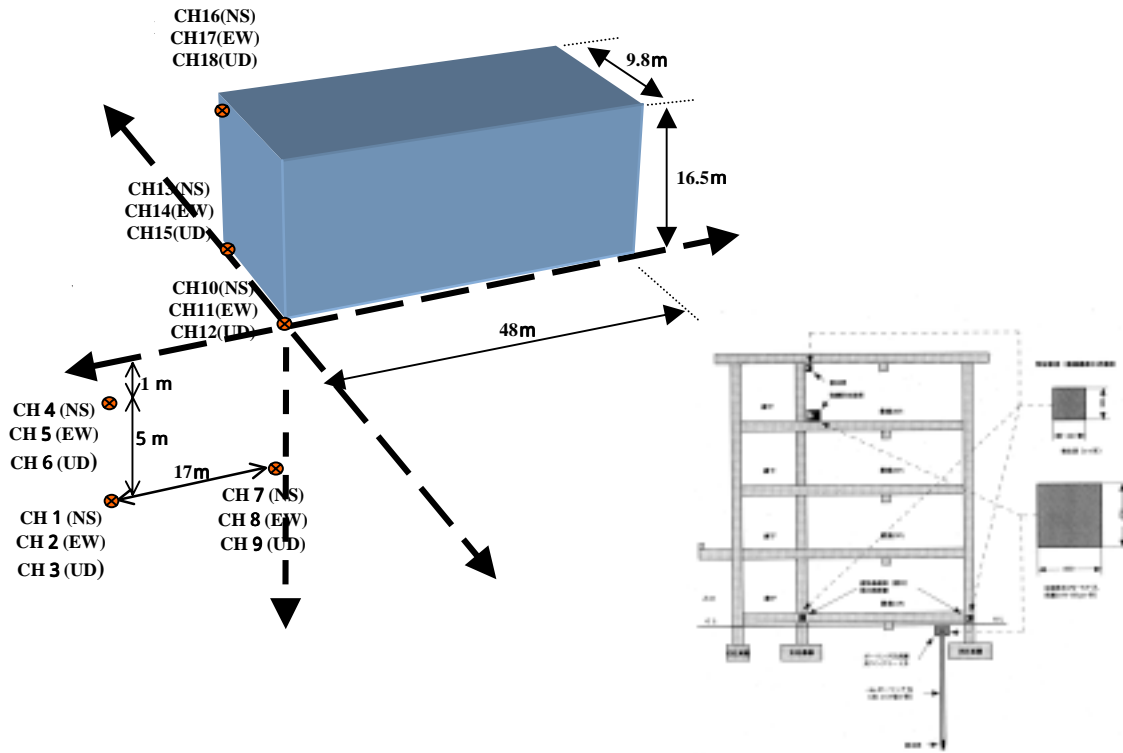


Figure 4. Location of accelerometers in D-building and near free field

2.3 Recorded data

A moderate earthquake motion was recorded on September 13, 1999. The acceleration data filtered with Butterworth order 4 at 0.1 Hz. The maximum accelerations of all the channels are listed in Table 1. The waveforms of the only NS component, which are used for the SSI analysis, are shown in Figure 5 with their Fourier spectrum.

Table 1. Maximum accelerations in gal

	component		
	NS	EW	UD
Free field GL-6m	10.05	11.30	5.25
Free field GL-1m	23.20	22.29	5.47
Beneath Building GL-6m	13.44	14.98	5.70
1st floor of building(south)	26.39	27.89	8.40
1st floor of building(north)	26.85	28.65	8.60
Roof level of building	60.70	52.20	7.64

2.4 Analysis of the building considering soil-pile-building interaction

The recorded data were simulated by the SSI model shown in Fig. 6. The building was idealized using three-line-element model for the wall. The sway and rocking are considered by the springs and dashpots connected to the rigid base.

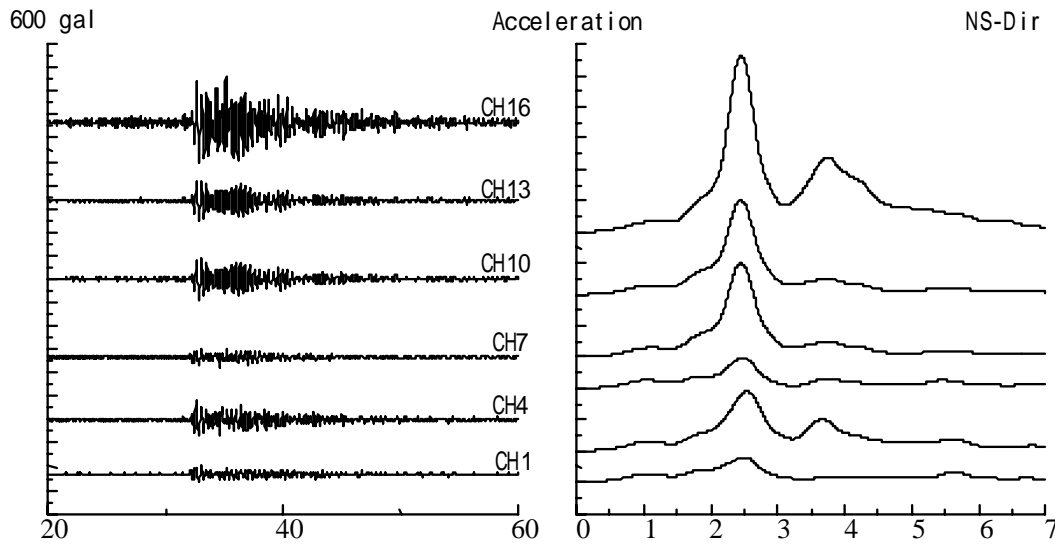


Figure 5 NS components of the accelerograms recorded on September 13, 1999, and the Fourier spectrum

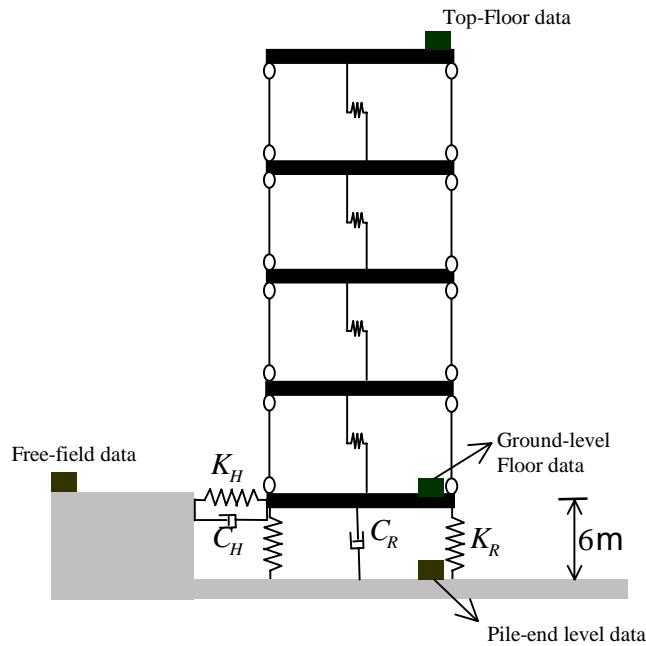


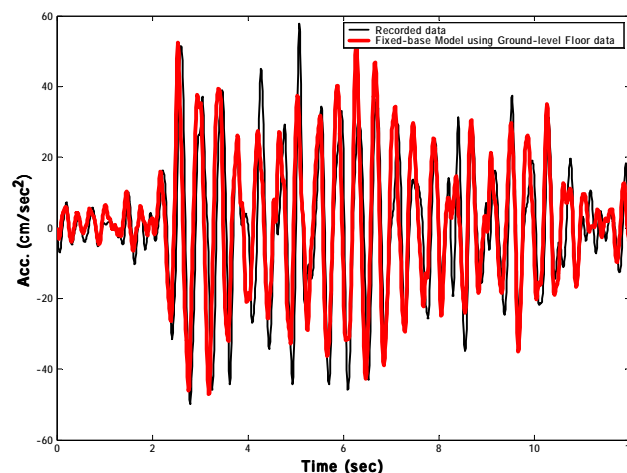
Figure 6 . SSI model for the simulation of the observed data

The characteristics of these springs for sway and rocking are determined as follows considering lateral stiffness of the piles in the soil (Novak, 1974). The response of building-foundation systems including seismic soil-pile-superstructure interaction (SSPSI) can be computed as the superposition of two effects: (1) a so-called kinematic interaction effect and (2) an inertial interaction effect. This superposition is exact for linear soil, pile and structure, and could be applied to moderately non-linear systems. For computational convenience and conceptual simplicity, each one of the above two stages can be further subdivided into two independent analysis steps, as follows:

(1) For the kinematic response: (a1) analysis of the free-field soil response (i.e. without the presence of piles) to vertically incident S-waves; and (a2) analysis of the interaction of the single pile or pile group with the surrounding soil, driven by the free-field response of step (a1).

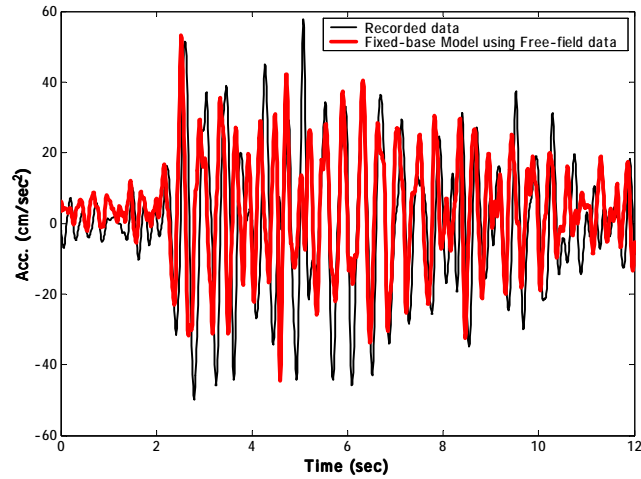
(2) For the inertial response: (b1) computation of the dynamic impedances at the pile head or the pile-group cap, associated with the swaying and rocking motion of the foundation; and (b2) analysis of the dynamic response of the superstructure supported on the springs and dashpots of the step (b1), subjected to the kinematic pile-head motion of the step (a2). The damping coefficients of the superstructure and the foundation were assumed as 0.05 and 0.10 respectively.

The calculated responses by the SSI model and the fixed base model are compared with the observed for the time-history of the roof level acceleration as shown in Figure 7. Figure 7(a) compares the analytical case where the responses are calculated by the fixed base model using the accelerogram (CH13) recorded at the base, on the foundation beam of the building. A good correlation is observed, from which it may be concluded that the modelling of the superstructure is rigorous. Figure 7(b) compares the analytical case where the responses are also calculated by the fixed base model using the accelerogram (CH4) recorded at the surface (GL-1m) of the free field. The calculated response are generally smaller than the observed. Figure 7(c) compares the analytical case where the responses are calculated by the SSI model using the accelerogram (CH7) recorded in the soil of GL-6m. under the building. A much better correlation is observed in the case (c) than in the case (b) where the free field motion is used.

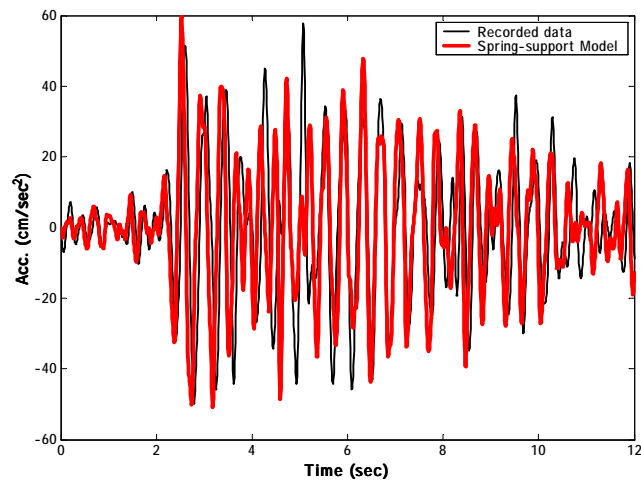


(a) Fixed base model under the accelerogram on the base of building

Figure 7 Calculated and observed responses of roof level acceleration



(b) Fixed base model under the accelerogram on the free field



(c) SSI model under the accelerogram in the soil of GL-6m

Figure 7. Calculated and observed responses of roof level acceleration

In the observed system, the fundamental frequencies of the ground and the SSI system are 2.5 Hz and incidentally identical as shown in Figure 5. Therefore, it is estimated that the response with the SSI system becomes larger than that of fixed base model under the free field record as is observed and calculated in above cases. As for the displacement response calculated from the accelerogram, the ratio of the roof level displacement due to the rocking was about half of the total deformation.

3. SIMPLE NON-LINEAR SSI ANALYSIS

It is well known that the earthquake response of the soil-structure interaction (SSI) system is generally smaller than that of the fixed base system, because the input energy to the SSI

system is dissipated by both radiation and hysteretic action in the soil. However, this is not always the case because of the hysteretic behavior of the structure and soil in the SSI system. That is, in case of elastic structure and elastic soil system (ESES_o) or elastic structure and inelastic soil system (ESIS_o), the response would generally be smaller by the effect of SSI. However, the responses of inelastic structure and elastic soil system (ISES_o) could be different. Furthermore, few studies have been conducted on the inelastic structure and inelastic soil system (ISIS_o), for which the effect has not yet been formulated in general. The specific objective of this study is to compare the earthquake responses of the four different SSI systems (ESES_o, ESIS_o, IPES_o, ISIS_o), characterized by the hysteretic behavior of the structure and soil, with the associated fixed base system in terms of energy dissipation.

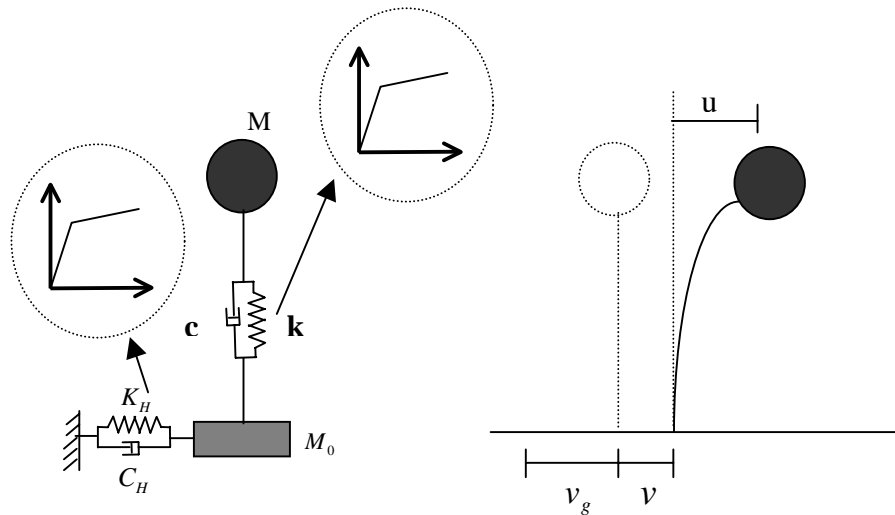


Figure 8. Single-degree-of-freedom system on flexible soil

A simple model was used for the SSI response analysis as shown in Figure 8, which consists of two masses: M representing superstructure is lumped at the height of H from the ground level and M_0 representing foundation with the radius of r . The inelastic springs of the superstructure and the soil are assumed to have a bilinear hysteretic restoring force with the yield strength of $Q_{y,str.}$ and $Q_{y,soil}$. The shear coefficients of the structure and the soil may be expressed using the total mass above the spring as $C_{y,str.} (= Q_{y,str.} / Mg)$ and $C_{y,soil} (= Q_{y,soil} / (Mg + M_0g))$, respectively. In this study, the initial stiffness, K_H , and damping factor, C_H , associated with the soil are assumed to be frequency-independent, because the hypothesis of frequency-independent soil parameters leads to results with

sufficient accuracy for most of buildings and the values used herein as follows (Parmelee, 1970);

$$K_H = \frac{6.77}{1.79 - \nu} Gr$$

$$C_H = \frac{6.21}{2.54 - \nu} \rho V_s r^2$$

where, ν : poisson's ratio for soil, G : shear modulus of soil, V_s : shear wave velocity of soil, ρ : mass density of soil.

As can be seen from Figure 8, only sway motion of foundation is considered. Hence, the equation of motion of the structure-foundation model in coupled horizontal translation can be written as follows:

$$M (\ddot{u} + \ddot{v} + \ddot{v}_g) + c\dot{u} + Q(k, \dot{u}, u) = 0$$

$$M_0 (\ddot{v} + \ddot{v}_g) + C_H \dot{v} + Q_0(K_H, \dot{v}, v) - c\dot{u} - Q(k, \dot{u}, u) = 0$$

In these equation, u is the horizontal displacement of the top mass relative to the base, which results from the deformation of the superstructure. $Q(k, \dot{u}, u)$ and $Q_0(K_H, \dot{v}, v)$ is the restoring force function of the structure and the foundation springs respectively, assumed as bilinear. The coefficients c and C_H are for the damping of the structure and the soil. v is the translation of the base mass in addition to the free field motion, whereas v_g is the field horizontal ground displacement. And the total energy dissipation in the SSI system, E_{SSI} is decomposed as follows:

$$E_{SSI} = E_{str} + E_{soil} = E_{D, str} + E_{Y, str} + E_{D, soil} + E_{Y, soil}$$

where, E_{str} is the total input energy to the structure, which is dissipated by the viscous damping ($E_{D, str}$), and the hysteretic energy ($E_{Y, str}$) in structure; E_{soil} is the total energy to the soil spring dissipated by the viscous damping ($E_{D, soil}$) and the hysteretic energy ($E_{Y, soil}$) in the soil.

A preliminary parametric study was conducted by using the parameters frequently discussed in the analysis of SSI system: (1) the ratio V_s / r of the shear wave velocity of the soil to the radius of the foundation, which characterizes the foundation properties, the ratio H / r of the height of the structure to the foundation radius, the ratio M_0 / M of the foundation mass to the mass of the superstructure, the percentage of critical damping of the structure in its fixed-base

condition, ζ , Poisson's ratio for the soil, ν , and the relative mass density for the structure and the soil, $\delta = M / \rho \pi r^2 H$.

Though the results obtained from these preliminarily parametric study are not presented here except for those from major parameters, V_s / r and H / r , because they are consistent with those of previous studies. As can be seen in Figure 9(a) resulted from the analysis of ESESo, the SSI effect on the maximum displacement response increase with H / r and decrease with V_s / r .

In terms of the energy dissipation in the soil, these results can be interpreted as follows: with increasing H / r and decreasing V_s / r , the energy dissipated by radiation damping in the soil, $E_{D,soil}$ is increased. This also means that the energy input to the structure, $E_{str.}$ is reduced (Figure 9b) and the response of the building therefore becomes small. The tendency of the effect was generally observed in the other SSI systems (ESISo, ISESo, ISISo) with inelastic properties of the springs, though the effect become smaller that in the elastic SSI system. It should be noted that the ratio H / r , known to the key parameter governing the rocking motion of the foundation, affects the SSI effect, although the rocking motion component is not considered here.

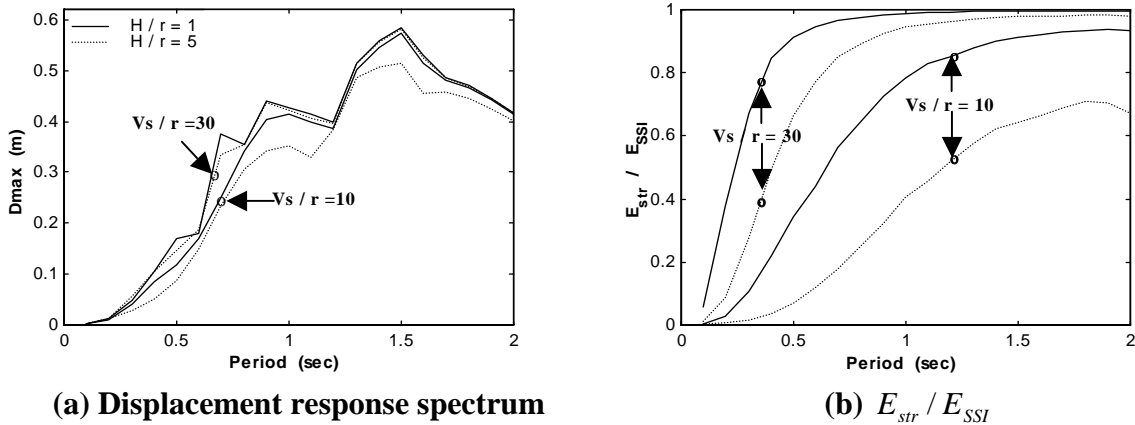
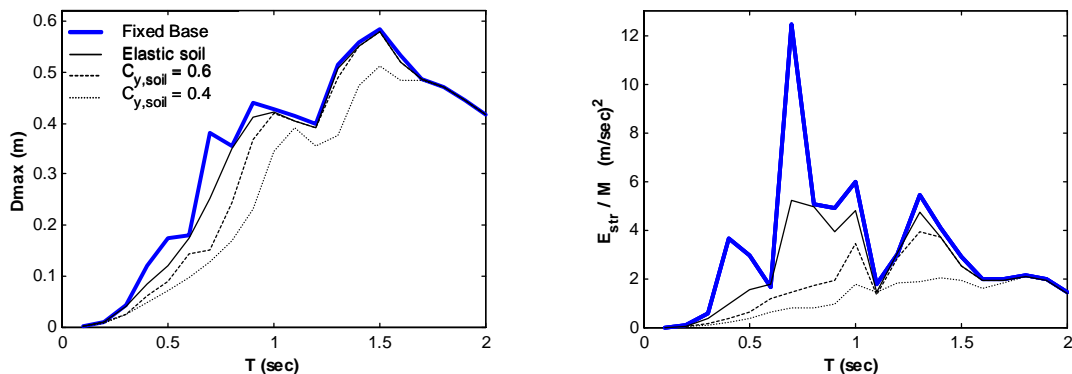


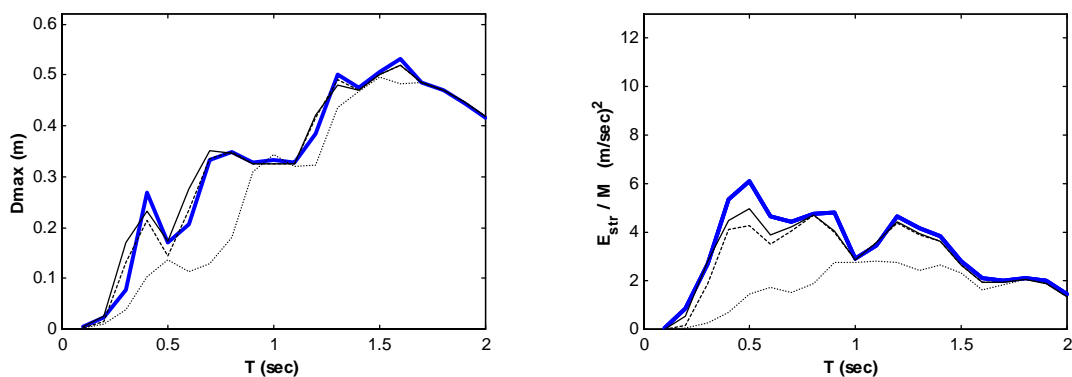
Figure 9. Effects of the parameter, H / r and V_s / r (ESES0)

Based on these results, a rather small value of V_s / r , 10 sec^{-1} is used for the analysis conducted herein, and M_0 / M is taken as 1.0; ζ as 0.02; and ν as 0.45. The rocking motion of the foundation not considered herein. A small value of H / r , 1 is used, for which the effect of rocking motion would be negligible compared to that of sway motion. Therefore, the main

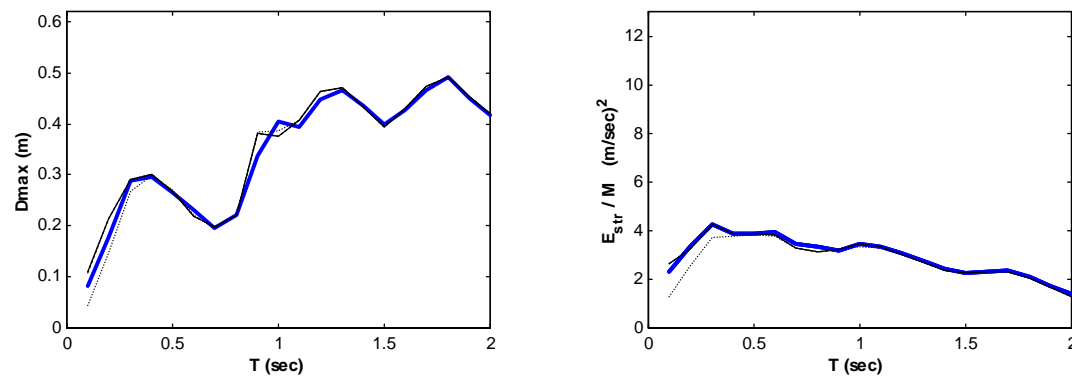
parameters used in the following analysis are the elastic or inelastic properties of the SSI systems and their shear coefficients, $C_{y, str.}$, $C_{y, soil}$.



(a) Elastic superstructure



(b) $C_{y, str} = 0.8$



(c) $C_{y, str} = 0.4$

Figure 10. Displacement response and energy spectrum

Several earthquake records are used for the analysis with the original acceleration levels, from which the responses to JMA Kobe(NS) are discussed in detail below. The displacement response spectrum and energy input to the four SSI systems are presented in Figure 10 with those of the fixed base system, from which the followings may be observed: (1) In the system

with inelastic soil, the differences of displacement response and the energy input to the structure between SSI system and fixed base system increase with decreasing $C_{y,soil}$ (Figure 10a). (2) SSI effect is less significant in case of inelastic response of the superstructure rather than in case of elastic response. (3) The responses of the system with inelastic structure and soil (ISISo) are not so different from those of the fixed base system. The response of SSI system exceeds that of the associated fixed base system in some period region (Figure 10b,c). (4) The displacement response of the fixed base system is not always larger than that of SSI system, though, in all systems, the energy input to the fixed base system is larger than that to the SSI system.

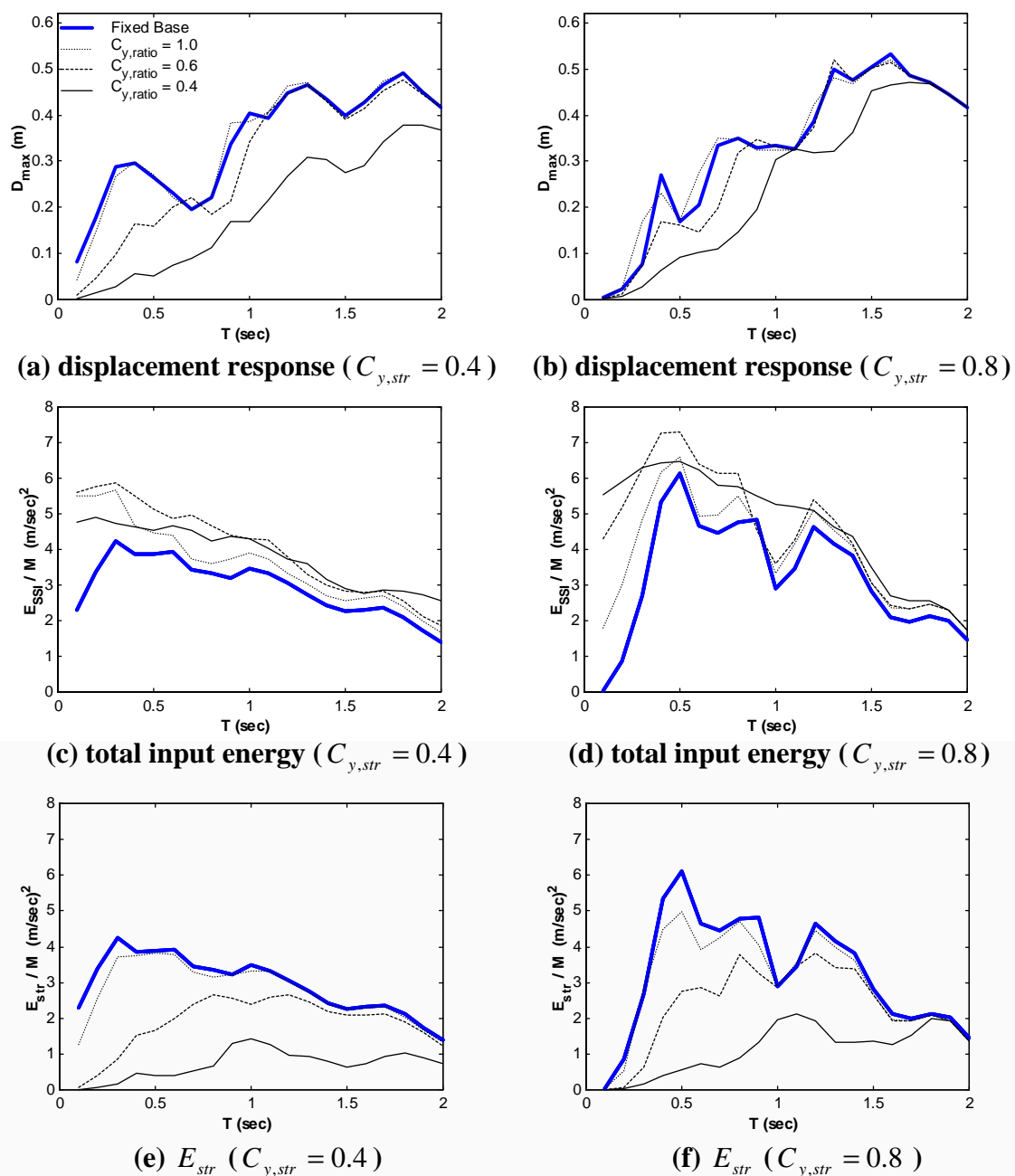


Figure 11. Displacement response and energy spectrum

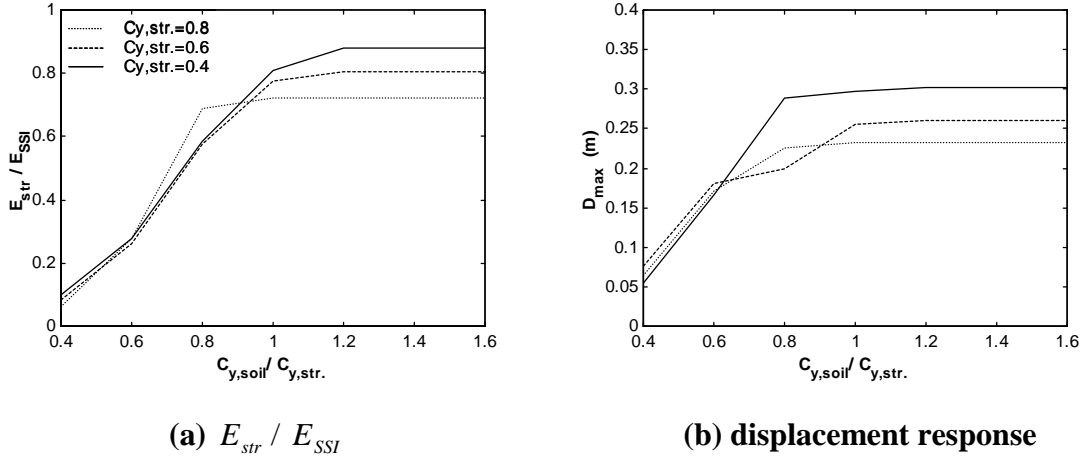


Figure 12. Energy and displacement response spectrum for the system with the fundamental period of $T=0.4$

It is revealed from these results that the SSI effects due to energy dissipation in the soil are dependent on the elastic or inelastic characteristics of the superstructure and soil of SSI system (ESES_o, ESIS_o, ISES_o, ISIS_o). Furthermore, it is greatly affected by the inelasticity of SSI system and the ratio of $C_{y,soil} / C_{y,str}$ governing the ratio $E_{Y,soil} / (E_{Y,soil} + E_{Y,str})$ of yielding energy dissipated in the soil to both in the soil and structure. For this reason, it is more instructive to plot the spectra for the value of $C_{y,ratio}$ ($C_{y,soil} / C_{y,str}$) rather than $C_{y,soil}$ and needed to plot the spectra for E_{SSI} in addition to the input energy to the structure, E_{str} for the SSI system of ISIS_o. Such plots are given in Figure 11 for ISIS_o with $C_{y,str} = 0.4, 0.8$.

It is clear from Figure 11c,d that the total energy input to the SSI system, E_{SSI} is larger than that of the fixed base system and the influence of $C_{y,ratio}$ on E_{SSI} is more significant in short period region rather than long one. And same as the above results, the dissipated energy in soil, E_{soil} ($E_{SSI} - E_{str}$), becomes large in the small value of $C_{y,ratio}$ and in the region of short period, which results in the small energy input to the structure, E_{str} and consequently small displacement response. The relationships between $C_{y,ratio}$ and E_{str} can be seen more clearly from Figure 12a and those between E_{str} and displacement response from Figure 12a and 12b. These relationships can be seen in other periods. From these facts, it is confirmed that whatever the value of $C_{y,str}$ is, the SSI effect in ISIS_o is mainly affected by $C_{y,soil} / C_{y,str}$.

4. CONCLUSION

The effects of soil-structure interaction (SSI) on the seismic response demand of the buildings are studied through observation and simulation. Dense observation system of seismographs on a school building and shallow soil has been set up. The observed responses under a moderate earthquake are analysed by the detailed frame models with and without SSI. A better correlation is reported in case of SSI analysis. A simple model is used to conduct a parametric study on the effects of SSI, taking elasto-plastic behavior in both structure and soil into account. The results indicate that SSI effects are much higher in case of inelastic soils. The SSI effect on the displacement response is interpreted based on the input energy dissipation by the structure and the soil. The theoretical background on the energy distribution need be studied further.

REFERENCE

- Bielak J.(1978): Dynamic response of non-linear building-foundation systems. *Earthquake Engineering & Structural Dynamics* 1978; 6:17-30.
- Jennings P, Bielak J.(1973): Dynamics of building-soil interaction. *Bulletin of the Seismological Society of America* 1973;63(1):9-48.
- Novak M.(1974) Dynamic stiffnesses and damping of piles. *Canad. Geotech. J.* 1974; 11:574-598.
- Parmelee, R.A.(1970): The influence of foundation parameters on the seismic response of interaction systems. *Proc. Third Japan Earthquake engineering Symposium.*
- Rodriguez M, Montes R.(2000) Seismic response and damage analysis of buildings supported on flexible soils. *Earthquake Engineering & Structural Dynamics* 2000; 29:647-665.
- Veletsos A, Meek J.(1974): Dynamic behavior of building-foundation systems. *Earthquake Engineering & Structural Dynamics* 1974; 3:121-138.

KEYWORDS

soil-structure interaction, SSI, non-linear, sway, rocking, foundation, pile, reinforced concrete building, seismic observation, seismograph

VALIDITY OF DEFORMATION DEMAND ESTIMATES USING NONLINEAR STATIC PROCEDURES

Sashi K. Kunnath¹ and Balram Gupta²

ABSTRACT

Static pushover methods are slowly gaining popularity as a viable alternative to fully nonlinear time-history analyses. Despite concerns over the potential drawback of the method for systems with high-mode effects, there appears to be some degree of confidence in using the technique for regular buildings. The objective of this paper is to explore the validity of nonlinear static methods, particularly those recommended in FEMA-273, in estimating seismic deformation demands and to further investigate the ability of these methods to predict potential story mechanisms across the height of the building. It is shown that for static procedures to reasonably reproduce the results of a nonlinear dynamic action, it is necessary to use fairly complex methods which consider the variation in lateral force distribution as a function of changing system characteristics. Innovative schemes which magnify the effects of critical high mode response parameters can also result in acceptable deformation demand predictions.

1. INTRODUCTION

Structural engineers in high seismic zones are faced with the daunting challenge of choosing an alternative approach to traditional force-based design procedures. The motivation for the move away from force-based design stems from numerous reasons, the most significant of which, in the context of this paper, are the following: (i) they do not account for force-redistribution following yielding, and (ii) they do not consider potential failure modes that result from mid and upper story mechanisms caused by the influence of higher modes. There is consensus among the research community that a more rational approach for seismic evaluation should be based on inelastic displacements rather than elastic forces (Bertero et al., 1991; Moehle, 1992; Nassar and Krawinkler, 1991; Miranda, 1993; Wallace, 1995).

It is not surprising, therefore, that the development of the *NEHRP Guidelines for the Seismic Rehabilitation of Buildings*, FEMA-273 (1997) brought into focus the importance of inelastic

¹ Department of Civil & Environmental Engineering, University of Central Florida, Orlando, FL 32816; kunnath@ucf.edu

² Saiful/Bouquet Consulting Structural Engineers, Pasadena, CA 91105; bgupta@sbise.com

analysis methods to achieve better estimates of deformation demands. The significance of this document is that it is a precursor to future performance-based seismic design codes. The publication of FEMA-273, however, is only a first step in the goal of advancing performance-based seismic design. The guidelines need to be systematically and critically evaluated before engineers can begin to use such methodologies with confidence.

A crucial step in the FEMA-273 evaluation process is the analysis of the building model which provides estimates of force and deformation demands in the various lateral force resisting elements in the building. Four analytical approaches are listed: two static procedures and two dynamic procedures. Of the two nonlinear procedures suggested in FEMA-273, it is reasonable to assume that structural engineers will prefer to use the nonlinear static procedure (NSP) over fully nonlinear time-history analyses. Three lateral force distributions are recommended to carry out the pushover analysis: an inverted triangular pattern, a uniform load pattern, and a lateral load pattern resulting from a modal combination of those modes that result in over 90% mass participation. These lateral load patterns will be evaluated in the first part of this study.

1.1 Objectives and Scope of Study

The main objective of this study is to examine the effectiveness of pushover procedures, based on the three FEMA-273 load patterns, to predict the seismic response characteristics of a typical building. A regular medium-rise reinforced concrete building with ductile non-degrading connections will constitute the baseline structure for all comparative evaluation tasks. Reasons for the inability of NSP to reproduce inelastic dynamic behavior will then be explored. An advanced pushover technique which overcomes these drawbacks will be presented. The sample structure will then be re-evaluated using the advanced pushover procedure. In each case, the predicted deformation demands and story mechanisms will be compared to results from a fully nonlinear time-history analysis. Finally, some simple yet effective lateral load patterns based on unique modal combinations will be investigated.

1.2 Typical Building Considered in Evaluation Studies

An 8-story office building with plan configuration shown in Figure 1 was used in a systematic evaluation study of different pushover methods. The lateral force resisting system consists of

four Special Moment Resisting Frames (SMRFs) in the longitudinal direction and six SMRFs in the transverse direction. A story height of 12 feet (3.66m) was assumed through out. The seismic design of the buildings was based on UBC-88 (1988) with R_w of 12, seismic zone factor, Z , of 0.4, and importance factor, I , of 1.0. Live loads on typical floors were assumed as 50 psf (2392.5 Pa). All concrete was assumed normal-weight with a *specified* compressive strength (f'_c) ranging from 4 to 6 ksi (27.6 – 41.4 MPa). The yield stress for all reinforcement was assumed as 60 ksi (414 MPa). All columns were assumed fixed at the base. P-delta and torsional effects were ignored. All buildings were designed to satisfy the drift criterion and the strong column-weak beam philosophy. Table 1 presents the member details for a typical frame. A typical longitudinal frame was considered for detailed evaluation in the present study.

Effective stiffness values, corresponding to secant stiffness at first yield of reinforcement, were used for the initial stiffness of all components. Moment curvature plots were generated using program BIAX (Wallace and Moehle, 1989) for all elements using *expected* strengths which were assumed at 120% of the *specified* strengths for concrete and 115% for reinforcement. Axial forces due to gravity loads were included in the moment-curvature computations of columns. The effective stiffness values used for columns varied from 45% to 55% of gross section properties while those for beams were in the range of 50% to 55%. FEMA-273 suggests effective stiffness values for columns and beams as 70% and 50% of gross values, respectively. Post-yield stiffness was assumed as 5% of the initial stiffness for all elements. Table 2 displays the dynamic properties of the building computed by eigenvalue analysis using effective stiffness properties. The values of periods appear to be high but are conservative for a displacement-based design.

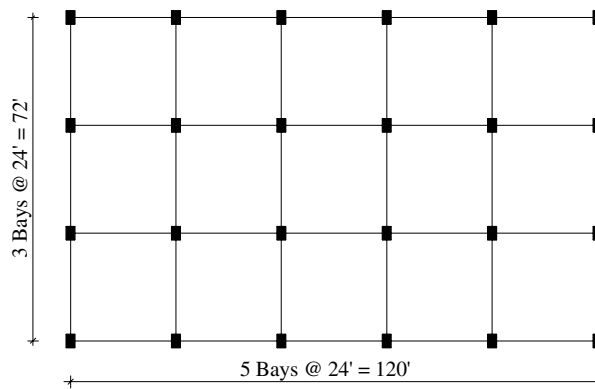


Figure 1: Typical plan of prototype structure used in evaluation study.

Table 1: Details of members for various frames used in validation study

# of Stories	Levels	Column Details			Beam Details			
		Size ^a	f_c'	Steel	Size ^a	f_c'	Top Steel	Bottom Steel
8	5-8	18x24	4	12-#8	18x24	4	4-#8	2-#8
	1-4	18x30	5	14-#9	18x24	4	3-#9+2-#8	3-#8

^a All dimensions are in inches

Table 2: Lateral vibration modes

Mode	1	2	3	4	5
Period (sec)	1.75	0.60	0.34	0.23	0.17
% Mass	81.8	10.6	3.5	2.0	1.0

2. EVALUATION OF FEMA-273 LATERAL LOAD PATTERNS

The target building selected for evaluation is a regular moment frame structure. Well-detailed, non-degrading connections were assumed so as to limit the variables in the study and allow a relatively simple comparison of the different methods being evaluated.

2.1 Benchmark Solution: Nonlinear Time History Analysis

It is assumed that the benchmark solution against which all other methods will be compared is a fully nonlinear time-history analysis. Program IDASS (Kunnath, 1995), a derivative of IDARC, was used in the time-history evaluation. Only a typical frame in the longitudinal direction was considered. The building was subjected to a magnitude-scaled S48W component of the Rinaldi Receiving Station free field motion recorded during the 1994 Northridge earthquake. The original record used in the analysis was taken from the SAC database and is classified as an event with a 10% probability of exceedance in 50 years. The accelerogram and spectra of the free field motion as used in the study are displayed in Figure 2. Results of the nonlinear time-history analysis are reported in succeeding sections along with the pushover response. The objective of selecting this record was to identify an earthquake that would induce high mode response in the system and produce deformations and damage of reasonable magnitude to facilitate a meaningful comparison of the different analytical methods.

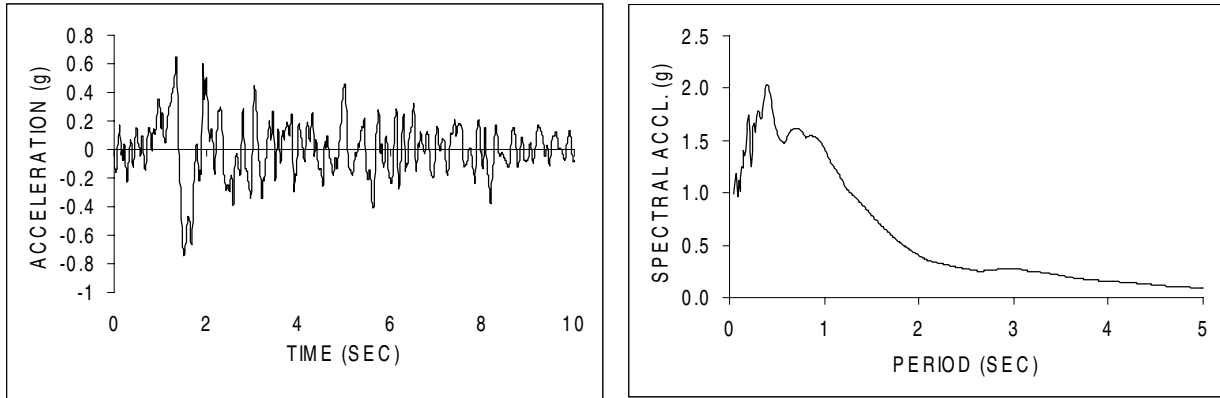


Figure 2: Strong motion duration and spectra of earthquake used in evaluation studies

2.2 Pushover Analyses

The structural model used in the time-history analysis was then subjected to equivalent lateral forces based on FEMA-273 load patterns. The following notation is used in representing the results of the different pushover procedures:

NSP-1: corresponds to the inverted triangular pattern with the period-dependent k-factor

NSP-2: represents a uniform pattern with lateral loads directly proportional to the floor mass

NSP-3: is based on a lateral load pattern proportional to the story shears obtained from a modal combination using a response spectrum analysis in conjunction with the earthquake spectra shown in Figure 2. All eight lateral modes were included in determining the story forces.

The target displacement used in each of the pushover procedures is the maximum roof displacement predicted by the nonlinear time history analysis (NTH). The results of the evaluation are summarized in Figure 3. The first plot in this figure shows the peak displacement profile. The peak displacements are generally well represented by load pattern *NSP-2*. The remaining two patterns underestimate the displacements at almost all levels. The adjacent plot which displays the peak inter-story drift clearly highlights the inability of nonlinear static methods to predict this critical deformation parameter. The importance of the inter-story drift demands in the upper stories is further demonstrated in Figure 4 which shows the predicted plastic hinges in the frame. The potential for the formation of a story mechanism in the upper stories can be overlooked with traditional pushover techniques. It is clear that the contribution of higher modes has not been captured in these static methods.

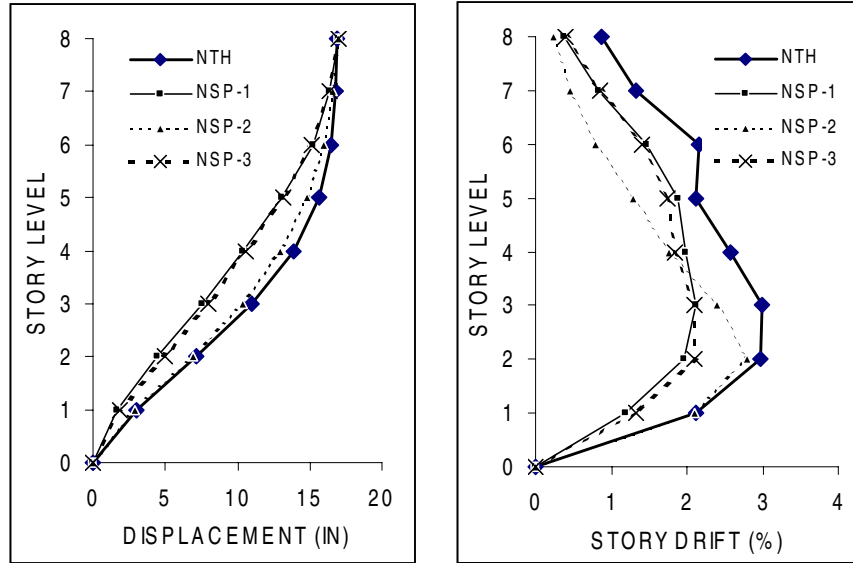
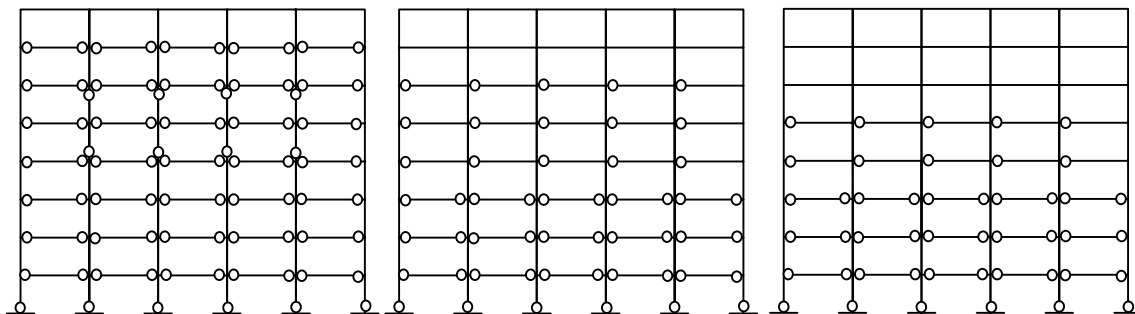


Figure 3: Displacement and drift profile using various analysis methods



(a) NTH

(b) NSP-1

(c) NSP-2

o: plastic hinge

Figure 4: Plastic hinge locations predicted using various analysis methods

3. DYNAMIC VS. STATIC METHODS

A clearer understanding of the behavior of the building under seismic loading is presented in Figure 5 which shows the variation of inter-story drift during the dynamic analysis. It is obvious that the peak drifts at different story levels occur at different times indicating the varying nature of the modal contributions to the response. Figure 6 contains the peak drifts of the building subjected to nine different earthquake motions. In each case, the profile is different suggesting that the contribution of the higher modes is not consistent and is a function of the frequency characteristics and magnitude of the earthquake.

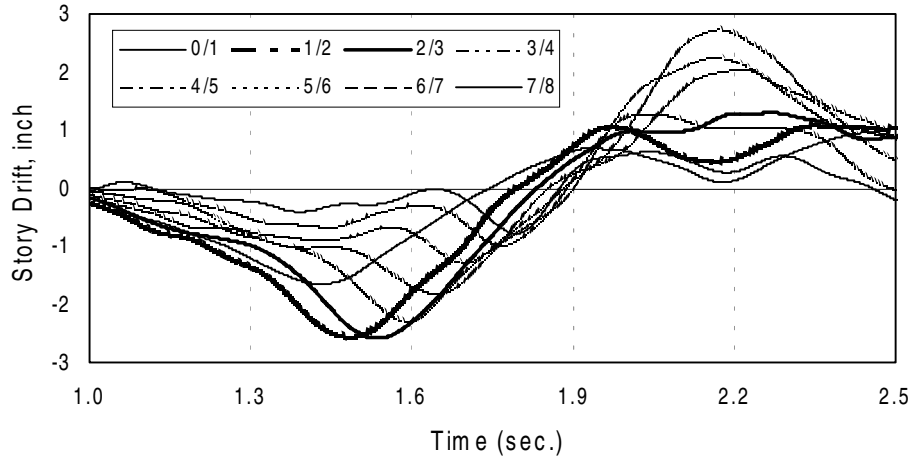
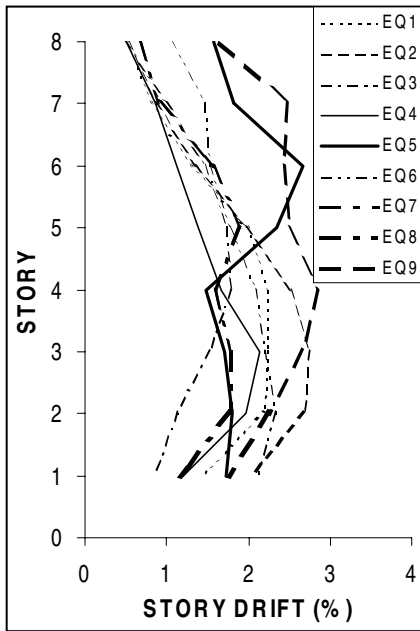


Figure 5: Variation of inter-story drift during dynamic response analysis
(numbers in legend indicate relative story numbers)



A static method, linear or nonlinear, in which an invariant load pattern is used, cannot incorporate these effects through simple modal combinations. Advanced methods which somehow take into account the varying dynamic characteristics of the structure are needed for pushover methods to work.

Figure 6: Variation of peak drifts for different earthquakes

4. ADAPTIVE PUSHOVER PROCEDURE

The primary differences between existing pushover methods and the proposed procedure are (i) the present method includes ground motion characteristics as part of the evaluation process; and (ii) the applied load pattern changes from one step to the next depending on the instantaneous dynamic properties of the system. The process consists of first specifying a hazard level using a design response spectrum and then carrying out the step-by-step lateral load analysis. Complete

details of the method including a comprehensive validation of the procedure for a variety of structural types and configurations can be found in Gupta and Kunnath (2000).

4.1 Loading

A unique feature of the proposed method is the specification of the seismic load in terms of a response spectrum. This will be used to determine the spectral accelerations for different modes as the analysis progresses and the dynamic properties of the system change due to yielding of elements. Two possible loading scenarios are possible: a response spectra based on actual recorded motions at the site, if available; or a NEHRP-type design spectra that characterizes the design earthquake. If actual ground motions are used, it is prudent to use several ground motions in order to obtain a statistical demand distribution.

4.2 Procedure

1. Create a mathematical model of the structure.
2. Specify the nonlinear force-deformation (moment-curvature) envelope for various elements in the structure. A bilinear or trilinear representation may be used depending upon the capabilities of the software being used.
3. Condense out the rotational and vertical degrees-of-freedom to create a reduced stiffness matrix which contains only the lateral floor degrees-of freedom. Perform an eigenvalue analysis of the reduced structural model at the current stiffness state. Using the story weights and the computed eigenvalues, determine the modal "participation" factors:

$$\Gamma_j = \sum_{i=1}^{i=N} m_i \phi_{ij} \quad (1)$$

where:

Γ_j = modal participation factor for j^{th} mode

Φ_{ij} = mass normalized mode shape value at i^{th} level and j^{th} mode

m_i = Mass of i^{th} story; and N = Number of Stories

4. Compute the story forces at each story level for each of the N modes (note that the number of modes is equal to the number of stories) to be included in the analysis using:

$$F_{ij} = \Gamma_j \Phi_{ij} W_i S_a(j) \quad (2)$$

where:

F_{ij} = lateral story force at i^{th} level for j^{th} mode ($1 < j < n$)

$S_a(j)$ = spectral acceleration corresponding to j^{th} mode

5. The story forces computed in the previous step are applied in small increments, which can be expressed as a fraction of the base shear. The magnitude of the force increments control the equilibrium errors that result in a non-iterative analysis.
6. Perform a static analysis of the structure using the scaled incremental story forces. This means that for modes other than the fundamental mode, the structure will be pushed and pulled simultaneously.
7. Compute element forces and deformations for each mode and combine them using any appropriate modal combination rule. In this study, an SRSS combination was used.
8. Check the accumulated member forces with their respective force-deformation envelopes. If any member has changed state (due to cracking, yielding or softening), re-compute the member stiffness, update the global stiffness matrix and return to Step 3.
9. Repeat the process until a limiting criteria, typically a specified story drift, is reached.

The above procedure is now applied to the target 8-story structure. To illustrate the difference in the methodology used in the adaptive procedure, the applied story forces for the first 3 modes at two stages of the analysis is shown in Figure 6. The values shown are the actual lateral loads applied in a single step. The total base shear (using an SRSS combination) resulting from the applied loads is the same in both stages. It is evident that the magnitude of the applied loads in the higher modes increases as the higher mode periods move into the amplified region of the response spectra.

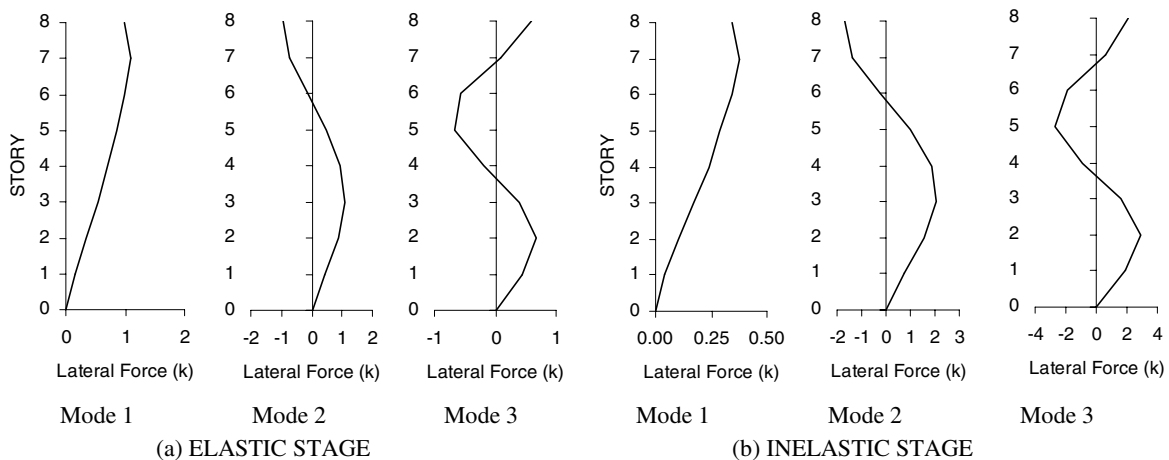


Figure 6: Applied lateral loads at different stages during adaptive pushover analysis

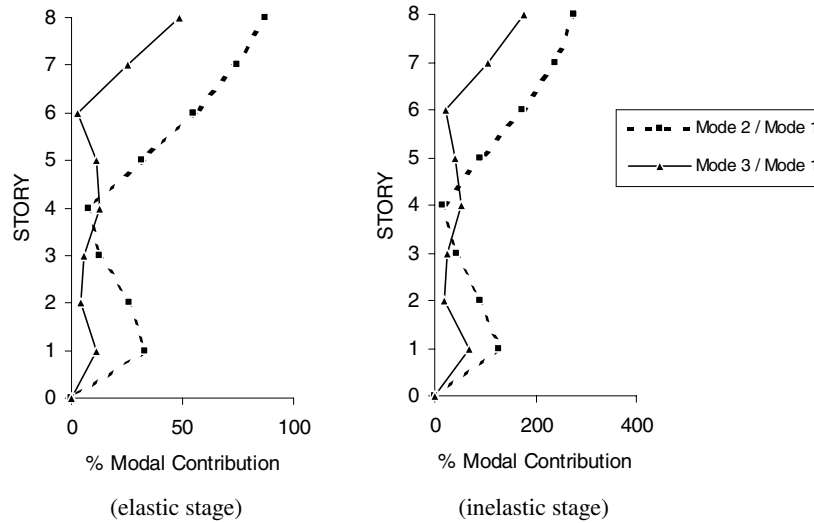


Figure 7: Ratio of modal drift contributions due to changes in dynamic characteristics

The effect of this loading pattern on the resulting modal drifts are shown in Figure 7. The cumulative effect of this “adaptive” lateral load distribution, as the stiffness characteristics of the system change, accounts for the ability of the method to incorporate the effects of high mode response in the analysis. The results of the adaptive pushover method are now compared to the time history evaluation. Both story drifts and plastic hinge distributions are shown in Figure 8. With reference to the time-history benchmark data presented earlier in Figures 3 and 4, it is demonstrated that the adaptive method is successful in estimating both the drift demands and the yielding in the upper stories of the building.

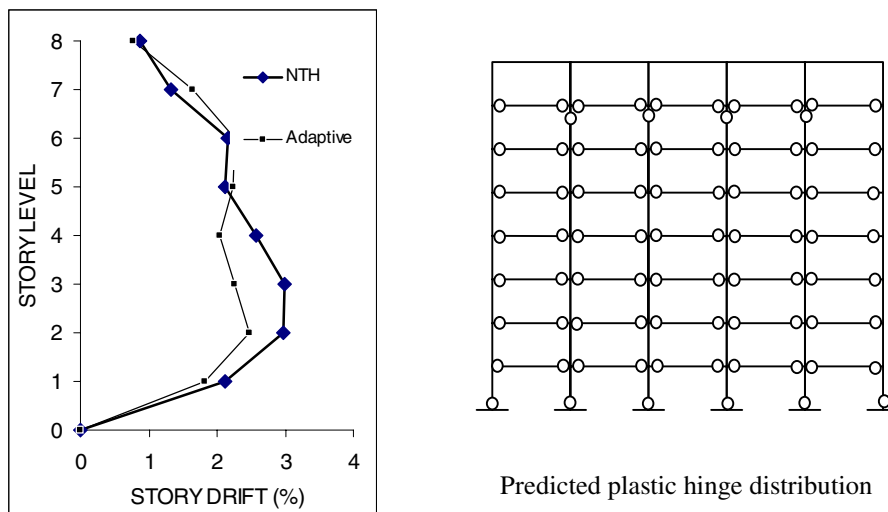


Figure 8: Results of the adaptive pushover analysis

4.2 Drawbacks and Limitations

The success of the adaptive method has been demonstrated in the previous section. However, there are a number of factors that presently restrict its use in routine evaluation of structures: (i) it requires a special purpose computer program to carry out the step-by-step analysis since modern computer codes do not provide the user with options to vary the load interactively during the analysis; (ii) equilibrium is not satisfied at every step since a modal combination is used, however, equilibrium errors can be minimized when small force increments are used; (iii) the SRSS combination tends to magnify certain modal contributions and results in over-conservative estimates at some story levels and likewise can underestimate demands at other levels.

5. ALTERNATIVE STRATEGIES

The adaptive pushover procedure needs to be simplified if it is to find practical application in routine structural analysis. A number of alternative strategies to magnify the effects of individual modes are possible. One such method was proposed by Matsumori et al. (1999) who suggested load patterns based on a modal combination of the difference and sum of the first two modes. The application of this technique is shown in Figure 9. The modal difference results in accurate drift predictions at the upper levels but severely under-predicts the drift at the lower levels. The modal sum produces the opposite effect. However, the envelope of the two sets provides useful information.

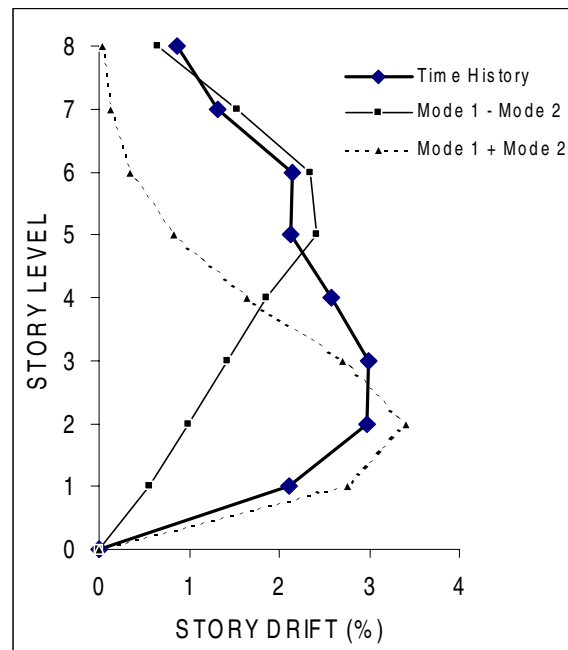


Figure 9: Alternative pushover method

As an extension of the above concept, it is possible to consider several unique combinations of modal shears so as to amplify the effects of selected modes. For taller structures, for example, the modal sum and differences of the first and third mode may be considered. Additional work on such combinations is underway.

6. CONCLUDING REMARKS

It is unlikely that nonlinear static procedures can fully replace nonlinear time-history analyses. However, given the current state-of-practice in seismic design, it is only reasonable to assume that approximate inelastic methods will continue to flourish until automated nonlinear computational tools for routine analysis of structures become commonplace. Given the complexity of interactions that govern a nonlinear response, the idea of a “simplified” pushover method may be unreasonable. However, as demonstrated in the previous section, it may still be possible to derive unique modal combinations that collectively “envelop” the expected seismic response of a building.

7. REFERENCES

- Bertero, V.V., Anderson, J.C., Krawinkler, H. and Miranda, E., 1991, Design guidelines for ductility and drift limits, *Report EERC 91/15*, University of California, Berkeley.
- FEMA-273, 1997, *NEHRP Guidelines for the Seismic Rehabilitation of Buildings*, Building Seismic Safety Council, Washington, D.C.
- Gupta, B. and Kunnath, S.K. (2000). Adaptive spectra-based Pushover procedure for seismic evaluation of structures, *Earthquake Spectra*, 16 (2), 367-392.
- Kunnath, S. K., 1995, Enhancements to program IDARC: modeling inelastic behavior of welded connections in steel moment-resisting frames, *Report No. NIST GCR 95-673*, National Institute of Standards and Technology, Gaithersburg, Maryland.
- Matsumori, T., Otani, S., Shiohara, H. and Kabeyasawa, T. (1999). Earthquake member deformation demands in reinforced concrete frame structures. US-Japan Workshop on Performance-Based Earthquake Engineering Methodology for RC Building Structures, Maui, 79-94.
- Miranda, E., 1993, Evaluation of site-dependent inelastic design spectra, *ASCE Journal of Structural Engineering*, **119**, 1319-1338.
- Moehle, J. P., 1992, Displacement-based design of RC structures subjected to earthquakes, *EERI Spectra*, **8** (3), 403-428.
- Nassar, A. A. and Krawinkler, H., 1991, Seismic demands for SDOF and MDOF Systems, *Report No. 95*, John A. Blume Earthquake Engineering Center, Stanford University (1991).
- Wallace, J. W. and Moehle, J.P., 1989, BIAX: A computer program for the analysis of reinforced concrete sections, *Report No. UCB/SEMM-89/12*. University of California, Berkeley.
- Wallace, J. W., 1995, Seismic design of RC structural walls. Part I: New code format, *ASCE Journal of Structural Engineering*, **121**, 75-87.

INELASTIC SEISMIC RESPONSE OF EXISTING REINFORCED CONCRETE BUILDINGS

T. Ichinose¹, Dinh V. Thuat², H. Kagohashi², and H. Umemura³

ABSTRACT

The response of existing reinforced concrete (RC) frame and wall buildings to future earthquake shaking is studied in terms of dissipating energies associated with collapse mechanism. For this purpose, RC wall structures with various story strengths are analyzed by nonlinear time-history analyses under three ground motion records and a number of their variations generated by the wavelet transform technique. A story-shear-safety factor is introduced to distinguish between the total-collapse and story-collapse mechanisms of structures and to investigate the height-wise distribution of plastic energy. In addition, an equation is developed to estimate the story response displacement under any level of future ground motion.

1. INTRODUCTION

Current improvements in the performance-based seismic design and engineering provide a useful tool for the seismic design of new buildings such as the capacity spectrum method (Freeman, 1978) and the displacement-based design (Priestley, 2000). These methods simply characterize a multistory building as an equivalent single-degree-of-freedom (SDOF) system on seismic structural performances. For this reason, the response behavior of a newly constructed building designed using these methods under seismic actions can be met if its properties (e.g., strength, stiffness, and energy dissipation capacity) satisfy reasonably the requirements for the designed deformation mechanism (i.e., weak-beam/strong-column mechanism) as well as the uncertainty in seismic structural response. However, for the seismic evaluation of existing buildings such methods may be applied only to those responding like SDOF systems or those with governing response in the first vibration mode of structure. In fact, an existing multistory building, designed by the conventional code, in fact may collapse in various ways (so-called total-collapse, story-collapse, or mixed-collapse types) during severe ground motions. Consequently, its energy dissipations in the plastic hinge zones in structural members and elements may also be concentrated on various stories over the height of the building, depending significantly on characteristics of earthquake ground motions and properties of building structures. Thus, an effectively simple method developed on the basis of the collapse mechanism (or energy-dissipating mechanism) of structures instead of the analysis of its equivalent SDOF systems is needed for the seismic evaluation of existing buildings. In Japan, the standard for seismic evaluation, which was compiled in 1977 and first revised in 1990, is in terms of the seismic index in each story

¹ Professor, Department of Architecture, Nagoya Institute of Technology, Japan, E-mail: ichinose@archi.ace.nitech.ac.jp

² Graduate students, Department of Architecture, Nagoya Institute of Technology, Japan, E-mail: k01@archi.ace.nitech.ac.jp

³ Dr. Eng., Department of Architecture, Nagoya Institute of Technology, Japan, E-mail: umemura@archi.ace.nitech.ac.jp

obtained as the product of the basic seismic index and the shape index (Okada, 1976; Aoyama, 1981). Currently, it is under review for the 2001 revision concerned with the uncertainties in the seismic response of structure. The objective of this paper is to study the seismic response of existing buildings in terms of dissipating energies with emphasis on story strengths. The results indicate that story-shear-safety factor must be considered as the basis for the seismic evaluation of RC existing buildings. In addition, this study may be extended for the seismic design of new buildings.

2. STRUCTURAL MODELS ANALYZED

Table 1 Model dimensions (cm)

Story	Wall			Frame	
	Column	Plate	Beam	Column	Beam
7~9	60 x 60	20	35 x 55	80 x 80	45 x 80
4~6	65 x 65	20	40 x 60	85 x 85	50 x 85
1~3	70 x 70	20	45 x 65	90 x 90	55 x 90

All analyzed models of both structural wall and moment-resistant frame buildings, as illustrated in Figure 1, have 9 stories, a constant story height of 3 m, and a span of 10 m and 7 m, respectively. The dimensions are shown in Table 1 and the constant story

weights are 1500 kN and 735 kN for wall and frame models, respectively (giving the fundamental period $T_1 = 0.42$ sec and 1.06 sec). Thus, the wall models can be considered as stiff buildings and the frame models as soft buildings in lateral response. Two boundary columns and a wall plate at each story of wall models are modeled as an equivalent column member with two plastic rotational springs at the top and bottom and a shear spring in the middle, where inelastic deformations may occur. The degrading trilinear model (Takeda model) is used for flexural deformation of all members and the origin-oriented degrading stiffness model is used for shear deformation of walls. The secant yield stiffness and the post-yield stiffness are assumed to be 0.3 and 0.01 times the initial stiffness, respectively. The viscous damping factor ζ is assumed as 0.05.

These models are designed and organized in three groups according to their height-wise variations in story yield strengths. Group 1 is for those having uniform yield strengths and Groups 2 and 3 are for those having a weak-first-story and weak-fifth-story, respectively (to be described below).

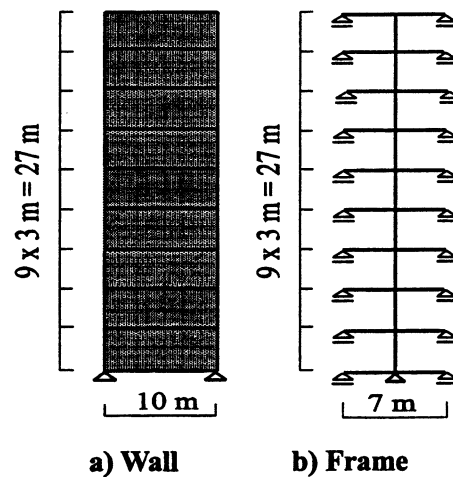


Figure 1 Analyzed models

Analyses to determine the moment and shear strengths for the wall models:

1. Perform a linearly elastic analysis of the building structure subjected to the lateral static forces distributed in accordance with the vertical distribution factor A_i specified by the Japanese Building Code. The base shear coefficient C_B is 0.6. The bending moments and shear forces at the i th story are denoted by M_{wi} and Q_{wi} , respectively.
2. Increase both the values of M_{wi} and Q_{wi} by a factor of ψ for each group while keeping the moment at the bottom of the first story and the shear force at a selected weak story in the case of weak-first-story or weak-fifth-story models unchanged as follows

Group 1 (uniform-shear-increase models)

$$M_i = M_{wi}, M_i = \psi M_{wi}, \text{ and } Q_i = \psi Q_{wi} (i = 1, 2 \dots n \text{ and } \psi = 1, 1.1, \dots \text{ or } 1.4) \quad (1)$$

Group 2 (weak-first-story models)

$$\text{The same as Equation (1) except } Q_1 = Q_{w1} \text{ and } \psi > 1 \quad (2)$$

Group 3 (weak-fifth-story models)

$$\text{The same as Equation (1) except } Q_5 = Q_{w5} \text{ and } \psi > 1 \quad (3)$$

where ψ is the strength modification factor for moments and shears in each story for each model and n is the number of stories.

3. Calculate the “minimum” required moment and shear strengths of the structure according to the data given in Table 1 and the minimum percentages of reinforcement required in the code. The concrete and reinforcement strengths are taken as 30 N/mm² and 400 N/mm², respectively.
4. Determine the yield moment and yield shear strengths at each story (M_{ywi} and Q_{ywi}) for each model as the larger of the corresponding values calculated on the above steps 2 and 3. The cracking strengths for all members are calculated in accordance with the AIJ (1999).

Analyses to determine the moment strengths of columns and beams for the frame models:

1. Perform a linearly elastic analysis of the structure subjected to the lateral static forces distributed in inverted triangular pattern and $C_B = 0.5$. The stiffness of structural members is calculated based on the data given in Table 1. As a result, the mean values of bending moments of columns and beams at two ends in the i th story are denoted by M_{ci} and M_{bi} , respectively.
2. Increase the value of M_{ci} by a factor of ψ to determine the yield moment strengths of columns for each group while keeping the moment at the weak story in groups 2 and 3 unchanged.

Group 1: (uniform-moment-increase models)

$$M_{yci} = \psi M_{ci} \quad (i = 1, 2 \dots n \text{ and } \psi = 0.8, 0.9, \dots \text{ or } 1.4) \quad (4)$$

Group 2 (weak-first-story models):

$$\text{The same as Equation (4) except } M_{ycl} = 0.8 M_{cl} \text{ and } \psi > 0.8 \quad (5)$$

Group 3 (weak-fifth-story models)

$$\text{The same as Equation (4) except } M_{yc5} = 0.8 M_{c5} \text{ and } \psi > 0.8 \quad (6)$$

where ψ is the strength modification factor for column moments in each story for each model.

- The yield moment strengths of beams are set equal to those obtained from the step 1 with the exception that the foundation and roof beams are intended to remain elastic so that their yield moment strengths are assumed to be 3 and 1.5 times those computed in the step 1, respectively. The cracking strengths for all members are assumed one-third those of the corresponding yield moments.

3. INPUT EARTHQUAKE GROUND MOTIONS

Table 2 lists three earthquake ground motions recorded in the United States and Japan with their peak values of velocity, V_s . Among them, the El Centro NS record is multiplied by 2.6 times to make its peak velocity equal 100 cm/sec. To consider uncertainties in characteristics of earthquake motions that may occur at the site of an existing building in the future and their effects on the response of structure, each of them is then generated based on the phase-variation method using the wavelet transform to produce twenty other motions. Figure 2 shows the Fukiai NS ground acceleration and an example of its generations.

4. STORY SHEAR SAFETY FACTOR

For a given existing building subject to se-

Table 2 Input earthquake motions

Earthquake records	V_s (cm/s)
1) 1940 El Centro NS (Imperial Valley)	38.1
2) 1994 Sylmar NS (Northridge)	130.1
3) 1995 Fukiai NS (Hyogo-ken Nambu)	123.3

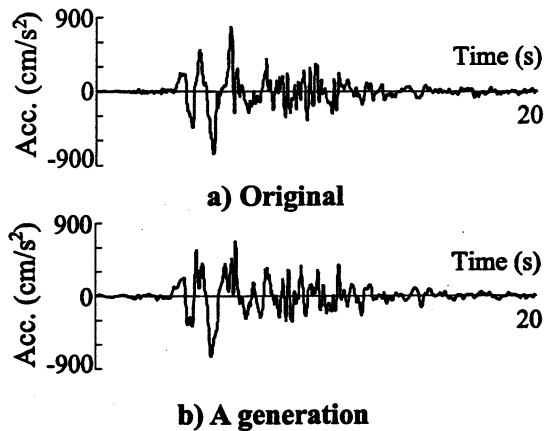
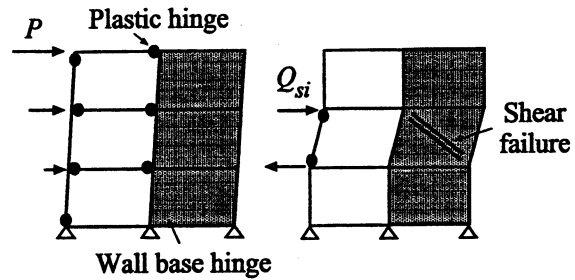


Figure 2 Fukiai NS ground motions

vere future earthquakes, a question being widely considered is whether it will fail in total-collapse type as expected in seismic design practice or in undesirable story-collapse type (Figure 3). If it fails in story-collapse type, how is the plastic energy distributed over its height or concentrated on a story? To consider the probability of story-collapse and plastic energy concentration of a building with emphasis on the story strength, a story-shear-safety factor for the i th story, f_i , is defined as the ratio of the story-collapse-resisting shear strength redundancy, ΔQ_i , over the story shear force, Q_{wi} , for ultimate state.

$$f_i = \Delta Q_i / Q_{wi}, \quad \Delta Q_i = Q_{si} - Q_{wi} \quad (f_i \geq 0) \quad (7)$$

where Q_{si} is the i th story shear strength with the assumption of the story-collapse shown in Figure 3b (shear failure develops in wall and flexural yielding in column). The value of Q_{wi} in Equation (7) can be obtained based on the nonlinear static pushover analysis at the ultimate state under the lateral static force, P , assumed to be distributed in triangularly inverted form or by



a) Ideal total-collapse b) Story-collapse
Figure 3 Energy-dissipating mechanisms

$$Q_{wi} = \frac{3(n+i)}{2(2n+1)} \cdot C_B^* \cdot \sum_{j=i}^n w_j \quad (8)$$

where C_B^* is the base shear coefficient determined with respect to the ultimate state under the force, P , against an expected level of future earthquakes and w_j is the j th story weight. Thus, the value of C_B^* can be less than or equal to the design value of C_B of the building used in section 2, depending on the property of each model analyzed. The minimum story-shear-safety factor, f_{min} , for each model is defined by

$$f_{min} = \min \{f_i\}; \quad i = 1, 2, \dots, n \quad (n = \text{number of stories}) \quad (9)$$

5. DISSIPATED PLASTIC ENERGY

5.1. Total Plastic Energy

The input energy by an earthquake on an inelastic building is in fact dissipated by viscous damping and hysteresis. But in order to make the procedure simple for the seismic evaluation of existing buildings, the plastic energies dissipated in a story are defined by the shaded areas

shown in Figure 4, E_m by flexural yielding and E_s by shear yielding (for wall models). The values of E_m and E_s in a given plastic region are determined based on the corresponding values of flexural and shear ductility factors (μ_m and μ_s) and the associated story yield moment and shear force (M_y and Q_y). Summing over all the stories of the building gives the total plas-

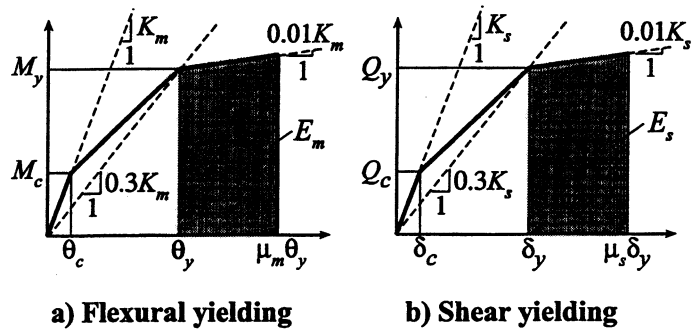


Figure 4 Dissipating plastic energy

(K_m and K_s = initial stiffness and θ_y and δ_y = flexural and shear yielding deformations)

tic energy E_p . Considering a mixed-collapse type building, the value of E_p is thus composed of two components, say E_{pt} and E_{ps} , corresponding to the contribution of total-collapse and story-collapse modes, respectively ($E_p = E_{pt} + E_{ps}$). Note that for particular cases, the value of E_{ps} can reach to E_p or zero if the building fails either in story-collapse or total-collapse type, respectively. Under a given motion, the value of E_{pt} is defined as the plastic energy dissipated by flexural yielding at the bottom of the first story for each wall model, and at all beam ends and at the bottommost and topmost of the columns for each frame model. The value of E_{ps} is then derived from summing the plastic energies of other plastic regions for each model.

5.2. Plastic Energy due to Story-Collapse and its Height-Wise Distribution

This section will show how the minimum story-shear-safety factor, f_{min} , affects the relative contributions of the collapse modes in a building during earthquake motions in terms of dissipating energies. For this purpose, the ratio E_{ps}/E_p is established to indicate how much the structure may behave in story-collapse mode, an undesirable behavior, during an expected level of future earthquakes. Figures 5a and 5b show the relationship between the ratio E_{ps}/E_p and the minimum story-shear-safety factor f_{min} for all the wall and frame models under all given earthquake motions (three recorded motions with each having twenty generations). From these figures, it can be seen that for buildings having the value of f_{min} greater than about 0.5, no plastic energy due to story-collapse is distributed ($E_{ps} = 0$). In other words, the structure fails in total-collapse type. A value of f_{min} less than 0.5 represents a structure that either fails in a mixed-collapse type (E_{ps} and $E_{pt} \neq 0$) or only total-collapse type ($E_{ps} = 0$ and $E_{pt} = E_p$) which may be attributed to the uncertainty in the seismic response of structure. For $f_{min} = 0$, the values of E_{ps} range from zero to unity of E_p for wall models and 0.03 to 0.85 for frame models. The mean and mean-plus-one-standard-deviation values of ratio E_{ps}/E_p are shown by the solid and broken lines, which have a tendency to decrease with increasing the factor f_{min} of the building. Compared with the large scatter due to different earthquake motions, the difference between the results of the frame models and those of the wall models is small. Thus it can be concluded that the contribution of story-

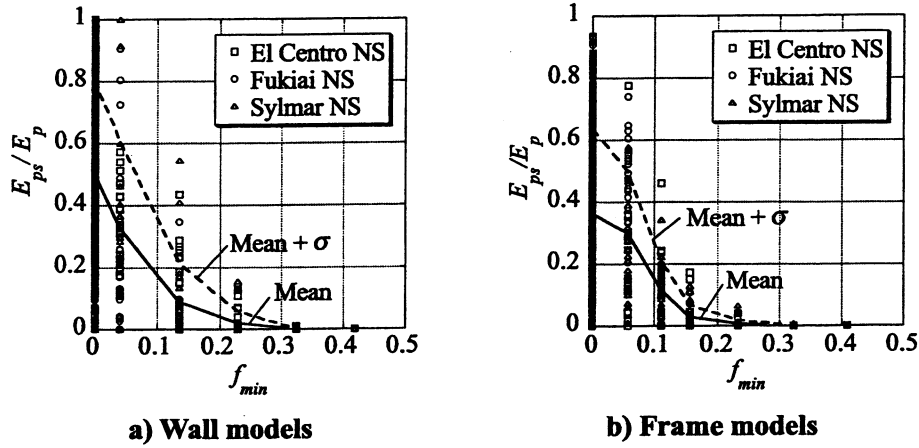


Figure 5 E/E_p and f_{min} relation (all Groups)

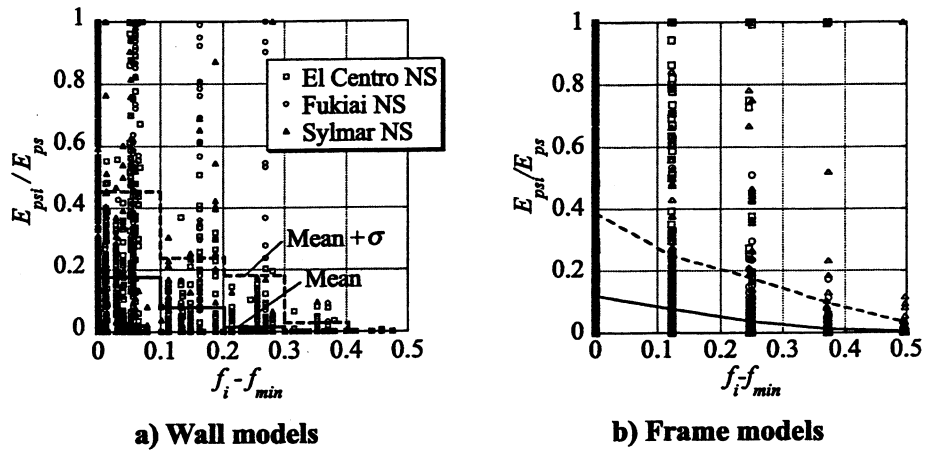


Figure 6 E_{pst}/E_{ps} and $f_i - f_{min}$ relation (all Groups)

collapse mode to the seismic response of a building tends to be lower as the factor f_{min} is larger, although it scatters depending on the characteristics of earthquake motions but not much on the type of structure. For convenience, we propose the following equation to estimate the mean values of E_{ps}/E_p .

$$\frac{E_{ps}}{E_p} = \frac{1}{2} \cdot (1 - 5f_{min}) \quad (10)$$

We now study how the plastic energy component due to story-collapse mode distributed (or concentrated) along the height of a building depends on the story-shear-safety factor during severe earthquake motions. Figures 6a and 6b show the plot of the ratio of E_{pst}/E_{ps} against the difference of $f_i - f_{min}$ where E_{pst} is the distribution of E_{ps} to the i th story. From these figures, it can be found that the plastic energy component due to story-collapse can be partly concentrated on some stories even where the story strengths are relatively strong ($f_i - f_{min}$ greater than zero), depending on the characteristics of earthquake motions. Hence, an inevitable scatter is observed at

the values of $f_i - f_{min}$ larger than zero for the models in Groups 2 and 3 ($f_{min} = 0$). For a few cases in particular, even though a story has the relatively large values of $f_i - f_{min}$, the plastic energy due to story-collapse mode is all concentrated on it ($E_{psi}/E_{ps} = 1$). In such cases, however, the resulting value of E_{ps} is quite small compared to the corresponding value of E_p . In general, the scattering of E_{psi}/E_{ps} decreases when $f_i - f_{min}$ increases. In addition, the mean and mean-plus-one-standard-deviation values of E_{psi}/E_{ps} computed for every ten percent in differences of $f_i - f_{min}$ except for the cases at $f_i - f_{min} = 0$ (as shown by the solid and broken lines) have a tendency to decrease as the value of $f_i - f_{min}$ increases. We propose the following equation to estimate the mean values of E_{psi}/E_{ps} .

$$\frac{E_{psi}}{E_{ps}} = \frac{1}{n} \cdot [1 - 2(f_i - f_{min})] \quad (11)$$

where n is the number of stories. For a building with story strengths corresponding to the inverted triangular forces, $f_i - f_{min}$ becomes zero and the above equation gives the uniform energy distribution.

6. ESTIMATE OF STORY RESPONSE DISPLACEMENT

6.1. Equation of Estimating Story Response Displacement

The story drift in each story, δ_p , imposed by seismic response is approximately estimated depending on the contributions of three components.

$$\delta_i = \delta_{psi} + \delta_{pti} + \delta_{ei} \quad (12)$$

where δ_{psi} , δ_{pti} , and δ_{ei} are the components of the story drift corresponding to the contribution of story-collapse, total-collapse, and elastic response modes, respectively. Assuming that the component δ_{psi} and the story strength Q_{si} cause the energy E_{psi} due to story-collapse mode, we have

$$\delta_{psi} = \frac{E_{psi}}{Q_{si}} \quad (13)$$

Assuming that the total-collapse mode causes uniform interstory drift angle ϕ over the height of the building, the component δ_{pti} in Equation (12) is determined as

$$\delta_{pti} = \phi \cdot h_i \quad (14)$$

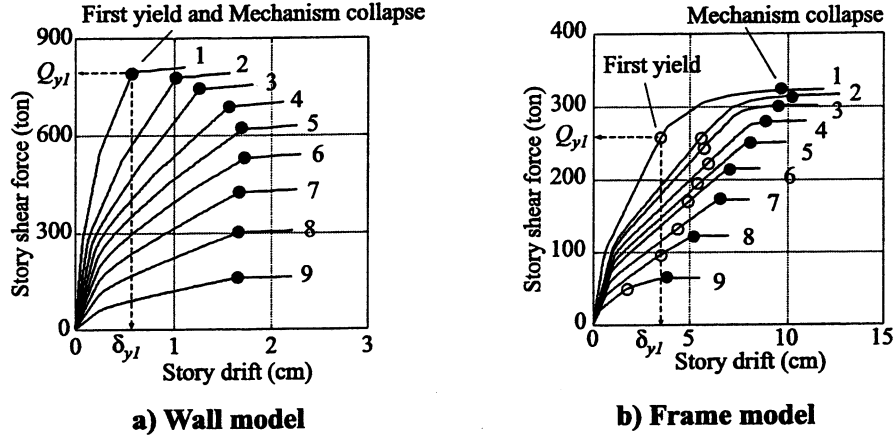


Figure 7 Story shear-drift relation for $\psi = 1.2$ models in Group 1

where h_i is the height of the i th story. We also assume that the drift angle ϕ and the story shear forces at yielding cause the energy E_{pt} due to total-collapse mode. Thus, we have

$$\phi = \frac{E_{pt}}{\sum_{j=1}^n (h_j \cdot Q_{yj})} \quad (15)$$

where Q_{yj} is the shear force of the j th story at the first yield shown by the solid circle in Figures 7a and 7b. Furthermore, we assume that the elastic component δ_{ei} is given as follows

$$\delta_{ei} = \kappa \cdot \delta_{yi} \quad (16)$$

where κ is a higher-mode modification factor in the elastic response range and simply assumed to be 1.2, and δ_{yi} is the i th story drift at the first yield. Thus Equation (12) is written as

$$\delta_i = \frac{E_{psi}}{Q_{si}} + \frac{E_{pt}}{\sum_{j=1}^n (h_j \cdot Q_{yj})} \cdot h_i + \kappa \cdot \delta_{yi} \quad (17)$$

Noting that the story stiffness in Figure 7a for the wall model are much larger than those in Figure 7b for the frame model, we may expect that the story shear-drift relations of most actual buildings would be formed in between those shown in Figures 7a and 7b.

6.2 Verification of the Proposed Equation

For the purpose of verifying the validity of Equation (17), the values of E_{pt} and E_{psi} in this equation are taken as those obtained from the time-history nonlinear dynamic analyses corresponding to each model and each earthquake motion. Figure 8 shows a comparison of the peak

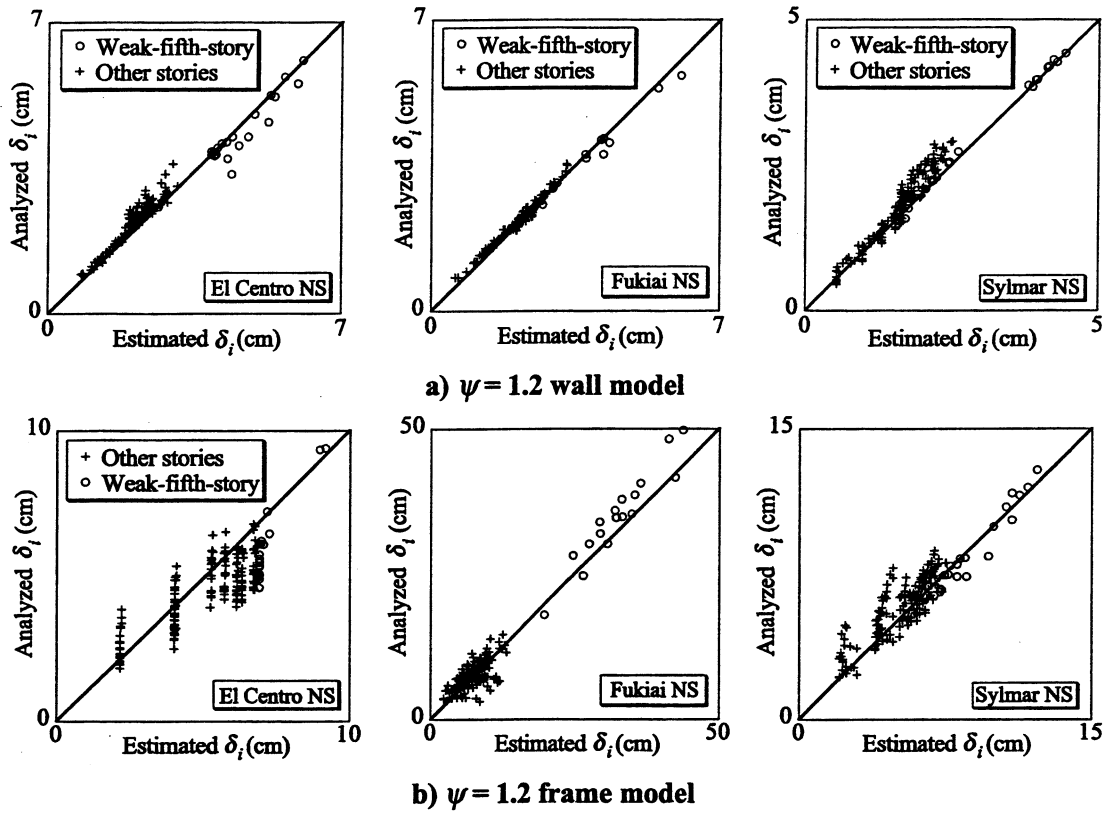


Figure 8 Comparison of estimated and analyzed story drifts in Group 3

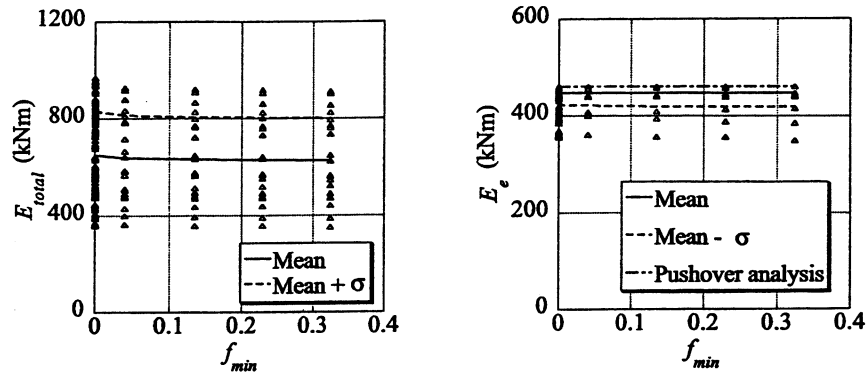
values of story drifts estimated by Equation (17) and those obtained by the dynamic analyses under the given earthquake motions for $\psi = 1.2$ models in Group 3. The results indicate that a relatively high degree of accuracy is generally observed for the models considered, particular in the wall models with high lateral stiffness.

6.3 Results of Estimating Mean Story Drift

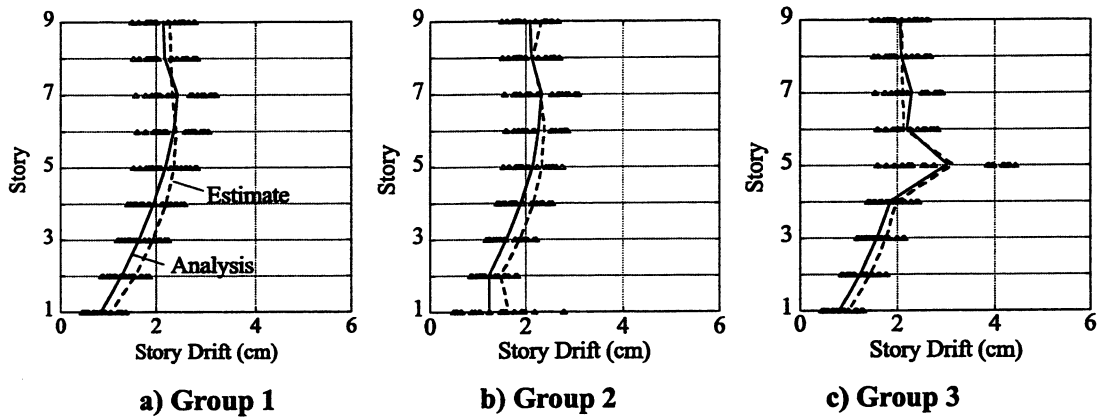
Figures 9a and 9b show the total input earthquake energy E_{total} and the total elastic energy E_e against the various f_{min} for all wall and frame models under the Sylmar NS record (21 motions). The chained line in Figure 9b shows the energy absorbed till the first yield in the story shear force-drift relation shown in Figure 7a. It is found that the scattering of E_e is generally small with a standard deviation value of approximately 3. In other words, the value of E_e can thus be estimated by the pushover analysis. Therefore, the total plastic energy E_p can be determined by the following equation.

$$E_p = E_{total} - E_e \quad (18)$$

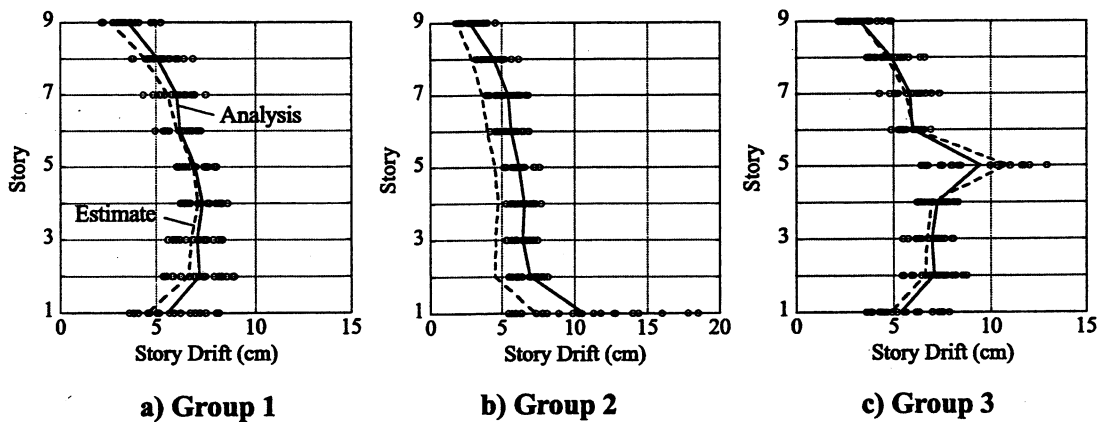
where E_e is the energy absorbed until the first yield during the pushover analysis. The values of E_{total} significantly depend on the earthquake intensity and weakly depend on the characteristics



a) Total energy b) Elastic energy
Figure 9 Energy for wall models (Sylmar NS)



a) Group 1 b) Group 2 c) Group 3
Figure 10 Estimate of mean story drifts for $\psi = 1.2$ wall models (Sylmar NS)



a) Group 1 b) Group 2 c) Group 3
Figure 11 Estimate of mean story drifts for $\psi = 1.2$ frame models (Sylmar NS)

of the structure (such as the fundamental period and the hysteresis), so that E_{total} can be determined based on the total input earthquake energy spectrum (Ichinose et. al., 1999).

An example of estimating the mean value of story drifts is presented in Figures 10 and 11 for $\psi = 1.2$ wall and frame models in all Groups 1, 2, and 3 under the Sylmar NS record. In these

figures, the solid lines indicate the mean values of analyses from the 21 motions and the broken lines indicate the mean values of estimate using Equation (17) and the mean values of energies shown in Figure 9. The results are rather good for all the models considered. The uncertainty of the response should be discussed in the future research.

7. CONCLUSIONS

1. The contribution of the story-collapse mode in a building during earthquake motions is reduced with increasing the minimum story-shear-safety factor.
2. The component of the plastic energy due to story-collapse mode that may be concentrated on a story of a building increases when the magnitude of its story-shear-safety factor decreases.
3. The story response displacement of a building to a selected level of future earthquake motions can be estimated using Equations (10), (11), and (17).

REFERENCES

- Aoyama, H., A (1981). Method for the evaluation of the seismic capacity of existing reinforced concrete buildings in Japan. *Bulletin of the New Zealand National Society for Earthquake Engineering*, Vol. 14, No. 3, pp. 105-130.
- Architectural Institute of Japan (1999). *Design Guidelines for Earthquake Resistant Reinforced Concrete Buildings Based on Inelastic Displacement Concept*. Tokyo, Japan. (in Japanese)
- Chopra, A. K. and Goel, R. K. (2000). Evaluation of NSP to Estimate Seismic Deformation. *Journal of Structural Engineering*, ASCE, Vol. 126, No. 4, pp. 482-490.
- Freeman, S. A. (1978). *Prediction of response of concrete buildings to severe earthquake motion*. SP-55, ACI, Detroit, USA, pp. 589-605.
- Ichinose, T., Umemura, H., Kanbayashi, H., Kagohasi, H., and Thuat, D. V. (2001). Seismic Evaluation of Reinforced Concrete Buildings. *Proceedings of the Tokai Region*, Architectural Institute of Japan, Japan, Parts 1-5. (in Japanese)
- Ichinose, T., Hanai, N., Umeno, T., and Idota, H. (1999). Probabilistic prediction of story displacement. *U.S.-Japan Workshop on Performance-Based Earthquake Engineering Methodology for Reinforced Concrete Building Structures*, Pacific Earthquake Engineering Research Center, Hawaii, pp. 145-158.
- Japan Association for Building Disaster Prevention (1990). *Standard for Seismic Capacity of Existing Reinforced Concrete Buildings*. Revised Edition, Tokyo, Japan. (in Japanese)
- Ohsaki, Y. (1994). *Introduction to seismic wave spectrum analyses*. Kajima Publication Co. Ltd., Tokyo, Japan. (in Japanese)
- Priestley, M. J. N. (2000). Performance based seismic design. *Proc. 12th World Conference on Earthquake Engineering*, Keynote Address, New Zealand, Vol. 33, No. 3, pp. 325-346.

SESSION A-3: RESPONSE BEHAVIOR OF FRAMES

Chaired by

◆ Rakesh Goel and Masaomi Teshigawara ◆

PERFORMANCE-BASED SEISMIC DESIGN OF NON-EMULATIVE PRECAST CONCRETE WALLS WITH FRICTION DAMPERS

Yahya C. KURAMA¹

ABSTRACT

Precast concrete structures in seismic regions have been traditionally designed to emulate the behavior of monolithic cast-in-place concrete structures largely because of limited knowledge about their seismic behavior. In recent years, a significant amount of research has been conducted on precast concrete walls which do not emulate monolithic cast-in-place concrete walls because of their economy, construction simplicity, and desirable seismic characteristics such as a self-centering capability and an ability to undergo “large” nonlinear lateral displacements with little damage. The greatest disadvantage of non-emulative precast walls in seismic regions is an increase in the lateral displacements as a result of small inelastic energy dissipation. It is possible to reduce these displacements by using friction dampers along vertical joints between the walls, without losing the desirable characteristics of the walls. The paper introduces a performance-based seismic design approach to reduce the maximum lateral displacements of the walls below a target displacement using supplemental friction dampers. Nonlinear dynamic time-history analyses of prototype walls with different fundamental periods of vibration show that the design approach is effective in reducing the lateral displacements to prevent significant damage in the walls under severe ground motions.

1. INTRODUCTION AND BACKGROUND

Recent research conducted as a part of the PREcast Seismic Structural Systems (PRESSSS) Program (Kurama et al. 1999; Priestley et al. 1999) has shown that the use of unbonded post-tensioning in non-emulative precast concrete walls results in desirable seismic characteristics such as a self-centering capability and an ability to undergo “large” lateral displacements with little damage. The greatest disadvantage of these walls in seismic regions is an increase in the lateral displacements as a result of small inelastic energy dissipation (Kurama 2000). Perez (1999) and Priestley et al. (1999) investigated the use of metallic yield dampers along vertical joints between multiple precast walls to reduce the displacements under extreme ground motions. The use of supplemental viscous fluid-dampers to reduce the displacements of the walls was investigated by Kurama (2000).

This paper addresses the seismic behavior and design of unbonded post-tensioned precast walls with supplemental friction dampers along vertical joints. Fig. 1(a) shows the plan layout of a prototype precast concrete office building in a region with high seismicity and a site with a medium soil profile. Figs. 1(b)-(d) show three prototype walls (Walls CW1, CW2, and CW3 with 6, 8, and 10 stories, respectively) which were designed for the building layout in Fig. 1(a).

The supplemental energy dissipation system uses the relative slip displacements which occur along the vertical joint between the walls as a result of gap opening along the horizontal joints as shown

¹ *Civil Engineering and Geological Sciences, University of Notre Dame, Notre Dame, IN 46556, U.S.A.
E-mail: Kurama.1@nd.edu*

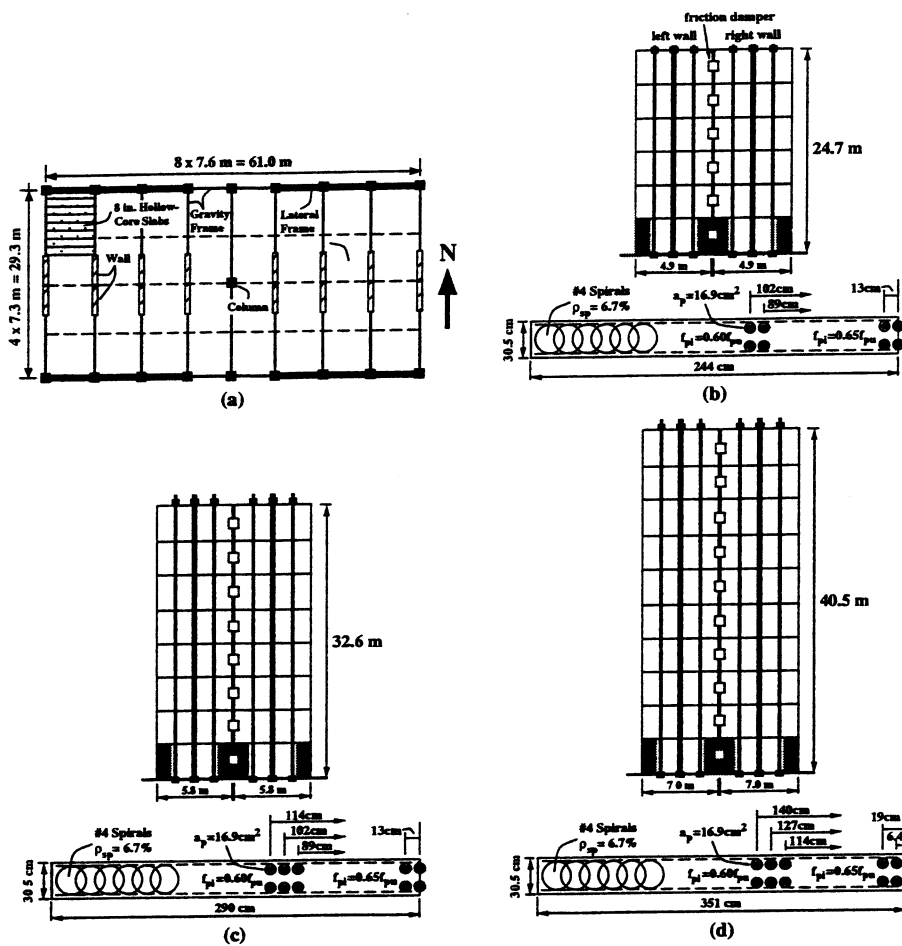


FIG. 1. Prototype buildings: (a) plan layout; (b) Wall CW1; (c) Wall CW2; (d) Wall CW3

in Fig. 2. It is noted that only the gap opening along the base-panel-to-foundation joint is shown in the idealized displaced shape of the wall in Fig. 2. In an actual wall, the slip displacements vary along the height of the wall as a result of the deformations of the wall including gap opening along the upper story horizontal joints. Recent tests of precast walls with metallic yield dampers along vertical joints at the University of California at San Diego (Priestley et al. 1999) have demonstrated that gap opening and slip displacements similar to Fig. 2 can occur without damaging the floor system.

Fig. 3 (a) shows the expected base-shear-roof-displacement ($V-u$) behavior of Wall CW1 without the friction dampers under combined gravity loads and cyclic lateral loads. The distribution of the lateral forces over the height of the wall is the same as the distribution of inertial forces corresponding to the first mode of vibration from a linear-elastic modal analysis of the structure. Fig. 3(a) shows that the hysteretic behavior of the wall is nearly nonlinear-elastic, characterized by loading and unloading curves that are very close to each other. The nonlinear behavior occurs primarily due to the opening of gaps along the horizontal joints (Kurama et al. 2000). The extremely narrow hysteresis loops show that the inelastic energy dissipation of the wall is very small.

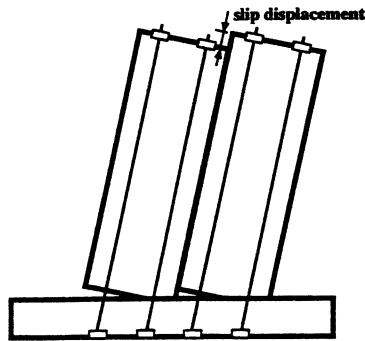


FIG. 2. Idealized slip displacements

Fig. 3(b) shows the expected $V-u$ behavior of Wall CW1 with friction dampers. The slip force for the dampers, F_s , is assumed to be equal to 583 kN. The results show that the inelastic energy dissipation capacity of the wall is significantly increased by the friction dampers as indicated by the much fuller hysteresis loops in Fig. 3(b). The self-centering capability of the wall (i.e., the ability of the wall to return towards its undisplaced position upon unloading from a large nonlinear displacement) is preserved.

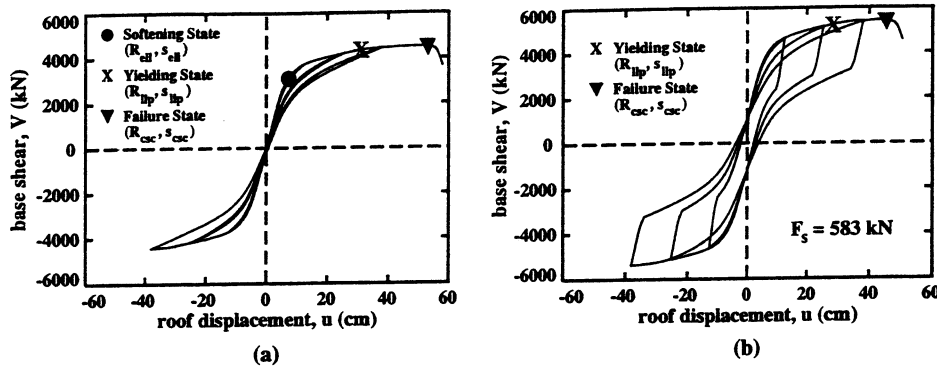


FIG. 3. Base-shear-roof-displacement relationship: (a) without dampers; (b) with dampers

Figs. 3(a) and (b) indicate that the lateral displacements of unbonded post-tensioned walls can be reduced by using friction dampers. A design approach for the walls without the dampers is described in Kurama et al. (1999). This paper proposes a performance-based

seismic design approach for the dampers to reduce the maximum roof displacements below a target roof displacement to prevent significant damage in the walls. The adequacy of the design approach is evaluated based on nonlinear dynamic time-history analyses of Walls CW1, CW2, and CW3.

2. ANALYTICAL MODEL

This section describes the analytical model which was developed for multi-story unbonded post-tensioned precast walls with supplemental friction dampers. As an example, Fig. 4(a) shows the model for Wall CW1. The analytical modeling of walls without dampers is discussed by Kurama et al. (1999) and is not described here in detail. Fiber beam-column elements are used to model the concrete wall panels and truss elements (not shown in Fig. 4(a)) are used to model the unbonded

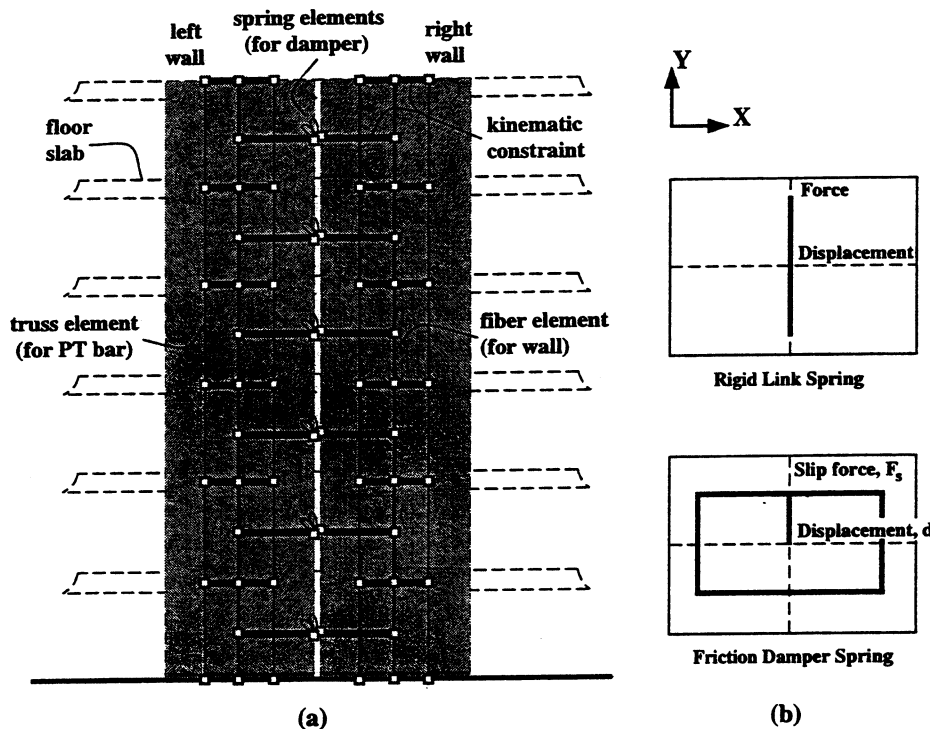


Fig. 4. Wall model: (a) multi-story wall; (b) spring elements

post-tensioning steel. The model, which is referred to as the fiber wall model, accounts for axial-flexural interaction, hysteretic behavior of the post-tensioning steel and concrete including crushing of concrete, and gap opening along the horizontal joints. The verification of the fiber wall model is described in Kurama (2000).

The friction dampers are modeled using zero-length spring elements as shown in Fig. 4(a). The X-displacement, Y-

displacement, and rotation degrees-of-freedom (DOF) of the damper nodes are kinematically constrained to the DOF of the corresponding wall nodes (at the same height as the damper nodes). Two zero-length spring elements are used between each pair of damper nodes. Fig. 4(b) shows the hysteretic force-displacement relationships of the spring elements. The first spring element is a rigid link element in the X-direction in order to ensure that the two walls go through the same lateral displacements. The second spring element is defined in the Y-direction to represent the behavior of the friction dampers along the vertical joint between the walls. The friction mechanism is characterized by close-to rectangular hysteresis loops, which are assumed to be generated by Coulomb friction. It is assumed that the anchorages between the walls and the dampers are properly designed for the maximum damper forces.

3. GROUND MOTION RECORDS

Two sets of ground motion records are used which are representative of maximum credible ground motions that can be expected in regions of the U.S. with high seismicity. The first set includes seven ground motions (five natural records and two generated records) selected and scaled at the University of Notre Dame as described in Kurama (2000). The Notre Dame (ND) ground motions are scaled to a constant maximum incremental velocity, MIV of 171 cm/sec. The MIV of a ground motion is equal to the maximum area under the acceleration time-history of the ground motion between two successive zero acceleration crossings. The ground motions are for sites with a medium soil profile similar to the site soil condition used in the design of the prototype walls. The second set includes twenty ground motion records (ground motions LA21 through LA40), having probabilities of exceedence of 2% in 50 years, as compiled and scaled by the SAC steel project (Somerville 1997).

4. SDOF REPRESENTATION OF THE UNDAMPED WALL SYSTEM

The seismic design of the friction dampers is based on a single-degree-of-freedom (SDOF) representation of the multi-degree-of-freedom (MDOF) wall system. For this purpose, the wall without the friction dampers is referred to as the “undamped” wall, which is assumed to have a viscous damping ratio of 3% in the first and third modes (using Rayleigh damping). The properties of the SDOF system are determined based on the linear-elastic first (i.e., fundamental) mode response of the MDOF system. The linear-elastic frequency and damping ratio of the SDOF system are assumed to be equal to the linear-elastic first mode circular frequency, ω_u and viscous damping ratio, ξ_u of the undamped MDOF wall, respectively.

The nonlinear force-displacement (R-s) relationship of the SDOF system is determined as follows. Fig. 5(a) shows a trilinear idealization of the base-shear-roof-displacement (V-u) relationship of Wall CW1 (without the dampers) in Fig. 3(a). The trilinear idealization of the V-u relationship is based on (Kurama et al. 1999): (1) the “softening” state (indicated by a ● marker) which identifies the beginning of a significant reduction in the lateral stiffness of the wall due to gap opening along the horizontal joints and nonlinear behavior of the concrete in compression (at a base shear and roof displacement of V_{e11} and u_{e11} , respectively); (2) the “yielding” state (indicated by a X marker) which identifies the point at which the strain in the post-tensioning steel reaches the limit of proportionality

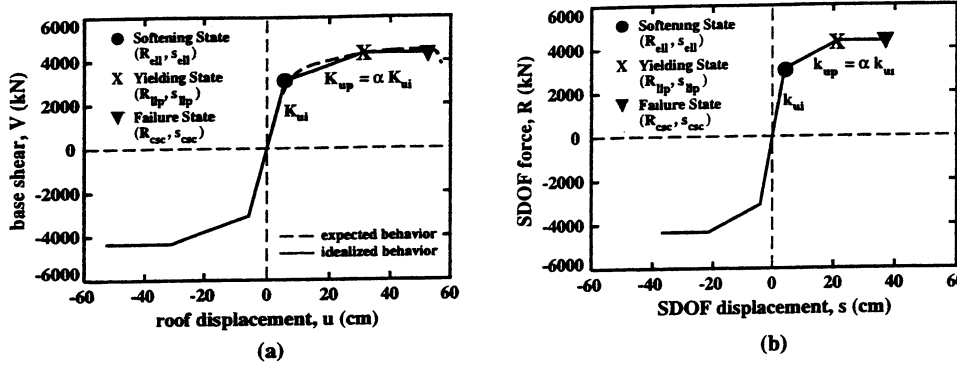


FIG. 5. SDOF representation of the undamped wall: (a) idealized MDOF model; (b) SDOF model

for the first time (at V_{llp} and u_{llp}); and (3) the “failure” state (indicated by a \blacktriangledown marker) which identifies axial-flexural failure of the wall as a result of crushing of the spiral confined concrete (Fig. 1) near the base (at V_{csc} and u_{csc}).

Fig. 5(b) shows the nonlinear force-displacement (R-s) relationship of the SDOF system to represent the idealized V-u relationship of the undamped MDOF system in Fig. 5(a). The SDOF displacements, s are determined by dividing the roof displacements of the MDOF system, u with the roof displacement participation factor, Γ based on the first linear-elastic mode shape of the wall as

$$\begin{aligned}
 s_{ell} &= \frac{u_{ell}}{\Gamma} \\
 s_{llp} &= \frac{u_{llp}}{\Gamma} \\
 \Gamma &= \frac{L}{M^*} \\
 L &= \{ \phi_{ui} \}^T [M] \{ 1 \} \\
 M^* &= \{ \phi_{ui} \}^T [M] \{ \phi_{ui} \}
 \end{aligned} \tag{1}$$

where L is the earthquake excitation factor and M^* is the generalized mass for the first mode, $\{ \phi_{ui} \}$ is the first linear-elastic mode-shape of the undamped wall normalized with respect to the roof, and $[M]$ is the diagonal mass matrix assigned to the wall. The mass of the SDOF system is assumed to be equal to the effective first mode mass, m of the MDOF system as $m = L^2 / M^*$ and, the initial stiffness, k_{ui} and post-softening stiffness, k_{up} of the SDOF system are calculated as

$$\begin{aligned}
 k_{ui} &= m \omega_{ui}^2 \\
 k_{up} &= \alpha k_{ui} \\
 \alpha &= \frac{V_{llp}/V_{ell} - 1}{u_{llp}/u_{ell} - 1}
 \end{aligned} \tag{2}$$

where α is the post-softening stiffness ratio of the undamped MDOF wall system. The hysteretic force-displacement relationship of the SDOF system in Fig. 5(b) is assumed to be nonlinear-elastic (i.e., with no inelastic energy dissipation). Thus, the small amount of inelastic energy dissipation of the MDOF system in Fig. 3(a) is ignored.

5. SDOF REPRESENTATION OF THE DAMPED WALL SYSTEM

Fig. 6(a) shows the shear forces and axial forces that develop at the base of the left wall and right wall as a result of the coupling between the two walls due to the damper forces. The coupling base shear, V_s and roof displacement, u_s corresponding to the slip of the dampers can be calculated as

$$V_s = \frac{n_d F_s l_w}{\bar{h}} \quad (3)$$

$$u_s = \frac{V_s}{K_s} = \frac{V_s}{K_{di} - K_{ui}}$$

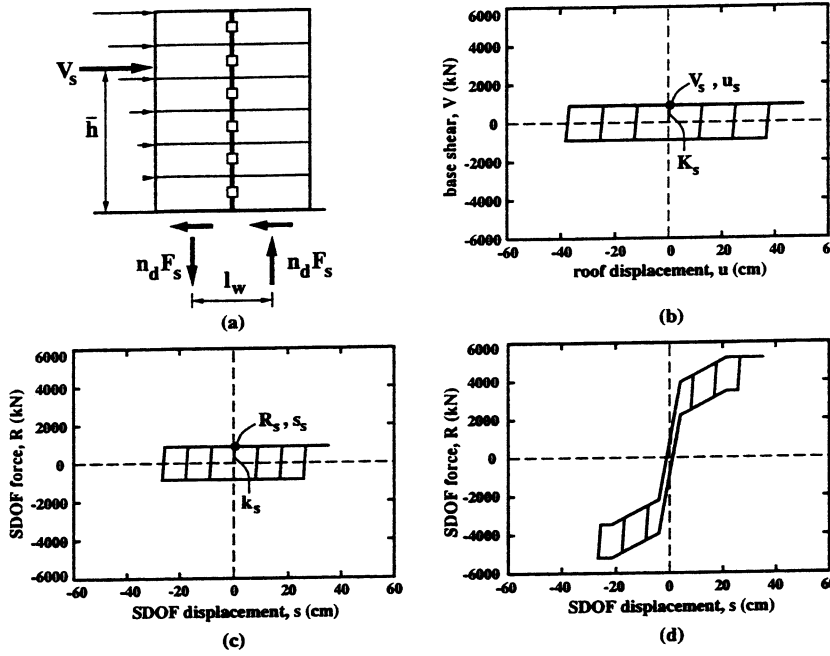


FIG. 6. SDOF representation of the damped wall: (a) coupling forces; (b) MDOF damper model; (c) SDOF damper model; (d) SDOF wall model

base-shear-roof-displacement relationship is shown in Fig. 6(c). The initial stiffness, k_s and slip displacement, s_s for the SDOF damper model in Fig. 6(c) are

$$k_s = k_{di} - k_{ui} = m \omega_{di}^2 \left(\frac{\omega_{di}^2}{\omega_{ui}^2} - 1 \right) \quad (4)$$

$$s_s = u_s / \Gamma$$

where ω_{di} is the linear-elastic first mode circular frequency of the damped MDOF wall system. It is noted that the linear-elastic first mode shape of the undamped wall system is used in the determination of \bar{h} , m , and Γ in Eqs. (3) and (4) since slip of the dampers occurs very early in the response, and thus, the response of the damped wall system is primarily governed by the mode shapes of the undamped wall system. The resulting SDOF force-displacement (R-s) relationship for

where n_d is the number of dampers, F_s is the slip force for one damper, l_w is the length of one wall, \bar{h} is the resultant height of first mode inertia forces, K_s is the increase in the initial lateral stiffness of the wall system due to the coupling between the walls, and K_{di} and K_{ui} are the initial lateral stiffness of the damped and undamped systems, respectively. It is assumed that all dampers slip at the same roof displacement.

Fig. 6(b) shows the coupling base-shear-roof-displacement relationship of the walls due to the damper forces. The SDOF representation of the coupling

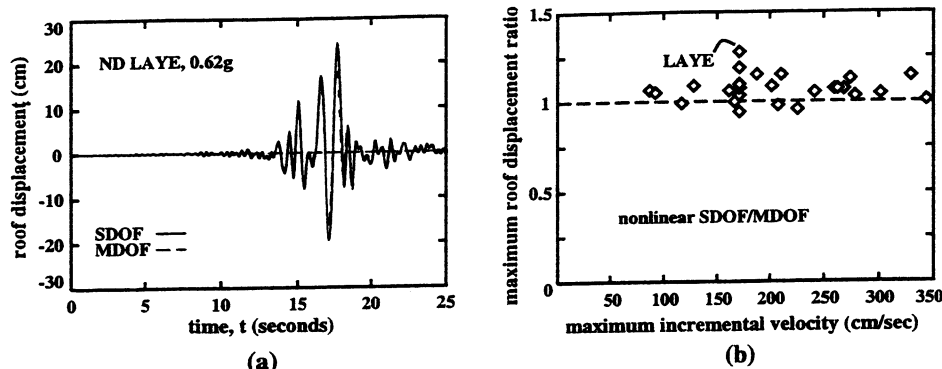


FIG. 7. Nonlinear SDOF model: (a) displacement time-history; (b) maximum displacement ratio

Fig. 7(a) compares the roof-displacement time-history of the damped MDOF system in Fig. 3(b) and the SDOF system in Fig. 6(d) under the ND Landers-Yermo (LAYE) ground motion. It is noted that the displacements of the SDOF system are multiplied with Γ . Fig. 7(b) shows the ratio between the maximum displacements of the SDOF system and the damped MDOF system under the 27 ND and SAC ground motions. On average, the ratio between the maximum displacements of the SDOF and MDOF systems is equal to 1.07.

It is concluded that the nonlinear SDOF system is capable of predicting both the maximum displacement and the roof-displacement time-history of the damped MDOF wall system reasonably well. The maximum displacement of the SDOF system is usually slightly larger than that of the MDOF system because of the small amount of inelastic energy dissipated by the undamped system (as shown in Fig. 3(a)) which is ignored in the SDOF system.

6. EQUIVALENT LINEARIZATION OF THE SDOF SYSTEM

For the SDOF system exhibiting the nonlinear properties in Fig. 6(d), the maximum displacement response can be reasonably approximated using an equivalent linear-elastic SDOF system whose stiffness and damping properties are expressed in terms of the properties of the nonlinear system as follows. Iwan and Gates (1979) have proposed an average stiffness method to determine the equivalent linear-elastic stiffness to represent a bilinear elasto-plastic system. This method is extended here to the trilinear undamped SDOF system shown in Fig. 5(b). It is noted that the increase in the initial stiffness of the wall due to the dampers is neglected since slip of the dampers occurs very early in the response. Thus, the equivalent linear-elastic stiffness is determined based on the undamped SDOF system only. According to the average stiffness method, the equivalent linear-elastic stiffness, k_e is calculated as

$$k_e = \frac{1}{s_{\max}} \int_0^{s_{\max}} k_u(s) ds \quad (5)$$

$$k_e = k_{ui} e_k$$

which, for the trilinear system in Fig. 5(b), results in

$$\begin{aligned}
(s_{ell} \leq s_{max} \leq s_{llp}) &\Rightarrow e_k = (1-\alpha) \frac{1 + \ln (s_{max}/s_{ell})}{s_{max}/s_{ell}} + \alpha \\
(s_{max} > s_{llp}) &\Rightarrow e_k = (1-\alpha) \frac{1 + \ln (s_{max}/s_{ell})}{s_{max}/s_{ell}} + \alpha \frac{1 + \ln (s_{max}/s_{llp})}{s_{max}/s_{llp}}
\end{aligned} \tag{6}$$

here s_{max} is the maximum displacement, s_{ell} and s_{llp} are defined in Eq. (1), and k_{in} and α are defined in Eq. (2).

The equivalent viscous damping ratio of the linear-elastic system is determined using a variation of the Resonant Amplitude Matching method (Iwan and Gates 1979) as

$$\begin{aligned}
\xi_e &= \frac{D_h}{2 \pi k_e s_{max}^2} + \xi_u \sqrt{\frac{1}{e_k}} \\
D_h &= 4 k_s s_s (s_{max} - s_s)
\end{aligned} \tag{7}$$

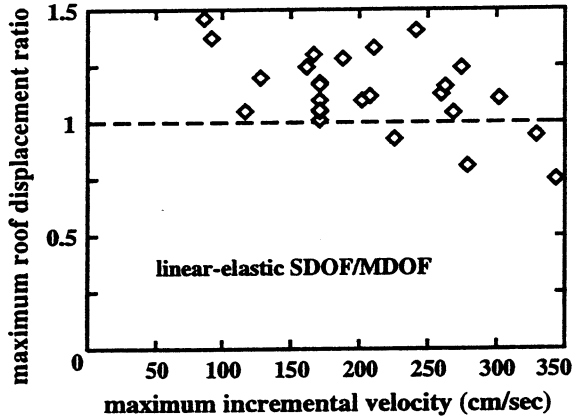


FIG. 8. Equivalent linear SDOF model

where D_h is the energy dissipated by the SDOF damper model in Fig. 6(c) during one cycle of response to the maximum displacement (i.e., between s_{max} and $-s_{max}$). The shift in the frequency of the nonlinear system is included in the estimation of ξ_e as indicated by the use of k_e in Eq. (7).

Fig. 8 shows the ratio between the maximum displacements of the linear-elastic SDOF system and the nonlinear MDOF system under the 27 ground motions. On average, the ratio between the maximum displacements of the two systems is equal to 1.13.

7. DESIGN APPROACH

This section describes the design of the supplemental friction dampers along the vertical joints. The seismic design of the walls without the friction dampers is discussed in Kurama et al. (1999) and is not described here. The objective of the design approach is to determine the required damper slip force to reduce the maximum roof-displacement of the walls below a target roof-displacement. This is achieved by comparing the capacity of the walls in the form of a generalized “capacity curve” with equivalent seismic demands in the form of average ground motion “demand spectra” as described in Kurama (2000). The design approach is demonstrated below using Wall CW1.

7.1 Ground motion demand spectra and structure capacity curve

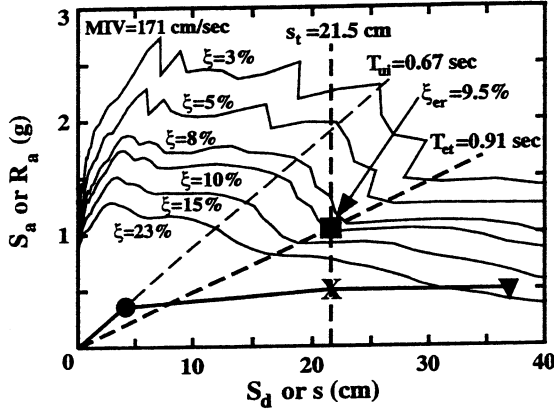


FIG. 9. Design approach

The demand spectra for a ground motion are constructed by plotting the linear-elastic SDOF pseudo-acceleration response spectra, S_a versus the displacement response spectra, S_d for different values of the viscous damping ratio, ξ . In the design of the dampers for the prototype walls, average demand spectra using the seven MIV-scaled ND ground motions are used. For this purpose, the thin solid lines in Fig. 9 show the average demand spectra (normalized with respect to g) of the ND ground motions for damping ratios of $\xi = 3, 5, 8, 10, 15,$ and 23% , respectively.

The capacity curve of the wall is determined from the nonlinear SDOF force-displacement (R - s) relationship of the undamped wall in Fig. 5(b). The SDOF force, R is converted to an equivalent SDOF acceleration, R_a by dividing with the effective first mode mass as $R_a = R/m$. The capacity curve for Wall CW1 is shown by the heavy solid line in Fig. 9. The light dashed radial line corresponds to the linear-elastic fundamental period of the undamped wall, $T_{00} = 2\pi/\omega_{00} = 0.67$ sec.

7.2 Target roof-displacement and equivalent fundamental period

As stated above, the objective of the design approach is to determine the required slip force of the dampers to reduce the maximum roof-displacement of the wall below a target roof-displacement, u_t . In order to prevent significant damage in the walls (Kurama 2000), the dampers are designed for a target roof-displacement of $u_t = u_{1p}$ (corresponding to the yielding state). The vertical dashed line in Fig. 9 shows the target roof-displacement for Wall CW1, $u_t = u_{1p} = 30.9$ cm converted to the target SDOF displacement, $s_t = s_{1p} = u_{1p}/\Gamma = 21.5$ cm.

The heavy dashed radial line in Fig. 9 represents the equivalent fundamental period, T_{et} for the wall corresponding to the target roof-displacement, u_t as $T_{et} = 2\pi(m/k_{et})^{0.5}$ where k_{et} is the equivalent stiffness of the wall corresponding to the target displacement, u_t . For $u_t = u_{1p}$, T_{et} is estimated as 0.91 sec. using Eqs. (5) and (6) with $s_{max} = s_t = 21.5$ cm. The estimated T_{et} represents a 35% elongation over the initial linear-elastic fundamental period of the undamped wall, $T_{00} = 0.67$ sec.

7.3 Required equivalent viscous damping ratio and damper slip force

The equivalent fundamental period T_{et} is used together with the capacity curve and the average demand spectra in Fig. 9 to estimate the required equivalent viscous damping ratio, ξ_{er} . The intersection point between the vertical line (at $s_t = 21.5$ cm) and the heavy radial line (at $T_{et} = 0.91$ sec.) gives the required equivalent viscous damping ratio, ξ_{er} to reduce the maximum roof-displacement below the target displacement. The estimated ξ_{er} for Wall CW1 is equal to 9.5%.

The required damper slip force, F_{sr} to achieve the required damping ratio, ξ_{er} is estimated for an assumed number of dampers, n_d using Eqs. (3), (4), and (7). It is assumed that the dampers have the

same slip force. For preliminary design $K_{di}/K_{ui} \approx (n_w l_w)^3/n_w l_w^3 = n_w^2$, where $n_w = 2$ is the number of walls may be used assuming that the dampers provide full coupling between the walls until slip occurs. Assuming that the system without the dampers has a viscous damping ratio of $\xi_u = 3\%$, the estimated required damper slip force for Wall CW1 is $F_{sr} = 537$ kN with $n_d = 6$ (Fig. 1(b)).

8. EVALUATION OF DYNAMIC RESPONSE

The proposed design approach for the friction dampers is evaluated based on nonlinear dynamic time-history analyses of Walls CW1, CW2, and CW3. The walls without the dampers (Table 1) were designed for a region with high seismicity and a site with a medium soil profile (site class D as defined in NEHRP-97 (FEMA 1998)) using a seismic design approach described in Kurama et al. (1999) and the provisions of NEHRP-97. In Table 1, the roof-displacements of the walls, u are given in terms of the roof-drift, Δ (%) by dividing the displacements with the wall height.

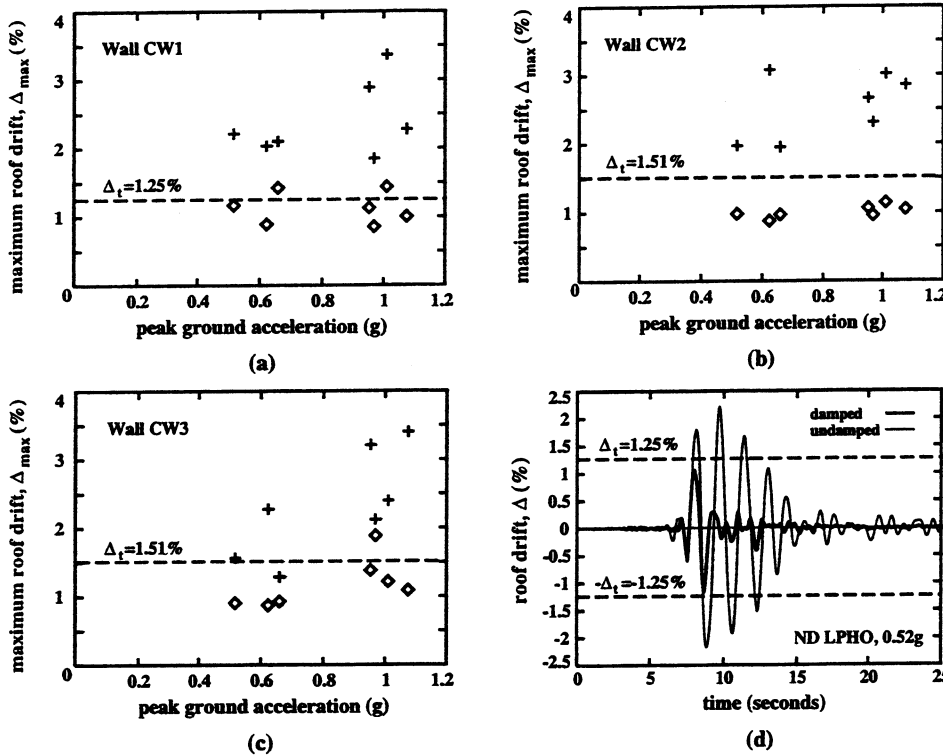


FIG. 10. Evaluation of dynamic response: (a)-(c) maximum roof-drift of Walls CW1, CW2, CW3, respectively; (d) roof-drift time-history for Wall CW1

ND ground motions and with a time step of 0.01 sec. Table 3 shows the average maximum roof-drift, $\bar{\Delta}_{max}$ of the walls from the dynamic analyses. The average maximum roof-drift, $\bar{\Delta}_{max}$ for the damped walls (i.e., with the friction dampers) are smaller than the corresponding target roof-drift, Δ_{llp} values in Table 2. Thus, the design objectives are on average achieved.

The dynamic analysis results indicate that the supplemental energy dissipation system is, on average, effective in significantly reducing the maximum roof-drift of the walls. The average ratio between the maximum roof-drift of the damped walls and undamped walls are equal to 0.48, 0.41, and 0.55

The friction dampers for the walls were designed as demonstrated above for Wall CW1. The estimated equivalent fundamental period, T_{er} , required equivalent viscous damping ratio, ξ_{er} , and required damper slip force, F_{sr} for the walls corresponding to the target roof-drift, $\Delta_t = \Delta_{llp}$ at the yielding state are in Table 2.

Figs. 10(a)-(c) show the maximum roof-drift, Δ_{max} from the dynamic analyses of the walls. The dynamic analyses were conducted using the seven MIV-scaled

for Walls CW1, CW2, and CW3, respectively. Figs. 10(a)-(c) also show that the scatter in the maximum roof-drift of the undamped walls is significantly larger than that of the damped walls.

Fig. 10(d) compares the roof-drift time-histories of Wall CW1 with and without the dampers under the MIV-scaled Loma Prieta-Hollister (LPHO) ground motion. The time-history results indicate that the dampers are very effective in reducing the large roof-drift cycles that occur in the undamped wall after the maximum roof-drift is reached.

The average maximum roof-acceleration, \bar{a}_{max} of the walls are shown in Table 3. The average ratio between the maximum roof-acceleration of the damped walls and undamped walls are equal to 0.83, 1.00, and 0.89 for Walls CW1, CW2, and CW3, respectively.

Table 1 - Walls without friction dampers.

Wall	h_w (m)	l_w (m)	T_{ui} (sec.)	V_{ell} (kN)	Δ_{ell} (%)	V_{llp} (kN)	Δ_{llp} (%)	Δ_{csc} (%)
CW1	24.7	2x4.9	0.67	3078	0.23	4342	1.25	2.15
CW2	32.6	2x5.8	0.90	3459	0.27	5041	1.51	2.26
CW3	40.5	2x7.0	1.05	4067	0.27	5799	1.51	2.78

Table 2 - Friction dampers.

Wall	T_{et} (sec.)	ξ_{ser} (%)	F_{sr} (kN)
CW1	0.91	9.6	537
CW2	1.23	12.0	733
CW3	1.43	10.6	567

Table 3 - Dynamic response of the prototype walls.

Wall	$\bar{\Delta}_{max}$ (%)		\bar{a}_{max} (g)	
	undamped	damped	undamped	damped
CW1	2.39	1.13	1.62	1.32
CW2	2.55	1.00	1.51	1.49
CW3	2.32	1.18	1.81	1.59

9. CONCLUSIONS

The paper proposes a seismic design approach for unbonded post-tensioned precast walls with friction dampers along vertical joints. The adequacy of the design approach is evaluated based on nonlinear dynamic time-history analyses of three prototype walls with and without friction dampers. The main contributions and conclusions of the paper are as follows.

1. The design approach uses an equivalent linear-elastic SDOF representation of the walls with the dampers. The estimation of the equivalent linear-elastic stiffness and damping properties for the walls is described in the paper.

2. The objective of the design approach is to reduce the maximum roof-drift to a target roof-drift to prevent significant damage in the walls. This is achieved by comparing the capacity of the walls in the form of a generalized "capacity curve" with equivalent seismic demands in the form of ground motion "demand spectra".

3. Nonlinear dynamic time-history analyses of 6, 8, and 10-story prototype walls with and without friction dampers show that the proposed design approach is, on average, effective in reducing the maximum roof-drift below the target roof-drift.

4. Walls with friction dampers have significantly smaller scatter in maximum roof-drift than walls without friction dampers. Furthermore, the large roof-drift cycles that occur in the walls after the maximum roof-drift is reached are effectively reduced by the friction dampers.

10. ACKNOWLEDGMENTS

The investigation is funded by the National Science Foundation (NSF) under Grant No. CMS 98-74872 as a part of the CAREER Program. The support of the NSF Program Director Dr. S. C. Liu is gratefully acknowledged. The opinions, findings, and conclusions are those of the author and do not necessarily reflect the views of the NSF or those acknowledged above.

11. REFERENCES

FEMA (1998). NEHRP recommended provisions for seismic regulations for new buildings and other structures. FEMA 302, Federal Emergency Management Agency, Washington, D.C.

Iwan, W. and Gates N. (1979). Estimating earthquake response of simple hysteretic structures. *Journal of Engineering Mechanics*, American Soc. of Civil Eng., Vol. 105, No. EM3, pp. 391-405.

Kurama, Y. (2000). Seismic design of unbonded post-tensioned precast walls with supplemental viscous damping. *ACI Structural Journal*, American Concrete Institute, Vol. 97, No. 4.

Kurama, Y., Pessiki, S., Sause, R., and Lu, L.W. (1999). Seismic behavior and design of unbonded post-tensioned precast concrete walls. *PCI Journal*, Pre./Prest. Conc. Inst., Vol. 44, No. 3, pp. 72-89.

Perez, F. (1998). Lateral load behavior of precast concrete walls with ductile vertical joint connectors. M.S. Thesis, Dept. of Civil and Env. Engineering, Lehigh University, Bethlehem, PA.

Priestley, M., Sritharan, S., Conley, J., and Pampanin, S. (1999). Preliminary results and conclusions from the PRESSS five-story precast concrete test building. *PCI Journal*, Vol. 44, No. 6, pp. 42-67.

Somerville, P. (1997). Development of ground motion time histories for phase 2 of the FEMA/SAC steel project. Report No. SAC/BD-97/04, SAC Joint Venture, Sacramento, CA.

12. KEYWORDS

Concrete, friction dampers, friction damping, precast concrete, precast wall, prestressed concrete, seismic design, shear wall, structural wall, supplemental damping, supplemental energy dissipation, unbonded post-tensioning.

SUB-STRUCTURE PSEUDO DYNAMIC TESTING ON 6-STORY REINFORCED CONCRETE FRAME WITH SOFT FIRST STORY

Hiroshi KURAMOTO¹ and Toshimi KABEYASAWA²

ABSTRACT

A sub-structure pseudo dynamic test for a six-story reinforced concrete frame with soft first story, which consisted of a bare frame in the first story and shear walls in the upper stories, was conducted to investigate the failure mechanism. The behavior of columns in the first story, which were subjected to high varying axial forces and shears, was especially focused in the investigation. The earthquake response analysis of the frame was also executed to confirm the possibility of simulating the test results. This paper shows an outline of the test and analysis.

1. INTRODUCTION

Many buildings suffered great damage in the 1995 Hyogoken-Nanbu Earthquake. Mentioned specially was the damage of reinforced concrete (RC) buildings with soft first story referred to as “*pilotis*-type buildings” in which the strength and stiffness of the first story are extremely lower than those of the upper stories. The damaged buildings were designed by not only the old seismic code before 1981 but also the code used in those days. In view of this kind of damaged buildings, the Ministry of Construction (MOC) immediately revised the Notification No.1997 that is related to the provision on the distribution of story stiffness along a building height, and showed some technical points to notice on the seismic design for RC buildings with soft first story¹⁾. Considering the immense damage of RC buildings with soft first story by the earthquake, the measure by MOC seems to be appropriate. However, since this was an emergency measure just after the earthquake, the technical points showed should be improved on the basis of the future research results. In particular, the causes of collapse in RC buildings with soft first story are not

¹ Associate Director for International Research Cooperation, Building Research Institute, Ministry of Construction, Tsukuba, Japan Email: kura@kenken.go.jp

² Professor, Earthquake Research Institute, the University of Tokyo, Tokyo, Japan
Email: kabe@eri.u-tokyo.ac.jp

made clear yet including the failure mechanisms, although the concentration of earthquake energy at the first story with large varying axial force and shear in the columns is pointed out as one of the causes in the past researches.

A sub-structure pseudo dynamic (PsD) test for a six-story RC frame with soft first story, which consisted of a bare frame in the first story and shear walls in the upper stories, was conducted to investigate the failure mechanism. The behavior of columns in the first story, which were subjected to high varying axial forces and shears, was especially focused in the investigation. The earthquake response analysis of the frame was also executed to confirm the possibility of simulating the test results. This paper shows an outline of the test and analysis.

2. SUB-STRUCTURE PSEUDO DYNAMIC TEST

2.1 Test Specimen

A two-story plane frame specimen of about two-fifth scale was fabricated, which simulated the lower two stories of the middle frame in a six-story RC residential building with soft first story shown in Fig. 1. As shown in Fig. 2, the specimen is one-span frame of which the length is 4,000mm with a stiff loading beam and a foundation stub in the top and bottom, respectively. The specimen had columns with a 400mm square section at the first and second stories and a beam with a section of 250mm x 400mm at the second story, and was infilled by a shear wall with a 80mm thickness at the second story. At the middle of each column at the first story, a load cell shown in Fig. 3 was installed to measure directly the varying axial force and shear in the columns. The details of bar arrangement in the specimen are listed in Table 1. The mechanical properties of the reinforcing bars and concrete used are also listed in Table 2.

2.2 Loading Method and Loading Apparatus

The sub-structure PsD testing method was applied to a six-story RC building with soft first story in which the lower two stories were an experimental portion (i.e. a specimen) and the upper four stories were corresponding to an analytical portion.

For conventional PsD tests, explicit integration schemes such as the central difference method are normally used to avoid iterative computations and the corresponding load reversal. However, when the explicit integration scheme is used for sub-structure PsD tests, the time interval applied has to be very small to meet the constraint of stability and this could make the experiment impracticable. About ten years ago, several unconditionally stable implicit and mixed implicit-explicit integration schemes have been successfully implemented for sub-structure PsD tests in the Building Research Institute (BRI)(Nakashima et al. 1990). Among them, it is found that the mixed implicit-explicit operator splitting (OS) method, originally proposed by Hughes et al. (1979) and successfully implemented for sub-structure PsD tests, is very convenient for incorporation into many existing dynamic response analysis codes using implicit integration procedures. The method of sub-structure PsD tests used in this study had been developed in BRI based on the above research. The algorithm is as follows:

- (a) Input external forces in the next loading ($i+1$) step, F_{i+1}
- (b) Predict the displacement and velocity at the $i+1$ step in both experimental and analytical portions, \bar{d}_{i+1} and \bar{v}_{i+1} :

$$\begin{aligned}\bar{d}_{i+1} &= d_i + \Delta t \cdot v_i + (\Delta t^2/4) \cdot a_i \\ \bar{v}_{i+1} &= v_i + (\Delta t/2) \cdot a_i\end{aligned}$$

where, d_i , v_i and a_i express the displacement, velocity and acceleration at the i step and Δt is an interval from i to $i+1$ steps.

- (c) Calculate restoring forces in the analytical portion, R_{i+1}^{ana} :

$$R_{i+1}^{ana} = K^{ana} \cdot \bar{d}_{i+1}$$

where, K^{ana} is the stiffness of a member in the analytical portion.

- (d) Calculate axial forces applied to the top of the experimental portion, P_{i+1}^{exp} , using R_{i+1}^{ana} .
- (e) Apply lateral story forces with keeping the axial forces of P_{i+1}^{exp} for the experimental portion, until the corresponding displacement reaches \bar{d}_{i+1} .
- (f) Measure restoring forces in the experimental portion, R_{i+1}^{exp}
- (g) Modify the external forces assumed in the $i+1$ step, F_{i+1}^*

$$\begin{aligned}
F_{i+1}^* &= F_{i+1} - C \cdot \bar{v}_{i+1} - R_{i+1}^{ana} - R_{i+1}^{exp} \\
a_{i+1} &= \left[M + (\Delta t/2) \cdot C + (\Delta t^2/4) \cdot K^{ana} \right]^{-1} \cdot F_{i+1}^* \\
v_{i+1} &= v_i + (\Delta t/2) \cdot (a_i + a_{i+1}) \\
d_{i+1} &= d_i + \Delta t \cdot v_i + (\Delta t^2/4) \cdot (a_i + a_{i+1})
\end{aligned}$$

(h) To next loading step.

In the developed method, the analytical portion is calculated using equivalent elastic frame models. In order to obtain the equivalent stiffness of members including shear walls of the upper four stories in the six-story frame, which is corresponding to the analytical portion, the inelastic push-over analysis for the whole frames using the Multi-Spring (MS) Model (Gu et al. (1988)) was executed before the test. The results indicated that the behavior of the upper four stories was almost elastic without occurring shear cracking in shear walls. Then, the upper four stories were analyzed as bare frames with equivalent elastic columns considering the structural properties of shear walls during the test. In the analysis during the test, the viscous damping was assumed to be 3% for the natural period of the first mode and be proportional to the initial stiffness.

Four earthquake ground motion records were used in the test. One was NS component of the 1995 Kobe Marine Observatory record of Japan Meteorological Agency (JMA). Other three were NS component of the 1940 El Centro records for which the level of the maximum velocity was normalized to 10cm/sec, 25cm/sec and 50cm/sec (EIC-10, EIC-25 and EIC-50), respectively. The input time was 7 seconds for each EIC motion and 4.5 seconds for JMA motion, respectively. The earthquake waves used for EIC-50 and JMA motions are drawn in Fig. 4.

In loading, as shown in Fig. 5, two horizontal actuators applied lateral story forces at the floor level of the third story which is 3,200mm in height from the column base, and two vertical actuators applied varying axial forces at the top of each column in the second story with an initial load of 441kN for each. As mentioned the above, the loading was conducted to be met the values of varying axial forces for each column and lateral displacement at the floor level of the third story calculated from the earthquake response analysis at each loading step.

3. TEST RESULTS

3.1 Failure Process

The final failure situation of the specimen after JMA input is sketched in Fig. 6. No crack occurred in the loading of EIC-10 input. In the loading of EIC-25 input, slightly flexural cracks of columns at the first story were observed in the bottom of the east side at the story drift angle of the first story, R_I , of 1/517 (1.8 sec), in the top of the west side at R_I of 1/388 (2.2 sec), in the bottom of the west side at R_I of -1/609 (3.8 sec), and in the top of the east side at R_I of -1/413 (4.2 sec), respectively. The occurrence and propagation of cracks were significant in the loading of EIC-50 input. Flexural cracks in a beam and slabs and shear cracks in a shear wall at the second story were observed at R_I of 1/366 to 1/179 (1.2 to 1.3 sec). The similar cracks in the beam, slabs and shear wall also occurred at R_I of about -1/140 (about 1.6 sec) in the loading of the opposite direction. In the loading of JMA input, crash of cover concrete in the top and bottom of the west side column at the first story was observed at R_I of about -1/60 (0.9 sec). Although the occurrence of new cracks was not so many, the propagation of cracks occurring in EIC-50 input was significant in this loading. Finally, the story collapse mechanism at the first story was formed with flexural yielding of columns.

3.2 Load versus Displacement Relations

Figure 7 shows the story shear versus lateral displacement relation for each earthquake motion inputted. In this figure, the vertical axis expresses shear applied at the floor level of the third story, and the horizontal axis shows story drift at the first story for dotted lines and the relatively lateral displacement from column bases at the second story for solid lines, respectively.

In the loading of EIC-10 input, the behavior of the specimen was elastic without the reduction of stiffness in both the first and second stories. The maximum story shear and drift for this input were 163.7kN and 1mm ($R_I=1/400$), respectively. In the loading of EIC-25 input, the stiffness of the first story was slightly reduced due to the occurrence of flexural cracks in the top and bottom of columns at the first story. This input induced the maximum story shear of 341.0kN and the

maximum story drift of 4.2mm ($R_f=1/333$). In the loading of EIC-50 input, the yield mechanism at the first story was almost formed and the maximum story shear and drift were 544.9kN and 14.8mm ($R_f=1/95$), respectively. The loading of JMA input induced large deformation in columns at the first story for the west direction at which the maximum story drift was 58.9mm ($R_f=1/24$) with the story shear of 543.9kN, although significant deterioration in load carrying capacity was not observed even after forming the yield mechanism.

Figure 8 shows the shear versus lateral displacement relations for columns at the first story in the loading of EIC-50 and JMA inputs. Chain and dotted lines in this figure give the flexural and shear strengths calculated, respectively. The shear measured was from load cells installed in the middle of each column. For both inputs, each column developed the flexural strength under both axial tension and compression. This means the frame formed the yield mechanism at the first story. The maximum lateral displacement of columns was about 14mm ($R_f=1/100$) for EIC-50 input and about 56mm ($R_f=1/25$) for JMA input, respectively. These values almost coincided with the maximum story drift at the first story.

3.3 External Force and Displacement in Each Story

Figure 9 shows the external force distribution at the maximum response for each earthquake motion inputted. As shown in Fig. 5, the loading system in this test was designed to make the external forces at the first and second stories concentrated at the second story, in order to avoid that the failure situation at the first story is affected by the existence of a loading stub which is to be installed at the floor level of the second story to apply the external force of the first story. In this reason, analyses in the sub-structure PsD test were executed for a five-story building model in which the mass of the first story was twice that of the other stories. Therefore, the external force applied at the second story is about twice that at the third story, while that at the first story is zero, as shown in Fig. 9. It is also indicated that the external forces at the third to sixth stories are almost the same value regardless of the level of earthquake motion inputted. This result implies that the external force distribution of the six-story frame tested was almost uniform at the maximum response.

The distributions of story drift along the building height at the maximum response for each earthquake motion inputted are shown in Fig. 10. The story drifts at lower two stories are measured and those at upper four stories are calculated. With an increase of the input level of earthquake motions, the drift at the first story increased extremely, while the increase of that at the other stories was not so much.

4. Comparison between Preliminary Analysis and Test Results

In this sub-structure PsD test, as mentioned before, lateral shear forces were applied for the specimen to be attained to the objective story displacement and axial forces of columns at the floor level of the third story obtained from the earthquake response analysis for the upper four stories in the six-story frame in each loading step. Therefore, the accuracy of the analysis during tests may seriously affect the test results. In order to confirm the accuracy of both the testing method and analytical tools used, a preliminary analysis was executed before the test, where modeling for the upper four stories was the same as that used in the sub-structure PsD test and the MS modeling was applied for the lower two stories, the experimental portion, as shown in Fig.11.

Figure 12 shows the time histories of story displacement at the first story, story shear at the second story and axial force of the east column at the first story for EIC-50 and JMA inputs. Solid and dotted lines in the figure express experimental and analytical results, respectively. Good agreement between experimental and analytical results was obtained for responses of not only the story shear and displacement but also the axial force of the column. These results give high reliability for the accuracy of the testing method and the validity of modeling in the analytical tools used.

5. CONCLUSIONS

For a six-story reinforced concrete plane frame with soft first story, sub-structure pseudo dynamic tests were conducted to investigate the failure mechanism. The maximum story drift

angle at the first story reaches to 1/95 for EIC-50 input and 1/24 for JMA input, respectively. The story collapse mechanism at the first story with the flexural yielding of columns was observed in the final stage. Almost uniform distributions for the external force of each story were formed at the maximum response for all earthquake motion inputted. The axial force of columns at the first story roughly ranged from –250kN to 980kN.

The preliminary earthquake response analysis executed in advance of the sub-structure pseudo dynamic test gave good predictions for experimental results on the story shear, the story drift and the axial force of columns at the first story. This implies high reliability for the accuracy of the testing method and the validity of modeling in the analytical tools used.

6. REFERENCES

- BCJ (1995). *Commentary on the Seismic Provisions and Design for Buildings*. Building Center of Japan.
- Gu J., Inoue N. and Shibata A. (1988). Inelastic Analysis of RC Member Subjected to Seismic Loads by Using MS Model. *Journal of Structural Engineering*. Architectural Institute of Japan. Vol. 44B: 157-166.
- Hughes T.J.R., Pister K.S. and Taylor R.L. (1979). Implicit-Explicit Finite Elements in Nonlinear Transient Analysis. *Computer Methods in Applied Mech. and Eng.* 17/18: 159-182.
- Nakashima M., Kaminosono T., Ishida M. and Ando K. (1990). Integration Techniques for Substructuring Pseudodynamic Test. *Proceedings of Fourth U.S. National Conference on Earthquake Engineering (Volume 2)*. Palm Springs, California.

7. KEYWORDS

Sub-Structure Pseudo Dynamic Test: Soft First Story: Story Collapse Mechanism: Varying Axial Load: Multi-Spring Model: Earthquake Response Analysis

Table 1 Detail of Bar Arrangement

Member	Story	b x D (cm)	Long. Reinf.	Trans. Reinf.
Column	1 and 2	40 x 40	16-D13	D6@50
Beam	2	25 x 40	12-D13	D6@80
Shear Wall	2	Thickness (cm)		Arrangement
		8		D6@80

Table 2 Mechanical Properties of Materials Used (Unit: N/mm²)

Concrete			
σ_B	ϵ_c	E_c	
29.8	0.213	2.64 x 10 ⁵	
Reinforcing Bar			
Diameter	σ_y	ϵ_y	σ_u
D6	376.9	0.221	515.8
D13	396.4	0.236	542.0

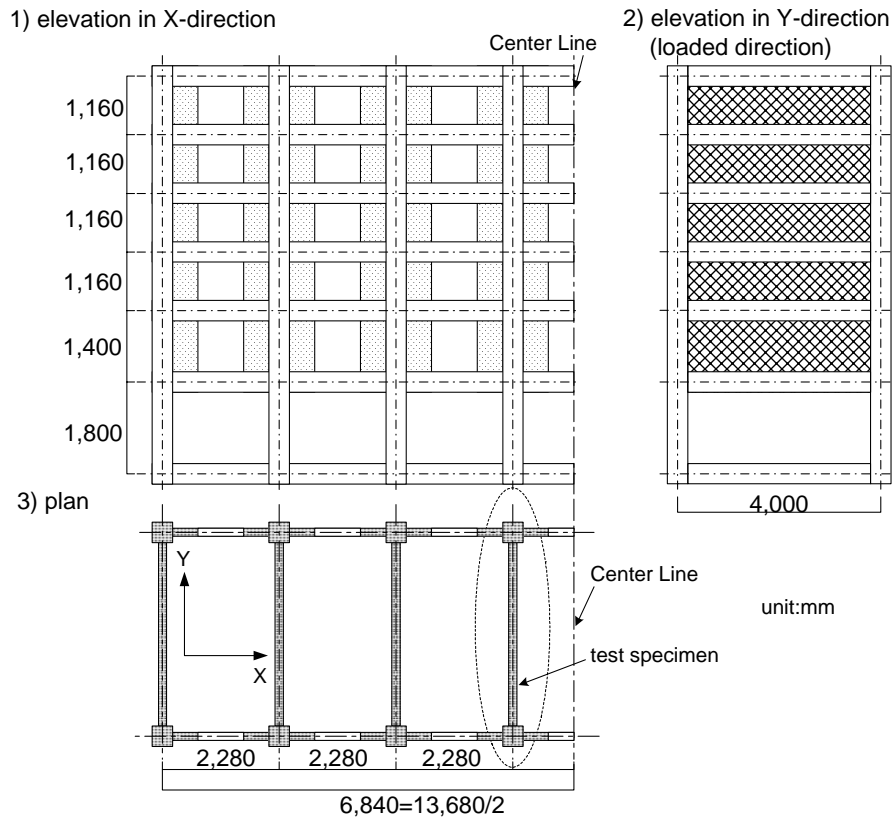


Fig. 1 Outline of Prototype Building

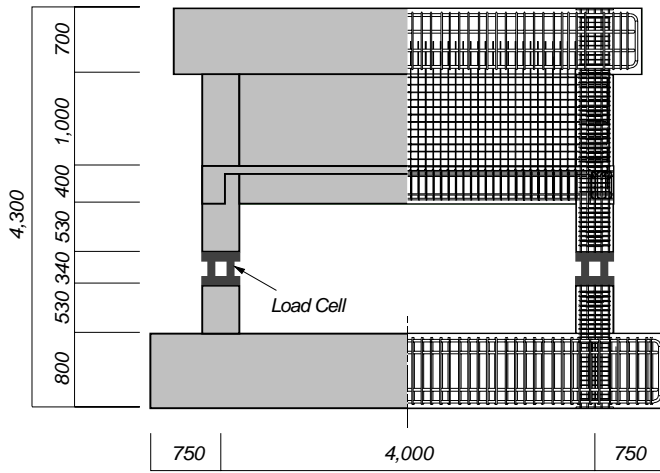


Fig. 2 Test Specimen

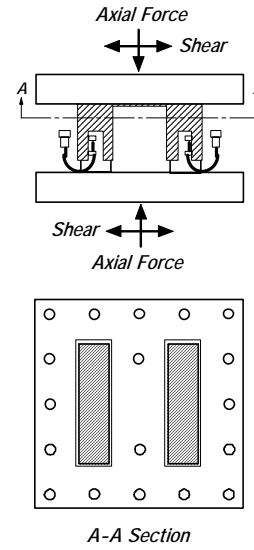


Fig. 3 Load Cell to Measure Stresses in Columns

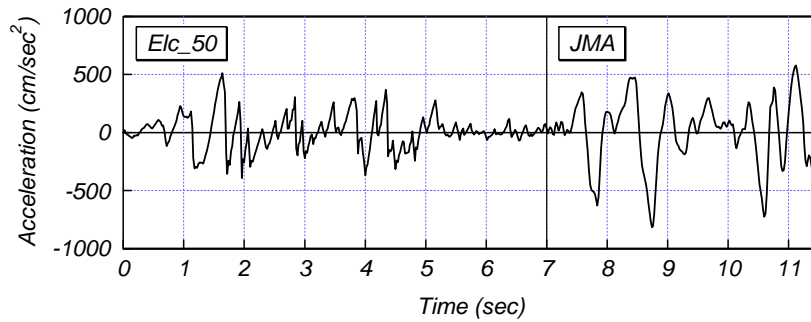


Fig. 4 Earthquake Ground Motions Inputted

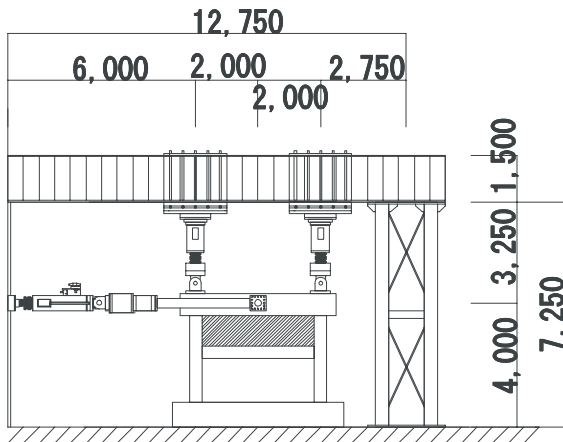


Fig. 5 Loading Apparatus

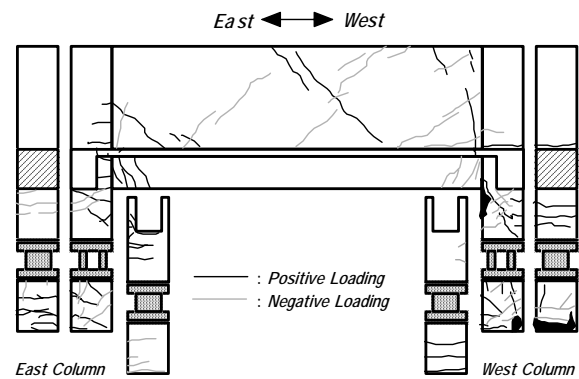


Fig. 6 Failure Situation after Testing

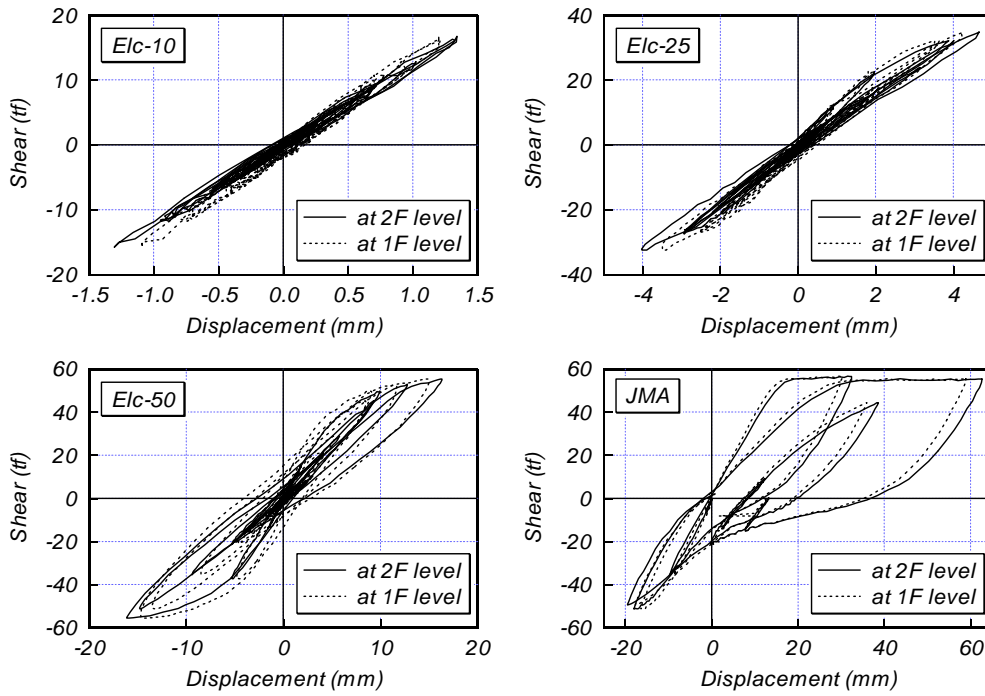


Fig. 7 Story Shear versus Lateral Displacement Relations

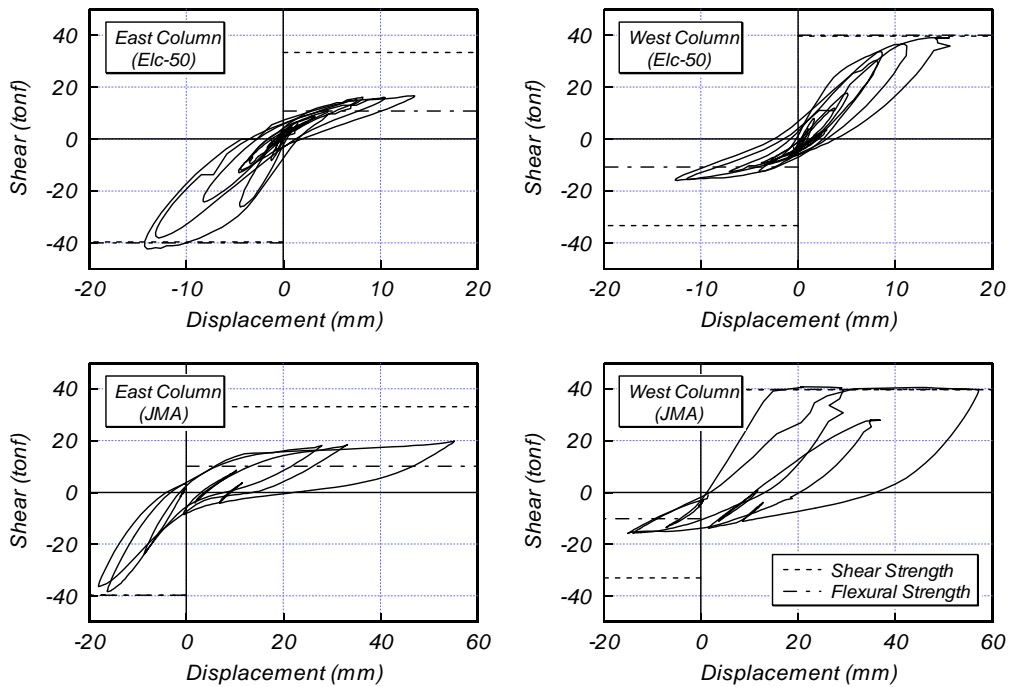


Fig. 8 Shear versus Lateral Displacement Relations for Columns at the First Story

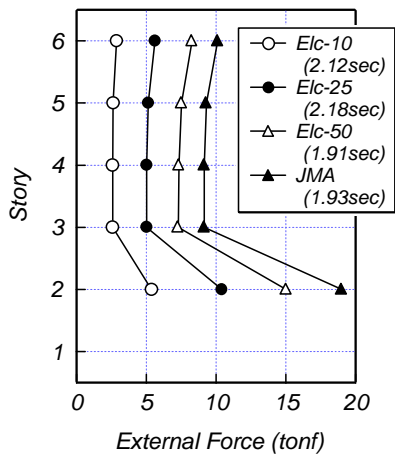


Fig. 9 External Force Distribution

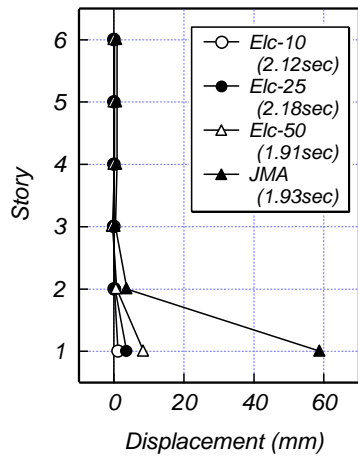


Fig. 10 Story Drift Distribution

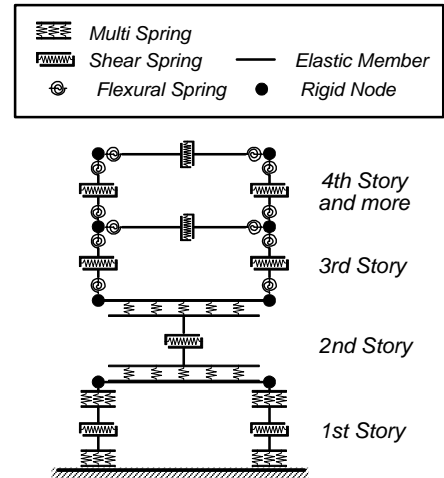
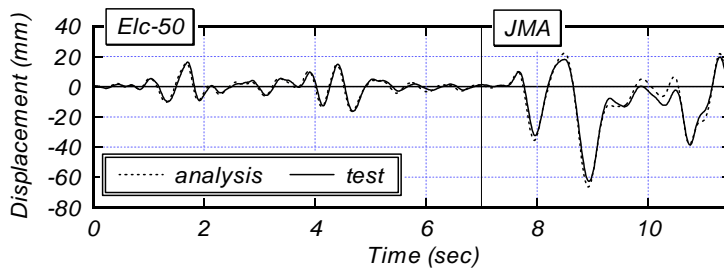
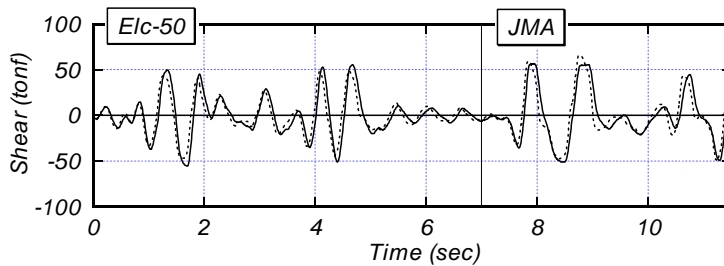


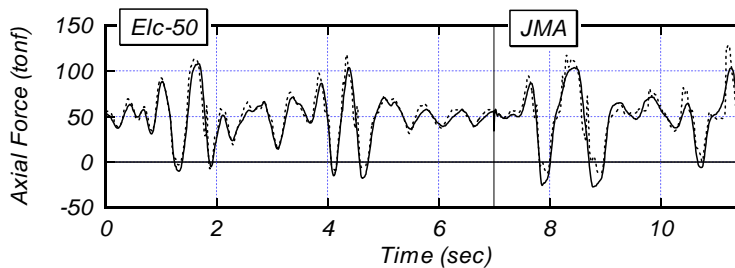
Fig. 11 Analytical Model



(a) Time History of Story Drift at the 1st Story



(b) Time History of Story Shear at the 1st Story



(b) Time History of Axial Force in East Column at the 1st Story

Fig. 12 Comparison between Experimental and Analytical Results

THE PRIMACY OF THE YIELD DISPLACEMENT IN SEISMIC DESIGN

M. A. ASCHHEIM and E. F. BLACK¹

ABSTRACT

Although seismic design traditionally has focused on period as a primary design parameter, relatively simple arguments, examples, and observations discussed herein suggest that yield displacement is a more stable and more useful parameter to begin the seismic design process with. The stability of the yield displacement is illustrated for four detailed examples, consisting of moment-resistant frame buildings. Each frame is designed to limit roof drift for a specific ground motion using an “equivalent” SDOF model in conjunction with Yield Point Spectra. The success of the simple design methodology is established by nonlinear dynamic analysis. Yield displacements were stable and consistent while fundamental periods of vibration (and lateral stiffness) varied substantially.

1. INTRODUCTION

Since the introduction of the response spectrum by Benioff (1934) and Biot (1941) (according to Miranda, 1993) it has become second nature to think of the seismic design task in terms of the fundamental period of vibration of a structure. For elastic response this is quite sensible, but when considering the design of structures responding nonlinearly, evidence suggests other views are better suited. This paper develops the idea that the yield displacement is a more natural and more useful parameter to use in seismic design. Relatively simple arguments, observations, and detailed examples are provided to support this claim. A displacement-based design approach having the objective of limiting system ductility and drift is discussed, and examples using Yield Point Spectra are provided that illustrate that design may be begun using an estimate of the yield displacement, without considering period as would be done in contemporary and traditional design approaches.

2. DESIGN AND THE KINEMATICS OF YIELD

The design process has meaning when focused upon an object, whether real or contrived. The design of the elements of the lateral force resisting system begins only after the type of lateral

¹ *Mid-America Earthquake Center, Department of Civil and Environmental Engineering, University of Illinois, Urbana.
Email: aschheim@uiuc.edu*

force resisting system and its geometric configuration have been determined. Approximate member depths and materials usually are identified early in the design process. Proportioning of members is typically directed at satisfying code requirements for strength. Code requirements on interstory drift may also influence member proportioning for flexible systems. Member depths usually change little as their strengths and stiffnesses are tailored to satisfy code requirements.

Consider first the yield displacement of a bracing member loaded in tension. The yield displacement is a function only of the length of the brace and the yield strain of the material. Increasing the strength of the brace by increasing its cross-sectional area has no effect on the yield displacement. For a beam in flexure, the yield displacement involves curvature contributions over the length of the beam, with the yield curvature being the ratio of the yield strain of the material and the depth to the neutral axis. Increases in the flexural strength of the beam achieved by increasing the longitudinal steel (if reinforced concrete) or the weight of the section (if steel) while maintaining the nominal member depth has little effect on the yield displacement. The addition or removal of material to affect strength causes concomitant changes in stiffness, for both the brace and the beam. These observations are fundamental and have been obvious to many (e.g. Priestley, 2000).

The treatment of multistory buildings responding to earthquakes is considerably simplified when the response may be assumed to occur predominantly in a single mode. The “capacity curve” is a plot of the base shear force versus roof displacement obtained in a nonlinear static (pushover) analysis, and may be developed by customary procedures (e.g. FEMA-273 and ATC-40) or alternative procedures (e.g. Gupta and Kunnath 2000). A yield displacement may be defined as the breakpoint in a bilinear curve fit to the capacity curve. Recognizing the inherent similarity between a building with structural walls and the behavior of a cantilever beam, one may accept the statement that the displacement of the roof at the moment that the wall reinforcement yields is primarily a function of the material yield strain and wall geometry, and that this displacement is nearly independent of the lateral strength provided to the wall. For moment-resistant frame buildings, supporting evidence may be of greater value. Figure 1, for example, shows the capacity curves obtained for two four-story moment-resistant frames, each having the same nominal geometry and member depths, but with section weights varied to affect a change in lateral strength. Yield displacements are nearly

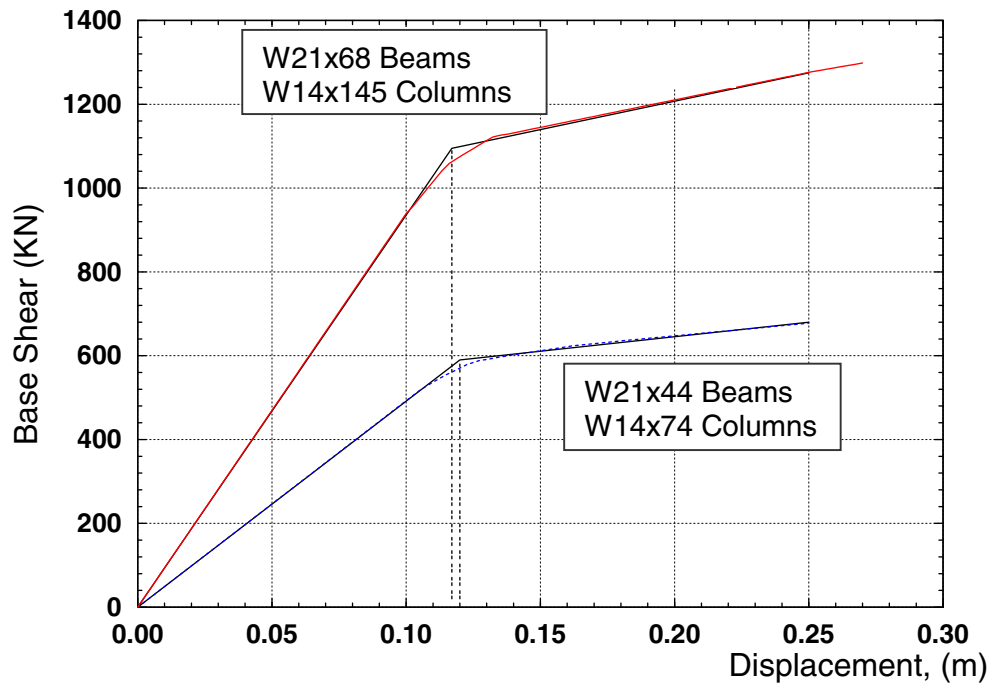


Figure 1. Nonlinear static (pushover) curves for two 4-story moment resistant frame, illustrating the relative stability of the yield displacement as the lateral strength of the frame is adjusted while member depths remain nominally constant.

invariant (about 0.75% of the height), while the strength and stiffness of the two frames differ considerably.

The preceding example considers the influence of strength on yield displacement for fixed geometry. It also is worthwhile to consider changes in geometry. Gupta and Kunnath (2000) report the capacity curves obtained using three pushover techniques applied to 4-, 8-, 12-, and 20-story reinforced concrete moment frame buildings. Each building has the same nominal floor plan, with 12-ft. (3.7 m) story heights and 24-ft (7.3 m) column spacings. Design was based on the 1988 Uniform Building Code, with $R_w = 12$ and $Z = 0.4$, but using the effective stiffnesses (corresponding to first yield) recommended by FEMA-273. The frames of the lateral force resisting system are located along each column line, meaning that all beams and columns are designated to participate in the lateral resistance. The fundamental periods of vibration computed for the buildings, after design, were 0.90, 1.75, 2.21, and 3.31 sec, respectively. The pushover curves, reproduced in Figure 2, display yield displacements of about 0.6, 0.6, 0.5, and 0.5 % of the building height, respectively, using the FEMA-273 technique. Clearly, periods of vibration vary considerably over the four buildings, while the

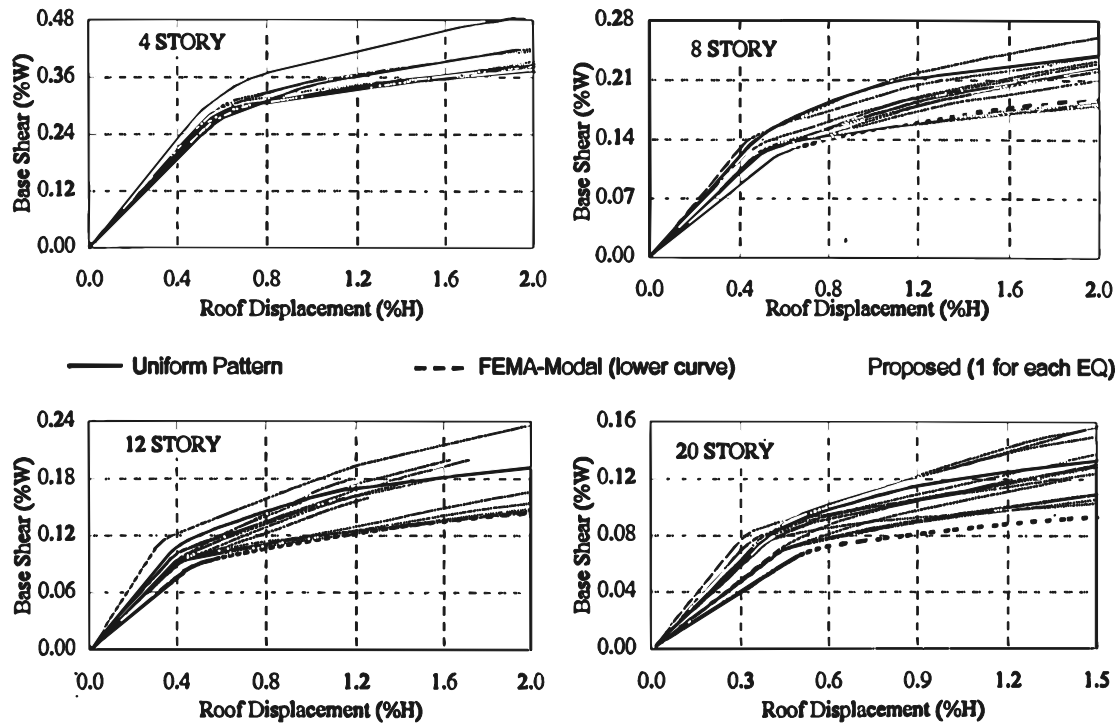


Figure 2. Capacity curves presented by Gupta and Kunnath (2000) for 4-, 8, 12, and 20-story reinforced concrete frames designed to satisfy the 1998 Uniform Building Code.

yield displacement remained nearly constant, relative to height. It would be absurd to speak of using an average period of 2.0 sec for design of the buildings, but it is feasible to design any of these buildings assuming the yield displacement to be about 0.5 or 0.6% of the building height.

Numerous other examples can be drawn from the literature or from readers' personal experience. Detailed examples are developed using steel moment-resisting frames in the remainder of the paper. Design of the frames is based on an estimated yield displacement to limit drift to satisfy a performance objective. The design is made using Yield Point Spectra, described next.

3. DESCRIPTION OF YIELD POINT SPECTRA

In essence, YPS are constant ductility spectra plotted on the axes of strength and yield displacement, for a range of oscillator periods and for a specified load-deformation relationship. The yield strength of the oscillator, V_y , is normalized by its weight, W , to obtain the yield strength coefficient, C_y . Figure 3 plots values of C_y versus the yield displacement Δ_y for displacement ductilities $\mu = 1, 2, 4, \text{ and } 8$, for a bilinear load-deformation response having

post-yield stiffness equal to 5% of the initial stiffness and viscous damping equal to 5% of critical damping. The classic 1940 NS El Centro record is used in this case. Periods are constant along radial lines emanating from the origin, and have the values indicated (in sec). Peak displacements Δ_u of the oscillators relative to the ground are given by $\mu\Delta_y$, with the value of μ estimated by interpolating between the curves of constant ductility. An example is shown in Fig. 3 for an oscillator having a period of 1.0 sec, a yield displacement equal to about 4 cm, and a yield strength coefficient equal to 0.18. Because the yield point falls on the $\mu = 2$ curve, the peak displacement is estimated to be twice the yield displacement. This choice of variables allows the influence of changes in strength or stiffness on peak ductility and displacement demands to be understood directly. A more complete description of Yield Point Spectra is given by Aschheim and Black (2000).

The curve for elastic response ($\mu = 1$) follows the 5% damped demand curve of the Capacity Spectrum method. For higher values of ductility the curves differ, since YPS explicitly plot Δ_y while the Capacity Spectrum Method and recent variants (such as Chopra and Goel, 1999, and Fajfar, 1999) explicitly plot Δ_u . The preference for plotting Δ_y comes from several considerations: (1) The effects of changing the strength and stiffness on response are apparent; (2) the yield displacement is at the boundary of the linear elastic and nonlinear domains, and thus allows nonlinear response to be considered while working directly with elastic quantities in design; (3) graphical methods are easily applied to handle multiple seismic performance objectives (described by Aschheim and Black, 2000), assuming the objectives can be stated in terms of limits on peak roof displacement and system ductility; and (4) design methods that make use of the stability of the yield displacement are easily implemented, allowing the strength required to control response to be determined directly using Yield Point Spectra.

Some additional benefits result, such as being able to handle varied load-deformation and hysteretic relations and avoiding the need for iterative solutions. It is not necessary to project back from Δ_u to Δ_y along a slope, representing the post-yield stiffness, as is required with capacity spectrum-type approaches. Oscillator response characteristics can be handled directly in the computations used to determine YPS (when ground motion records are available) or may be handled by applying suitable R - μ - T relationships to smoothed design response.

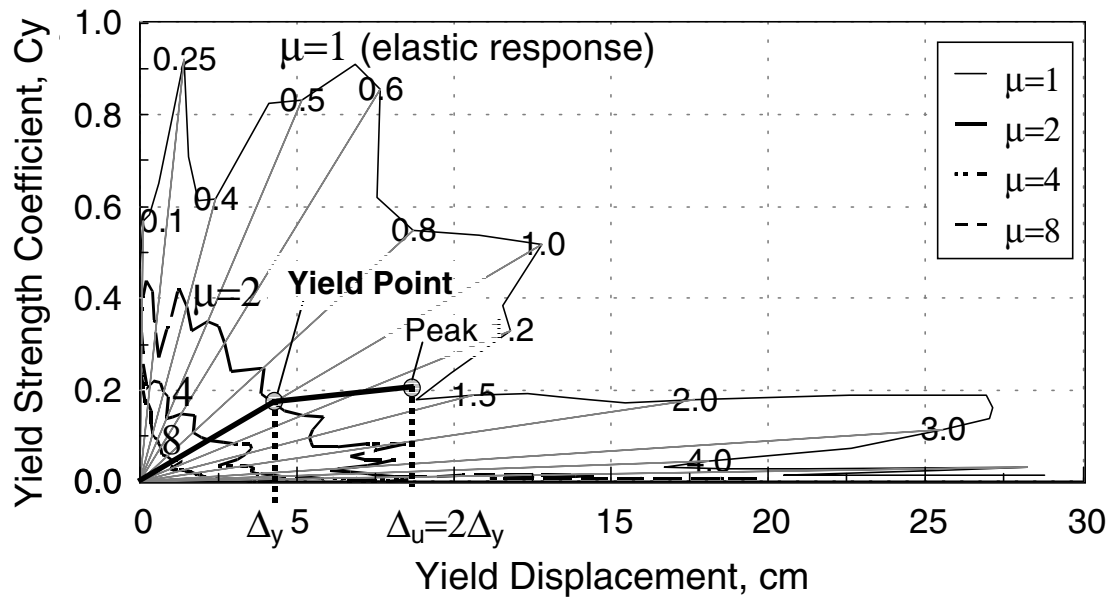


Figure 3. Yield Point Spectra computed for the 1940 NS El Centro record. The response of a 1-sec period oscillator with yield point on the $\mu=2$ curve is illustrated, schematically.

spectra. Direct computation has the benefit of revealing the sensitivity of SDOF demands to oscillator properties and ground motion variability.

4. DESIGN TO LIMIT DRIFT AND DUCTILITY

Performance-based seismic design aims to control the damage or loss of function that may occur under ground motions having varied probabilities of occurrence. Performance objectives stated as limits on drift and system ductility for a designated earthquake hazard level allow control, at a gross level, of the degree of damage to structural and nonstructural components. Estimates of the yield displacement for a particular structural system may be made based on a previous nonlinear static analysis, experience, or explicit formulae that consider the framing system, geometry, yield strain, and an approximate mode shape or displacement profile. The minimum lateral strength that satisfies both drift and ductility limits is the greater of the lateral strengths that separately satisfy these limits. The general situation is described graphically by the concept of an admissible design region, as discussed by Aschheim and Black (2000). For design of specific structures, simple algebraic relations are more useful, and these are used in the following design procedure:

Step 1: Estimate the yield displacement that would be observed in a nonlinear static (pushover) analysis of the building. In the four examples that follow, the yield displacement is estimated to be 0.75% of the height.

Step 2: Based on the performance objectives, determine the allowable ductility for the system. This is the minimum of (1) the system ductility limit associated with the performance level, and (2) the ratio of the drift limit associated with the performance level and the yield displacement estimated in Step 1.

Step 3: Determine properties of the “equivalent” single-degree-of-freedom structure. This requires an estimate of the term Γ_1 , often referred to as the modal participation factor, and an estimate of the term α_1 , referred to as the mass participation factor. Often the use of reasonable assumptions leads to good results; no attempt is made here to recommend best practices. Tabulated ranges of these parameters for the case of uniformly distributed mass are provided by Abrams (1985) and Black and Aschheim (2000).

Step 4: Using Yield Point Spectra or other techniques, determine the yield strength coefficient, C_y , required to limit the ductility demand of the SDOF oscillator to the value determined in Step 2, for a demand consistent with the earthquake hazard level. The required base shear coefficient for the building is $\alpha_1 C_y$.

Step 5: Distribute the base shear over the height of the building and design the building according to the equivalent static lateral force procedure of a modern building code. Black and Aschheim (2000) used the UBC (ICBO 1997) lateral force distribution for design of the beams and employed additional criteria for sizing the columns to ensure that weak story mechanisms did not result.

If multiple performance objectives are to be considered, Steps 2 and 4 are repeated for each performance objective, and design (Step 5) continues with the largest of the base shear coefficients determined in Step 4. Design need not require the benefit of nonlinear static (pushover) analysis. For example, the beam strengths required for the lateral forces of Step 5 were provided while ensuring the fundamental period of the frame matched the period of the equivalent SDOF system (a function of C_y and the estimated SDOF yield displacement). Only after the frames were designed was a nonlinear static (pushover) analysis done, as part of the documentation and validation of the methodology. While nonlinear static (pushover) analysis was not required for design, pushover analyses are useful for validating design assumptions and for accounting for sources of overstrength.

5. DESIGN EXAMPLES

To test the above design methodology, four regular moment-resistant frame buildings were designed. Steel was chosen for simplicity to permit bilinear load-deformation models to be

used, but the findings are equally applicable to reinforced concrete frames, for which stiffness-degrading responses ideally should be embodied in the Yield Point Spectra. The frames were designed and analyzed only for lateral load to test the design methodology without introducing complications resulting from overstrength, such as would result if load factors were applied to gravity loads. Details are provided in Black and Aschheim (2000).

Each frame was designed to limit roof drift to 1.5% of the building height for a specific earthquake ground motion. Two 4-story frames were designed, one for a relatively weak earthquake and one for a relatively strong earthquake. Two 12-story buildings also were designed for this drift limit, again for a relatively weak and a relatively strong earthquake. The 1.5% drift limit corresponds to peak drifts of 25.5 and 73.5 cm for the 4- and 12-story buildings, respectively. Frames designed for relatively weak earthquakes were relatively flexible, and were designated “Flexible-4” or “Flexible-12,” while the others were designated “Rigid-4” and “Rigid-12.”

For design purposes, yield displacements were estimated to be 0.75% of the height. Because peak roof displacements were limited to 1.5% of the height, the ductility response of the frames were to be limited to a target value of $1.5/0.75 = 2$. This controlled over any ductility limits associated with limiting structural damage to the frames. Mass was uniformly distributed over the height of the frames. As a simple approximation, the mode shape assumed for Step 2 was triangular, leading to $\Gamma_1 = 1.33$ and 1.44 and $\alpha_1 = 0.86$ and 0.79 for the 4- and 12-story frames, respectively, following tabulated data provided by Abrams (1985) and reproduced by Black and Aschheim (2000). These values are based on mode shapes normalized to unit amplitude at the roof. Table 1 identifies the design parameters for each frame, and Figures 4 and 5 identify the members that comprise the lateral-force-resisting systems.

Table 1: Frame Design Parameters

Designation	Design Motion-Component	Peak Roof Drift, cm	Base Shear Coefficient	Fundamental Period, sec
Flexible-4	1992 Landers-Lucerne-250	25.5	0.258	1.13
Rigid-4	1994 Northridge-Newhall-360	25.5	0.688	0.70
Flexible-12	1985 Michoacan-SCT-270	73.5	0.174	2.18
Rigid-12	1995 Kobe-Takatori-360	73.5	0.474	1.32

Nonlinear static (pushover) analyses were done using Drain-2DX (Prakash et al. 1993) using forces applied proportional to the actual elastic mode shape. Bilinear curves were fit to the

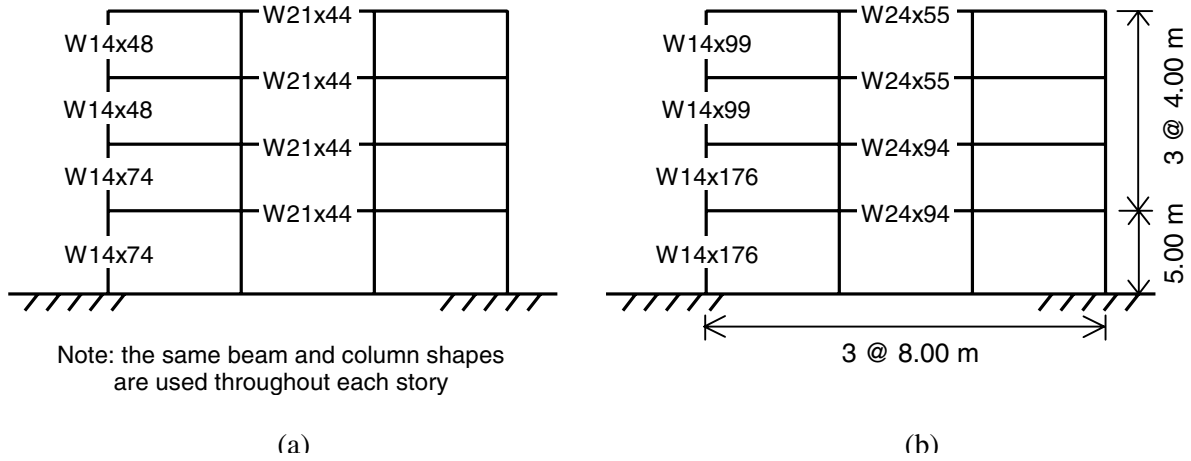


Figure 4. Framing configurations determined for (a) Flexible-4 and (b) Rigid-4 frames.

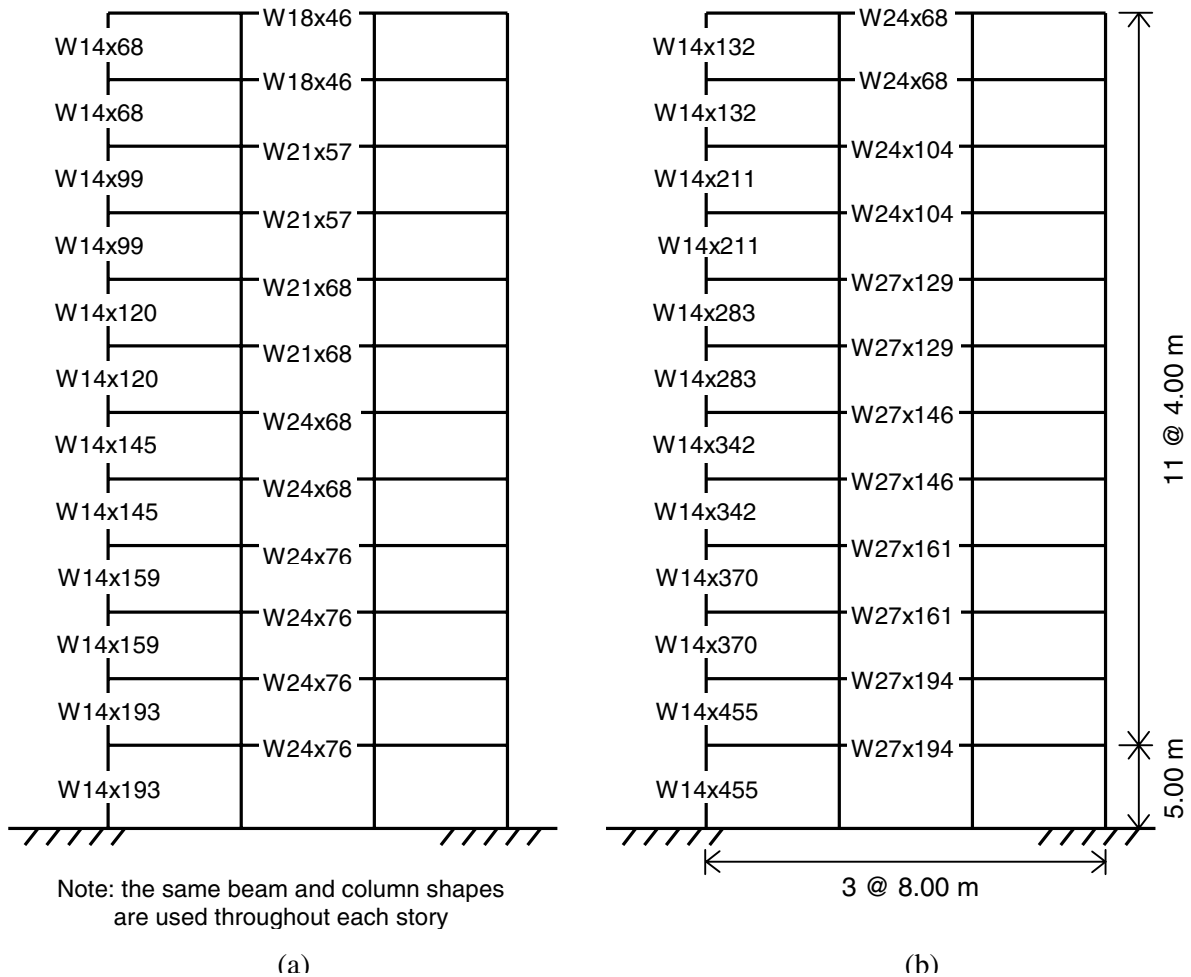


Figure 5. Framing configurations determined for (a) Flexible-12 and (b) Rigid-12 frames.

resulting capacity curves, leading to the values of base shear coefficient and yield displacement shown in Table 2. Nonlinear dynamic analyses of the frames subjected to the design ground motions resulted in the peak roof drifts shown in Table 2.

Table 2: Frame Characteristics and Performance Based on Nonlinear Analysis

Designation	Yield Displacement, cm	Base Shear Coefficient (at Yield)	Fundamental Period, sec	Peak Roof Drift, cm
Flexible-4	12.9	0.265	1.16	24.1
Rigid-4	13.3	0.681	0.71	22.3
Flexible-12	35.3	0.173	2.17	66.7
Rigid-12	33.5	0.469	1.25	65.0

The yield displacements (Table 2) range between 0.68 and 0.78% of the height of the building. These values are relatively stable despite large differences in the lateral strengths (0.17 to 0.68 times dead load), heights (17 and 49 m), and fundamental periods (0.71 to 2.17 sec). The peak roof drifts determined by nonlinear dynamic analysis for the design ground motions were within 13% of the target values (25.5 and 73.5 cm) for the four frames.

The present examples suffice to demonstrate control of drift and ductility demands for a range of building heights and earthquake intensities using a simple methodology that is based on assuming the yield displacement to be stable. Simple assumptions are employed and no nonlinear analyses were done to refine the designs. The success of the methodology suggests it is robust. Extensions to consider overstrength, irregularities, eccentricities, and second-order effects merit further consideration.

6. CONCLUDING REMARKS

Evidence in the form of logical argument and empirical data were presented that show that: (1) for a given structural configuration, yield displacements remain approximately constant as lateral strength is adjusted, and (2) for a given structural composition (bay sizes, member spans and depths, etc.) the yield displacement as a fraction of the height of the structure is nearly invariant as the number of stories varies. On this basis it appears feasible to approach design from the perspective of constant yield displacement. The examples provided illustrated the effectiveness of a yield displacement approach in satisfying performance objectives for 4- and 12-story frames subjected to earthquake records of varied intensities. Fundamental periods of vibration varied significantly, even among frames of a given height. Yield

displacements were nearly constant, and were close to the values assumed in design. Peak displacement responses computed in the nonlinear dynamic analyses were within 13% of the target values associated with the design objectives. Design approaches based on an assumed or computed period would not have been as simple and effective.

7. ACKNOWLEDGMENTS

Support for the preparation of this paper was provided by a CAREER Award from the National Science Foundation (Grant No. CMS-9984830). This support, under the direction of Program Manager Vijaya Gopu, is gratefully acknowledged. This work made use of Earthquake Engineering Research Centers Shared Facilities supported by the National Science Foundation under Award Number EEC-9701785. Figure 2 was reproduced with the consent of the Earthquake Engineering Research Institute.

8. REFERENCES

Abrams, D. A. (1985). *Nonlinear Earthquake Analysis of Concrete Building Structures*, final report on a study to the American Society for Engineering Education.

Aschheim, M., and Black, E. (2000). Yield Point Spectra for seismic design and rehabilitation. *Earthquake Spectra*, 16(2):317-336.

ATC-40 (1996). *Seismic Evaluation and Retrofit of Concrete Buildings*, Volumes 1 and 2, Report No. ATC-40, Applied Technology Council, Redwood City, California, Nov.

Benioff, H. (1934). The physical evaluation of seismic destructiveness. *Bull. Seismological Society Am.*, 24(2):398-403.

Black, E., and Aschheim, M. (2000). *Seismic Design and Evaluation of Multistory Buildings Using Yield Point Spectra*, CD Release 00-04, Mid-America Earthquake Center, University of Illinois, Urbana, July.

Biot, M. A. (1941). A mechanical analyzer for the prediction of earthquake stresses. *Bull. Seismological Society Am.*, 31(2):151-171.

FEMA-273 (1997). *NEHRP Guidelines for the Seismic Rehabilitation of Buildings*, Report No. FEMA-273, Federal Emergency Management Agency, Washington, D.C., Oct.

Chopra, A. K., and Goel, R. K. (1999). "Capacity-demand-diagram methods based on inelastic design spectrum," *Earthquake Spectra*, 15(4):637-656.

Fajfar, P., (1999). "Capacity spectrum method based on inelastic demand spectra," *Earthquake Engineering and Structural Dynamics*, 28:979-993.

Gupta, B., and Kunnath, S. K. (2000). Adaptive spectra-based pushover procedure for seismic evaluation of structures. *Earthquake Spectra*, 16(2):367-391.

ICBO (1997). *Uniform Building Code*, International Conference of Buildings Officials, Whittier, California.

Miranda E. (1993). Evaluation of site-dependent inelastic seismic design spectra. *Journal of the Structural Division*, American Society of Civil Engineers, 119(5):1319-1338.

Prakash, V., Powell, G.H., and Campbell, S. (1993). *Drain-2DX Base Program Description and User Guide, Version 1.10*. Report No. UCB/SEMM-93/17, Structural Engineering, Mechanics, and Materials, University of California, Berkeley, Nov.

Priestley, M. J. N. (2000). Performance based seismic design. *Proceedings of the 12th World Conference on Earthquake Engineering*, Auckland, New Zealand, Jan. 30 – Feb. 4.

**SESSION A-4: SEISMIC RESPONSE AND
DESIGN OF STRUCTURES**

Chaired by

◆ Norman Abrahamson and Kazuyoshi Kudo ◆

THE EFFECT OF VERTICAL EXCITATION ON STRUCTURAL RESPONSE CHARACTERISTICS

-Comparison the characteristics of vertical ground motion with horizontal one-

Koichi KUSU¹, Yoshiaki NAKANO² and Tsuneo OKADA³

ABSTRACT

Under an earthquake, structures might vibrate not only horizontally but also vertically due to the vertical excitation. Now the effect of the vertical excitation however is not considered directly or with scientific justification. The effect of the vertical excitation must be studied to improve the seismic capacity of structures under real earthquakes. In this paper, the characteristics of the vertical excitation are discussed comparing with the horizontal excitation using 12 ground acceleration records including 1995 Hyogo-ken Nanbu Earthquake records as the first step. As the results, these can be said that the maximum vertical ground acceleration is generally smaller than the horizontal, the vertical input energy due to ground motion is less than the horizontal, but the vertical response acceleration is larger than the horizontal, and the simultaneity of the horizontal and vertical responses should be considered so that the horizontal and vertical maximum response acceleration should occur at the same time.

1. INTRODUCTION

The earth would quake not only horizontally but also vertically under earthquake. Recently vertically high ground accelerations were recorded especially at sites close to the epicenter. For example, the horizontal and vertical maximum ground accelerations at the Northridge/San Fernando Valley Earthquake of January 17, 1994 (CSMPI, 1994) are shown in Table 1. The vertical maximum ground acceleration is almost the same or even larger than the horizontal at some sites. Structures would vibrate vertically by this large vertical excitation, and additional varying axial force might act on columns due to the vertical vibration. The restoring moment force of column would vary caused by this additional varying axial force.

¹ Koichi Kusu, Building Research Institute, Ministry of Construction, Tsukuba, Japan

E-Mail : kusunoki@kenken.go.jp

² Yoshiaki Nakano, Institute of Industrial Science, University of Tokyo, Tokyo, Japan

E-Mail : iisnak@iis.u-tokyo.ac.jp

³ Tsuneo Okada, Shibaura Institute of Technology, Tokyo, Japan

E-mail : okada@sic.shibaura-it.ac.jp

In Japan, the effect of the vertical excitation is considered in Technical Guideline for Generation of Design Basis Earthquake (JEA, 1987) and Technical Guideline for Generation of Design Basis Earthquake (BRI, JBC, 1992). In first reference, the effect of the vertical excitation is considered as the static force of which intensity is a half of the horizontal depending on the importance of structures. However, it does not have scientific justification; why the vertical intensity is a half of the horizontal. And in second reference, this is not for the static design but to make an artificial ground motion record for analysis. The vertical response acceleration spectrum is proposed in this guideline of which natural period is 0.0 ~ 10.0. Since the vertical natural period of structure is generally very short, the vertical response spectrum of short natural period range is needed for the structural design. And the relationships between horizontal and vertical response characteristics of structures must be taken into consideration.

And the other guidelines or standards do not consider the effect of the vertical excitation directly. It is not considered also in Japanese Standard for Structural Calculation of Reinforced Concrete Structures (AIJ, 1991). One of the reasons why the effect of the vertical excitation is not considered in this standard is that redundant strength of allowable unit stress for long sustained loading would include the effect of vertical excitation if assumptions that the maximum vertical ground acceleration is a half of the horizontal and vertical response magnification ratio is less than horizontal, are true.

Also in Design Guidelines for Earthquake Resistant Reinforced Concrete Buildings Based on Ultimate Strength Concept (AIJ, 1990), the effect of the vertical excitation is not taken into consideration. Especially in this guideline of which concept is yield mechanism shall be the beam-yielding type, column can yield based on the axial force-moment curve of a section due to the additional axial load by the vertical excitation. The reason why is that the dimension and bar arrangement of a member section are usually decided based on the ultimate strength concept so that the axial force-moment curve of the restoring force would be comprehend the maximum stress when the collapse mechanism is formed. If the varying axial force due to the vertical excitation would act on the column, it depends on the redundant strength of the column but there is a possibility of yielding as shown in Fig. 1.

Followings must be studied to improve the seismic capacity of buildings against the

earthquake real ground motion.

1. Comparison the characteristics of the vertical ground motion with the horizontal.
2. Comparison the vertical response characteristics of structures with the horizontal.
3. To study the effect of the vertical excitation especially on the response of column with non-linear Dynamic response analysis under bi-axial ground motion.

Finally, the design method must be established based on the ultimate strength concept considering the vertical excitation from results of above three subjects. In this paper, the first subject, comparison the characteristics of the vertical ground motion with the horizontal one, is discussed.

**Table 1 Maximum ground acceleration at each site
at the Northridge/San Fernando Valley Earthquake of January 17, 1994 (CSMIP, 1994)**

Place	Maximum Acceleration (G)	
	Horizontal	Vertical
Tarzanna Codar Hill Nursery	1.82	1.18
Arleta Nordhoff Ave. Fire Station	0.35	0.59
Pacoima Kagel Canyon Fire Sta.	0.44	0.19
Sylmar 6-story County Hospital	0.91	0.60
Century City LACC North	0.27	0.15
Los Angels Hollywood Strange Bldg. Free Field	0.41	0.19
Los Angels Hollywood Strange Bldg.	0.41	0.19
Santa Monica City Hall Ground	0.93	0.25
LA-Baldwin Hilla	0.24	0.10
Los Angels Pico and Sentous	0.19	0.07
Los Angels Temple and hope	0.19	0.10

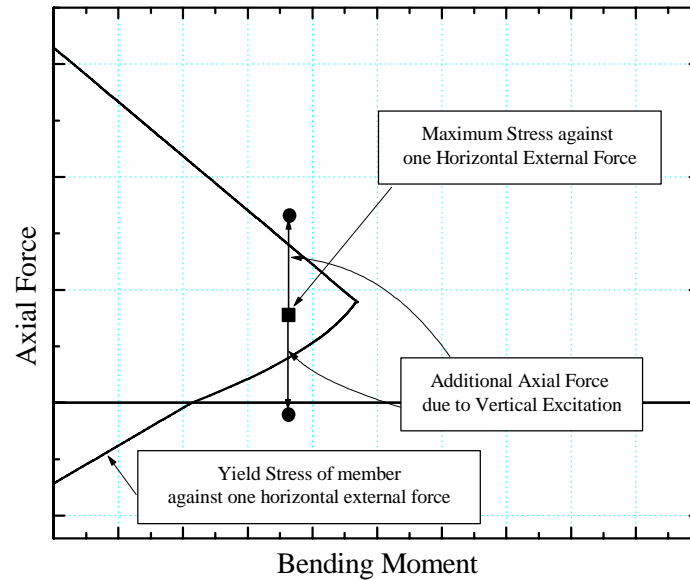


Fig. 1 The effect of additional varying axial force due to vertical excitation on axial force-moment curve

2. COMPARISON THE CHARACTERISTICS OF VERTICAL GROUND MOTION WITH HORIZONTAL

2.1 Maximum Ground Acceleration

To compare the characteristics of the vertical ground motion with the horizontal, 12 earthquake records were studied. The maximum ground accelerations of each direction and maximum ground acceleration ratio (vertical / horizontal) are shown in Table 2. Chiba was recorded at 1987 Chibaken-Toho-Okai Earthquake in Chiba Experiment Station of Institute of Industrial Science (Ryoichi TAMURA, 1984). El Centro was recorded at 1940 Imperial Valley Earthquake, Hachinohe was recorded at 1968 Tokachi-Okai Earthquake and Taft was recorded at 1952 Kern County Earthquake. These records are usually used for the structural design. And Kobe1 ~ Kobe7 were recorded at 1995 Hyogo-ken Nanbu Earthquake in JMA sites^[7] and KPI was also recorded at 1995 Hyogo-ken Nanbu Earthquake in Kobe Port Island (artificial land) (CEOR,1995). City names, latitude north and longitude east of each JMA site are shown in Table 3. There were two records for the horizontal ground motion (EW and NS components). In Table 2, the underlined ratios were calculated with the horizontal record of which maximum ground acceleration was larger than the other.

As shown in Table 2, the maximum vertical ground acceleration of KPI record was larger than the horizontal because of the effect of the liquefaction, but it can be said that the maximum vertical ground acceleration is generally less than the horizontal. It is also generally spoken that the maximum vertical ground acceleration ratio against the horizontal depends on the following three factors (Katsuhiko ISHIDA, et. al, 1976).

1. Soil Condition
2. Distance between site and epicenter
3. Earthquake intensity

Since these factors are correlated each other and only twelve records were studied in this paper, so not general characteristics of vertical excitation using statistical inference but comprehensive characteristics of these records are discussed.

Table 2 Maximum ground acceleration and ratio of each record

Record	Max. Acceleration			Ratio	
	EW	NS	UD	UD/EW	UD/NS
Chiba	222.7	401.4	118.2	0.53	<u>0.29</u>
El Centro	210.1	341.7	206.3	0.98	<u>0.60</u>
Hachinohe	182.9	225.0	114.3	0.62	<u>0.51</u>
Kobe1	41.5	33.0	10.1	<u>0.24</u>	0.31
Kobe2	146.9	136.7	39.1	<u>0.27</u>	0.29
Kobe3	617.1	817.8	332.2	0.54	<u>0.41</u>
Kobe4	52.2	66.9	39.4	0.76	<u>0.59</u>
Kobe5	59.1	77.3	35.9	0.61	<u>0.46</u>
Kobe6	65.9	80.8	64.5	0.98	<u>0.80</u>
Kobe7	74.2	76.7	14.7	0.20	<u>0.19</u>
KPI	284.3	341.2	555.9	2.00	<u>1.63</u>
Taft	175.9	152.7	102.9	<u>0.58</u>	0.67

Table 3 JMA records at 1995 Hyogo-ken-Nanbu Earthquake (JMA, 1995)

Record	Longitude East	Latitude North	Location	Trigger Time
Kobe1	136°14''	36°03''	JMA Fukui	05:46:54
Kobe2	136°15''	35°16''	JMA Hikone	05:46:46
Kobe3	135°11''	34°41''	JMA Kobe	05:46:27
Kobe4	135°19''	35°27''	JMA Maizuru	05:46:40
Kobe5	135°55''	34°39''	JMA Okayama	05:46:40
Kobe6	135°31''	34°41''	JMA Osaka	05:46:31
Kobe7	134°14''	35°29''	JMA Tottori	05:46:43

2.2 Response Acceleration Spectrum

At first, the period T_{max} at the maximum response acceleration of each record as shown in Fig. 2 was calculated to compare the characteristics of frequency. The T_{max} of each record are shown in Fig. 3. From this result, it can be said that the superior period of the vertical excitation is shorter than that of the horizontal.

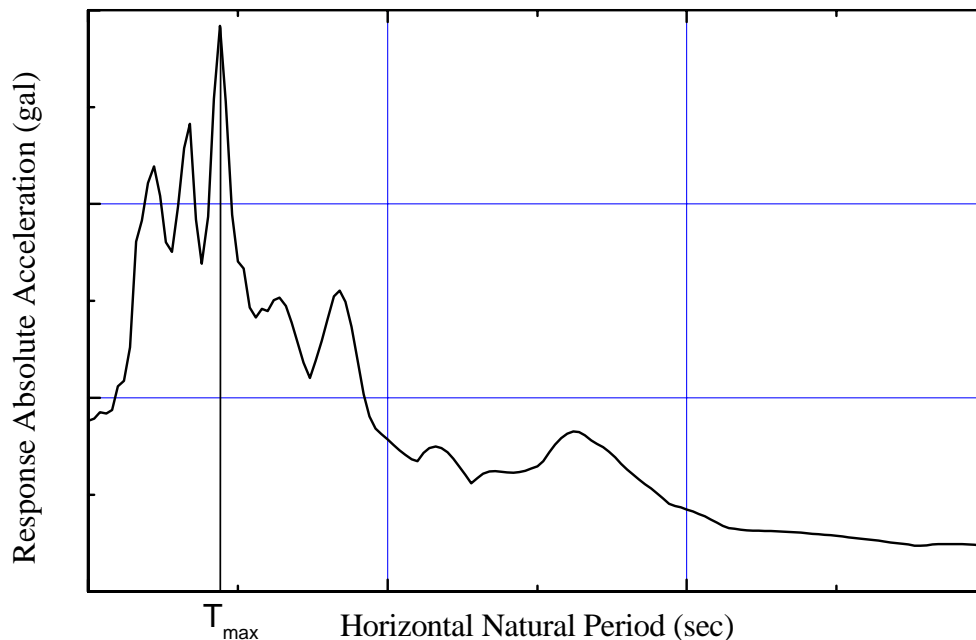


Fig. 2 The Period T_{max} when the response acceleration is maximum

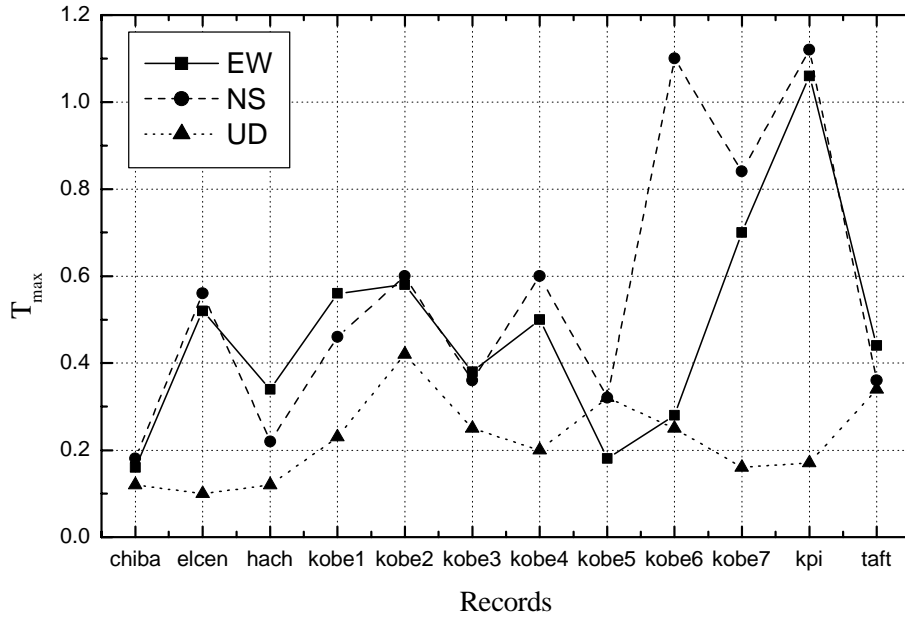


Fig. 3 T_{max} of each record

To discuss the effect of the vertical excitation on the response characteristics of structures, the difference between the vertical and horizontal natural periods of structures must be taken into account. The horizontal natural period ratio to the vertical can be calculated easily as the ratio of the length to the depth of column, H/D (Equation (2)), with following six assumptions.

ASSUMPTIONS

1. horizontal and vertical stiffness have no correlation each other
2. floors are rigid
3. dimensions of all members are the same
4. moment distribution of column is antisymmetric
5. shear deformation of member is negligible
6. sections of columns are rectangular

The ratio H/D is calculated as follows. The horizontal stiffness K_H and the axial stiffness K_V of one column are calculated as Eq.1.

$$\begin{cases} K_H = \frac{12EI}{H^3} \\ K_V = \frac{EA}{H} \end{cases} \quad (1)$$

Horizontal and vertical eigen-value equations can be calculated independently as follows. In these equations, ω_H and ω_V are the horizontal and vertical natural angular frequency, $[M]$ is the mass matrix, and $\{U_H\}$ and $\{U_V\}$ are horizontal and vertical eigenvectors.

$$\begin{cases} (-\omega_H^2[M] + [K_H])\{u_H\} = 0 \\ (-\omega_V^2[M] + [K_V])\{u_V\} = 0 \end{cases}$$

Then, these two stiffness matrix $[K_H]$ and $[K_V]$ have the relationship as $[K_V] = a \cdot [K_H]$ with Equation (1) and assumptions. The relationship between ω_H and ω_V is derived from the vertical eigenvalue equation as follows.

$$\therefore \omega_V = \sqrt{a} \omega_H$$

The horizontal natural period ratio against vertical can be calculated as Equation (2).

$$\begin{aligned} \frac{T_H}{T_V} &= \frac{1}{\sqrt{a}} = \sqrt{\frac{K_V}{K_H}} = \sqrt{\frac{\frac{EA}{H}}{\frac{12EI}{H^3}}} = \sqrt{\frac{AH^2}{12I}} = \sqrt{\frac{bDH^2}{12 \frac{bD^3}{12}}} \\ &= \frac{H}{D} \end{aligned} \quad (2)$$

The ratio of vertical maximum response acceleration to the horizontal was studied considering the difference of the horizontal and vertical natural periods with Equation (2). The ratio of the vertical maximum response acceleration to the horizontal (referred to be as Response Acceleration Ratio) at $H/D=6.0$ of each record are shown in Fig. 4. Since two directional accelerations (EW and NS components) were recorded as horizontal ground motions, the record of the direction of which maximum ground acceleration is larger than the other was used for calculation. The value of Response Acceleration Ratio is larger than 1.0 within the wide range of the natural period except extremely short period. From this result, it can be said that the vertical response acceleration is generally larger than the horizontal of structure.

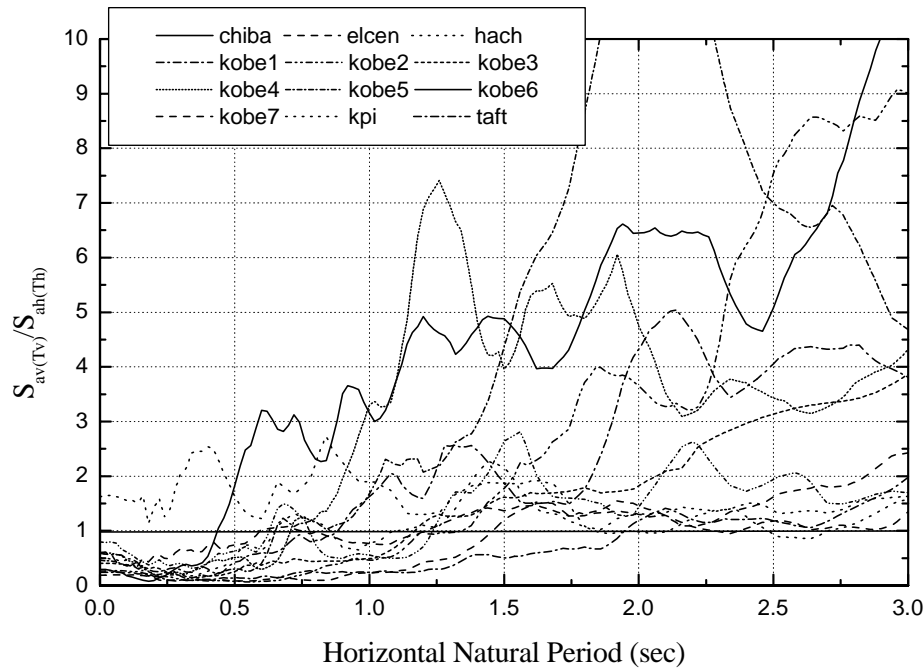


Fig. 4 The ratio of vertical maximum response acceleration to horizontal of each records

2.3 Response Velocity Spectrum

Response Velocity Ratio was studied considering the difference of horizontal and vertical natural periods of structure as Response Acceleration Ratio. The Response Velocity Ratio is shown in Fig. 5. The ratio is less than 1.0 within all natural periods. From this result, it can be said that the vertical response velocity of structure is generally less than the horizontal, then the vertical input energy due to earthquake is generally less than the horizontal because the response velocity is correspondent to input energy due to earthquake.

2.4 Simultaneity of horizontal and vertical response

The other important factor to discuss the effects of the vertical excitation on the response characteristics of structures is the simultaneity of the horizontal and vertical responses. To study the simultaneity of the horizontal and vertical elastic responses, one mass and two-degree-of-freedom (horizontal and vertical) model was used as a structure (Fig. 6). The way to study the simultaneity is described as follows. At first, the time history of horizontal response absolute acceleration was calculated at each horizontal natural period T_H with each horizontal record. In this study, the horizontal natural period T_H was varied from 0.0 to 2.0

sec. Secondly, the time history of vertical response absolute acceleration was calculated at each vertical natural period T_V with each vertical record. At this time, T_V can be calculated as $T_H \cdot D/H$ based on the natural period ratio as mentioned before. H/D of 6.0 was used in this

study. The $R_{(t)} = 0.5 \left(\frac{A_{h(t)}}{A_{h \max}} + \frac{A_{v(t)}}{A_{v \max}} \right)$ was used as the index of the simultaneity depends on

time using the horizontal and vertical maximum response absolute accelerations $A_{h \max}$, $A_{v \max}$ and the horizontal and vertical response absolute accelerations $A_{h(t)}$, $A_{v(t)}$. In this equation, the absolute value of $A_{v(t)}$ was not used as because of the assumption that only additional tensile axial force due to vertical excitation would decrease the seismic capacity of structures. $R(t)$ can vary from 0.0 to 1.0 depending on time, the maximum of $R(t)$ was used as the index of the response simultaneity.

The results of the response simultaneity of El Centro, Kobe1(JMA Fukui) and Kobe3(JMA Kobe) are shown in Fig. 8, Fig. 9 and Fig. 10. From these figures, the response simultaneities of each record were grouped into three classes as follows.

- . The simultaneity is not so high at all natural period of structure.
- . The simultaneity is high at only the particular natural period of structure.
- . The simultaneity is high within the wide natural period region.

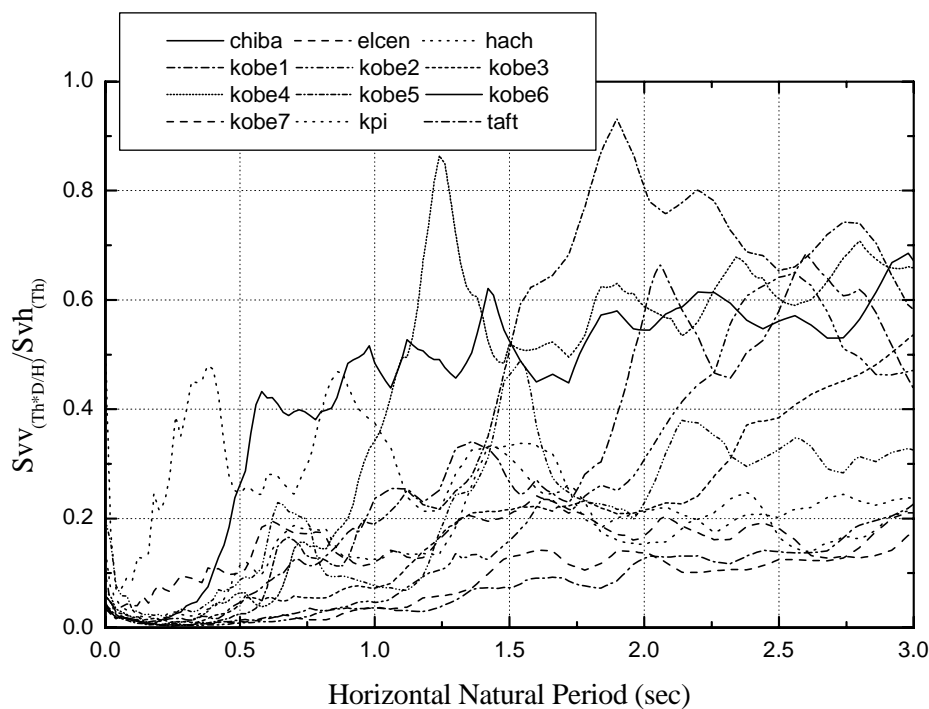


Fig. 5 Maximum Response Velocity Ratio

The classifications of each record are shown in Table 4. The simultaneity of JMA Kobe was especially high within the region of $T_H=1.0 \sim 1.5$ sec. But it is difficult to get the general tendency of the simultaneity. It can be said that it is safe to use R as 1.0 so that the maximum horizontal and vertical response acceleration would occur at the same time.

Table 4 Result of simultaneity of response

Simultaneity	Records
	El Centro , Hachinohe
	Kobe1 , Kobe2 , Kobe4 , Kobe5 , Kobe6 , Kobe7 , KPI
	Chiba , Kobe3 , Taft

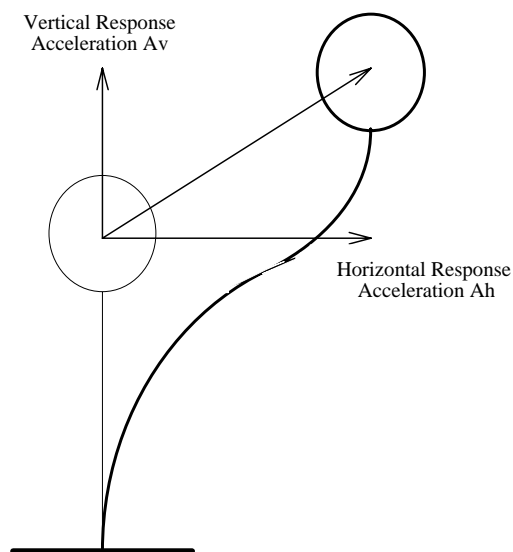


Fig. 6 Model to study simultaneity

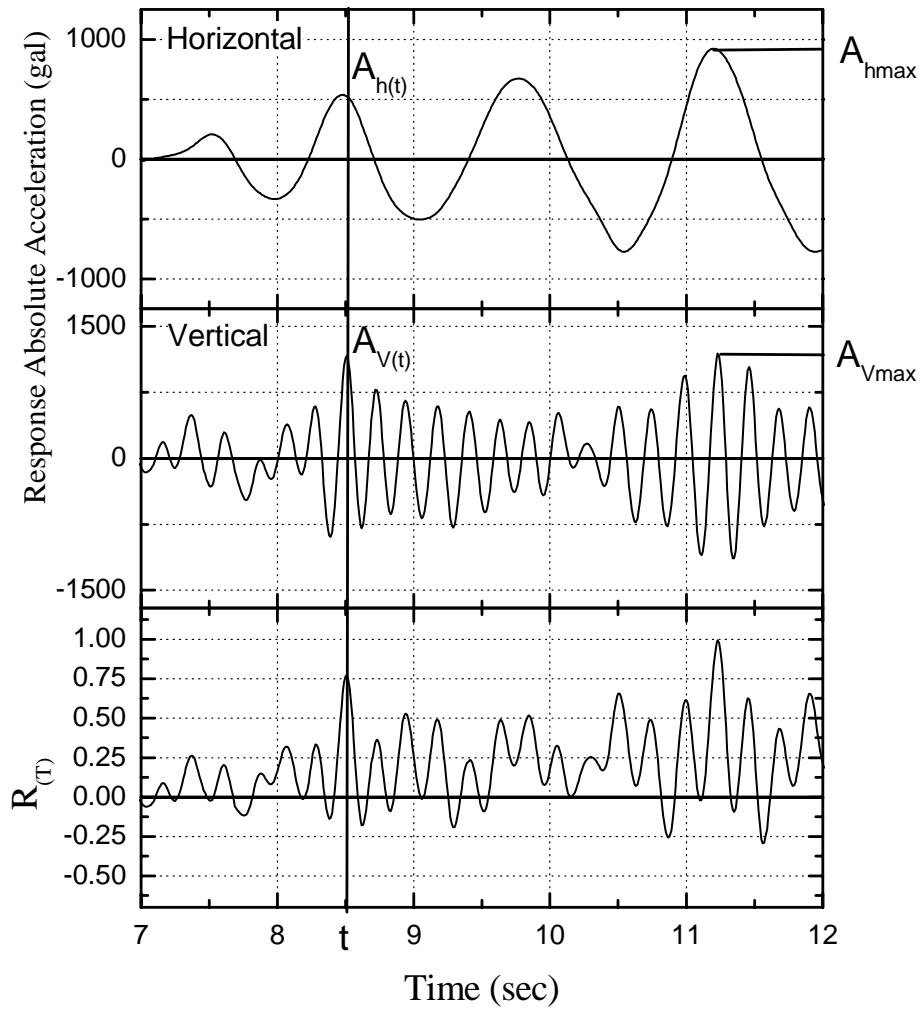


Fig. 7 Index of response simultaneity $R(t)$

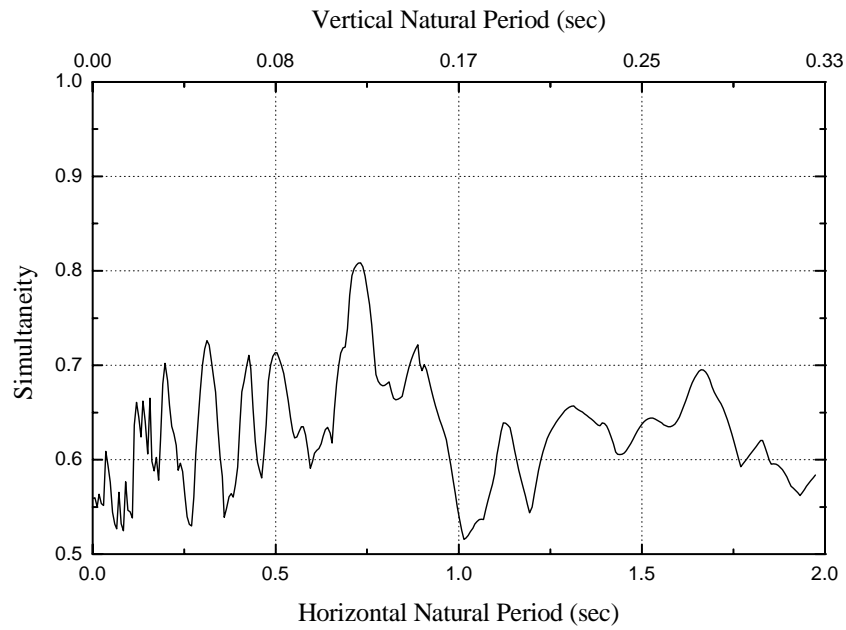


Fig. 8 Simultaneity of El Centro

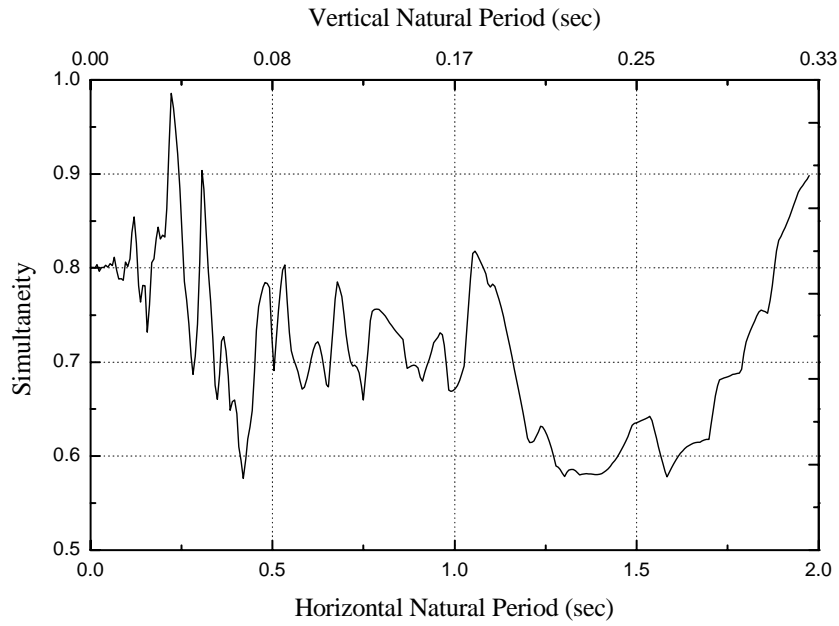


Fig. 9 Simultaneity of Kobe1 (JMA Fukui)

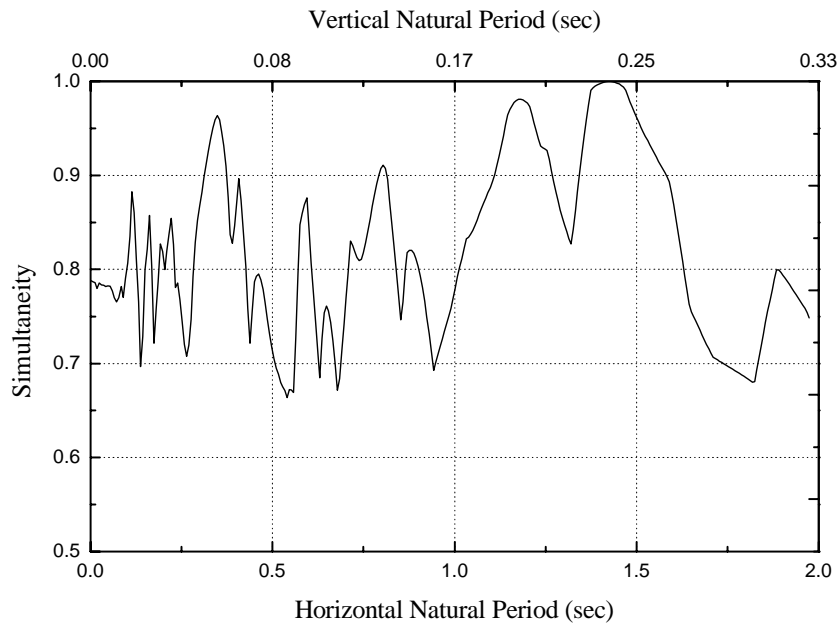


Fig. 10 Simultaneity of Kobe3 (JMA Kobe)

3. CONCLUDING REMARKS

To compare the characteristics of the vertical excitation with the horizontal, 12 earthquake ground motion records were studied. The following main conclusions can be drawn for the emphasis.

1. The maximum vertical ground acceleration is generally less than the horizontal.
2. The vertical response due to the vertical ground acceleration is superior in shorter natural period than the horizontal.
3. In a structure, the vertical response acceleration is superior to the horizontal in wide natural period range.
4. The vertical input energy due to earthquakes is generally inferior to the horizontal.
5. There are some records that the simultaneity of the horizontal and vertical response is high. However, it is difficult to get the general tendency of the simultaneity. So it is safe to use R as 1.0 so that the maximum horizontal and vertical response acceleration would occur at the same time.

4. REFERENCES

- [1] AIJ, *Standard for Structural Calculation of Reinforced Concrete Structures*, 1991
- [2] AIJ, *Design Guidelines for Earthquake Resistant Reinforced Concrete Buildings Based on Ultimate Strength Concept*, 1990
- [3] Building Research Center, Japan Building Center, *Technical Guideline for Generation of Design Basis Earthquake*, 1992
- [4] California Strong Motion Instrumentation Program, *Fourth Quick-Report on CSMIP Strong-Motion Data from the Northridge/San Fernando Valley Earthquake of January 17, 1994*, 1994
- [5] Japan Electric Association, *Technical Guideline for Aseismic design of nuclear power plant JEAG 4601*, 1987
- [6] KATSUHIKO ISHIDA, MAKOTO WATABE, and YORHIKO OSAKI, Analysis on Earthquake Ground Motions including Vertical Components (Part 1. Factor Analysis based on Statistical Method on Vertical Component of Seismogram), *Transactions of the architectural institute of Japan*, No. 273, November 1976
- [7] RYOICHI TAMURA, Observation of Earthquake Response of Reinforced Concrete Weak-Model Structure, *Doctor Thesis of University of Tokyo*, 1984
- [8] Strong-motion accelerogram of Japan Meteorological Agency, 1995
- [9] The committee of earthquake observation and research in the Kansai area

DEVELOPMENT OF A TWO-PARAMETER SEISMIC INTENSITY MEASURE AND PROBABILISTIC ASSESSMENT PROCEDURE

Paul P. Cordova¹, Gregory G. Deierlein², Sameh S.F. Mehanny³, and C.A. Cornell⁴

ABSTRACT

A method to evaluate the seismic collapse performance of frame structures is presented, considering uncertainties in both the ground motion hazard and inelastic structural response to extreme input ground motions. The procedure includes a new seismic-intensity scaling index that accounts for period softening and thereby reduces the large record-to-record variability typically observed in inelastic time-history analyses. Equations are developed to combine results from inelastic time history analyses and a site-specific hazard curve to calculate the mean annual probability of a structure exceeding its collapse limit state.

1. INTRODUCTION

Research on performance-based earthquake engineering poses many challenges, among them being the need for a consistent methodology to predict structural collapse as a function of the earthquake ground motion intensity. Components to an assessment methodology for collapse should include (1) definition of the seismic hazard, (2) simulation of structural response to input ground motions, including stiffness and strength degradation, and (3) statistical interpretation of results. The methodology must rigorously account for variability in performance prediction arising due to uncertainties in the inherent seismic hazard and the nonlinear simulation of structural response.

A large source of variability in seismic performance assessment arises from simplifications in defining earthquake intensity relative to the true damaging effects of ground motions on structures. Current codes in the United States, such as the *International Building Code* (ICC 2000), define earthquake hazard in terms of spectral response coefficients, typically spectral acceleration measured at the first mode period of vibration, $S_a(T_1)$. First mode spectral acceleration is the basis of equivalent lateral force design procedures, and it is often used as the default earthquake intensity scaling parameter for time-history analyses. While first mode

¹ Research Assistant, John A. Blume Earthquake Engineering Center, Stanford Univ., Stanford, CA 94305-4020

² Prof., Dept. of Civil & Env.l Engrg., Stanford Univ., Stanford, CA 94305-4020, email: ggd@stanford.edu

³ Simpson Gumpertz and Heger, Inc., San Francisco, CA., email: SSFMehanny@sgh.com

⁴ Prof., Dept. of Civil & Env.l Engrg., Stanford Univ., Stanford, CA 94305-4020, email: cornell@ce.stanford.edu

spectral acceleration is an accurate index for structures that respond elastically, this single parameter does not reflect many of the aspects of earthquake ground motions that affect inelastic stiffness and strength degradation. An objective of this paper is to examine a new two-parameter hazard intensity index that can improve the accuracy of structural performance predictions based on inelastic time history analyses. A related objective is the development of reliability-based equations for interpreting the performance limit state to compare the effect of using a single versus two-parameter intensity measure.

The scope and approach of this paper is as follows. First, the general concepts of earthquake ground motion intensity measures are introduced, including an overview of traditional measures and the development of attenuation functions for the new proposed index. Second, a series of case study buildings are introduced and analyzed to determine their collapse limit state using incremented inelastic time-history analyses coupled with a post-earthquake stability analysis. Results of the case study analyses are used to calibrate the new earthquake intensity measure. Next, a probability-based assessment procedure is developed to describe the collapse performance in terms of mean annual probability of exceedance and an equivalent load and resistance format. Finally, the probabilistic assessment procedure is demonstrated through an application to one of the case study buildings.

2. HAZARD INTENSITY MEASURES

Traditionally, building codes have quantified earthquake intensity as a function of either peak ground motions (acceleration or velocity) or linear response spectrum quantities (acceleration, velocity, or displacement). As implied by their name, linear response spectrum quantities do a good job at characterizing earthquake effects in structures that respond elastically, but they do not necessarily capture inelastic behavior. More elaborate indices, which seek to improve characterization of earthquake ground motions, have been the subject of continuing studies. For example, Housner (1975) proposed combining spectral acceleration together with strong motion duration. More recently, Luco (2001) has proposed extending linear spectral quantities into the nonlinear realm through the use of inelastic spectral response demands. While they are generally more accurate, one drawback of the nonlinear spectral values is that they imply a coupling between the earthquake hazard definition and the inelastic structural properties. This complicates

development of seismic hazard maps for general use. Another topic of recent research concerns near fault directivity effects and whether these warrant specialized treatment in earthquake hazard characterization (e.g., Alavi & Krawinkler 2000). These are just a few examples of research to investigate the damaging features of earthquake ground motions and develop improved hazard intensity measures to represent these effects.

Common to most studies of improved intensity measures is the goal to characterize ground motion hazards in a statistically meaningful way for predicting structural performance. This implies that the best intensity measures are those that result in the least record-to-record variability, measured with respect to a common intensity index, when evaluating structural performance to multiple earthquake records. Of course, even with the best ground motion characterization, uncertainties will persist in characterizing the geologic earthquake hazard and in simulating inelastic structural performance.

Improved Hazard Intensity Measure - $S_a(T)R_{Sa}^\alpha$

The *International Building Code* (ICC 2000) and most other earthquake engineering design standards in the United States define hazard intensity as the spectral acceleration of the ground motion, typically calculated at the fundamental (first mode) period of the structure. A known shortcoming of this measure is that it does not account for inelastic lengthening of the period as the structure softens under stiffness degradation. As illustrated in the response spectra plots of Fig. 1, two ground motions characterized on the basis of their first-mode spectral response may result in significantly different inelastic response, depending on the slope of the spectra at lengthened periods. For example, when normalized with respect to $S_a(T_1)$, record #2 will inevitably produce larger inelastic deformations than record #1. This trend is not accounted for in the single spectral quantity, $S_a(T_1)$.

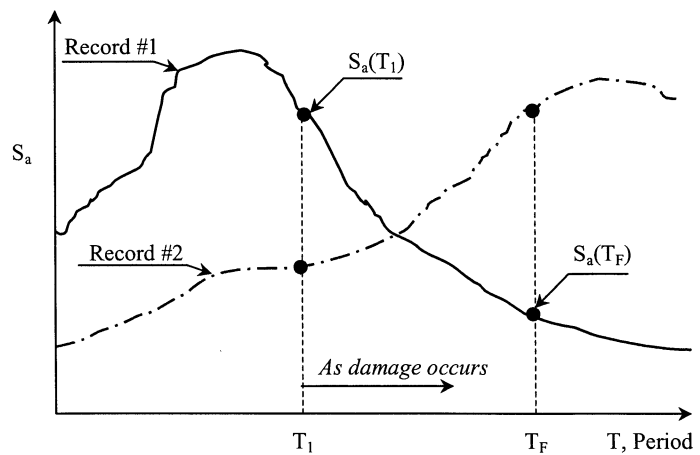


Figure 1 – Effects of structural softening.

A simple extension to current practice that can help capture the period shift effect is to introduce a second intensity parameter that reflects spectral shape. The proposed parameter to do this is a ratio of spectral accelerations at two periods,

$$R_{S_a} = S_a(T_f) / S_a(T_1) \quad (1)$$

where T_1 is the first mode period and T_f is a longer period that represents the inelastic (damaged) structure. This ratio can then be combined with the first mode spectral acceleration, $S_a(T_1)$, to give the following new two-parameter hazard intensity measure

$$S^* = S_a(T_1) R_{S_a}^\alpha \quad (2)$$

where α and the ratio T_f/T_1 are determined by calibration to optimize the intensity index by minimizing the variability in computed results.

Attenuation Functions for Two-Parameter Index

Given the prevalence of linear spectral acceleration in codes and practice, most hazard assessment techniques and data are geared toward this predicting this quantity. For example, national hazard maps available from USGS define earthquake hazard in terms of spectral acceleration at two periods (roughly $T = 0.2$ second and 1 second) representative of short and long period structures. In devising new intensity measures, it is convenient if they can be derived by manipulating existing models and hazard data.

Since the proposed intensity measure, S^* , is simply a function of the spectral acceleration at two different periods (T_1 and T_f), it is relatively straightforward to modify existing attenuation function to accommodate this index. Equations 3 and 4 show the transformation of a single parameter attenuation function, $E[\ln S_a(T_x)]$, to the modified function, $E[\ln S^*]$, where $E[\ln \dots]$ is read as the “expected value of the natural log of the given parameter” and other variables are as defined previously:

$$\ln S^* = (1 - \alpha) \ln S_a(T_1) + \alpha \ln S_a(T_f) \quad (3)$$

$$E[\ln S^*] = (1 - \alpha) E[\ln S_a(T_1)] + \alpha E[\ln S_a(T_f)] \quad (4)$$

In addition to the expected value of S^* , the standard deviation, $\sigma_{\ln S^*}$, must also be defined. This in turn requires the correlation between spectral accelerations at the two periods, $S_a(T_1)$ and

$S_a(T_f)$. Inoue (1990) provides the following empirical correlation coefficient, $\rho_{\ln S_{a_1} \ln S_{a_f}}$, that fills this need:

$$\rho_{\ln S_{a_1} \ln S_{a_f}} = 1 - 0.33 \left| \ln(1/T_1) - \ln(1/T_f) \right| \quad (5)$$

Given this correlation expression, the standard deviation of S^* can be defined as follows:

$$\sigma_{\ln S^*}^2 = (1 - \alpha)^2 \sigma_{\ln S_{a_1}}^2 + \alpha^2 \sigma_{\ln S_{a_f}}^2 + 2\rho_{\ln S_{a_1} \ln S_{a_f}} (1 - \alpha)\alpha \sigma_{\ln S_{a_1}} \sigma_{\ln S_{a_f}} \quad (6)$$

Most spectral attenuation relationships define empirical coefficients as a function of frequency or period that can be manipulated to calculate S^* according to Eq. 4. For example, Abrahamson & Silva (1997) define an attenuation function as follows:

$$E[\ln S_a] = a_1 + a_4(m - m_1) + a_{12}(8.5 - m)^n + [a_3 + a_{13}(m - m_1)] \ln(R) \quad (7)$$

where the a -coefficients are tabulated by Abrahamson & Silva, m is the earthquake magnitude, m_1 is a given base magnitude, and R is the distance from the epicenter to the site. Substituting Eq. 7 into Eq. 4, one obtains the following relationship for modified coefficients that can be applied in the otherwise standard attenuation relationship to obtain S^* :

$$a_x^* = (1 - \alpha)a_{xT1} + \alpha a_{xT2} \quad (8)$$

These new relationships can then be applied in a standard probabilistic site hazard analysis where the required performance is evaluated on the basis of this new intensity, S^* .

3. BUILDING TESTBEDS

In related research (Mehanny et al., 2000, 2001) several moment frame structures have been developed and analyzed to exercise seismic assessment and design provisions for composite construction. These frames are utilized here to provide the basis for calibrating the new intensity measure parameters, α and T_f/T_1 , and illustrate their application in a probabilistic performance assessment. The case study structures consist of three six-story frames and one twelve-story frame, all of which are designed according to provisions of the *International Building Code* (ICC 2000) and *AISC Seismic Provisions* (1997) for a site in a high seismic region of California. Due to space limitations the frames are only briefly introduced here. For further details the reader is referred to Mehanny et al. (2000, 2001).

Three of the case study structures are composite moment frames composed of reinforced concrete columns and steel beams (referred to as RCS systems), and the fourth is a steel space frame. An elevation of one of the frames, a six-story RCS perimeter frame, is shown in Fig. 2. Beam sizes in the frames were generally governed by drift requirements while the reinforced columns were governed by the strong column weak beam criterion. As summarized in Table 1, vibration periods for the frames range from $T_1 = 1.3$ to 2.1 seconds (note – other data reported in Table 1 is discussed later).

Inelastic static and dynamic (time history) analyses are conducted using an analysis program developed by El-Tawil et al. (1996) that takes into account second-order geometric behavior and spread-of-plasticity effects in the beam-columns and connections. Inelastic component properties are based on the expected (as compared to nominal) material strengths, where the expected strengths are taken as 1.15 times the nominal strengths. Static pushover and inelastic time history analyses are run simultaneously with gravity loads equal to 100% dead load and 25% live load. Summarized in Table 1 are static lateral overstrengths of the frames, defined as $\Omega_o = V_u/V_d$ where V_u is the ultimate base shear and V_d is the IBC design base shear. The overstrengths range from roughly $\Omega_o = 2.6$ for the six-story RCS perimeter frame up to $\Omega_o = 6.1$ for the six-story steel space frame. The overstrengths are relatively large compared to the typical expected values of $\Omega_o = 2$ to 3, due to the following sources of overstrength: (1) expected versus minimum specified material strengths, (2) minimum stiffness (*drift*) criteria, (3) structural redundancy, (4) strong column criterion, and (5) discrete member sizing.

Table 1 – Testbed frame data

Frame ID	First Mode Period, T_1 (sec)	V_u/V_d , Ω	IDA Dispersion Data for Alternative Intensity Measures					
			General Records			Near Fault Records		
			$\sigma_{In(IDR Sa)}$	$\sigma_{In(IDR SaRsa)}$ (Optimized)	$\sigma_{InIDR SaRsa}$ (2.0, 0.5)	$\sigma_{In(IDR Sa)}$	$\sigma_{In(IDR SaRsa)}$ (Optimized)	$\sigma_{In(IDR SaRsa)}$ (2.0, 0.5)
6S_RCS_S	1.3sec	3.9	0.42	0.28 (1.9, 0.65)	0.29	0.45	0.22 (1.8, 0.9)	0.27
6S_S_S	1.3sec	6.1	0.27	0.20 (1.2, 2.4)	0.23	0.30	0.18 (1.6, 0.8)	0.19
12S_RCS_S	2.1sec	4.4	0.24	0.19 (1.6, 0.6)	0.22	0.26	0.21 (2.4, 0.4)	0.22
6S_RCS_P	1.5sec	2.6	0.30	0.23 (1.65, 0.45)	0.24	-	-	-

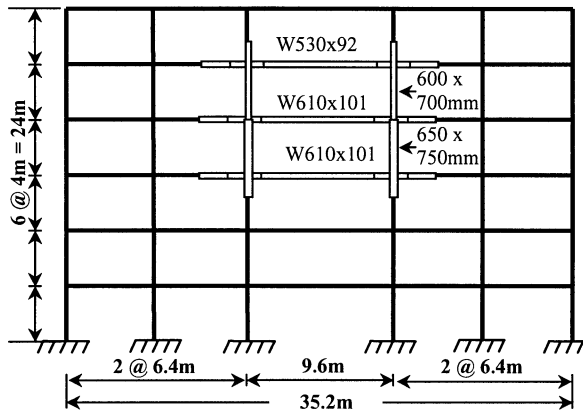


Figure 2 – Elevation of RCS perimeter frame.

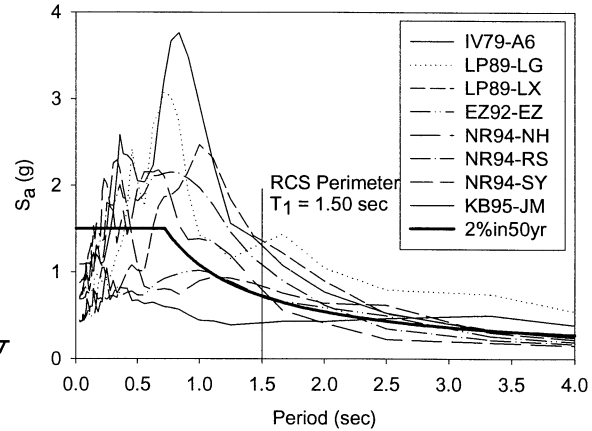


Figure 3 – Near Fault Response Spectrum

4. COLLAPSE ANALYSIS TECHNIQUES

Incremented Dynamic Analysis

Seismic performance is assessed through nonlinear time history analyses using two sets of ground motions – one comprised of eight general records and another of eight near-fault records with forward directivity. Response spectra for the near-fault records are superimposed on the 2% in 50-year design hazard spectrum used to design the case study buildings in Fig. 3. Acceleration components of the records are scaled, where the resulting ground motion intensity is reported in terms of either spectral acceleration, $S_a(T_1)$, or the proposed new index, $S_a R_{S_a}^\alpha$. Shome and Cornell (1997) have demonstrated that such scaling of records will not bias the results and is an appropriate technique for multi-level hazard analysis. More details on the ground record properties and scaling issues for the records are summarized by Mehanny (2000).

Results of the time history analyses are summarized by plotting the scaled intensity measure versus maximum Interstory Drift Ratio (IDR), creating what are referred to herein as Incremented Dynamic Analysis (IDA) curves. Shown in Fig. 4 are examples of the IDA curves for the RCS perimeter frame building subjected to the general records, where each data point corresponds to the peak IDR resulting from a single time history analysis. The collection of data points for a single ground record scaled to multiple hazard levels forms the IDA curve. Results are plotted in terms of the $S_a(T_1)$ intensity in Fig. 4a and $S_a R_{S_a}^\alpha$ in Fig. 4b.

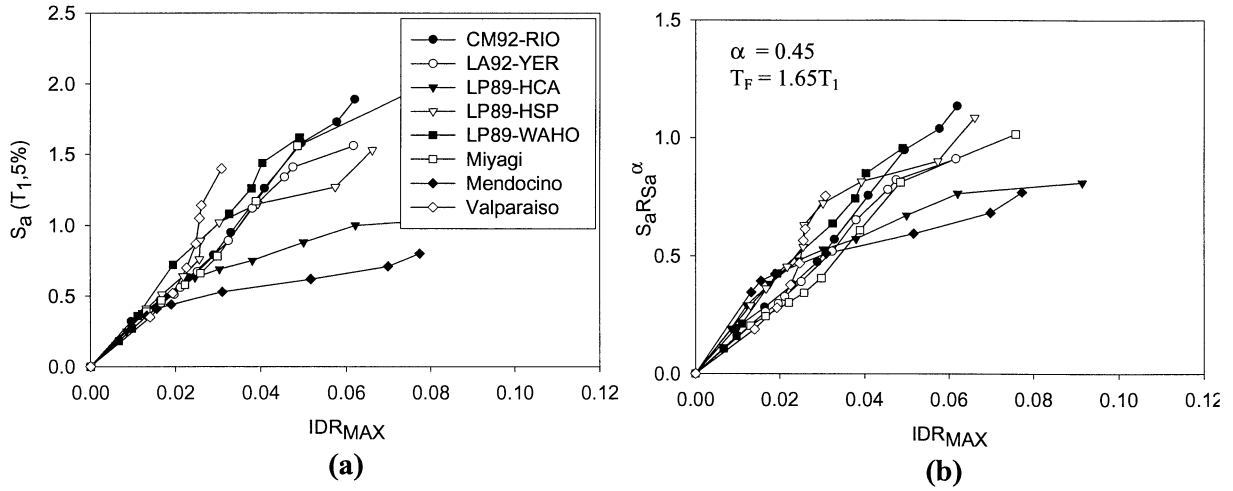


Figure 4 – IDA plots for 6S_RCS_P Frame: (a) IDR vs. $S_a(T_1)$ (b) IDR vs. $S_a R_{s_a}^\alpha$

Comparing the graphs in Fig. 4, it is obvious that the two-parameter intensity measure (Fig. 4b) results in significantly less record-to-record variability than $S_a(T_1)$ (Fig. 4a). The variability can be quantified in terms of dispersion of the drift response conditioned on the ground motion intensity measure. Dispersion is calculated according to the following equation as the mean squared deviation of the drift data from an average response curve obtained by linear regression in log-log space between drift and the seismic intensity (of the form, $\ln IDR_{MAX} = A + B \ln IM$):

$$\sigma_{\ln IDR_{MAX} | intensity\ measure} = \left[\frac{\sum_{i=1}^n (\ln IDR_{MAX,i} - \ln \hat{IDR}_{MAX})^2}{n-1} \right]^{\frac{1}{2}} \quad (9)$$

where $IDR_{MAX,i}$ is the i th response calculated for a given intensity, \hat{IDR}_{MAX} is the value from the regression curve, and n is the total number of observations ($n=8$ in this case).

Comparing Figs. 4a and 4b, the dispersion $\sigma_{\ln(IDR,Sa)} = 0.45$ for the $S_a(T_1)$ index is roughly twice that of $\sigma_{\ln(IDR,SaR)} = 0.22$ for $S_a R_{S_a}^\alpha$. This result is based on using the optimized coefficients of $\alpha=0.45$ and $T_f/T_1 = 1.65$ for the $S_a R_{S_a}^\alpha$ index, determined by varying these factors so as to minimize the dispersion. Note that these optimal values are specific to the RCS six-story perimeter frame under the set of eight ground motions. Reduction in the dispersion in this way helps reduce the number of records necessary to simulate time history response within a specified confidence interval.

While the two-parameter index reduces the overall dispersion, this reduction is most apparent at larger drifts, where the structure behaves nonlinearly. In fact, comparing Figs. 4a and 4b, in the elastic range (at lower drifts), the two-parameter $S_a R_{S_a}^\alpha$ index results in more variability than $S_a(T_1)$. This follows from the fact that $S_a(T_1)$ provides a nearly exact correlation with drift for the linear case, whereas the period shift captured in $S_a R_{S_a}^\alpha$ works best when the structure behaves nonlinearly. This suggests that an improved index would be one where the α and T_f parameters are devised to vary with the degree of inelastic action, similar in some ways to how the period is shifted using the capacity spectrum method for calculating the target displacement for nonlinear static pushover analyses.

While the IDA's provides useful information on the structural response, it is apparent from the curves in Fig. 4 that the IDA's do not reveal a definitive stability limit state. Some curves, such as the one for the LP89-HCA record, asymptotically approach a bounding strength (in terms of the intensity measure), but others do not. For example, the CM92-RIO and Valparaiso plots maintain positive slopes at very large earthquake intensities and drifts. This reflects inherent limitations of the inelastic time-history analysis to fully capture the strength and stiffness degradation at large inelastic deformations.

Frame Stability Limit State Determination

To evaluate global instability, the authors have employed a procedure that integrates local damage indices, computed during the time-history analysis, through a supplementary stability analysis of the damaged structure. The basic procedure, described in detail by Mehanny and Deierlein (2001), entails a post-earthquake second-order inelastic stability analysis to assess the loss of gravity load capacity due to damage incurred during the earthquake. This procedure, which leads to the plot of an intensity measure versus gravity stability index λ_u shown in Fig. 5, entails three basic steps. (1) *Perform a nonlinear time-history analysis and calculate the cumulative damage indices.* This provides the basis to quantify the localized (distributed) damage caused by a given earthquake ground motion. The damage indices are empirical equations that track the structural damage as a function of cumulative plastic deformations. (2) *Modify the analysis model based on the damage incurred during the time-history analysis.* This

involves reducing element stiffness and strengths as a function of the cumulative damage indices and incorporating the residual (permanent) building drift into the structural topology. (3) *Reanalyze the modified structural model through a second-order inelastic static analysis under gravity loads up its inelastic stability limit.* The resulting stability index, λ_u in Fig. 5, is defined as the ratio of the vertical load capacity to the applied gravity loads, where the gravity loads are assumed as full dead load plus 25% of the live load.

The stability index, λ_u , provides a global failure criterion that integrates the effect of local damage sustained under each earthquake record and intensity. Figure 5 shows the evolution of the stability index for the six-story RCS space frame, where there is a one-to-one correspondence between stability points in Fig. 5 and the maximum interstory drifts in Fig. 4. The initial value of $\lambda_{uo} = 5.5$ (on the horizontal axis in Fig. 5) is the index for the undamaged structure, implying that the undamaged frame has sufficient lateral strength/stiffness to maintain stability under 5.5 times the gravity load. This large value reflects the fact that the structure has significant gravity-load overstrength as a result of the high seismic loads. The point where the curves cross $\lambda_u = 1.0$ is point at which the structure can no longer sustain stability under its self-weight due to extensive seismic damage. The stability index at this point is defined as λ_f and the associated median value of the seismic hazard value is $\hat{\mu}_{\lambda_f}$. This level is defined as the ‘capacity’ – or collapse limit state – of the structure. Between these limits, λ_{uo} and λ_f , a third limit point is identified at $\lambda_u = 0.95\lambda_{uo}$, corresponding to the point at which the lateral stability begins to

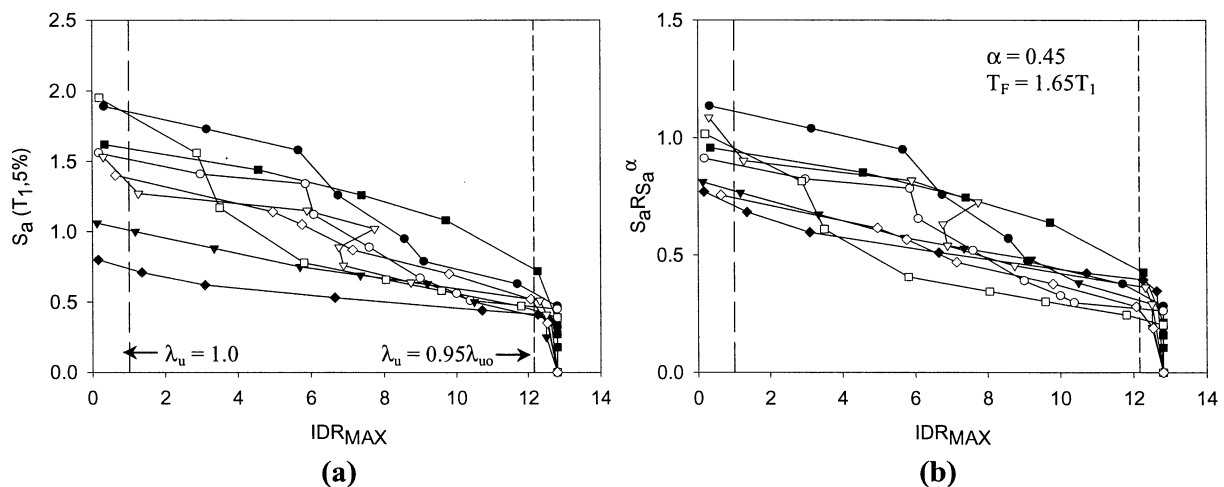


Figure 5 – Stability curves versus IM, (a) $IM = S_a$, (b) $IM = S_a R_{sa}^\alpha$

significantly degrade. This point, referred to as λ_{OD} (Onset of Damage) defines where there is a sharp transition in the $S_a(T_1)$ or $S_a R_{S_a}^\alpha$ versus λ_u stability curve, representing the intensity level beyond which the stability index degrades rapidly.

Similar to the IDA plots (Fig. 4), the $S_a(T_1)$ index shows much larger record-to-record variability in the λ_u response than the $S_a R_{S_a}^\alpha$ index. The standard deviations of $S_a(T_1)$ at λ_{OD} and λ_f are equal to 0.40 and 0.49, respectively, compared to 0.26 and 0.15 using $S_a R_{S_a}^\alpha$. This reduced variability leads to a better approximation of the expected collapse performance.

5. DETERMINATION OF GENERAL α AND T_f

The examples described above show how the proposed intensity measure, $S_a R_{S_a}^\alpha$, can significantly reduce the record-to-record variability in calculating the seismic performance. What remains to determine is optimum values of α and the period multiplier, $C=T_f/T_1$, which minimize dispersion for a broad class of building frames. To accomplish this, we will utilize analysis results of the four case study structures introduced previously.

To determine the optimal calibration for α and C , IDA and λ_u stability analyses are run for each of the four structures under the sixteen ground motions (eight general and eight near fault). Next, the $S_a R_{S_a}^\alpha$ response data is plotted for various combinations of α and C , the average response curve is fit to the data, and the dispersion is calculated. This results in many α and C pairs for each structure, each with its own dispersion, σ_{mIDR} . The optimal α and C pair for each structure is one that yields the least dispersion. The graphs in Fig. 6 show the resulting relationships between α , C , and the resulting dispersion for each structure and bin of ground motions. The optimum alpha-coefficient is plotted versus the corresponding C in Fig. 6a, and the associated dispersions for the corresponding pairs of α and C are plotted in Fig. 6b.

Determination of one general pair of α and C obviously compromises the preciseness that can be achieved with multiple pairs tailored for each structure and each ground record. Nevertheless, a

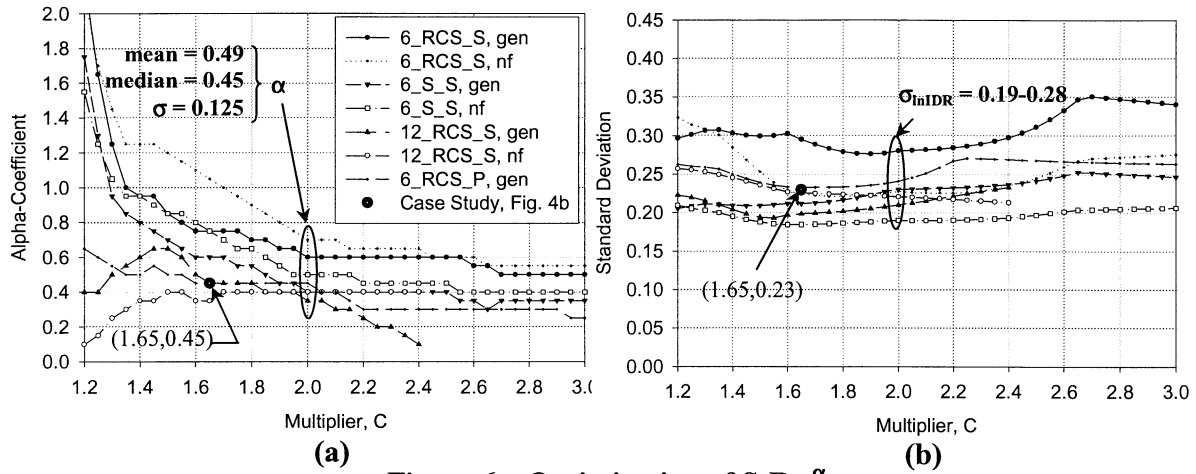


Figure 6 – Optimization of $S_a R_{S_a}^\alpha$,

(a) Range of optimum α -C pairs and (b) Dispersion on α -C pairs.

common calibration is desired to make the procedure convenient for generalized use. Referring to Fig. 6b, on average the dispersion turns out to be relatively constant over a large range of C and α pairs. Further, from Fig. 6a we see that the optimal α (given C) is relatively stable for $2 < C < 3$. This indicates that the intensity measure is somewhat insensitive, within a certain range, to the choice of period multiplier. Based on these observations, a pair of $C = 2.0$ ($T_f = 2.0T_1$) and $\alpha = 0.5$ is proposed for general use. Thus, the proposed intensity measure takes the specific definition:

$$S^* = S_a(T_1) \left[\frac{S_a(2.0T_1)}{S_a(T_1)} \right]^{0.5} = S_a R_{S_a}^{0.5} \quad (10)$$

Based on this definition, the data in Figs. 4b and 5b are re-plotted and shown in Fig. 7. Dispersion data for all three intensity measures ($S_a(T_1)$, the optimal $S_a R_{S_a}^\alpha$, and the generalized $S_a R_{S_a}^{0.5}$) are summarized for each frame in Table 1.

Referring to Table 1, in all cases the proposed intensity measure ($S_a R_{S_a}^\alpha$) consistently reduces the variability in the calculated structural response, compared to the $S_a(T_1)$ index. The two-parameter index with optimum coefficients ($S_a R_{S_a}^\alpha$) obviously does a better job than the average index ($S_a R_{S_a}^{0.5}$ per Eq. 10), but the average index still does well – particularly where the dispersion is large for the original $S_a(T_1)$ index. Conversely, the only cases where the new index fails to make a significant impact is those instances where the variability of the response is

already low when scaled by spectral acceleration alone. Comparing results for the average two-parameter index (Eq. 10) with $Sa(T_1)$, the two-parameter index reduces the range of dispersion from 0.24-0.45 for $Sa(T_1)$ to 0.19-0.29 for $SaR_{Sa}^{0.5}$.

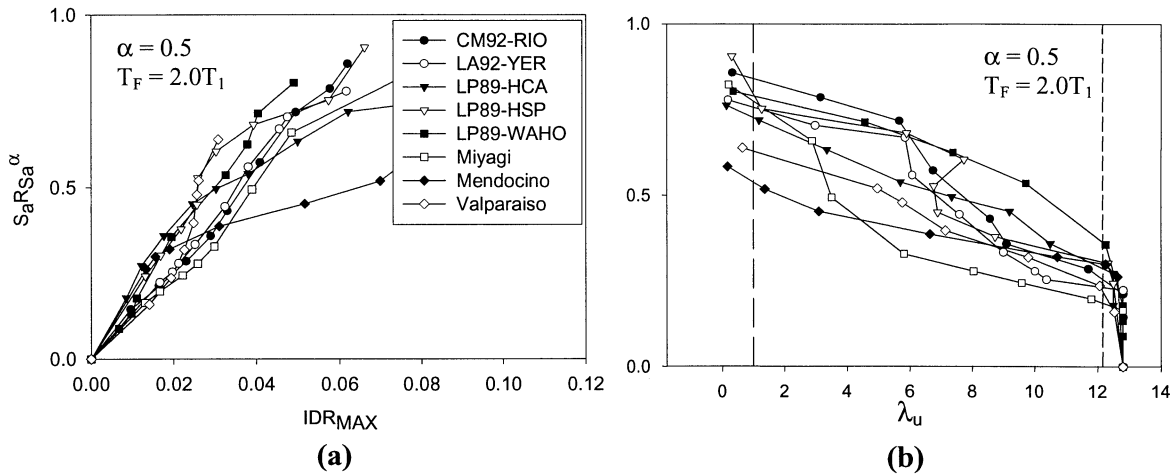


Figure 7 – Updated Behavior Curves with $IM = S_a R_{S_a}^{0.5}$
(a) IDA and (b) stability curves

6. PROBABILITY ASSESSMENT OF COLLAPSE PREVENTION

Using the inelastic time-history and stability analysis method described above, the “collapse prevention” performance for a given set of ground motion records is defined by the stability limit, $\hat{\mu}_{\lambda_f}$, defined in terms of the seismic hazard intensity – either $Sa(T_1)$ or $SaR_{Sa}^{0.5}$. The next step in the performance assessment is to compare the stability limit to the seismic hazard, considering the uncertainty in both the calculated response indices and the site hazard curve.

Mean Annual Probability of Exceedance

Defining failure (collapse) by the likelihood of the ground motion intensity exceeding the stability limit $\hat{\mu}_{\lambda_f}$ the mean annual probability of collapse can be described by the following:

$$P_f = P[IM \geq \hat{\mu}_{\lambda_f}] \quad (11)$$

Where P_f is the mean annual probability of failure and IM is the seismic hazard demand expressed using an intensity measure consistent with that used to define the stability limit, $\hat{\mu}_{\lambda_f}$.

In this case, the two alternative intensity measures considered are $S_a(T_1)$ or $S_a R_{S_a}^{0.5}$. The

seismic demands are expressed in terms of a probabilistic hazard curve (the annual probability of exceeding a specified intensity measure), determined either explicitly by a probabilistic seismic hazard analysis or using published hazard maps.

Equation 11 can be further expanded into the following form using the total probability theorem:

$$P_f = \int_0^{\infty} H_{IM}(u) f_{\lambda_f}(u) du \quad (12)$$

Where u is the intensity measure, $H_{IM}(u)$ is the hazard curve, and $f_{\lambda_f}(u)$ is the probability density of the structural stability limit. To permit closed-form solution of the probability integral, the hazard function is assumed to take the following form:

$$H_{IM}(u) = k_o u^{-k} \quad (13)$$

where k_o and k are coefficients that fit Eq. 13 to the hazard data. Further, $f_{\lambda_f}(u)$ is assumed as a lognormal distribution with the median $\hat{\mu}_{\lambda_f}$ and the dispersion δ_{λ_f} (or $\sigma_{\ln(\lambda_f)}$). Given these assumptions, the integral solution to Eq. 12 is as follows:

$$P_f = H_{IM}(\hat{\mu}_{\lambda_f}) e^{\frac{1}{2}k^2\delta_{\lambda_f}^2} \quad (14)$$

where $H_{IM}(\hat{\mu}_{\lambda_f})$ is the mean annual probability from the hazard curve evaluated at the median capacity $\hat{\mu}_{\lambda_f}$, and the other terms are as defined previously.

LRFD-like Format of Collapse Probability

An alternative way to envision the mean annual collapse probability is by rearranging Eq. 14 so as to compare the hazard demand to the structural capacity in a format similar to that used for *Load and Resistance Factor Design* (LRFD) provisions. Setting the failure probability in Eq. 14 to a maximum acceptance probability criteria, $P_f < P_{acceptance}$, Eq. 13 and 14 can be combined to give the design requirement:

$$k_o \hat{\mu}_{\lambda_f}^{-k} e^{\frac{1}{2}k^2\delta_{\lambda_f}^2} < P_{acceptance} \quad (15)$$

Rearranging this equation, the required capacity $\hat{\mu}_{\lambda_f}$ to ensure that the probability of failure is less than the acceptance criterion, $P_{acceptance}$, is given by the following:

$$\hat{\mu}_{\lambda_f} \geq IM_{P_{acceptance}} e^{\frac{1}{2}k\delta_{\lambda_f}^2} \quad (16)$$

where $IM_{P_{acceptance}}$ is the hazard intensity measure with the annual probability, $P_{acceptance}$, of being exceeded (i.e. $P_{acceptance} = H_{IM}(IM_{P_{acceptance}})$). The term, $e^{\frac{1}{2}k\delta_{\lambda_f}^2}$, which reflects the variability of the median stability limit $\hat{\mu}_{\lambda_f}$, can be moved to the left side of Eq. 16, resulting in the following:

$$e^{-\frac{1}{2}k\delta_{\lambda_f}^2} \hat{\mu}_{\lambda_f} \geq IM_{P_{acceptance}} \quad \text{or} \quad \phi \hat{\mu}_{\lambda_f} \geq \text{“seismic demand”} \quad (17)$$

where $\phi = e^{-\frac{1}{2}k\delta_{\lambda_f}^2}$. This equation is similar to LRFD equations that are prevalent in code provisions where the “design strength” on the left side (the nominal strength reduced by a phi factor) is compared to the load effect or “seismic demand”. In this case there is no load factor on the seismic demand since the recurrence interval of the demand is implicit in its definition.

An important but perhaps misleading coincidence in Eq. 17 is that the probability associated with the demand term (on the right side) turns out to be equal to the desired limit on the probability of exceeding the median stability intensity, $\hat{\mu}_{\lambda_f}$. This is different than saying that one is designing for a given hazard with a specified probability of exceedance. From Eq. 15, the underlying probability statement implied in Eq. 17 is related to the likelihood of exceeding the stability criterion, $\hat{\mu}_{\lambda_f}$ taking into account both variability in the ground motion hazard and the record-to-record variability in the stability index.

Essentially, Eq. 17 enables one to establish whether a structure meets the collapse performance objective with a mean annual probability of exceedance, $P_{acceptance}$. There are two basic input requirements for the procedure: (1) the “seismic demand” for the desired probability of exceedance, $IM_{P_{acceptance}}$, determined using either hazard maps or a probabilistic seismic hazard analysis; and (2) the median stability limit, $\hat{\mu}_{\lambda_f}$, of the structure and the corresponding dispersion δ_{λ_f} for a representative set of ground motions.

7. APPLICATION OF PROBABILISTIC COLLAPSE ASSESSMENT

This example will go through a collapse performance assessment for the 6-story RCS perimeter frame. The hazard analysis is based on a site at Yerba Buena Island (in San Francisco Bay)

where the San Andreas and Hayward faults govern the seismic hazard. The seismic hazard is characterized two ways: (1) through an explicit probabilistic seismic hazard analysis of the site and (2) using spectral acceleration hazard maps from building code provisions.

Annual Hazard Curves

Probabilistic Seismic Hazard Analysis (PSHA): Using the Abrahamson and Silva attenuation relationship presented in Eqs. 7 and 8, annual hazard curves for spectral acceleration, $S_a(T_1)$, and the proposed intensity measure, $S_a R_{S_a}^{0.5}$, can be developed through a standard probabilistic seismic hazard analysis for the Yerba-Buena Site site. Details of the hazard analysis are beyond the scope of this paper, but basically, this analysis provides a probabilistic assessment of earthquake magnitude and distance (M-R) pairs for the site, given its proximity to nearby faults.

Code Based Technique: An alternative (simplified) technique to obtain the hazard curve is to infer it from mapped spectral and site coefficients such as those provided by the seismic design provisions of the *International Building Code* (ICC 2000). The first step is to calculate the spectral acceleration for the site using the following equation:

$$S_a = F_v S_l / T_1 \quad (18)$$

where F_v is a tabulated site coefficient, given as a function of the site (soil) class and the spectral coefficients, and S_l is the spectral hazard coefficient obtained from seismic hazard maps with an average probability of occurrence of 2% in 50-years. Implied by Eq. 18 is a $1/T$ spectral curve in the long period range. Using Eq. 18, one can directly obtain the 2% in 50 year ($P_o = 0.0004$) spectral acceleration at the first mode period T_1 , i.e., $S_a(T_1)$. One can also approximate the two-parameter index $S_a R_{S_a}^{0.5}$, by assuming that $R_{S_a} = 2 \langle = S_a(T_1) / S_a(2T_1) = 2T_1 / T_1 \rangle$. Two approximations inherent in this assumption are that there is full correlation between the hazard values of $S_a(T_1)$ and $S_a(2T_1)$ and the $1/T$ design spectrum accurately represents the hazard spectrum. Once the 2% in 50 year spectral values are known, the full hazard curve is constructed assuming $k = 4$, and then back-calculating the k_o parameter.

Hazard Curve Comparison: Hazard curves for $T_1 = 1.5$ seconds (the natural period for the six-story RCS perimeter frame) are shown in Fig. 8, and the corresponding hazard curve parameters

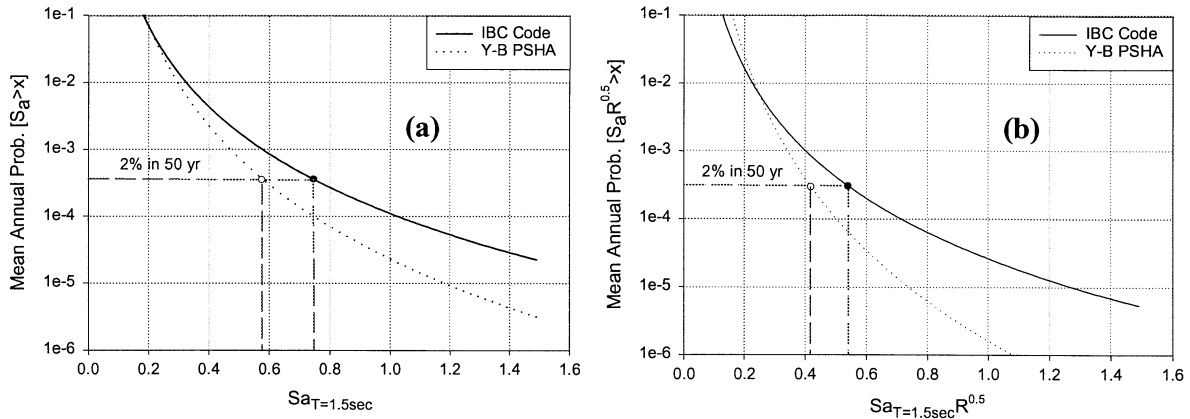


Figure 8 – Site Hazard Curves (a) S_a and (b) $S_a R^{0.5}$ ($T_1 = 1.5$ seconds)

are summarized in Table 2. Also summarized in Table 2 are capacity statistics $\hat{\mu}_{\lambda_f}$ and δ_{λ_f} for the frame. Referring to Fig. 8a, the 2% in 50 year value of $S_a(T_1)_{PSHA} = 0.57g$ from the probabilistic seismic hazard analysis is about 20% less than the code-value of $S_a(T_1)_{Code} = 0.72g$, and there are corresponding differences over the entire hazard curve. Presumably the PSHA results are more accurate, but further studies would need to be done to confirm this. Referring to Fig. 8b, the difference between the PSHA and code approach at the 2% in 50 year level for the $S_a R_{sa}$ index is also about 20%, $S_a(T_1)R_{Sa}^{0.5}_{PSHA} = 0.40$ versus $S_a(T_1)R_{Sa}^{0.5}_{Code} = 0.51g$.

Table 2 – Hazard curve coefficients and mean and dispersion of capacity

IM	Yerba Buena Site		Code Based Technique		$\hat{\mu}_{\lambda_f}$	δ_{λ_f}
	k_o	k	k_o	k		
$S_a(T_1)$	2.3×10^{-5}	5.0	1.1×10^{-4}	4	1.45	0.31
$S_a R_{Sa}^{0.5}$	1.6×10^{-6}	6.0	2.6×10^{-5}	4	0.76	0.15

Probability of Failure

Summarized in Table 2 are all the necessary data to compute the mean annual failure probabilities for the six-story RCS perimeter frame using the two alternative hazard intensity measures, $S_a(T_1)$ and $S_a(T_1)R_{Sa}^{0.5}$, and two alternative hazard curves (PSHA and building code approach). Substituting these data into Eqs. 13 and 14, the resulting collapse probabilities, P_f , are calculated and summarized in Table 3.

For the code hazard spectra and the $S_a(T_1)$ index, the mean annual probability of exceeding the stability (collapse) performance is about 0.00005 or roughly a 0.3% chance of exceedance in 50

years. Using the $S_a R_{S_a}^{0.5}$ index the probability roughly doubles to a mean annual value of 0.00009 or roughly a 0.5% in 50-year level. Since these probabilities are less than one-fourth of the 2% in 50-year seismic hazard probability commonly used as the target for collapse prevention performance, these data suggest that current code provisions result in a conservative design for this case. Moreover, the failure probabilities are less by about a factor of five using the PSHA intensity data, implying an additional degree of conservatism in the design.

Another interesting question raised by the results in Table 3 concerns the different results obtained using the $S_a(T_1)$ versus $S_a R_{S_a}^{0.5}$ index. The fact that the two-parameter index results in higher failure probabilities suggests that for predicting collapse performance, simple scaling based on $S_a(T_1)$ may be unconservative. This follows from the logic that the two-parameter index more accurately represents the damaging effects of earthquakes in the hazard curve. Note, however, that the difference between the two indices is not too large for the Yerba Buena site analysis (PSHA) where the correlation between $S_a(T_1)$ and $S_a(T_p)$ is modeled more accurately than in the code-based technique.

Table 3 – Failure probability and capacity factor design factors

		Yerba Buena Site	Code Based Technique
Probability of Failure	$P_f(S_a(T_1))$	1.19×10^{-5}	5.37×10^{-5}
	$P_f(S_a R_{S_a}^{0.5})$	1.24×10^{-5}	9.29×10^{-5}
IM = $S_a(T_1)$	ϕ	0.78	0.82
	$\phi \mu_M$	1.13g	1.19g
	<i>10%in50year</i>	0.41g	0.48g
	<i>2%in50year</i>	0.56g	0.72g
IM = $S_a R_{S_a}^{0.5}$	ϕ	0.94	0.96
	$\phi \mu_M$	0.72g	0.73g
	<i>10%in50year</i>	0.30g	0.34g
	<i>2%in50year</i>	0.40g	0.51g

Factored Capacity versus Nominal Demand

An alternate way of assessing the analysis results is through the LRFD-like approach described by Eq. 17. Data for this method are summarized in the lower half of Table 3, where limiting values are reported for 2% in 50-year (0.0004) and 10% in 50-year (0.002) probability levels. Referring to Table 3, the ϕ factor ranges from $\phi = 0.78$ to 0.82 for the $S_a(T_1)$ index and from $\phi = 0.94$ to 0.96 for the $S_a R_{S_a}^{0.5}$ index. The large difference between these ranges is directly

related to the reduced dispersion achieved using the two-parameter $S_a R_{S_a}^{0.5}$ index as compared to the $S_a(T_1)$ index.

According to the criteria, $\phi \hat{\mu}_{\lambda_f} \geq IM_{P_{acceptance}}$, the frame collapse performance limit passes the 2% in 50-year and 10% in 50-year probability checks in all cases. These comparisons do reflect the relative difference in results between the $S_a(T_1)$ and $S_a R_{S_a}^{0.5}$ indices that is similar to the difference observed in the failure probabilities described previously. For example, consider the ratio $\phi \hat{\mu}_{\lambda_f} / IM_{P_{acceptance}}$ between the factored capacity and the hazard intensity. Using data from the Yerba-Buena PSHA at the 2% in 50-year level, the ratios are $\phi \hat{\mu}_{\lambda_f} / Sa_{2\%in50} = 1.13/0.56 = 2.0$ for the $S_a(T_1)$ index and $\phi \hat{\mu}_{\lambda_f} / SaR_{Sa2\%in50} = 0.72/0.4 = 1.8$ for the $S_a R_{S_a}^{0.5}$ index.

8. SUMMARY AND CONCLUSIONS

A method to assess seismic response and probabilistic collapse performance of structures is presented and demonstrated by application to a composite moment frame building. Included is a proposal for a new two-parameter earthquake hazard intensity measure $S_a R_{S_a}^{0.5}$ that reflects both spectral intensity and spectral shape, thus accounting for inelastic strength and stiffness degradation (period elongation). Data are presented which show that this proposed index significantly reduces the record-to-record variability in predicted response obtained from inelastic time history analyses. This has practical implications on improving the accuracy of seismic assessment methods and reducing the number of records necessary to obtain a given confidence in the results.

Equations are developed to interpret the probability of collapse using data from incremented dynamic analyses. The equations are presented in two formats, one that directly computes the probability of failure for a structure, and another, which mimics an LRFD format by applying a “phi-factor” to the capacity of the structure and comparing it to a specified hazard.

ACKNOWLEDGMENTS

This paper is based on research supported by the National Science Foundation (CMS-9632502 and CMS-9975501), the Pacific Earthquake Engineering Research center (NSF Award Number EEC-9701568), and Stanford University (graduate fellowship support for the first author).

REFERENCES

- Abrahamson, N.A., and Silva, W.J. (1997), Empirical Response Spectral Attenuation Relations for Shallow Crustal Earthquakes, *Seismological Research Letters*, 68(1), 94-127.
- AISC (1997), *Seismic Provisions for Structural Steel Buildings*, American Institute of Steel Construction, Chicago, IL
- Alavi, B., Krawinkler, H. (2000), Consideration of Near-Fault Ground Motion Effects in Seismic Design, *Proc. of 12th World Conf. on Earthquake Engrg.*, New Zealand, 8 pg.
- El-Tawil, S., and Deierlein, G.G. (1996), *Inelastic Dynamic Analysis of Mixed Steel-Concrete Space Frames*, Struct. Engrg. Report No. 96-5, Cornell Univ., Ithaca, NY.
- Housner, G. W. (1975), Measures of severity of earthquake ground shaking, *Proceedings of the U.S. National Conference on Earthquake Engineering-1975*, Earthquake Engineering Research Inst., Oakland, California, June 1975, pages 25-33.
- Inoue, T. (1990). Seismic Hazard Analysis of Multi-degree-of-freedom Structures, *Report No. RMS-8*, Stanford University, Stanford, CA.
- ICC (2000), *International Building Code*, International Code Council, contact: BOCA, Country Club Hills, IL.
- Luco, N. (2001), "Probabilistic Seismic Demand Analysis, SMRF Connection Fractures, and Near-Source Effects", Ph.D. Thesis, CEE Dept., Stanford Univ., Stanford, CA.
- Mehanny, S.S., Deierlein, G.G. (2000), Modeling and Assessment of Seismic Performance of Composite Frames with Reinforced Concrete Columns and Steel Beams, *J.A. Blume Earthquake Engineering Center, Technical Report No. 135*, Stanford, CA.
- Mehanny, S.S., Cordova, P.P., and Deierlein, G.G. (2001), Seismic Design of Composite Moment Frame Buildings – Case Studies and Code Implications, *Composite Construction IV*, ASCE, in press.
- Mehanny, S.S., Deierlein, G.G. (2001), Seismic Damage and Collapse Assessment of Composite Moment Frames, *Jl. of Structural Engineering*, 127(9), ASCE, (to appear).
- Shome, N., and Cornell, C.A. (1997), "Probabilistic Seismic Demand Analysis of Nonlinear Structures," *Report No. RMS-35*, Stanford University, Stanford, CA, 320 pgs.

SUGGESTED IMPROVEMENTS TO PERFORMANCE-BASED SEISMIC DESIGN GUIDELINES

Joe MAFFEI¹

ABSTRACT

Recent performance-based seismic guidelines have improved structural engineering practice in the United States, and a number of further improvements can be made. Based on the author's experience over the last four years on several seismic evaluation and retrofit projects, this paper gives recommendations for simplifying and clarifying performance-based guidelines. The paper advocates more explicit instruction on the capacity-design approach, which is a prerequisite to considering nonlinear structural behavior. This involves clarifying key definitions and simplifying the basic seismic evaluation procedure. The recommended procedure emphasizes the capacity side of seismic evaluation rather than the demand side. The procedure highlights six essential steps that should be common to any analysis procedure from linear-static to nonlinear dynamic time-history. The procedure applies to either force-based or displacement-based methods of determining acceptability. An example is given on how, beyond the framework of general performance-based guidelines, specific structural criteria can be defined. The example provides detailed recommendations for the evaluation of concrete wall buildings for immediate occupancy performance.

1. INTRODUCTION

In the United States, recent performance-based seismic guidelines such as *FEMA 273* [ATC 1997] and *ATC 40* [ATC 1996] have improved the awareness of practicing engineers on important issues in structural engineering for earthquakes. The codification of nonlinear static procedure of analysis contributes to an improved appreciation of mechanisms of nonlinear response. The tabulation of acceptability limits can lead to a better understanding of the behavior modes of structural components.

The new guidelines represent a landmark advance over previous practice, and may provide the best available engineering framework to date for seismic retrofitting. The documents are relatively new, however, and there is significant opportunity for improving the guidelines.

Case studies of the *FEMA 273* guidelines were recently carried out on some 40 buildings of various structural characteristics spread throughout the United States. Engineering consultants conducted seismic evaluations and retrofit designs for each building. A number of recommendations were made towards improving the guidelines. [Merovich 1999, Maffei 1999].

The findings of these case studies, plus my experience over the last four years with performance-based seismic evaluation and retrofit design of buildings in California, lead me to suggest improvements to our practice. Some of the most important recommendations and areas of study are outlined in this paper. They include suggestions to:

¹ Senior Technical Consultant, Rutherford & Chekene, and Consulting Structural Engineer, San Francisco, California.
Email: jmaffei@ruthchek.com

- Clarify and simplify key definitions and procedures of performance-based design, according to the principles of capacity design.
- Correlate, compare, and simplify force-based and displacement-based methods of determining the acceptability of a structure to seismic criteria.
- Consider the appropriateness of using nonlinear analysis methods.
- Develop detailed criteria for the performance-based design of specific structure types and performance levels.

2. CAPACITY DESIGN BASIS

For new structures, *capacity design* is a seismic design approach in which distinct structural components, such as member plastic hinges, are chosen and detailed for energy dissipation according to a desired mechanism of nonlinear lateral deformation. All other structural components and actions are provided with sufficient strength to prevent failure under the chosen mechanism. When capacity design is applied to the evaluation of existing structures, the expected strength of structural components is determined and then the mechanism of nonlinear lateral deformation is identified.

The evaluation and retrofit guidelines *FEMA 273* [ATC 1997] and *ATC 40* [ATC 1996] establish, in part, this approach. As pointed out by Powell [1994], a capacity-design approach is in fact a prerequisite to using a nonlinear static procedure. However, the Case Studies project [Merovich 1999] has shown that the *FEMA 273* document does not clearly explain to users that a capacity-design approach must be followed. The *FEMA 273* and *ATC 40* guidelines should provide more explicit instruction in this regard.

Central to the use of *FEMA 273* and *ATC 40*, and to the issue of clearly explaining the capacity-design basis, are the definitions of the terms “force-controlled” and “deformation-controlled.” Even the authors of the documents and the expert reviewers on the Case Studies project were not clear or in agreement as to the meanings of these terms. Users of the documents are invariably confused by the lack of clarity in the definitions.

I recommend that the terms force-controlled and deformation-controlled be defined along the lines of capacity-design principles as shown below:

Deformation-controlled action: A component action that reaches its capacity under the governing mechanism. Deformation-controlled actions are the weak links or fuses of the structural response. The demand on deformation-controlled component actions derives from the deformation caused by the earthquake motion. Deformation-controlled actions must be ductile for the response of the structure to be ductile.

Force-controlled action: A component action that does not reach its capacity under the governing mechanism. Force-controlled actions are not the weak links of the structural response. The demand on force-controlled component actions derives from the forces delivered by deformation-controlled actions. Force-controlled actions need not be ductile for the response of the structure to be ductile.

Governing mechanism: The mechanism of inelastic lateral deformation — determined from a plastic analysis, a nonlinear analysis, or a comparison of relative strengths — that establishes which component actions reach their capacity under the expected pattern of seismic lateral forces.

3. RECOMMENDED EVALUATION PROCEDURE

Another improvement that can be made to seismic evaluation and retrofit guidelines is a simplification and clarification of the evaluation procedure. I recommend the seven-step procedure shown in Table 1.

The procedure can be used with either a computer analysis or hand/spreadsheet calculations. In my experience, the procedure tends to lead engineers to using more simplified analysis procedures than they had at first contemplated. This is because the procedure emphasizes the “capacity side” of the evaluation rather than the “demand side.”

Table 1 Recommended Procedure for Seismic Evaluation

Procedure	Remarks
1. Establish expected material strengths.	See Table 3 for an example.
2. Calculate the strength of critical sections (i.e., of deformation controlled actions).	See proposed definition of “deformation-controlled actions.”
3. Identify the governing post-elastic mechanism and the associated base shear, V .	See proposed definition of “governing mechanism.”
4. Calculate V/W , equal to base shear divided by seismic weight.	
5. Determine the fundamental period, T , and the effective initial stiffness.	Given T and V/W , a simplified envelope of the nonlinear force deformation response can be constructed.
6. Determine the governing behavior modes of the components (e.g., flexure, shear, sliding shear, boundary compression, foundation rocking) to verify the mechanism.	This step requires checking that capacity exceeds demand for all force-controlled actions, and thus that the assumed mechanism indeed governs. <i>FEMA 306</i> (ATC 1999) provides guidance on Behavior modes for concrete and masonry walls.

7. Given the mechanism, behavior mode, V/W , T , and response spectra, determine acceptability.	Acceptability can be checked using either force-based or displacement-based procedures. Recommend studies to simplify the currently used procedures.
---	---

The engineer begins with calculations of the strengths of the structural components, for example in shear and in flexure, and from that information identifies the governing mechanism (Step 3). This can usually be done by a hand plastic analysis, meaning that computer analysis, if used, is not applied until the last step. By doing most of the hand calculations first, the engineer gains a better understanding of the structure, and a greater ability to judge what the analysis model really needs to include. It becomes easier for him or her to come to grips with modeling issues such as the following:

- What are the critical elements and locations for which forces and displacements must be checked?
- Can two-dimensional modelling be used instead of 3-D?
- Given the location of the center of strength [Paulay 1996], does plan torsion need to be specially addressed?

The earthquake demand, represented by the response spectra of the defined earthquake hazard level, is not checked until the last step.

Comparison to Other Procedures

The procedure is somewhat opposite of a traditional structural engineering calculation, which stems from the procedures used for an elastic gravity-load evaluation. In such an evaluation, the loads are known quantities, which are input into an analysis and then checked against capacities. For nonlinear response to earthquake forces, by contrast, the demands are more variable than the capacities, and the forces in fact depend on the capacities. The procedure of Table 1 starts with what (a) is known best and (b) provides the most information to the engineer: the capacities. As a practical matter, the procedure tends to discourage engineers from getting bogged down in a falsely precise analysis of demands.

The basic procedure is applicable to either force-based or displacement-based methods of determining acceptability, which are discussed later in this paper. The procedure is also applicable to either static or dynamic analysis methods. The first six steps of the procedure are in fact identical whether force- or displacement-based methods are used, and whether static or dynamic analyses are carried out. Thus the procedure emphasizes six essential steps that should be common to any analysis procedure: linear static, linear dynamic, nonlinear static, or nonlinear dynamic time-history.

For most structures the procedure of Table 1 would require a similar level of effort to a conventional linear analysis. However, the procedure also provides the essential insights that

would be gained with a nonlinear procedure — namely, that of identifying the governing mechanism and behavior modes. Other aspects of nonlinear procedures can be incorporated if displacement-based acceptance procedures are used.

As in any engineering procedure, iteration between steps may be required. The procedure here is written for seismic evaluation, but it is also applicable to the subsequent phase of seismic retrofit design by applying the same steps to a proposed design.

The procedure proposed in Table 1 was written based on the seismic evaluation work done by Rutherford & Chekene Engineers on a number of buildings in the San Francisco Bay area [R&C 1999]. In practice the procedure as proven to be expedient and effective. The procedure is similar to, but broader than, a force-based procedure proposed by Park [1997] for the seismic evaluation of concrete moment-frame buildings.

4. FORCE-BASED OR DISPLACEMENT BASED ACCEPTANCE CRITERIA

Various procedures proposed for seismic evaluation are referred to as either force-based or displacement-based. For example, the linear static and linear dynamic procedures of *FEMA 273* [ATC 1997] are force-based, while the nonlinear static procedure is displacement-based. Priestley [1995], among others, has recently proposed a displacement-based procedure. As indicated in the previous section, most of the essential steps of seismic evaluation are identical for both types of procedures — the method of determining acceptability is the central difference.

Inelastic Demand based on Elastic Demand

Both force-based and displacement-based methods require an estimate of inelastic demand based on elastic demand. In force-based methods, a global reduction factor, R , has been used for new buildings [ICC 1998, UBC 1997]. The linear procedures of *FEMA 273* use component modification factors, m , in combination with a number of global response factors. Essentially these approaches are ductility-based — the R or m factors depend principally on assumed ductility capacity. The New Zealand structural code [SANZ 1992] makes direct use of displacement ductility, μ , and provides corresponding inelastic design spectra.

In displacement-based methods, two options are referred to in *FEMA 273* [ATC 1997] and *ATC 40* [ATC 1996], the Displacement Coefficient Method, and the Capacity Spectrum Method. As shown in Figure 1, these two procedures can give divergent estimates of displacement demand for the same building and earthquake input, sometimes by a factor of 2 or 3 [Aschheim et al 1998]. The basic technical assumptions behind the two methods also differ markedly. To reduce displacement demands, the Coefficient Method leads the engineer to add stiffness to a building with little concern for strength, while the Capacity Spectrum Method leads to the opposite conclusion.

Under the category of performance-based design, there has been considerable attention paid to various displacement-based and force-based methods, with different procedures each having proponents. The different acceptability procedures have not been correlated with each other, and often the algorithm for applying a procedure is more complicated than it needs to be. Given the disparity of results, the recently proposed procedures may offer little advantage over simpler methods such as the equal displacement and equal energy assumptions that were developed nearly 40 years ago [Blume et al 1961].

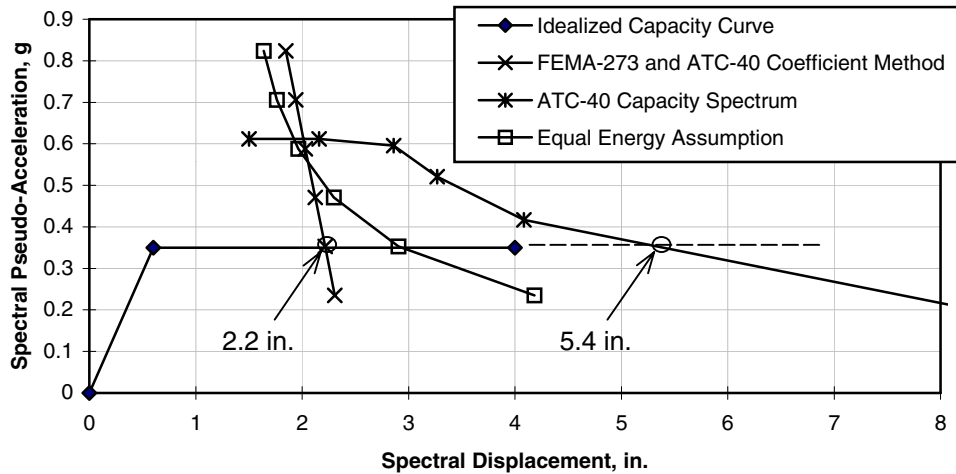


Figure 1 Comparison of Displacement Demands predicted by Displacement Coefficient and Capacity Spectrum Method [Aschheim et al 1988]

Recommended Study

To resolve issues of what methods of determining acceptability are most appropriate, a more direct comparison of different proposed methods is needed. Reformatting different procedures towards a more common basis would facilitate this comparison. It appears, for example, that any displacement-based procedure could be reformulated as a force-based procedure, and vice-versa. The technical issue of how to relate inelastic demands to elastic demands should be investigated in separation from how different procedures are formatted or presented. The input variables to this problem (as indicated in Table 1, Step 7) are the five characteristics listed below:

- Mechanism of response, which can affect the relationship between global and local ductility.
- Behavior mode of the critical (deformation-controlled) actions, which indicates strength degradation and stiffness degradation.
- V/W , the lateral strength of the structure divided by its weight.
- T , the structure period, which indicates effective initial stiffness.
- The response spectra of the design earthquake input.

The above recommendations characterize the problem of determining acceptability according to a global basis, but the results of the proposed study could also be applied to component-by-component acceptability procedures.

5. APPROPRIATENESS OF ANALYSIS METHODS

Many engineers assume that, compared to conventional design, performance-based design always requires a more complicated structural analysis, such as a nonlinear static procedure. This should not be the case.

In many instances, performance-based design is used when a building owner desires better than life-safety performance: either immediate occupancy, or some measure of damage control. Nonlinear procedures are actually less important to use for immediate-occupancy or damage-control performance levels than they are for life-safety or collapse-prevention performance levels. The reason is that for the stricter performance levels such as immediate occupancy, nonlinear response is limited, and thus an elastic model can acceptably capture the behavior. An example of specific structural criteria for immediate occupancy performance, based on a linear analysis, is discussed subsequently in this paper.

Currently in California, nonlinear procedures are used more frequently for existing buildings than for new buildings. This is somewhat illogical because many of the existing buildings being evaluated have little ability to achieve nonlinear deformations, whereas new buildings in high seismic zones are intended to have high ductility capacities. Except for seismic-isolated structures, nonlinear analysis procedures are not required for new buildings [ICBO 1997]. If the capacity-design procedure proposed in this paper is used, few buildings, new or existing, should require nonlinear analyses. When a nonlinear analysis procedure is used for an existing structure with non-ductile components, the ability of the procedure to properly account for strength degradation in the components should be carefully examined.

6. DEVELOPMENT OF DETAILED GUIDELINES

An example of specific performance-based structural criteria is given in Table 2 and Table 3. The criteria were initially developed for a hospital building in California, for immediate occupancy performance for the given design response spectra. The criteria are rewritten here to apply to any typical concrete wall building with concrete beam and column gravity framing, as shown in Table 2. The criteria are force-based, use a linear analysis, and include requirements for component actions for the reinforced concrete walls, columns, and beams. The analysis is made without reducing the input or results, for example by an R factor. The full elastic response is used.

In a conventional evaluation, the walls of the building would be designated as the seismic-force-resisting system and the columns and beams would not be designated as part of the seismic force-resisting system. For the criteria given here, this distinction is unnecessary. The columns and beams do not need to be included in the computer model because they will have only a small, and beneficial, effect on the force and displacement results. The actions on the columns and beams can be approximated by a hand analysis that applies the displacement results of the computer analysis.

Table 2 Example of Specific Performance-Based Structural Criteria

Performance Objective:	Immediate Occupancy for the 10% in 50 year ground motion
Building Type:	Concrete wall building with concrete beam and column “gravity” framing.
Analysis Method:	Linear static or response spectrum analysis using unreduced demand. Beams and columns can either be explicitly included in the model, or beam and column actions can be calculated subsequently from the induced displacement, where the unreduced elastic displacement is used.

Mechanism Check:	A comparison of member strengths, or a more formal plastic analysis, verifies that a story mechanism (for example a weak-pier, strong spandrel mechanism) does not occur. A range of possible vertical distributions of lateral forces should be considered.
Acceptability Method:	Force based, using actions (such as M and V) from analysis, compared to component nominal strengths (such as M_n and V_n) using $\phi = 1.0$ and expected material strengths.
Acceptable Displacement:	Nonstructural elements must be designed to accommodate the seismic displacements, The unreduced elastic displacements can be used, magnified somewhat for short-period buildings.

Displacement and nonstructural components

The design of nonstructural building components, such as cladding, partition, ceilings, equipment, ductwork, piping, and electrical components can be a key part of achieving the desired performance level. The nonstructural components must be designed considering both seismic displacements and accelerations.

Components that connect across more than one level of a structure, such as cladding or partitions, must be designed to accommodate the relative seismic displacements of the different levels. Typically the designer should first calculate the displacements for the structure, and then design or specify the nonstructural components accordingly. For concrete wall structures and most other seismic systems, it is usually not practical or necessary to adjust the structural design to achieve a displacement criterion. (Structures that use only moment frames to resist lateral forces may need to be designed using displacement criteria.)

Nonstructural components must withstand the seismic accelerations that occur at the floor level where they are located in the building. Unreduced floor accelerations resulting from a linear-elastic analysis should provide an upper bound that can be used in design. Conventional code requirements for forces on components can also be used, but further study is needed to determine the seismic performance that results from such requirements.

Behavior Modes and Detailing

The proposed criteria explicitly consider a number of possible behavior modes that can occur in concrete wall structures [ATC 1999, Paulay and Priestley 1992]. For brittle behavior modes such as wall shear in diagonal tension, the criteria require the structure to remain elastic, or for the behavior mode not to govern over ductile behavior modes. For ductile behavior modes such as wall moment or foundation rocking, a limited amount of nonlinear response is permitted.

Generally, a displacement ductility of up to 2.5 is considered acceptable for ductile behavior modes. At such a ductility level, flexural cracks that open upon yielding are likely to close again and residual crack width will be small. If compression strains are kept below 0.003, spalling is not expected. Strains can be estimated using the procedure of the SEAOC Blue Book [SEAOC 1999].

Detailing for confinement is required for collapse prevention in the maximum credible ground motion, but it is not necessary for immediate occupancy performance. Because compression strains are limited to 0.003 for immediate occupancy performance, the cover concrete is not

expected to spall, and thus there is no demand for confinement of the concrete core. The seismic evaluation handbook, *FEMA 310* [ASCE 1998] implies an opposite conclusion; the document incorrectly requires confined wall boundaries for immediate occupancy performance but not for life-safety performance.

Table 3 Specific Performance Requirements and Acceptability Criteria

Action	Performance Requirement	Acceptability Criteria
Wall Moment:	Flexural cracks to remain small (e.g., 1/8 inch) and no significant spalling should occur.	$M \leq 2.5 M_n$, and $\epsilon_c \leq 0.003$ (strain calculation per 1997 UBC). Boundary confinement is not required for immediate occupancy. Flexural yielding to low ductility is acceptable.
Wall Shear in Diagonal Tension	Shear failure does not occur. Any shear cracks are minor.	$V \leq V_n = V_c + V_s + V_p$, per <i>FEMA 306</i> [ATC 1999]. V_c is based on $0.25\sqrt{f'_c}$ MPa ($3\sqrt{f'_c}$ psi) times factors α and β .
Wall Sliding Shear	Sliding shear does not occur	$V \leq V_{nf}$ (ACI 318 shear friction) and $V \leq 0.67\sqrt{f'_c}$ MPa ($8\sqrt{f'_c}$ psi)
Wall Overturning	Foundation overturning permitted to limited displacement.	$M \leq 2.5 M_R$, use 1.0D for resisting moment. Check for induced displacement on beams and columns per criteria given below.
Wall Diagonal Compression	Diagonal compression (web crushing) failure does not occur.	$V \leq 0.67\sqrt{f'_c}$ MPa ($8\sqrt{f'_c}$ psi), based on <i>FEMA 306</i> information
Lap Splice Length	Allow only limited lap-splice slip.	Check for class A lap length per ACI 318-99 Section 12.2.3. If necessary consider references given in <i>FEMA 306</i> .
Beam moment:	Flexural cracks to remain small (e.g., 1/8 inch) and no significant spalling should occur.	$M \leq 2.5 M_n$
Beam Shear	Shear failure does not occur. Any shear cracks are minor.	$V \leq V_n = 3\beta\sqrt{f'_c} + V_s$, similar to <i>FEMA 306</i>
Column Moment	Flexural cracks to remain small (e.g., 1/8 inch) and no significant spalling should occur.	$M \leq 2.5 M_n$, and $\epsilon_c \leq 0.003$
Column Shear	Shear failure does not occur. Any shear cracks are minor.	$V \leq V_n = V_c + V_s + V_p$, per Priestley and Kowalsky

Expected Strength

The criteria proposed here are based on expected material strengths, rather than lower-bound strengths, and strength-reduction factors, ϕ , are not used. Typically, expected strength of reinforcing steel is about 1.15 times the specified yield strength [ATC 1999, Park 1997]. Table 4 gives expected material strength values used for a 1960s-designed concrete building in California. The values were based on test data that were available from other buildings of the same era.

Table 4 Example of Expected Material Strengths

Material	Specifications given in the structural drawings	Expected Strength
Reinforcing Steel, 25mm (#8) and larger	ASTM A432	$f_y = 450 \text{ MPa (65 ksi)}$
Reinforcing Steel, 22mm (#7) and smaller	none	$f_y = 340 \text{ MPa (49 ksi)}$
Concrete	25.8 MPa (3750 psi) regular weight	$f'_c = 31 \text{ MPa (4500 psi)}$

Comparison to New Building Requirements

The criteria allow flexural demands up to 2.5 times greater than capacities, which is roughly consistent, in the case of concrete wall buildings, with requirements for new buildings that are essential facilities. By the Uniform Building Code [ICBO 1997] the building would be designed with an R factor of 5.5 and importance factor, I of 1.5. With a ϕ factor of 0.85 and a ratio of expected strength to nominal strength of 1.15, the proposed value of 2.5 compares to a value of 2.7 from by the UBC. The calculation is $(5.5 \times 0.85)/(1.5 \times 1.15) = 2.7$.

The value of 2.5 for flexural demands should possibly be reduced, to 2.0 say, in cases where buildings have a shorter period than the site period. This is similar to the C_I variable of FEMA 273 [ATC 1997]. The proposed criteria for shear behavior modes is generally more restrictive than what is used for new buildings that are essential facilities. These two points indicate that codes for new essential facilities may not be sufficient to provide immediate occupancy performance. The situation can be worse for structural systems such as moment frames that use higher R values.

Recommendations

The proposed criteria tend to give much more specific requirements to the engineers than *FEMA 273*. I recommend that specific requirements such as in Table 3, focused on a particular building types and performance levels, should be developed as part of a revision, expansion, and calibration of *FEMA 273*. This would greatly improve the usability and reliability of the document.

To my knowledge, no one has examined from a performance-based perspective whether the codes for new essential facilities would provide immediate occupancy performance. This would be a useful study.

7. CONCLUSION

Recent performance-based seismic guidelines such as *FEMA 273* [ATC 1997] have been developed in a “top-down” fashion, with issues being identified and characterized based on the general experience of the contributors. Much of the effort to date on the guidelines has focused on establishing definitions and categorizing structural systems and issues. Application of the guidelines to real buildings shows that more work is needed to develop detailed criteria applicable to specific building types and characteristics.

The performance-based seismic guidelines have succeeded in improving the awareness of practicing engineers in considering nonlinear response and the behavior modes of structural components. The guidelines have the potential to be much more useful to practitioners. The recommendations given throughout this paper are some of the essential changes and expansions that should be made to performance-based guidelines to improve their usability and effectiveness

8. REFERENCES

- ASCE, 1998, *Handbook for the Seismic Evaluation of Existing Buildings — A Pre-standard*, prepared by the American Society of Civil Engineers for the Federal Emergency Management Agency, Report No. *FEMA 310*, Washington D.C.
- ATC, 1996, *Seismic Evaluation and Retrofit of Concrete Buildings*, prepared by the Applied Technology Council (ATC-33 project) for the California Seismic Safety Commission, Report No. *ATC-40*, Redwood City California
- ATC, 1997, *NEHRP Guidelines for the Seismic Rehabilitation of Buildings*, prepared by the Applied Technology Council (ATC-33 project) for the Building Seismic Safety Council, published by the Federal Emergency Management Agency, Report No. *FEMA 273*, Washington D.C.
- ATC, 1997, *NEHRP Guidelines for the Seismic Rehabilitation of Buildings*, prepared by the Applied Technology Council (ATC-33 project) for the Building Seismic Safety Council, published by the Federal Emergency Management Agency, Report No. *FEMA 273*, Washington D.C.
- ATC, 1999, *Evaluation of Earthquake Damaged Concrete and Masonry Wall Buildings*, prepared by the Applied Technology Council (ATC-43 project) for the Partnership for Response and Recovery, published by the Federal Emergency Management Agency, Report No. *FEMA 306*, Washington D.C.

- Aschheim, Mark, Joe Maffei, and Edgar Black, 1998, "Nonlinear Static Procedures and Earthquake Displacement Demands," *Proceedings, Sixth U S National Conference on Earthquake Engineering*, Seattle, Washington, Earthquake Engineering Research Institute, June
- Blume, John A., Nathan A. Newmark, and Leo H. Corning, 1961, *Design of Multistory Reinforced Concrete Buildings for Earthquake Motions*, Portland Cement Association, Skokie, Illinois.
- BSSC, 1992, NEHRP Handbook for the Seismic Evaluation of Existing Buildings, prepared by the Building Seismic Safety Council for the Federal Emergency Management Agency, Report No. FEMA 178, Washington D.C.
- ICBO, 1997, *Uniform Building Code*, Volume 2, Structural Engineering Design Provisions, International Conference of Building Officials, Whittier California.
- ICC, 1998, *International Building Code 2000*, Final Draft, International Code Council, Falls Church Virginia, July
- Maffei, Joe, 1999, *Case Studies of FEMA 273, NEHRP Guidelines for the Seismic Rehabilitation of Buildings, Final DAP Report*, J. Maffei, member of the Design Assessment Panel, Oakland CA, June
- Merovich, A. T., 1999, *Case Studies of the NEHRP Guidelines for the Seismic Rehabilitation of Buildings, Final Project Report*, prepared for the Building Seismic Safety Council, Washington D.C.
- Park, R., 1997, "A Static Force-Based Procedure for the Seismic Assessment of Existing Reinforced Concrete Moment Resisting Frames," *Bulletin of the New Zealand National Society for Earthquake Engineering*, Vol. 30, No.3, September
- Paulay, T., 1996, Seismic Design for Torsional Response of Ductile Buildings, *Bulletin of the New Zealand National Society for Earthquake Engineering*, Vol. 29, No.3, September
- Paulay, T. and M. J. N. Priestley, 1992, *Seismic Design of Reinforced Concrete and Masonry Buildings*, John Wiley and Sons, New York
- Powell, Graham., 1994, "Nonlinear Analysis," *The Developing Art of Seismic Engineering, SEAONC Fall Seminar Papers*, Structural Engineers Association of Northern California, San Francisco, CA, November
- Priestley, M. J. N., 1995, "Displacement Based Seismic Assessment of Existing Reinforced Concrete Buildings," *Proceedings of Pacific Conference on Earthquake Engineering*, Vol. 2, Melbourne, pp 225-244.
- R&C, 1999, *Seismic Evaluation Reports for Edwards Building, Quillen and Blackwelder Buildings, Mudd Chemistry Building, Herrin Hall and Labs, Wurster Hall, Briggs Hall*. (Individual project reports from 1997 to 1999) Rutherford & Chekene Consulting Engineers, San Francisco CA
- SANZ, 1992, *Code of Practice for General Structural Design and Design Loads for Buildings NZS4203*, Standards Association of New Zealand
- SEAOC, 1999, *Recommended Lateral Force Requirements and Commentary*, Seismology Committee, Structural Engineers Association of California, Sacramento California.

SESSION B-1: COLUMNS

Chaired by

◆ Julio Ramirez and Hitoshi Shiohara ◆

DAMAGE EVALUATION OF REINFORCED CONCRETE COLUMNS UNDER MULTIAXIAL CYCLIC LOADINGS

Susumu KONO¹ and Fumio WATANABE²

ABSTRACT

This study aims to propose a method to evaluate damage to reinforced concrete columns which have experienced severe cyclic reversal loadings in multiaxial directions. In the experimental program, eight column base models with 242 mm square section were tested under the reversals of unidirectional or bidirectional lateral displacement with constant or variable axial force. Damage progressed severely for specimens under variable axial force or bidirectional horizontal displacement. In the analytical program, the stress-strain model of confined concrete was modified and the hinge length was determined in order to accommodate effects of strain gradient, intensity of axial force, and loading paths. The new analytical model was validated by comparing the axial strain-curvature relations with experimental results. Based on the modified stress-strain relation of confined concrete, a moment capacity damage index, $I(M)$, is proposed which can be evaluated from the maximum strain experienced by the concrete without knowing the complete stress-strain history. The moment capacity damage index, $I(M)$, is compared to the reduction factor of moment capacity carried by the concrete, R_c , which represents the degraded moment capacity of the concrete. The comparison showed that the moment capacity damage index can be used reliably to evaluate damage of reinforced concrete columns.

1. INTRODUCTION

After several large-scale earthquakes in the 1990's, more post-earthquake interest has been paid to evaluation of the damage level of buildings from the viewpoint of economics. Damage evaluation is also important to establish criteria for a performance based design method. For a building structure to have a reliable beam side sway mechanism, the most critical section is a hinge zone at the base of ground level columns, which are subjected to variable axial force with bidirectional lateral displacement. Extensive studies have been made for years in order to predict the hysteretic behavior of column hinges. However, it is still difficult to correctly predict that behavior. Consequently, a method to assess the damage and estimate the remaining capacity in displacement and strength after earthquakes has not been

¹ Assistant Professor, Dept. of Architecture, Kyoto University

² Professor, Dept. of Architecture, Kyoto University

established. Rao et al. [1] and Park et al. [2] proposed damage models but their models need the complete history of the load-displacement relation of members or frames and are not necessarily developed for post-earthquake examinations. In this study, eight column base models with 242 mm square section were tested under multiaxial reversal cyclic loading to investigate the sensitivity of the damage process to different loading paths and axial force intensities. A damage index, which is assessed in terms of the maximum axial strain experienced by the concrete, is proposed to evaluate the degraded moment capacity carried by the concrete.

2. EXPERIMENTAL PROGRAM

2.1 Test setup

Eight cantilever column models with a 242 mm square section and a shear span ratio of $L/D=2.5$, as shown in Figure 1, were tested under quasi-static lateral displacements combined with axial compression force. All test columns were reinforced with twelve deformed bars of 13 mm diameter, giving a longitudinal reinforcement content of 2.44%. The flexural failure of core concrete was designed to precede shear failure in the plastic hinge zone. The specimen was connected to a three-jack hydraulic system which enabled orthogonal horizontal displacements to be applied at the top of cantilever columns as shown in Figure 2. The major variables were horizontal displacement patterns and the intensity of axial force.

(I) Horizontal displacement patterns (See Figure 4 (a) for a history):

- Linear pattern; Loading consisted of two cycles of linear path to displacement $\pm \Delta x$ of $\Delta x/L = 0.25\%$, 0.5% , 1.5% , 2% , 3% , and 4% as shown in Figure 3(a), where L is a shear span length of 625 mm.
- Circular pattern; Loading consisted of two circles with a radius, Δ , of $\Delta/L = 0.25\%$, 0.5% , 1.5% , 2% , 3% , and 4% as shown in Figure 3(b).

(II) Intensity of axial force:

- Constant force; Intensity was either $N=0.3 f'c Ag$ or $0.6 f'c Ag$, where $f'c$ is the cylinder compressive strength of the column concrete and Ag is the gross sectional area of the column.

- Variable force; Intensity was proportional to the sum of M_x and M_y as shown in Figure 4(b), where M_x and M_y are moments about the two major axes. In the figure, point (0, 0.3) was fixed and the slope, k , was varied as shown in Table 1.

Displacements were measured by LVDT's as shown in Figure 1(c). The concrete for the test units was a standard mix type, with a maximum aggregate size of 20 mm, supplied by a local commercial ready-mix concrete company. Material strengths are included in Table 1.

Table 1 Variables of specimens and analytical results

	Specimen	Material properties				Control parameters			Analytical results	
		Concrete f'c (MPa)	Longitudinal reinforcement fy (MPa)	Shear reinforcement		Axial force N/D ² f'c	Horizontal loading directions	k in Fig. 3	Confining effect	Hinge length
				fyh (MPa)	ph (%)				a	Lp (mm)
Fluctuating axial force	D1NvA	26.8	467	604	1.39	Varied	1	1.39	2.7	250
	D1NvB							2.79	2.0	250
	D2NvA						2	1.04	2.6	250
	D2NvB							1.66	2.5	250
Constant axial force	D1N3	37.6	461	486	1.53	1	0.0	0.3	2.6	230
	D1N6							0.6	4.9	160
	D2N3					2		0.3	3.8	170
	D2N6							0.6	7.1	230

ph: Volume ratio of shear reinforcement

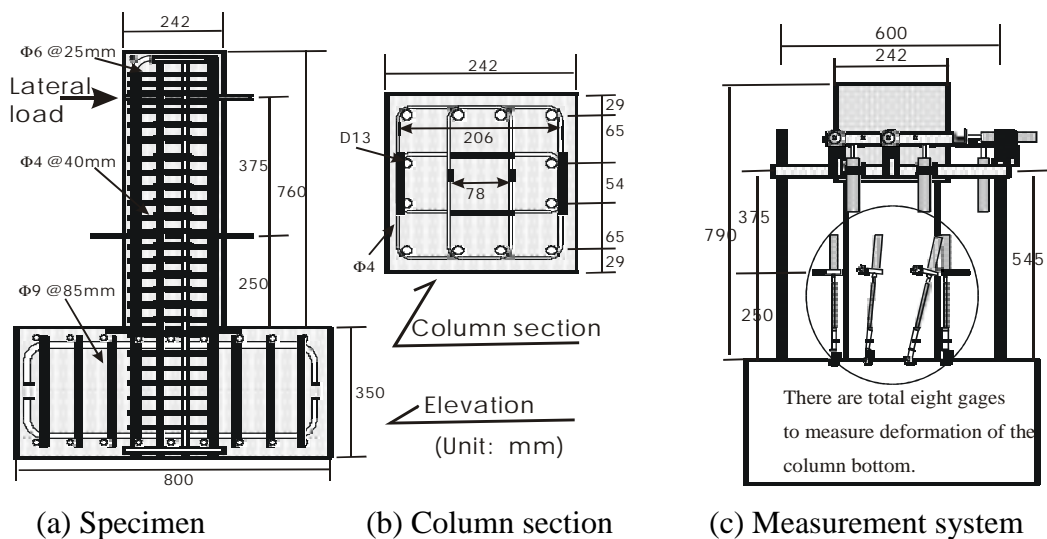


Figure 1 Dimension and reinforcement of column specimens

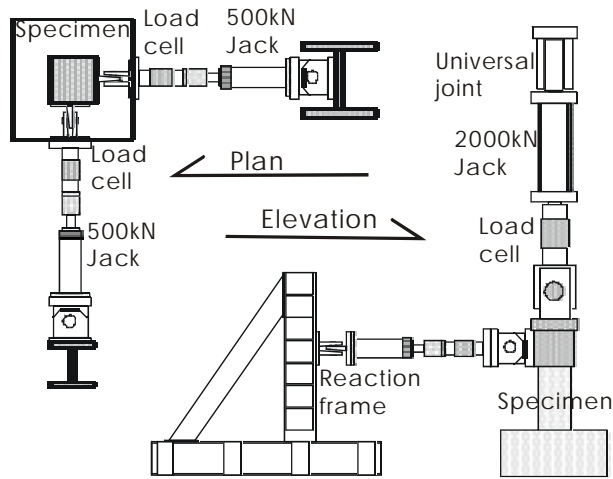
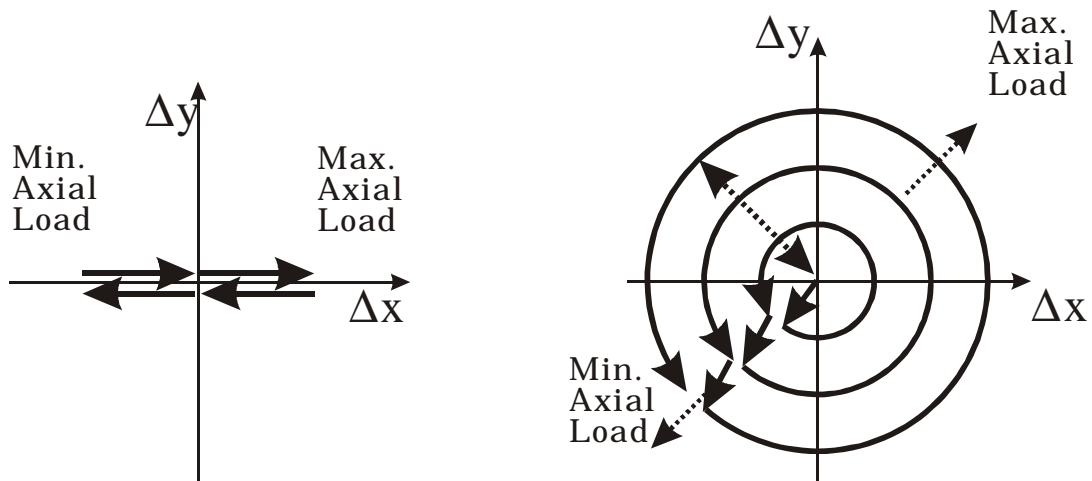


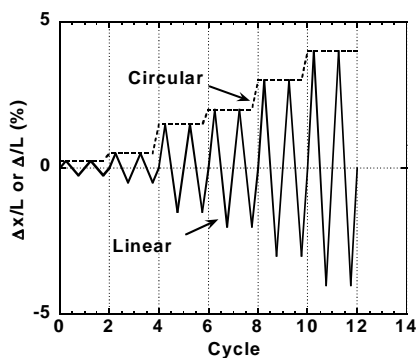
Figure 2 Loading system



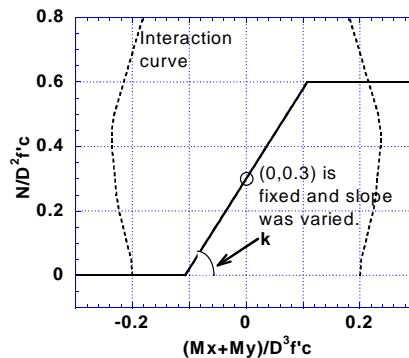
(a) Linear pattern

(b) Circular pattern

Figure 3 Displacement patterns at the loading point



(a) Loading history in lateral direction



(b) Variable axial force

Figure 4 Dimension and reinforcement of column specimens

2.2 Experimental results

All specimens showed ductile flexural behavior and their damage at the end of testing are shown for four specimens in Figure 5. D1N3 and D2N3 had constant axial force and damage patterns are symmetrical about the axis of bending. D1NVA and D2NVB, which had variable axial force, showed asymmetrical damage. The concrete subjected to large axial force had more damage than that subjected to small axial force. In Figure 6, the average curvatures at the bottom of the columns are shown. The average curvature was computed from the displacements measured with 8 displacement gages circled in Figure 1(c). The average curvature for the measured height is large for large axial force and small for small axial force. This is possible if the large curvature is distributed over the measured height under large axial force and the even larger curvature concentrates over a shorter height inside the measured height under small axial force, under the condition that both curvatures create the same amount of lateral displacement at the loading point. The evidence in Figures 5 and 6 indicates that the hinge length under large axial force must be taken as larger than that under small axial force. It can be seen from the experimental axial strain-curvature relations shown in Figure 7 that the bidirectional lateral displacement pattern shortened the column much more than the linear displacement pattern. The shortening effect for large axial force of $N=0.6 f'c Ag$ was also as large as that for the bidirectional lateral displacement.

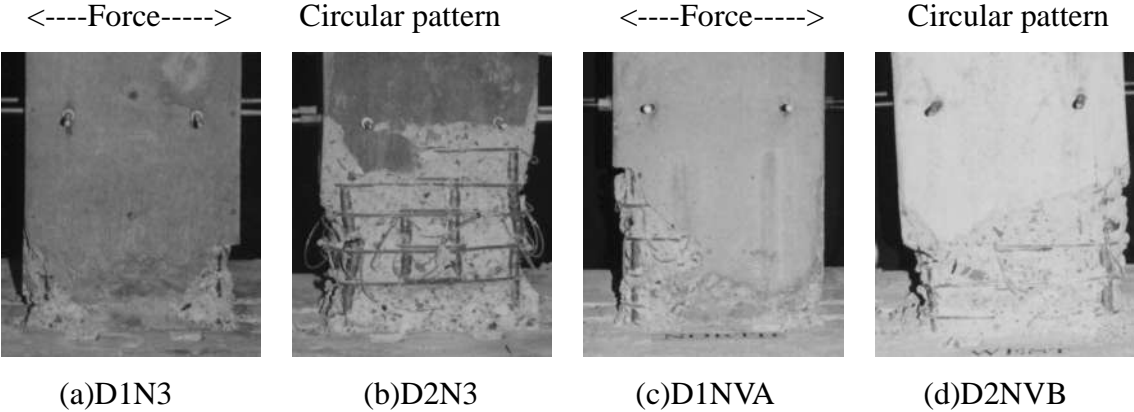


Figure 5 Damage at the end of testing

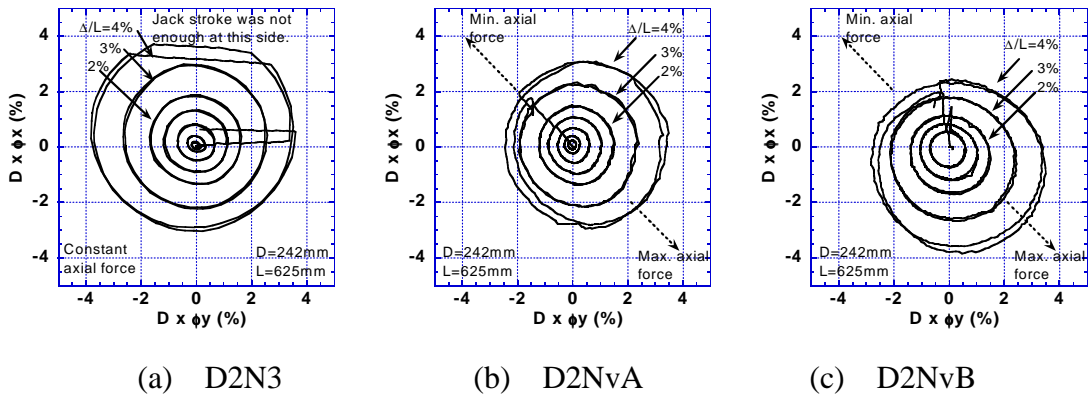


Figure 6 Curvature measured at the column bottom region

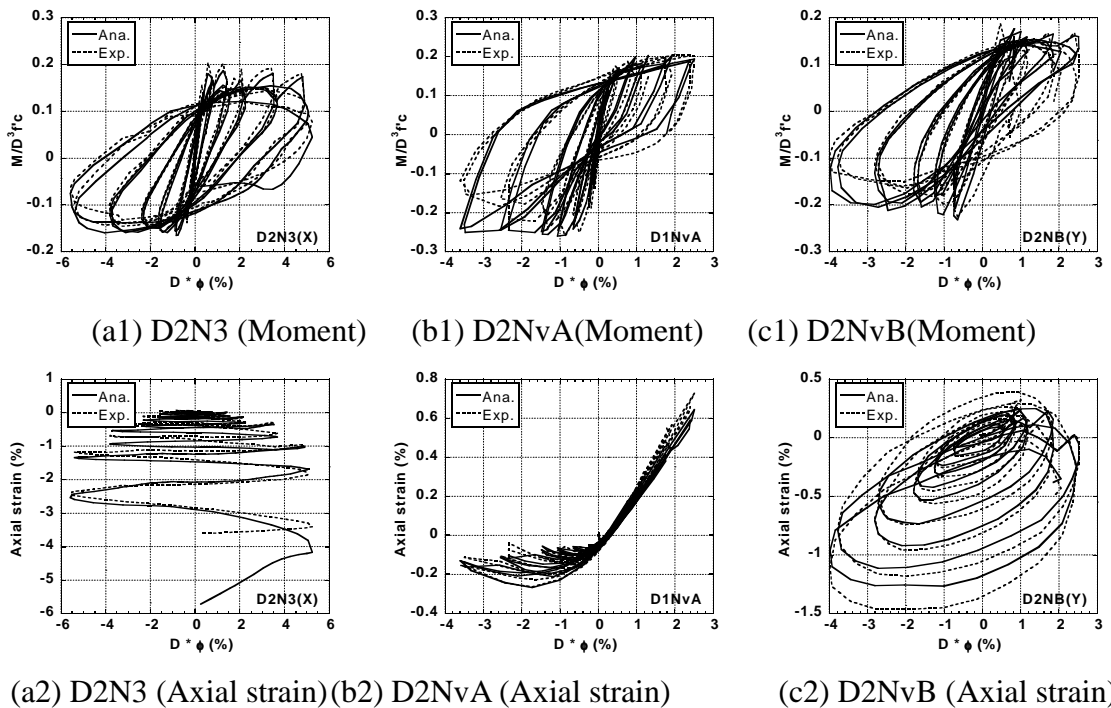


Figure 7 Analytical results compared with experiment results

3. ANALYTICAL PROGRAM

3.1 Section analysis

Section analysis was carried out assuming Bernoulli's theory (Plane section remains plane) for concrete and longitudinal steel. The scheme is to subdivide the column cross section into concrete and reinforcing steel fibers and obtain the section response from the integration of fiber stresses and stiffnesses. Each fiber follows the uniaxial stress-strain relation for

reinforcing steel or concrete. The skeleton curve of the stress-strain relation for concrete is based on the study by Sakino and Sun [3]. The enhanced strength, f_{peak} , due to confinement is expressed as follows.

$$f_{peak} = f'_c + \kappa \cdot \rho_h \cdot f_{hy} \quad (1)$$

$$\kappa = 11.5a \left(\frac{d}{C} \right) \left(1 - \frac{s}{2D_{core}} \right) \quad (2)$$

where f'_c is the cylinder compressive strength without confinement, k , the coefficient of strength enhancement due to confinement, ρ_h , f_{hy} , d , and C the volume ratio, yield strength, diameter, and unsupported length of shear reinforcing bars, respectively, s the distance between adjacent shear reinforcement, and D_{core} the area of confined concrete. In this study, a simple modification was made in the stress-strain relation. In Eq. 2, the coefficient, a , was added to the original equation to take into account the effects of strain gradient. Value a is taken greater than 1.0 and used to increase the strength and ductility of confined concrete. Without a , the analytical model gave moment capacities much lower than the experimental results. The hinge length, L_p , was also adjusted for each specimen. In the analysis, a and L_p were varied so that the analytical results in axial strain-curvature relations that best fitted the experimental results, where axial strain is the longitudinal strain at the centroid of the column section. The optimized a and L_p values are listed in Table 1. The analytical predictions for moment-curvature relations are compared with experimental results in Figure 6, together with axial strain-curvature relations.

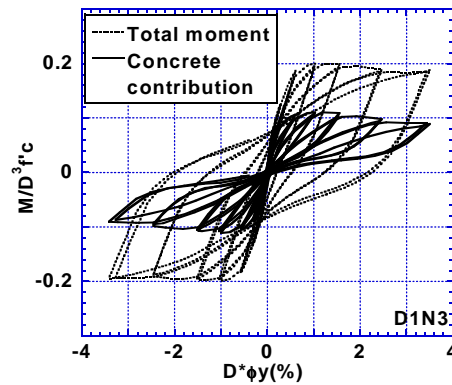


Figure 8 Moment-curvature relations and concrete contribution

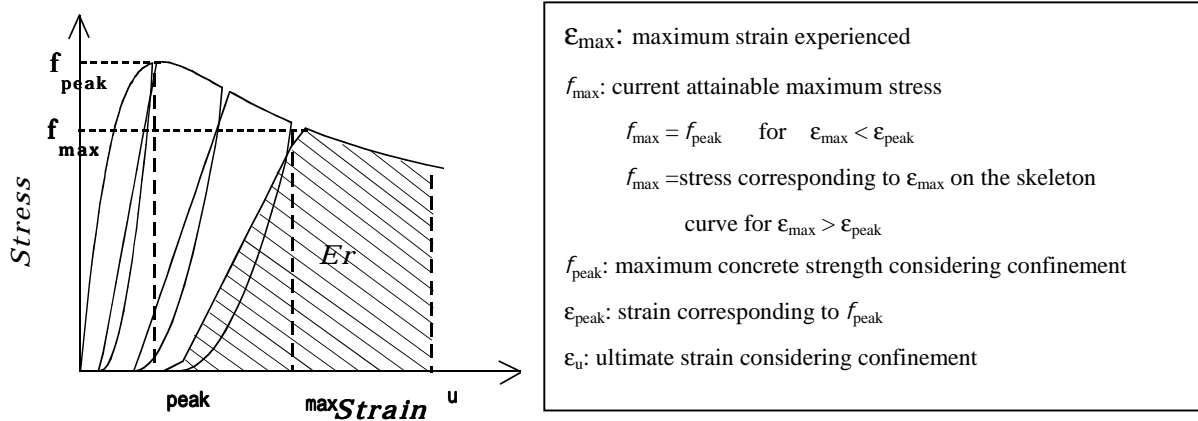


Figure 9 Stress-strain curve for confined and unconfined concrete

3.2 Physical damage of columns

Since the major role of the column is to sustain the vertical load, the vertical load carrying capacity was taken as an indicator of physical damage. As load is cyclically applied to the column and concrete damage progresses, the column shortens and the load carried by the concrete gradually shifts to the longitudinal reinforcement. If this shifting progresses, the vertical load carrying capacity of the column is finally lost because axial shortening becomes excessive or the longitudinal reinforcement buckles. Based on this concept, the axial force carried by the concrete was computed and its variation with respect to the number of cycles was checked. For a variable axial force, the axial force varies by a large amount and does not seem to represent the physical damage to the columns. Instead, the moment - curvature relation was used to evaluate the damage to the column in this study. Figure 8 show the total moment and the moment carried by concrete with respect to the curvature. It can be seen that the maximum values of total moment for each cycle stay almost the same but the moment carried by the concrete gradually decreases. The reduction factor, Rc , is defined as Equation (3) and computed in terms of the moment carried by the concrete:

$$Rc = \frac{\text{Maximum value for each cycle}}{\text{Maximum value for whole history}} \quad (3)$$

Since the experimental data were not sufficient to obtain Rc , Rc was computed from the analytically obtained moment-curvature relation as shown in Figure 8.

3.3 Damage index

If excitation gives the stress-strain history shown in Figure 9 at an arbitrary point in the concrete at the column section, the moment capacity damage index, $I(M)$, is defined as follows:

$$I(Mx) = \frac{\int_A f_{\max} \cdot |y| dA}{\int_A f_{\text{peak}} \cdot |y| dA} \quad \text{and} \quad I(My) = \frac{\int_A f_{\max} \cdot |x| dA}{\int_A f_{\text{peak}} \cdot |x| dA} \quad (4)$$

where A is the area of the column section, and X and y are coordinates from the center of gravity of the section. Figure 10 compares the variation of $I(Mx)$ and Rc with respect to the number of cycles. Here, index $I(Mx)$ was computed for each quadrant of the column section and the most damaged value was used. $I(Mx)$ and Rc show similar degradation as the number of cycles increases except for D1N6 and D2N6. Rc represents the damage to a column from the viewpoint of moment carrying capacity and can be obtained if the whole history of the moment-curvature relation is known. On the other hand, $I(M)$ can be computed only if the maximum compressive strain experienced is known and the Rc value can be predicted reliably. Since recording the maximum experienced axial strain is more practical and easier than recording the stress-strain history, $I(M)$ can play an important role in post-earthquake damage assessment.

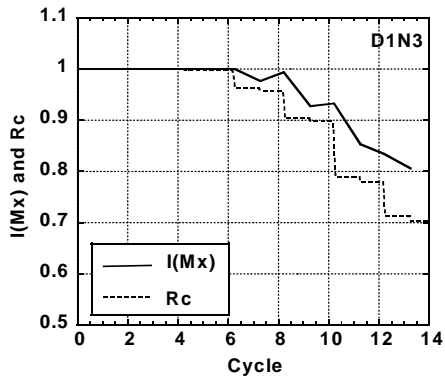
The methodology to evaluate damage has been explained and that knowledge is important in order to restore the original functions of reinforced concrete columns. It is also equally important to evaluate the remaining capacity of columns, that is, to assess the remaining capacity with respect to axial force, moment, displacement, and energy in order to know the risk for expected earthquakes. This assessment can be done, for example, by considering the remaining strain energy absorption capacity, E_r , shown in Figure 9 and such a study is currently in progress.

4. CONCLUSIONS

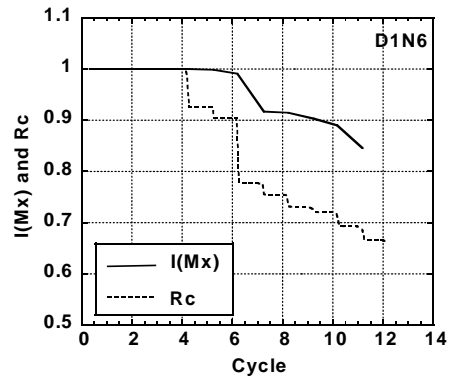
Eight column base models with 242 mm square section were tested under unidirectional or bidirectional lateral reversal cyclic displacements with constant or variable compressive axial force. The experimental results showed that the damage in plastic hinge zones was sensitive to the moment history and axial load intensity. Plastic hinge length needs to be determined taking into account the loading history.

The experimental results indicated that the hinge length under large axial force must be taken larger than that under small axial force.

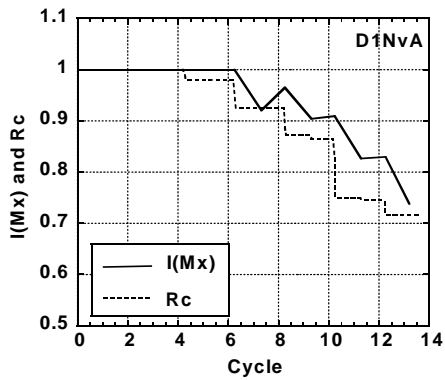
The moment capacity damage index, $I(M)$, was proposed which can be computed from the maximum experienced strain only. It was shown that $I(M)$ can predict the degraded contribution of the concrete to the moment carrying capacity and can be used to evaluate the remaining load carrying capacity and to consider the retrofit strategy in post-earthquake damage assessment.



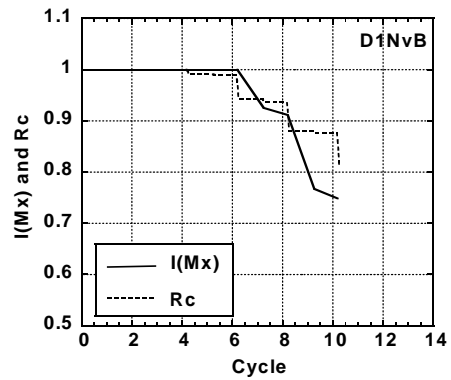
(a) D1N3



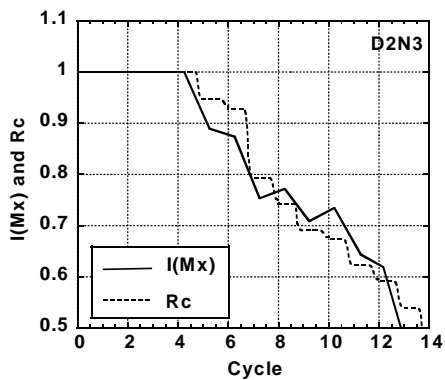
(b) D1N6



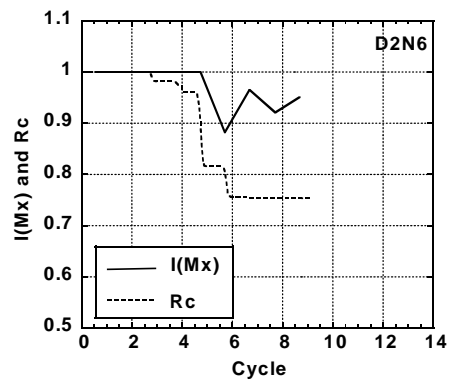
(c) D1NvA



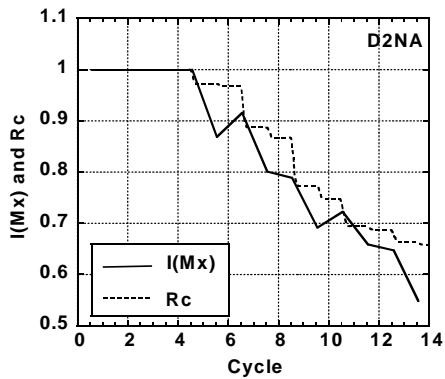
(d) D1NvB



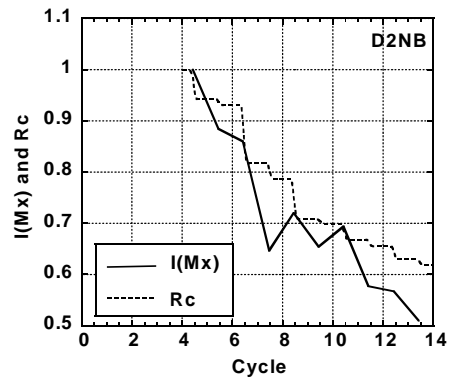
(e) D2N3



(f) D2N6



(g) D2NvA



(h) D2NvB

Figure 10 Comparison between $I(Mx)$ and Rc

5. ACKNOWLEDGEMENTS

Financial support for this project of the Japan Ministry of Education (Grant No. 11209204 and No. 11305039) is gratefully acknowledged. The paper is based on experiments and analyses conducted by T. Kuroyama, T. Ikeuchi, and R. Fujimoto, former graduate students in the Department of Architecture at Kyoto University.

6. REFERENCES

1. Rao, P. S., Sarma, B. S., Lakshmanan, N., and Stangenberg, F., “Damage Model for Reinforced Concrete Elements under Cyclic Loading”, • ACI Materials Journal, Vol. 95, No. 6, pp. 682-690, 1998.
2. Park, Y. J., Ang, A. H. S., and Wen, Y. K., “Seismic Damage Analysis of Reinforced Concrete Buildings”, • Journal of Structural Engineering, ASCE, Vol. 111, No. 4, pp. 740-757, April, 1985.
3. Sakino, K, and Sun, Y., “Stress-strain curve of concrete confined by rectilinear hoop”, • Journal of structural and construction engineering, Architecture Institute of Japan, No. 461, pp. 95-104, Jul. 1994. (In Japanese)
4. Hiraishi, H. and Inai, E., “Theoretical study on deformation capacity of R/C columns beyond flexural yielding”, • Journal of structural and construction engineering, Architecture Institute of Japan, No. 408, pp. 21-30, Feb. 1994. (In Japanese)

SHEAR FAILURE AND AXIAL LOAD COLLAPSE OF EXISTING REINFORCED CONCRETE COLUMNS

J. P. Moehle, K. J. Elwood, H. Sezen¹

ABSTRACT

Earthquake reconnaissance has identified failure of reinforced concrete columns as a primary cause of collapse of older existing reinforced concrete building frames during earthquakes. Apparent column failure, however, does not always result in building collapse. A study of columns tested in the laboratory examines loss of lateral and vertical load capacities. Correlations with geometric, materials, and loading characteristics are identified.

1. INTRODUCTION

Before the introduction of special requirements in the 1970s, reinforced concrete building frames constructed in zones of high seismicity in the US had details and proportions similar to frames designed primarily for gravity loads. Columns generally were not designed to have strengths exceeding beam strengths, so column failure mechanisms often prevail. Relatively wide spacing of transverse reinforcement was common, such that column failures may involve some form of shear or flexure-shear failure. As shear failure proceeds, degradation of the concrete core may lead to loss of axial load carrying capacity of the column. As the axial capacity diminishes, the gravity loads carried by the column must be transferred to neighboring elements. A rapid loss of axial capacity will result in the dynamic redistribution of internal actions within the building frame and may progressively lead to collapse. This sequence is the focus of the ongoing study reported here.

Particular incentive for this research has been provided by the experience of engineers involved in the seismic retrofit of buildings in California. Many have found, using prevailing rehabilitation methodologies, that it is not economically feasible to limit the building design displacements such that the columns are protected from shear failure. Thus, there is a need to

¹ *Pacific Earthquake Engineering Research Center, U.C. Berkeley, CA, USA*
Email: moehle@peer.berkeley.edu, elwood@ce.berkeley.edu, sezen@ce.berkeley.edu

improve understanding of column shear strength, as well as to understand how the gravity loads will be supported after a column fails in shear.

Reconnaissance of recent earthquakes provides evidence of the importance of column shear failure on collapse, as well as the possibility that shear failure of individual columns need not lead to collapse of the building. Laboratory experiments provide corroborating evidence, and suggest improvements to methods for estimating shear strength and deformation at loss of gravity load capacity. This paper summarizes the findings and the status of ongoing studies.

2. OBSERVATIONS FROM EARTHQUAKES

Earthquakes [Northridge, 1994; Kobe, 1995; Kocaeli, 1999; Chi-Chi, 1999; and others] have demonstrated that columns in older reinforced concrete building frames may be vulnerable to shear failures (Figure 1). While several experimental programs have illustrated that the lateral resistance of these columns is limited after shear failure, the residual axial capacity and stiffness have not been adequately investigated. Methods for reliably assessing the conditions under which axial load capacity is exhausted have not been identified.

In many cases, column damage in recent earthquakes has all but eliminated their axial capacity, yet the building has not collapsed (Figure 2). These examples illustrate the need to consider the whole system when evaluating a building for the collapse limit state. Mechanisms that may contribute to the capacity of a system to resist collapse include:

- catenary action of slabs and beams allowing gravity loads to span to adjacent elements,
- vierendeel truss action from the moment frame above a damaged column, and
- gravity load support provided by shear walls or non-structural elements such as partitions and infills.

Some gravity load collapses during earthquakes can be attributed to shear failure, and the subsequent loss of axial load carrying capacity, of multiple columns in a single story (Figure 3). The story-wide failures may be the result of massive internal redistribution of internal forces, possibly amplified by dynamic effects; however, the specific mechanisms leading to gravity load collapse of reinforced concrete frames are not well understood.

3. DEVELOPMENT OF A SHEAR STRENGTH MODEL

There is considerable uncertainty in calculating the shear strength of lightly-confined reinforced concrete columns. A database of tests described in Moehle et al. (1999), and summarized in Table 1, is used to evaluate a new shear strength model.

As with ACI 318, the model assumes the shear strength can be represented by:

$$V_n = V_c + V_s \quad (1)$$

The concrete contribution, V_c , is assumed to be related to the calculated nominal principal tension stress in the column. Principal tension stress capacity was set equal to $f_{tc} = 0.5\sqrt{f'_c}$ (MPa). According to traditional stress transformation relations, the shear stress at which the principal tension stress capacity is reached is given by Equation 5.

$$\tau_{xy} = 0.5\sqrt{f'_c} \sqrt{1 + \frac{P}{0.5A_g \sqrt{f'_c}}} \quad (\text{MPa}) \quad (2)$$

In a concrete column with flexure, this shear strength is reduced because of interaction with flexural stress and redistribution of internal actions as cracking occurs. This effect can be represented approximately by introducing an aspect ratio term, a/d , where a = distance from maximum moment to inflection point. Multiplying by the cross-sectional area, A_g , results in

$$V_c = k \left(\frac{0.5\sqrt{f'_c}}{a/d} \sqrt{1 + \frac{P}{0.5A_g \sqrt{f'_c}}} \right) A_g \quad (3)$$

No bounds are placed on the aspect ratio a/d , though it is noted that the range of values was limited to between 2.0 and 3.9 in the database. Some limits may be appropriate for columns having aspect ratios outside this range.

In Equation 6, the term k is a modifier to account for strength degradation within the flexural plastic hinges. Similar terms have been introduced in other shear strength models (Aschheim, 1993; Priestley, 1994). For this data set, k was defined as shown in Figure 4. Degradation relations proposed by other researchers [Aschheim, 1993; Priestley, 1994], as developed from

data sets including columns with higher quantities of transverse reinforcement, were found to overestimate the rate of degradation for this data set.

The steel contribution, V_s , is defined by:

$$V_s = k \frac{A_{sw} f_y d}{s} \quad (4)$$

The shear strength contribution associated with transverse reinforcement is assumed to degrade with increasing ductility using the same coefficient k (defined by Figure 4) as was used for the concrete contribution in Equation 6. Studies on the data in Table 1 showed that alternative expressions such as proposed by Aschheim (1993) and Priestley (1994) overestimated the contribution of hoops. It is noteworthy that for the columns considered in this study, the calculated value of V_s typically was half or less of the calculated value of V_c . The reduction for ductility is reasonable considering that the truss mechanism associated with steel and concrete is likely to degrade in much the same way as does the concrete mechanism, especially (perhaps) for small quantities of transverse reinforcement.

Work is currently being conducted by others to justify the choice of values for k applied in the V_s term based on Bayesian updating of the shear strength equation using a large database of experimental data (Gardoni et al., 2000).

Figure 5 plots ratios of measured to calculated strengths using the alternative procedure. The correlation is relatively uniform for the range of ductilities shown. The mean ratio of test to calculated strength is 1.01; the mean minus one standard deviation is 0.90.

4. AXIAL CAPACITY OF CONCRETE COLUMNS AFTER SHEAR FAILURE

4.1 Experimental Evidence

Most tests of columns have been terminated shortly after loss of lateral load capacity. The resulting data are useful for columns considered as part of the lateral-force-resisting system. Considering traditional notions of safety (that is, once shear failure begins, axial load collapse cannot be far behind), the data also probably define a practical upper-bound displacement capacity even for columns not considered part of the lateral-force-resisting system in new

building designs. For existing buildings, whether being evaluated for seismic resistance or for seismic rehabilitation, a less conservative approach is required by economic and functionality considerations. If a column can reliably carry gravity load after its lateral strength degradation begins, it may be possible to achieve considerable savings by considering the column as a secondary component. It was mainly for this reason that the tests by Lynn (1996) and Sezen (2000) were conducted (see Table 1).

Figure 6 plots drift ratios corresponding to significant events for the twelve columns reported by Lynn and Sezen. For columns having lower axial loads, the tendency is for axial load failure to occur at relatively large drifts, regardless of whether shear failure had just occurred or whether shear failure had occurred at much smaller drift ratios. For columns with larger axial loads, axial load failure tended to occur at smaller drift ratios, and might occur almost immediately after loss of lateral load capacity.

4.2 A Shear-Friction Model

A shear-friction model can be used to represent the general observation from Figure 6 that the drift at axial load failure is inversely related to the magnitude of axial load. Figure 7 shows a free-body diagram for the upper portion of a column under shear and axial load. The external moment vector at the top of the column is not shown and will not enter the equilibrium equations written here. The external shear force V will be assumed equal to zero, under the assumption that the column has lost most of its lateral load resistance. The inclined free surface at the bottom of the free-body diagram is assumed to follow a critical inclined crack associated with shear damage. In this presentation, the “critical” crack is one that, according to the idealized model, results in axial load failure as shear-friction demand exceeds the shear-friction resistance along the crack.

Dowel forces from the transverse reinforcement crossing the inclined crack are not shown; instead, the dowel forces are assumed to be included implicitly in the shear-friction force along the inclined plane. Shear resistance due to dowel action of the longitudinal bars depends on the spacing of the transverse reinforcement, and reasonably can be ignored for the columns considered in this study.

Relative movement across the shear failure plane tends to compress the longitudinal reinforcement. Given the tendency for buckling, especially in the limit, the axial force capacity of the longitudinal reinforcement will be assumed equal to zero.

In light of the above discussion, equilibrium of the forces shown in Figure 7 results in the following equations:

$$\sum F_y \rightarrow P = N \cos \theta + V_{sf} \sin \theta \quad (5)$$

$$\sum F_x \rightarrow N \sin \theta = V_{sf} \cos \theta + \frac{A_{sw} f_y h \tan \theta}{s} \quad (6)$$

The literature documents shear-friction models that relate V_{sf} and N (Mattock and Hawkins, 1972; Mau and Hsu, 1988). The classic shear friction model, included in ACI 318 since 1977, idealizes the crack, across which shear must be transferred, as a flat plane with a coefficient of friction, μ , and computes the shear capacity as:

$$V_{sf} = N\mu \quad (7)$$

Substitution of equation 7 into equations 5 and 6, and eliminating the case where $\mu = \tan \theta$, gives the following expression for the axial capacity of the column:

$$P = \frac{A_{sw} f_y h}{s} \tan \theta \left(\frac{\cos \theta + \mu \sin \theta}{\sin \theta - \mu \cos \theta} \right) \quad (8)$$

The inclination θ of the shear failure plane can be estimated by considering the magnitude of the axial load in the column at the time of shear failure. A simplistic approach is to define θ as the angle of the nominal principal tension stress at the instant when it reaches the tensile capacity of concrete under combined shear and axial load, using the same model used to establish Equation 2. This approach, however, invariably results in an angle steeper than that observed in tests. An empirical approach is suggested instead. Figure 8 plots observed average angle of critical shear cracks observed in the tests by Lynn (1996) and Sezen (2000). (The authors estimated the angles subjectively from photographs.) The angle could be approximated as 60 degrees relative to horizontal, or could have the linear variation suggested by the unbroken line in the figure. The

straight line has an intercept at 55° for zero axial load and passes through the angle 90° for $P/P_o = 1$. In Figure 8, P_o is the pure axial capacity of the column given by $P_o = 0.85f'_c(A_g - A_s) + f_y A_s$ where A_s = area of longitudinal steel and the other variables are defined previously. (The outlying datum at $P/P_o \approx 0.21$ was for Column 3CMH18 (see Table 1). That column had a critical crack that was somewhat less steep over most of its length, with a vertical segment near column mid-depth, resulting in the relatively large reported critical crack angle.) All of the columns tested by Lynn and Sezen had a height to width ratio greater than 6.0. For columns with low height to width ratio, it is expected that the maximum crack angle will be limited by the aspect ratio of the column (that is, $\theta_{max} = \arctan(\text{height}/\text{width})$).

An empirical approach was used to define the shear-friction coefficient in Equation 8, as follows. The critical crack angle θ for each column was assessed visually (Figure 8). Knowing this angle and all the other quantities in Equation 8, the value of the shear-friction coefficient was calculated. Figure 9 plots the calculated values as a function of the lateral drift ratio at which column collapse occurred. The data apparently follow a trend that can be approximated by a line.

The data of Figure 9 suggest that the apparent shear-friction coefficient is a function of the drift angle at failure. This relation is plausible considering that increased deformation (and increased sliding along the critical shear plane) degrades the roughness of the shear plane and reduces the effective friction. It is worth recalling that the increased deformation capacities are associated with reduced axial loads (Figure 6).

The presented relations lead to the hypothesis that the drift at axial load collapse decreases as the axial load increases and as the quantity of transverse reinforcement decreases. Figure 10 organizes the data by the approximate quantity of transverse reinforcement (the quantity $(A_{sv}f_y h/s)/P_o \approx 0.01, 0.02$ and 0.03), and for that organization plots the drift capacity as a function of axial load ratio. The hypothesized trend is clear in the plotted data.

The relation between axial load and crack angle (Figure 8), the relation between drift and friction coefficient (Figure 9), and the relation among axial load, transverse reinforcement, crack angle, and friction coefficient (Equation 8) can be combined to produce relations among column axial load, column transverse reinforcement, and drift ratio at loss of axial load capacity. The

relations, which are plotted in Figure 11, also support the hypothesis that drift capacity at axial load collapse decreases with decreasing transverse reinforcement and increasing axial load.

To convey a sense of the accuracy implicit in the relations of Figure 11, those relations were used to estimate the drift capacity of ten of the twelve columns reported by Lynn and Sezen. Of the remaining two columns, Column 2CVD12 was subjected to varying axial load and Column 2SLH18 sustained lap-splice failure, so they were not included in the comparison. The results are plotted in Figure 12. The mean ratio of calculated to measured drift at collapse is 0.92; the standard deviation is 0.36. The results of Figure 11, if applied, should be used only with full understanding that a significant number of columns are likely to fail at drifts below the calculated quantities. The relatively large scatter may be a product of inherent randomness associated with the complicated failure mechanism. Additional data and analyses may well improve our ability to predict the onset of gravity load failure of columns.

5. CONCLUSIONS

Shear failure of columns is identified as a primary cause of collapse of older reinforced concrete building frames in earthquakes. Test data were gathered to understand the effects of materials, geometry, and loading on failure mechanisms. A new shear strength equation is developed and found to give accurate estimates of shear strength for the selected database of column tests. Subsequent collapse of columns is examined using a shear-friction model. The model identifies some variables controlling column collapse. Results of the model are compared with test results. Significant scatter between calculated and measured results suggests that additional study may be fruitful.

ACKNOWLEDGMENT

The authors gratefully acknowledge the significant contribution of Professor Abe Lynn, California Polytechnic State University, in the development of the alternative shear strength equation. This work was supported in part by the Pacific Earthquake Engineering Research Center through the Earthquake Engineering Research Centers Program of the National Science Foundation under Award number EEC-9701568 and by the National Science Foundation under Grant No. BCS-9120214. The experimental studies by Lynn and Sezen were conducted in the

research laboratories of PEER at the University of California, Berkeley. Photographs in Figures 1 and 2 are used courtesy of the National Information Service for Earthquake Engineering.

KEYWORDS

Reinforced concrete; Buildings; Columns; Shear; Axial Load; Collapse; Design; Earthquakes; Experimentation

REFERENCES

- ACI Committee 318 (1999) *Building Code Requirements for Structural Concrete (318-99) and Commentary (318R-99)*, American Concrete Institute, Farmington Hills, Michigan.
- Architectural Institute of Japan (1997) *Report on Hanshin-Awaji Earthquake Disaster: Building Series Volume 1, Structural Damage to Reinforced Concrete Building*.
- Aschheim, M. A., Moehle, J. P. and Werner, S. D. (1993) Deformability of Concrete Columns, *Dames and Moore Technical Report to the California Department of Transportation, Contract 59Q122*.
- Bett, B. J., Klingner, R. E., and Jirsa, J. O. (1985) Behavior of Strengthened and Repaired Reinforced Concrete Columns Under Cyclic Deformations, *Phil M. Ferguson Structural Engineering Laboratory (PMFSEL)*, PMFSEL Report No. 85-3, 75 pages.
- P. Gardoni, A. Der Kiureghian, and K. M. Mosalam, (2000), Seismic Fragility of Reinforced Concrete Columns Subjected to Shear, *8th ASCE Specialty Conference on Probabilistic Mechanics and Structural Reliability PMC2000-285*, Notre Dame, Indiana.
- Ikeda, A. (1968) Report of the Training Institute for Engineering Teachers, *Yokohama National University*, Japan.
- Kokusho, S. (1964) Report by Building Research Institute, *Building Research Institute*, Tsukuba, Japan.
- Kokusho, S., and Fukuhara, M. (1965) Report by Kokusho Lab., *Tokyo Industrial University*.
- Lynn, A. C., Moehle, J. P., Mahin, S. A., and Holmes, W. T. (1996) Seismic Evaluation of Existing Reinforced Concrete Columns, *Earthquake Spectra*, Earthquake Engineering Research Institute, Vol. 12, No. 4, pp. 715-739.
- Mattock, A.H., and Hawkins, N., (1972) Shear Transfer in Reinforced Concrete - Recent Research, *Journal of Prestressed Concrete Institute*, V. 17, No. 2.
- Mau, S.T., and Hsu, T.T.C., (1988) Discussion, *PCI Journal*, V. 33, No. 1.
- Moehle, J. P., Lynn, A.C., Elwood, K.J., and Sezen, H., (1999) "Gravity load collapse of reinforced concrete frames during earthquakes", *First US-Japan Workshop on Performance-Based Design Methodology for Reinforced Concrete Building Structures*, Maui, Hawaii, PEER report 1999/10. Berkeley, Calif.: Pacific Earthquake Engineering Research Center, University of California.

Preistley, M. J. N., Verma, R., and Xiao, Yan (1994) Seismic Shear Strength of Reinforced Concrete Columns, *Journal of the Structural Division*, ASCE, Vol. 120, No. ST8.

Sezen, H. (2000) Evaluation and Testing of Existing Reinforced Concrete Columns, *CE 299 Report*, Dept. of Civil and Environmental Engineering, UC Berkeley.

Umemura, H. and Endo, T. (1970) Report by Umemura Lab, *Tokyo University*.

Table 1 Test specimen materials and details

Specimen	b	d	a	l _{splice}	No. bars	ρ_{long}	A _{sw}	s	Tie type	f' _c	f _{y-long}	f _{y-tran.}	P	fail. mode	V _u	δ_y	δ_u	μ_δ
	mm	mm	mm	mm	no.		mm ²	mm		MPa	MPa	MPa	kN		kN	mm	mm	
Lynn and Moehle, 1996																		
3CLH18	457	381	1473	none	8	0.03	142	457	r90	25.6	331	400	503	SCF	271	19.3	30.5	1.58
3SLH18	457	381	1473	25	8	0.03	142	457	r90	25.6	331	400	503	SCF	267	17.3	29.2	1.69
2CLH18	457	381	1473	none	8	0.02	142	457	r90	33.1	331	400	503	FSCF	240	18.3	76.2	4.17
2SLH18	457	381	1473	20	8	0.02	142	457	r90	33.1	331	400	503	FSCF	231	17.3	45.7	2.65
2CMH18	457	381	1473	None	8	0.02	142	457	r90	25.7	331	400	1512	STF	316	7.9	15.2	1.94
3CMH18	457	381	1473	None	8	0.03	142	457	r90	27.6	331	400	1512	SCF	338	7.1	15.2	2.14
3CMD12	457	381	1473	None	8	0.03	245	305	d90	27.6	331	400	1512	SCF	356	9.1	22.9	2.50
3SMD12	457	381	1473	25	8	0.03	245	305	d90	25.7	331	400	1512	SCF	378	8.4	22.9	2.73
Sezen and Moehle, 2000																		
2CLD12	457	394	1473	None	8	0.025	245	305	d90	21.1	441	469	667	SCF	323	26.9	78.2	2.91
2CHD12	457	394	1473	None	8	0.025	245	305	d90	21.1	441	469	2669	SCF	347	13.5	51.6	3.86
2CVD12	457	394	1473	None	8	0.025	245	305	d90	20.9	441	469	Var.	SCF	311	19.1	55.6	2.92
2CLD12M	457	394	1473	None	8	0.025	245	305	d90	21.8	441	469	667	SCF	300	30.5	91.2	2.99
Bett, Klingner and Jirsa, 1985																		
1-1	305	264	457	None	8	0.02	129	203	d135	29.9	462	414	289		209	4.8	14.5	3.00
Ikeda, 1968																		
43	200	173	500	None	6	0.02	58	100	r135	19.6	434	558	80	FSCF	73.9	3.0	15.0	4.84
44	200	173	500	None	6	0.02	58	100	r135	19.6	434	558	80	FSCF	76.3	3.0	15.0	5.00
45	200	173	500	None	6	0.02	58	100	r135	19.6	434	558	67	FSCF	82.2	3.0	15.0	4.87
62	200	173	500	None	10	0.02	58	100	r135	19.6	345	476	80	FSCF	57.7	2.5	13.2	5.28
63	200	173	500	None	10	0.02	58	100	r135	19.6	345	476	156	FSCF	68.5	2.3	14.0	5.79
64	200	173	500	None	10	0.02	58	100	r135	19.6	345	476	156	FSCF	68.5	2.0	16.8	8.00
Umemura and Endo, 1970																		
205	200	180	600	None	6	0.02	58	100	r135	17.6	462	324	156	STF	71.3	4.3	13.0	3.07
207	200	180	400	None	6	0.02	58	100	r135	17.6	462	324	156	STF	105.9	3.3	6.4	1.88
208	200	180	400	None	6	0.02	58	100	r135	17.6	462	324	391	FSCF	135.0	2.5	7.9	3.20
214	200	180	600	None	6	0.02	58	200	r135	17.6	462	324	391	SCF	82.7	3.8	10.7	2.86
220	200	180	400	None	6	0.01	26	120	r135	32.9	379	648	156	FSCF	78.3	2.3	23.9	10.00
231	200	180	400	None	6	0.01	26	100	r135	14.8	324	524	156	FSCF	50.9	1.8	16.3	9.00
232	200	180	400	None	6	0.01	26	100	r135	13.1	324	524	156	FSCF	58.2	2.8	23.9	8.89
233	200	180	400	None	6	0.01	26	100	r135	13.9	372	524	156	FSCF	69.1	2.8	13.7	4.93
234	200	180	400	None	6	0.01	26	100	r135	13.1	372	524	156	FSCF	67.0	2.8	16.0	5.71
Kokusho, 1964																		
372	200	170	500	None	4	0.01	65	100	r135	19.9	524	352	156	FSCF	74.4	2.5	10.7	4.12
373	200	170	500	None	4	0.02	65	100	r135	20.4	524	352	156	FSCF	88.1	3.6	9.9	2.78
Kokusho and Fukuhara, 1965																		
452	200	170	500	None	4	0.03	65	100	r135	21.9	359	317	391	FSCF	110.1	3.0	7.6	2.53
454	200	170	500	None	4	0.04	65	100	r135	21.9	359	317	391	FSCF	110.1	2.3	5.1	2.32

Notation: A_{sw} = area of tie steel; a = shear span; b = square column dimension; d = depth to centerline of tension reinforcement; f_{y-long} = long. reinf. yield strength; f_{y-tran} = trans. reinf. yield strength; l_s = lap splice length; P = axial load (Var = varying axial load); s = hoop spacing; V_u = peak shear; δ_y = yield displacement; δ_u = displacement when 20 percent of peak shear is lost; ρ_{long} = total long. steel ratio; $\mu_\delta = \delta_u/\delta_y$. Tie types are: r90 - rect. w/ 90° hooks; r135 - rect. w/ 135° hooks; d90 - rect. and diamond w/ 90° hooks; d135 - rect. and diamond w/ 135° hooks. Failure modes are: FSCF - flexural shear compression failure, several inclined cracks; SCF - shear compression failure, many inclined cracks; STF - shear tension failure, very large inclined crack.



Figure 1 Column shear failure from 1999 Kocaeli Earthquake



Figure 2 Apparent loss of column axial load capacity without collapse of building frame from 1999 Chi-Chi Earthquake



Figure 3 Gravity load collapse from 1995 Kobe Earthquake (AIJ, 1997)

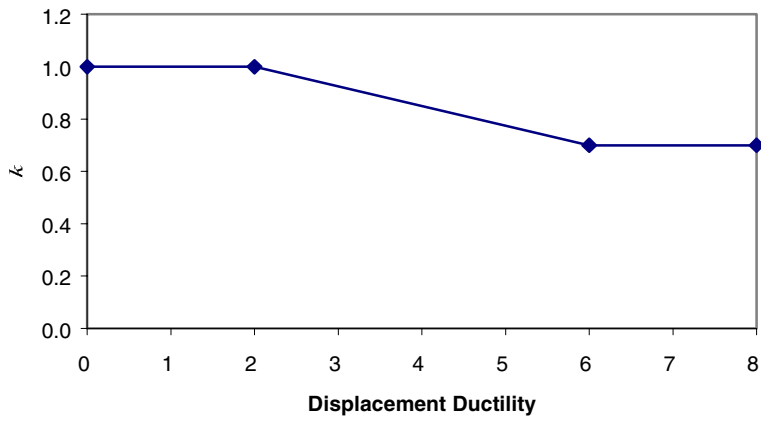


Figure 4 Parameter k

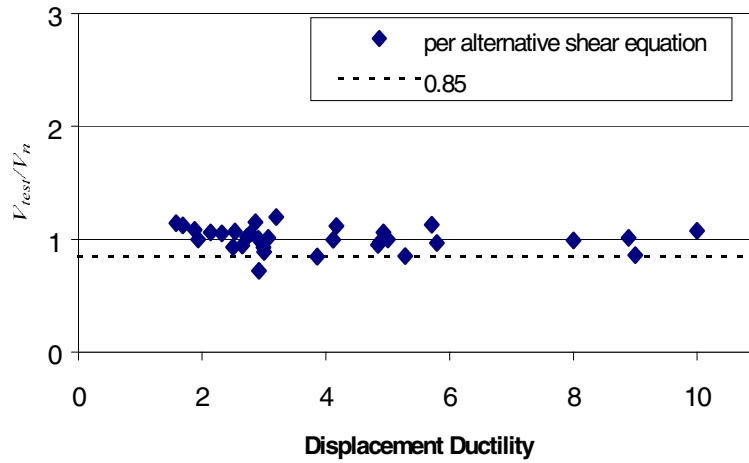


Figure 5 Comparison of measured strengths with strengths calculated by alternative shear strength model

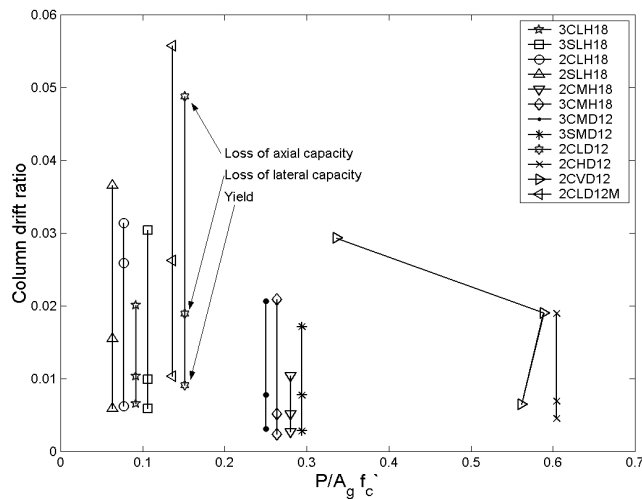


Figure 6 Measured column drift ratios as a function of axial load

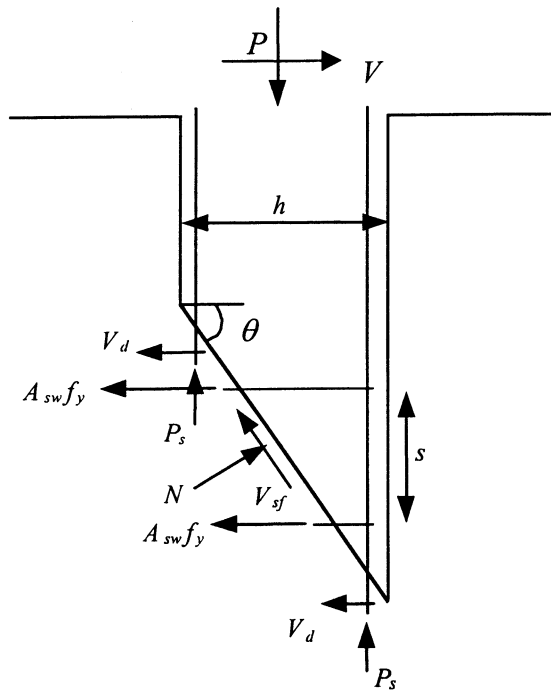


Figure 7 Free body diagram of column after shear failure

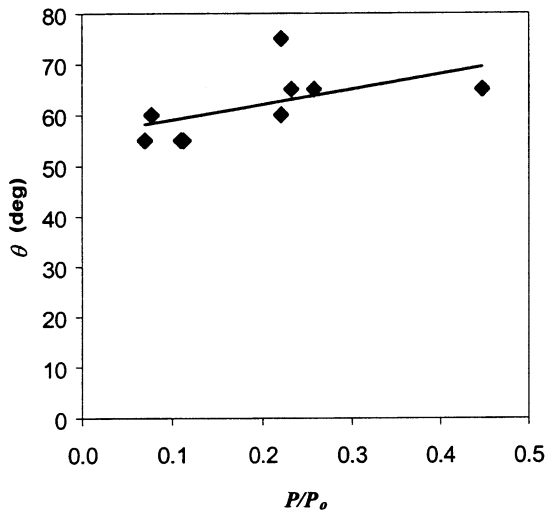


Figure 8 Observed angles of critical cracks near axial load failure of columns

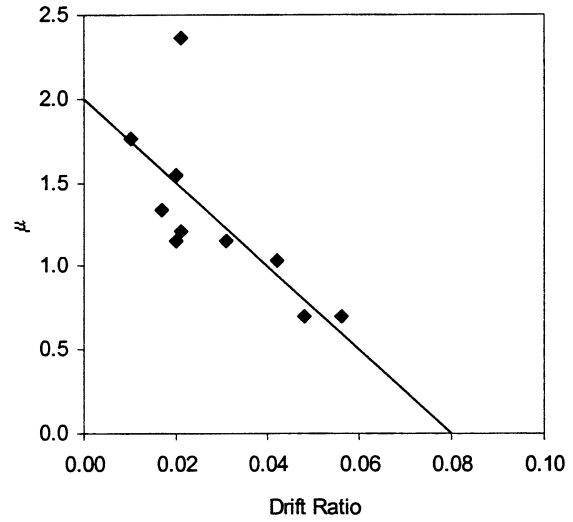


Figure 9 Relation between inferred shear-friction coefficient, μ , and drift ratio at axial load failure.

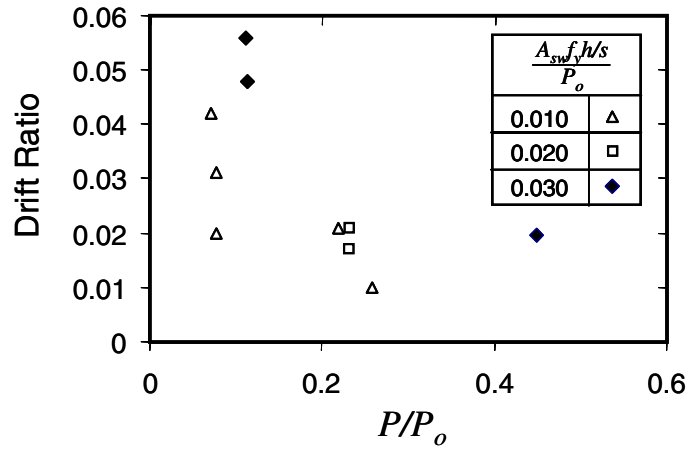


Figure 10 Measured variation of drift capacity with axial load ratio and transverse reinforcement ratio

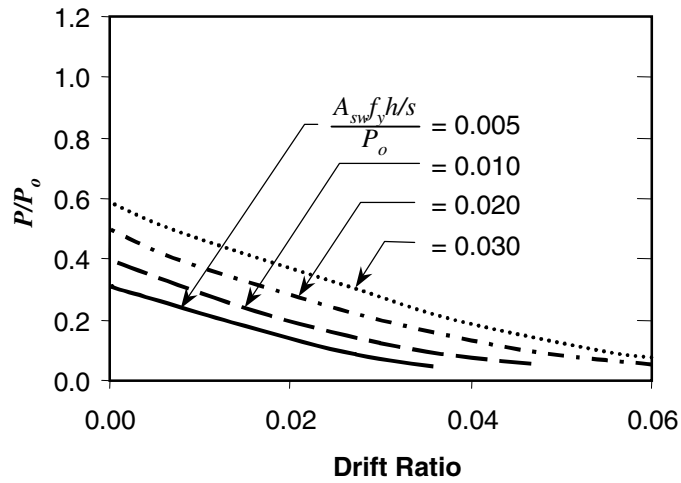


Figure 11 Derived relation among axial load, transverse reinforcement, and drift capacity at axial load failure.

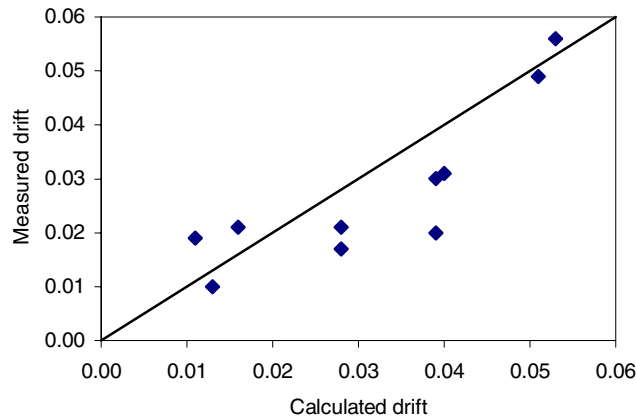


Figure 12 Comparison of calculated and measured drift capacities at axial load failure for test columns

RESIDUAL AXIAL CAPACITY OF REINFORCED CONCRETE COLUMNS DURING SHEAR DETERIORATION

Akira TASAI¹

ABSTRACT

The degradation of axial capacity of reinforced concrete columns during shear deterioration after flexural yielding was studied experimentally. Deterioration of the axial strength was influenced strongly by the generation of diagonal shear cracks. Although the axial capacity during shear deterioration cannot be evaluated by the inelastic flexural analysis, the plastic analysis based on truss and arch mechanisms well predicted the deterioration of axial strength. The restorability of the axial capacity was also studied. The injection of epoxy resin into the diagonal shear cracks was effective to recover the lateral and axial performance perfectly.

1. INTRODUCTION

Present knowledge to evaluate the residual capacity or restorability of structures or elements after an earthquake cannot be expressed to be sufficient. Especially, to estimate precisely the ability of damaged vertical elements to sustain the gravity load of a structure is one of the complicated problems. The author has been studying about the axial capacity or the restorability of moment resisting columns after an earthquake in order to define a damage restorable limit for the performance seismic engineering design. The observed deterioration in the axial strength of flexural columns including post-repair was explained by the analysis using a modified nonlinear fiber mode (Kitada, 1998) (Watanabe, 1999).

In the practical design, there is a case of insufficient margin of shear capacity against bending one. In this study, the axial capacity of reinforced concrete columns during shear deterioration after flexural yielding was investigated experimentally. The restorability of the axial capacity after the deterioration was also studied.

¹ Dept. of Architecture and Building Science, Faculty of Engineering, Yokohama National University, Yokohama 240-8501, Japan

Email: tasai@arc.ynu.ac.jp

2. OUTLINES OF THE TEST

Five column specimens A9 – A13 with same dimensions, reinforcement and materials were tested. They were designed that the shear capacity was equivalent to the flexural capacity. The properties and the reinforcement details are shown in Table 1 and Figure 1, respectively. The dimensions of the section were 300×300 mm and the shear span to depth ratio was 1.5. Eight D16 bars(SD 345) were arranged as longitudinal reinforcement, and 9ϕ bars(SD235) as lateral reinforcement. The main parameter of the test was the loading deformation level related to the deterioration of shear and axial capacity. After cyclic lateral loading, all columns were loaded in the axial direction. The prism specimens with the same section properties with the columns as shown in Table 2 were also tested in order to obtain the uniaxial stress-strain relationship in the direction of the column axis. The material properties are listed in Table 3.

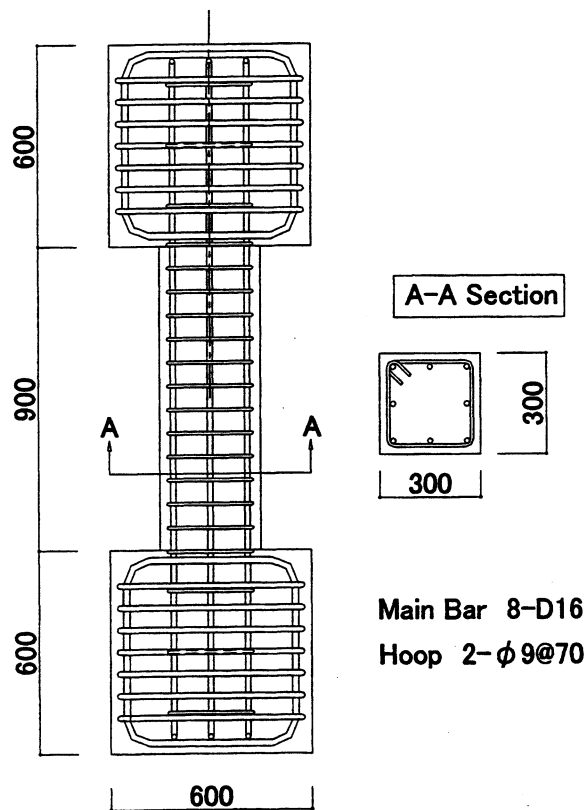


Figure 1 Reinforcement Details of Specimens (unit:mm)

Table 1 Properties of Column Specimens

Sections (mm)	Shear Span Ratio	Main Bar	Hoop	Pg (%)	Pw (%)	Qsu/Qmu	Constant Axial Stress
300 × 300	1.5	8-D16 SD345	2-9 ϕ @70 SR235	1.76	0.60	1.00	0.2 σ _B

Qsu : Shear Capacity
Qmu : Flexural Capacity

Table 2 Properties of Prism Specimens

Specimen	Main Bar	Hoop	Property	Height (mm)	Axial Capacity by Test
D1	-		Plain	600	2079
D2					1370
D3					2446
D4	8-D16	2-9 ϕ @70	Similar to Column Specimen		2598
D5					2097
D6					No Cover

Table 3 Properties of Materials

Concrete (100 ϕ × 200mm)

Age (days)	Young's Modulus × 10 ⁴ (N/mm ²)	Compressive Strength (N/mm ²)
14	2.48	24.2
28	-	25.5
35	-	25.1

Reinforcement

Size and Quality	Young's Modulus × 10 ⁵ (N/mm ²)	Yield Stress (N/mm ²)	Maximum Stress (N/mm ²)
D16(SD345)	1.91	375	562
9 ϕ(SR235)	2.02	335	466

Epoxy Resin for Repair

Young's Modulus (N/mm ²)	Compressive Strength (N/mm ²)	Tensile Strength (N/mm ²)
1891	69.9	44.3

Specimens were loaded by the apparatus as shown in Figure 2. They were subjected to lateral forces in a cyclic manner producing anti-symmetric bending moment distribution under a constant axial load equivalent to $0.2\sigma_B$ in the compressive stress level (σ_B : compressive strength of concrete). The lateral deformation amplitude was increased 1/800 radian in the member rotation angle at every loading cycle; i.e. the amplitude of $\pm 1/800$ rad. in the first cycle, $\pm 2/800$ rad. in the second cycle, $\pm 3/800$ in the third, and so on. It was possible to observe the softening in the restoring force characteristics by the way of the loading. In order to investigate the relation between the deterioration of axial capacity and the degradation of shear capacity of

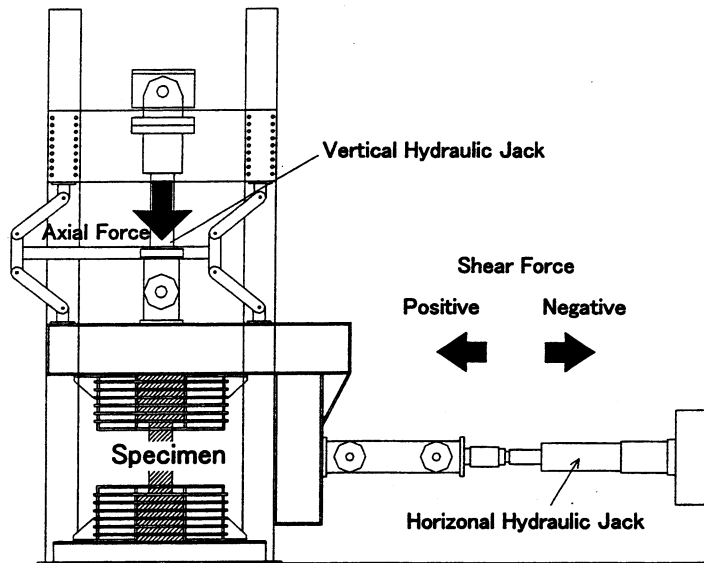


Figure 2 Loading Apparatus

columns, the degree of degraded shear capacities was chosen as the main parameter of the test. Each specimen was loaded in the axial direction after corrected the residual deformation by the lateral loading. One of the specimens, specimen A13, was repaired by epoxy injection into cracks occurred by the original loading and was investigated the restorability of axial capacity by the repair. The loading procedure of each specimen was as follows.

- A9: loaded laterally until 30% of the lateral maximum capacity, and axial compression,
- A10: loaded laterally until 80% of the lateral maximum capacity, and axial compression,
- A11: loaded laterally until the lateral maximum capacity, and axial compression,
- A12: loaded laterally until 60% of the lateral maximum capacity, and axial compression,
- A13: loaded laterally until 80% of the lateral maximum capacity, and repaired,
- A13R(A13 after the repair): the same loading as A11.

Specimen A9 was loaded at the beginning of the test. Other specimens were loaded laterally based on the results of specimen A9. Shear capacity level of 80% to the maximum capacity in the specimen A13, corresponds to the usual capacity level to define the ultimate deformation of members. The specimen was repaired under a condition that only deadweight of the apparatus (90kN) was loaded. After the crushed cover concrete was removed, epoxy resin was injected into cracks. The crushed part was replaced by super-rapid hardening type cement mortar after one day curing. However, the replaced part to the new cement mortar was little area.

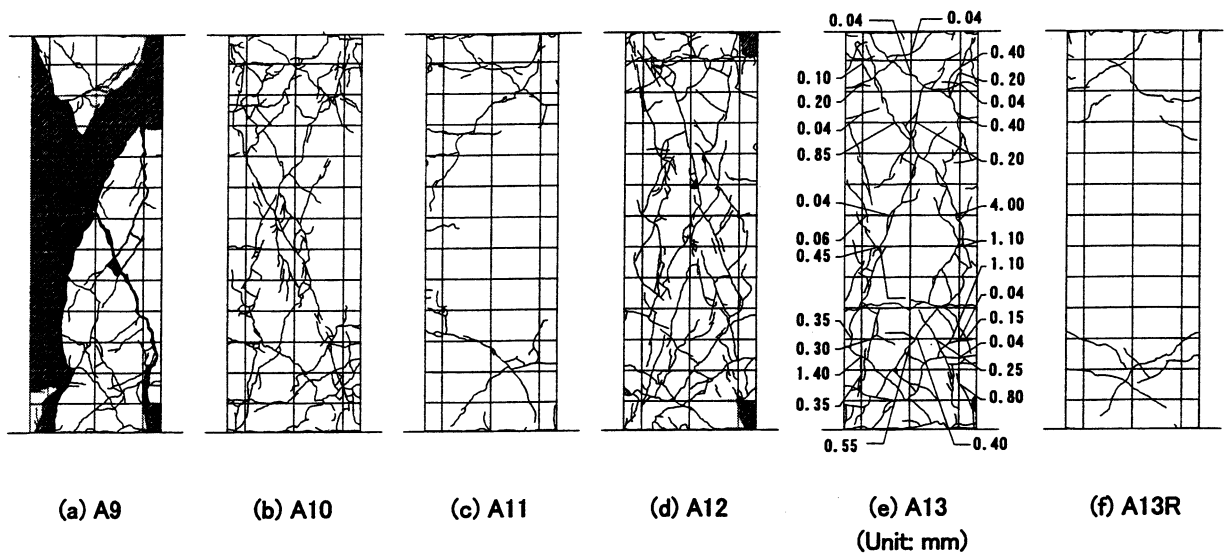


Figure 3 Crack Patterns in the Final Cycle

3. TEST RESULTS

Crack patterns in the final cycle of each specimen are shown in Figure 3. Development of cracks is quite similar among specimens. First flexural cracks occurred at both column ends at a rotation angle of $1/800$ rad. And the generation and development of flexural shear cracks were observed at the region within the length equivalent to the depth, D , from column ends. At a rotation angle of $11/800$ rad., diagonal shear cracks generated at the mid-span of column. After that, new dominant flexural cracks did not occur. In the specimen A9, At a rotation angle of $30/800$ rad., crush of cover concrete at the column ends and sliding along the dominant shear cracks were observed. Longitudinal bars yielded at a rotation angle of $4/800$ rad. and lateral bars yielded at $16/800$ rad..

Figure 3(e) shows crack widths of specimen of A13R before repair. Generally, the injection of epoxy resin is effective when crack width is over 0.2mm. It was judged that the epoxy injection of this specimen was successful, because widths of many cracks were over 0.2mm before repair. During the loading of the specimen A13R, cracks due to original loading did not open and new cracks generated.

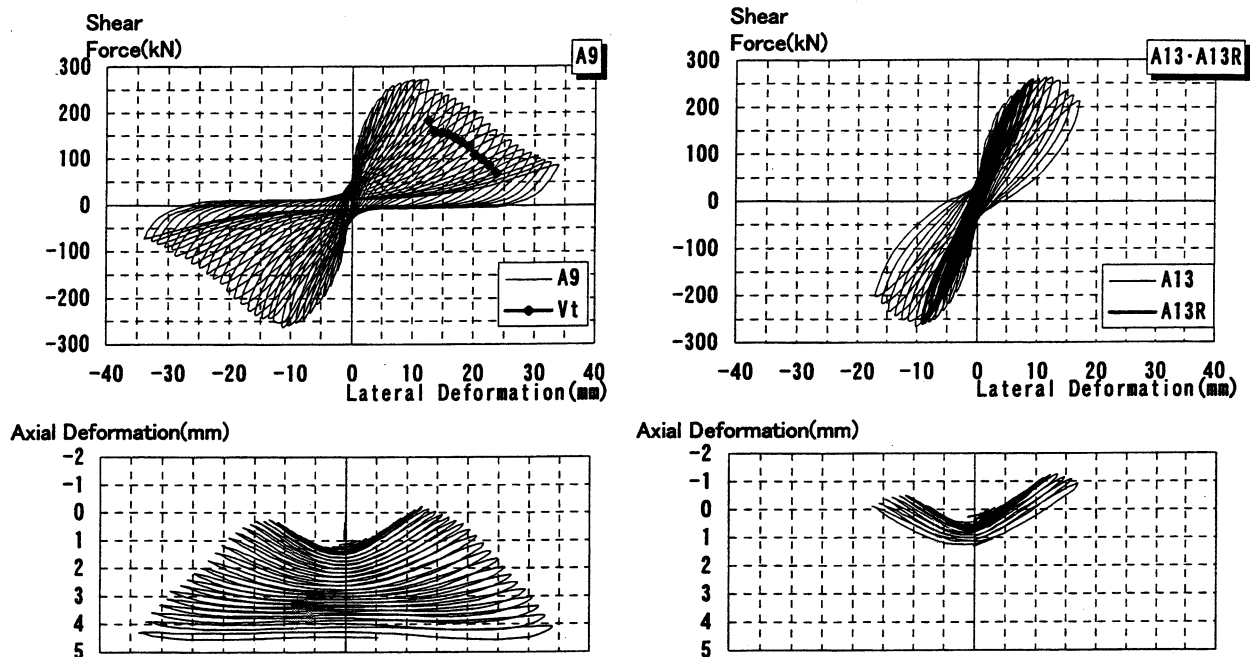


Figure 4 Shear Force-Lateral Deformation Relations and Axial Deformation

Restoring force characteristics and axial deformations of specimens A9, A13 and A13R are shown in Figure 4. In both specimens A9 and A13, immediately after the generation of dominant diagonal shear cracks, lateral resistances started to decrease, while the axial deformations gradually increased proportionally to the decrease of lateral resistances. In the repaired specimen A13R, the restoring force characteristics were by no means inferior to the original one.

The axial compressive loading was applied to the specimens A11 and A13R before dominant diagonal shear cracks occurred by the lateral loading. In Figure 5, the axial capacity of each specimen obtained from the axial loading was plotted for the ratio of deteriorated lateral capacity to the maximum capacity. The axial strength of the specimen A11 was 2932 kN. This value was higher than that of the corresponding prism

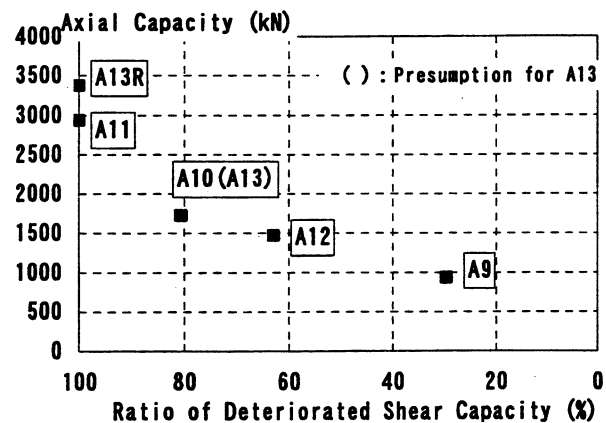


Figure 5 Deterioration of Axial Capacity

specimen. Therefore, the loading up to the maximum lateral load did not deteriorate the axial strength. On the other hand, in specimens A10, A12 and A9, remarkable sliding along the dominant diagonal shear cracks was observed during axial loading, and the axial strength was significantly lower than that of specimen A11. The axial strength was deteriorated proportionally to the decrease in the lateral shear capacity. In the specimen A13R, which was repaired after the original loading, the diagonal shear cracks due to original loading did not open during the lateral reloading and the axial strength was completely restored. These results indicate that the deterioration in the axial capacity was caused by the damage due to shear cracks. In addition, it is possible to restore the deterioration by the repair.

4. DISCUSSION ON THE AXIAL CAPACITY

4.1 Evaluation by Inelastic Flexural Analysis

The deterioration of the axial strength was evaluated by the inelastic flexural analysis using the fiber model. The method well predicted the axial capacity for the columns failed in flexure (Tasai, 2000). In the analysis, after the moment vs. curvature relationship of the cross section was analyzed according to the rotation observed in the test, both moment and curvature were converged to the original point, and then the strain vertical to the section was increased

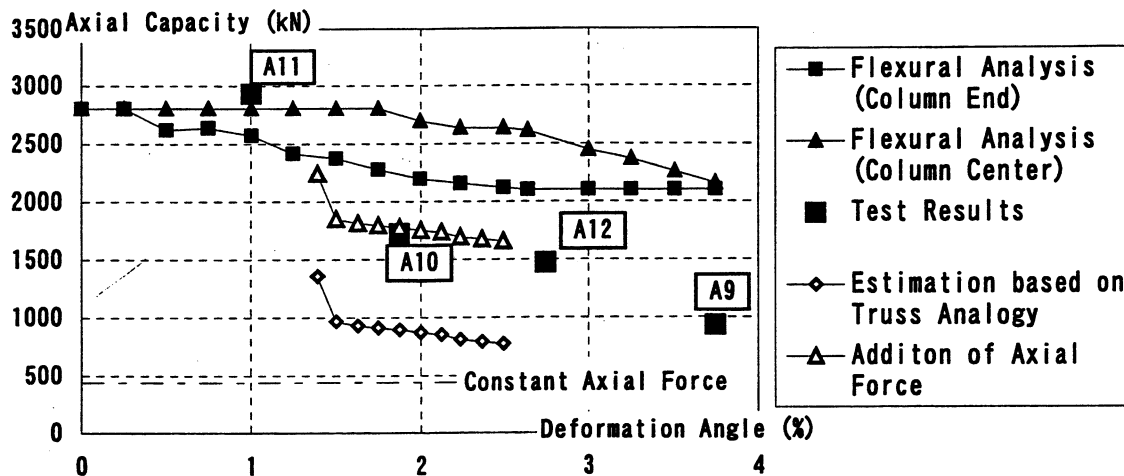
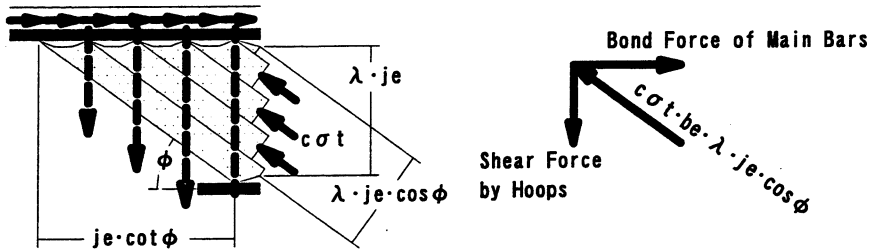


Figure 6 Axial Capacity-Rotation Angle Relations

uniformly up to the maximum axial strength. The uniaxial stress strain relationships of confined core concrete and unconfined cover concrete were determined from the prism and material tests. The results of the analysis are shown in Figure 6. The axial strength by the test was considerably lower than the analytical results after the maximum lateral resistance. It is concluded that the axial capacity during shear deterioration cannot be evaluated by the inelastic flexural analysis.

4.2 The Deterioration of Shear Capacity

The lateral shear capacity deteriorated obviously caused by the damage due to shear in the test. The deterioration was analyzed according to the concept of the truss mechanism proposed in Design Guidelines for Earthquake Resistant Reinforced Concrete Buildings on Inelastic Displacement Concept (AIJ, 1999). The outline of the concept is shown in Figure 7. The figure represents the equilibrium among concrete stress in the compression strut of analogous truss, the force of shear reinforcement and the required bond force along main bars. Distribution of strain along main bars and strain of hoops were measured in the mid-span of the column specimens. Examples of bond stress in main bars and hoop stress derived from the measurement of strain in the mid-span of specimen A9 are shown in Figure 8 and Figure 9. The change of the angle of concrete strut, ϕ , was calculated based on the bond stress and hoop stress as shown in Figure 10. The value of $\cot\phi$ rapidly decreased after the generations of dominant shear cracks, which probably indicated the formation of truss mechanism. The shear force carried by the truss mechanism, V_t , was calculated from the hoop stress and the $\cot\phi$. In the Figure 4, the calculated V_t is plotted in the restoring force characteristics of specimen A9. A constant difference about 80 kN between the shear force and estimated V_t is observed during the deterioration in shear. When the constant axial load of 440 kN in the test was assumed to be carried by the arch mechanism as shown in Figure 11, the additional shear force V_{aN} satisfying the equilibrium was 74 kN, which almost coincides with the difference between the observed shear force and V_t . Therefore, it is surely presumed that a constant compressive stress σ_a was always carried by the arch mechanism caused by the axial load in the test.



b_e : Effective Width of Section for Truss Mechanism $c\sigma_t$: Diagonal Compressive Stress of Concrete
 j_e : Effective Height of Section for Truss Mechanism λ : Coefficient of Effective Area in Truss Mechanism

Figure 7 Truss Mechanism

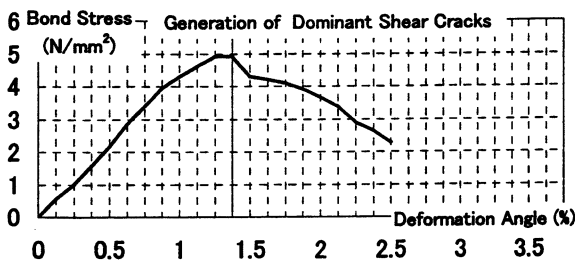


Figure 8 Bond Stress-Rotation Angle Relations

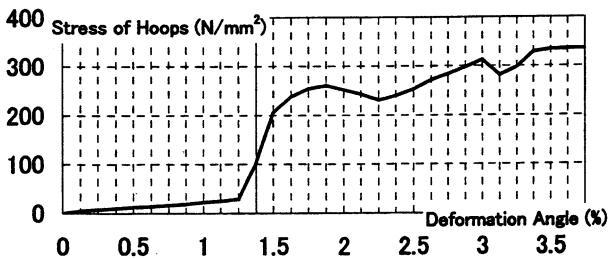


Figure 9 Stress of Hoops-Rotation Angle Relations

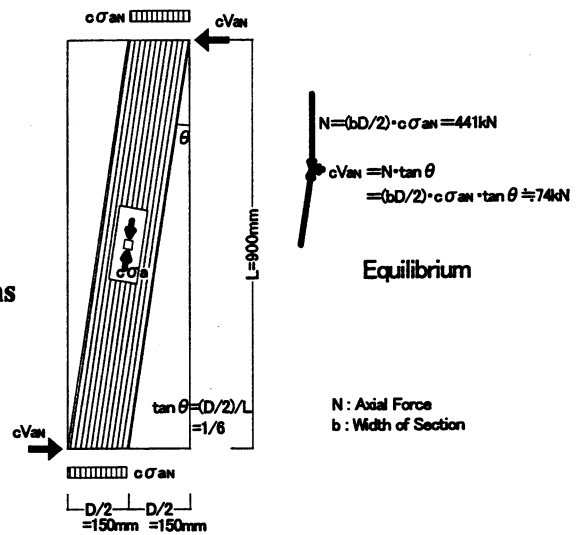


Figure 11 Arch Mechanism

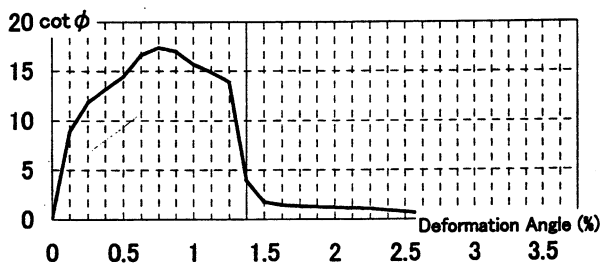


Figure 10 cot φ -Rotation Angle Relations

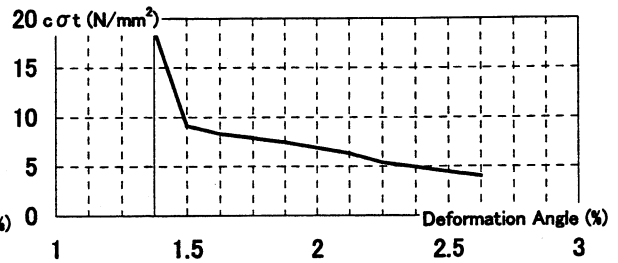


Figure 12 cσt-Rotation Angle Relations

4.3 Evaluation of the Deterioration in Axial Capacity

If the effective concrete compressive strength is known, it may be possible to evaluate the deteriorated axial capacity. The observed concrete compressive stress of strut in the truss mechanism, ${}_c\sigma_t$, calculated by assuming the equilibrium in the Figure 7, is shown in Figure 12. The stress ${}_c\sigma_t$ gradually decreased according to the magnitude of lateral deformation. This implies a deterioration of the effective concrete strength. The effective strength was assumed to be represented by a summation of ${}_c\sigma_t$ and ${}_c\sigma_a$, neglecting the difference in directions of these stresses. Here, ${}_c\sigma_a$ is the stress of the arch mechanism that was mainly formed by a constant vertical load in the test (see Section 4.2). The axial capacity of column, N_d , was evaluated by the following equation.

$$N_d = {}_c\sigma_t \cdot b_e \cdot \lambda \cdot j_e + {}_c\sigma_a \cdot b \cdot D + \sigma_y \cdot A_s \quad (1)$$

Where, $b_e \cdot \lambda \cdot j_e$: effective area of truss mechanism according to the AIJ Guidelines, $b \cdot D$: total cross section area of a column, σ_y : yield stress of main bar, and A_s : total area of main bars.

The evaluated N_d is plotted in Figure 6. It was judged that the deteriorated axial capacity of column was well predicted by the equation (1).

5. CONCLUSIONS

The residual axial capacity of reinforced concrete columns during lateral shear deterioration after flexural yielding was investigated experimentally and analytically. The following conclusions were obtained.

- (1) It was observed that the deterioration of the axial strength was caused by dominant diagonal shear cracks in the mid-span of columns, and the deterioration was significantly large immediately after the shear cracks occurred.
- (2) The analysis based on truss and arch mechanisms well predicted the deterioration of axial strength, which related strongly the deterioration of concrete compressive stress of strut in

truss mechanism

- (3) The injection of epoxy into the diagonal shear cracks was effective to recover the lateral and axial strength perfectly.

ACKNOWLEDGEMENT

The author is grateful to the subsidization for this study from JSPS's Grant-in-Aid for Scientific Research (Basic Research C, No.11650600, Researcher: Tasai,A.,1998), and also grateful to Miss Yasuko Ohsugi, a graduate student, ERI University of Tokyo, who helped the author in preparing the manuscript.

REFERENCES

- Kitada, T. and Tasai, A. (1998). Study on residual axial capacity and damage restorability of flexural columns after earthquake. *Proceedings of JCI*, 20, 3: 433-438. (in Japanese)
- Watanabe, A. and Tasai, A. (1999). Residual axial strength and damage restorability of flexural columns under varying axial load after earthquake. *Proceedings of JCI*, 21, 3: 619-624. (in Japanese)
- Tasai, A. (2000). Residual axial capacity and damage restorability of reinforced concrete columns after earthquake. *Proceedings of twelfth WCEE*. CD-ROM.
- Architectural Institute of Japan (1999). Design guidelines for earthquake resistant reinforced concrete buildings on inelastic displacement concept. *AIJ*.

COLUMN SPLICES: OBSERVED EARTHQUAKE DAMAGE, MODELING APPROACHES, AND THE PEER/UCLA RESEARCH PROGRAM

John W. WALLACE and Murat MELEK¹

ABSTRACT

Splices in reinforced concrete columns in older buildings, or within the non-participating frames in some newer buildings, were typically designed as compression lap-splices. Compression lap-lengths are typically short (20 to $24d_b$), and only light transverse reinforcement is provided over the lap-length. Observations of column damage following earthquakes have revealed that these splices perform poorly; however, relatively sparse information exists to assess the expected performance for typical conditions. To address these needs, a PEER Center research program was undertaken at UCLA to conduct testing of full-scale columns under a variety of conditions, as well as to develop modeling techniques appropriate for column splices and complete systems. Test specimens consist of cantilever columns with a point load applied at the top. The 450 mm square column sections tested under reversed cyclic lateral load with either constant or variable axial load. Primary variables include the connection type, the level of axial load, the ratio of moment to shear, and the load history. An overview of this project, as well as relevant observations from column damage in recent earthquakes, is provided.

1. INTRODUCTION

Splices of column longitudinal reinforcement in older buildings (e.g., pre-1973) were commonly designed for compression only with relatively light transverse reinforcement enclosing the lap. For example, a lap splice length of 20 longitudinal bar diameters with widely spaced transverse reinforcement (equal to the least column dimension or 16 longitudinal bar diameters) was commonly used in older buildings. Observations following damaging earthquakes have revealed that columns with compression lap splices and widely spaced transverse reinforcement, especially at the perimeter of the building, perform poorly. Under earthquake actions, the column longitudinal reinforcement may be subjected to significant tensile stresses, particularly if the splice is located just above the floor slab, which is common in older construction. Given that required lap lengths for tension substantially exceed those for compression, slip occurs along the splice length at load levels less than required to reach the nominal moment capacity of the column, resulting in significant and rapid loss in column moment capacity.

¹ Department of Civil and Environmental Engineering, University of California, Los Angeles, 5731 Boelter Hall, Los Angeles, California, 90095-1593 USA; Email: wallacej@ucla.edu

Splices of column longitudinal reinforcement for moment frames in new buildings (e.g., designed according to ACI 318-99 provisions) require that the splices be located within the middle third of the column, encased within that tightly-spaced transverse reinforcement, and that they develop the yield stress of the bar in tension. Deformation compatibility requirements govern the design of splices for columns not designed to be part of the lateral-force-resisting system (see UBC-94, Section 1631.2.4 and UBC-97, Section 1633.2.4). More stringent requirements for transverse reinforcement for these non-participating columns were incorporated within ACI 318-95, and subsequently in UBC-97, following damage observed in the 1994 Northridge earthquake. The need for these new provisions indicates that substandard lap-splice (and shear reinforcement) details were used even in relatively recent building construction (pre-1995).

Relatively little research has been conducted on the behavior of columns with deficient lap splices. Early work focused primarily on developing rehabilitation options for splices. Testing was conducted on columns subjected to pure tension (Valluvan et al., 1993), and columns subjected to uniaxial bending with no superimposed axial load (e.g., Aboutaha et al, 1996). Rehabilitation measures studied included the addition of external and internal ties, as well as the use of jackets (e.g., steel angles with straps or steel-plate jackets with and without through-bolts). For most rehabilitation options, brittle splice failures were suppressed and substantial inelastic (flexural) deformations were observed prior to failure.

Deficient column splices are likely to exist in a majority of building columns at several locations over the height of a building and rehabilitation methods typically result in substantial disruption to building functions and possibly even displacement of the occupants. Therefore, although acceptable performance could be achieved with a variety of rehabilitation options, it often is not economical or practical to rehabilitate column splices in buildings. To address these issues, rehabilitation options that minimize the impact on the occupants and building operations are sought. A common strategy employed is to limit the drift imposed on the columns by adding bracing, shear walls, or a protective system (e.g., isolators, dampers) to the building such that the lateral deformations of the building are minimized. By limiting the lateral building deformations, the forces imposed on the column splice are limited such that the spliced reinforcement is not

subjected to significant tension. Rehabilitation guidelines (“Guidelines,” 1997) have been developed in recent years that are used by the engineering profession to accomplish this task.

Although the overall rehabilitation strategy is well accepted and the guidelines exist to assist in implementing the selected strategy, very sparse data exist on the performance of columns with “deficient” lap splices. This lack of knowledge on how the lateral-load behavior of column splices is influenced by important parameters such as axial load, shear, and load history leads to considerable uncertainty, and conservative and costly rehabilitation measures.

The PEER Center research program at UCLA was developed to provide vital data on the performance of column lap splices. Background information and important aspects of the research program are outlined in the following sections. Damage observations from recent earthquakes and relevant research are first reviewed, followed by a summary of the research program.

2. OBSERVATIONS FROM EARTHQUAKE DAMAGE

Brief summaries of splice damage observed in the 1994 Northridge, 1999 Izmit, and 1999 Chi-Chi earthquakes are provided to identify common damage patterns as well as to establish important performance issues.

Following the Northridge Earthquake, shear and splice failures in reinforced concrete columns were commonly observed in older buildings and in building columns designed as non-participating elements. Splice damage at the base of an exterior column in a one-story parking structure is shown in Figure 1 (Sherman Oaks, near the 101/405 interchange). The column is approximately 450 mm square with $20d_b$ lap splices. Cross sections of the interior columns of this structure had been significantly increased to provide longer seat lengths for the precast floor girders; however, no apparent changes had been made to the exterior columns. Damage to the column indicated that slip had occurred along the splice, with spalling of concrete, which is fairly common for splice failures. Diagonal cracks in some of the exterior columns indicated that the shear capacities of these columns may have been compromised. The shear distress in some

columns (and the lack of significant observed damage in the splice region) indicates a range of behavior for columns with presumably similar details.



(a) One Story Parking Structure



(b) 8-Story Parking Structure

Figure 1 Splice Damage – Northridge Earthquake

Damage to columns of an eight-story parking structure located across the street from the structure shown in Figure 1. The structure was designed using the 1982 UBC, and built in the mid-eighties. Although the columns in this structure had been designed with the lap splice near the mid-height of the column, “non-structural” reinforced concrete elements cast directly against the columns, created a captive column. The maximum moment for the captive column was shifted to the splice region, possibly leading to the observed damage. Splice damage was limited in this structure due to the use shear walls.

Poor behavior of splices in exterior columns may have been a significant contributing factor in the collapse of buildings in the 1999 Izmit, Turkey and Chi-Chi, Taiwan earthquakes. Figure 2 shows a close-up of a typical beam-column connection region for a five or six story apartment building just east of Golcuk, Turkey. Straight anchorage lengths were used on the interior column bars, and the exterior column bars were extended through the joint and anchored with short hooks into the top of the column. The failure surface between the column and the floor slab indicates that the interior column longitudinal bars were inadequately anchored, and pulled-out,



(a) Connection region – Golcuk, Turkey



(b) 12-Story Building – Nantou

Figure 2 Anchorage and Splice Damage

most likely at relatively low load-levels, allowing the column to rotate freely. Lateral loads imposed on the columns under this condition lead to higher axial compression in the column (because the axial load for lateral and gravity loads add). The axial compression, when coupled with the column rotation caused by reinforcement slip, could lead to premature buckling of the exterior column longitudinal reinforcement passing through the joint.

Damage in the splice region was observed in a 12-story building in Nantou (Figure 2), Taiwan; however, the use of shear walls was a significant factor in limiting the damage to the columns. Damage was also observed at some beam-column connections in a three-story building near Nantou, Taiwan. Failure at the connection regions may have been initiated by slip along the interior column splice bars, leading to significant rotation of the column. Under the column rotation, large compression would be exerted at the column edge, potentially leading to the peeling away of the concrete in the joint region, as observed.

In summary, column damage associated with the poor performance of splices has been consistently observed in recent earthquakes. In cases where the building system contains well-distributed shear walls, column damage has not led to collapse. Damage to exterior columns observed in the 1999 earthquakes in Turkey and Taiwan may have been significantly impacted by splice behavior.

3. BRIEF LITERATURE REVIEW

A brief literature review, covering both experimental and modeling studies, is summarized in the following subsections.

3.1 Experimental Studies

Valluvan et al. (1993) constructed and tested twelve, approximately two-thirds scale, column specimens to investigate rehabilitation measures for column splices. The test columns were 300 mm square and reinforced with 11 mm longitudinal bars and 6 mm hoops spaced at 300 mm on center. One column was used as a reference case, whereas rehabilitation measures were employed on the other 11 columns (two with welded splices, five with steel angles and straps, three with external ties, and one with internal ties). The specimens were subjected to reversed, cyclic axial loads (no bending). The reference specimen exhibited poor behavior, with a sudden loss in capacity at approximately $2/3$ of the nominal moment capacity of the section based on bar yield. Use of external steel angles and straps or ties was effective provided grout was used to achieve good contact between the existing concrete and new steel. Welding splices worked well provided additional ties are provided to resist outward thrust; use of internal ties was less effective because removing concrete cover caused micro-cracking in the concrete.

Aboutaha et al. (1996) investigated the use of steel jackets on square and rectangular column cross sections to improve the behavior of columns with inadequate splice lengths. Reinforcing details for the columns conformed to ACI 318 provisions (“Building,” 1956, 63). Specimens were approximately full-scale, and tested under uniaxial bending (no axial load). Four specimens were tested without rehabilitation measures to serve as benchmarks. As expected, performance of these specimens was poor, with brittle failures prior to reaching the nominal moment capacity of the section. Steel jackets with various anchor bolt arrangements were used on seven columns. Columns were tested laterally with no axial load. Steel jackets were very effective in improving load-displacement behavior provided anchor bolts were used and the jacket was longer than the column dimension in the direction of the applied load.

The studies conducted by Valluvan and Aboutaha focused primarily on identifying promising rehabilitation strategies; therefore, a relatively simple test configuration was used. Lynn et al. (1996), on the other hand, tested columns with pre-1970's construction details with and without splices to investigate behavior. Eight, 450-mm square columns with eight longitudinal reinforcing bars (either 25 or 36 mm diameter) and 8-mm diameter hoops/ties at 300 or 450 mm on center were constructed and tested. Five specimens had continuous reinforcement whereas three had $20d_b$ splices at the base of the columns. The specimens were subjected to reversed cyclic lateral displacements while the axial stress was held constant for the duration of the test at either $0.12f'_c$ or $0.35f'_c$. Although the yield stress was reached in the spliced bars, cracks along the lap splice lead to strength degradation and eventually shear failure (just above the splice) in the specimen with low axial stress. For the specimens with high axial stress, abrupt shear failures were observed for columns with and without the lap splice; therefore, the splice did not substantially influence the observed behavior.

3.2 Modeling Bond-Slip

Modeling the bond-slip relations for reinforcing bars is commonly accomplished using uniaxial springs (e.g., see Angelokos, 1999; Xiao, 1997). Moment versus rotation relations also may be derived from uniaxial spring relations and used to model the effect of slip (Reyes, 1999). Uniform spring properties may be used, or they may be varied to account for factors such as the amount of concrete confinement provided. Angelokos (1999) used this approach, by defining different bond properties at well and lightly-confined regions. Xiao (1997) assumed bond was lost along the splice region within the calculated plastic hinge length, and placed bond springs only on the remaining portion of the spliced bars to study the influence of splices on the lateral load behavior of columns. Relations to model the bond-slip relations between reinforcement and concrete include those developed by Popovic (1973), Ciani et al. (1981), Eligenhausen et al. (1983), and Giurani (1991). An example relation is given in Figure 3.

An alternative approach to modeling bond-slip behavior at the local level (using springs) is to modify moment-rotation relations used at potential plastic hinge locations to account for the influence of bond-slip on the strength and stiffness deterioration. In this case, experimental studies are helpful to calibrate the model, although relatively sparse data exist for this purpose.

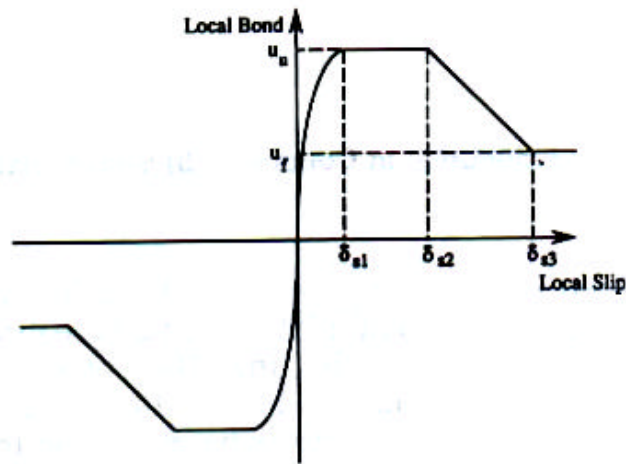


Figure 3 Typical Bond-Slip Relation (Eligenhausen et al, 1983)

4. PEER/UCLA RESEARCH PROGRAM

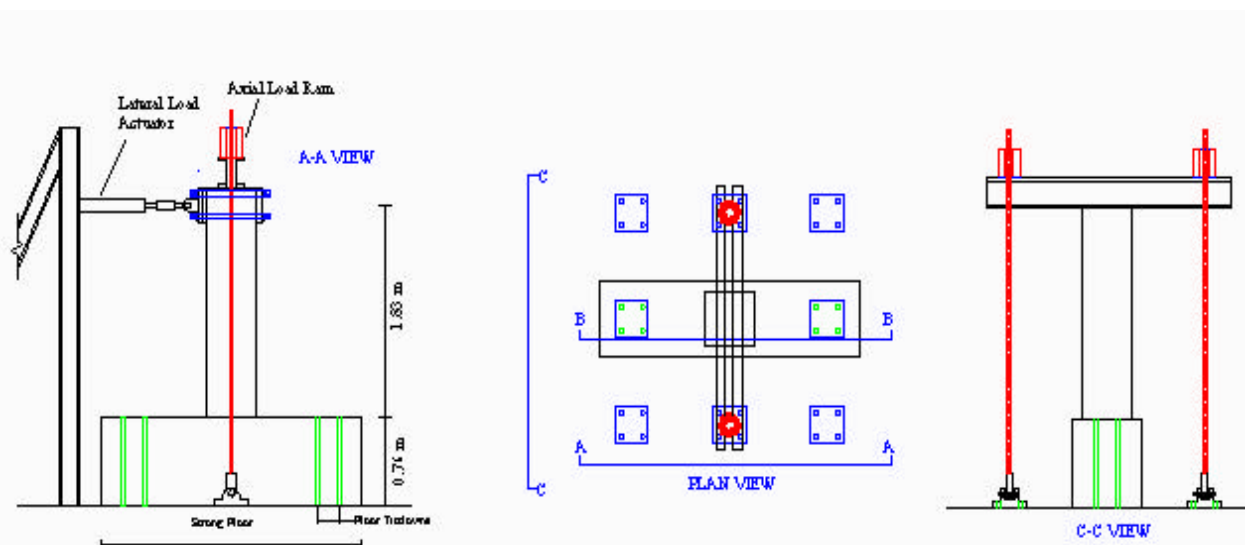
The primary focus of the research program is to produce essential and well-documented data on the behavior of full-scale columns with lap splices subjected to axial load and cyclic lateral load. The results of the test program will then be used to conduct analytical studies of complete building systems to assess the impact of splice behavior of building performance.

4.1 Experimental Program

The test specimens consist of a cantilever column with a foundation block attached to a strong floor. The test setup for the interior and exterior column specimens is shown in Figure 4. The specimens represent the building column from column mid-height between floors to the column-joint interface for the interior column. Typical reinforcing details will be used with the joint region of the specimen representing exterior columns. A column height of approximately 1.83 meters with a 457 mm square cross section is used. The column cross-section and longitudinal reinforcement are the same as the UC Berkeley test program.

The column height was selected to ensure the shear strength of the column (using ACI 318 Eq. 11-4 and 11-15) is sufficient to develop the flexural strength at the base of the column, where the lap splice is located. A lap splice length of $20d_b$ is used based on the requirements used for

compression splices in older buildings. Three levels of axial load ($0.1, 0.2$ and $0.3A_gf'_c$) and two arrangements of transverse reinforcement (minimum and moderate levels) are investigated. A majority of the specimens will be subjected to constant axial load and cyclic uniaxial bending. The load history will be fairly typical, and consists of three cycles at each displacement level with monotonically increasing drift levels ($0.1, 0.25, 0.5, 0.75, 1.0, 1.5, 2.0, 3, 5, 7.5,$ and 10%). One objective of the tests is to apply large displacement amplitudes to assess both loss of lateral load capacity and loss of axial load carrying capacity. The latter is important in evaluating life-



safety and collapse prevention performance levels. A pulse-type load history also will be used on one or two specimens. This history will consist of a few cycles at low-to-moderate displacement levels, followed by essentially monotonic loading in one direction until failure.

Table 1 provides an overview of the test program with the primary variables. The first three specimens represent interior columns, and will be tested under the standard cyclic lateral load history with the axial load held constant for the duration of the tests at $0.1, 0.2,$ and $0.3A_gf'_c$. For the splice length used ($20d_b$), the splice should fail when the moment in the column reaches approximately 70 to 80% of the nominal moment capacity. The objective of the tests is to assess the influence of axial load on lap splices with moderate shear stress and light transverse reinforcement (single hoops at 40 mm on center are used). Column reinforcing details are shown in Figure 5.

The second series of three specimens will be companions to the first three, and be used to assess the importance of shear and load history on splice behavior. Two specimens will be tested with a shear stress level approximately equal to the shear strength of the column. The axial load levels for these two specimens will be 0.2 and $0.3A_gf'_c$. For the third specimen, the axial load will be $0.2A_gf'_c$ and the load history will be modified to represent a short duration pulse (quasi-static application).

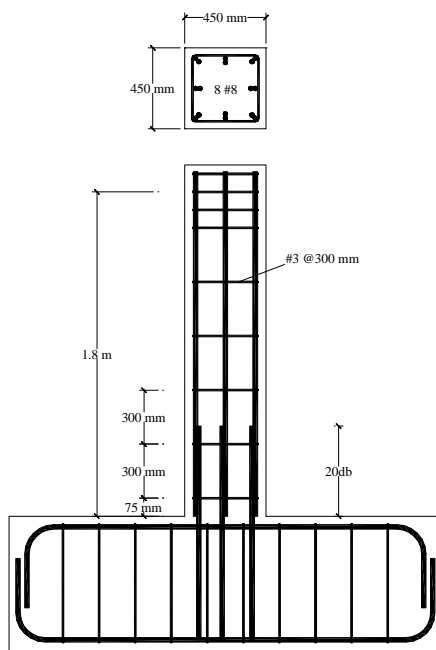


Figure 5(a) Reinforcing Details

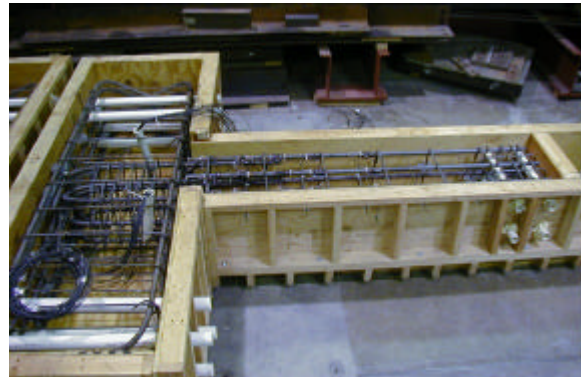


Figure 5(b) Photos of Reinforcing Cages

Four specimens, representing exterior columns, will be tested in the third phase of the test program. The axial load on the specimens will be initially set to $0.15A_gf'_c$ and then increased/decreased proportionally with the lateral load to minimum and maximum values of 0.0 and $0.3A_gf'_c$, respectively. The shear stress will be approximately three-quarters of the shear developed at the nominal moment capacity of the column for all specimens. In three specimens, light transverse reinforcement will be used within the joint region, and the fourth will have moderate transverse reinforcement. Three of the specimens will contain a lap splice, while the fourth will have continuous longitudinal reinforcement. A conventional load history will be used for three of the four specimens.

Table 1 Tentative Test Matrix

Specimen	Splice 20d _b	Axial Load % A _g f' _c	Shear (V _u @ M _n)/V _n	Load History	Hoop Spacing (mm)	TYPE
2S10MI	YES	10	0.60	STD	300	Interior
2S20MI	YES	20	0.65	STD	300	Interior
2S30MI	YES	30	0.70	STD	300	Interior
2S20HI	YES	20	1.00	STD	300	Interior
2S30HI	YES	30	1.00	STD	300	Interior
2S20MIN	YES	20	0.70	NEAR	300	Interior
2S30ME	YES	0 to 30	0.70	STD	300	Exterior
2C30ME	NO	0 to 30	0.70	STD	300	Exterior
2S30MEN	YES	0 to 30	0.70	NEAR	300	Exterior
2S30MEJ	YES	0 to 30	0.70	STD	300/150 ¹	Exterior

¹Column spacing/Joint spacing

Column testing is underway and will continue through the summer of 2001. Preliminary test results for specimen 2S10MI (Figure 6) are shown in Figures 7 and 9. Figure 7 plots the measured lateral load versus lateral column top displacement history.

The tests indicate that the column splice slipped at an imposed displacement level between 1.0% and 1.5%, prior to yielding of the longitudinal reinforcing bars. Strain histories for several gauges affixed to the longitudinal reinforcing bars along the splice are shown in Figure 9. Gauges located at the splice midpoint on both the bar anchored into the footing, as well as the bar extending vertically that is spliced to the footing bar, show very similar strain histories prior to the first cycle to 1.5% drift. During the cycle to 1.5% drift, the strain in the bars drops off substantially, indicating that slip is occurring.



Figure 6 – Specimen 2S10MI

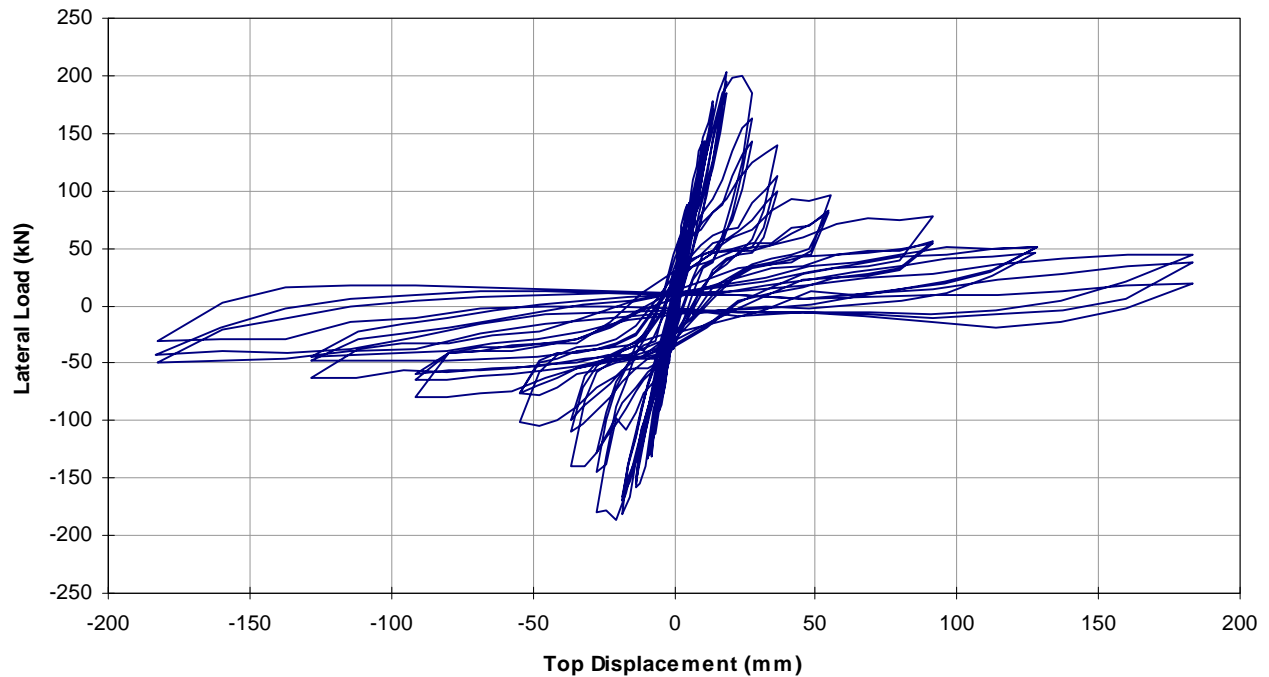


Figure 7- Load-Displacement (Specimen 2S10MI)

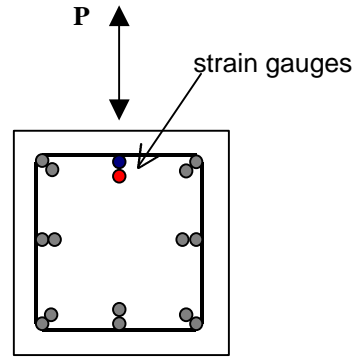
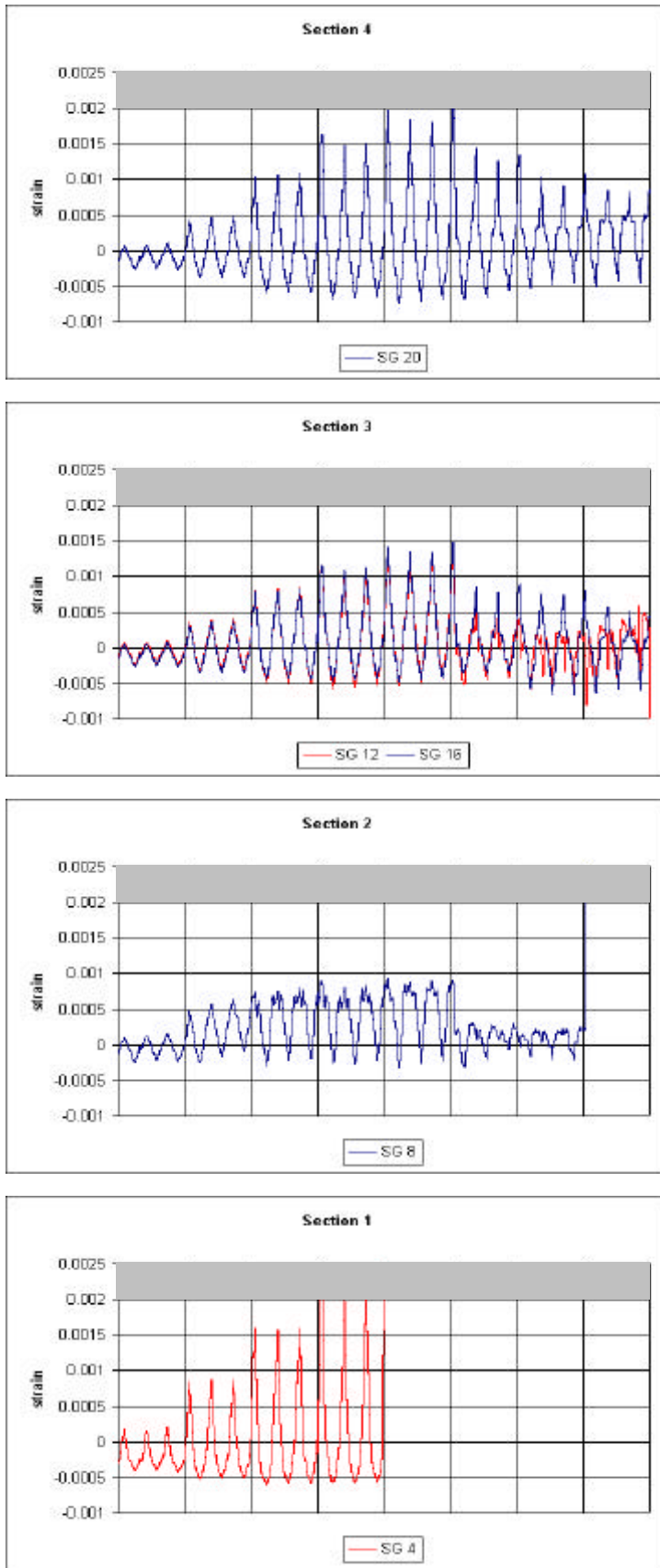
These cycles are followed by 2, 3 and 5% drift levels. Specimen 2S10MI at 5% drift is shown on Figure 8. Ultimately, three cycles of lateral drift at 7.5% and one cycle at 10% were imposed on the column without loss of axial load carrying capacity. At the completion of the test, with no applied lateral drift, the column was



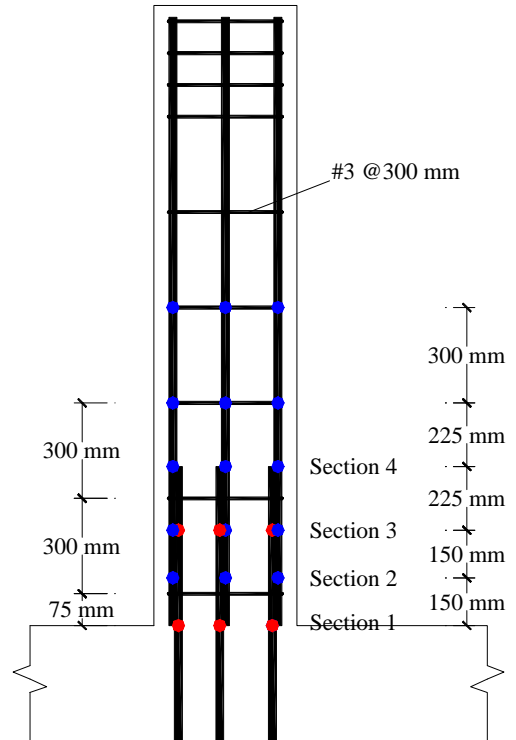
Figure 8

loaded under pure compression up to approximately $0.15A_g f'_c$ prior to loss of axial load carrying capacity.

Completion of the tests will provide valuable data to assess the impact of splices on building performance under a variety of conditions, as well as essential data to improve splice modeling.



- spliced bar
- longitudinal bar



Yield strain

Figure 9

4.2 Analytical Program

The test results will be used to calibrate existing models for degrading flexural strength and stiffness to assess the impact of splice behavior on the performance of building systems. Approximately 3, 5, and 8-story frame and frame-wall systems will be analyzed. A wall macro-model will be used that realistically accounts cyclic response with neutral axis migration. This model is currently being developed as part of a NSF sponsored research project.

5. CONCLUSIONS

Poor splice behavior has been observed in recent earthquakes and, in some instances, may have played a significant role in the partial collapse of some buildings. Existing information on splice behavior is very limited, and focuses mainly on rehabilitation options; however, rehabilitation of column splices is often not a viable solution. A common rehabilitation strategy involves adding new structural elements to limit the drift imposed on brittle elements, such as columns with deficient lap splices. The ongoing PEER/UCLA research program is designed to provide a wealth of data to address performance issues for buildings with column lap splices.

6. REFERENCES

- Aboutaha, R., Engelhardt, M. D., Jirsa, J. O., Kreger, M. E., (1996), "Retrofit of Concrete Columns with Inadequate Lap Splices by the Use of Rectangular Steel Jackets," *Earthquake Spectra*, Vol. 12, No. 4, November 1996, pp. 693-714.
- Alsawat, J., Saatcioglu, M., "Reinforcement Anchorage Slip under Monotonic Loading," *Journal of Structural Engineering*, ASCE, 118(9), 1992, pages 2421-2438.
- Angelakos, B. (1999), "The Behavior of Reinforced Concrete Knee Joints Under Earthquake Loads," PhD Thesis, University of Toronto, Department of Civil Engineering, Canada.
- "*Building Code Requirements for Reinforced Concrete: ACI 318*," American Concrete Institute, Farmington Hills, MI, 1956, 1963, 1995, and 1999.
- Eligehausen, R, Popov, E. P., Bertero, V. V., "Local Bond Stress-Slip Relationships of Deformed Bars under generalized excitations: experimental results and analytical model," *Report No. UCB/EERC-83/23*, EERC, Richmond, CA, 169 p.
- Giuriani, E., Plizzari, G., Schumm, C., "Role of Stirrups and Residual Tensile Strength of Cracked Concrete on Bond", *Journal of Structural Division*, ASCE V. 117, No. 1, January 1991, pp.1-17.

- “Guidelines for the Seismic Rehabilitation of Buildings,” *Report No. FEMA-273*, Federal Emergency Management Agency, October 1997.
- Lynn, A. C., Moehle, J. P., Mahin, S. A., Holmes, W. T. (1996), Seismic Evaluation of Existing Reinforced Concrete Building Columns,” *Earthquake Spectra*, Vol. 12, No. 4, November 1996, pp. 715-739.
- Popovic, S. (1973), “A numerical approach to the complete stress-strain curves for concrete,” *Cement and Concrete Research*, 3(5), 583-599.
- Reyes, O.; Pincheira, J. (1999), “RC Columns with Lap Splices Subjected to Earthquakes,” *Structural Engineering in the 21st Century: Proceedings, 1999 Structures Congress*, April 18-21, 1999, New Orleans, Louisiana, ASCE, Reston, Virginia, 1999, pp. 369-372.
- “*Uniform Building Code*,” International Conference of Building Officials, Whittier, CA, 1994, 1997.
- Valluvan, R., Kreger, M. E., Jirsa, J. O. (1993), “Strengthening of Column Splices for Seismic Retrofit of Nonductile Reinforced Concrete Frames,” *ACI Structural Journal*, V. 90, No. 4, July-Aug. 1993, pp 432-440.
- Xiao, Y., Ma, Rui (1997), “Seismic Retrofit of RC Circular Columns Using Prefabricated Composite Jacketing,” *Journal of Structural Engineering*, ASCE, 123(10), pp. 1357-1374.

KEYWORDS

Column, splice, lap splice, frame, frame-wall, experiments, testing, cyclic loads, lateral load, column shear, rehabilitation, performance-based design.

SESSION B-1: COLUMNS

Chaired by

◆ Julio Ramirez and Hitoshi Shiohara ◆

EVALUATION OF PERFORMANCE OF R/C COLUMNS

Daisuke KATO¹ and Koichi OHNISHI²

ABSTRACT

The objective of this paper is to reconstruct methods to evaluate load-deformation characteristics of reinforced concrete column members, relating with their limit states which are introduced in the performance based seismic design procedure. Limit states of reinforced concrete members are generally defined by damage levels of concrete and reinforcement, which are subjected to tensile and compressive stress. In this paper limit states are discussed paying attention to limit states caused by compressive stress. Calculated crushing point of cover concrete, which correspond to operation limit state, was found to be conservative and effective for design equation. Calculated crushing point of core concrete, which correspond to repair limit state, was found to be conservative and effective for design equation. Three calculated deflection angles, which correspond to safety limit state, were found to be conservative for observed deflection angles when specimens lost axial load carrying capacities and effective for design equation.

1. INTRODUCTION

Recent earthquake resistant design concept of structures places explicit emphases on limit state design. The objective of this paper is to reconstruct methods to evaluate load-deformation characteristics of reinforced concrete column members, relating with their limit states which are introduced in the performance based seismic design procedure. Limit states of reinforced concrete members are generally defined by damage levels of concrete and reinforcement, which are subjected to tensile and compressive stress. In this paper limit states are discussed paying attention to limit states caused by compressive stress.

2. LOAD DEFORMATION CHARACTERISTICS AND LIMIT STATES OF COLUMNS

Figure 1 shows load deformation relationship of a typical reinforced concrete column member subjected to axial force. Two points should be emphasized, i.e. i) behavior of core concrete only is dominant after crushing of cover concrete and ii) behavior after maximum strength depend on

*1 Department of Architecture, Faculty of Engineering, Niigata University, Niigata, Japan
Email: dkato@eng.niigata-u.ac.jp*

2 Graduate Student, Niigata University, Niigata, Japan

the loading history, i.e. specimens with cyclic loading apt to show smaller deformation capacities comparing to those with monotonic loading. This is called cyclic loading effect in this study and previous study indicated that column specimens with constant axial load whose axial load ratio were higher than 1/3 showed the cyclic loading effect (Kato 1996).

Some characterized points are highlighted in this figure, i.e. flexural cracking of concrete, commencement of yielding of longitudinal steel, commencement of crushing of cover concrete, commencement of crushing of core concrete, point where restoring force degrades to design lateral load (lateral load at yielding of longitudinal reinforcement) and point where the column loses capacity to carry design axial force. Those highlighted points are related with limit states of the column as shown above or below the relationship. It must be noted that limit states based on the compressive behavior of concrete and reinforcement are shown above the relationship and those based on the tensile behavior are shown below. Limit states based on compressive behavior are more important comparing to tensile behavior because columns are characterized by the subjected axial force. From this view point limit states based on the compressive behavior are discussed in this paper. In other words limit states based on the tensile behavior of materials are considered to be given by evaluating methods of beam members.

Three limit states are discussed, i.e. operation limit, repair limit and safety limit. Operation limit state is defined as a limit state within which buildings can be fully operational after earthquake, which is considered to correspond to commencement of crushing of cover concrete in this study. Repair limit state is defined as a limit state within which buildings can be repaired under rational cost. It seems better to classify repair limit into 2 groups(and) because of the wide range of this limit state. Repair limit state is considered to correspond to commencement of crushing of core concrete because repair of only cover concrete is enough within this condition. It seems reasonable to consider that safety limit state corresponds to losing point of axial load carrying capacity of the column. However losing point of design axial load is also effective to represent safety limit state because of the large amount of experimental data which can be used to examine the feasibility of evaluating methods. From this view point two kinds of experimental data are discussed for safety limit state.

3. EVALUATING METHODS OF LIMIT STATES

Characterized points on the load deformation relationship can be calculated by basic flexural theory under the assumption that plane remains plane after bending. Figure 2 shows stress strain relationship of core concrete and assumed edge strain of core concrete at repair and safety limit states.

3.1 Operation Limit State

As described in Chapter 2, operation limit state is considered to correspond to commencement of crushing of cover concrete. Curvature at commencement of crushing of cover concrete can be calculated assuming that the edge stress of cover concrete reaches maximum stress of stress-strain relationship of plain concrete. Deformation for this curvature can be given by assumed deformation mechanism of the column shown in Fig. 3 suggested by Hiraishi(Hiraishi 1990).

3.2 Repair Limit State

Repair limit state is considered to correspond to commencement of crushing of core concrete. Curvature at commencement of crushing of core concrete can be also calculated assuming that the edge stress of core concrete reaches maximum stress of stress-strain relationship of confined core concrete(see Fig.2).

3.3 Safety Limit State (Rf)

Safety limit state is considered to correspond to losing point of axial load carrying capacity of the column. However this point can not be given theoretically. So three kinds of method are chosen and their feasibility as design equations are examined. Deflection angles obtained by these methods are symbolized as Rf in this study.

i)k1k3max point : Coefficients k1 and k3 to determine stress block of concrete are widely

introduced to replace stress strain relationship in the practical design. The point when the multiplication of coefficients k_1 and k_3 becomes maximum can represent the losing point of axial load carrying capacity of the column. This method was applied to specimens without cyclic effect in this paper.

ii) point where concrete stress equals to axial load stress: Some researchers indicated that the point where concrete edge stress equaled to average axial load stress could represent the losing point of axial load carrying capacity of the column (Hiraishi 1990, for example). This method was also applied to specimens without cyclic effect in this paper.

iii) Empirical equation: Empirical equation was proposed by Kato (Kato 1996). Edge strain of core concrete $1.9\epsilon_{cp}$ (ϵ_{cp} : strain at maximum stress point of confined concrete) was assumed at the ultimate point. This edge strain was obtained empirically using column specimens with cyclic loading effect. It must be added that it can be also applied for specimens without cyclic loading effect with equivalent axial load (see Fig. 4).

4. FEASIBILITY OF EVALUATING METHODS

4.1 Specimen Examined

Figure 5 shows the range of properties of 122 reinforced concrete column specimens tested in Japan. Figure 6(a) shows frequency of subjected axial load of specimens with constant axial load and Fig. 6(b) shows that of specimens with varying axial load. As explained in Chapter 2, specimens with constant axial load whose axial load ratio are higher than 1/3 apt to suffer cyclic loading effect and show smaller deformation capacities. Other specimens (specimens with constant axial load whose axial load ratio are lower than 1/3 and specimens with varying axial load) are called specimens without cyclic loading effect in this paper.

4.2 Concrete Model for Core Concrete Confined by Transverse Reinforcement

In this study the concrete model proposed as a result of the New RC Projects (New RC Project 1993) was used for core concrete confined by square hoop reinforcement. This model was developed to match with a variety of experimental data conducted not only during the New RC Projects but by overseas researchers. The maximum strength of concrete and transverse reinforcement used in examined specimens was 132 and 1109 MPa, respectively. The maximum stress σ_p and the strain at the maximum strength ϵ_p of confined concrete are expressed as follows.

$$\sigma_p = \sigma_B + \kappa \cdot \rho_{wh} \cdot \sigma_{wy} \quad (1)$$

$$\epsilon_p = \begin{cases} \epsilon_c \cdot (1 + 4.7 \cdot (K - 1)) & K \leq 1.5 \\ \epsilon_c \cdot (3.35 + 20 \cdot (K - 1.5)) & K > 1.5 \end{cases} \quad (2)$$

$$\kappa = 11.5 \cdot (dw/c) \cdot (1 - 0.5 \cdot s/je)$$

$$\epsilon_c = 0.93(\sigma_B)^{1/4} \cdot 10^{-3} \quad (\sigma_B: \text{MPa})$$

$$K = \sigma_p / \sigma_B$$

where, σ_B denotes strength of plain concrete (MPa), c denotes length between effective supports of hoop, ϵ_c denotes axial strain at maximum point of plain concrete, ρ_{wh} denotes volumetric ratio of reinforcement to concrete core, je denotes core depth (mm), σ_{wy} denotes yielding strength of hoop (MPa, $\sigma_{wy} < 687 \text{ MPa}$), dw and s denote diameter and spacing of hoop (mm).

4.3 Safety Limit Determined by Shear Failure after Flexural Yielding (Rp)

Losing point of axial load carrying capacity of the column is not only determined by flexural failure but shear failure after flexural yielding. In this study deflection angle to lose axial load carrying capacity due to shear failure was assumed to be obtained as R_p value proposed by Architectural Institute of Japan (1990). The R_p value was originally proposed as deformation

capacity determined by shear failure after flexural yielding.

4.4 Comparison between Calculation and Experiment

4.4.1 Operation limit state

Figure 7 shows the relations between deflection angle at commencement of crushing of cover concrete observed during the test and calculation. Only specimens conducted in Niigata Univ. are compared because commencement of crushing of cover concrete was not usually described in previous papers. The result indicates that calculated crushing point of cover concrete is conservative and it seems effective for design equation.

4.4.2 Repair limit state

Figure 8 shows the relations between deflection angle at commencement of crushing of core concrete observed during the test and calculation. However commencement of crushing of core concrete could hardly be observed during the tests. From this reason in Figure 8(a) experimental data were replaced by points where first revealing of reinforcement were observed during the tests. In order to compare with more experimental data, maximum strength point was chosen as the test result for this limit state in Figure 8(b). Calculation is found to be conservative for both of two kind of experimental data, which means it seems effective for design equation.

Figure 9 shows comparison between observed limit states. Figure 9(a) compares deflection angles at maximum strength with those when commencement of crushing of cover concrete was observed during the test, which indicates the latter are roughly half of the former. Figure 9(b) compares deflection angles at maximum strength with those when first revealing of reinforcement was observed during the test, which indicates the latter are roughly twice of the former.

4.4.3 Safety limit state

Figure 10 shows the relations between observed deflection angles when specimens lost axial load carrying capacities and calculation shown in Section 3.3. It must be noted that both vertical and horizontal axes were normalized by R_p value to eliminate the effect of deformation capacity determined by shear failure after flexural yielding. In other words the feasibility of the evaluating method of R_f should be discussed using the experimental data with R_f/R_p value of less than 1. The empirical equation is compared with both specimens without and with cyclic loading effect whereas other two methods are compared with specimens without cyclic loading effect. Those figures indicates that the calculation shows conservative, which means it seems effective for design equation.

Figure 11 compares calculated edge strain of core concrete at safety limit state with the strain at maximum stress of core concrete ϵ_{cp} , which indicates edge strain by empirical equation were roughly comparable with the result by k_1k_3 max point.

In order to compare with more experimental data, observed deflection angles when restoring force of specimens degraded to 80% of the maximum strength were chosen as the test result for this limit state in Figure 12. Note that this deflection angle could represent the observed deflection angles when specimens lost design lateral load in the previous study (Kato 1996). The empirical equation is found to be conservative whereas other two methods are not conservative.

5. CONCLUSIONS

(1) Crushing point of cover concrete corresponds to operation limit state. Calculated crushing point was found to be conservative for operation limit state and effective for design equation.

(2) Crushing point of core concrete, which corresponds to repair limit state, can be replaced by maximum strength point. Calculated crushing point of core concrete was found to be conservative for repair limit state and effective for design equation.

(3) Deflection angles when specimens lose axial load carrying capacities correspond to safety limit state. Three calculated deflection angles were found to be conservative for safety limit state and effective for design equation.

(4) Observed deflection angles when specimens lose design lateral can represent safety limit state. Calculated deflection angles by empirical equation were found to be conservative for observed deflection angles when specimens lost design lateral force whereas other two method were found to be not conservative.

6. REFERENCES

Architectural Institute of Japan (1990), *The design guidelines for earthquake resistant reinforced concrete buildings based on ultimate strength concept (in Japanese)*

Hiraishi, H. and Inai, E. (1990)., *Theoretical Study on Deformation Capacity of R/C Columns beyond Flexural Yielding, Journal of Structural and Construction Engineering, No.408*

Summary report on NEWRC project in 1992(1993), *c-7)state of the art report on characteristics of confined concrete, Research center on national land development, (in Japanese)*

Kato, D., Honda, Y., Suzuki, H. and Shiba, J. (1996)., *Confinement of Concrete of R/C Members under Varying Axial Load, The 11-th World Conference on Earthquake Engineering*

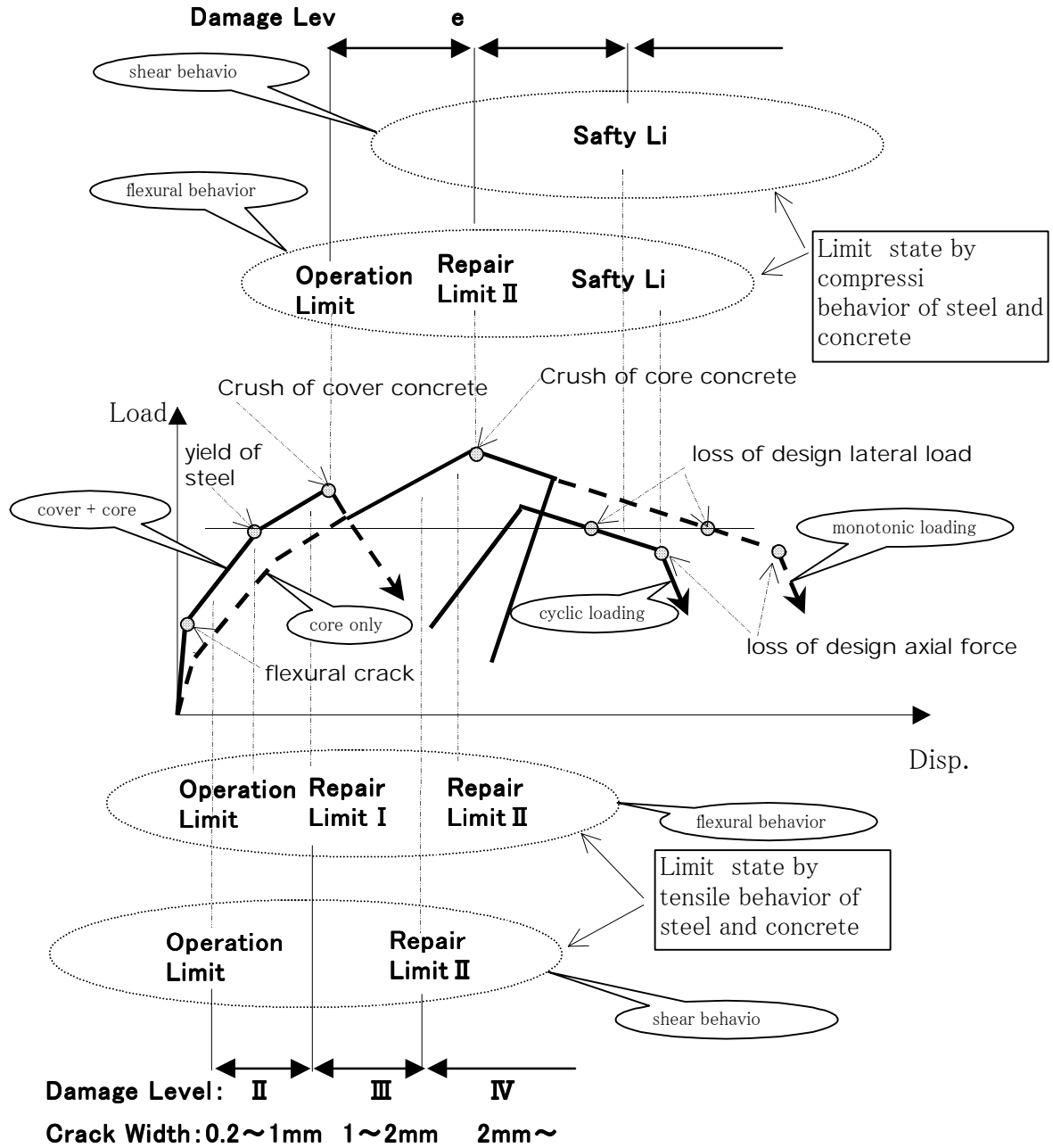


Figure 1 Load deformation characteristics and limit states of columns

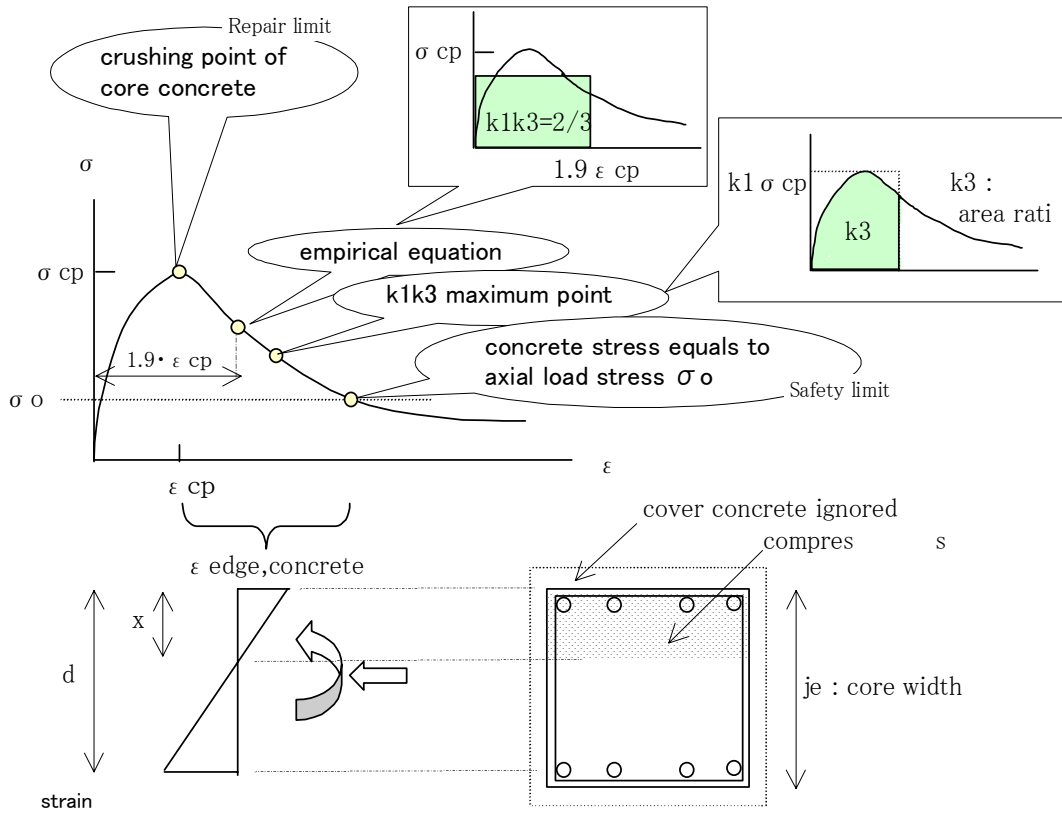
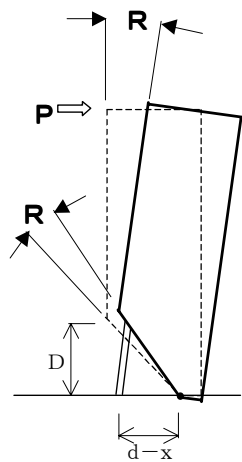
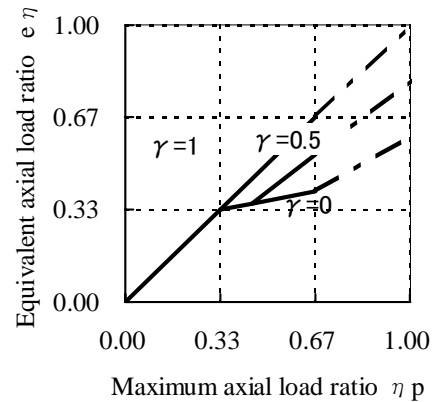


Figure 2 Stress strain relationship of core concrete and assumed edge strain of core concrete at repair and safety limit state



$$R = \delta_{\text{main}} / (d-x) = \phi \cdot D$$

δ_{main} : elongation of main bar in hinge region
 D : length of hinge region
 $\phi = \epsilon_{\text{main}} / (d-x)$
 $\epsilon_{\text{main}} = \delta_{\text{main}} / D$

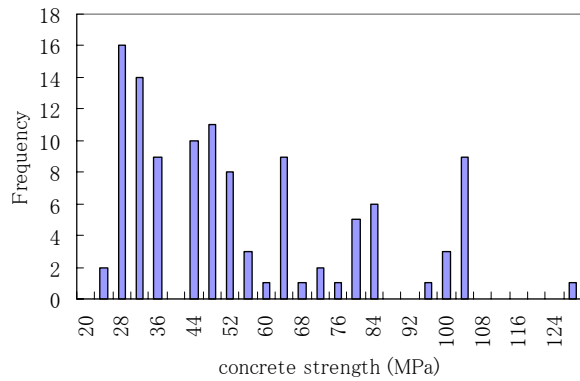


$$e\eta = \begin{cases} \eta_p & 0 < \eta_p \leq 1/3 \\ \eta_p/5 + 4/15 & 1/3 < \eta_p < 2/3/(1+\gamma) \\ (3+2\cdot\gamma)/5 \cdot \eta_p & 2/3/(1+\gamma) \leq \eta_p \leq 2/3 \end{cases}$$

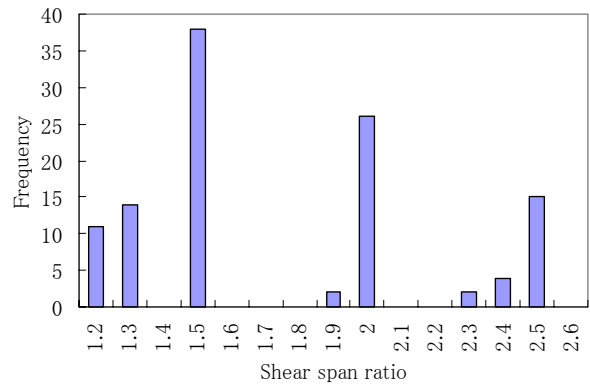
$$\gamma = \frac{\text{minimum axial load}}{\text{maximum axial load}}$$

Figure 3 Deformation mechanism of column

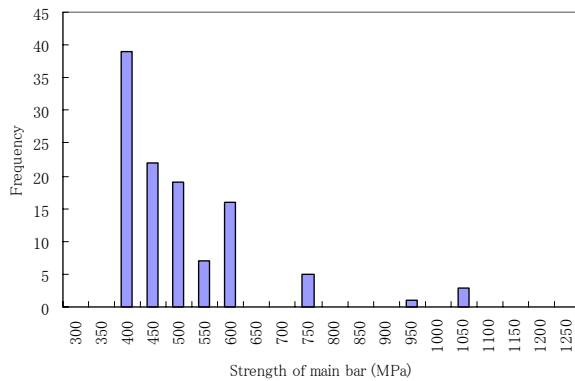
Figure 4 Equivalent axial load used to apply empirical equation



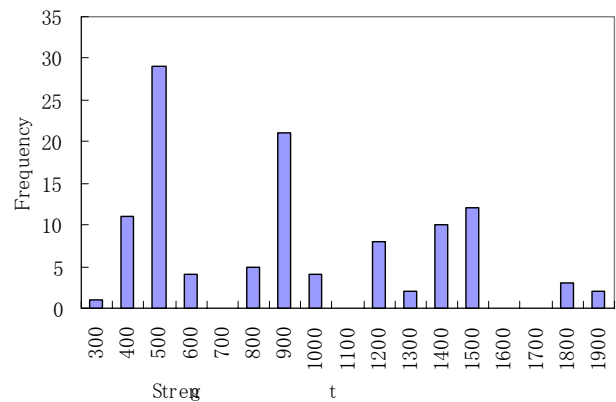
(a) Frequency of concrete strength



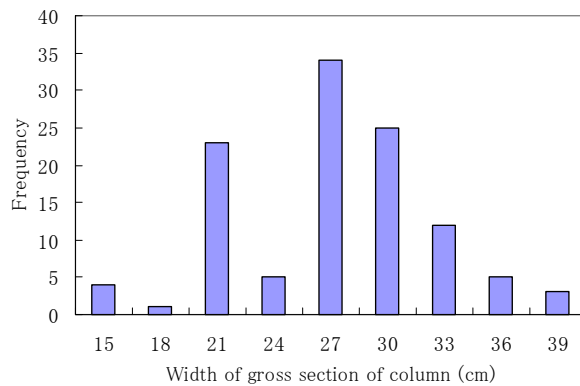
(b) Frequency of shear span ratio



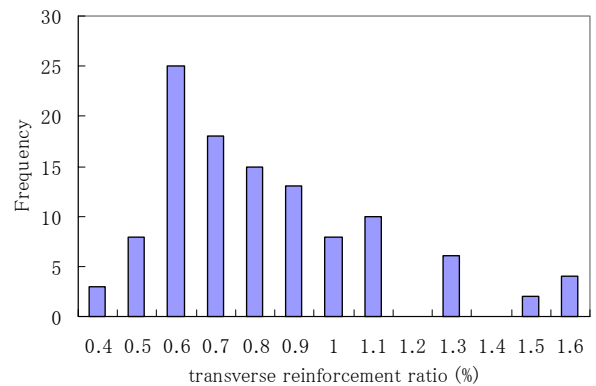
(c) Frequency of strength of main bar



(d) Frequency of strength of hoop reinforcement



(e) Frequency of width of column



(f) Frequency of hoop reinforcement ratio

Figure 5 Properties of examined specimens

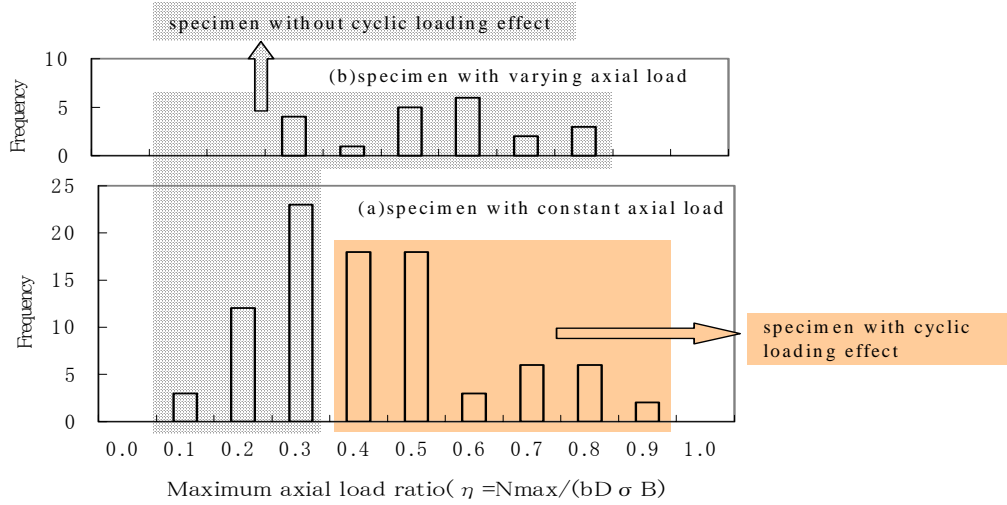


Figure 6 Frequency of subjected axial load of examined specimens

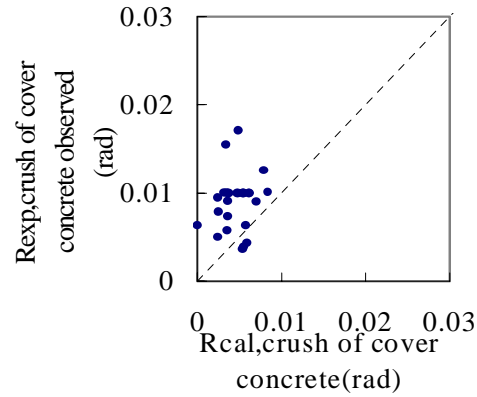
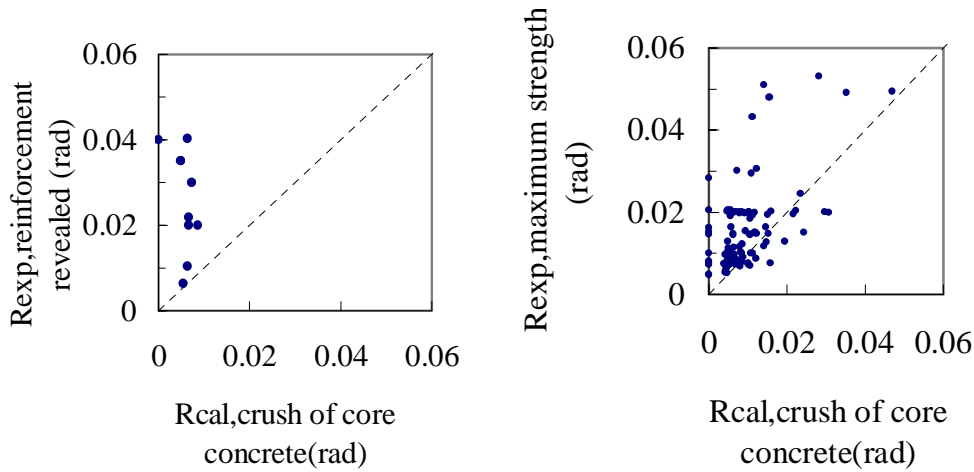
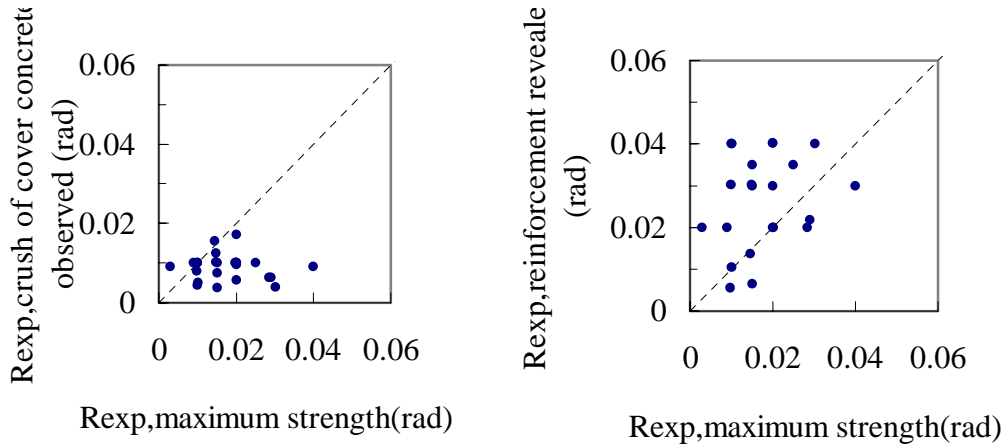


Figure 7 Comparison of deflection angle at operation limit state between calculation and experiment (point where crushing of cover concrete was observed)



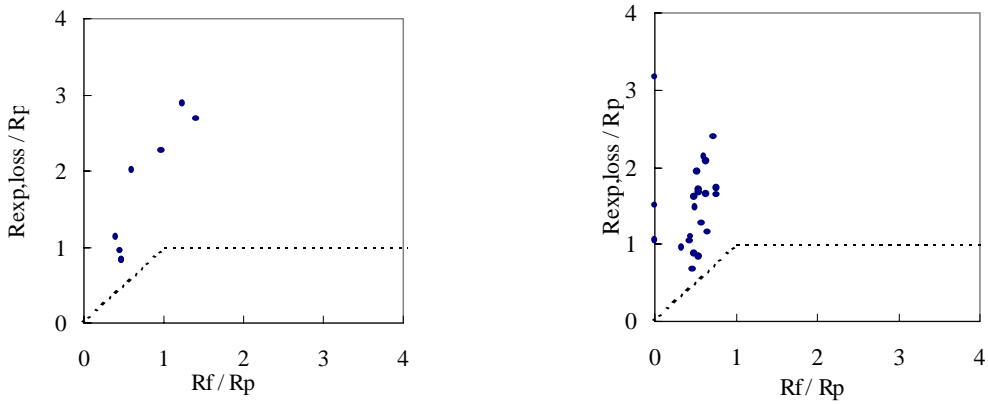
(a) point where revealing of reinforcement was observed (b) at maximum strength

Figure 8 Comparison of deflection angle at repair limit state between calculation and experiment



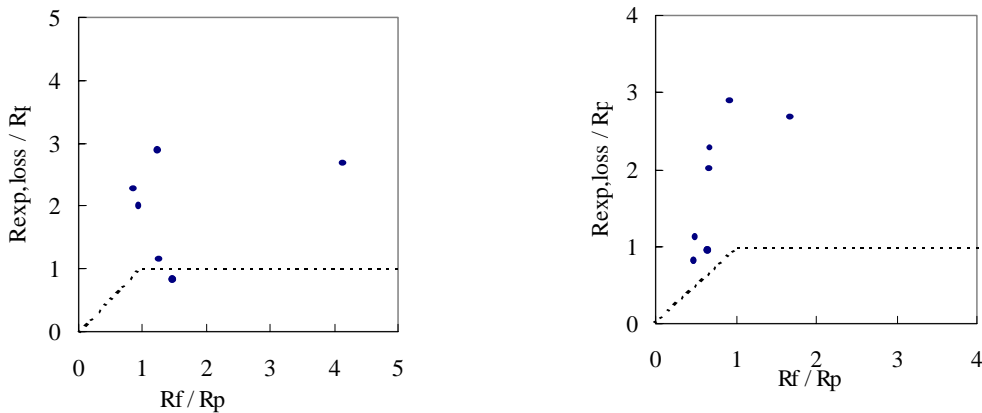
(a)maximum strength –crush of cover concrete (b)maximum strength-reinforcement revealed

Figure 9 Comparison between observed limit states



(a-1)specimen *without* cyclic loading effect (a-2)specimen *with* cyclic loading effect (using equivalent axial load)

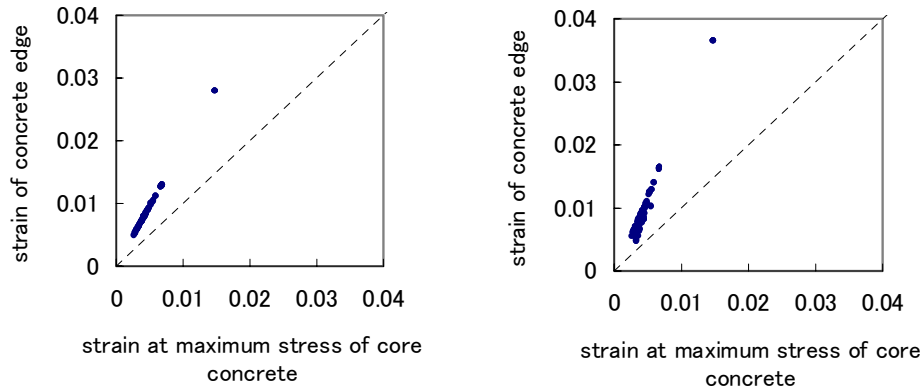
(a) calculation : Empirical equation using $\epsilon_u=1.9\epsilon_{cp}$ and $k_1k_3=2/3$



(b) calculation : point where concrete stress σ_c equals to applied axial load stress σ_o (specimen *without* cyclic loading effect)

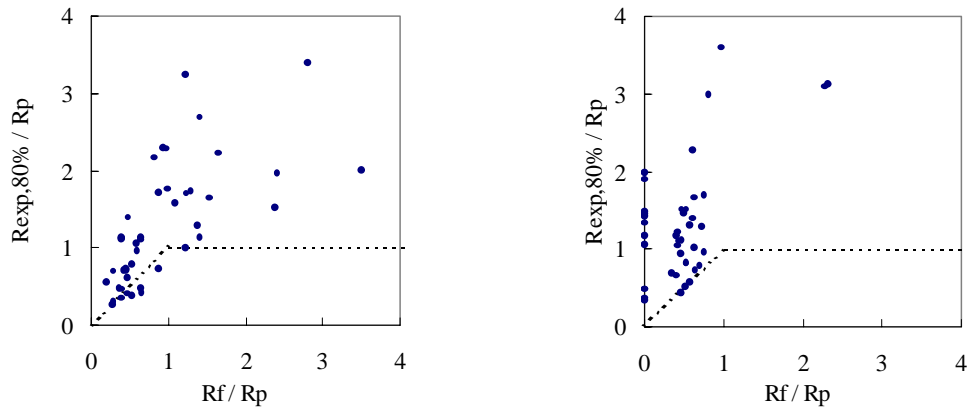
(c)calculation : point where ratio k_1k_3 becomes maximum (specimen *without* cyclic loading effect)

Figure 10 Comparison of deflection angle at safety limit state between calculation(R_f) and experiment($R_{exp,loss}$ defined as point where specimen lost axial loading capacity)



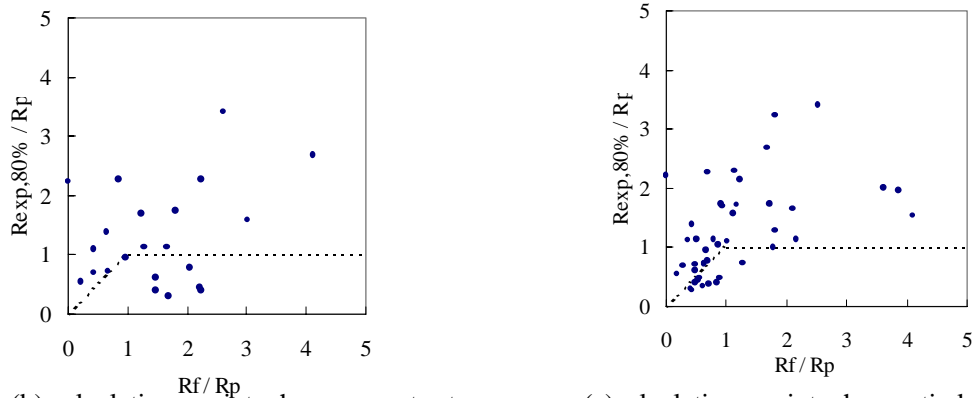
(a) empirical eq. (b) point where ratio $k1k3$ becomes maximum

Figure 11 Calculated edge strain of core concrete at safety limit state



(a-1) specimen *without* cyclic loading effect (a-2) specimen *with* cyclic loading effect (using equivalent axial load)

(a) calculation : Empirical equation using $\epsilon_u = 1.9\epsilon_{cp}$ and $k1k3 = 2/3$



(b) calculation : point where concrete stress σ_c equals to applied axial load stress σ_o (specimen *without* cyclic loading effect) (c) calculation : point where ratio $k1k3$ becomes maximum (specimen *without* cyclic loading effect)

Figure 12 Comparison of deflection angle at safety limit state between calculation(R_f) and experiment($R_{exp,80\%}$ defined as point where restoring lateral force degraded to 80% of maximum force)

SEISMIC EVALUATION OF WAFFLE SLAB SYSTEMS FOR INDUSTRIAL FACILITY

Khalid M. MOSALAM¹, Clay J. NAITO² and Erik KUNKEL³

ABSTRACT

This paper presents an experimental investigation for the seismic evaluation of the structural performance of reinforced concrete waffle slab systems commonly used in industrial facilities. For the purpose of equipment installation and usage, circular perforations and sometimes discontinuous concrete walls are encountered. In this way, the system behaves as a grid-like floor supported on columns and partially infilled frames. Accordingly, Concerns related to the performance of such systems when subjected to large gravity load in conjunction with seismic loading motivated the experimental investigations. Two types of subassemblies were tested. The first focused on the bi-directional seismic response of grid/column system while the second was concerned with grid/partially infilled frame system subjected to unidirectional loading parallel to the infill wall. Ductile response of the first subassembly was observed with formation of column plastic hinging. In the second subassembly, depending on the selected simulated soil model in the test setup, two distinct modes of failure were obtained, namely, punching failure of the waffle for flexible soil or formation of short column mechanism for stiff soil.

1. INTRODUCTION

Several existing high technology fabrication plants in western United States were mainly designed for the weight of heavy sensitive equipments and for limiting their exposure to micro-vibrations. Accordingly, deep waffle slab floors with span to depth ratio of approximately five were generally selected. In addition, reinforced concrete walls were sometimes constructed between columns to reduce lateral deformations. For accessibility to both sides of the floor for equipment installation and usage, perforations were commonly introduced between the joists of the waffle slabs rendering the floor system a grid-like structure. Moreover, walls were sometimes terminated approximately 2 ft (610 mm) below slabs leading to structural action similar to partial infill walls.

¹ Assistant Professor, Department of Civil and Environmental, University of California, Berkeley, USA
Email: mosalam@ce.berkeley.edu, Fax: (510) 643-8928

² Post-doctoral Researcher, Department of Civil and Environmental, University of California, Berkeley, USA
Email: naito@ce.berkeley.edu

³ Graduate Student, Department of Civil and Environmental, University of California, Berkeley, USA
Email: kunkel@ce.berkeley.edu

The gravity load design approach of the perforated waffle slab system leads to absence of shear reinforcement in the joists off the column gridlines. Moreover, the large gravity loads due to equipment weight and the possible earthquake loading lead to two major concerns. The first is the possible loss of gravity load resistance especially if shear failure takes place in the floor system where the shear stress in the slab at the slab-column connection may be high enough to cause punching failure. The second concern is due to the expected formation of short column mechanism in the laterally unsupported length of the columns adjacent to the partial infill walls.

The selected prototype building is an industrial facility where large gravity load due to heavy equipment should be supported. It consists of a single reinforced concrete waffle slab floor with circular perforations between the joists. The floor is directly supported on reinforced concrete circular columns and in some locations on partially infilled frames as shown in Figure 1 where two regions are identified. Region 1 represents grid/circular column system while Region 2 is a grid/partially infilled frame system.

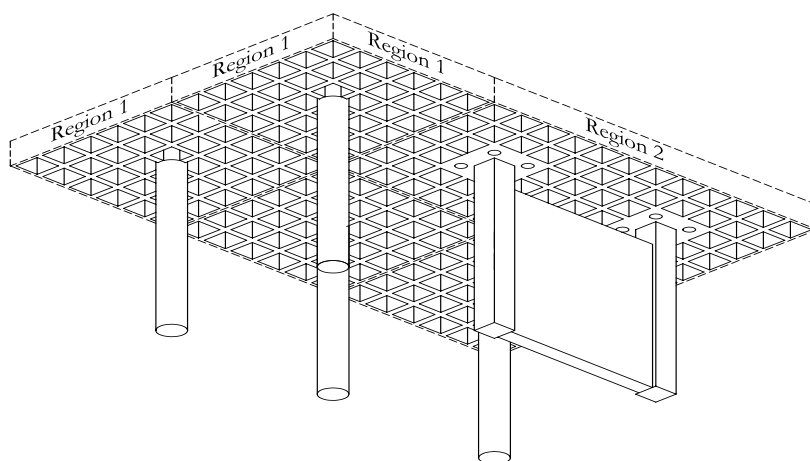


Figure 1: Isometric view of the prototype building

2. TEST SUBASSEMBLIES

Four subassemblies (A1 & A2 for Region 1 and B1 & B2 for Region 2) were tested with 60% scale in inverted positions. Concrete geometry and reinforcement details for group A subassemblies are shown in Figures 2 to 4 where half bay on all four sides of the column and half the column height are modeled. For group B, Figures 5 to 7 represent the geometry and details with full bay modeled including half bay on all four sides of the partially infilled frame. Material properties of the used concrete and reinforcing steel are listed in Tables 1 and 2, respectively.

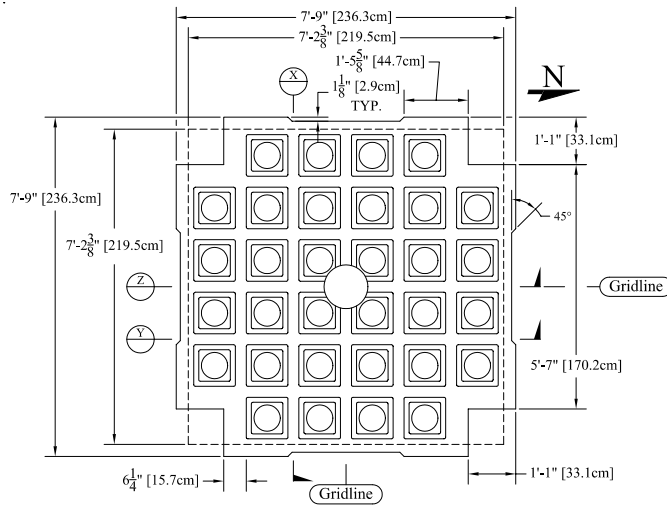


Figure 2: Plan view of group A subassemblies

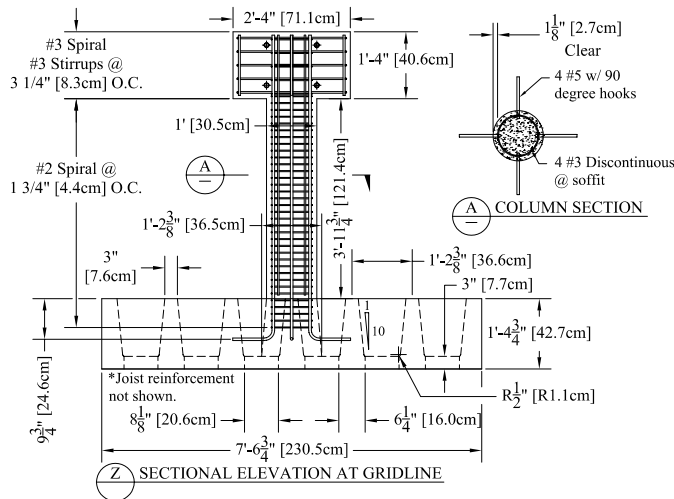


Figure 3: Sectional elevation of group A subassemblies

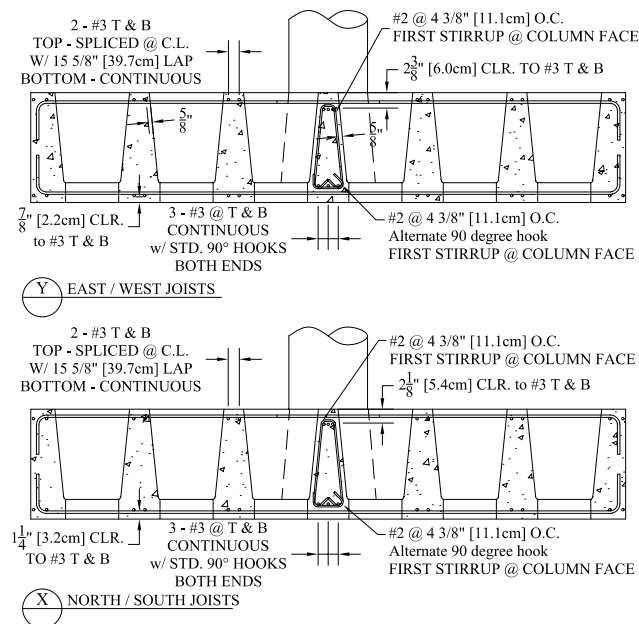


Figure 4: Reinforcement details of joists in group A subassemblies

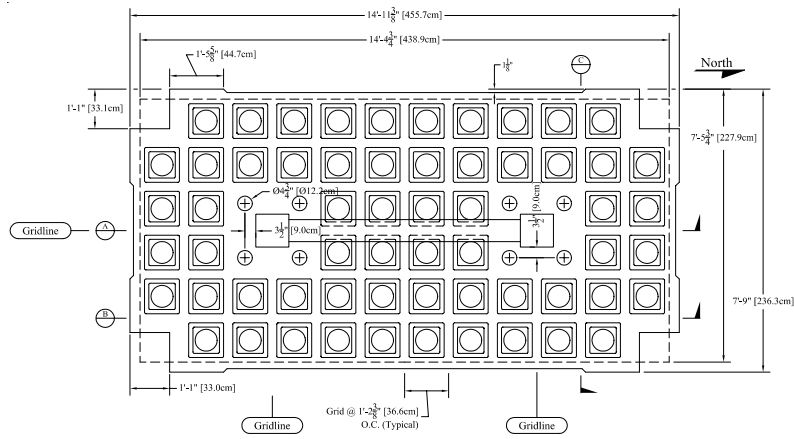


Figure 5: Plan view of group B subassemblies

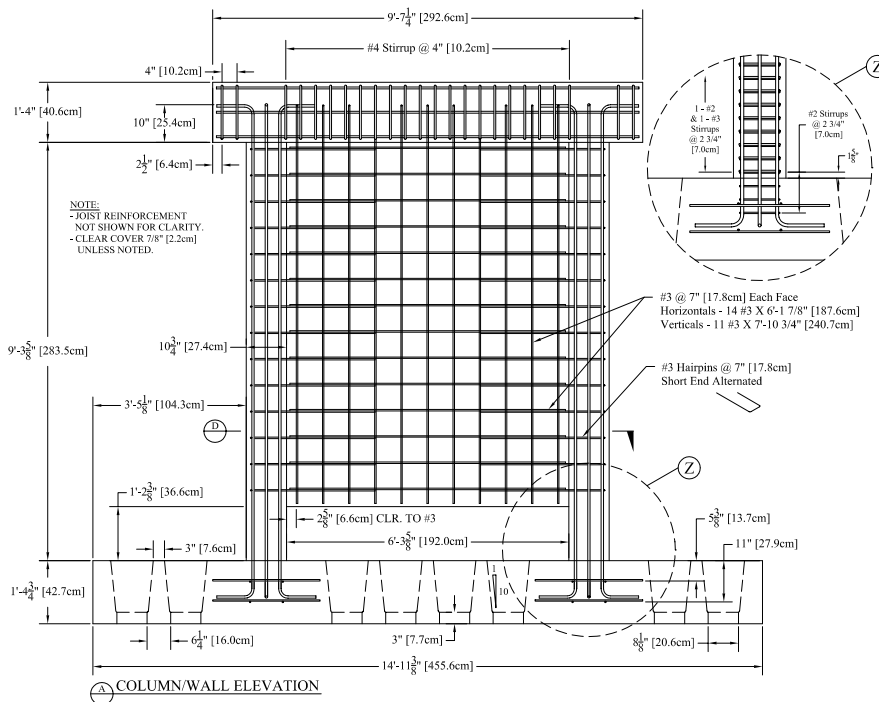


Figure 6: Front elevation of group B subassemblies

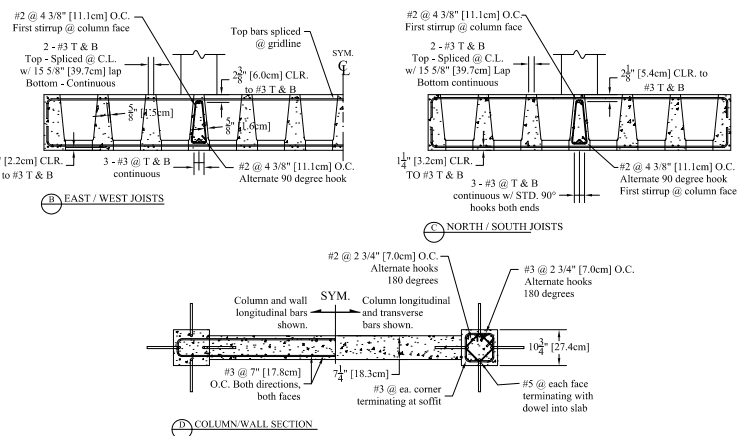


Figure 7: Cross-section details of group B subassemblies

Table 1: Average concrete material properties

Subassembly	Location	f'_c [MPa]	f'_t [MPa]	E_c [MPa]
A1	Waffle slab	29.0	2.6	19900
	Column	32.7	2.9	22500
A2	Waffle slab	34.5	3.2	20400
	Column	30.1	2.8	19100
B1	Waffle slab	32.7	2.4	23.3
	Columns and wall	31.7	2.8	23.9
B2	Waffle slab	30.1	2.8	20.4
	Columns and wall	32.2	2.8	21.0

Table 2: Reinforcing steel material properties

Bar	Reinforcement usage	Grade	f_y [MPa]	ϵ_y	f_u [MPa]
#2	Joist and column stirrups	N.A.	394	0.0020	519
#3	Column stirrups	A615	533	0.0027	743
#3	Joist, columns, and wall (longitudinal)	A615	438	0.0022	710
#5	Column longitudinal bars	A615	477	0.0024	744

A preliminary analytical study was conducted to determine the appropriate boundary conditions of the subassemblies. The adopted approach attempted to match the bending moments and shearing forces at the critical sections of the subassembly with those from a larger building model. This analytical study of the boundary conditions was based on simplified linear elastic analysis where gravity loads consisting of 12 kN/m² dead load and 12 kN/m² live load were applied. The corners of the subassemblies were prevented from translations and allowed rotations in the three global directions. Several configurations of the boundary conditions were considered. These configurations included different arrangements of the locations of vertical roller supports (indicated by the ⊗ mark in Figure 8) which prevent vertical translation only. The building and the subassembly models were subjected to the full gravity load and representative lateral target deformation according to the recommendations by FEMA-273 (Mosalam and Naito, 2000a). The shear forces and bending moments at different sections in the joists were compared and accordingly the models shown in Figure 8 for groups A and B gave the best match with the results obtained from the analyses of the building models.

Schematics of the test setup and loading protocols for both groups A and B are given in Figure 9 with the displacement values listed in Tables 3 and 4. Complete discussions on the development of the test specimens and their loading protocols can be found in (Mosalam and Naito, 2000a) and (Mosalam and Naito, 2000b).

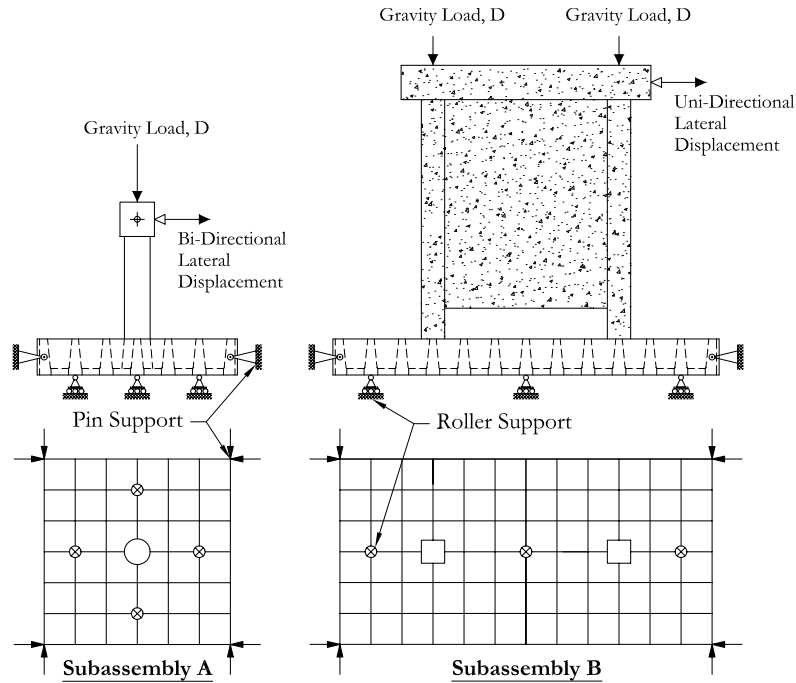


Figure 8: Boundary conditions for the waffle slab subassemblies

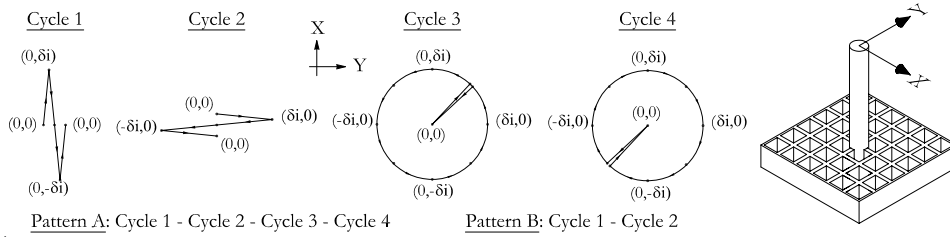


Figure 9: Subassembly type A bi-directional displacement pattern

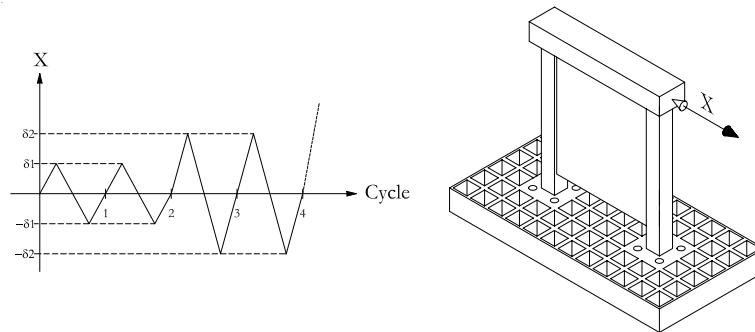


Figure 10: Subassembly type B unidirectional displacement pattern

Table 3: Applied displacement history for group A subassemblies

Cycle Group #	1	2	3	4	5	6	7
Drift Ratio [%]	0.09	0.15	0.27	0.43	0.58	0.72	0.84
Pattern	A	A	A	A	A	A	A
Cycle Group #	8	9	10	11	12	13	14
Drift Ratio [%]	1.01	0.15	1.20	1.40	0.15	2.10	2.79
Pattern	A	B	A	A	B	A	A
Cycle Group #	15	16	17	18	19	20	21
Drift Ratio [%]	0.15	3.48	4.14	0.15	6.84	0.15	11.04
Pattern	B	A	A	B	A	B	A

Table 4: Applied displacement history for group B subassemblies

Cycle #	1-2	3-4	5-6	7-8	9-10	11-12	13-14
Drift [%]	0.07	0.13	0.26	0.41	0.53	0.65	0.78
Cycle #	15-16	17	18-19	20-21	22	23-24	25
Drift [%]	0.90	0.13	1.10	1.27	0.13	1.90	0.13

4. MODELLING SOIL STIFFNESS FOR GROUP B

To evaluate the effect of soil conditions on the tested subassemblies of group B, a detailed nonlinear finite element (FE) model was developed and is illustrated in Figure 11. This FE model accounts for cracking and plastification of the concrete. The reinforcement is modeled using embedded reinforcing bars, which add stiffness and strength to the concrete FE's. In the FE analysis, the soil stiffness is accounted for using the recommendation of FEMA-273 (Mosalam and Naito, 2000b).

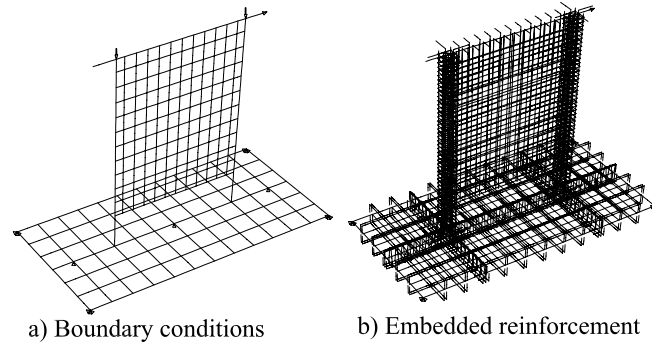


Figure 11: FE model of group B test subassembly

For soil shear modulus G_s and Poisson's ratio ν_s and columns supported on rectangular footings with length L and width B with foundation shape factor α and embedment factor β , the soil spring constant $k = \alpha \beta [4 G_s R / (1 - \nu_s)]$ with $R = \sqrt{B L / \pi}$ is determined. Using typical values, the soil spring constant $k = 1714$ kN/cm. Another solution to determine the unit sub-grade spring coefficient $k_{sv} = 1.3 G_s / B (1 - \nu_s)$ is based on the assumption of flexible foundation. In that case, the soil spring constant $k = 835$ kN/cm. Four cases are considered in the FE analytical study: (1) Infinitely stiff soil, i.e. rotation of the footing is prevented with $k = \infty$, (2) Finite soil stiffness with $k = 1714$ kN/cm and (3) $k = 835$ kN/cm, and (4) Free rotation of the footing, i.e. no soil effect with $k = 0$.

Introducing flexible supports at the column end is similar to changing its axial load with the applied lateral displacement. Accordingly, column axial loads were varied to control the rotation of the top beam (footing) in the test setup. Comparison between the analytical solutions of the determined column loads in the tension and compression

sides for the studied four cases is presented in Figure 12. It is to be noted that the case of free rotation of the top loading beam is shown as constant column load at 136 kN. In this study, to model the soil flexibility, the sum of the two column loads were kept constant at $2 \times 136 = 272$ kN, with column loads varying as functions of the applied displacement as illustrated by the idealized loading of Figure 12. Two cases were adopted for the experimental study; the first, evaluated in specimen B1, investigated the behavior under free rotation, the second, evaluated in specimen B2, investigated the behavior of the specimen with a finite soil stiffness of approximately 835 kN/cm.

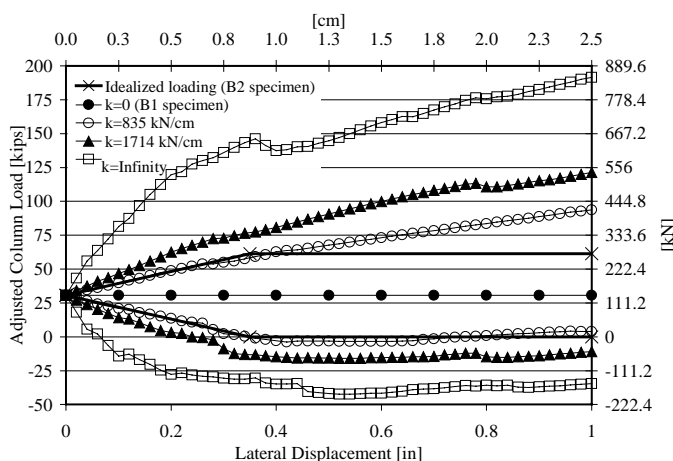






Figure 12: Analytical solutions for the column loads (compression is positive)

5. RESULTS AND DISCUSSIONS

For group A, the two specimens A1 and A2 were identical to investigate repeatability of results. Results from specimen A2 is reported herein. The photographs in Table 5 present the progression of main events. The full-scale load-drift ratio response is shown in Figure 13. From this figure, one observes the strength and stiffness degradation due to cycling and the dissipation of hysteretic energy. The East-West direction is lower in strength and stiffness than the North-South direction due to the selected loading path (cycles in the North-South were applied first). Moment-rotation relationships for the plastic hinge response are developed using the two techniques shown by the insert of Figure 14. This figure compares the experimental relationships (after scaling them to the full-scale dimensions) with the analytical predictions based on section analysis. The plots of Figure 14 demonstrate that the analytical model over-estimated the response compared with the backbone curve. This difference is expected since the backbone curve accounts for cyclic loading effects, which are not included in the section analysis.

Table 5: Damage progression in subassembly A2

	
<p>2.8% Drift – Cracking on column and joists</p>	<p>3.5% Drift – Spalling from interface into joists</p>
	
<p>6.8% Drift – Excessive spalling</p>	<p>11% Drift – Column bars buckling & fracture</p>

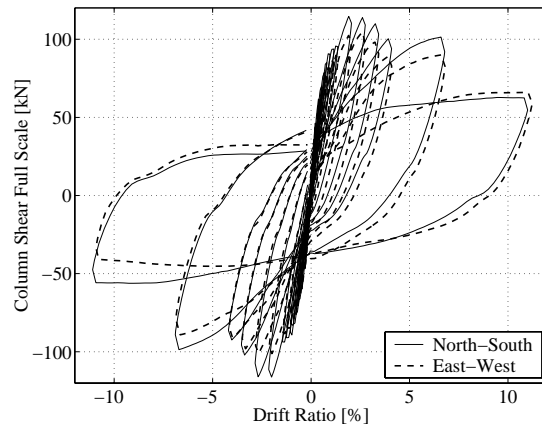


Figure 13: Load–drift ratio relationships for subassembly A2

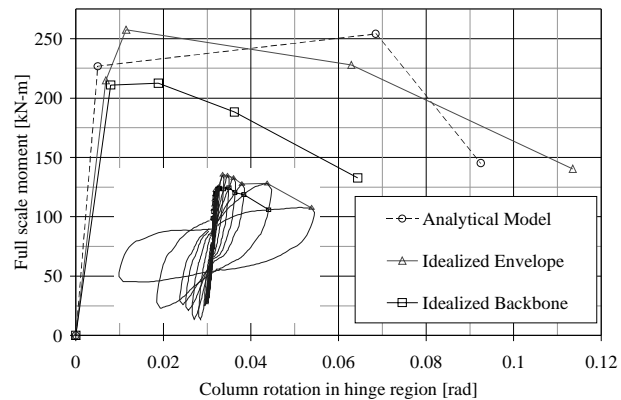


Figure 14: Circular column plastic hinge models for subassembly A2

The method used for modeling soil stiffness in subassembly B2 was successful in reducing the footing rotation as demonstrated by the comparison of Figure 15. The load-displacement relationships for specimens B1 and B2 are shown in Figure 16, which indicates symmetric response for B1 and asymmetric one for B2. This is attributed to the obtained modes of failure of B1 and B2 as discussed subsequently. Higher peak load in the positive (North) direction is observed for B2 since the North column of B2 did not punch through the slab and instead failed in compression-shear manner.

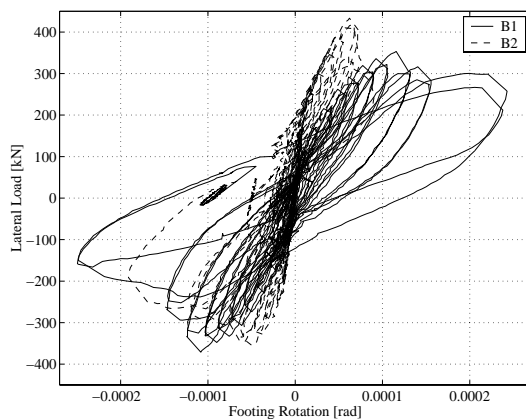


Figure 15: Lateral load-footing rotation relationships for group B

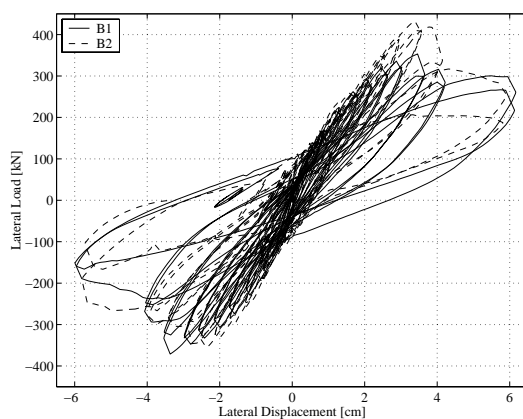
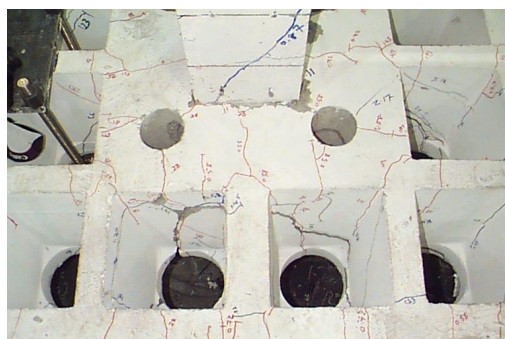


Figure 16: Lateral load-displacement relationships for group B

Damage of group B specimens followed a similar progression. Damage initiated with formation of flexure cracks in the longitudinal joists (i.e. joists parallel to the plane of the wall) due to the gravity loads. This was followed by formation of flexure cracks along the interfaces between the columns and the waffle slab. Subsequently, formation of flexure cracks within the laterally unsupported length of the columns took place with increase of cracking along the column height. Formation of flexure-shear cracks in the joists occurred due to torsional effects in the transverse joists (i.e. joists perpendicular to

the plane of the wall). Moderate shear cracks within the laterally unsupported length of the columns formed and extended along the compression diagonal of the walls. Failure modes of specimens B1 and B2 differed as shown in Figure 17. Ultimate response of B1 (with free footing rotation) was controlled by a brittle punching failure of the waffle slab at both columns. The punching failure surfaces are cylindrical and extend in the transverse direction (Figure 18). The ultimate response of B2 (accounting for soil stiffness) was controlled by punching of the slab at the South column (comparable to punching surfaces of B1) followed immediately by shear failure of the North column.



a) North column punching (B1)



b) North short column failure (B2)

Figure 17: Failure mechanisms of group B

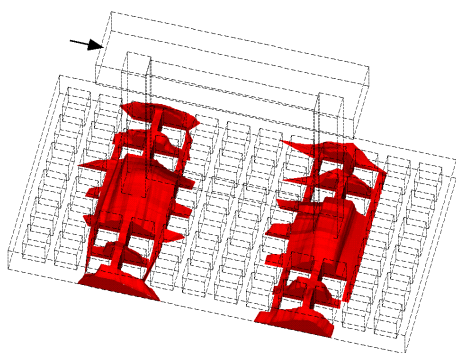


Figure 18: Punching surfaces of B1

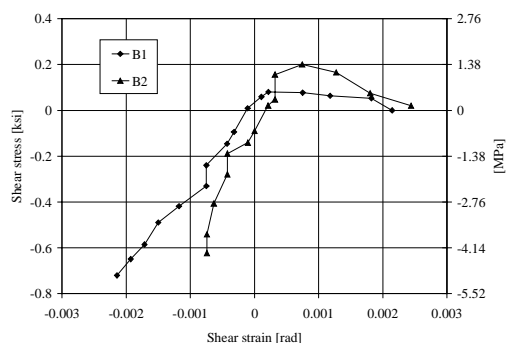


Figure 19: South column results

Envelopes of the shear stress-strain relationships of B1 and B2 are shown in Figure 19. In this figure, negative shear stress corresponds to the state when the column is under axial tension. The behavior is asymmetric due to the compression strut action of the wall and its interaction with the bounding frame elements. Under the combined action of shear and compression, the column forms a mechanism and is unable to resist any additional shear load. Conversely, under the combined action of shear and tension, the columns behave almost elastically and do not soften prior to the ultimate lateral load capacity of the system.

6. CONCLUDING REMARKS

From the above results, the following conclusions may be inferred:

1. The dominant mode of failure of group A is formation of column plastic hinging at the vicinity of the column/waffle slab interface. This took place in a ductile manner without loss of gravity load resistance up to 10% of applied column drift ratios.
2. The perforated waffle slabs of group A suffered minor damage up to 10% applied column drift ratio. This is due to formation of plastic hinging at the column/waffle connection. The existence of plane of weakness due to the cold construction joint between the column and the stiff waffle slab led to early isolation of the waffle slab floor from the relatively flexible column leading to an overall flexible system.
3. The ductile system response of group A was achieved by proper detailing of the column/waffle slab connection. The anchorage of column longitudinal reinforcing bars and concrete core confinement by the column transverse reinforcement shown in Figure 3 proved to be very effective for achieving the observed ductility.
4. The FE analysis for the effect of the soil stiffness in group B on the footing rotation was essential for developing realistic boundary conditions of the tested system.
5. The global lateral load-displacement responses of B1 and B2 were comparable. On the contrary, the local response and mode of failure were significantly affected by the assumed soil stiffness. Reducing footing rotation (i.e. stiff soil) resulted in a local compression-shear failure and punching failure. On the other hand, free footing rotation (i.e. soft soil) resulted in only punching failure.
6. The punching failure in group B took place with cylindrical failure surface extending in the transverse direction normal to the direction of the lateral loading.
7. Interaction between the partial infill wall and the short column led to asymmetric shear stress-strain relationships due to the shear-axial interaction. Small demand is observed with axial compression and elastic response is obtained with axial tension.

7. REFERENCES

- Mosalam, K. M. and C. J. Naito (2000a). Seismic evaluation of gravity load-designed column-grid system. *Submitted to J. of Structural Engineering, ASCE.*
- Mosalam, K. M. and C. J. Naito (2000b). Seismic evaluation of reinforced concrete grid supported by partially infilled frame. *Submitted to J. of Structural Engineering, ASCE.*

8. KEYWORDS

Waffle slab, Infill wall, Bi-directional load, Punching, Short column, Soil stiffness

ULTIMATE LIMIT STATE OF RC COLUMNS

Manabu YOSHIMURA¹ and Noriyuki YAMANAKA²

ABSTRACT

During the 1995 Kobe earthquake, about thirty concrete buildings, mostly steel encased RC construction, suffered complete collapse at an intermediate story. Such collapse is believed to be due to that columns at a certain intermediate story underwent severe shear failure and eventually came to be unable to sustain their axial load. To study this, seismic tests of RC columns subjected to rather low axial load corresponding to the intermediate story were conducted. The ultimate limit state, as was defined in this paper as a state of the loss of axial load carrying capacity or collapse, was mainly discussed. The major findings from the study are as follows:

- (1) The lateral deformation, axial deformation and input energy at the ultimate limit state vary depending on the deformation path imposed on each specimen, in other words, it can not be said that the collapse occurs when any of them reaches a certain value.
- (2) On the contrary, the deformation increment ratio, ratio of vertical deformation increment to lateral deformation increment, at the ultimate limit state does not vary depending on the deformation path. And the reason for this is explained by plastic theory in such that the collapse occurs when the failure surface is reduced to a certain size.
- (3) The collapse occurs when the lateral load decreases to about 10 % of the maximum load.

1. INTRODUCTION

During the 1995 Kobe earthquake, about thirty concrete buildings, mostly steel encased RC construction, suffered complete collapse at an intermediate story (Architectural Institute of Japan, 1998). Such collapse is believed to be due to that columns at a certain intermediate story underwent severe shear failure and eventually came to be unable to sustain their axial load. In the past a number of seismic tests of RC columns, where loaded up to the loss of axial load carrying capacity, were conducted. However, they were mostly those subjected to high axial load and those subjected to low axial load corresponding to the intermediate story were very few (Yamanaka and Yoshimura, 2000).

This paper is intended to clarify how RC columns subjected to rather low axial load come to lose their axial load carrying capacity during earthquake actions. The column's loss of such capacity or collapse directly jeopardizes human lives, therefore, is considered the clearest

¹ *Department of Architecture, Tokyo Metropolitan University, Hachioji, Japan*
Email: myoshim@arch.metro-u.ac.jp

² *Department of Architecture, Maebashi Institute of Technology, Maebashi, Japan*

definition of the ultimate limit state. The discussions to be stated below put main emphasis on what is a good index to express the ultimate limit state so defined among those such as reduction of lateral load, lateral deformation, axial deformation, input energy and something different from them.

2. SPECIMENS AND TEST PARAMETERS

Two test series were planned. One was of a type failing in shear after flexural yielding, referred to as FS (Flexure-Shear) series, and the other was of a type initially failing in shear, referred to as S (Shear) series. Specimens of the both series are outlined in Table 1 and their reinforcement details are shown in Fig. 1. The specimens were rendered a cantilever shape considering the easiness of loading. Test apparatus is shown in Fig. 2. The loading point was 900 mm high from the column base, 600 mm (height of specimen) plus 300 mm (height of universal joint). Hereafter lateral deformation is expressed by the deformation measured at the loading point divided by 900 mm.

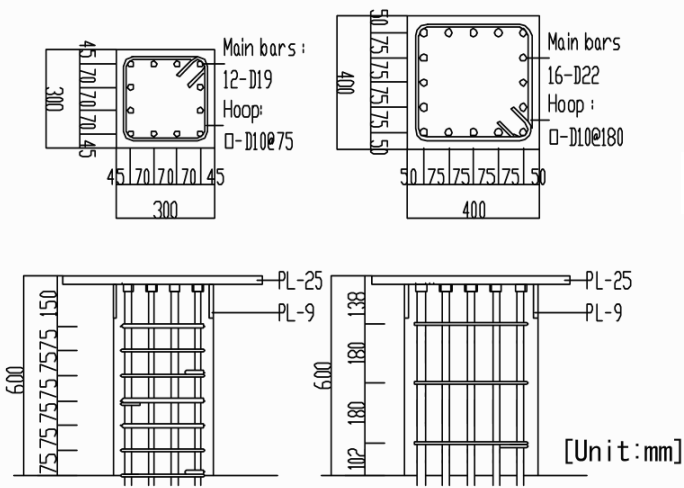
A loading manner was test parameter. Four loading manners were considered, as shown in Fig. 3: (1) monotonic loading to X-direction (1D(Monotonic), FS0 in Table 1), (2) cyclic loading to X-direction (1D(Cyclic), FS1 and S1), (3) bilateral loading with square deformation path (2D(Square), FS2 and S2), and (4) bilateral loading with rectangular deformation path (2D(Rectangular), S2A), where Y-deformation was set half X-deformation. FS0 was loaded to X-direction until constant axial load could not be maintained. All other specimens, after a few cycles of loading with small (basically 1% and 2%) deformation

Table 1 Test specimens

Series	Specimen name	Loading manner	Shear span ratio	Axial stress level	Flex. st./ Shear st.
FS	FS0	1D (Monotonic)	3.00	0.26	1.19
	FS1	1D (Cyclic)			
	FS2	2D (Square)			
S	S1	1D (Cyclic)	2.25	0.20	0.47
	S2A	2D (Rectangular)			
	S2	2D (Square)			

levels, were loaded to X-direction with Y-deformation being kept zero until constant axial load could not be maintained.

Yield stress of main bars and concrete strength were 387 and 27.0 MPa, and 547 and 25.1 MPa, respectively for FS and S series. Yield stress of hoop was 355 MPa for both series. Axial stress levels were set as 0.26 and 0.20 times as much as concrete strength, respectively for FS and S series.



(1) FS Series (2) S Series
Fig. 1 Reinforcement details

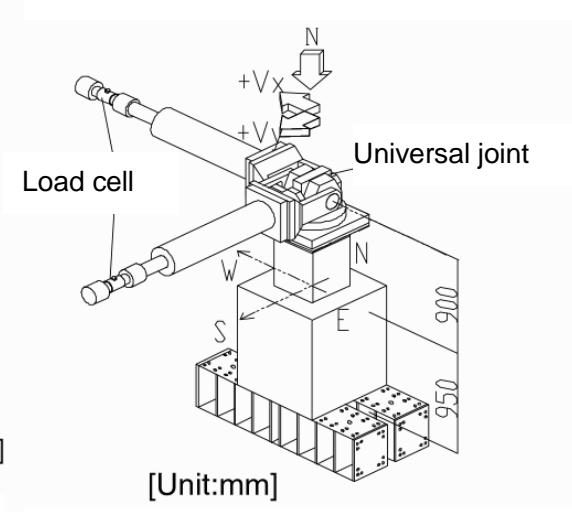


Fig. 2 Test apparatus

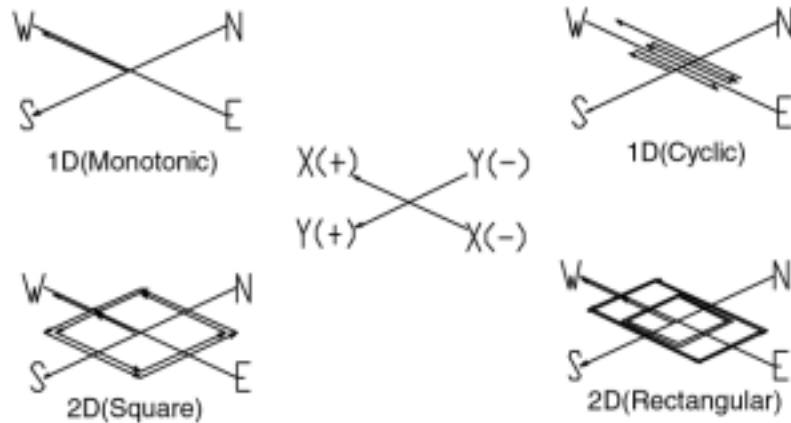
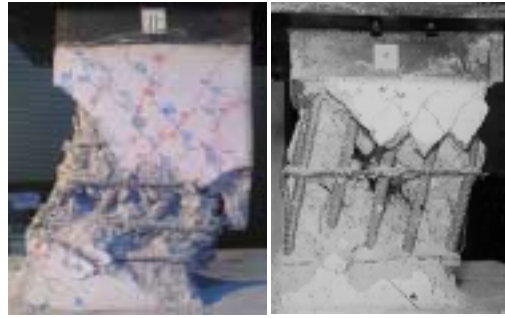


Fig. 3 Loading manners

3. TEST RESULTS AND DISCUSSIONS

As an example, final failure of FS1 and S1 was shown in Fig. 4. All specimens finally lost their axial load carrying capacity.



(1) FS1

(1) S1

Fig. 4 Final failure (North face)

3.1 Lateral Load - Lateral Deformation Relations

Lateral load - lateral deformation relations are shown in Fig. 5. Lateral load was estimated by considering P- effect produced by the axial load and the other lateral load. MLP (Maximum Load Point) and ULP (Ultimate Limit Point) were defined as a point where lateral load (estimated by SRSS of two lateral loads for the bilateral loading case) was maximum and a point where the axial load carrying capacity was lost, respectively.

The deformation and load of FS0 and FS1 at ULP and MLP (the latter case is shown in the parentheses) were 9.1 % and 19kN (2.0 % and 207 kN), and 8.4 % and 31kN (2.0 % and 198 kN), respectively. And the SRSS deformation and load of FS2 at ULP and MLP were 5.3 % and 18 kN (1.4 % and 175 kN). The fact that the deformation of FS2 at ULP was pretty smaller than the other two is believed to be due to the effect of the bilateral loading.

The deformation and load of S1 at ULP and MLP were 8.6 % and 39 kN (-2.0 % and -400 kN). And the SRSS deformation and load of S2A and S2 at ULP and MLP were 8.8 % and 34 kN (1.4 % and 388 kN), and 6.7 % and 31 kN (1.4 % and 378 kN), respectively. The fact that the deformation of S2 at ULP was smaller than the other two is believed to be due to the effect of the severe bilateral loading for S2 (the deformation path imposed on S2 was severer than on S2A).

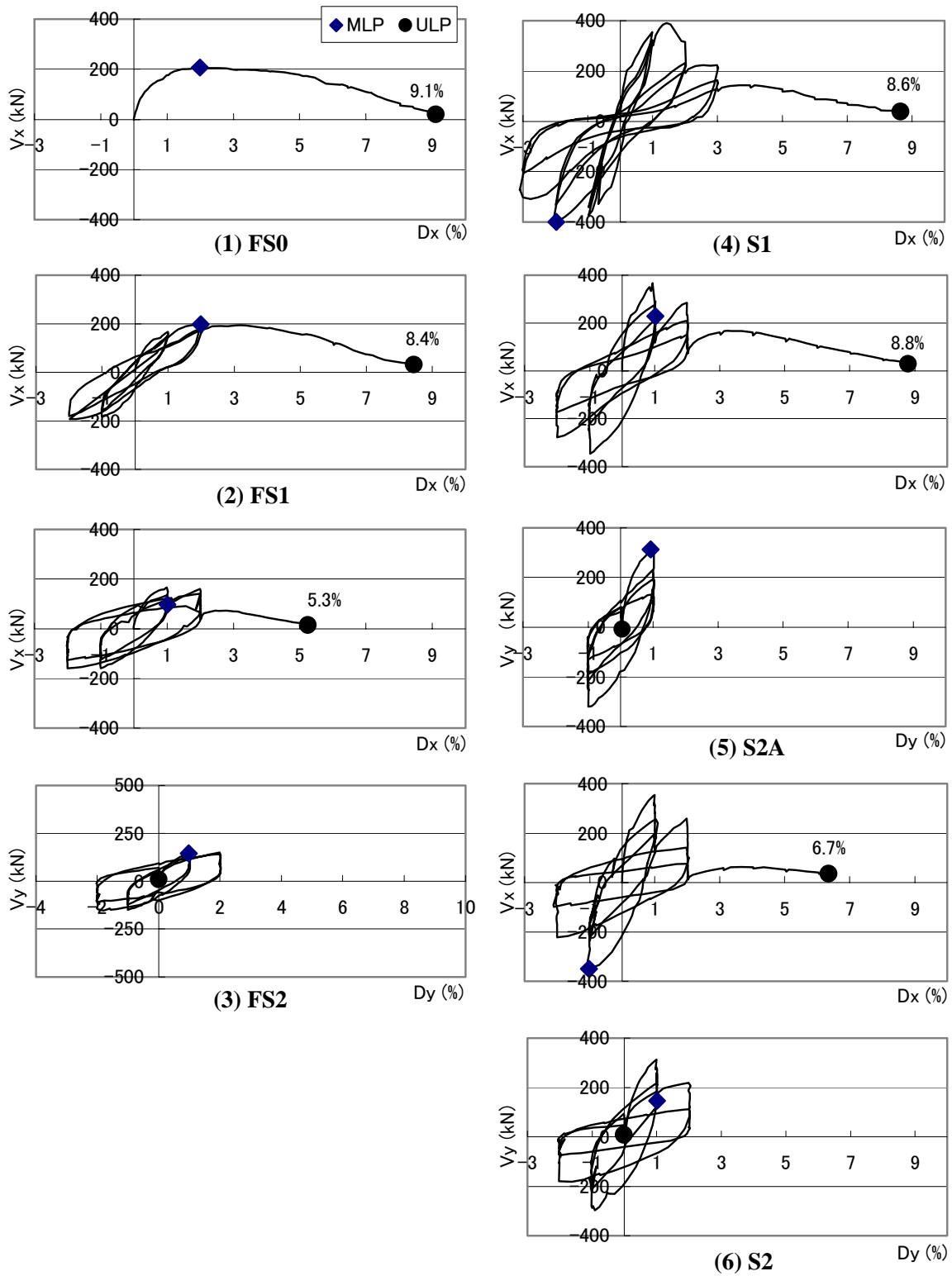


Fig. 5 Lateral load - lateral deformation relations

3.2 Axial Deformation

Axial deformation - lateral deformation relations are shown in Fig. 6. Axial deformation was measured at 620 mm high from the column base.

For FS0 the axial deformation first showed elongation and turned into shortening. Axial shortening at ULP was 5.4 mm. The behavior of FS1 was very close to FS0 (no influence of the cyclic loading). And for FS2 axial shortening, being accumulated during the bilateral loading, reached 9.4 mm at ULP, which was larger than the other two.

For S1 the axial shortening, being not much accumulated during the cyclic loading, was 10.3 mm at ULP. The behavior of S2A was very close to S1 (no influence of this type of bilateral loading). And for S2 the axial shortening, though accumulated during the bilateral loading, remained as small as 8.0 mm at ULP, which was smaller than the other two.

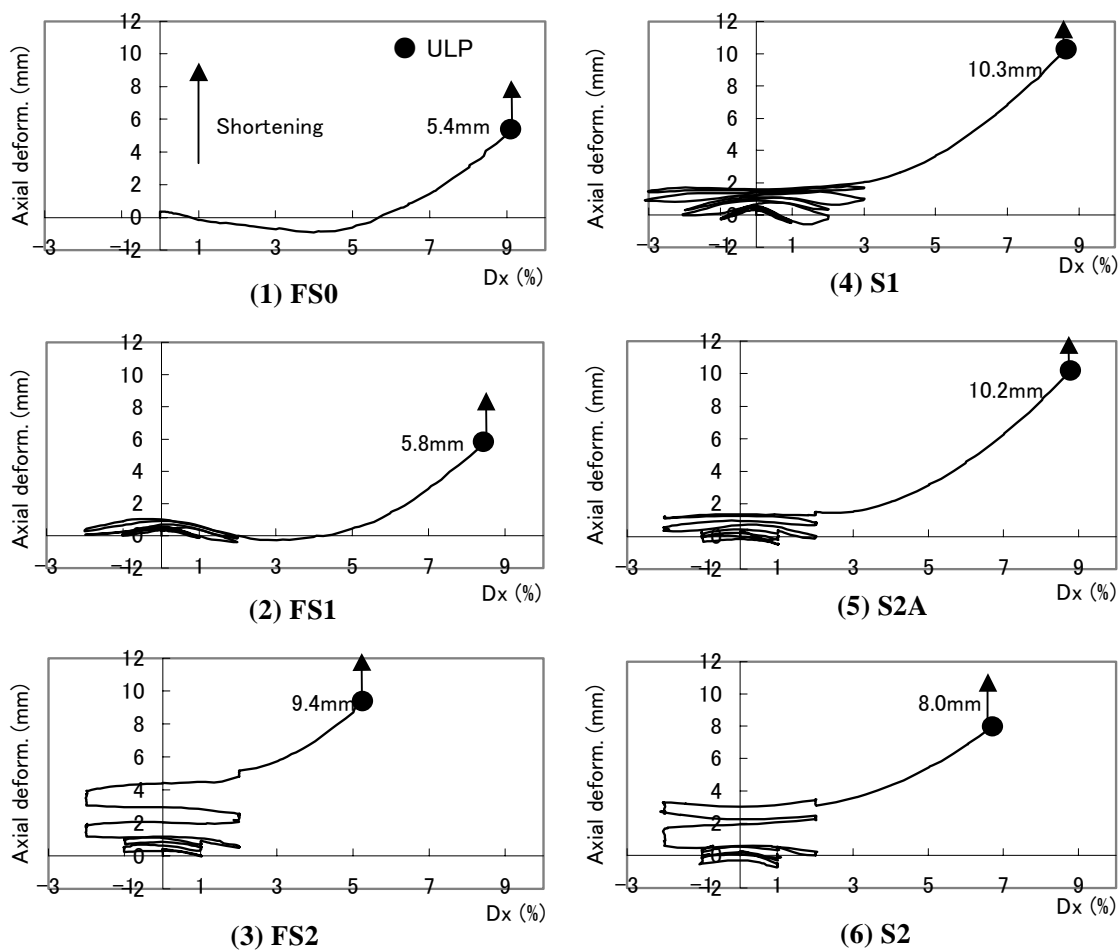


Fig. 6 Axial deformation - lateral deformation relations

Load and deformation data on the ultimate limit state are outlined in Figs. 7 through 10. As shown in Fig. 8, the lateral load at ULP was from 9.2 to 15.7 % of the maximum load for FS series and from 8.2 to 9.8 % for S series, indicating for both series that the loss of axial load carrying capacity occurred when the lateral load decreased to about 10 % of the maximum load. And Figs. 9 and 10 indicate that the lateral deformation and axial deformation at the ultimate limit state varied depending on the deformation path imposed on each column. In other words it can not be said for both series that the loss of axial load carrying capacity occurred when the lateral deformation or axial deformation reached a certain value (such trend is more pronounced for FS series).

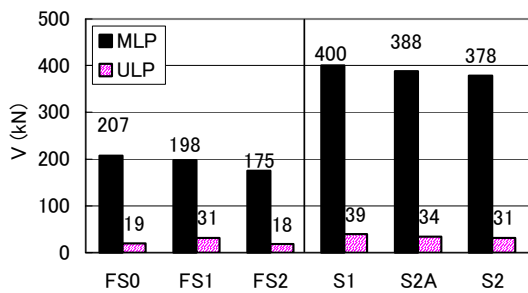


Fig. 7 Load at MLP and load at ULP

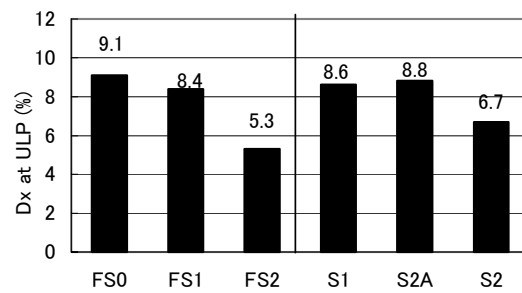


Fig. 9 Lateral deformation at ULP

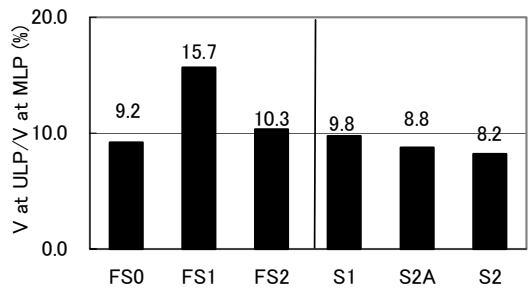


Fig. 8 Load at ULP / load at MLP

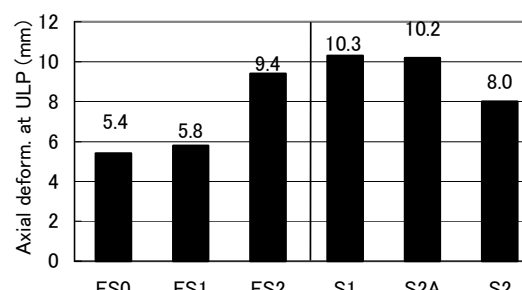


Fig. 10 Axial deformation at ULP

3.3 Input Energy

The external works of lateral load and axial load (E_h and E_v) were computed. The sum of E_h and E_v (total energy) and E_v (vertical energy) are shown in Figs. 11.

For FS0 the total energy and vertical energy at ULP were 15 and 3.3 kN·m. For FS1 the total energy, being accumulated during the cyclic loading, and vertical energy, being not

accumulated during that period, were 22 and 3.5 kN·m at ULP. And for FS2 the total energy, being accumulated much during the bilateral loading, and vertical energy, being not accumulated during that period, were 40 and 5.7 kN·m at ULP.

For every specimen of S series the total energy was accumulated much during the cyclic or bilateral loading while the vertical energy was not. The total energy and vertical energy at ULP were from 44 to 51 kN·m and from 5.9 to 7.8 kN·m, respectively.

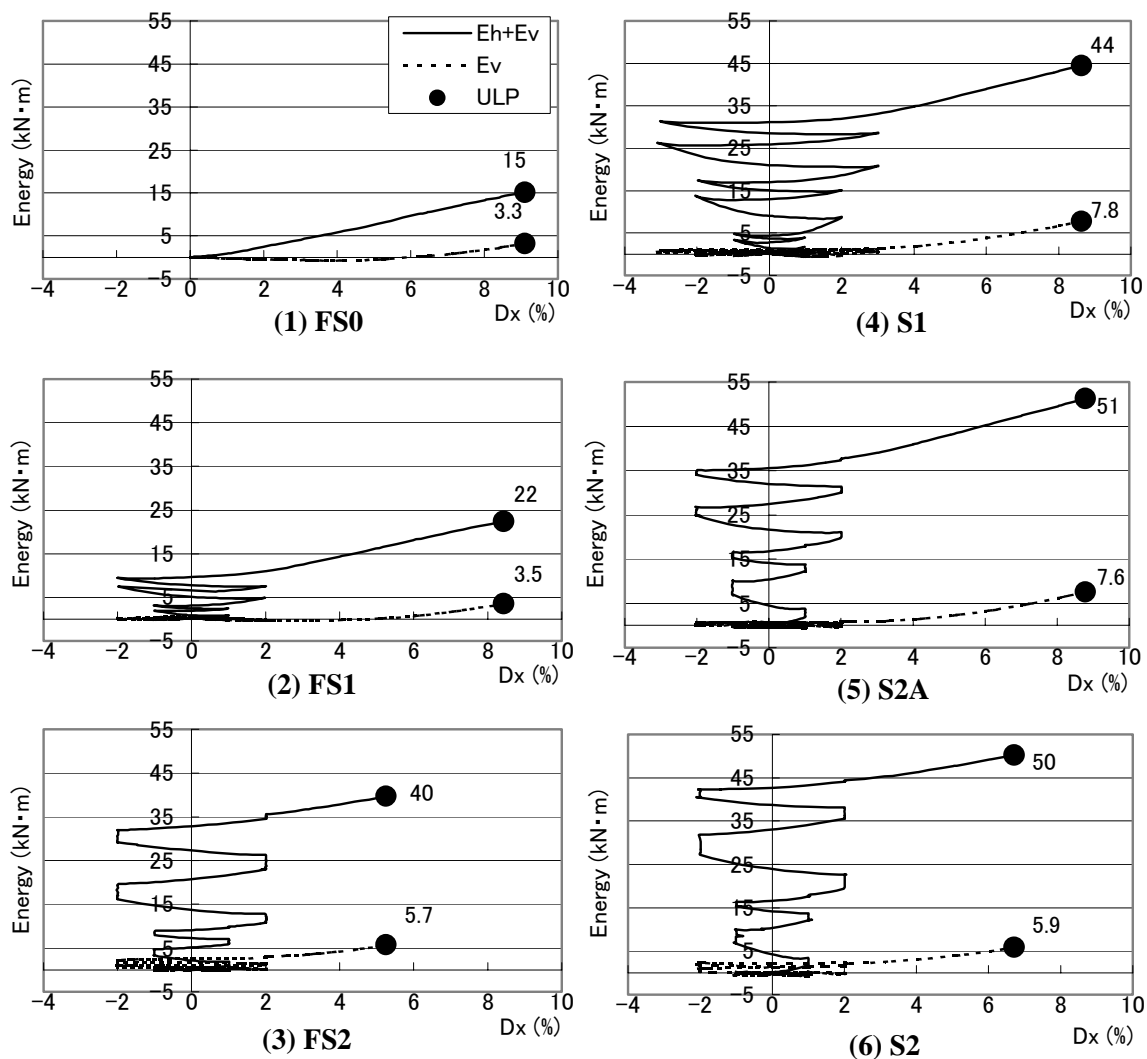


Fig. 11 Energy - lateral deformation relations

Energy data on the ultimate limit state are outlined in Figs. 12 and 13. It can not be said for both series that the loss of axial load carrying capacity occurred when total energy or vertical

reached a certain value (such trend is more pronounced for FS series). This result indicates that the input energy at the ultimate limit state varied depending on the deformation path imposed on each column. And from the discussions made up to now it is clear that any of the lateral deformation, vertical deformation and input energy can not be a good index to express the ultimate limit state.

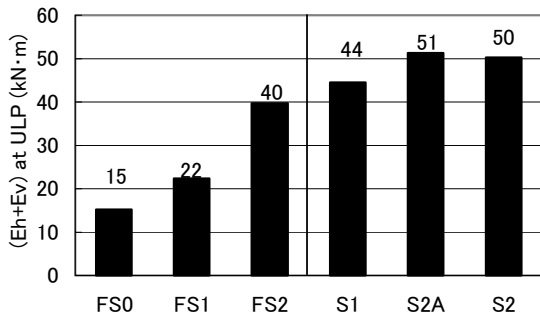


Fig. 12 Total energy at ULP

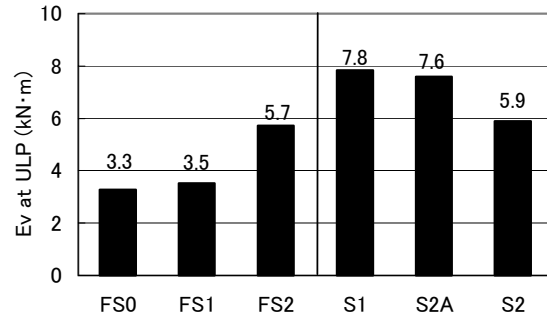


Fig. 13 Vertical energy at ULP

3.4 Deformation Increment Ratio

Figure 14 demonstrates the ratio of vertical deformation increment to lateral deformation increment for FS series. Note that for the simplicity of discussions only the last loading to X-direction with lateral deformation more than 2% was considered for FS1 and FS2. This ratio is called hereafter DI (Deformation Increment) ratio. The graph, though includes some plots where DI ratio changes very rapidly, show clear tendency that DI ratio increases as the loading proceeds. DI ratio at ULP ranges from 0.17 to 0.31.

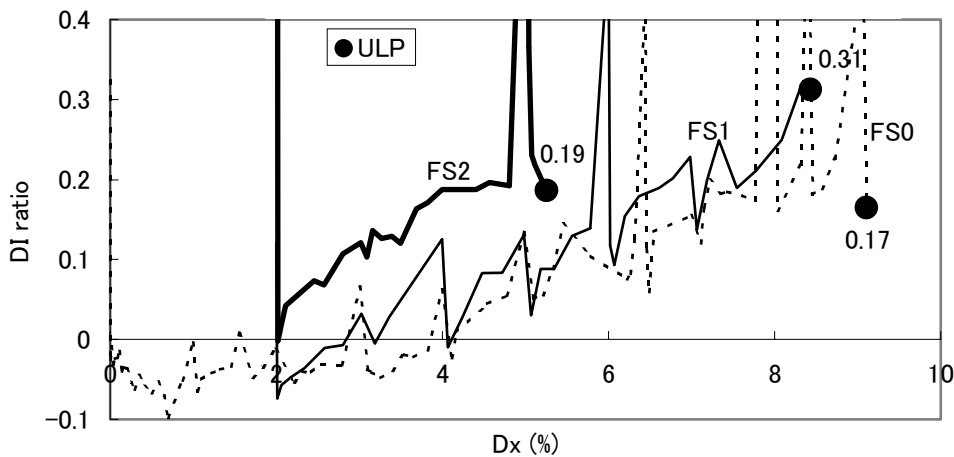
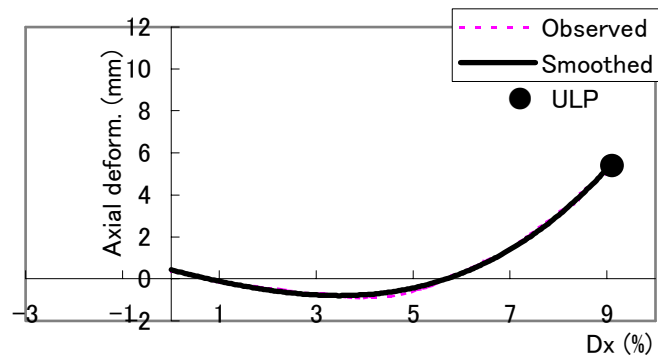
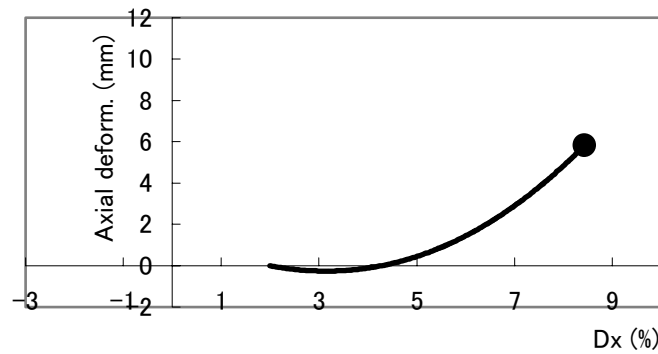


Fig. 14 DI ratio - lateral deformation relations (FS series)

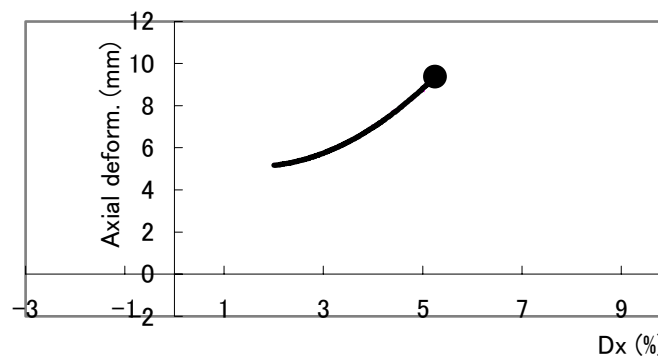
To have a clearer understanding of DI ratio, it was attempted to smooth the observed data. Figure 15 compares the observed vertical deformation - lateral deformation relations and smoothed ones. The smoothing was done in such that the observed data were approximated by a cubic equation using the least square method. The smoothed curve just fits the observed. DI ratio based on the smoothing is shown in Fig. 16. DI ratio at ULP is almost equal for the three specimens. The smoothed DI ratio at ULP is shown in Fig. 17, where the results for S series are also included. This result indicates for both series that DI ratio at the ultimate limit state did not vary or that the loss of axial load carrying capacity occurred when DI ratio reached a certain value (such trend is more pronounced for FS series).



(1) FS0



(2) FS1



(3) FS2

Fig. 15 Smoothed axial deformation - lateral deformation relations (FS series)

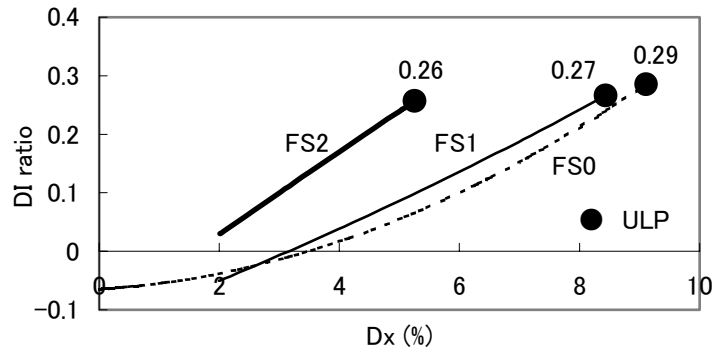


Fig. 16 Smoothed DI ratio - lateral deformation relations (FS series)

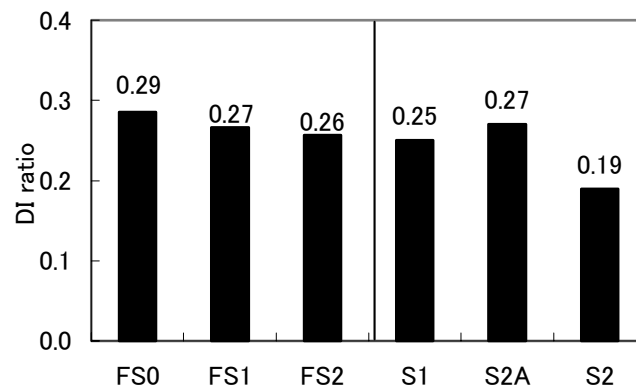


Fig. 17 Smoothed DI ratio at ULP

The reason that DI ratio at ULP was close for each series will be discussed below. Figure 18 shows a conceptual sketch of lateral strength - axial strength interaction curve (failure surface). Initial failure surface in the figure, which corresponds to the state of MLP, was depicted such that the points of initial axial compression strength and initial axial tension strength lay on it. The failure progress occurring after MLP is believed to accompany the deterioration of concrete, resulting in the reduction of axial compression strength as well as lateral (shear) strength. But axial tension strength is considered to keep an initial value because it is not affected by concrete strength. The reduced failure surface in the figure was depicted by considering the above. One can know from the flow rule in plastic theory that DI ratio is equivalent to a direction normal to the failure surface. Though exactly speaking DI ratio has to be evaluated on the basis of plastic deformation, it is not a problem because elastic deformation is negligible small for this case. As is shown in the figure, as the loading proceeds (the failure surface is reduced), DI ratio is increasing, which coincides with the observations. And the fact that DI ratio at ULP was close for each series regardless of the

deformation path seems to indicate the loss of axial load carrying capacity occurs when the failure surface is reduced to a certain size.

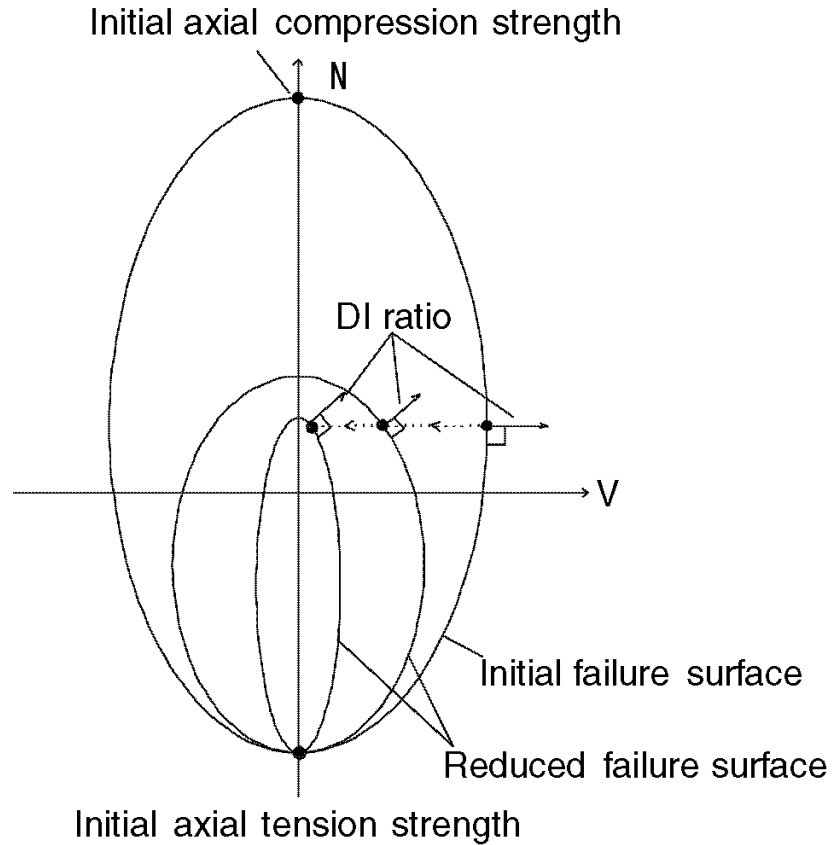


Fig. 18 Reduction of failure surface and changes of deformation increment ratio

It was attempted to estimate how the failure surface was reduced. Figure 19 shows the results estimated for FS series at some specified load points: DI of 0.0, 0.1 and 0.2, and ULP.

For the estimation the followings were assumed:

- (1) Failure surface is idealized as ellipse.
- (2) Axial tension strength is not to change.
- (3) The specified load point lies on the failure surface.
- (4) DI value observed at the specified load point gives a direction normal to the failure surface.

This figure is considered to show the reduction process of failure surface up to the ultimate limit state. The failure surface at the ultimate limit state is fairly close for the three specimens.

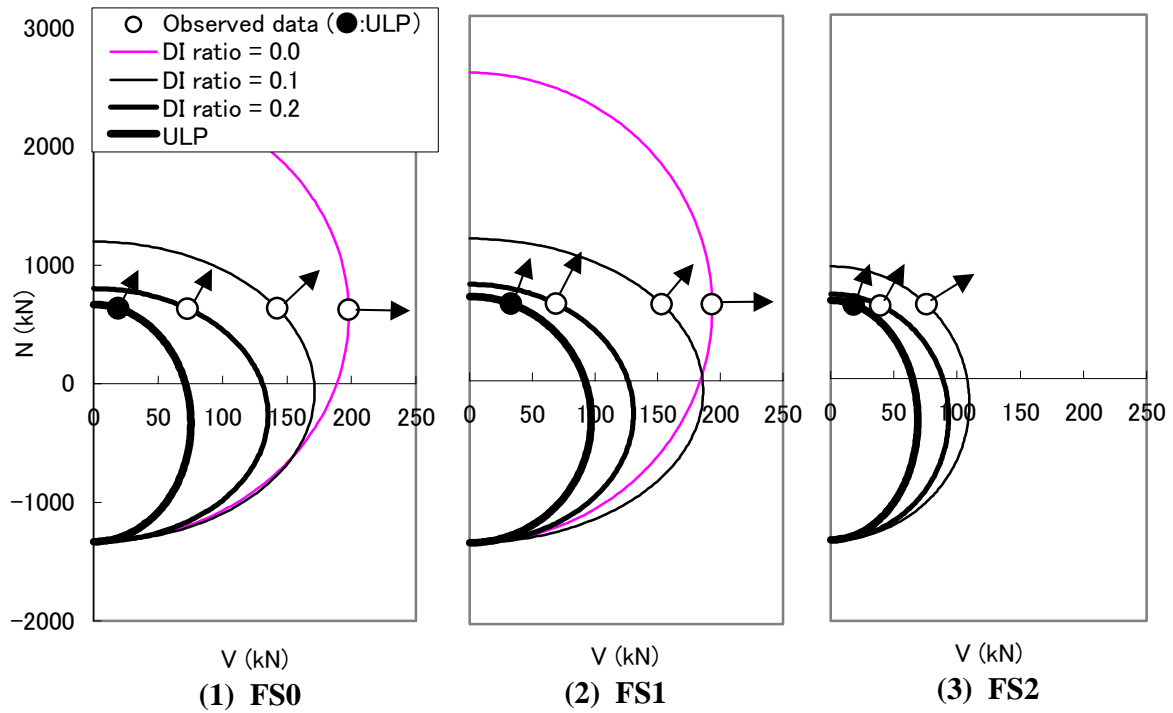


Fig. 19 Estimated reduction of failure surface

4. CONCLUSIONS

The seismic tests of RC columns subjected to rather low axial load were conducted to clarify the ultimate limit state, as was defined as a state of the loss of axial load carrying capacity or collapse. The major findings from the study are as follows:

- (1) The lateral deformation, axial deformation and input energy at the ultimate limit state vary depending on the deformation path imposed on each specimen, in other words, it can not be said that the collapse occurs when any of them reaches a certain value.
- (2) On the contrary, DI ratio, ratio of vertical deformation increment to lateral deformation increment, at the ultimate limit state does not vary depending on the deformation path. The reason for this is explained by plastic theory in such that the collapse occurs when the failure surface is reduced to a certain size.
- (3) The collapse occurs when the lateral load decreases to about 10 % of the maximum load.

5. REFERENCES

Architectural Institute of Japan. (1998). Recommendation to RC structural design after Hanshin-Awaji earthquake disaster – Cause of particularly noticed damages and corresponding RC structural design details

Yamanaka, N. and Yoshimura, M. (2000). Collapse of flexure-shear and shear failing RC columns subjected to low axial load. Proceedings of the Japan Concrete Institute. Vol.22. No.3. 325-330

6. KEYWORDS

Collapse, Intermediate story, Ultimate limit state, Axial load carrying capacity, Deformation increment ratio, Flow rule, Failure surface, Shear Failure

SESSION B-3: COLUMNS AND BEAM-COLUMN JOINTS

Chaired by

◆ Michael Valley and Susumu Kono ◆

DATABASE STUDY ON CAPACITIES OF R/C COLUMNS STRENGTHENED WITH FRP SHEETS*

Shigeru FUJII,¹

Yasuhiro MATSUZAKI², Katsuhiko NAKANO² and Hiroshi FUKUYAMA³

ABSTRACT

Using the database consisting of 236 R/C column specimens conducted in Japan, the characteristic behaviors of strengthening by fiber wrapping were analyzed. The following findings were obtained: (1) The amount of shear reinforcement, the span to depth ratio, the axial compressive stress level influence on the strength and deformation capacities of retrofitted columns by fiber sheet wrapping (2) Shear strength of retrofitted columns can be predicted by previous design equations based on the strut and tie models as same as for usual R/C columns, in which the effective fiber strains of about 1% is appropriate. (3) There are few test data about the confining effect of fiber sheet wrapping on bond resistance of longitudinal bars. Further research effort is required to evaluate the shear strength of columns governed by the splitting of cover concrete along longitudinal bars. (4) The ductility ratio can be roughly estimated as a function of the shear to flexural strength ratio. (5) For the specimens with plain round longitudinal bars, the previous equations based on the strut and tie model cannot be applied because of the poor bond capacity.

1. INTRODUCTION

In the past ten years, a lot of experimental research has been conducted around the strengthening of RC columns by fiber sheet wrapping in Japan. To develop the design guidelines, the committee for 'Structural Use of New Fiber Reinforcing Materials' in Architectural Institute of Japan (AIJ) has been collecting the test data. This paper reports on the database analysis of column capacities and the applicability of current R/C design equations for shear and splitting bond failures. The characteristic behavior and the

* This report was presented at International Symposium on Fiber-Reinforced-Plastic Reinforcement for Concrete Structures (FRPRCS4) held at Baltimore, US in 1999.

¹ Department of Global Environment Engineering, Kyoto University, Japan
Email:fujii@archi.kyoto-u.ac.jp

² Department of Architecture, Science University of Tokyo, Japan

³ Institute of Seismology and Earthquake Engineering at the Building Research Institute, Japanese Ministry of Construction, Tsukuba, Japan

strengthening effect by fiber sheet wrapping are discussed. For the strengthened specimens preceded by flexural yielding, the improvement of ductility by fiber sheet wrapping is analyzed.

2. CONTENTS OF DATABASE

The compiled database contains a total of 236 column specimens with rectangular sections. Table 1 shows the classification of the data regarding the types of the strengthening method and the observed failure modes. Table 2 shows the variations of the experimental parameters.

Table 1 Classifications of regular column data

Specimens types yielding	flexural failure	shear failure	bond failure	shear failure after flexural	total
RC	3	27	4	9	53
Carbon Wrap	32	41	9	20	102
Aramid Wrap	11	20	0	11	42
Steel Jacket	11	3	1	1	16
total	57	101	14	41	213

Table 2 Variations of experimental parameters

	concrete strength σ_B (MPa)	sheet reinf. ratio p_{wf} (%)	shear span to depth ratio M/VD	tensile reinf. ratio p_t (%)	axial stress ratio $P/A_c\sigma_B$	column depth D (mm)
min.-max.	17-37	0.01-0.45	1.5-6.0	0.5-2.5	0.0-0.6	200-600
frequent range	21-30	0.04-0.10	1.5-2.0	1.0-1.5	0.1-0.2	200-300

3. MECHANICAL PROPERTIES OF FIBER SHEET

The fiber types used in the experiments are limited to carbon and two types of aramid fibers. Figure 1(a) and (b) show the comparisons between nominal and experimental mean values of the tensile strength and the modulus of elasticity of fiber sheet. The nominal tensile strength is smaller than the measured mean experimental values. Nominal strength is the

manufacture-guaranteed catalogue value considering the safety allowance of 3σ (σ : standard deviation). It is noted that the tensile strength of fiber sheet is defined for the total sectional area of only fibers not including the binding epoxy-resin. On the other hand, the nominal value of the modulus of elasticity closely coincides with the experimental mean values.

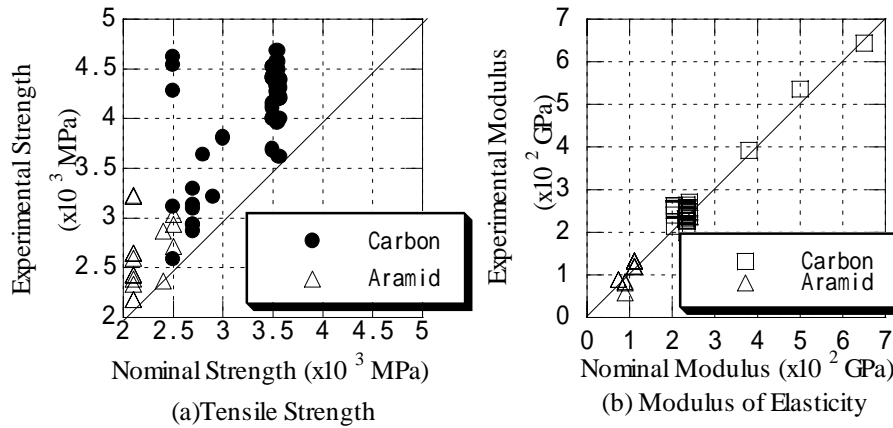


Fig.1 Mechanical Properties of Fiber Sheet

4. IMPROVEMENT OF SHEAR AND BOND STRENGTHS

Effective shear reinforcement amount -- Tests indicate that the shear strength improvement is larger for the specimens with carbon fibers than aramid fibers because of the different modulus of elasticity. To evaluate the shear strengthening effect it is convenient to define the effective shear reinforcement amount $p_{we}\sigma_{we}$,

$$p_{we}\sigma_{we} = p_{ws}\sigma_{sy} + p_{wf}E_f\varepsilon_f \quad (\text{Eq.1})$$

Where, p_{ws} and p_{wf} : the reinforcement ratio of steel hoops and fiber sheet,
 E_f : modulus of elasticity of fiber sheet,
 σ_{sy} : yield strength of steel hoops, ε_f : effective fiber strain

The observed fiber strain at maximum shear is usually less than its potential elongation capacity because of the elastic property of fiber reinforcement. In this study, a constant value of 1.0% as the effective strain ε_f is used for the analysis as the first step, which is the roughly estimated average value of the measured fiber strains in shear cracking regions in several previous test specimens.

Applications of previous R/C shear strength equations -- The shear strength equation (Eq.2) in AIJ Design Guideline(1) was used in the analysis.

$$V_{cal} = b j_t p_w \sigma_{wy} \cot \phi + \tan \theta (1 - \beta) b D v \sigma_B / 2 \quad (\text{Eq.2})$$

Where $\tan \theta = \{(L/D)^2 + 1\}^{0.5} - L/D$ (Eq.3)

$$\beta = \{(1 + \cot^2 \phi) p_w \sigma_{wy}\} / (v \sigma_B) \quad (\text{Eq.4})$$

b, D : width and overall depth of the section
 j_t : distance between the top and bottom bars;
 L : clear span of the member; σ_B : compressive strength of concrete,
 σ_{wy} : strength of the shear reinforcement, p_w : shear reinforcement ratio,
 $v = 0.7 - \sigma_B / 200$ (in N/mm^2): effective concrete compressive strength,
 ϕ : angle of the compressive strut in the truss mechanism,
 $\cot \phi$: minimum of $(2.0, j_t / (D \tan \theta), \{v \sigma_B / (p_w \sigma_{wy}) - 1\}^{0.5})$

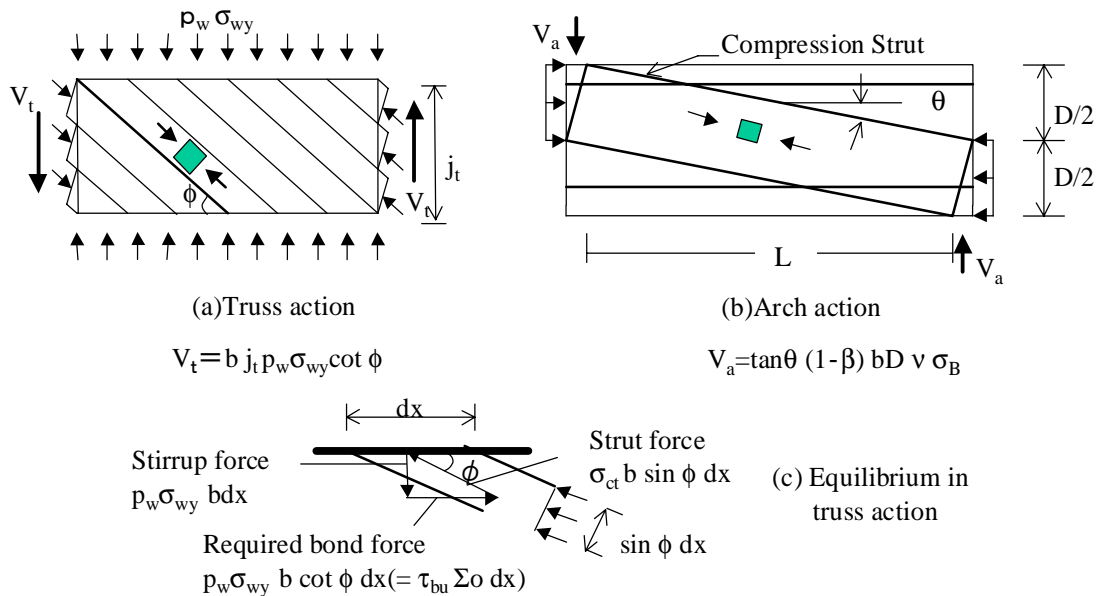


Fig.2 Concept of Applied Shear Strength Equation (AIJ Design Guidelines)

Figure 2 illustrates the truss and strut action on which the equation is based. Here, the shear reinforcement amount $p_w \sigma_{wy}$ was replaced by $p_{we} \sigma_{we}$ (Eq.1) with $\epsilon_f = 0.01$. Figure 3 shows the comparisons between the calculated strength V_{cal} and the experimental maximum shear loads V_{exp} of the 101 specimens, which failed in shear before flexural yielding. For all the specimens, the average ratio of V_{exp} / V_{cal} is $m = 1.13$ with standard deviation $\sigma = 0.36$. On the

other hand, the individual average ratios of V_{exp}/V_{cal} are 1.31 for the specimens with usual hoops and/or steel jackets, 0.98 with carbon fiber wrapping and 1.07 with aramid fiber wrapping respectively. It indicates that the effective strains of fiber sheets ε_f in Eq.1 should be taken as less than 1% and/or the upper reinforcing limit should be introduced to give the same safety factor as for the usual RC columns. It is noted that the data includes the specimen with high-modulus carbon fiber sheet ($E_f=650\text{GPa}$), which is highly over-estimated ($V_{exp}/V_{cal}=0.58$). It failed in much a brittle manner because the breakage of fibers progressed rapidly along the diagonal cracks. The small elongation capacity of the high-modulus carbon fibers affects the shear capacity.

Figure 4 shows the average fiber strains at maximum loads reported in several papers. Similar notice should be taken for aramid fibers ($E_f=80\text{-}120\text{GPa}$), whose effective strain is somewhat higher than carbon fibers. The effectiveness of fibers decreases with an increase of reinforcement amount. The analysis shows that the strength equation for RC is fundamentally available for retrofitted columns by fiber wrapping using the modulus of elasticity of fibers. However, the influence of characteristic natures of each fiber type, such as the small elongation capacity, the poor resistance against the direct shear and the smaller strength at the bent portions etc. should be taken into account.

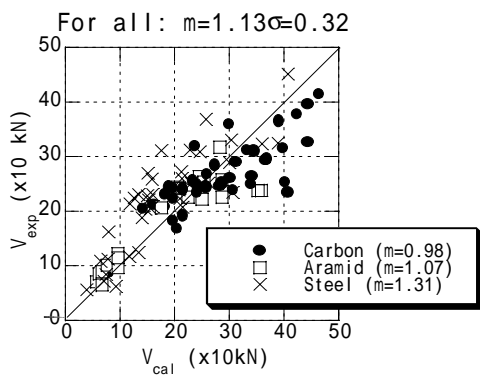


Fig.3 Comparisons between Calculated and Measured Shear Strength

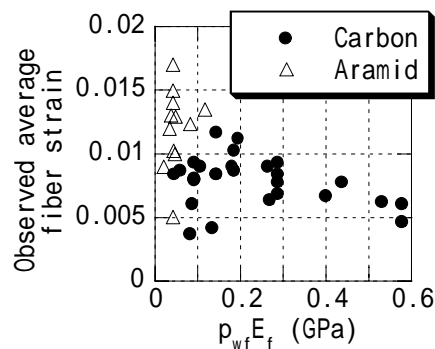


Fig.4 Observed Average Fiber Strain at Maximum Shear

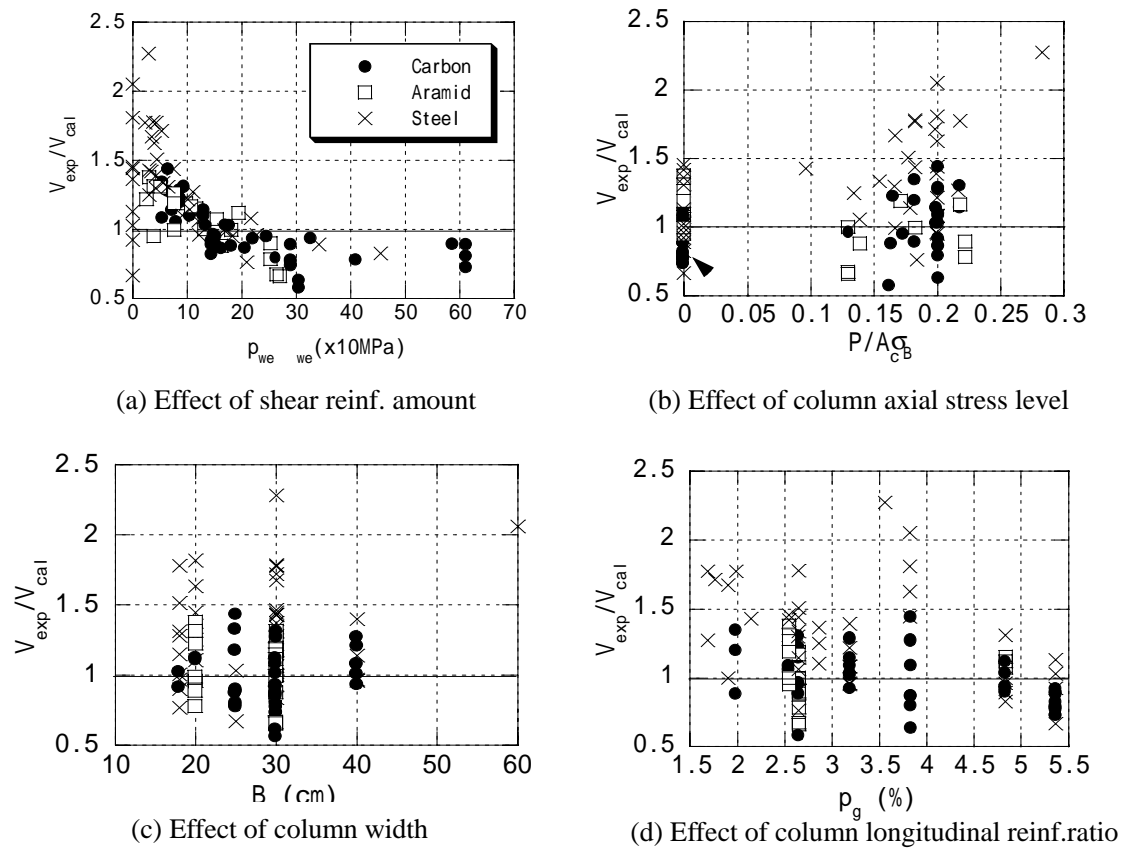


Fig.5 Effects of Several Parameters on Shear Strength

Effect of several parameters on shear strength -- Figure 5(a), (b), (c) and (d) show the variations of measured to calculated shear strength ratios of specimens that failed in shear against shear reinforcement amount ($p_{we}\sigma_{we}$), column axial stress to concrete strength ratio ($P/A_c\sigma_B$), column width (B) and longitudinal reinforcement ratio (p_g) respectively. It is significant that the larger $p_{we}\sigma_{we}$, the smaller the ratio of measured to calculated strength. It suggests that the fiber strain at shear failure becomes smaller as the $p_{we}\sigma_{we}$ becomes larger, which coincides with the finding in Fig.4. The strength equation tends to over-estimate the shear strength for specimens with larger p_g , which indirectly means worse bond properties of longitudinal bars. The influences of B and $P/A_c\sigma_B$ on shear strength are not clear. Considering that the fiber sheet in one-directional strengthening material and the form of external wrapping, it is important to add the data of large scaled specimens.

Splitting bond failures of columns -- In Japanese design practice, it is considered that the

bond failure along column longitudinal bars is one of the brittle failure modes to be prevented. Referring to Figure 2(c), maximum shear force transferred by the truss action is limited by either of the shear reinforcement force, the bond force or the compressive capacity of diagonal concrete strut. If the bond stress reaches the critical value (τ_{bu}) first, the contribution of truss action is given by

$$V_{bond} = \tau_{bu} \cdot \Sigma O \cdot j_t \tag{Eq.5}$$

Where ΣO : total nominal perimeter of the bars
 j_t : distance between the compressive and tensile longitudinal bars

Shear strength governed by the splitting bond failure V_{bu} can be evaluated by replacing the first term of Eq.2 with Eq.5. The splitting bond strength τ_{bu} was given by the equation proposed by Morita et al.(2), ignoring the effect of fiber sheet wrapping on bond. (The Orangun, Jirsa and Breen’s equation (3) will give similar bond strengths.) Assuming the angle $\phi=45$ degree in truss action, the shear strengths were predicted for 115 data. (Fourteen specimens failed in bond were added to 101 shear-failure specimens.). Here, the calculated value is given as the smaller value between shear strength V_{su} by Eq.2 and the bond governed shear strength V_{bu} . Figure 6 shows the result. Comparison with Figure 3 indicates a considerable number of specimens are judged as bond failure. It suggests that it is important to consider the bond capacity for shear strength evaluation. The effect of fiber sheet wrapping on bond strength should be made clear. Recently conducted research reported that the fiber sheet wrapping was more effective than hoops by several times, when the bond strength increment was formulated by the function of the sectional area of transverse reinforcement (not including the fiber strength in the bond strength equation).

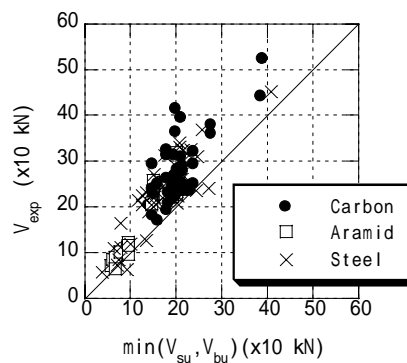


Fig.6 Comparisons between Measured and Calculated Strengths Considering Bond Failure

5. DUCTILITY OF STRENGTHENED COLUMNS

Database contains the information on load-deformation curve of each specimen. The ductility factor μ_{exp} is defined by,

$$\mu_{exp} = \frac{R_u}{R_y} \quad (\text{Eq.6})$$

Where, R_y : deflection angle at yielding of longitudinal bars,
 R_u : deflection angle in the envelope curve when the load decreased to 85% of the maximum.

Figure 7 shows the relationships between the ductility factors and the calculated shear to flexural strength ratios (V_{su}/V_{mu}) of the 98 specimens subjected to load reversals of inelastic range. Here, the shear strength V_{su} was calculated by Eq.2 with $\varepsilon_f = 0.01$. The flexural strength V_{mu} was calculated by the Japanese practical design equation. There is a tendency the larger the ratio V_{su}/V_{mu} , the larger the μ_{exp} . Selecting the 41 specimens that failed in shear or bond after load reversals in plastic range, the V_{su}/V_{mu} vs. μ_{exp} relationships were plotted in Figure 8. The linear regression analysis gave Eq.7 for a rough prediction of ductility.

$$\mu_{cal} = 2 \frac{V_{su}}{V_{mu}} + 0.7 \quad (\text{Eq.7})$$

To investigate the reasons of the scatter shown in Figure 7, the variations of the measured to calculated ductility ratios (μ_{exp}/μ_{cal}) against several influencing factors were plotted in Figure 9(a), (b) and (c). These figures indicate that the Eq.7 has a tendency to over-estimate the deformation capacity for the specimens with larger axial compressive stress level ($P/A_c\sigma_B$), for the specimens with larger transverse reinforcement amount ($p_{we}\sigma_{we}$), and for the specimens with smaller span to depth ratio (M/VD). Modification of the effective fiber strain depending on the fiber type and the reinforcement ratio is required in shear strength equation and the reduction should be considered for short columns and for columns subjected to high compressive load in ductility assessment. In addition, the damage of bond resistance of longitudinal bars, which has not been considered in the analysis, is also important because the bar slip due to bond failure causes significant degradations of the

stiffness and energy dissipation capacity.

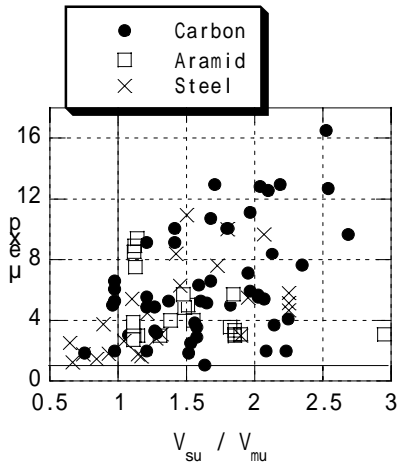


Fig. 7 Measured Ductility vs. Calculated Shear to Flexural Strength Ratio

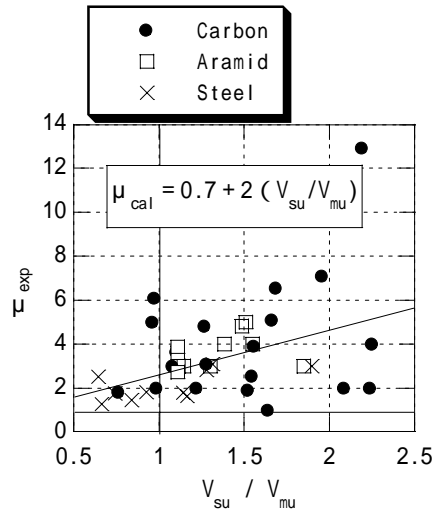
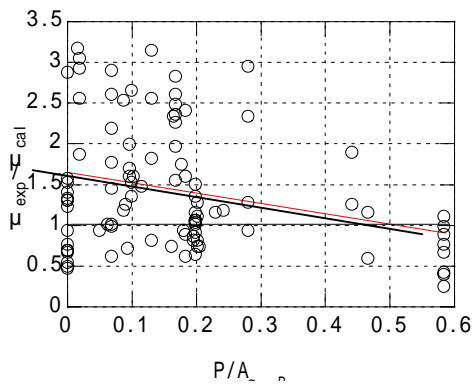
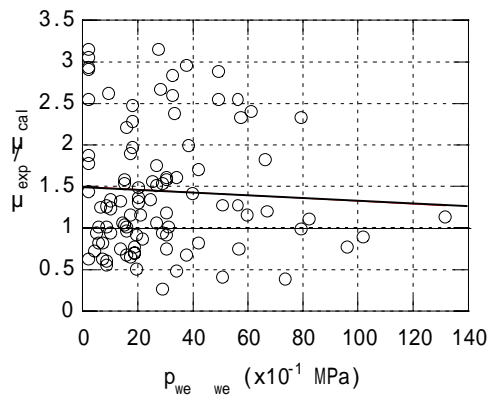


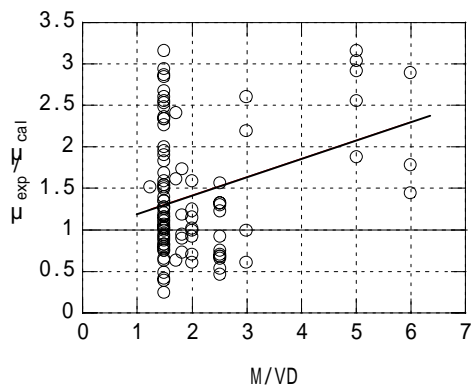
Fig.8 Relationship between ductility ratio and V_{su}/V_{mu} for Shear Failed Specimens



(a) Effect of column axial stress level



(b) Effect of shear reinf. amount



(c) Effect of shear to span ratio

Fig.9 Effect of Several Parameters on Ductility in Reversed Cyclic Loadings in Plastic Range

6. COLUMNS WITH PLAIN ROUND BARS

There are 23 column test data with plain round longitudinal bars. For such columns, the shear strength contribution by truss action is very small due to poor bond property, which means that the Eq.2 cannot be available directly. In Japan, the empirical equation proposed by Arakawa (5) has been used widely in practical design, which was based on many test data including the data with plain round bars. The equation is given by

$$V_{Arakawa} = \left(\frac{0.53 p_t^{0.23} (\sigma_B + 180)}{M / (V \cdot d) + 0.12} + 2.7 \sqrt{p_{we} \sigma_{we}} \right) \cdot b \cdot j + \frac{0.1P}{A_c \cdot \sigma_B} \quad (\text{Eq.8})$$

Where p_t : longitudinal tensile reinforcement ratio, P : column axial load
 b : column width, j : internal lever arm ($=7d/8$), A_g : overall column area
 (cm in length, kgf in force and kgf/cm² in stress)

Figure 10(a) and (b) shows the applicability of the equations, Eq.2, and Eq.8 to the data, where the shear reinforcement amount with effective fiber strain of 1.0% was used. Arakawa's equation predicts the strength comparatively well apparently. However, the function of square root of $p_{we} \sigma_{we}$ in the equation result in the calculated values are not sensitive to the reinforcement amount, which seems unrealistic. The behaviors of these specimens are quite different from columns with deformed bars. Most specimens showed the comparatively large deformation capacities in envelope curves without clear observation of flexural yielding at critical sections, although the stiffness in load-deflection curves and energy dissipating capacity are low. The concrete crush and fiber sheet breakage at the column ends is the final failure patterns without significant damages in the mid-span. It indicates that the roles as the confinement for the compressive concrete and against buckling of longitudinal bars might be larger in addition to the shear reinforcing effect. The different treatment for flexural and shear strength evaluations and the different ductility assessment considering the poor bond property should be established.

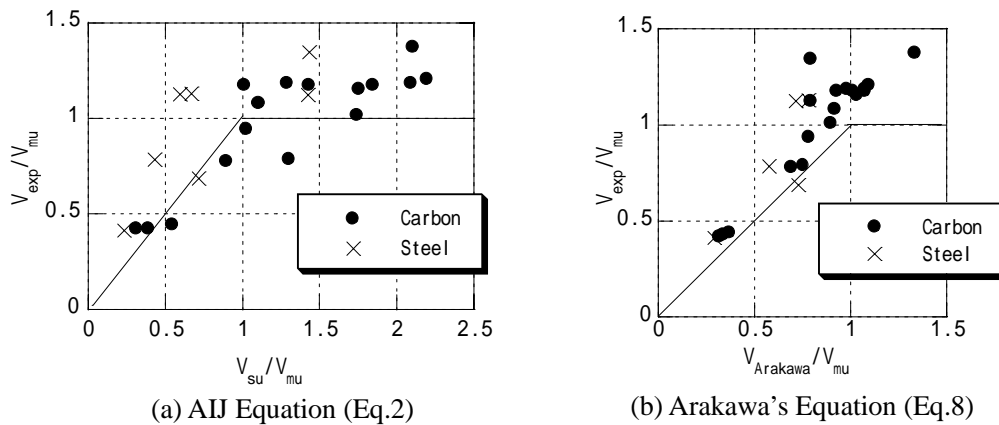


Fig. 10 Strength Evaluation for Specimens with Plain Round Bars

7. CONCLUSIONS AND FUTURE RESEARCH NEEDS

Based on the analysis of the 236 column retrofitting test data conducted in Japan, the following findings were obtained:

- (1) Shear strength of retrofitted columns using fiber sheet can be predicted by previous equations for R/C columns. Consideration of the modulus of elasticity and the effective strain around 1% of fiber sheets seems essential.
- (2) The effective strain in fibers at maximum load becomes smaller for columns with larger shear reinforcement ratio. The effective strain of aramid fiber ($E_f=80-120\text{GPa}$) is higher than that of carbon fiber. Quantitative evaluations of these behaviors improve the applicability of strength equation.
- (3) Use of high modulus type carbon fiber sheet ($E_f=400$ or 600GPa) did not give the larger shear capacity..
- (4) There are few test data about the effect of fiber sheet wrapping on bond resistance of longitudinal bars. Further research effort is required.

(5) The larger the shear to flexural strength ratio, the larger the ductility factor. For short columns and columns with high compressive stress level, the ductility factor is decreased in comparison with regular columns.

(6) In the case of columns with plain round bars, the effect of fiber wrapping is different. The rational evaluation of flexural and shear capacities considering the poor bond property is required.

8. ACKNOWLEDGEMENT

The assistance of H. Katsumata, M. Tanigaki, N. Hayashida and other members of AIJ Subcommittee in gathering and analyzing data are gratefully acknowledged.

9. REFERENCES

- 1) *Design Guidelines for Earthquake Resistant Reinforced Concrete Buildings Based on Ultimate Strength Concept* (1990), Architectural Institute of Japan (English version, 1994)
- 2) Morita, S. and Fujii, S. (1982): Bond Capacity of Deformed Bars due to Splitting of Surrounding Concrete, '*Bond in Concrete*', Applied Science Publishers, (Proc. of International Conference at Paisley, Scotland), pp.331-341
- 3) Orangun, C.O, Jirsa, J.O. and Breen, J.E. (1977): A reevaluation of test data on development length and splices, *Journal of ACI Proc.*, Vol.74, Mar.
- 4) Katsumata, H, Hagio, H. and Kobatake, K. (1997): Retrofit of RC Columns by Carbon Fiber Wrapping, *Summary Report of AIJ Annual Convention*, pp.671-672
- 5) *AIJ Standard for Structural Calculation of RC Structures* (Revised in 1999), Architectural Institute of Japan

10. KEYWORDS

database, carbon, aramid, column retrofit, strengthening, shear, ductility

ON THE DEFORMATION CAPACITY OF REINFORCED CONCRETE COLUMNS SUBJECTED TO LATERAL SHEAR REVERSALS INTO THE NONLINEAR RANGE

Julio A. Ramirez¹ and Turel Gur²

ABSTRACT

Several approaches to proportion reinforced concrete columns to resist lateral shear reversals into the nonlinear range are reviewed. Two types of approaches are discussed in this paper. The first group consists of models specifically addressing the reinforced concrete column shear strength. The second type of approach aims at estimating the amount of transverse reinforcement from a single hypothesis for concrete failure under the combined effect of normal and shear stresses. The approaches discussed are applied in the evaluation of an elevated highway pier.

1. INTRODUCTION

The current seismic design philosophy allows nonlinear behavior of the structure to reduce strength requirements. This implies that the structure must be able to retain its integrity under cycles of displacement into the nonlinear range. Often, columns become a critical source of energy dissipation. Experimental observations have shown that if a reinforced concrete column is subjected to cycles of shear reversals into the range of nonlinear response, the displacement limit at which it can sustain the lateral shear corresponding to its yield strength tends to decrease compared with the displacement limit for monotonically increasing load. Priestley et al. (1994) referred to this failure mechanism as a ductile shear failure, where a degree of ductility develops hinges in the column before shear failure occurs. A number of variables have been identified as playing a role on the capacity of a column to withstand lateral shear reversals. Among those, the magnitude of axial and shear stresses, the strength of concrete and steel, the displacement history, and the amount and configuration of the reinforcement are important. In this paper, two approaches for proportioning columns to resist lateral shear reversals into the nonlinear range are examined. One approach considers the shear strength required. Five shear strength models for columns are summarized under this heading. A second approach aims at calculating the required amount of transverse reinforcement for a given maximum drift. The amount of transverse reinforcement is

¹ Professor of Structural Engineering and Assistant Head for Graduate Programs, School of Civil Engineering, Purdue University, West Lafayette IN 47907-1284. Email: ramirez@ecn.purdue.edu.

² Doctoral Graduate Research Assistant, School of Civil Engineering, West Lafayette IN 47907-1284

determined as a function of the axial load, shear force, drift, and the dimensional and material properties of the given column.

2. SHEAR STRENGTH MODELS

The shear models reviewed are:

- ACI 318-99 Code
- FEMA 723 (1997)
- Moehle, Elwood, and Sezen (2000)
- Priestley, Verma and Xiao (1994)
- Standard Specification for Design and Construction of Concrete Structures, JSCE 1986, Part 1 (Design)

2.1 ACI 318-99 (U.S. Customary)

The ACI 318-99 considers separate contributions from the concrete, V_c , and the transverse steel reinforcement, V_s , to the nominal shear strength, V_n . The effect of increasing displacement demand into the nonlinear range is included in a simplified form. The ACI 318-99 calls for the shear strength, V_c , attributed to the concrete to be ignored in regions where yielding is likely to occur in connection with inelastic lateral displacements provided that:

- The maximum calculated lateral shear force resulting from considering earthquake induced forces exceeds more than $\frac{1}{4}$ of the total required strength, and
- The factored axial compression force is less than $0.05f'_cA_g$

For columns with axial loads equal to or greater than $0.05f'_cA_g$, the equations to estimate the shear strength are as follows:

$$V_n = V_c + V_s \quad (1)$$

$$V_c = 2 \left\{ 1 + \frac{P}{2000A_g} \right\} \sqrt{f'_c} b_w d \quad (2)$$

$$V_s = \frac{A_v f_{yv} d}{s} \quad (3)$$

where V_n = nominal shear strength, V_c = contribution from concrete, V_s = contribution from tie reinforcement, P = axial load, A_g = gross concrete area, f'_c = concrete

compressive strength (psi), b_w = width of the section, d = effective depth, A_v = area of tie steel crossing the potential failure crack within the spacing, s , and f_{yv} = yield strength of the tie steel. In the U.S. the concrete contribution has been derived from test results. The steel contribution has been estimated as the contribution provided by a truss with constant inclination concrete diagonals.

2.2 FEMA 273 (1997)(U.S. Customary)

The NEHRP Guidelines for Seismic Rehabilitation of Buildings (FEMA 273, 1997) shear strength evaluation method was developed from column tests with relatively high amounts of transverse reinforcement. The FEMA 273 guidelines also establish the nominal shear strength of the member, V_n , as calculated in Eq. (1). The contribution from the ties is estimated using Eq. (3) except in yielding regions of columns where the transverse reinforcement is considered effective only if $s \leq d/2$ and hoops have hooks embedded into the concrete core. The concrete contribution, V_c , is:

$$V_c = 3.5 \left\{ k + \frac{P}{2000A_g} \right\} \sqrt{f'_c} bd \quad (4)$$

where $k = 1.0$ for displacement ductility less than 2, otherwise $k = 0$.

2.3 Moehle, Elwood and Sezen (2000)(U.S. Customary)

This model also follows the format of Eq. (1). The concrete contribution, V_c , is related to calculated nominal principal tension stress in the column. The limiting principal tension stress is set equal to $6\sqrt{f'_c}$. The concrete contribution is also made a function of the aspect ratio of the column, a/d , to reflect the interaction with flexural stresses in the case of column subjected to combined flexure and axial load. The parameter a = distance from the maximum moment to the inflection point. The resulting expression is

$$V_c = k \left\{ \frac{6\sqrt{f'_c}}{\frac{a}{d}} \sqrt{1 + \frac{P}{A_g * 6\sqrt{f'_c}}} \right\} A_g (psi) \quad (5)$$

No limits are placed on the aspect ratio, though it is noted by the authors that the range of values in the database used was limited to between 2.0 and 3.9. In Eq. (5), the term k is a modifier to account for strength degradation in flexural hinging regions. For the data set evaluated by Moehle et al., k was defined as shown in Figure 1. The steel contribution, V_s , is defined as

$$V_s = k \frac{A_v f_{yv} d}{s} \quad (6)$$

Equation (6) is similar to Eq. (3) except for the factor k . This factor represents a degradation term of the steel contribution to the shear strength of the member with increasing ductility demand. This modification was introduced to reflect the test results of columns with low amounts of transverse reinforcement considered by Moehle et al. (2000) where the estimated steel contribution was half or less of the calculated value of the concrete contribution. The technical argument presented by the authors was the likely degradation of the truss mechanism represented by the V_s term.

2.4 Priestley, Verma and Xiao (1994)(U.S. Customary)

In this model, the nominal shear strength of a reinforced concrete column is taken as:

$$V_n = V_c + V_P + V_s \quad (7)$$

The concrete contribution term is separated into two components. A limiting diagonal tension component, V_c , without axial load, plus an axial force component, V_P , respectively

$$V_c = k\sqrt{f'_c} A_e \quad (8)$$

where k depends on the displacement ductility demand, as well as on whether the column is expected to be subjected to uniaxial or biaxial ductility demand (see Fig. 2). The effective shear area A_e is taken equal to 0.8 times the gross cross sectional area A_g . The upper limit for k of 3.5 is chosen to represent a concrete limit value for principal diagonal tension without the axial load effect, and

$$V_p = P \tan \alpha = P \left(\frac{D - c}{2a} \right) \quad (9)$$

where D = the overall section depth or diameter, c = the depth of the compression zone, $a = L$ for cantilever columns and $L/2$ for a column in reverse bending. It must be noted that V_p is not degraded with increasing ductility demand. Equation (9) indicates that as the aspect ratio of the column decreases, the axial load contribution to the shear strength will increase, and that for slender columns, the axial load contribution decreases. This argument is similar to the one presented by Moehle et al. to introduce the aspect ratio in their proposed concrete contribution term. Equation (9) also indicates that as the axial load increases, the contribution from this mechanism to the column shear strength will decrease since the depth of the compression zone, c , increases. The contribution of the transverse reinforcement is given by a truss mechanism using a 30° angle between the truss compression diagonals and the longitudinal axis of the column, unless limited to larger angles by the inclination of the potential corner to corner crack. This component is given by the expressions below for circular and rectangular columns respectively

$$V_s = \frac{\pi A_{sh} f_{yh} D'}{2 s} \cot 30^\circ \quad (10a)$$

$$V_s = \frac{A_v f_{yv} D'}{s} \cot 30^\circ \quad (10b)$$

where, D' = the distance between centers of the tie or spiral, A_{sh} = area of cross section in the form of spiral or hoop, $f_{yh} = f_{yv}$ = yield strength of transverse reinforcement, s =

spacing of transverse reinforcement along the member axis, and A_v = total area of transverse reinforcement within a distance s . Equations (10a) and (10b) differ from Eqs. (3) and (6). In (10a) and (10b), the distance between centers of hoops or spiral is used instead of the distance between the centroid of the tension reinforcement and the extreme compression fiber, d . No degradation of the truss contribution is envisioned due to increasing ductility demand. A 30° angle is employed instead of the traditional 45° to estimate the contribution of the transverse reinforcement.

2.5 Standard Specification for Design and Construction of Concrete Structures, JSCE-1986, Part 1 (Design)(Metric)

The JSCE-1986 Part 1 (Design) requirements for the design of concrete structures are based on limit states approach. For columns, the design shear capacity is obtained using Equation (1), where V_c = design shear capacity provided by the concrete, and V_s = design shear capacity provided by the transverse reinforcement. For comparison with the other models presented, the member and material factors are taken equal to the unity. The concrete and the steel contributions are given by Equations (11) and (16) respectively.

$$V_c = f_{vcd} b_w d \quad (11)$$

$$f_{vcd} = 0.9(\beta_d)(\beta_p)(\beta_n) \sqrt[3]{f'_{cd}} \quad (\text{kg/cm}^2) \quad (12)$$

$$\beta_d = \sqrt[4]{100/d} \quad (d \text{ in cm}), \beta_d \leq 1.5 \quad (13)$$

$$\beta_p = \sqrt[3]{100 p_w} \quad \beta_p \leq 1.5 \quad (14)$$

$$\beta_n = 1 + \frac{M_0}{M_d} \quad \text{for compression, } \beta_n \leq 2.0 \quad (15)$$

where f_{vcd} = design shear strength of the concrete, b_w and d are as previously defined, β_d = size effect coefficient, β_p = longitudinal reinforcement coefficient, β_n = axial force

coefficient, f'_{cd} = design concrete compressive strength, $p_w = A_s/b_w d$, M_o = decompression moment required to cancel the axial force compressive stress at the extreme tension fiber corresponding to M_d (gross section properties), M_d = design moment, and the steel contribution, V_{sd} , provided by hoops or ties is

$$V_{sd} = [A_v f_{yv} z] / s \quad (16)$$

where A_v = area of hoops or ties in spacing s , f_{yv} = yield strength of the shear reinforcement (no more than 4000 kgf/cm²), $z = d/1.15$, and s = spacing of hoops or ties measured along the length of the member. An upper limit to the shear force, given by Eq. (17), is imposed to control failures due to concrete crushing in the web of the member.

$$V_{wcd} = f_{wcd} b_w d \quad (17)$$

where

$$f_{wcd} = 4\sqrt{f'_c} \quad (\text{kgf/cm}^2) \quad (18)$$

3. DEFORMATION CAPACITY MODELS- PUJOL ET AL. (2000)(U.S. CUSTOMARY)

The approach discussed herein deviates from the notion that the ability of a column to undergo nonlinear cycles of shear reversal can be addressed with traditional shear strength models. In this approach, a physical criterion is used to develop a relationship to establish the required amount of transverse reinforcement. The hypothesis is that the main function of the transverse reinforcement is to confine the concrete core subjected to combined normal and shear stresses rather, than to resist shear induced diagonal tension in addition to improve deformability under axial compression. It is an approximate formulation to determine the amount of transverse reinforcement for columns of reinforced concrete frames subjected to nonlinear lateral shear reversals. It is assumed that the combined effects of shear and normal stress are a function of the maximum drift

ratio. The effect of the combined stresses is interpreted using Coulomb's failure criterion (1773) as shown in Figure 3. In this approach the slope, m , of the line representing Coulomb's criterion is taken equal to 0.75, and only the ordinate of the failure criterion ($_ = 0$) is assumed to change due to shear reversals as a function of the number of cycles and displacement history. Based on these assumptions, and on the calibration with data from 29 tests of reinforced concrete columns from six different investigations (Pujol et al. 2000), the effect of the ratio of drift to aspect ratio, $(_{max}/L)/(a/d)$, on the ordinate at the origin, v_0 , normalized against f'_c was evaluated and Eq. (19) was proposed.

$$k_1 = \frac{v_0}{f'_c} = \frac{1}{7} \left[1 - \frac{100 * \Delta_{max}}{3 * L * \frac{a}{d}} \right] \geq 0 \quad (19)$$

The equations for the rest of the parameters in Figure 3 are

$$\sigma_a = \frac{P + T}{h_c * b_c} \quad (20)$$

where $_a$ = mean axial compressive stress on the core, P = applied axial load, T = force in the tension reinforcement $\approx (1/2) * A_s * f_y$, A_s = area of longitudinal reinforcement, f_y = longitudinal reinforcement yield stress, h_c = depth of core measured center to center of peripheral hoop reinforcement, and b_c = width of core measured center to center of peripheral hoop reinforcement, and

$$v = \frac{V}{h_c b_c} \quad (21)$$

where v = mean shear stress, and V = shear force, and

$$\sigma_t = \frac{A_v f_{yv}}{s * b_c} \quad (22)$$

where $_t$ = mean stress exerted on the concrete core by the peripheral hoops assumed to be at yield (implies that the tie has adequate detailing), A_v = area of hoop reinforcement at

spacing s , and f_{yv} as previously defined. Pujol et al. (2000) derived Equation (23) to determine the required transverse reinforcement ratio, $r = (A_v/(s*b_c))$.

$$r = \left[\left(\frac{3}{8} \right) \left(\frac{4k_1 f'_c}{\sigma_a} + 3 \right) + 1 - \frac{5}{8} \sqrt{ \left(\frac{4k_1 f'_c}{\sigma_a} + 3 \right)^2 - \left(\frac{4v}{\sigma_a} \right)^2 } \right] * \left(\frac{\sigma_a}{f_{yv}} \right) \quad (23)$$

where the terms are as defined in Equations (19)- (22). Equation (23) is limited to design conditions satisfying the following assumptions:

- The maximum column drift capacity is not less than the calculated drift corresponding to the column yield capacity.
- The shear force corresponding to the column shear capacity exceeds the lateral shear at inclined cracking.
- The static shear strength of the column is greater than the column shear corresponding to the development of the anticipated maximum moment(s) at the column end(s) based on increased yield stress primarily to recognize strain hardening of the reinforcement.
- The column core is confined by transverse reinforcement properly anchored to reach its yield capacity.
- The governing drift cycles occur primarily in the plane defined by one of the principal axis of the cross section.

4. ELEVATED HIGHWAY PIER EVALUATION

The pier height is 50 meters (164.2 ft) measured from the top of the footing. The pier is assumed fixed at the base. The cross section at the base of the column is shown in Figure 4 and additional data is given in Table 1. The design concrete compressive strength is 35 MPa (5075 psi), and the design yield strength for all reinforcement is 500 MPa (72,500 psi). The evaluation is conducted for only one of the principal axis of the column.

Table 1. Section A at the Base of the Pier- Strong Axis (transverse direction)

Axis of M	A_g , m ² (ft ²)	Axial Load, tons (kips)	d , m (ft)	b_w , m (ft)	s , mm (in)	Clear Cov. mm (in)	r , %	A_{st} , m ² (ft ²)	A_{sw} , m ² (ft ²)
Y	15.4 (166)	3500 (7719)	7.5 (24.6)	1.20 (3.9)	10 (3.9)	40 (1.6)	0.0104	0.507 (5.47)	0.075 (0.81)

A moment-curvature analysis was conducted for the section at the base. The results from the analysis are listed in Table 2 including the depth of the flexural compression zone, c . The values of the yield displacement, Δ_{yield} , maximum displacement, Δ_{MAX} , and the resulting displacement ductility, μ_{Δ} , were determined using the following procedure. A secant was defined by the origin (zero load and zero displacement) and the point where a horizontal line at 70% of the maximum a calculated shear intersected the envelope curve. The yield displacement was then defined by where the secant intersected a horizontal line passing through the envelope curve at the shear corresponding to the maximum moment capacity, M_{MAX} , (maximum calculated shear force, V_{MAX}). The maximum displacement was defined as the displacement corresponding to a limit compressive strain value of 0.005 at the extreme fiber at the base of the pier. A plastic hinge region at the base of the column having a length equal to the effective depth of the member was used to determine the nonlinear component of the total displacement. Table 3 gives results of the evaluation results from the five shear models discussed in Section 2.

Table 2. Flexural Analysis Result for Section A at the Base of the Pier

Axis for Moment	M_{MAX} kN-m (ft-kip)	V_{MAX} kN (kips)	Δ_{yield} m (ft)	Δ_{MAX} m (ft)	μ_{Δ}	C mm (ft)
Y	800,000 (589,971)	16,000 (3597)	0.558 (1.83)	1.049 (3.44)	1.88	2490 (8.17)

Table 3. Evaluation Results for Strong Axis

Method	Shear Area in²	V_c Kips (kN)	No. of Hoops Active	V_s Kips (kN)	V_n Kips (kN)	V_{MAX} Kips (kN)	V_{MAX}/V_c
ACI 318-99	13950	2307 (10261)	d/s	10575 (47038)	12882 (57299)	3597 (16000)	1.56
FEMA- 273	13950	4037 (17957)	d/s	10575 (47038)	14612 (64994)	3597 (16000)	0.89
Moehle et al.	23937	2050 (9118)	k*d/s	10575 (47038)	12625 (56156)	3597 (16000)	1.73
Priestley et al.	19150	5238 (23299)	1.73* d/s	19429 (86420)	24667 (109719)	3597 (16000)	0.69
JSCE- 1986	13,950	817 (3634)	0.87* d/s	9211 (40971)	10028 (44605)	3597 (16000)	4.35

Equation (23) results in a required ratio of transverse reinforcement, $r = 0.001$ (near minimum level for shear) for a maximum calculated drift of 2.1%. The provided amount in the strong direction of the section is 0.0104 (754 psi or 5.2 MPa). Based on the Moehle et al. approach, the amount of reinforcement calculated from Eq. (23) would result in a shear capacity of the section, V_n , of 3061 kips (13615 kN) whereas the Priestley et al. model would estimate a capacity of 7045 kips (31336 kN). The results from this evaluation indicate that the amount of transverse reinforcement is controlled by confinement requirements. It is debatable whether current confinement specifications are applicable to this type of column. The scatter in the calculated capacities from the different approaches also points out an area of needed work.

5. SUMMARY

Two approaches to determine the required amount of transverse reinforcement in columns subjected to lateral shear reversals into the nonlinear range were reviewed. One approach looks at improved design requirements in reference to shear. An alternate proposal determines the required amount of transverse reinforcement based on a single

hypothesis of concrete failure under combined effect of normal and shear stresses. In the improved shear strength models, the traditional sectional approach used in the static domain, is extrapolated into the dynamic domain through the incorporation of a strength degradation factor, k . The factor is a function of the displacement ductility demand. Only in the Moehle et al. model, the degradation factor is applied to both the concrete and the steel contributions. In the other four models, the reduction is applied to the concrete contribution alone, and in the Priestley et al. model, the component due to the axial load is not degraded. In the Priestley et al. model, an increased contribution of the transverse reinforcement with respect to the other four models by a factor equal to about 1.73 is used. It must be noted that the JSCE 1986 Part 1 method includes a size, and a longitudinal tension reinforcement factors applied to the concrete contribution, V_c . In the shear strength models, the common approach of deriving a concrete contribution from the evaluation of test results and the steel contribution from a truss with constant inclination diagonals has been followed. In the alternate approach, the amount of transverse reinforcement is determined for a given limit drift. This approach provides a new perspective to the phenomenon of column behavior under later shear reversals into the nonlinear range. The evaluation of the elevated highway pier with the methods discussed in this paper resulted in a considerable scatter in the predicted capacities and in the different contributions of the separate components of the shear capacity. This observation suggests the need for additional work in this area. Another area of work appears to be related to the confinement requirements for larger scale members.

6. REFERENCES

ACI Committee 318 (1999), *Building Code Requirements for Structural Concrete (318-99) and Commentary (318R-99)*, American Concrete Institute, Farmington Hills, Michigan.

Coulomb, C.A. (1773). "Essai sur une Application des Règles de Maximis & Minimis à quelques Problèmes de Statique Relatifs à l'Architecture." *Mémoires de Mathématique & de Physique, Présentés à l'Académie Royale des Sciences par divers savans, & lûs dans ses assemblées*, Paris, France, 7, pp. 343-382.

FEMA 273 (1997) NEHRP Guidelines for the Seismic Rehabilitation of Buildings, *Federal Emergency Management Agency*, Washington DC, October 1997.

JSCE Part 1 (Design) (1986), *Standard Specification for Design and Construction of Concrete Structures*, JSCE SP-1, Japan Society of Civil Engineers, Tokyo, 160 Japan.

Moehle, J.P., Elwood, K.J., and Sezen, H. (2000), "Gravity Load Collapse of Building Frames During Earthquakes," M. Uzumeri Symposium, Special Publication, American Concrete Institute.

Priestley, M. J. N., Verma, R., and Xiao, Y. (1994), "Seismic Shear Strength of Reinforced Concrete Columns," *Journal of Structural Engineering, American Society of Civil Engineers (ASCE)*, Vol. 120, No. 8, August, pp. 2310-2329.

Pujol, S., Sozen, M. A., and Ramirez, J. A. (2000). "Transverse-Reinforcement Requirement For Columns of RC Frames to Resist Earthquakes." *Journal of Structural Engineering, American Society of Civil Engineers (ASCE)*, Vol. 126, No. 4, April, pp. 461-466.

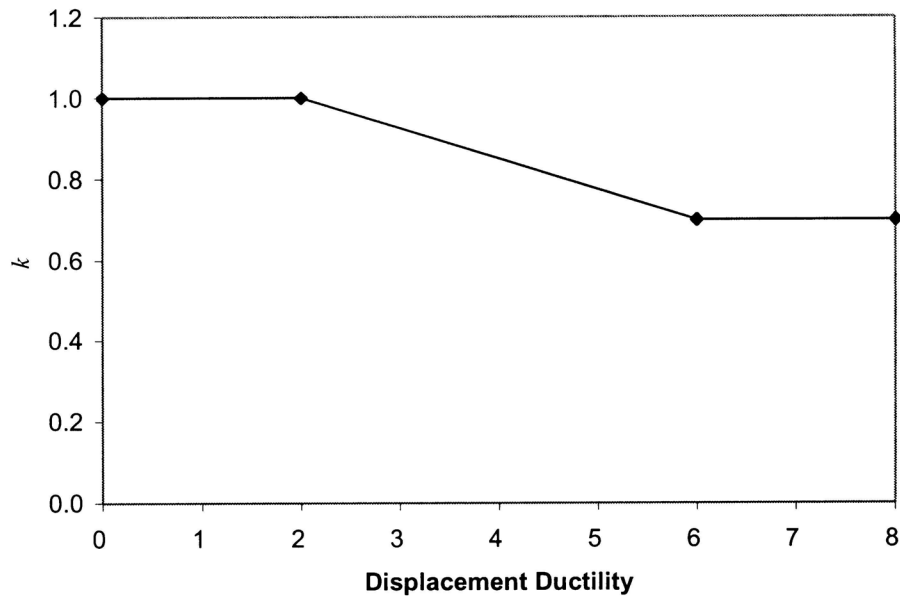


Figure 1. Parameter k, Moehle et al. (2000)

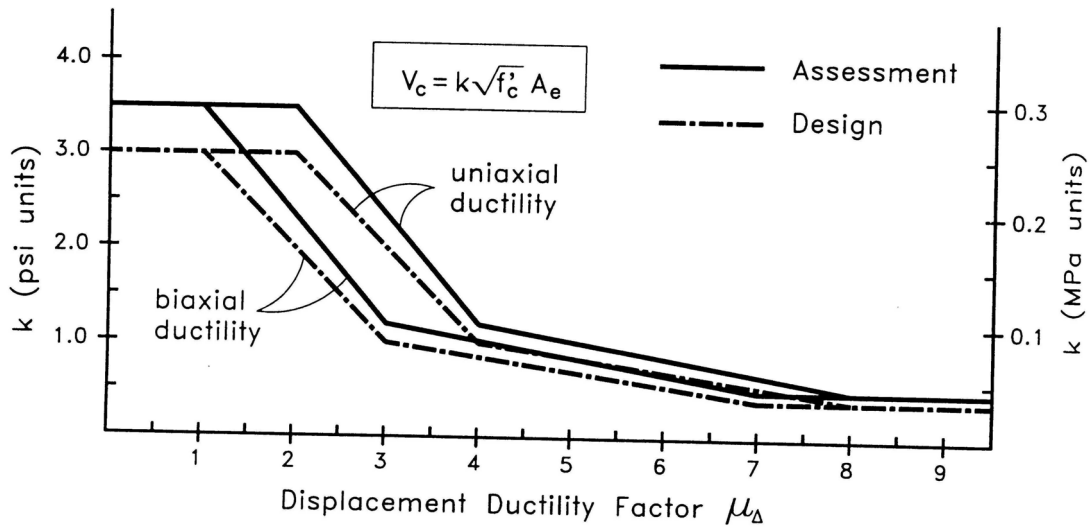


Figure 2. Relationship between ductility and strength, Priestley et al. (1994)

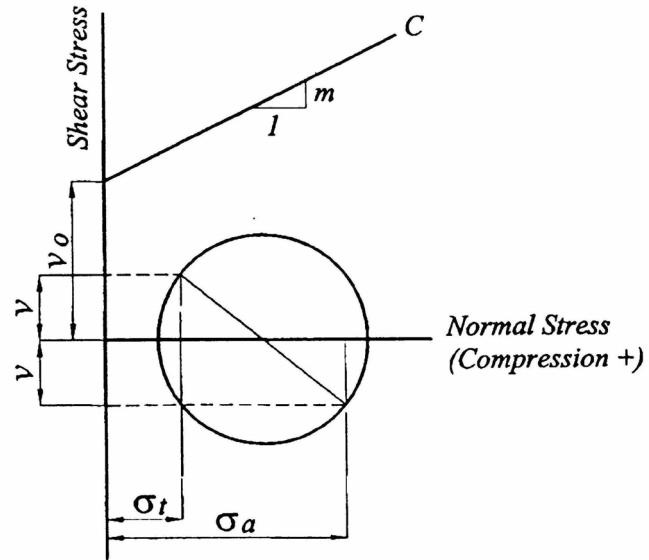


Figure 3. Coulomb's Criterion

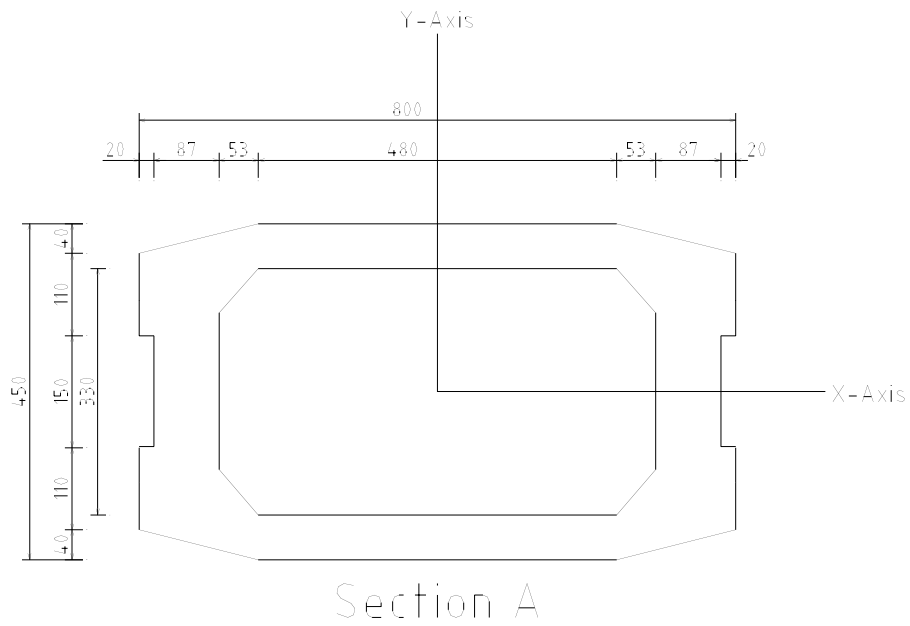


Figure 4. Cross Section at the Base of the Elevated Highway Pier

INFLUENCES OF BEAM AND COLUMN BAR BOND ON FAILURE MECHANISM IN REINFORCED CONCRETE INTERIOR BEAM-COLUMN JOINTS

KITAYAMA Kazuhiro *1, TAJIMA Yuji *2, OKUDA Makoto *3 and KISHIDA Shinji *4

ABSTRACT

Reinforced concrete (R/C) interior beam-column joint specimens were tested under the column axial loading and the reversed cyclic lateral loading to study on the joint failure mechanism and the relation between story shear and joint shear. The bond transfer from the beam and column longitudinal bars to surrounding concrete in a joint was important to enhance the story shear. It was judged that the joint core concrete failed by diagonal compression since the compressive principal strain within a joint panel increased with the story drift and exceeded the strain at the concrete compressive strength in cylinder tests. The joint shear force computed from the beam bar forces in which residual tensile forces at the story shear of zero were eliminated on the basis of the measured beam bar strains at beam critical sections decreased with the decrease in the story shear.

1. INTRODUCTION

The strength and the failure types in reinforced or prestressed concrete interior beam-column joints were interpreted by Shiohara [1] through the consistent mathematical models without using empirical rules. The paper said as follows. The deterioration of moment resisting mechanism in a beam-column joint, caused by the loss of anchorage ability along the beam longitudinal bars within a joint, results in the joint failure. Both the anchorage capacity along the beam bars passing through a joint and the concrete compressive strength dominate the joint strength. On the contrary, the joint failure type is dominated by the moment resisting capacity in a joint panel or the flexural capacity at the beam critical sections whichever is smaller. Thus the principal factors which settle the strength or the failure type of a beam-column joint are not necessarily coincident with each other. In other words, the joint failure type has nothing to do with the joint input shear force.

Therefore the test results are reported in this paper on the influence of the bond ability along beam and column longitudinal bars passing through a joint on the behavior of R/C interior beam-column joints under earthquake motions. The steel plates were set at beam critical sections to improve the anchorage capacity along beam bars within a joint for three specimens. The additional steel bars were welded to beam longitudinal reinforcement only in a joint for one specimen.

2. OUTLINE OF TEST

2.1 SPECIMENS

*1 Associate Professor, Graduate School of Engineering, Tokyo Metropolitan University, Dr. Eng.

*2 Konoike Corporation, M. Eng.

*3 Kajima Corporation, Tokyo Branch.

*4 Research Associate, Graduate School of Engineering, Tokyo Metropolitan University, Dr. Eng.

Table 1 Properties of specimens and material properties of concrete

Specimen	PB-1	PNB-2	PNB-3	PBU-4
Column Axial Load, kN	883 (Compression, stress ratio:0.33)			
Column Longi. Bars	16-D22			
Beam Longi. Bars	Top: 4-D25, Bottom: 4-D25			
Joint Lateral Bras	2-D10 3 sets			
Anchorage Plates	○	○	○	None
Welded Bars to Beam Bars	None	None	None	○
Bond along Beam Bars	○	None	None	○
Bond along Column Bars	○	○	None	○
Concrete Compressive Strength, MPa	21.0	21.0	21.9	22.2
Concrete Tensile Strength, MPa	2.10	2.38	2.07	2.38
Young's Modulus(*1), GPa	25.1	25.7	26.0	25.8

*1: Secant modulus at one-fourth of concrete compressive strength

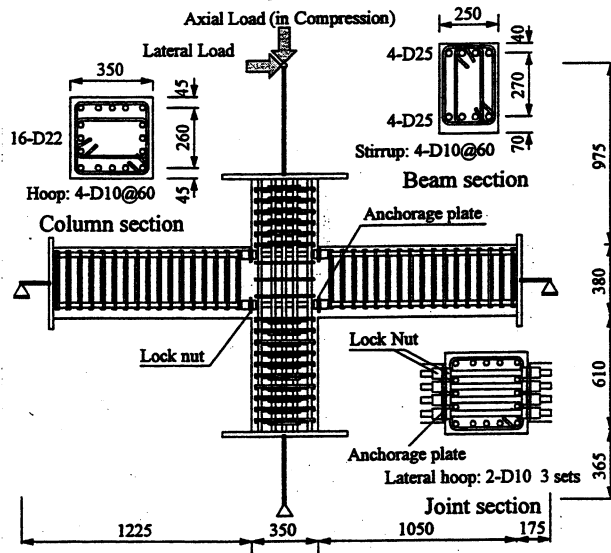


Fig. 1 Section dimensions and reinforcement details

Table 2 Material properties of steel bars

Diameter	Yield Strength, MPa	Tensile Strength, MPa	Fracture Strain, %
D10	404	629	14.0
D22	517	674	17.8
D25	534	685	18.0

Table 3 Material properties of steel plate

Standard	Yield Strength, MPa	Tensile Strength, MPa	Fracture Strain, %
SM490	388	583	20.4

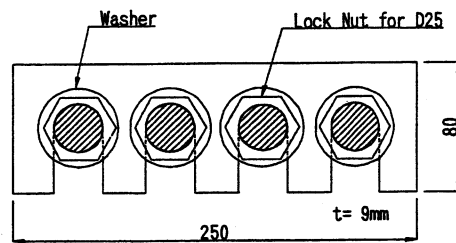


Fig. 2 Detail of anchorage plate

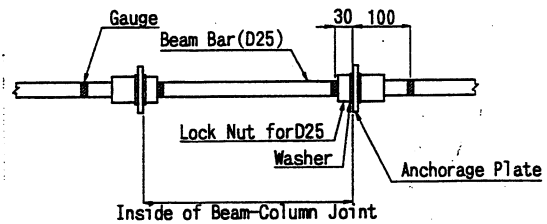


Fig. 3 Anchorage plates and strain gauge locations

Properties of specimens and material properties of concrete are summarized in Table 1. Material properties of steel are listed in Tables 2 and 3. Section dimensions and reinforcement details are shown in Fig. 1. Four plane cruciform subassemblage specimens with one-half scale were tested. Section dimensions and the specified concrete strength (18 MPa) were common for all specimens. The column section was square with 350mm depth. The depth and the width of a beam section were 380mm and 250mm respectively. Three sets of 2-D10 were arranged as the joint lateral reinforcement for all specimens. Test parameter was the bond condition along beam and column longitudinal bars within a joint.

Reinforcing details in a beam-column joint are illustrated in Fig. 4 for all specimens. The anchorage steel plates as shown in Figs. 2 and 3 were placed at the beam critical sections by screwing nuts along beam bars for Specimens PB-1, PNB-2 and PNB-3. These plates were considered to be available for preventing the concrete at beam ends from compressive failure which gives ill effect to the research for the influence of the bond along longitudinal bars within a joint on the behavior of beam-column joints. The bond along beam bars was eliminated within a joint for Specimen PNB-2 by stuffing clay into the dents along deformed bars and wrapping vinyl-sheets. The bond along both beam bars and column bars within a joint was eliminated for Specimen PNB-3 by the same manner as Specimen PNB-2. Deformed steel bars with the diameter of 25mm were welded to each beam bars only in a joint for Specimen PBU-4 in order to increase the sectional area and the perimeter length of beam bars.

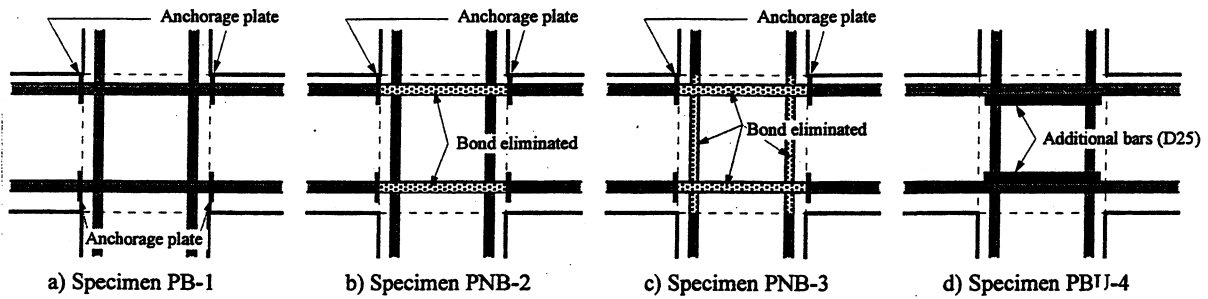


Fig. 4 Reinforcing details in joint

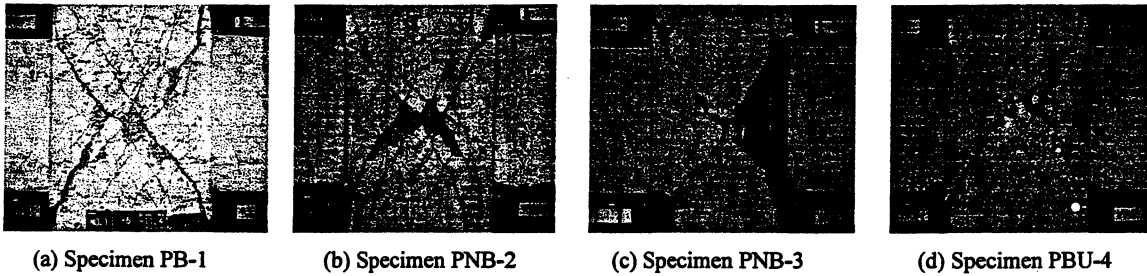


Fig. 5 Crack patterns at story drift angle of 1/33

2.2 LOADING METHOD AND INSTRUMENTATION

The beam ends were supported by horizontal rollers, while the bottom of the column was supported by a mechanical hinge. The reversed horizontal load and the column axial load in constant compression were applied at the top of the column. Specimens were controlled by the story drift angle for one cycle of 1/400, two cycles of 1/200, 1/100 and 1/50 respectively, one cycle of 1/33 and two cycles of 1/25. The lateral force applied to the top of a column, the column axial load and the shear forces of both beam ends were measured by load-cells. A story drift, beam and column deflections, and local displacements of a joint panel were measured by displacement transducers. The strains of beam bars, column bars and the joint lateral reinforcement were measured by strain gauges.

3. TEST RESULTS

3.1 GENERAL OBSERVATIONS

The crack patterns after the story drift angle of 1/33 are shown in Fig. 5. Diagonal shear cracks were observed in a joint panel for all specimens. The crack width along the main diagonal strut in a joint panel expanded dominantly for Specimens PNB-2 and PNB-3 in which the bond transfer along longitudinal bars was removed within a joint. The shell concrete spalled off in a joint panel. The only one of column bars yielded at the story drift angle of 1/25 for all specimens. The beam bars hardly yielded. Therefore it was judged that beams and columns did not yield.

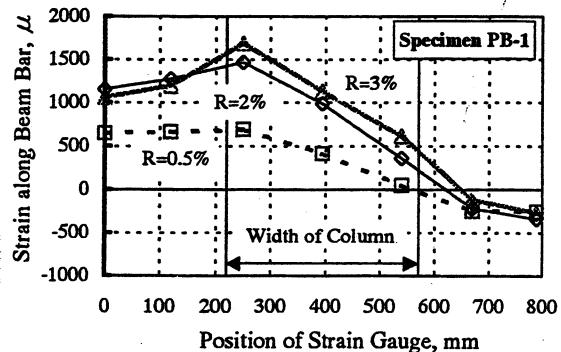


Fig. 6 Strain distribution along beam bar for Specimen PB-1

The strain distributions along a beam bar are shown in Fig. 6 for Specimen PB-1. Bond along beam bars deteriorated within a joint. However tensile forces of beam bars at a critical section could be developed by the anchorage plate placed at opposite beam critical section for Specimens PB-1, PNB-2 and PNB-3. Then the stress of beam bars within a compressive region at beam end remained compression, resulting in the reduction of concrete compressive force at the beam critical section. Consequently concrete compressive failure at beam ends could be avoided for all specimens.

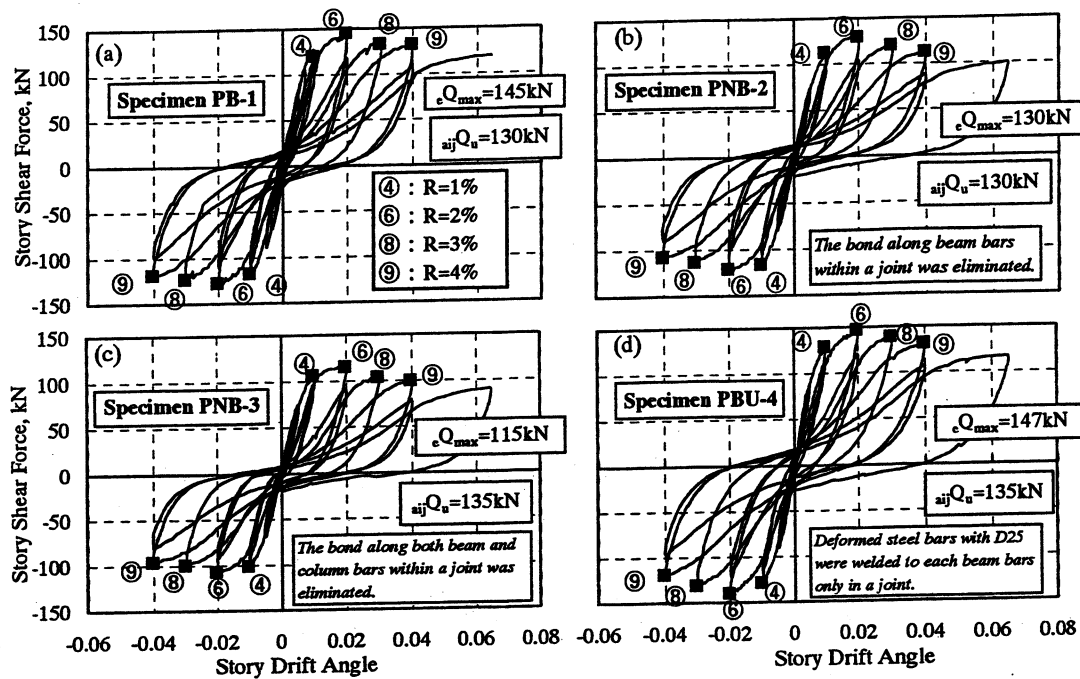


Fig. 7 Story shear force - story drift relations

The contribution of joint shear distortion to the story drift increased with cyclic loading and exceeded the half of the total story drift after story shear force reached at the maximum value. It was concluded on the basis of the research as mentioned above that all specimens eventually failed in joint shear.

3.2 STORY SHEAR - DRIFT RELATIONS

The story shear force – story drift relationships are shown in Fig. 7. The story shear force was computed from moment equilibrium between measured beam shear forces and the horizontal force at the supported point on the top of the column. The story shear reached at the maximum force at the story drift angle of 1/50 and decreased gradually after the drift angle. The maximum story shear for Specimen PBU-4 with twice larger amount of beam bar sectional areas within a joint than other specimens was almost equal to that for Specimen PB-1 with the steel plates for the anchorage of beam bars. The maximum story shear for Specimen PNB-2 where the beam bar bond was eliminated within a joint and Specimen PNB-3, where the bond along both beam and column bars was eliminated, diminished to 89 percent and 79 percent of that for Specimen PB-1 respectively. Therefore the bond ability along beam and column bars within a joint played an important role for the story shear capacity.

The story shear force at joint shear failure computed according to the provisions by Architectural Institute of Japan [2], denoted as ${}_{aj}Q_u$ in Fig. 7, was smaller than the measured maximum story shear denoted as ${}_{e}Q_{max}$ for Specimens PB-1 and PBU-4, which derived conservative estimation. On the contrary, the provisions by AIJ overestimated the measured story shear for Specimens PNB-2 and PNB-3.

Pinching hysteresis loops were obtained for Specimen PBU-4 similarly with Specimen PB-1 although the bond along beam bars within a joint for Specimen PBU-4 was kept good (see Fig. 12) comparing with that for Specimen PB-1. Then the pinching hysteresis shape was caused by shear deterioration in a beam-column joint.

4. DISCUSSION OF TEST RESULTS

Kusuhara and Shiohara [3] proposed that the beam-column joint does not fail in a shear, but fails by the increase in the flexural compression of the concrete at the beam critical section caused by the bond deterioration along beam bars within a joint. Therefore the relationship between the joint shear failure and the transition of a story shear force was investigated. The stresses of beam bars used in the paper were obtained from measured strains by strain gauges through Ramberg-Osgood

Model for the stress-strain relationship for steel.

4.1 JOINT SHEAR - SHEAR DISTORTION ANGLE RELATIONS

The joint shear force was computed in two manners as the following.

a) Tensile force of beam bars was supposed by dividing beam bending moment on a critical section by a constant lever arm length. The joint shear force V_j is obtained by following equation.

$$V_j = \frac{M_{b1}}{j_{b1}} + \frac{M_{b2}}{j_{b2}} - V_c \quad (1)$$

where M_{b1} and M_{b2} are beam bending moments on critical sections, j_{b1} and j_{b2} are lever arm lengths on a beam critical section and V_c is the story shear force. The lever arm lengths were assumed to be the constant value of 7/8 times the beam effective depth.

b) Tensile force of beam bars was computed directly from beam bar stresses at a critical section. The joint shear force is obtained by the equation below.

$$V_j = \sum a_{st} \cdot \sigma_{st} + \sum a_{sb} \cdot \sigma_{sb} - V_c \quad (2)$$

where a_{st} and a_{sb} are the sectional areas of the top and bottom beam bar, σ_{st} and σ_{sb} are the stresses of the beam bar on a critical section computed from the interpolation between stresses measured at two locations close to the beam critical section as depicted in Fig. 3. Equation (2) however may overestimate joint shear force because stresses of beam bars at both critical sections are enhanced due to the confining action against lateral expansion of damaged concrete within a joint panel. Lateral displacement of the joint panel for Specimen PNB-3 is shown in Fig. 8. There was residual displacement at the story shear of zero after the story drift angle of 1/50. Then the third method to compute joint shear force is indicated below.

c) The schematic stress field in a beam-column joint region is illustrated in Fig. 9 when story shear force returns to zero under reversed cyclic loading. The tensile forces of beam bars at beam critical sections develop as the reaction forces to lateral confinement by framing beams into a joint. The beam tensile forces in this situation do not contribute to the joint shear force as a matter of course. Therefore residual tensile forces should be removed from the beam tensile forces at the peak drift under half cycle of loading when calculating joint shear force as indicated by Equation (3).

$$V_j = \sum a_{st} (\sigma_{st} - \sigma_{t0}) + \sum a_{sb} (\sigma_{sb} - \sigma_{b0}) - V_c \quad (3)$$

Where σ_{t0} and σ_{b0} are the residual tensile stresses of beam top and bottom bars at the story shear of zero just prior to the peak drift.

Joint shear stresses of Specimens PB-1, PNB-2 and PNB-3 obtained by three methods are shown in Fig. 10. The joint shear stress was computed by dividing joint shear force by the effective sectional area of a joint panel that was the product of the average width of the column and beam multiplied by the column depth. The joint shear computed by Equation (2) increased with the increase in joint shear distortion. The joint shear computed by Equation (3), on the contrary, decreased after the story drift angle of 1/25 to the end of the test for Specimen PB-1. The joint shear by Equation (3) was almost equal to that computed by Equation (1) for Specimens PNB-2 and PNB-3 up to the story drift angle of 1/25.

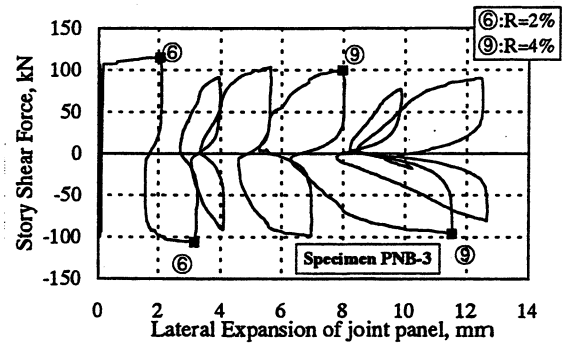


Fig. 8 Lateral expansion of joint panel for Specimen PNB-3

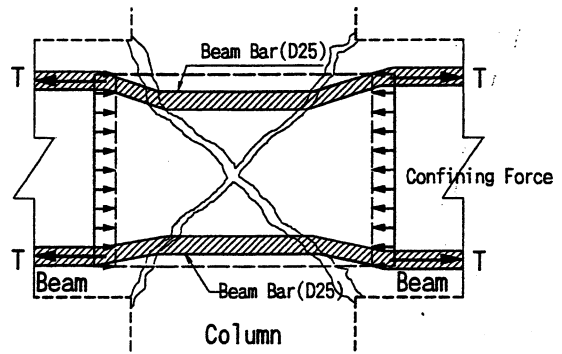


Fig. 9 Schematic stress field in joint at story shear of zero

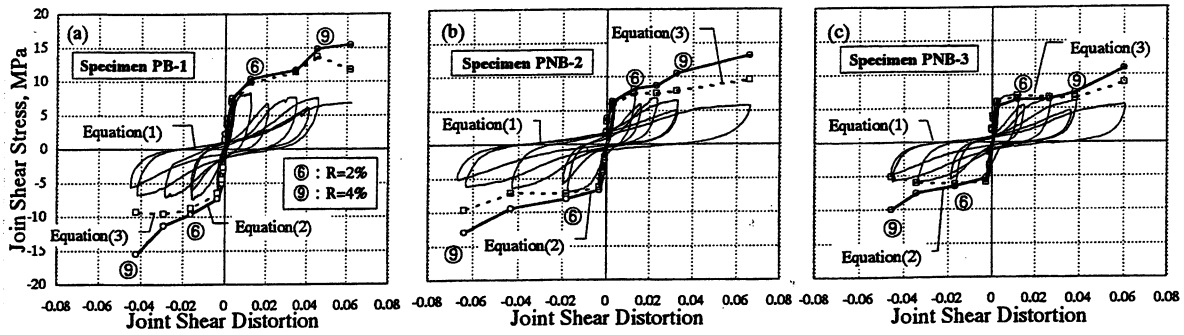


Fig. 10 Joint shear stress - shear distortion relations

4.2 BEAM BAR STRAIN AT CRITICAL SECTION

The beam bar stress within a joint adjacent to a beam critical section for Specimen PB-1 is shown in Fig. 11. Tensile forces of beam bars increased with cyclic loading to the end of the test for all specimens nevertheless the maximum story shear force was attained at the story drift angle of 1/50. The residual tensile force at the story shear force of zero became remarkable after the story drift angle of 1/50 although the strain of beam bars remained to be elastic. It is necessary to take account of residual tensile forces due to damage in a joint core concrete when joint shear force is computed from beam bar forces measured directly.

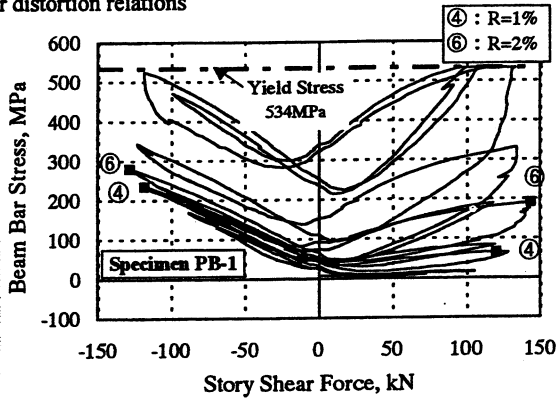


Fig. 11 Beam bar stress adjacent to beam critical section

4.3 BOND ALONG BEAM AND COLUMN BARS

The average bond stresses along a beam bar within a joint for all specimens are shown in Fig. 12. The average bond stress was computed by the difference of the pair of beam bar forces adjacent to column faces. Beam bar bond stress for Specimen PB-1 decreased after the story drift angle of 1/50 whereas tensile force of beam bars at critical sections increased to the end of the test. It is judged that the decrease in bond stress along beam bars within a joint resulted from bond deterioration. Beam bar bond stress for Specimen PBU-4 increased up to the story drift angle of 1/25 though story shear force reached at the maximum at the story drift angle of 1/50 and decreased after the drift. Then the decay of story shear resistance was not caused by bond deterioration along beam bars within a joint.

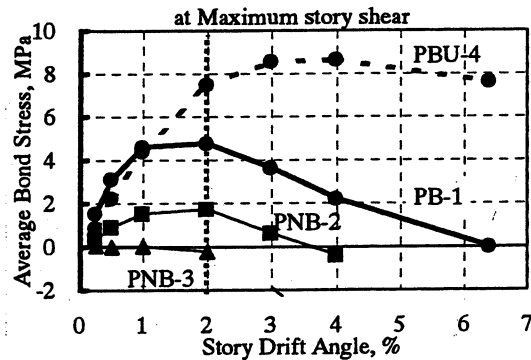


Fig. 12 Average bond stress along beam bar within joint

The average bond stresses along a column bar within a joint are shown in Fig. 13. Column bar bond stress reached at the maximum stress of 3 MPa at the story drift angle of 1/50. Bond deterioration along column bars occurred within a joint after the story drift angle of 1/50.

4.4 DEFORMATION IN JOINT PANEL

The lateral and vertical average strains in a joint panel are shown in Figs. 14 and 15 respectively. The tensile principal strain - compressive principal strain relationships in a joint panel are shown in Fig. 16. These strains were computed by using average displacements measured by two horizontal, vertical and

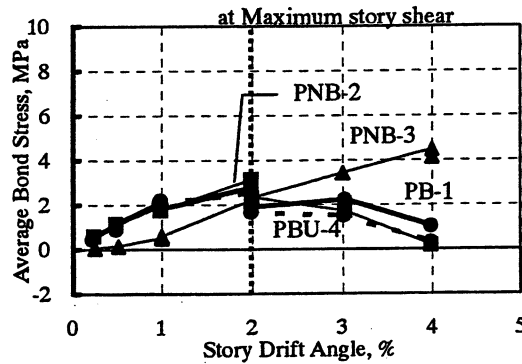


Fig. 13 Average bond stress along column bar within joint

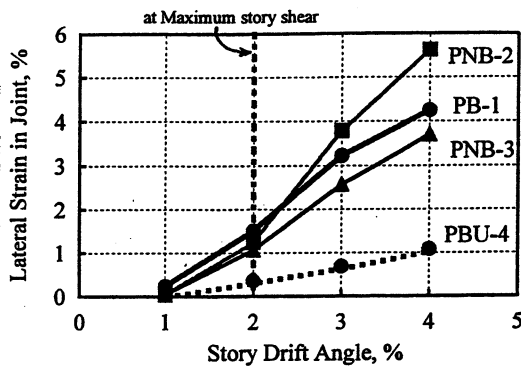


Fig. 14 Lateral average strain in joint panel

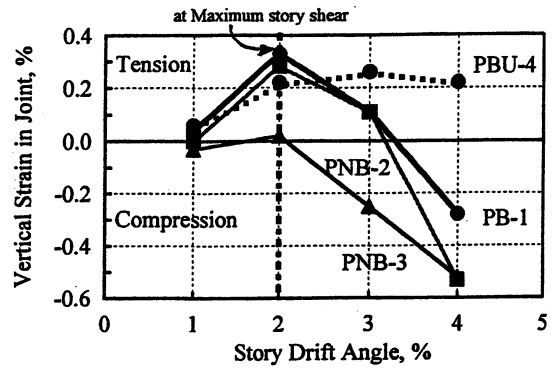


Fig. 15 Vertical average strain in joint panel

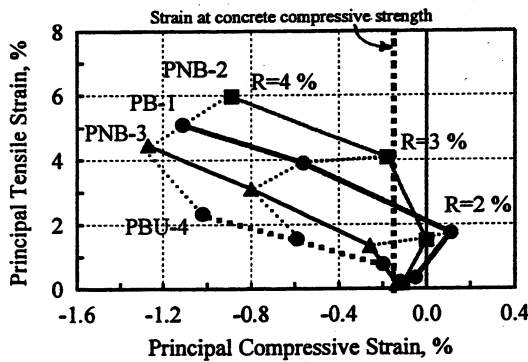


Fig. 16 Principal strains in joint panel

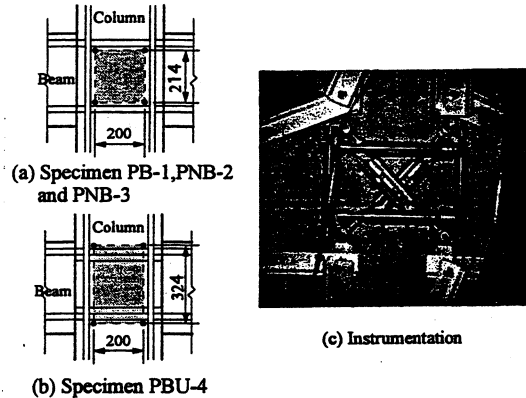


Fig. 17 Instrumentation for joint panel distortion

diagonal displacement transducers respectively as illustrated in Fig. 17.

Lateral strains for Specimens PB-1, PNB-2 and PNB-3, where anchorage steel plates were placed at beam critical sections, increased abruptly at the story drift angle of 1/50. On the contrary, lateral strain for Specimen PBU-4 which had the twice amount of beam cross-sectional areas in a joint region comparing with other specimens was smaller than other specimens. Vertical strains of a joint panel changed from elongation to shrinkage at the story drift angle of 1/50 except for Specimen PBU-4. This means that compressive failure in joint core concrete was progressing after the story drift angle of 1/50.

Tensile principal strain in a joint panel augmented suddenly for all specimens at the story drift angle of 1/25 as shown in Fig. 16. The strain in Specimen PBU-4 however was less than the half in other specimens since the lateral expansion of joint core concrete was restricted by beam longitudinal bars passing through a joint with additional welded bars. Compressive principal strain exceeded the strain of 0.16% at the concrete compressive strength by cylinder tests at the story drift angle of 1/50 for Specimens PNB-3 and PBU-4, at the story drift angle of 1/33 for other specimens. Therefore it is considered that the compressive failure of core concrete took place in a joint panel.

Mohr's strain circles are shown in Fig. 18 at the story drift angle of 1/50 by shaded area, 1/33 by dashed line and 1/25 by solid line to investigate deformation property of a joint panel in more detail. The half angle of inclination of the diameter drawn in the Mohr's circle to the abscissa represents the direction of compressive principal strain to the vertical axis along a column. It means that the larger Mohr's circle is, the severer the damage in a joint core concrete is. The strain circle of Specimen PBU-4 was the smallest among specimens. This indicates that the increase in the cross-sectional areas of beam bars within a joint contributed to restrict joint damage caused by shear. Although bond capacity however was improved simultaneously along beam bars for Specimen PBU-4 as mentioned above, the story shear strength was almost equal to that of Specimen PB-1. This was derived from the following mechanism;

a) compressive principal strain increased beyond the strain of 0.16% at the concrete compressive strength at the story drift angle of 1/50 because isotropic expansion of the joint panel concrete for Specimen PBU-4 was restrained, which can be supposed from the fact that the center of the Mohr's strain circle at the story drift angle of 1/50 was the most adjacent to the point of origin among specimens although the shear distortion angle of 1% approximately was almost same as other specimens.

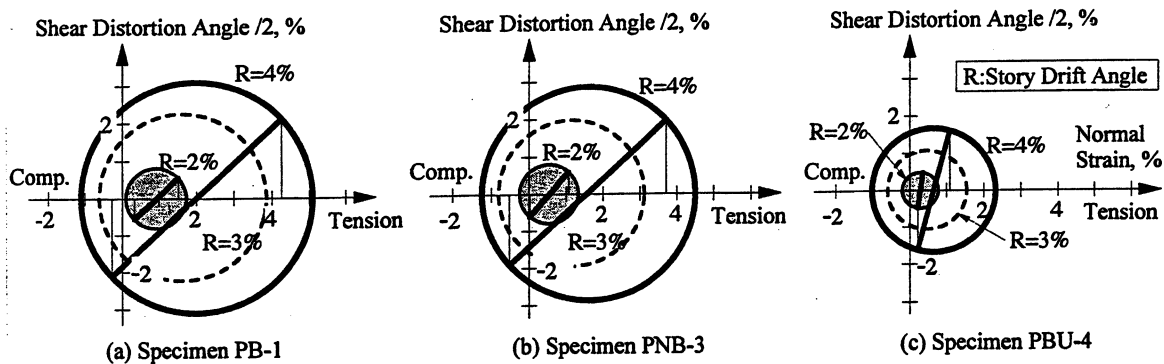


Fig. 18 Mohr's strain circles for joint panel

b) then the concrete within a joint panel failed uniformly by compression. This was judged from two phenomena. The one is that fine diagonal shear cracks occurred in a joint panel whose direction was 45 degrees approximately for Specimen PBU-4 whereas the direction of other specimens stood up more steeply. The other is that the bond transfer to beam bars within a joint was effective to carry joint shear.

5. CONCLUDING REMARKS

The following conclusions can be drawn from the present study.

- 1) The story shear capacity of beam-column subassemblages, where the beam bar bond or both the beam and column bar bond was eliminated within a joint, decayed to 89 percent or 79 percent respectively that of control specimen (PB-1). Thus the bond transfer performance along longitudinal bars passing through a beam-column joint provided important influence to story shear capacity.
- 2) The story shear capacity for Specimen PBU-4, in which bond condition along beam bars was kept good in a joint due to additional deformed bars welded to beam bars, was equal to that for Specimen PB-1 where good anchorage ability was provided to beam longitudinal bars within a joint by steel plates placed at beam critical sections. Joint core concrete failed by compression for both specimens. However the deformation properties as expressed by Mohr's strain circle were fairly different between two specimens.
- 3) The increase in the amount of beam longitudinal bars only in a joint was effective to delay the progress of concrete damage in a joint panel because additional bars within a joint were useful to confine lateral expansion of joint core concrete. Story shear strength however could not be enhanced because of concrete compressive failure developing simultaneously in a joint.
- 4) The joint shear stress computed by Equation (2), where tensile forces of beam bars obtained from measured strains at critical sections were used directly, increased successively to the end of the test. On the contrary, the joint shear stress computed by Equation (3), where residual tensile forces of beam bars caused by lateral expansion in a joint panel were considered, decreased or was kept almost constant for some specimens.

ACKNOWLEDGMENT

The study reported in the paper was sponsored by a Grant-in-aid for Scientific Research of the Ministry of Education and Science. Authors wish to express their gratitude to Tokyo Tekko Co. in offering steel bars.

REFERENCES

- (1) Shiohara, H., "Failure Mechanism of Beam-Column Joints," Proceedings for Symposium of "Present or Future Design Method for Prestressed Concrete Structures," Architectural Institute of Japan, pp.204-239, 2000, (in Japanese).
- (2) Architectural Institute of Japan, "Design Guidelines for Earthquake Resistant Reinforced Concrete Buildings Based on Inelastic Displacement Concept," 1999.
- (3) Shiohara, H. and F. Kushihara, "Re-evaluation of Joint Shear Tests of R/C Beam-Column Joints Failed in Shear," Proceedings of the Japan Concrete Institute, Vol.19, No.2, pp.1005-1010, 1997, (in Japanese).

SEISMIC PERFORMANCE OF REINFORCED CONCRETE BEAM-COLUMN JOINTS

Dawn E. LEHMAN, W. Greg MOSIER, and John F. STANTON¹

ABSTRACT

Reliable methods for assessing the performance of beam-column joints must be developed before performance-based engineering can be applied to reinforced concrete structures in seismic regions. This research addresses joint performance using both analytical and experimental methods. Initially, previous research results were gathered to assess the influence of various parameters on the cyclic response and to guide the development of the experimental program. Preliminary results suggest that a previously unmeasured parameter, the cyclic deformation demand, is one of the most important. Analytical models were developed to relate the joint shear strength to the cyclic demand. Experiments are being conducted to quantify more precisely the effect of cyclic demand on joints without confinement reinforcement. Preliminary results are presented.

1 INTRODUCTION

Performance-based methods for design and assessment of reinforced concrete structures have attracted considerable interest in the last five years. However, implementation of these methods requires quantification of the performance of structural elements to a more detailed and accurate level than was necessary in the past. Much of the attention has been paid to columns, both because they have consistently suffered damage in past earthquakes and because of their importance in maintaining the integrity of the structure. By contrast little attention has been paid to joints. Design of new joints and assessment of existing ones may depend on quite different criteria. A structure with weak joints could be retrofitted by installing a stiff wall, in which case the forces on the joint are controlled by the maximum drift as dictated by the wall. In a new joint, the forces are controlled by strength of the beam reinforcement. A better understanding, both qualitative and quantitative, of the performance of joints is needed to implement performance-based design and assessment methodologies. The research program described here was undertaken to improve that understanding using analytical and experimental methods. The objectives of the analytical component are to

¹ *Department of Civil and Environmental Engineering, University of Washington, Seattle, WA, 98103 USA*

Email: delehman@u.washington.edu

identify the parameters that most influence the performance and to develop analytical models that predict different performance states. The experimental component specifically targets the seismic performance of joints in existing construction. Most research programs have concentrated on the response of confined joints, but many existing buildings in the US were designed for gravity only and their joints contain little or no confinement reinforcement. This reflects the fact that restrictions on the joint shear stress level and minimum requirements for reinforcement were not instituted until the early 1970s. Typically those columns decrease in size up the building but the beam size remain the same, so the joint shear stress in the upper stories can become very high and may exceed $20\sqrt{f'_c}$ (psi). Such joints almost certainly require retrofit, but the process is cumbersome and may be prohibitively expensive. In order to make it feasible, reliable guidelines are needed, but they cannot be developed until performance is accurately quantified.

2 PREVIOUS RESEARCH RESULTS

Previous results from research from Japan, New Zealand and the United States were gathered and analysed. This study was performed for several reasons. Most importantly, these results were used to gain an understanding of the parameters that influence the seismic performance of beam-column connections. The study parameters of the experimental test program were based on the results from this analysis. In addition, the results were used to evaluate existing models used to assess the joint shear capacity. Most models estimate the joint shear strength as a function of several aspects of the joint loading and reinforcement, most importantly the joint reinforcement ratio, average bond demand, and the axial load ratio (e.g., FEMA 1997, Pantazopoulou 1992). Other researchers have also included the effect of the deformation demand (e.g., Zhang 1982, Lin 2000).

In this study, the influence of these parameters was quantified. The data from 32 relevant specimens were analysed. The study was restricted to interior joints in exterior frames without transverse beams. In addition, joints that appeared to fail due to inadequate bond capacity were excluded because the bond capacity of some of the specimens appeared to be reduced by the presence of the strain gauges. The study only included specimens that fail as a result of inadequate joint shear strength and beam hinging.

For the specimens used in the study, the geometry, reinforcement and loading were tabulated. Using this data, the joint shear stress, the equivalent uniform bond demand and the

cumulative deformation capacity were calculated for each specimen. Details of the procedures used and the data that was used for the evaluation may be found in (Mosier 2000). These results were used to evaluate the influence of salient joint properties.

2.1 Joint Shear Strength

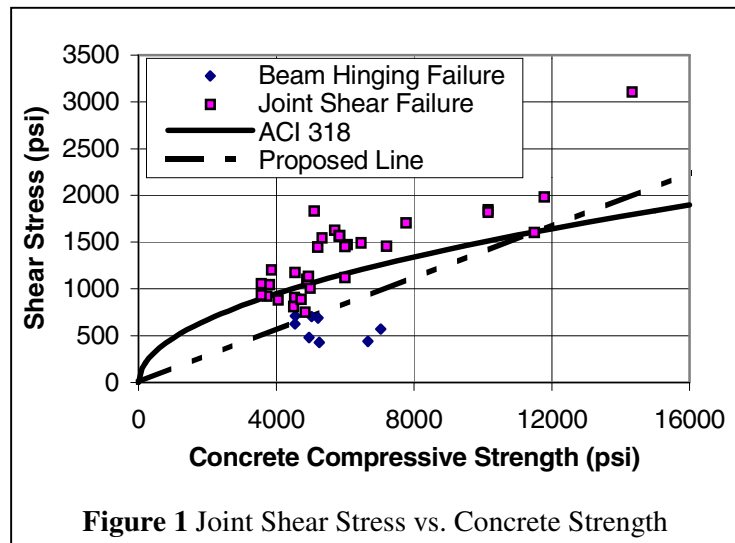
In the United States, joint shear strength is the primary indicator of joint performance (ACI 1999). For new construction, the joint shear strength of an interior joint in an exterior frame is given by Equation Error! Not a valid link., in which f'_c is the specified compressive strength of the concrete, A_j is the equivalent joint area, and V_j is the maximum joint shear force.

$$V_j = 15\sqrt{f'_c(\text{psi})}A_j \quad \text{Eq. 1}$$

This method of assessing joint performance assumes that the joint shear strength is directly proportional to the concrete tensile strength which is in turn proportional to $\sqrt{f'_c}$. However, most tests show that the peak joint force occurs long after cracking and is precipitated by concrete crushing (Mosier 2000). Therefore, it may be more reasonable use f'_c as the critical measure as defined by Equation Error! Not a valid link.. The ratio is termed as the normalized joint shear-stress ratio.

$$\frac{v_j}{f'_c} = \frac{V_j}{f'_c A_j} \quad \text{Eq. 2}$$

A comparison of the two methods is provided in Figure Error! Not a valid link.. The joint shear stress, V_j/A_j , is plotted relative to the measured compressive concrete strength for each specimen. The data are divided into two categories, specimens that fail by joint-shear mode and those that fail by beam hinging. The solid line indicates the ACI joint shear stress limit; some of the joint-shear failure specimens lie below this line. The dashed line in the figure represents Equation Error! Not a valid link. and has a slope of 0.14. Note that the line separates the beam-hinging and joint-shear failures.



This indicates two things: (1) expressing the joint shear stress relative to the concrete compressive strength gives a better indication of the joint performance and (2) a joint shear stress limit of $0.14 f'_c$ is a simple method for ensuring beam hinging.

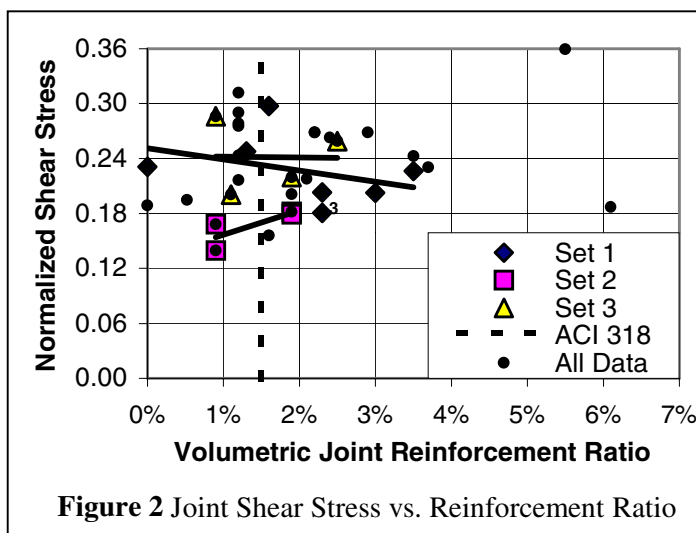
The following sections use the data to analyse the effect of the joint reinforcement ratio and the axial load ratio on the joint shear capacity. In both cases, all of the experimental data were analysed. In addition, to assess the influence of a single parameter, individual data sets were isolated and studied. In the isolated data set, the study parameter was varied but the others were held approximately constant. For example, to determine the influence of the joint reinforcement ratio, data sets were constructed using specimens that had similar axial load ratios and equivalent uniform bond demands. These data sets are used to better assess the influence of each parameter.

2.1.1 Joint Reinforcement Ratio

Previous research results do not demonstrate clearly the effect of the joint reinforcement ratio on the joint shear strength. For example, Meinhiet and Jirsa (1977) tested 5 specimens with volumetric joint reinforcement ratios that ranged from 1.1% to 5.2%. The researchers concluded that although the amount of reinforcement did not influence the cracking strength, it did effect the ultimate joint shear strength. In contrast, Fujii and Morita (1991) tested 4 specimens with volumetric joint reinforcement ratios that ranged from 0.8% to 2.2% and found that the joint shear strength was not increased with an increase in joint reinforcement.

The data were used to assess the influence of the joint reinforcement on the joint shear strength. Figure Error! Not a valid link. shows the normalized joint shear stress ratio as a

function of the joint reinforcement ratio. The joint reinforcement ratio required by ACI 318 (1999) is shown with a dashed line. The isolated data sets are shown using larger markers. Three isolated data sets are shown. The three sets have approximately constant values of axial load ratio and average bond stress demand. The results do not provide a discernible



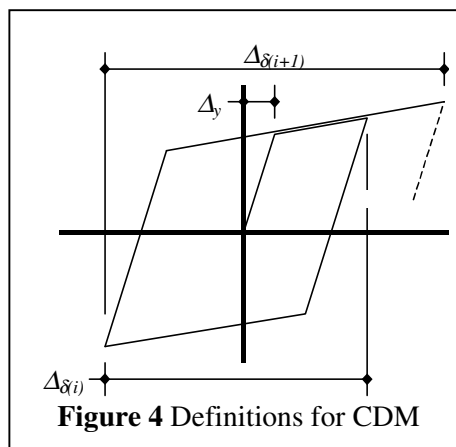
trend. Therefore, it is not possible to determine a reliable relationship between the normalised joint shear stress and the joint reinforcement ratio using the experimental data.

deformation. Therefore the procedure used in this study to evaluate the cyclic deformation is explained in Section 2.2.1. The subsequent sections used this measure to assess the influence of the joint reinforcement ratio and the axial load ratio on the cumulative ductility measure.

2.2.1 Cumulative Ductility Measure

Study of experimental results indicates that cycling influences the performance of beam-column connections. Although joint shear strain is a logical measure of joint performance, it is seldom reported. Instead, the displacement ductility was adopted to quantify the cyclic deformation. Use of this imperfect measure was used because all researchers reported the force-displacement response.

Previous researchers have used displacement ductility to quantify the cyclic load effects. The model by Baik et al. (1988) was adapted to quantify the cumulative ductility. However, the Baik model used the plastic deformation to quantify the effect of cycling. Experimental results demonstrate that joint damage may accumulate at displacement demands that are less than the yield displacement, therefore, the proposed measure is based on the total deformation. The



cumulative ductility measure (CDM), Λ , is defined by Equation 4 and the components are described in Figure Error! Not a valid link. in which $\Delta_{\delta i}$ is the total displacement range for cycle i , Δ_y is the yield displacement, and n is the number of half cycles.

$$\Lambda = \sum_{i=1}^n \left(0.5 |\Delta_{\delta i}| / \Delta_y \right)^{1.5} \quad \text{Eq. 4}$$

The cumulative ductility measure has an exponent of 1.5. Qualitatively, this indicates that the larger deformation demands are more damaging.

2.2.2 Joint Shear Strength

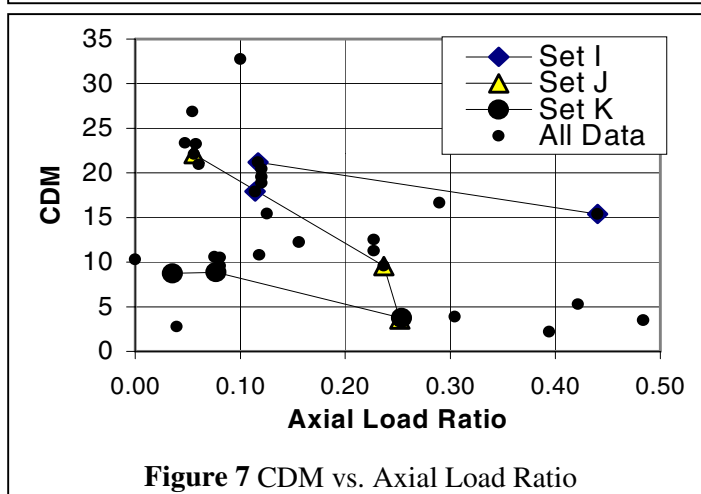
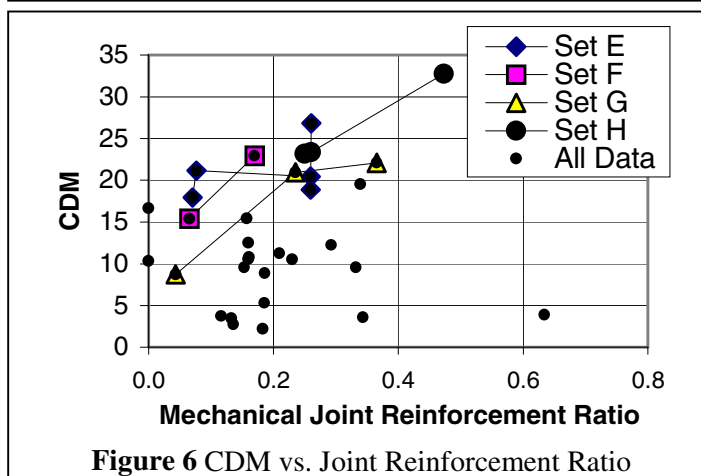
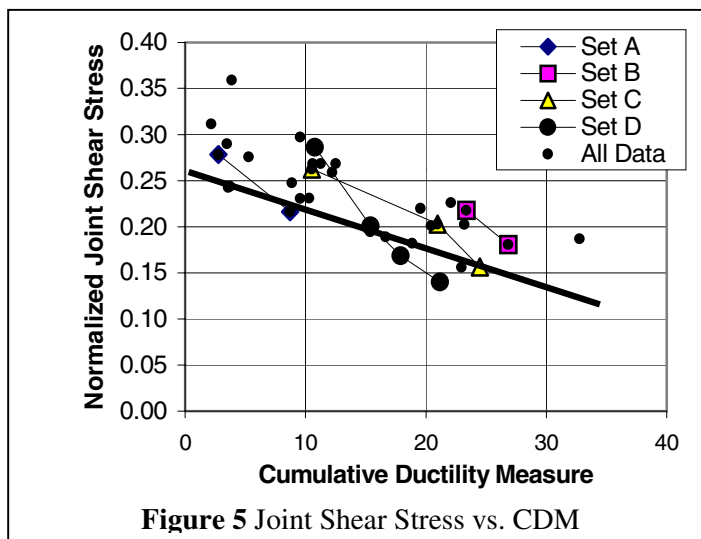
Experimental results indicate that the joint shear strength decreases with an increase in the cyclic deformation demand (Meinheit 1977, Milburn 1982). Figure 5 also shows this trend. This trend is also supported by the isolated data sets. All four sets indicate that the joints with lower normalised joint shear stress ratios sustained a larger cumulative ductility measure.

2.2.3 Joint Reinforcement Ratio

The data were used to evaluate the influence of the joint reinforcement ratio on the cycle deformation capacity. Previous researchers have noted an increase in the cyclic deformation capacity with an increase in the joint reinforcement ratio (e.g., Meinheit 1977, Durrani 1982). In the Figure Error! Not a valid link., the complete data set shows no discernible trend. However, the isolated data sets provides more insight. Three of the four indicate that increasing the joint reinforcement ratio increases the cumulative ductility measure.

2.2.4 Axial Load Ratio

Finally, the influence of the axial load ratio on the cumulative deformation measure was considered. Figure Error! Not a valid link. shows all of the data and three isolated data sets. Both indicate the cumulative ductility measure is larger for beam-column joints with smaller axial load ratios.



2.3 Expressions to Evaluate Joint Shear Strength

The research results presented herein were used to develop two predictive expressions to calculate the joint shear strength. The first, given by Equation 5, is described by the solid line shown in Figure Error! Not a valid link.. This model relates the normalized joint shear stress to the cumulative ductility measure.

$$\frac{v_j}{f'_c} = -\frac{\Lambda}{170} + 0.31 \quad \text{Eq. 5}$$

Equation **Error! Not a valid link.** can be expanded to include the influence of the joint reinforcement ratio and the axial load ratio. Equation 6 gives this expression and reflects the trends shown in Figures 6 and 7.

$$\frac{v_j}{f'_c} = 6 \frac{(1 + \rho_{vj} f_{yh} / f'_c)}{(\Lambda + 14) * (1 + P / (A_g f'_c))} \quad \text{Eq. 6}$$

Of the two proposed models, the first model (Equation **Error! Not a valid link.**) is simpler to use, but it fits the experimental data less well. The model provided by Equation 6 matches the test data more closely because it accounts for the additional parameters that have been found to be important. On average, the ratio of the predicted to measure joint shear strength is 0.99 and standard deviation is 0.13 (Table **Error! Not a valid link.**) and a maximum ratio of 1.24. These statistics show the improvement available for Model 2 relative to Model 1.

Table 1 Comparison of Predicted/Measured Ratios

Model	Average	Standard Deviation	Coeff. Of Variation	Maximum Deviation
Model 1 (Eq. 5)	1.05	0.22	0.22	50%
Model 2 (Eq. 6)	0.99	0.13	0.13	24%

3 EXPERIMENTAL RESEARCH STUDY

The experimental portion of the research was designed to build on and improve upon the previous research results. As shown in Figure **Error! Not a valid link.**, few experimental studies have focused on joints without reinforcement. These results are required to develop performance-based seismic methodologies for non-ductile reinforced concrete buildings. To achieve this, the experimental research study was designed to assess the seismic performance of beam-column joints in non-ductile building frames.

To develop the test matrix, the previous research results were considered. Although the results indicate that the cumulative displacement demand is one of the most influential parameters, previous experimental research programs have not been designed to specifically study this effect. In this study, the influence of the displacement history will be studied by subjecting nominally identical specimens to different displacement histories. Three other

specimens will be constructed to study the axial load ratio, the concrete strength, and the joint shear stress ratio, since the research results indicate that these are significant as well.

3.1 Test Matrix

The test matrix consisted of seven specimens constructed at approximately 2/3-scale. The specimens were constructed to relate to a reference specimen. The reference specimen is shown in Figure Error! Not a valid link.. The reference specimen had a joint shear stress ratio of approximately $0.14f'_c$, an axial load ratio of 0.1 (relative to the gross cross sectional

properties), and a concrete strength of approximately 5 ksi. The reference specimen was tested using a displacement history labelled “Standard” which consisted of three cycles at increasing drift levels. Specimen yield occurred at approximately 0.75% drift. The post-yield drift levels included 1%, 1.5%, 2%, 3%, 4%, and 5%. The specimen

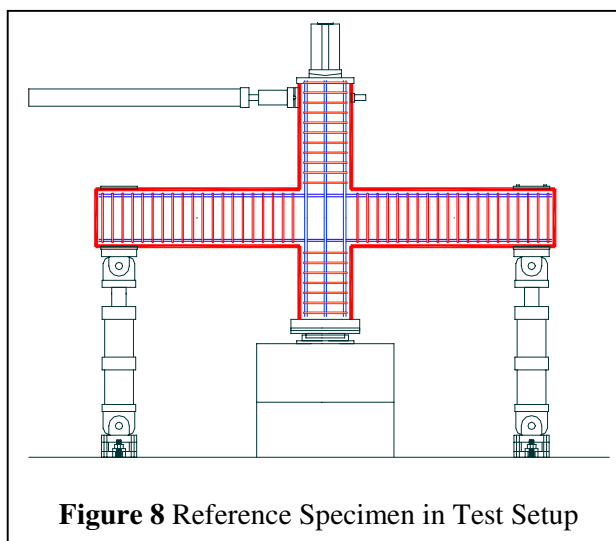


Figure 8 Reference Specimen in Test Setup

was tested until the majority of its lateral load carrying capacity was lost.

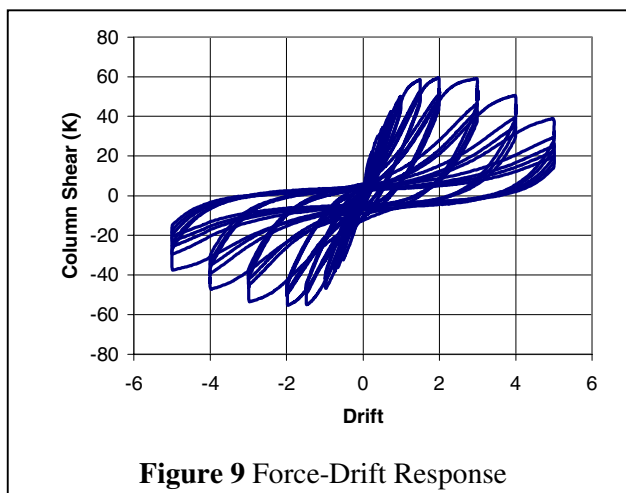
The remaining specimens relate to the reference specimen as shown in Table Error! Not a valid link.. The study parameter for each of the remaining specimens is identified in bold. Three additional specimens will be tested using constant amplitude displacement histories. It is expected that drift levels of 0.75%, 1.5%, and 3% will be targeted. The remaining specimens differ from the reference specimen in their axial load ratio, concrete strength, or normalized joint shear stress.

Table 2 Test Matrix

Specimen	Drift History	Axial Load	Concrete Strength	Shear Stress
Reference	Standard	$0.1f'_cA_g$	5 ksi	$\approx 0.14f'_c$
CD1	Constant: 0.75%	$0.1f'_cA_g$	5 ksi	$\approx 0.14f'_c$
CD2	Constant: 1.5%	$0.1f'_cA_g$	5 ksi	$\approx 0.14f'_c$
CD3	Constant: 3%	$0.1f'_cA_g$	5 ksi	$\approx 0.14f'_c$
Axial	Standard	$0.25f'_cA_g$	5 ksi	$\approx 0.14f'_c$
Concrete	Standard	$0.1f'_cA_g$	7-8 ksi	$\approx 0.14f'_c$
Joint Shear	Standard	$0.1f'_cA_g$	5 ksi	$\approx 0.22f'_c$

3.2 Results

At the time of this writing, only the reference specimen has been tested. The force-displacement response is shown in Figure 9. During testing, damage was closely monitored. The progression of joint damage was as follows: (1) initial joint cracking: 0.5% drift, (2) first yield of beam bars: 0.75% drift, (3) open residual crack widths: 2% drift, (4) initial spalling: 1% drift, (5) loss of 20% of lateral load carrying capacity: 3-4% drift, and (6) loss



of 50% of lateral load carrying capacity: 5% drift. As might be expected for a beam-column joint without ties, the force-displacement response is pinched relative to the hysteretic response of a ductile element, such as a beam or column. However, the maximum lateral load is retained to a drift level of approximately 3%, which is the maximum drift level that might be expected for an existing building that has been retrofitted with stiff elements or the maximum drift that the building might experience in a moderate level earthquake. Even at a drift level of 5%, the joint sustains a portion of the lateral load and its entire axial load.

4 SUMMARY AND CONCLUSIONS

Study of previous research results indicates that the seismic response of beam-column connections is influenced by several parameters, including the joint reinforcement ratio and the column axial load ratio. Previous research has studied the influence of these parameters on the joint shear strength. However, study of these research results does not show a strong relationship between the joint shear strength and the joint reinforcement ratio or the column axial load ratio. Instead it was shown that the cyclic deformation demand has a larger influence on the joint shear strength. In addition, the research indicates that the axial load ratio and the joint reinforcement ratio can influence the cyclic deformation capacity.

Using these results, an equation was developed to predict the joint shear strength. The equation is a function of the parameters identified earlier, including the cyclic deformation capacity and the results indicate that it is reliable.

Finally, the findings were used to develop the experimental program. The program will study the performance of joints in non-ductile construction and was designed to evaluate the influence of the cyclic displacement history. The research program is underway and the results will be used to evaluate and modify the prediction equation.

5 ACKNOWLEDGEMENTS

This work was supported in part by the Pacific Earthquake Engineering Research Center through the Earthquake Engineering Research Centers Program of the National Science Foundation under Award number EEC-9701568. The authors would like to thank the laboratory staff and graduate student researchers Chris Yeargin and Stephen Walker at the University of Washington for their help with the experiments. The assistance of the library staff at the PEER center is gratefully acknowledged.

6 REFERENCES

- ACI Committee 318 (1999). *Building Code Requirements for Structural Concrete (ACI 318-99) and Commentary (ACI 318R-99)*, American Concrete Institute, Farmington Hills, MI.
- Baik, S., Lee, D., Krawinkler, H. (1988), A Simplified Model for Seismic Response Prediction of Steel Frame Structures, *Proceedings of the 9th World Conference on Earthquake Engineering*, V:375-380.
- Beckingsale, C.W. (1980), *Post Elastic Behavior of Reinforced Concrete Beam-Column Joints*, Department of Civil Engineering, University of Canterbury, Christchurch, New Zealand.
- Birss, G.R. (1978), *The Elastic Behavior of Earthquake Resistant Reinforced Concrete Interior Beam-Column Joints*, Department of Civil Engineering, University of Canterbury, Christchurch, New Zealand.
- Blakeley, R.W.G., Megget, L.M., Priestley, M.J.N. (1975), Seismic Performance of Two Full Size Reinforced Concrete Beam-Column Joint Units, *New Zealand Society for Earthquake Engineering*.
- Castro, J. J., Imai, H., Yamaguchi, T. (1992), Seismic Performance of Precast Concrete Beam-Column Joints, *10th World Conference on Earthquake Engineering*, 6:3131-3137.
- Durrani, A.J., Wight, J.K. (1982), *Experimental and Analytical Study of Internal Beam to Column Connections*, Department of Civil Engineering, University of Michigan, Ann Arbor, MI.
- Englekirk, R.E., Llovet, D. (1998), Cyclic Tests of Cast-In-Place High Strength Beam-Column Joints FEMA Publication 273 (1997), *NEHRP Guidelines for the Seismic Rehabilitation of Buildings*, Building Seismic Safety Council, Washington, D.C.
- Fujii, S., Morita, S. (1991), Comparison Between Interior and Exterior RC Beam-Column Joint Behavior, *Design of Beam Column Joints for Seismic Resistance*, ACI, Farmington Hills, MI, pp. 145-165.
- Hatamoto, H, Bessho, S. (1988), Structural Behavior of Columns and Beam-Column Subassemblages in a 30 Story Reinforced Concrete Building, *9th World Conference on Earthquake Engineering*, IV:627-632.
- Hwang, S.J., Lee, H.J. (2000), Analytical Model for Predicting Shear Strengths of Interior Reinforced Concrete Beam-Column Joints for Seismic Resistance, *ACI Structural Journal*, 97:35-44.
- Kitayama, K., Lee, S., Otani, S., Aoyama, H. (1992), Behavior of High-Strength R/C Beam-Column Joints, *Proceedings of the 10th World Conference on Earthquake Engineering*, 6:3151-3156.
- Kitayama, K., Otani, S., Aoyama, H. (1991), Development of Design Criteria For RC Interior Beam-Column Joints, *Design of Beam Column Joints for Seismic Resistance*, ACI, Farmington Hills, MI.
- Lin, C. (2000), *Seismic Behavior and Design of Reinforced Concrete Interior Beam-Column Joints*, Department of Civil Engineering, University of Canterbury, Christchurch, New Zealand.
- Meinheit, D.F., Jirsa, J.O. (1977), *The Shear Strength of Reinforced Concrete Beam-Column Joints*, Department of Civil Engineering, University of Texas, Austin, TX.
- Milburn, J.R., Park, R. (1982), *Behavior of Reinforced Concrete Beam-Column Joints Designed to NZS 3101*, Department of Civil Engineering, University of Canterbury, Christchurch, New Zealand.

- Mosier, G. (2000), *Seismic Assessment of Reinforced Concrete Beam-Column Joints*, University of Washington, Seattle, WA.
- Noguchi, H., Kashiwazaki, T. (1992), Experimental Studies on Shear Performances of RC Interior Column-Beam Joints with High-Strength Materials, *10th World Conference on Earthquake Engineering*.
- Noguchi, H., Kurusu, K. (1988), Correlation of Bond and Shear in RC Beam-Column Connections Subjected to Seismic Forces, *9th World Conference on Earthquake Engineering*, IV:597-602.
- Oka, K., Shiohara, H. (1992), Tests of High-Strength Concrete Interior Beam-Column-Joint Subassemblages, *10th World Conference on Earthquake Engineering*, 6:3211-3217.
- Owada, Y. (1992), Seismic Behaviors of Beam-Column Joint of Reinforced Concrete Exterior Frame Under Varying Axial Load, *10th World Conference on Earthquake Engineering*, 6:3181-3184.
- Pantazopoulou, S., Bonacci, J. (1992), Consideration of Questions about Beam-Column Joints, *ACI Structural Journal*, 89:27-36.
- Park, R., Gaerty, L., Stevenson, E.C. (1981), Tests on an Interior Reinforced Concrete Beam-Column Joint, *Bulletin of the New Zealand National Society for Earthquake Engineering*, 14:81-92.
- Pessiki, S. P., Coneley, C. H., Gergely, P., White, R. N. (1990), *Seismic Behavior of Lightly-Reinforced Concrete Column and Beam-Column Joint Details*, Cornell University, Ithaca, NY.
- Yunfei, H., Chingchang, H., Yufeng, C. (1984), Behavior of Reinforced Concrete Beam-Column Joints under Reversed Cyclic Loading, *8th World Conference on Earthquake Engineering*, 6:485-492.
- Zhang, L., Jirsa, J.O. (1982), *A Study of Shear Behavior of Reinforced Concrete Beam-Column Joints*, Department of Civil Engineering, University of Texas, Austin, TX.

keywords: beam-column joints, cyclic, non-ductile, seismic, performance, joint shear strength

**SESSION B-4: BEAM-COLUMN JOINTS AND
EXISTING BUILDINGS**

Chaired by

◆ John Wallace and Daisuke Kato ◆

SEISMIC DAMAGE AND PERFORMANCE EVALUATION OF R/C BEAM-COLUMN JOINTS

Masaru TERAOKA¹ and Shigeru FUJII²

ABSTRACT

To establish the performance-based seismic design, it is necessary to prepare the evaluation methods for seismic performance and damage of structural members with sufficient accuracy. In this report, the seismic damage and the shear performance of beam-column joints were focused on. The shear failure process in joints was shown, and the shear stress - shear distortion relationship in joint panels was modeled. According to database analysis of reversed cyclic loading experiment on RC interior beam-and-column subassemblages, the relationship between damage progress and shear stress-shear distortion characteristic was examined. Based on above examinations, the relationship between the damage and the experienced shear distortion was summarized as the damage map, and the schematic relationship among experienced shear distortions and observed damage conditions and residual seismic performance was shown. By applying these relationships and expected frame ductility requirement, the design criteria to control the damage to beam-column joints was proposed.

1. INTRODUCTION

To establish the performance-based seismic design, it is necessary to prepare the evaluation methods for strength and deformation capacity of structural members with sufficient accuracy. Moreover, it is important to make clear the relationship between the expected seismic damage, such as crack behavior and concrete crushing, and restoring force-deformation characteristics. It is required that the remaining performance of the damaged building after the earthquake can be evaluated by observed damage conditions. Structural engineers must have the judgment materials for its serviceability, reparability and safety for the collapse (Fujii, 1999a).

In RC moment resisting frame structures, recent research works show that the seismic performance of beam-column joints significantly affects the frame behaviors. The seismic performances to be evaluated for the beam-column joints are: (1) the shear performance of the joint panels, (2) the performance on bond and anchorage of beam and column longitudinal reinforcement, and (3) the performance of supporting the axial load of upper floors at the joint as a part of the column. In this report, the shear performance of beam-column joints is focused on. The relationship between load-deformation curves and observed damages are examined. The standard values of various limit conditions of serviceability, reparability and safety for collapse are discussed. And the design criteria to control the damage to beam-column joints is proposed.

2. SHEAR FAILURE PROCESS IN JOINTS

Previous experimental results showed that the relationship between the joint shear force and the shear distortion ($\tau - \gamma$ curve) is generally given by the curve in Figure 1.

¹ *Technology Development Division, Fujita Corporation, Kanagawa, Japan*
E-mail: teraoka@fujita.co.jp

² *Department of Global Environment Engineering, Kyoto University, Kyoto, Japan*
E-mail: fujii@archi.kyoto-u.ac.jp

The envelope of the reversed cyclic $\tau - \gamma$ curve is given by the dotted line in the figure, where three characteristic points can be defined: the point A (the shear cracking), the point B (beginning of the shear compressive failure at panel zone concrete) and the point C (the stage at the maximum shear strength) (Sasaki et al., 1993).

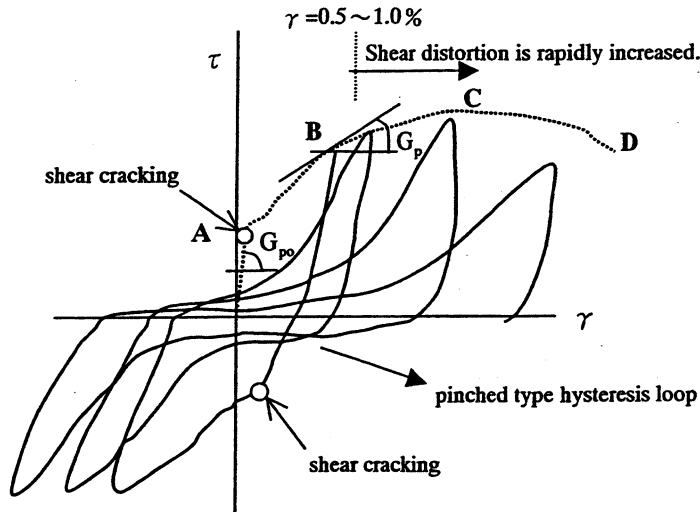


Figure 1 Model of the relationship between shear force and shear deformation in joint panels

2.1 Region A-B: Process of development, increase in number and widening of shear crack

Before joint shear crack occurs, the joint region behaves elastically. After the shear crack occurs, the stiffness in $\tau - \gamma$ curve is reduced. The region A-B corresponds to the process of an increase in the number of cracks and an increase of crack width. The cracks intersect diagonally under reversed cyclic loadings and the number and crack width increase in proportion to the increase of the applied shear stress. The shear distortion of the joint panels in the region A to B is mainly originated by a diagonal extension due to the progress of cracks, not by the concrete compression in the other direction. It seems that the diagonal extension can be controlled by joint shear reinforcement and the intermediate column reinforcement. As the shear stress increases, the diagonal compressive strain gradually increases and the crushing of panel zone concrete starts at the point B. Previous test results show that, the shear distortion angle of the joint panels is around 0.4% and the maximum shear crack width is about 0.4 mm at the point B. However, the strain in joint shear reinforcement is in the range of elasticity in general cases (Teraoka et al., 2000). Therefore, after unloaded from this region A-B, the cracks close. The axial compression force in the column also contributes to crack closing. The influence on the remaining performance is the decreasing rigidity at reloading.

2.2 Region B-C : Progress of compressive strain of concrete

In the region B-C, when the shear stress level becomes larger, the concrete compressive failure develops as well as cracks open and develops. Joint shear reinforcement reaches the yield strain. It was pointed out that once the shear distortion angle attains to about 0.4-0.5%, the shear distortion angle of the joint panels increases rapidly by subsequent loadings (Kaku et al., 1989). In this stage, the compressive failure progress and the shear lag along cracks appears. Cracks do not close after unloading and the width becomes larger. After the point B, not only the crack width but also the concrete compressive failure observation comes to be

the damage index to judge the experienced stress level and evaluate the residual resistance. In this stage, the damage condition is influenced by the frequency of the cyclic loading and the axial load level of column also affects these damages. The residual performance is greatly reduced in the shear rigidity of $\tau - \gamma$ curve and in cyclic joint shear.

2.3 Maximum strength point C

At the maximum strength, the large compressive concrete strain causes the dilatation, and the spalling of the cover concrete. The shear distortion angle at the maximum shear stress is about 1 %.

2.4 Region C-D

The compressive failure and the spalling of cover concrete in the joint panels occur after the maximum strength is reached. In most cases, the joint shear resistance gradually decreases, not rapidly. It seems that it is because the joint panel is the area that is confined by beams and columns.

3. MODEL OF SHEAR STRESS - SHEAR DISTORTION RELATIONSHIP ($\tau - \gamma$ CURVE) IN JOINT PANELS

The experimental results on the $\tau - \gamma$ characteristic are widely scattered because it is not easy to measure γ with accuracy. As the envelope relationship of the $\tau - \gamma$ curve up to maximum strength, two models have been proposed: the bi-linear model (Kitayama, 1992) that was introduced in AIJ Design Guidelines for Earthquake Resistant R/C Buildings Based on Inelastic Displacement Concept(1999b), and the above-mentioned tri-linear model. In the model of the former, neither properties after the maximum strength nor the hysteresis characteristic are formulated, and in a latter model, recently the characteristic of hysteresis was formulated (Teraoka et al., 2000). In this paper, the simplified model is introduced based on these models (When a detailed examination is required please refer to original works). Here, the envelope curve is formulated by quadri-linear curve divided by the characteristic point A, B, C, and D as shown in Figure 1.

3.1 Point A : Shear cracking point (τ_{sc}, γ_{sc})

The shear cracking point can be estimated using the principal stress equations and the shear modulus of concrete in following equations:

$$\tau_{sc} = \sqrt{f_t^2 + f_t \cdot \sigma_0} \quad (1.a)$$

$$\gamma_{sc} = \tau_{sc} / G_c \quad (1.b)$$

where, f_t : tensile strength of concrete, assumed to be $f_t = 0.4\sqrt{\sigma_B}$ (N/mm²),
 σ_B : concrete strength in N/mm²,
 σ_0 : axial compressive stress in column,
 G_c : shear modulus of concrete.

3.2 Point B : Shear compression failure occurrence point (τ_{fc} , γ_{fc})

Overviewing the previous test results, the shear compression failure of joint concrete occurs when the joint shear stress of joints panels reaches about 85% of ultimate shear strength. The shear distortion of joint panels is around 0.4%,

$$\tau_{fc} = 0.85 \tau_{ju} \quad (2.a)$$

$$\gamma_{fc} = 0.4\% \quad (2.b)$$

The definition of the joint shear stress and the formulation of the maximum joint shear stress τ_{ju} is given in 3.3.

3.3 Point C : Ultimate shear strength point (τ_{ju} , γ_u)

Ultimate joint shear strength point can be estimated by following equations:

$$\tau_{ju} = \frac{V_{ju}}{b_j D_j} = \kappa \phi F_j \quad (3.a)$$

$$\gamma_u = 1.0\% \quad (3.b)$$

where, V_{ju} : ultimate joint shear force,

κ : factor dependent on the shape of beam-column joints (1.0 for interior joints, 0.7 for exterior joints and 0.4 for a corner knee joints),

ϕ : factor on the effect of transverse beams (1.15: joints with transverse beams on the both sides of the joint, 1.0: other type joints),

F_j : standard value of the joint shear strength, which is assumed to be

$$F_j = 0.8 \times \sigma_B^{0.7} \text{ (N/mm}^2\text{)},$$

σ_B : concrete strength in N/mm²,

D_j : column depth for an interior connection, or projected development length of anchored beam bars with 90-degree hook for exterior and knee joints,

b_j : effective width of beam-column connection, given by following equations:

$$b_j = b_b + b_{a1} + b_{a2}$$

where, b_b : beam width,

b_{a1} , b_{a2} : the smaller of one-quarter of column depth and one-half of distance between beam and column face on either side of beam.

This strength evaluation is based on the AIJ Design Guideline 1999. As the design equation has a safety margin, it is noted that the safety factor of about 1.0 was used in this paper by changing the factor ϕ from 1.0 (Guideline) to 1.15 for interior joints and from 0.85 to 1.0 for exterior joints. The power function of the equation was originally given by the statistical examination of previous test data (Teraoka et al., 1991&1992, Murakami et al., 1998). According to the comparative study using the above equations for previous test data, the average ratio of measured-to-calculated values were 1.01 for interior joints and 1.14 for exterior joints, with standard deviations of 0.10 and 0.21, respectively.

3.4 C-D region: Strength decreasing region

Although there exists the effect of cyclic loading on resistance degradation after peak behavior, a few test data is available. Based on the previous test data, the post-peak behavior was roughly estimated here as follows.

$$\tau_{jd} = 0.8\tau_{ju} \quad (4.a)$$

$$\gamma_{jd} = 2.0\% \quad (4.b)$$

4. RELATIONSHIP BETWEEN DAMAGE PROGRESS AND SHEAR STRESS-SHEAR DISTORTION CHARACTERISTIC

As the damage indices for beam-column joints, the shear crack width and concrete crushing area can be used. Here, some simplification of recent research work (Teraoka et al., 1997&2000) is made for practical purpose.

Thirty-three interior beam-column joint specimens were employed for this study. The dimension of column section is in the range of 300~540mm in width and depth, respectively, and the dimension of beam section is in the range of 240~365mm in width and in the range of 300~560mm in depth.

4.1 Relationship between shear distortion and maximum shear crack width

Figure 2 shows the example of the relationship between joint shear maximum crack width and shear distortion ($w-\gamma$). Maximum crack width becomes larger in proportion to the shear distortion. There is a large scatter in crack width at the range of $\gamma > 0.5\%$. The average crack width at $\gamma = 0.4\%$, when the panel concrete starts to crush, is about 0.4mm. The average crack width at $\gamma = 1.0\%$, when the maximum joint shear strength is reached, is about 1mm.

Figure 3 shows the example of the relationship between the residual crack width after unloading (w_r) and the experienced maximum crack width (w). The different relationship between w_r and w is observed for the range of $w < 0.4\text{mm}$ and $w > 0.4\text{mm}$. When the experienced shear distortion was smaller than 0.4%, the cracks almost close or resulted in minor after unloading.

Figure 4 shows the stiffness degradation (G/G_0) in $\tau-\gamma$ curve with an increase of maximum crack width (w), where the G is the tangent shear modulus in reversed cyclic loadings and the G_0 is the initial tangent shear modulus. According to this figure, tangent modulus (G) has decreased to about 0.1-0.2 of initial modulus (G_0) when w is larger than 0.4mm.

Figure 5 shows the example of the relationship between average strain of joint hoops ($\bar{\epsilon}$) and maximum crack width (w), which were obtained from the previous tests with ordinary strength joint-hoops. Most transverse reinforcements remained in elastic range when w is smaller than 0.4-0.5mm.

These behaviors show that the shear distortion angle of 0.4% is one of the boundaries for the recovery performance. The joint shear reinforcement yields when w becomes larger than 0.4mm. After this stage the concrete crushing of panel zone becomes significant.

When the joint experiences over 0.4% of shear distortion, the degree of compressive failure of panel zone concrete should be added to the crack width. To analyze this behavior, the fractal dimension analysis was introduced (Teraoka et al., 2000). This method made possible to evaluate the compressive failure progress continuously as a function of shear distortion. As a simplification, the compressive failure damage conditions are given in the figures in Table 1

in this paper. When a detailed examination is required, please refer to the reference.

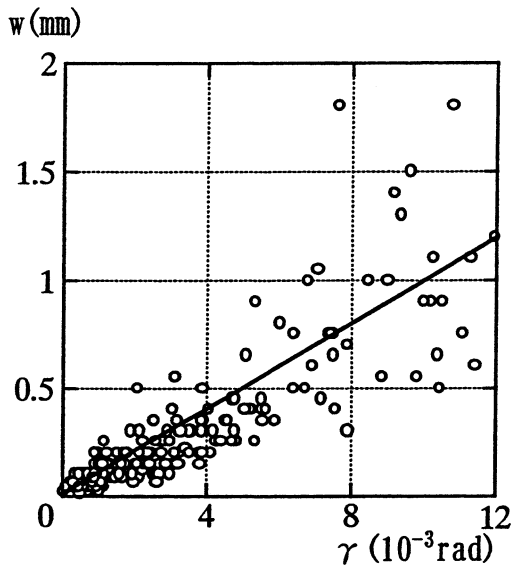


Figure 2 Relation between shear distortion (γ) and maximum shear crack width (w)

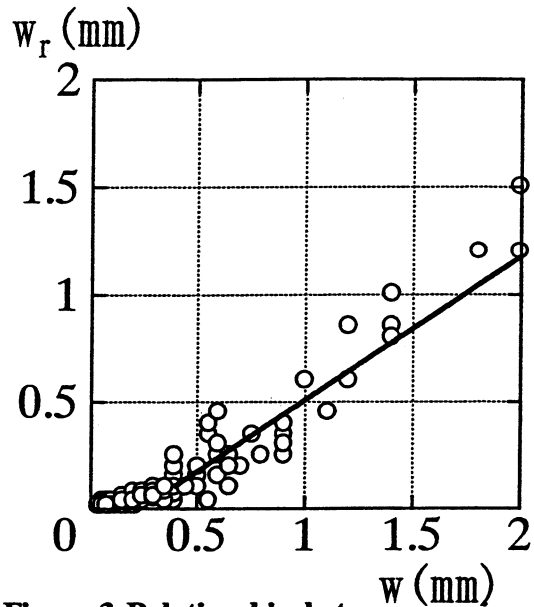


Figure 3 Relationship between maximum shear crack width (w) and maximum residual shear crack width (w_r)

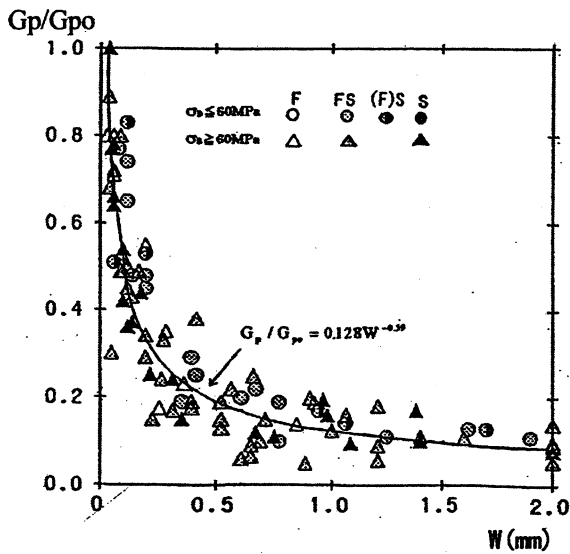


Figure 4 Relationship between stiffness degradation (G_p/G_{p0}) and maximum shear crack width (w)

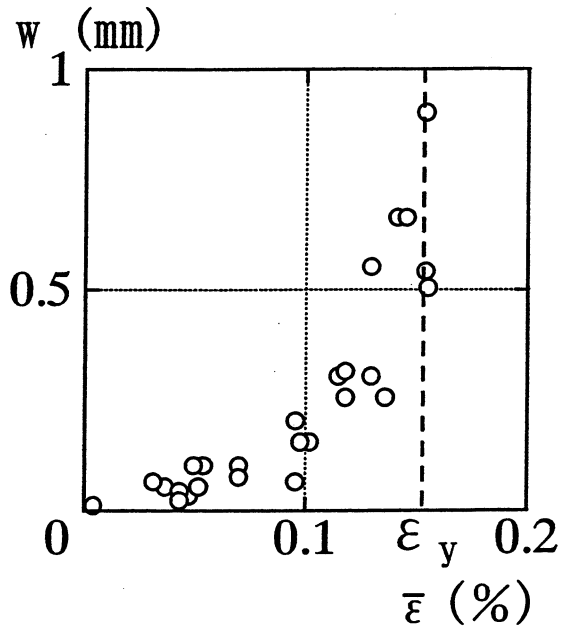


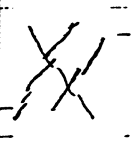




Figure 5 Relationship between the maximum shear crack width (w) and average strain of transverse reinforcement ($\bar{\epsilon}$)

4.2 Relationship between experienced shear distortion and damage condition, and seismic performance

Based on the above-examinations, the relationships between the damage and the experienced shear distortion (shear stress level), can be summarized in Table 1. This table can be used as the damage map.

Figure 6 shows the schematic relationship among experienced shear distortions and observed damage conditions and residual seismic performances (serviceability, repairability, and safety for collapse). Serviceability, repairability and safety are estimated to degrade linearly from the point A, B and C respectively. There have not been enough test data on the repaired and strengthened specimens (Teraoka et al., 1997). Limited test data show that it was possible to recover the shear strength but not in stiffness. And it is also the point that the effective strengthening method for joint shear capacity has not been proposed yet.

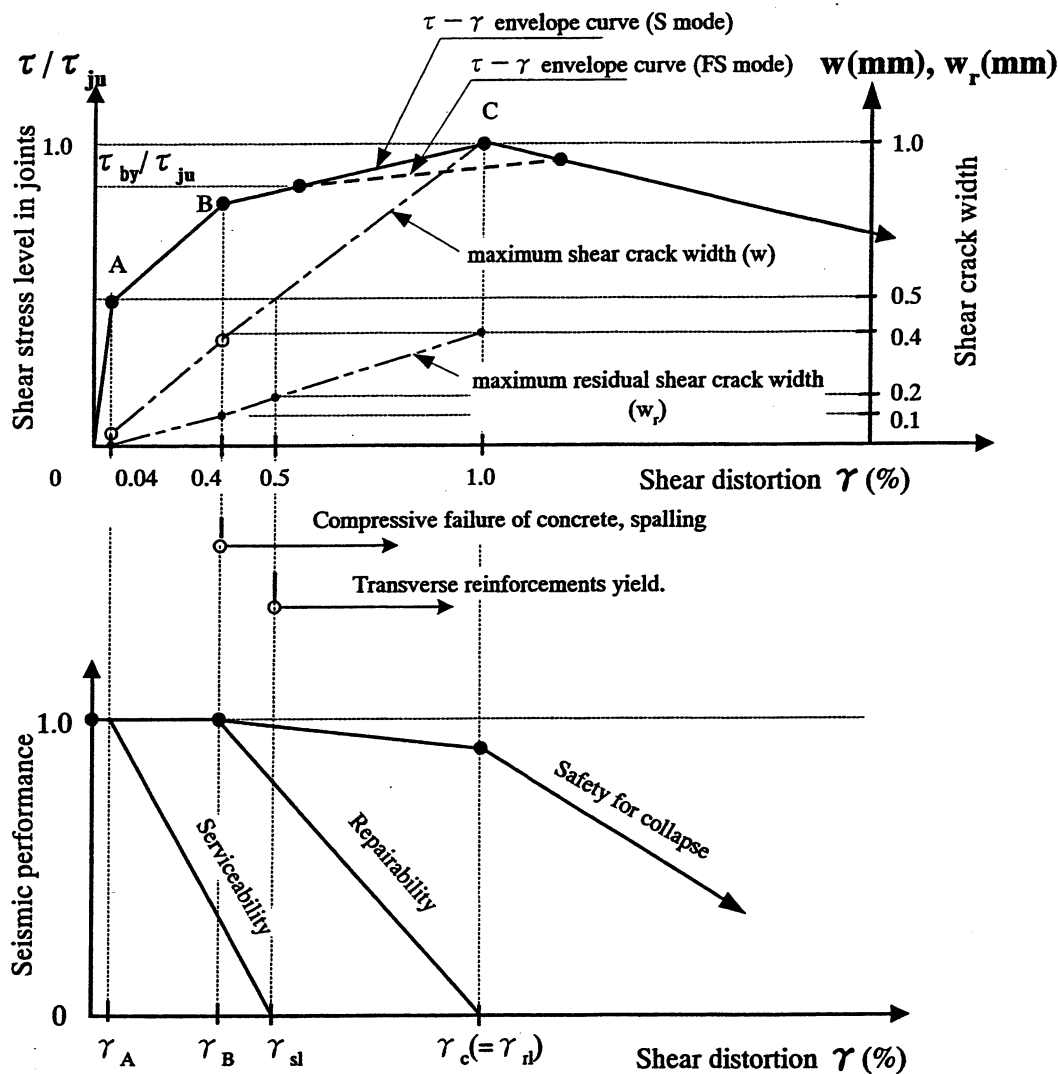
Table 1 Damage condition and experienced shear distortion (Experienced shear stress level)

Point in Figure 1	A		B	C	D	
Experienced shear distortion γ (%)	below 0.04	0.2	0.4	1.0	2.0	4.0
Experienced shear stress level (τ / τ_w)	below 0.5	0.65	0.85	1.0 (0.85~1.0)*	1.0 (1.0~0.6)**	1.0 (0.9~0.5)**
Maximum shear crack width w (mm)	0	0.2	0.4	1.0	—	—
Experienced maximum residual crack width w_r (mm)	0	0.05	0.1	0.4	—	—
Damage condition						
Notes	<ul style="list-style-type: none"> • Almost no damage 	<ul style="list-style-type: none"> • 3-4 cracks occur. • No transverse reinforcement yield 	<ul style="list-style-type: none"> • 6-8 cracks occur. • Transverse reinforcement is not yield almost 	<ul style="list-style-type: none"> • About ten cracks occur. • The cracks connect, and shear lag along crack occurs. • Compressive failure occurs • Spalling of part concrete • Transverse reinforcement yields 	<ul style="list-style-type: none"> • Wide shear lag along crack occurs, • Compressive failure of the core concrete expands, and the range of spalling extends 	<ul style="list-style-type: none"> • Spalling is remarkable • Transverse reinforcement exposure
					Strength decrease region (Strength decrease by cyclic loading is remarkable)	

Note) w and w_r : the average value of the experiment data shown in Figure 2 and Figure 3,

*: failure mode is FS type (joint shear failure after beam flexural yielding),

** : ratio of remaining strength (including the influence of the cyclic loading).



- γ_A : Limit shear distortion in the case serviceability keeps good (0.04%)
- γ_{sl} : Limit shear distortion in the case serviceability loses completely (0.5%), $w_r=0.2\text{mm}$
- γ_B : Limit shear distortion in the case it is easy to repair (0.4%)
- γ_d : Limit shear distortion in the case it is very difficult to repair (1.0%)
- γ_c : Limit shear distortion in the case safety begins to lose rapidly (1.0%)

Figure 6 Relationship among shear distortion and damage condition, residual seismic performance (serviceability, repairability and safety for collapse)

5. DESIGN CRITERIA ON SHEAR PERFORMANCE OF JOINT PANELS

The anticipated joint shear distortion and damage condition can be predicted directly by the static or dynamic response analysis of the frame considering the joint shear-distortion relationship. Here, the model for the joint shear deterioration due to cyclic load input after beam hinging was available (Teraoka et al., 2000). The hysteresis model and comparison of measured and calculated V_j - γ restoring force characteristics is shown in Figure 7 and 8, respectively.

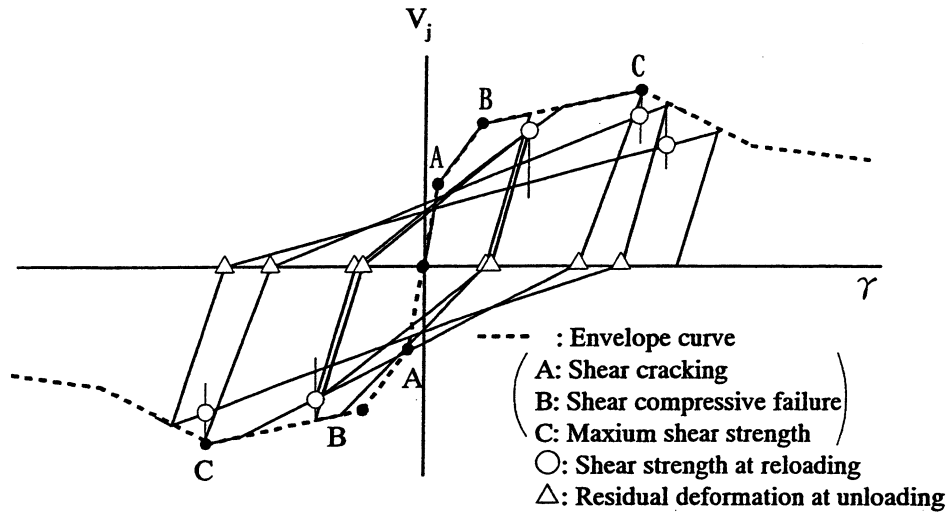


Figure 7 Hysteresis model

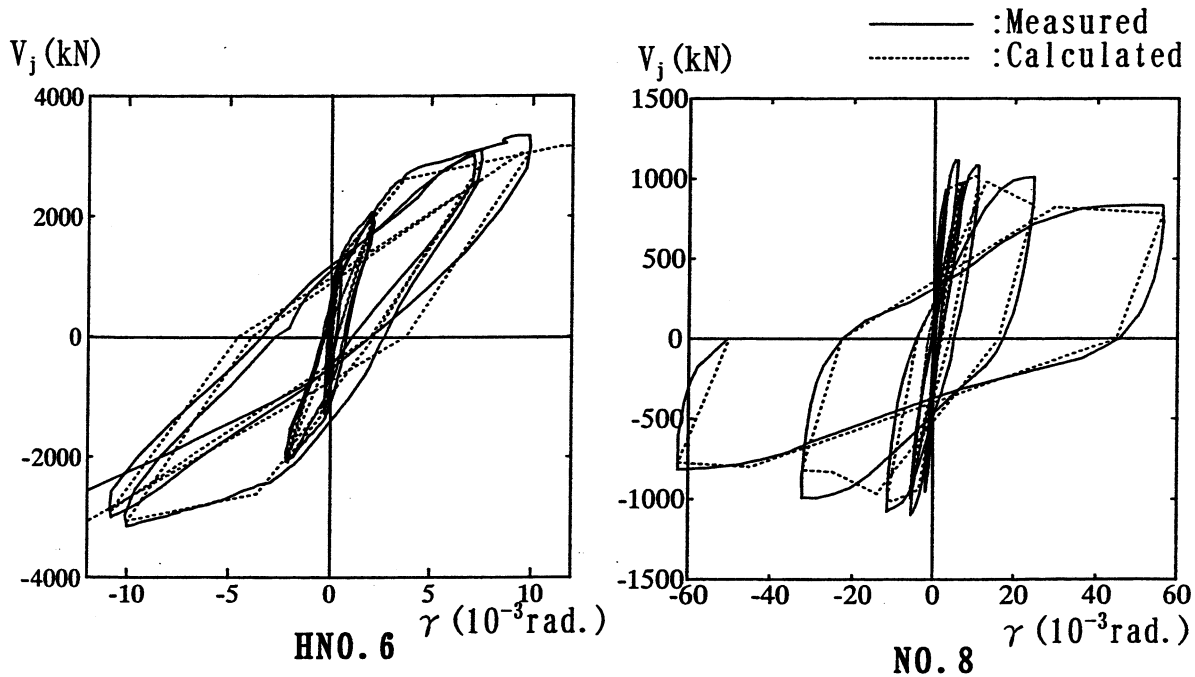


Figure 8 Comparison of measured and calculated V_j - γ restoring force characteristics

On the other hand, it is also possible to control the joint shear deterioration corresponding to the expected frame ductility requirement in design indirectly. Safety factor against joint shear failure (the ratio of joint shear strength to the shear input at beam flexural yielding) can be used as an index for the damage progress in reversed cyclic loadings in inelastic range. The failure mode discrimination method (Teraoka et al., 1991) and examination of deformation capacities (Teraoka et al., 1996, Murakami et al., 2000) can be available. Database analysis showed that the larger the safety factor, the larger the ductility ratio of the frame response for the specimens failed in joint shear after beam flexural yielding as shown in Figure 9(Murakami et al., 2000). When the safety factor was over 1.35, the ductility of 4.0 was obtained. Table 2 shows one of the design criteria to control the damage to beam-column joints.

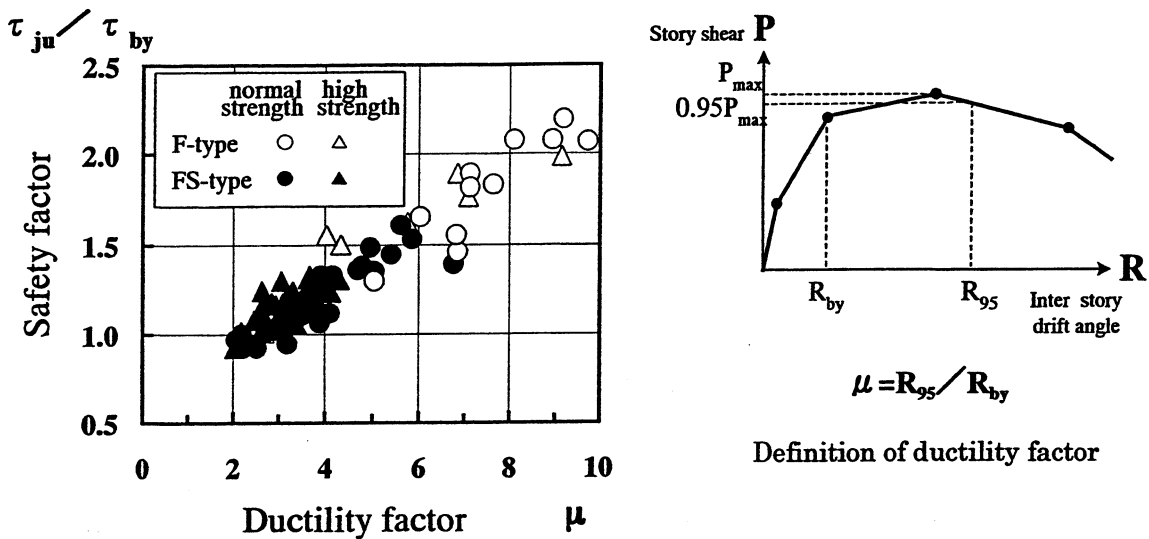


Figure 9 Relationship between safety factor (the ratio of joint shear to flexural strength) and ductility factor of the frames

Table 2 Standard example of criteria of shear critical state and the judgment method

Level of demand	Assumed damage level	Influence on frame structure	Judgment method
No damage	Shear cracking is not occurred		$\tau_{sc} / \tau_{by} \geq 1.0$
Slight damage	0.2mm in shear crack width	Hoop does not yield.	$\tau_{ju} / \tau_{by} \geq 1.70$
Moderate damage	0.4mm in shear crack width 0.1mm in residual shear crack width	Hoop is yet elastic. The influence on response is small.	$\tau_{ju} / \tau_{by} \geq 1.35$
Severe damage	Compressive failure of concrete, shear slip	Around peak, the influence on response is large	$\tau_{ju} / \tau_{by} < 1.35$
Great damage	Spalling of concrete, instability of axial load maintaining	Strength decreasing region after the maximum shear strength	"

note) 1) $\tau_{sc} = \sqrt{f_t^2 + f_t \cdot \sigma_0}$ (minimum shear crack strength by the principal stress equation),
 where, f_t : tensile strength of concrete, which is assumed to be $0.15\sqrt{\sigma_B}$ (N/mm^2),
 σ_0 : axial stress of column

2) τ_{by} : joint shear stress corresponding to beam flexural yielding (equation of AIJ)

3) τ_{ju} : ultimate shear strength of joint panels (equation (3.a))

6. CONCLUSIONS

In this report, the seismic damage and the seismic performance of the beam-column joint panels in structural frames were focused on. The shear failure process in joints was shown, and the shear stress - shear distortion relationship in joint panels was modeled. According to test data analysis, the relationship between damage progress and shear stress-shear distortion characteristic was examined. Based on above examinations, the damage and the experienced shear distortion were summarized as the damage map, and the schematic relationship among experienced shear distortions and observed damage conditions and residual seismic performance was shown. By applying these relationships and expected frame ductility requirement, one of the design criteria to control the damage to beam-column joints was

proposed.

Following are the point that the further research effort seems to be required on:

- (1) Interactions between bond deterioration behaviors of beam and column bars and shear performance on beam-column joints,
- (2) Interactions between shear capacity and performance of supporting axial load in beam-column joints,
- (3) Size effect for seismic damage and seismic performance of beam-column joints, and
- (4) Effective strengthening method for joint shear capacity.

ACKNOWLEDGEMENT

The authors wish to express their deep appreciation for Messrs. Kazuya Hayashi, Satoshi Sasaki and Naoki Takamori, Fujita Corporation, for their contribution to this study.

REFERENCES

- Architectural Institute of Japan (1999a). *Performance Based Design and Various Critical States of Reinforced Concrete Structure*, (5) Confirmation of Performance on Beam-Column Joints and Earthquake Resistant Shear Walls (by Fujii, S.):29-38 (in Japanese).
- Architectural Institute of Japan (1999b). *Design Guidelines for Earthquake Resistant Reinforced Concrete Buildings Based on Inelastic Displacement Concept*. AIJ, Tokyo.
- Kaku, T., Asakusa, H., (1989). Ductility Estimation of Exterior Beam-Column Subassemblages in Reinforced Concrete Frames. *Journal of Structural and Construction Engineering (Transactions of AIJ)*, No. 401: 87-96(in Japanese).
- Kitayama, K., (1992). Restoring Force Characteristics in Reinforced Concrete Beam-Column Joints. *Transactions of the Japan Concrete Institute*, Vol.14, No.2: 431-436, (in Japanese).
- Murakami, H., Fujii, S., Ishiwata Y. and Morita, S., (1998). Shear Strength of R/C Interior Beam-Column Joint panels (Database study on beam-column joint panels part 1). *Journal of Structural and Construction Engineering (transaction of AIJ)*, No.503:85-92 (in Japanese).
- Murakami, H., Fujii S., Ishiwata Y. and Morita S.(2000). Shear Strength and Deformation Capacity of Interior R/C beam-Column Joint Subassemblage. *Proceedings on 12th World Conference on Earthquake Engineering*, No.0679.
- Sasaki, S., Teraoka, M., and Kanoh, Y., (1993). Shear Force and Shear Distortion Relationship in RC Beam-Column Joint Panels. *Proceedings of the Japan Concrete Institute*, Vol.15, No.2:571-576 (in Japanese).
- Teraoka, M., Kanoh, Y. and Kobayashi K., (1991). Study on the Shear Strength of RC Interior Beam-Column Joints -In the Case of Using Normal Concrete Without Transverse Beams-. *Journal of Structural Engineering, Architectural Institute of Japan*, Vol.37B, March 1991: 365-378 (in Japanese).
- Teraoka, M., Sasaki, S., and Hayashi, K., (1992). Study on Ultimate Strength of RC Exterior Beam-Column Joints. *Summaries of Technical Papers of Annual Meeting of Architectural Institute of Japan*: 205-206 (in Japanese).
- Teraoka, M., Kanoh, Y., Sasaki, S., and Hayashi, K., (1996). An Estimation of Ductility in Interior Beam-Column Subassemblages of Reinforced Concrete Frames. *Journal of the Society of Materials Science Japan*, Vol. 45, No. 9: 1033-1041 (in Japanese).
- Teraoka, M., Hayashi, K., and Sasaki, S., (1997). A proposal of Criteria on Damage Level

and a Choice of Repair / Strengthening Works for RC Beam-Column Joints Damaged by an Earthquake. *Summaries of Technical Papers of Annual Meeting of Architectural Institute of Japan*: 497-498 (in Japanese).

Teraoka, M., Hayashi, K., Sasaki, S., and Takamori, N., (2000). Estimations of Shear Behaviors and Damage in RC Interior Beam-Column Joints (part 1-3). *Summaries of Technical Papers of Annual Meeting of Architectural Institute of Japan*: 805-810 (in Japanese).

Shear strength of beam-column joints are reviewed in Noguchi, H., Fujii, S. and Teraoka, M., Shear Strength of Beam-Column Joints with High-Strength Materials. *ACI SP-176* : 329-356, 1998.

KEYWORDS

reinforced concrete; beam-column joint; seismic damage; seismic performance; restoring force characteristic; shear crack width; shear distortion; evaluation method; design criteria; serviceability; repairability; safety for collapse

DEVELOPING STANDARDS FOR THE EVALUATION AND REHABILITATION OF EXISTING CONCRETE BUILDINGS

Michael Valley¹

ABSTRACT

This paper describes the special challenges faced in the evaluation and rehabilitation of existing buildings and the consequent difficulties that arise in the development of codes and standards to govern such work. Technical challenges are encountered in applying the seismic design philosophy to existing concrete buildings because the materials, detailing, and controlling behavior of such structures often violate rules of modern seismic-resistant design. It should be noted that existing construction varies widely, the background research is incomplete, and practitioners have addressed the technical issues differently in the past; therefore, standards committees must deal with significant procedural difficulties as well.

The U.S. earthquake engineering community has addressed these conditions by developing and implementing a performance-based seismic evaluation and rehabilitation methodology. The methodology attempts to reconcile the results of post-earthquake observations, physical testing, and advanced analysis. Originally published as handbooks and guidelines, the documents that embody this approach are presently being developed into consensus standards. This paper also identifies several areas for future research to improve the documents.

1. INTRODUCTION

The tenets of the U.S. seismic design philosophy are to provide a safe structure; to limit damage in small, frequent earthquakes; and to allow ductile, inelastic response to reduce construction costs. In the design of new buildings, these goals are generally achieved by:

- Selecting the controlling behavior,
- Providing special detailing to promote ductile response,
- Carefully controlling material properties (e.g., concrete strength, reinforcement yield and tensile strength, and reinforcement weldability), and
- Reducing engineering requirements by limiting explicit design consideration to one level of ground shaking with implied performance for other levels of hazard.

Using this approach, improved performance for “essential facilities” (hospitals, fire and police stations, etc.) is obtained by amplifying the design forces and applying slightly more stringent drift and detailing provisions. Although adequate performance is implied by these measures, the

¹Skilling Ward Magnusson Barkshire, Seattle, Washington, U.S.A.
Email: mtv@skilling.com

U.S. codes and standards for new building design (FEMA, 1998b; ICC, 2000) do not require explicit consideration of performance.

The following technical challenges face practitioners who evaluate and rehabilitate existing buildings:

- Elements with undesirable controlling modes of behavior may not be able to survive cyclic, inelastic demands.
- The existing detailing often is unable to provide adequate confinement, ductility, or reliable reserve gravity capacity.
- The properties of the existing materials may not be known (if test results and/or drawings do not exist) and even when known are not easily modified.

These differences from new building design approach favor the implementation of an explicit performance-based approach for the evaluation and rehabilitation of existing concrete buildings. In some cases, the performance objective will be the same as that for new buildings. However, the use of a performance-based methodology affords the owner or jurisdiction the opportunity to select higher or lower performance objectives.

2. BASIS FOR THE EVALUATION AND REHABILITATION OF EXISTING BUILDINGS

The criteria for seismic evaluations and rehabilitations are generally based on post-earthquake observations, physical testing, and/or structural analysis. Each of these bases has different strengths and limitations, and the results may be contradictory.

Post-earthquake reconnaissance is an important source of information that leads to better designs for seismic resistance. Significant earthquakes in recent decades have led to the generation of a sizeable body of largely anecdotal performance observations. Projects undertaken by the Applied Technology Council in the 1980s culminated in the development of a handbook for seismic evaluation of existing buildings (FEMA, 1992) that is primarily based on the observed performance of various building types that are common in California. This anecdotal basis has the advantages of identifying the most significant problems and of capturing, at least partially, behavior that is not yet fully understood. However, this approach suffers from a few potentially significant disadvantages in that the database of observations is quite small compared with the at-risk inventory, construction methods and building types vary significantly from region to region,

behavior that is not fully understood cannot be readily extended to different conditions, and trained observers often attribute the same poor performance to different (or even conflicting) sources. For instance, despite considerable research effort, the causes of middle-story collapses in the Kobe earthquake and fractures of welded steel moment-resisting frame connections in the Northridge earthquake are still the subject of some controversy.

Physical testing is at the heart of modern structural codes and standards. This method allows more accurate quantification of behavior, provides insight into the expected performance of components and systems for which field observations are not available, and allows the identification of separate parameters that affect the overall response. However, such testing is generally expensive, the number of conditions that can be tested is severely limited, researchers often focus their efforts on the development of new and better systems rather than on a more complete understanding of archaic systems, limitations of the test equipment and protocols often lead researchers to neglect gravity loading effects, and research projects have generally focused on the performance of fairly small components rather than entire systems. With increased computational power, advanced analysis methods have grown in popularity among both researchers and practitioners. Such analyses can capture important nonlinear and dynamic features of response, and the global and local behavior of complex structures may be readily predicted. However, nonlinear dynamic analysis is much more sensitive to small changes in the underlying assumptions than is linear static analysis. Although modern digital computers permit rapid solution of large numbers of nonlinear equations, the volume of numerical results and the complex interplay of various parameters can easily exceed the cognitive capacity of analysts.

3. U.S. STANDARDS DEVELOPMENT PROCESS

In general, the U.S. government does not directly develop building codes. Although various government agencies support the work on which codes and standards are based, the production and maintenance of such documents is usually the charge of volunteer committees that follow a process accredited by the American National Standards Institute. Members of a committee are balanced in representing three interest groups: producers, consumers, and general interest. No organization or individual claims responsibility for the standards developed. Because most committee members volunteer the time to participate, it is possible for outspoken individuals to significantly affect the results--to the benefit or detriment of the standards. The significant influence of individuals and turnover of committee membership can lead to differences that are

more substantial than the changes in the underlying research. To counter that potential, some committees have gone to the other extreme--allowing the negative votes of a small group or an individual to stifle progress.

4. SEISMIC EVALUATION OF EXISTING BUILDINGS

A new standard for the seismic evaluation of buildings is being developed by a standards committee of the American Society of Civil Engineers, Structural Engineering Institute. This standard is the result of a two-year ballot process that began with a pre-standard developed with funding from the Federal Emergency Management Agency (FEMA, 1998a). Publication of the standard is expected in 2001.

This standard, which blends the three bases for evaluation described above, sets forth a three-tiered approach.

- Tier 1 involves *screening* based on checklists of deficiencies observed in similar buildings subjected to past earthquakes. These checklists succeed those contained in FEMA 178, having been recast in mandatory language, updated to reflect more recent observations, extended to apply to additional building types across the U.S., and modified for application to two distinct performance levels--Immediate Occupancy and Life Safety.
- Tier 2 entails quantitative *evaluation* using calculations that are generally much simpler than those required for new building design. The evaluation may be complete--applicable to all of the major lateral- and gravity-load-resisting elements of the structural system as well as nonstructural and foundation elements, or partial--applicable only to those items that were found noncompliant in Tier 1.
- Tier 3 *detailed evaluation* is based on the Rehabilitation Guidelines discussed below.

5. SEISMIC REHABILITATION OF EXISTING BUILDINGS

The same ASCE Standards committee that is finishing the evaluation standard has just begun the ballot process for a rehabilitation standard. This rehabilitation standard will be based on a prestandard developed under funding from the Federal Emergency Management Agency (FEMA, 2000b) which, in turn, is based on previously developed guidelines for seismic rehabilitation and an associated commentary (FEMA, 1997b; FEMA, 1997a). During the development of the rehabilitation prestandard, a large number of areas for future improvement

were identified (FEMA, 2000a) and a series of case studies was commissioned to assess the technical validity, useability, and economic implications of the rehabilitation approach (FEMA, 1999).

Like the evaluation standard described above, the rehabilitation standard builds on all three bases for evaluation and rehabilitation: observed performance, testing, and analysis. The document includes two rehabilitation approaches: simplified and systematic.

Application of simplified rehabilitation is limited to small structures that fit one of the common building types. The rehabilitation measures need only address deficiencies identified using the evaluation standard. Because this approach is founded almost entirely on the anecdotal basis, the resulting level of building performance is less certain than when the systematic approach is taken.

Systematic rehabilitation requires analysis of the complete building system. Four analysis procedures are available, as described below. Detailed guidance is provided for the establishment of material properties, element capacities, analytical modeling of the structural and foundation elements, and acceptance criteria. Qualitative and quantitative measures of expected performance are provided. The document also provides detailed discussion of rehabilitation strategies to address deficiencies.

6. DETAILS OF THE SYSTEMATIC REHABILITATION APPROACH

The systematic rehabilitation approach in the FEMA 356 *Prestandard* requires explicit consideration of performance objectives. The selected objective may involve any combination of hazard and performance level, but a Basic Safety Objective is defined and suggested for general use. This Basic Safety Objective is based on achieving Life Safety and Collapse Prevention for ground shaking hazards with probabilities of exceedance in 50 years of 10 percent and 2 percent, respectively. FEMA 356 contains detailed provisions governing the selection of appropriate material properties, element capacities, analysis procedures, and element modeling and acceptance criteria, as described below.

6.1 Material Properties and Element Capacities

Because identification of expected performance (not simply acceptable performance) is one of the basic requirements of performance-based earthquake engineering, FEMA 356 requires the

consideration of the statistics of material properties and element capacities. Structural behavior is classified as deformation-controlled (ductile) or force-controlled (brittle). Expected (average) material properties are used for ductile limit states, and lower-bound (mean minus one standard deviation) material properties are used for brittle limit states. The incorporation of test results and recent research by users is encouraged. Such results and feedback from users (practical and case studies) were considered in the course of the project to convert the FEMA 273 *Guidelines* to the FEMA 356 *Prestandard*. The prestandard project team also commissioned ten special studies that aimed to bring recent improvements in the state-of-the-art into FEMA 356. One of these special studies resulted in significant changes in the acceptance criteria and calculated shear strength of concrete columns, based on work by Lynn and Moehle.

6.2 Analysis Procedures

Each of the four analysis procedures permitted in FEMA 356 has a place in current engineering practice. The linear static procedure is similar to the traditional U.S. approach used in the design of new buildings. This method is still widely used for verification of more complex analyses, for scaling of dynamic analysis results (in new building design), and on small projects. Because the method cannot reflect localized inelastic response or higher mode effects, its use is limited to fairly regular buildings with short fundamental periods and only moderately nonlinear response. The linear dynamic procedure is generally consistent with the most common U.S. approach taken in the design of complex new buildings. The response of buildings with stiffness irregularities and those with higher mode effects can be adequately captured using this method.

The nonlinear static procedure has enjoyed a recent increase in popularity. This method provides useful information concerning the expected progression of inelastic response for buildings with dynamic response dominated by the first mode, but it is not suitable for buildings with significant higher mode effects. Various demand estimation methods may be used in “pushover” analysis. Details on the two most common methods (coefficient and capacity spectrum) are provided elsewhere (FEMA, 2000b; ATC, 1996). The nonlinear dynamic procedure is the most rigorous and probably the most sensitive approach. The use of this method is not widespread among U.S. practitioners, except for specific applications with limited nonlinearity (e.g., buildings with seismic isolation or added damping).

6.3 Element Modeling and Acceptance Criteria

FEMA 356 provides modeling and acceptance criteria for a wide range of structural elements and components. The values provided were developed (during the preparation of FEMA 273) based on a search of the available literature, a standard characterization of inelastic cyclic response, and expert judgement. Some of the criteria were revised during the development of the FEMA 356 *Prestandard* on the basis of more recent research. FEMA 356 also defines a testing protocol and data reduction methodology to allow users to develop additional acceptance criteria. Some recent research has resulted in the development of FEMA 356 acceptance criteria based on explicit reliability studies (FEMA, 2000c; FEMA, 357).

7. CONCLUSIONS AND RECOMMENDATIONS

Because of the technical challenges involved, explicit consideration of performance (preferably by the practitioner, but at least by standards writers) is an important part of the seismic evaluation and rehabilitation of existing concrete buildings. The standards that govern this work should make use of anecdotal performance data, available analysis tools, and the best available research. This requires that practitioners be conversant with past and ongoing research and that researchers be aware of the needs of the user community. Current research is not (and will never be) complete, but great strides can be made if researchers make a point of considering the detailing of existing construction, sensitivity to gravity loading, and performance of entire systems (rather than focusing solely on isolated, small-scale components). Researchers and standards writers should assess the reliability of performance predictions using the available documents and procedures. This could well involve the extension of the reliability-based research recently completed for welded steel moment-resisting frames (FEMA, 2000c).

Finally, practitioners, standards writers, and researchers must recognize the strengths and weaknesses of the standards development process. The process serves to balance the influence of various interest groups. Those involved should strive for a reasonable level of stability and consistency in the standards developed while keeping in mind that the process is largely unfunded and holds no one responsible, although outspoken individuals can make significant contributions or cause significant problems.

8. REFERENCES

ATC (1996). *Seismic Evaluation and Retrofit of Concrete Buildings* (Report No. ATC 40), developed by the Applied Technology Council for the California Seismic Safety Commission.

FEMA (1992). *NEHRP Handbook for the Seismic Evaluation of Existing Buildings* (Report No. FEMA 178), developed by the Building Seismic Safety Council for the Federal Emergency Management Agency.

FEMA (1997a). *NEHRP Commentary on the Guidelines for the Seismic Rehabilitation of Buildings* (Report No. FEMA 274), developed by the Building Seismic Safety Council for the Federal Emergency Management Agency.

FEMA (1997b). *NEHRP Guidelines for the Seismic Rehabilitation of Buildings* (Report No. FEMA 273), developed by the Building Seismic Safety Council for the Federal Emergency Management Agency.

FEMA (1998a). *Handbook for the Seismic Evaluation of Buildings - A Prestandard* (Report No. FEMA 310), prepared by the American Society of Civil Engineers for the Federal Emergency Management Agency.

FEMA (1998b). *NEHRP Recommended Provisions for Seismic Regulations for New Buildings and Other Structures* (Report No. FEMA 302), prepared by the Building Seismic Safety Council for the Federal Emergency Management Agency.

FEMA (1999). *Case Studies: An Assessment of the NEHRP Guidelines for the Seismic Rehabilitation of Buildings* (Report No. FEMA 343), prepared by the Building Seismic Safety Council for the Federal Emergency Management Agency.

FEMA (2000a). *Global Topics Report on the Prestandard for the Seismic Rehabilitation of Buildings* (Report No. FEMA 357), prepared by the American Society of Civil Engineers for the Federal Emergency Management Agency.

FEMA (2000b). *Prestandard for the Seismic Rehabilitation of Buildings* (Report No. FEMA 356), prepared by the American Society of Civil Engineers for the Federal Emergency Management Agency.

FEMA (2000c). *Recommended Seismic Evaluation and Upgrade Criteria for Existing Welded Steel Moment-Frame Buildings* (Report No. FEMA 351), developed by the SAC Joint Venture for the Federal Emergency Management Agency.

ICC (2000). *International Building Code*, International Code Council.

9. KEYWORDS

Codes; Concrete; Evaluation; Existing buildings; Rehabilitation; Seismic; Standards.

EFFECTS OF INTERACTION BETWEEN JOINT SHEAR AND BOND STRENGTH ON THE ELAST-PLASTIC BEHAVIOR OF R/C BEAM-COLUMN JOINTS

Hitoshi SHIOHARA¹

ABSTRACT

The effects of the interaction between (a) joint shear force and (b) anchorage strength of beam bars passing through joint on the strength and failure modes of interior R/C beam-column joint are investigated by a new analytical model proposed by the author. The model considers two deformation modes, i.e. beam mode, due to the opening of the crack at the end of beam, and joint mode, due to the opening of the diagonal crack in joint. It is revealed that the shear strength at joint failure and failure modes are independently affected by induced joint shear force as well as anchorage force. In particular, the anchorage strength of beam bars passing through joint was found to have opposite effects i.e. good anchorage enhances joint strength while it cause an increase of joint deformation.

1. INTRODUCTION

Current building codes for reinforced concrete structures place limits on input joint shear force and ratio of column dimension to bar diameter in beams to avoid ill behavior of beam-column joints (ACI 1995, AIJ 1994, NZS 1995) for earthquake resistant design. In those codes, a) shear strength of joint and b) bond-capacity are regarded as independent factors affecting the failure mode and hysteresis loops of beam-column joints respectively. However, it is obvious from the past tests that a significant interaction among these factors does exist. ACI318 Commentary (ACI 1995) states that amount of transverse reinforcement in beam-column joint is not sensitive to joint shear strength, but it is also well known that joint shear deformation decreases by increasing of transverse reinforcement in beam-column joints. Cheung (Cheung 1991) proposed a refined model based on truss and strut mechanism (Pauley 1978) considering the bond slip effects. These example suggests the factor of shear strength of joint does not alone influence on failure mode. Hakuto (Hakuto 1999) recognized the strength degradation due to the weak bond capacity of beam bar passing through beam-column joint. Researchers in New Zealand reported (Liu 2000) a

¹ *Department of Architecture, School of Engineering, The University of Tokyo, 7-3-1 Hongo, bunkyo-ku, Tokyo, Japan*
Email: shiohara@rca.arch.t.u-tokyo.ac.jp

test to evaluate the performance of beam-column joint designed by the old building code using plain bars for beam bars. No shear failure of beam-column joints was observed in the tests. Review of test data by Teraoka (Teraoka1997) revealed that the increase of amount of beam bars in beam-column joints enhance the joint shear strength. These facts suggest that factors including shear strength of joint and bond strength have influences on both strength and deformation behavior of joints in such a complex manner. These type of interaction need to be identified and they should be reflected into a design of beam-column joint. This paper reports a preliminary work to develop a new analytical model which is available for design by predicting the strength and failure mode of beam-column joint reflecting the interaction of those factors in a consistent way.

2. MODELLING OF BEAM-COLUMN JOINTS

2.1 Real behavior of joint shear failure

The author demonstrated facts in joint shear failure (Shiohara 1998) using test data. The real behavior was summarized as follows. (1) shear deformation of beam-column joint increases mainly due to diagonal expansion, (2) remaining shear resisting capacity of the joint is reserved while, (3) story shear gradually decreases. The degradation in story shear is caused by the upper limit of anchorage capacity of straight beam bars passing through the beam-column joint. It is not caused by the failure of joint shear resisting system. Existing behavior model for beam-column joints such as truss mechanism or strut mechanism (Pauley 1978), are not useful to account for these facts accurately.

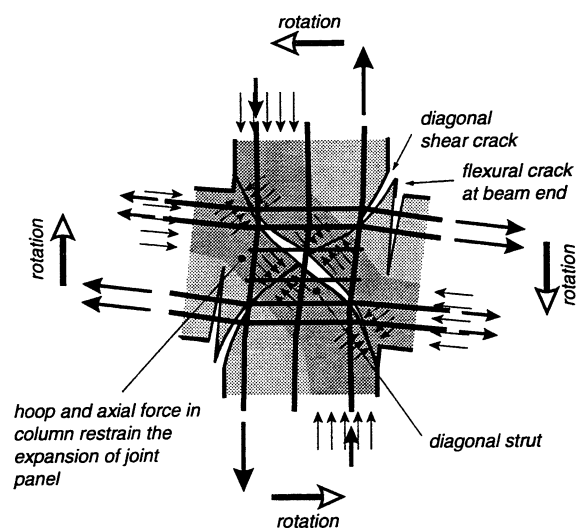


Figure 1: Behavior model for joint shear failure and force flow in beam-column connection

2.2 New model for moment resisting system in a beam-column joint

A new behavior model for shear failure in a interior beam-column joint was proposed as illustrated in Fig. 1 (Shiohara 1998). In the model, shear deformation is represented by the rotation of the four triangular concrete segments. As shown in Fig. 2 (a), the vertical and horizontal spring

connecting the segments prevent them from going into pieces. The moments acting on these segments are resisted by the system of the segments and springs. This model is useful to explain how the beam-column joint could resist to applied moment and how the joint shear failure occur, because the real behavior is that shear deformation of beam-column joint increases while shear resisting capacity of the connection remains.

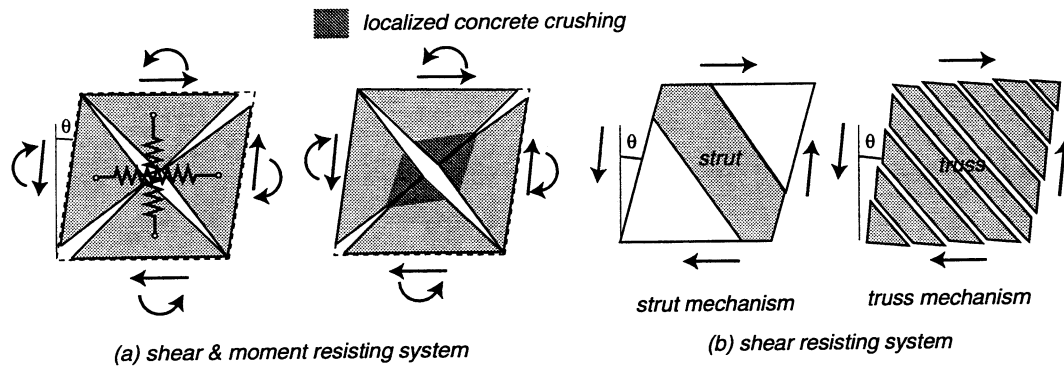


Figure 2: Comparison of mechanisms for the new model and existing models

2.3 Overall Behavior of Beam-Column Joint Subassembled

When the upper limit of bond capacity is attained, the story shear degradation begins. Then longitudinal strain in beam bars usually distribute as shown in Fig. 3. The total elongation of beam bars in beam-column joint equals to the area under the line of distribution of longitudinal strain.

By considering the deformation compatibility in beam bars and concrete, the elongation of beam bars cause opening of crack in concrete. Figure 4 shows two typical crack patterns. The elongation of beam bars may contribute to opening crack at column face as depicted in Fig. 4(a), which contribute to beam end rotation. Another possibility is that the elongation of beam bars may contribute to opening diagonal cracks in joint panel as shown in Fig. 4(b), which contribute to rotation of segments consisting joint shear panel as already introduced in Fig. 2(a). The other possibility of deformation in joint panel is shown in Fig. 4(c). This failure is very special type caused by the real compressive failure of concrete diagonal strut in specially designed beam-col-

umn joint. But this type of failure have not be reported scarcely before. Thus the last type of failure is not considered in this paper.

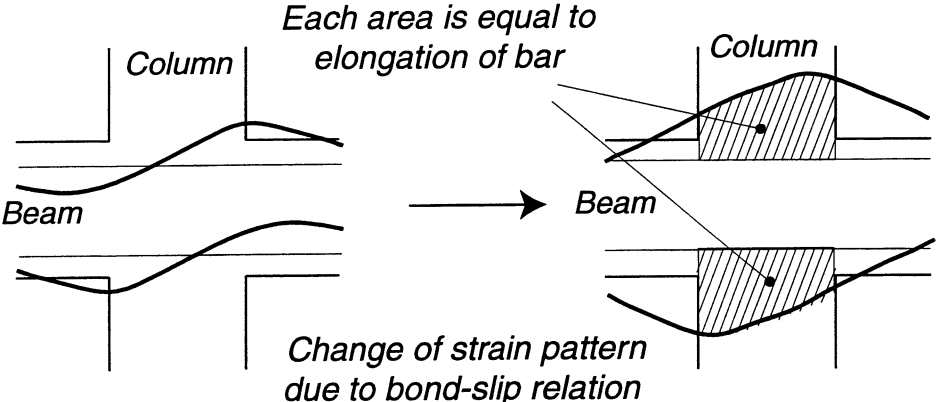


Figure 3: Elongation of beam bars passing through a beam-column joint

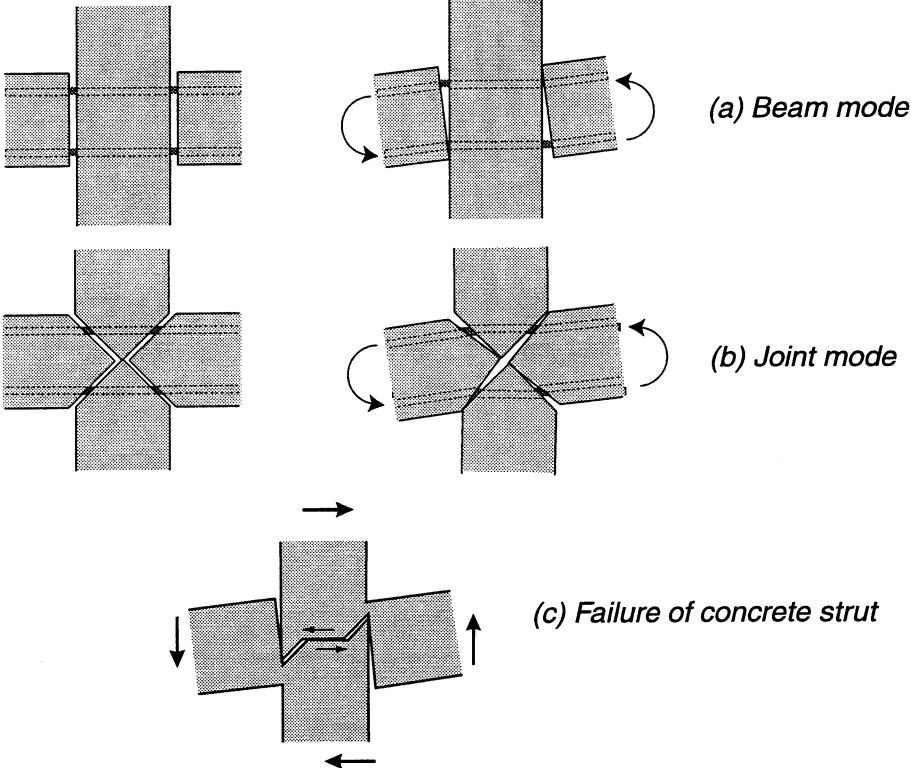


Figure 4: Overall behavior of beam-column connection subassemblage

2.4 Two Deformation Modes in Beam-Column Joints

The deformation mode shown in Fig. 4(a) is a favorable deformation mode because the deformation in a joint is relatively small. Hereafter the deformation mode is called “B (Beam)-mode.” The other deformation mode shown in Fig. 4(b) is not favorable because large shear deformation in the joint cause local crushing of concrete at the center of the joint due to large rotation of the segments as shown in Fig. 2(b). Hereafter the deformation mode is called “J (Joint)-mode.” To preclude J-mode behavior in design, mathematical model is necessary to understand how one of the two deformation modes become distinct.

2.5 Prediction of deformation mode based on strength

Each deformation mode has its own moment resisting mechanism inherent to each deformation mode. Thus the lateral resistance of beam-column joint for each deformation mode can be calculated provided an appropriate models are developed. If the calculated resistance for B-mode is smaller than that for J-mode, contribution of B-mode deformation to total story drift is smaller. By this way, the deformation mode in beam-column joint may be predictable. The lateral resistance of beam-column joint subassembled are going to be discussed in the following sections.

3. STRENGTHS FOR B-MODE AND J-MODE

3.1 Assumption in Critical Sections

Figure 5 defines two sets of critical section corresponding to B-mode and J-mode respectively. B-mode assumes critical sections at beam ends for flexural action, while J-mode assumes diagonal lines as critical sections. To define the longitudinal stress in straight beam bars passing through at the critical sections, notations of T_1 and T_2 are used respectively. The basic idea used here is coincident with flexural theory of section. However, the assumption of plain section remains plain is not used, because in beam-column joint, the effects of bond slip is significant and not negligible. Thus the value of T_1 and T_2 are assumed as independent variables. It should be noted that the value of $T_1 - T_2$ is equal to the anchorage force resisting by bond action between the surface of beam bars and concrete in a beam-column joint.

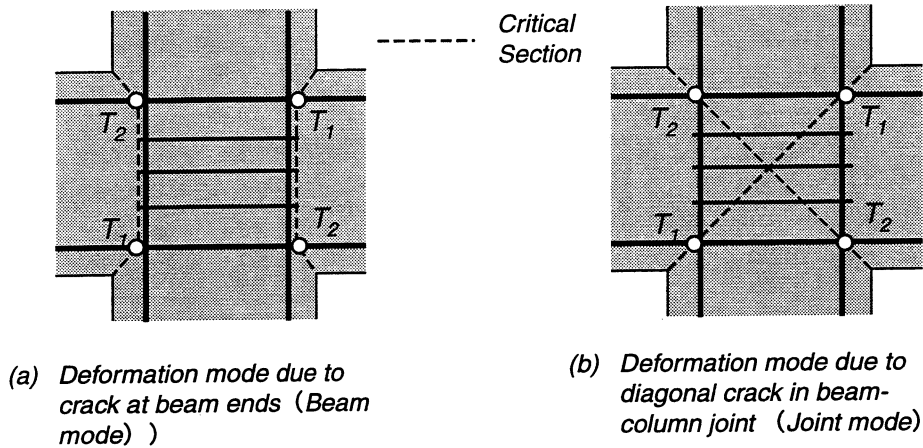


Figure 5: Two sets of flexurally critical section

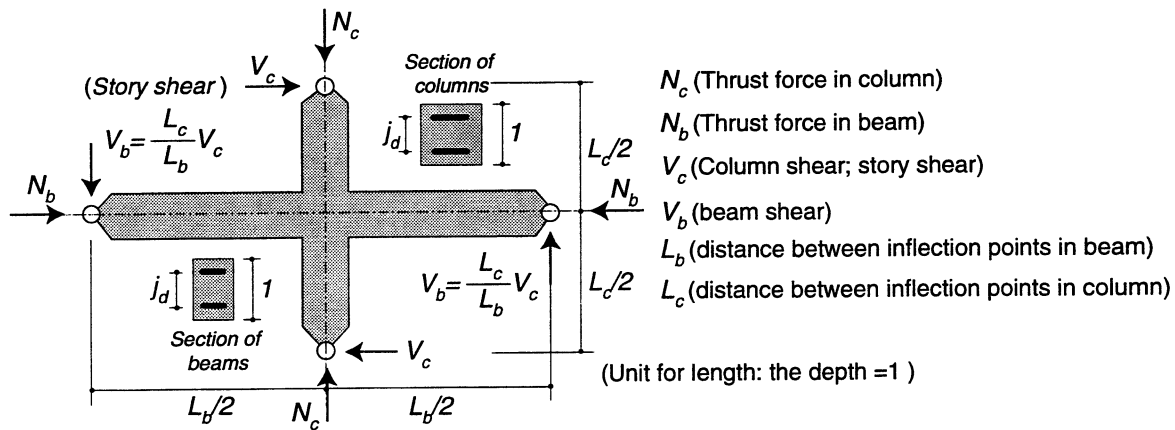


Figure 6: Definitions and notations for external forces acting on a beam-column joint subassembled

3.2 Definition of a Generic Beam-Column Joint Substructure

The geometry, dimensions and external forces are defined in Fig. 5. The relation between the tensile forces T_1, T_2 ; stress in beam bars, tensile force T_5 ; total stress in joint hoops, and joint shear stress τ_j is derived with respect to this generic substructure. The geometry and pattern of external forces acting on this structure assumed to be symmetric for simplicity. The depth of beams and columns are assumed identical, which is also used as the unit of length. Notations L_B and L_C is the distance between two contra flexure points in beams and columns respectively. Notations b_c and b_b define the width of column and beam respectively. The force T_1, T_2, T_5 and other notations for

forces represented by normalized with coefficient ($b_c D_c \sigma_c$), where σ_c is the concrete compressive stress at concrete stress block.

3.3 Strength for B-Mode Deformation

3.3.1 Assumptions and Notations in Analysis

By considering the equilibrium of horizontal force and moment at the critical section at the end of beam, the relation of the internal force T_1 , T_2 and moment M_b at the critical section is derived as the Eq. 1.

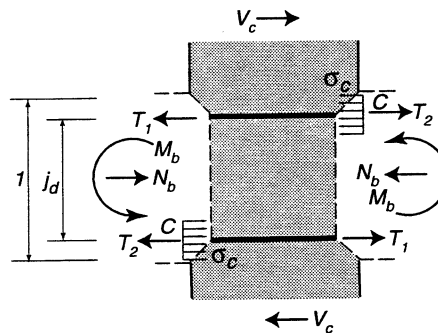


FIG 7

Figure 7: Definitions and notations of internal forces acting on the critical sections considering B-mode deformation

$$M_b = \frac{T_1 - T_2}{2} j_d + (T_1 + T_2 + N_b) \left(\frac{1}{2} - \frac{b_c T_1 + T_2 + N_b}{b_b} \right) \quad (1)$$

The beam shear V_b and the column shear V_c are easily derived from the value of M_b considering the geometry of substructure. Finally the joint shear stress τ_{jB} ; strength of B-mode is obtained using assumptions that the length of stress resultants at beam section j is equal to $7/8$ of effective depth of beam d and the effective area of beam-column joint for shear resistance is equal to the A_{eff} given by the AIJ Guidelines (AIJ 1991). The last assumptions are not essential but just conventions. By using this assumptions, the τ_{jB} is always proportional to M_b , V_b and V_c .

3.3.2 An example of numerical solution

Figure 8 is an example of numerical solution, which shows the surface of joint shear stress τ_{jB} for each point represented by a set of value (T_1 , T_2) in three dimensional space. It is obvious from the

Fig. 8 that the joint shear strength increased when the anchorage force $T_1 - T_2$ increases. The strength of B-mode is not the function of T_5 . Hence the amount of joint hoops has no influences on the strength.

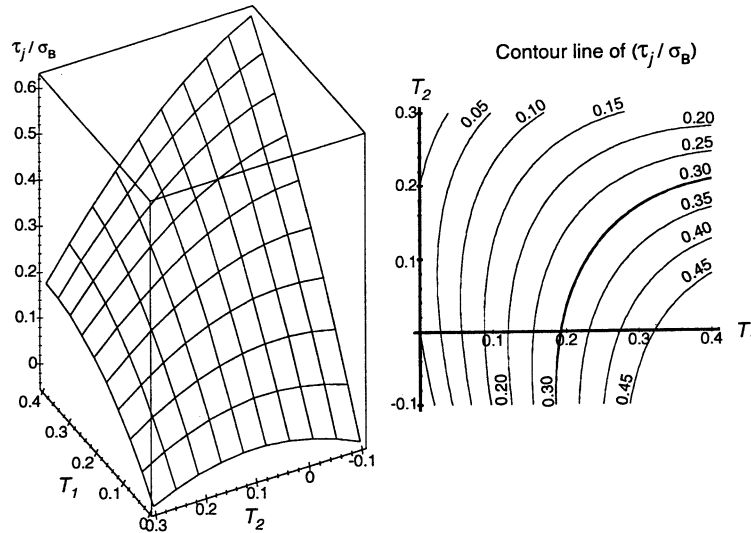


Figure 8: An example of numerical solution for strength for B-Mode

3.4 Strength for J-Mode Deformation

3.4.1 Assumptions and Notations in Analysis

Figure 9 shows the notations necessary to define the set of internal forces at the critical sections for the J-mode. The notations T_1, T_2, T_3, T_4 (positive in tension) represent tensile forces in longitudinal reinforcing bars in beams and columns. Tensile force T_5 is used to represent tensile force in joint hoops distributed in height direction where, they are assumed to concentrate at the mid height. The compressive force C_1, C_2 (positive in compression) in concrete are shown in Fig. 9(b). They are the x and y component of forces acting perpendicular to the boundary of segment. Thus the principal stress decline 45 degree in beam-column joint. Column shear V_c is identical to story shear and beam shear is V_b . All the forces with notation N, T, C and V , in this paper are normalized with $(b_c D_c \sigma_c)$.

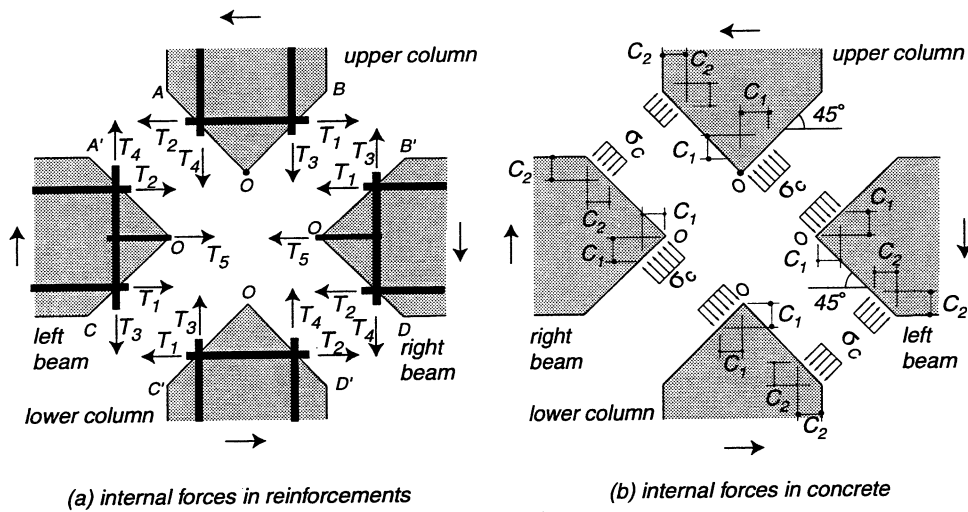


Figure 9: Definition of internal forces and their notations

3.4.2 Equilibrium in Forces Acting on the Segments

The number of equations is three necessary to define equilibrium in a rigid plane body. In this system, twelve equations exist to define equilibrium because a beam-column joint subassembly consists of four rigid bodies. Because a symmetric geometry is assumed, the number of required equations decreases to six. In addition to that, the column shear V_c and the beam shear V_b is proportional and not independent. Hence, the number of independent equations representing the equilibrium is five. The five equations are given as follows. The equilibrium of x and y directional forces on the right beam are expressed as,

$$-T_1 - T_2 - T_5 + C_1 + C_2 - N_b = 0 \quad (2)$$

$$T_3 - T_4 - C_1 + C_2 - \alpha V_c = 0 \quad (3)$$

respectively. The equilibrium of moment with respect to the center point O (see Fig. 9) on the right beam is given.

$$\frac{L}{2}\alpha V_c + \frac{1}{2}j(T_3 - T_4) + \frac{1}{2}j(T_1 - T_2) + C_2(1 - C_2) - C_1 C_1 = 0 \quad (4)$$

The equilibrium of x and y directional forces on the upper column are,

$$T_1 - T_2 - C_1 + C_2 - V_c = 0 \quad (5)$$

$$-T_3 - T_4 + C_1 + C_1 - N_c = 0 \quad (6)$$

respectively. The simultaneous equations of second order from Eq. (2) to Eq. (6) give a solution for five unknown variables, provided the value of the other variables are confirmed.

By solving the equations from Eq.(2) to Eq.(6), the story shear V_c is calculated. Hereafter, V_c , T_3 , T_4 , C_1 and C_2 are chosen as an unknown variables, whereas, the T_1 , T_2 and T_5 is assumed to be given. Finally the joint shear stress τ_{jJ} of J-mode is obtained as a function of T_1 and T_2 using same assumptions on length of stress resultants at beam section and effective area of joint used for B-mode in the previous section.

3.4.3 An example of numerical solution

Figure 10 is an example of numerical solution obtained by solving the equations from Eq. (2) to Eq. (6). It show the surface of joint shear stress τ_{jJ} . The shape of the surface of J-mode is different from the surface of M-mode. It is the shape of a dome. Most significant difference compared to that of B-mode is that the joint strength τ_{jJ} decreases provided the force T_2 is negative, i.e. the T_2 is in compression. This means that good anchorage in beam-column joint jeopardize the strength of J-mode.

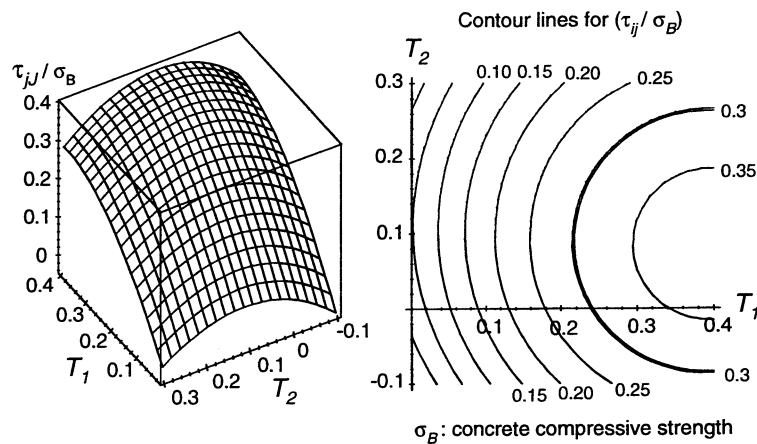


Figure 10: An example of numerical solution for strength of J-Mode

3.5 Difference in Strengths for J-mode and B-mode

The functions of stress τ_{jJ} and τ_{jB} are not identical and show different characteristics as shown in Fig.9 and Fig. 10. Figure 11 shows the contour lines of larger value $\{\tau_{jJ}, \tau_{jB}\}$ for each set of value (T_1, T_2) . Fig. 11(a) is the result for $T_5 = 0.04$, i.e. amount of joint hoops are almost equal to minimum requirement. Fig. 11(b) is the result, in which the amount of joint hoops is increased 250 percent to compare the effect of transverse reinforcement. The boundary curves are also plotted on (T_1, T_2) plane, which connects the points at which τ_{jJ} equals to τ_{jB} . Provided the point (T_1, T_2) locates in the upper left of the boundary curve, the value of τ_{jJ} is always larger than τ_{jB} . In this region, the strength of B-mode is smaller and B-mode deformation is dominant while the J-mode deformation is minor. On the contrary, J-mode deformation is dominant if the point (T_1, T_2) locates in the lower right region. Thus the boundary curves is useful to distinguish the deformation mode provided the values of T_1 and T_2 are known. Hereafter the two regions divided by the boundary line are B-region and J-region, where joint shear deformation become dominant. It is revealed by the comparison of Fig. 11(a) and Fig. 11(b) that the boundary line move right by increasing of joint hoops. As a result, this model account for the reason why the increase of joint hoops have an effect to reduce the joint shear deformation. This model also explain the effect of bond capacity on the strength and deformation modes. If beam straight bar has small bond capacity such as plain bar, the anchorage capacity is small and $T_1 - T_2$ is almost zero. It means the points (T_1, T_2) always stay on the 45 degree line passing the origin of the $T_1 - T_2$ plain. As shown

in Fig. 11, that line of 45 degree always lie in the B-region. Therefore, the B-mode deformation is dominant for the beam-column joint with no bond. This model account for the reason why the beam-column joint with plain bars did not show joint shear failure. By this way, this model explain the interaction of many factors including (1) input joint shear, (2) bond strength, (3) amount of joint hoops, (4) beam axial force, (5) column axial force and so on how these factors have influence on the behavior of beam-column joint in a consistent way.

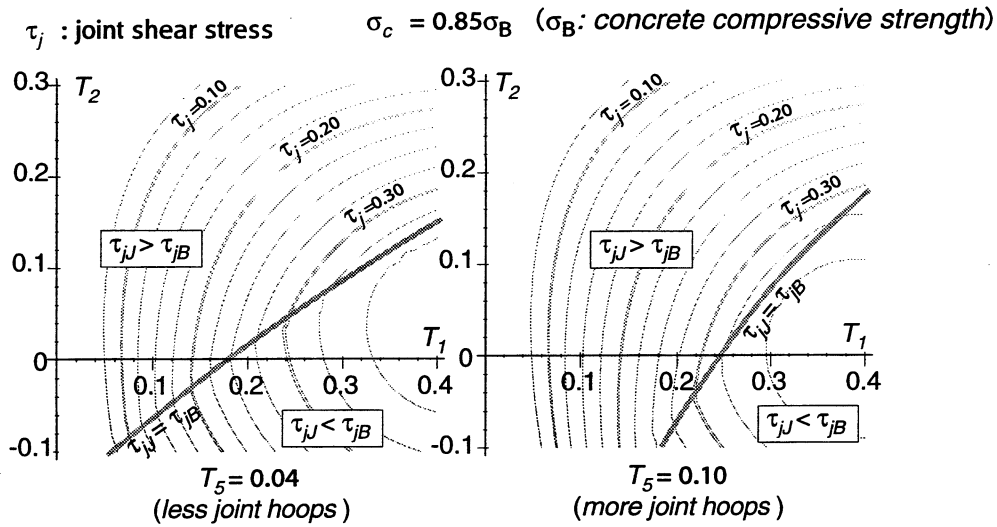


Figure 11: Calculated joint shear stress by the new model

4. APPLICATION OF THE NEW MODEL FOR PREDICTION OF FAILURE MODE

4.1 Loading path

In order to apply this model to practical application, the possible loading pass in the plain of (T_1 , T_2) should be taken into account. There are two physical constraint on the range for T_1 and T_2 . One constraint is tensile strength of beam bars. The other constraint is anchorage capacity of beam straight bar through beam-column joint. Upper bound of the value of T_1 and T_2 is determined by the tensile strength of steel. The upper bound of anchorage force T_1 - T_2 is determined by the anchorage capacity. Figure 12 shows a typical loading pass in beam column joint. When a beam-column joint subassembledge is loaded monotonically, the T_1 and T_2 will increase proportionally, as far as the bond is capable to resist to the input bond force like a line OA shown in Fig.

12(b). However once the bond capacity attains to its capacity B_u , the loading path will turn the direction moving on the 45 degree line like a line AB.

If these constraint is taken into account, the behavior of beam-column joint is predictable. Provided the point of (T_1, T_2) at which beam bars yield is within the B-region, the behavior is predicted as it shows so-called beam-yield failure mode. If enough amount of beam bars with high strength are provided such that the bond strength B_u is attained before beam bars yield, the loading path will be change the direction and moves on the line AB as shown in Fig. 12. Then it will finally attain the point B or B' at which maximum joint strength is given. By this reason, joint shear strength increases provided the anchorage capacity is higher and higher. If the bond capacity of B_u is known from the geometry and the material properties, this model is also useful to predict the joint strength by this way. This model is also applicable to different type of beam-column joints such as a joint with prestressing in horizontal or vertical direction. Currently there is little test data on the behavior of such a beam-column joint under seismic action.

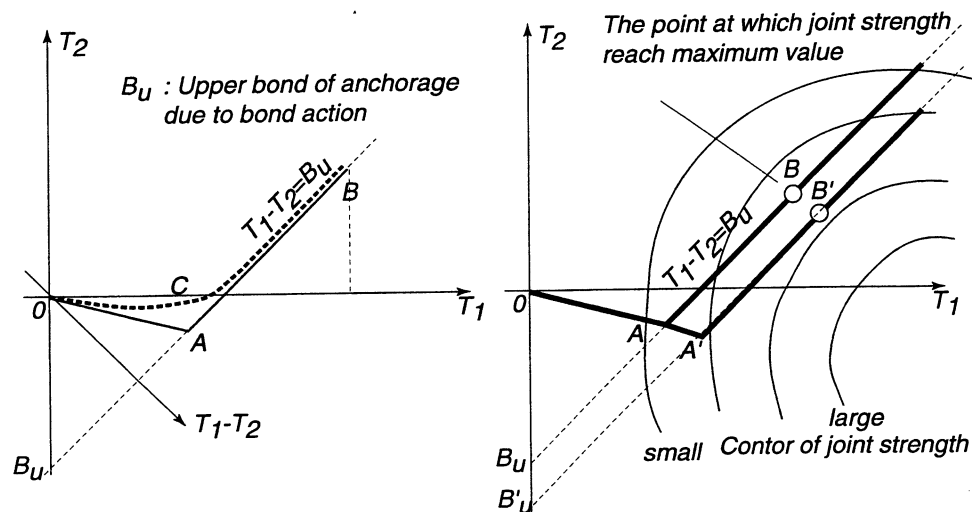


Figure 12: Possible loading pass considering the constraint of bond capacity

5. CONCLUSIONS

A new model is proposed to account for the interaction of factors affecting the behavior of reinforced concrete beam-column joint. The prediction of the model is as follows,

1. The strength and deformation of beam-column joint are strongly affected by two factors, i.e., the input joint shear and bond strength and their interaction. They are not independent. Each factor have independent influences on the strength and deformation mode of beam-column joint.
2. In particular, the bond strength is one of the important factor which have influences on both strength and failure mode of beam-column joints. Larger bond capacity increase the joint strength. But larger bond capacity increase the joint shear deformation.

6. REFERENCES

- 1) ACI Committee 318 (1995) *Building Code Requirements for Structural concrete and Commentary (ACI 318-95)*, Farmington Hills, Michigan.
- 2) Architectural Institute of Japan, (1994). *AIJ Structural Design Guidelines for Reinforced Concrete Buildings*. Tokyo, Japan.
- 3) Cheung, P. C., Paulay, T. and Park, R. (1991) Some Possible Revisions to the Seismic Provisions of the New Zealand Concrete Design Code for Moment Resisting Frames, Proceeding of the Pacific Conference on Earthquake Engineering, New Zealand, November 1991, 79-90.
- 4) Liu, Aizhen and Park, R. (2000). Seismic Behavior of Existing Moment-resisting Frames with Plain Roud Reinforcing Bars Designed to Pre-1970S Codes, Proc. of 12WCEE, January 2000, Paper No. 1030.
- 5) Hakuto S., Park, R. and Tanaka, H., (1999). "Effect of Deterioration of Bond of Beam Bars Passing through Interior Beam-Column Joints on Flexural Strength and Ductility." *ACI Structural Journal*, 96(5), 858-864.
- 6) NZS, (1995). *NZS3101 Concrete Structures Standard: Part1 - The Design of Concrete Structure:1995*, Wellington, New Zealand.
- 7) Paulay, T., Park, R., and Priestley, M. J. N., (1978). "Reinforced Concrete Beam-Column Joints Under Seismic Actions." *Journal of ACI*, 75(11), 585-593.
- 8) Shiohara, H. (1998) "New model for joint Shear failure of reinforcement concrete beam-column Joint," *Journal of the School of Engineering, The University of Tokyo*, Vol. XLV, 1998, pp. 15-40.
- 9) Teraoka, M., (1997). "A study on seismic design of R/C beam-column joint in high rise frame structure." Research Report of Fujita Institute of Technology, Extra Issue No. 5, Tokyo, Japan (in Japanese).

TEST OF AN INNOVATIVE REINFORCING DETAIL FOR HIGH PERFORMANCE R/C INTERIOR BEAM-COLUMN CONNECTIONS SUBJECTED TO SEISMIC ACTION

Hitoshi SHIOHARA¹, Safaa ZAID¹ and Shunsuke OTANI¹

ABSTRACT

Two half scale reinforced concrete interior beam-column joints were tested under statically cyclic lateral load. They were designed such that joint shear failure would occur by increasing the number and size of beam bars passing through the joint. The beam-column joint reinforced with a new detail showed lateral story shear resistance 28% larger than that of the other joint with no special joint reinforcing detail. The new detail was effective to enhance the story shear capacity and joint shear stiffness as well as to alter the failure mode from joint shear failure to beam yielding which is favorable for earthquake resistant design of moment resisting frames.

1. INTRODUCTION

Beam-column joints are critical components in reinforced concrete moment resisting frames designed for inelastic response under severe seismic attack. Hence, recent building codes for reinforced concrete buildings have provisions against the ill behavior of beam-column joints. ACI code (ACI 1995) and AIJ guidelines (AIJ 1991) put restrictions on joint shear to preclude failure of beam-column joints and put restrictions on the diameter of longitudinal bars passing through the beam-column joint to prevent from hysteresis loop with slip having poor energy dissipating performance. Those design provisions do not allow any relaxing of the restrictions by joint reinforcing method. Thus, a test program was planned to examine the effectiveness of a new joint reinforcing detail. The new detail was intended to enhance the strength and stiffness of monolithic beam-column joints as well as to alter failure mode to more favorable one. Two half scale reinforced concrete interior beam-column joints were tested under statically cyclic lateral load and the performance of the beam-column joint was compared with that of the conventionally detailed

¹ Department of Architecture, School of Engineering, The University of Tokyo, Tokyo, Japan
Email: shiohara@rcs.arch.t.u-tokyo.ac.jp

beam-column joint. The new joint detail was found that it significantly enhanced the performance. This paper describes the test results and discusses the force transfer mechanism in the new reinforcing detail.

2. TEST PROGRAM

2.1 Specimens and Test Parameter

Two half-scale reinforced concrete crucial beam-column joints S3 and S4 were tested. They were designed such that joint failure would initiate before beam's flexural yielding by using large amount of beam bars passing through the joints. Difference in the two specimens is joint reinforcing detail. The specimen S3 has a conventional detail in the joint and does not have any special reinforcement

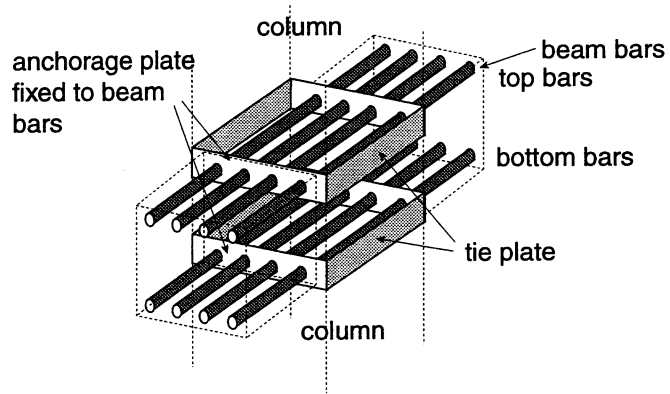


Figure 1: Concept of the new joint reinforcing detail

while the specimen S4 has a novel joint reinforcing detail depicted in Fig. 1. In the specimen S4, the beam bars are fixed to anchorage plates. In addition to that, those anchorage plates were connected to the tie plates which provide horizontal confinement to the beam-column joint to reduce joint deformation. However there is no additional joint hoops or diagonal reinforcement. This concept was implemented as shown in Fig. 2. Deformed reinforcing bars with screw thread passing through the beam-column joint were fixed with double nuts to steel angles. The four steel angles (90x75x9mm) perpendicular to beam axis were welded to the ends of the steel tie plates with 3.2mm thickness and 90 mm width. All the other properties are common for S3 and S4. The cross section of the columns and beams were 300x300mm and 300x200mm respectively. Five D16 bars were arranged at the top and the bottom of the section respectively. Reinforcements in the columns are 12-D19 bars. Four sets of hoops of D6 were placed in beam-column joints. Calculated joint shear stress and diameter of beam bars are much larger than the restrictions specified in the current design codes^{1), 2)}.

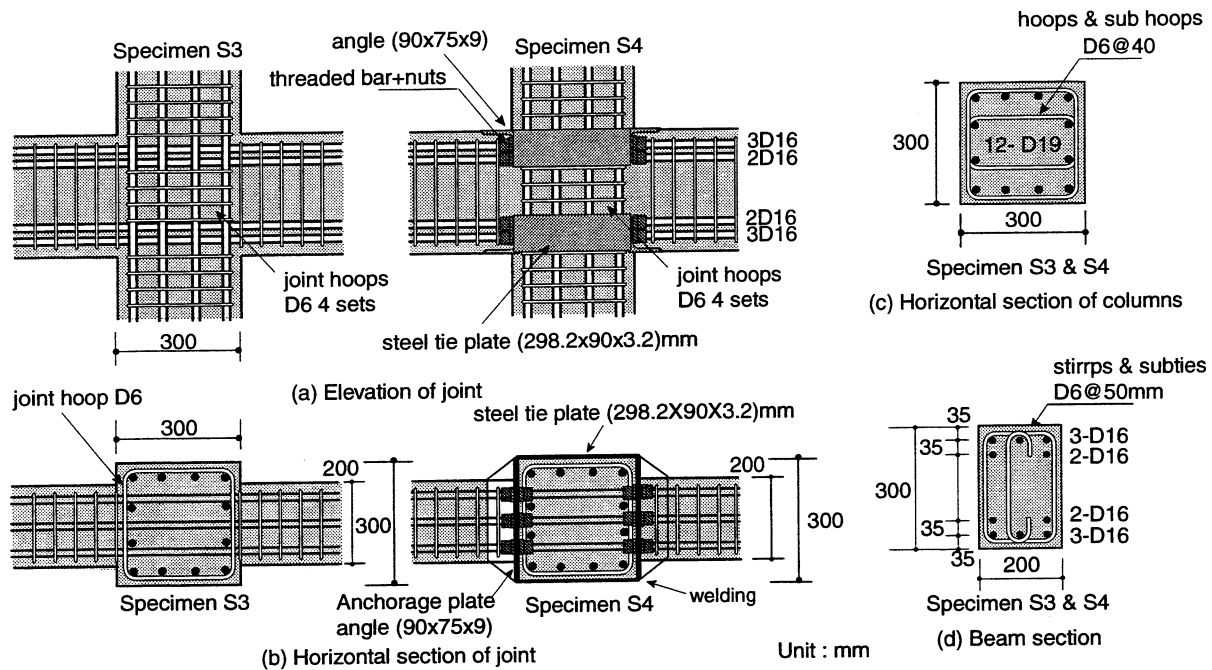


Figure 2: Geometry and reinforcing detail of beam-column joint

2.2 Material

Normal portland cement concrete with design compressive strength of 24MPa was used. The averaged compressive strength of the concrete was 28.0 MPa. The SD390 steel were used for D16 and D19 bars while SD345 steel was used for D6 bars. The mechanical properties of the deformed bars and the tie plates are listed in Table 1.

Table 1: Mechanical properties of steel

Reinforcing bars and steel plate	Sectional area (mm ²)	Yield Strength (MPa)	Tensile strength (MPa)	Young's modulus (GPa)
D6	32	390	580	185
D16	199	470	660	194
D19	287	450	680	208
Tie plate	288	353	475	205

2.3 Test Setup and Loading Sequence and Measurement

The loading set up is shown in Fig. 3. The specimens were supported in vertical position. The top of the column was loaded by two actuators in vertical and horizontal directions. The beam ends were supported by horizontal rollers, while the bottom of the column was supported by a universal pin. Constant axial load of 100kN was applied by load control with the vertical 1000kN actuator, while statically horizontal cyclic load was applied by displacement

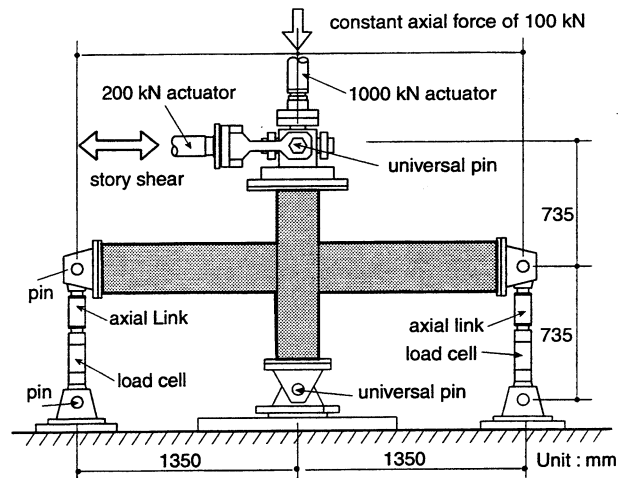


Figure 3: Test setup and loading rig

control with the horizontal actuator with capacity of 200kN. Two cycles of the same amplitude in story drift were repeated before a displacement amplitude was increased. Exception is the one cycle to the story drift of 1% was repeated after the cycles of 2%. Each specimen was instrumented to monitor the applied displacements, corresponding loads, the resulting strains and deformation with emphasis on joint deformation.

3. TEST RESULT AND DISCUSSION

3.1 Development of Cracks

The cracking patterns of specimens at story drift of 3% are compared in Fig. 4. In the specimen S3, diagonal cracks were concentrated on joint. Beam bars did not show yielding until 4% story drift. In the specimen S4, flexural cracks on beams were uniformly distributed along the entire length of the beam and number of cracks was larger than that of crack in the joint. At story drift of 3%, the beam bars showed yielding. When the story drift exceeded 4%, a series of diagonal short cracks aligned horizontally grew up at the mid height

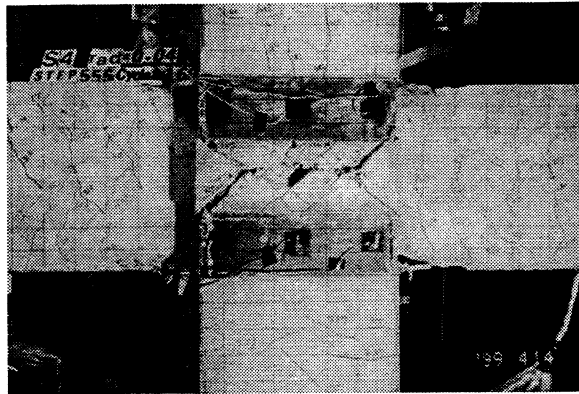


Figure 4: Sliding shear failure of joint (S4)

of the joint. As increasing the story drift, horizontal dislocation increased and a horizontal line of sliding shear failure occurred (see Fig. 5). It is observed that tensile strain in tie plate increased when the story drift increased. The value of tensile strain in the tie plates reached yield strain at

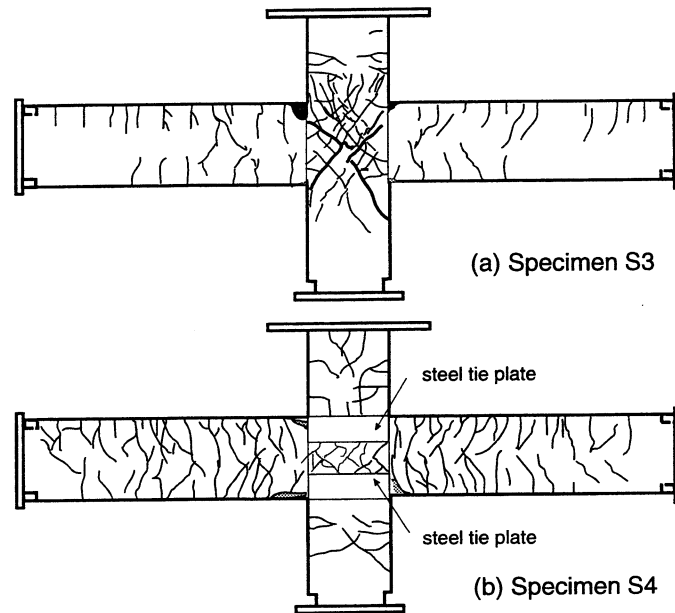


Figure 5: Observed crack patterns after 3% story drift

4% story drift. The yielding of the tie plates may have triggered the occurrence of sliding shear failure of the joint observed in the specimen S4.

3.2 Story Shear-Story Drift Relation

Figure 6 compares relations of story shear and story drift. Specimen S4 held hysteresis loops with a spindle shape with steady dissipation of energy without degradation of story shear until the end of the loading cycle 4% drift. Maximum story shear of 165kN was attained at first cycle of 3% story drift. On the contrary to that, the specimen S3 experienced a degradation of story shear and clear pinching loops due to joint shear deformation and decay of resistance starting after story drift 2%. Attained maximum story shear was 128.4 kN. The strength of the specimen S4 in terms

of story shear was 28% larger than that of S3. This test result proves that lateral resistance of the beam-column joint is enhanced by using the new joint reinforcing detail.

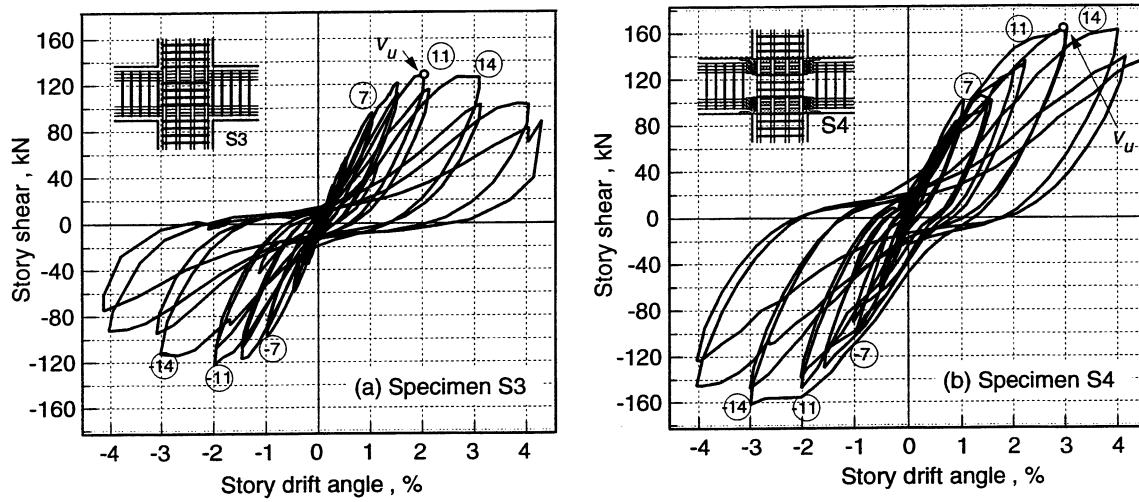


Figure 6: Story shear-Story drift relation

Table 2: Calculated and observed story shear

Specimens		S3	S4
Calculated	V_{uf} : Story shear at flexural yield of beam, in kN	140	140
	V_{uj1} : Story shear at joint shear specified in AIJ 1991 ¹⁾ , in kN	127	127
	V_{uj2} : Story shear at joint shear specified in AIJ1997 ³⁾ , in kN	106	106
Observed	V_{exp} : Maximum story shear, in kN	128	165
Ratio of V_{exp} to the minimum of the calculated story shear		1.21	1.55

3.3 Comparison of Predicted and Observed Story Shear

Table 2 lists the calculated and observed maximum story shear. The story shears (V_{uf}) are calculated one at flexural yielding of beam using flexural theory and mechanical properties of material. Story shear at joint shear strength specified in codes (V_{uj1} and V_{uj2}) was calculated assuming that the length of moment lever arm was equal to 7/8 of effective depth of the beam section. Observed maximum story shear (V_{exp}) of the specimens S3 was almost equal to V_{uj1} , or the calculated story shear obtained by using AIJ 1991 guidelines¹⁾. It is significantly less than V_{uf} . The observed max-

imum story shear V_{exp} of the specimen S4 was 55% larger than the calculated story shear V_{uj2} at joint failure using the conservative recommendation of AIJ guidelines³⁾ in 1997. Moreover maximum observed story shear V_{exp} of the specimen S4 was larger than V_{uf} . So it is concluded that the new joint reinforcing detail successfully converted the failure mode of the beam-column joint from unfavorable joint shear failure to more favorable ductile beam yielding.

3.4 Joint Shear Stress

The joint shear V_j was calculated based on the tensile stress in tensile beam bars at the section of column face.

$$V_j = T_1 + T_2 - V_c \quad (1)$$

where, T_1, T_2 is total tensile force and total compressive force in beam bars at column face respectively, and V_c is column shear. A non-linear stress-strain model considering plastic yield plateau with very small slope and a non-linear strain hardening was used to calculate steel stress from the strain gauge readings⁴⁾. Then the averaged joint shear stress was obtained by dividing the V_j with effective joint area considering the column depth(=300mm) and effective joint width (=250mm). The envelope curves of the relation between story shear and story drift are plotted in Fig. 7a. Although the behavior of the specimens S3 and S4 before story drift of 1.5% is almost identical, the story shear of the specimen S4 is extremely higher than that of the specimen S3.

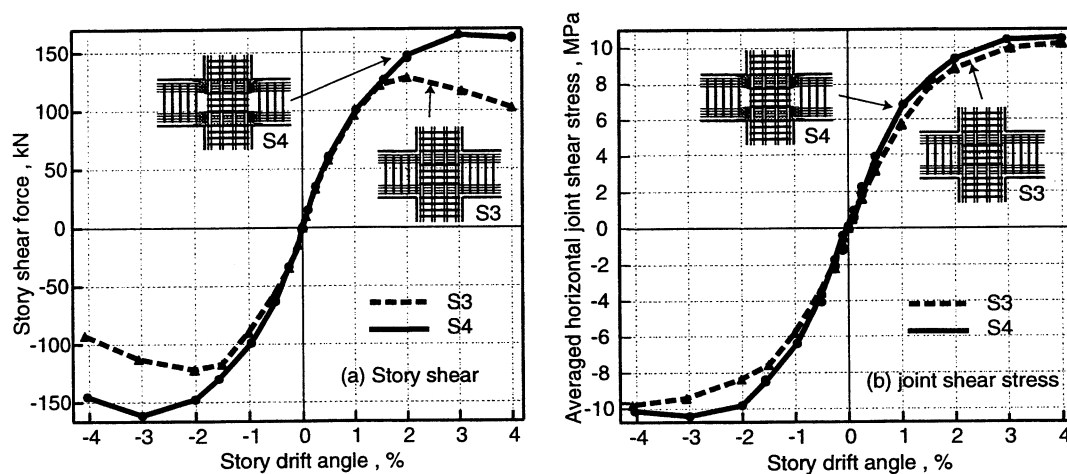


Figure 7: Envelope curves for story shear and joint shear stress

Envelope curves of the averaged joint shear stress are plotted against story drift in Fig. 7b. It is observed that relation between joint shear and story drift for the specimen S3 is similar to that of the specimen S4. Joint shear stress seems continuously increasing as story drift increases. In addition to that the attained maximum joint shear stress of Specimen S3 and Specimen S4 is almost identical.

Hence, it is concluded that the increase of joint shear deformation and the degradation of the story shear observed in Specimen S3 was not related to the degradation of the joint shear stress. Thus, the level of joint shear stress level is an inappropriate index for evaluation of the vulnerability of beam-column joints to joint shear failure, as far as this particular experimental results concerns. Further investigation is necessary on this point.

3.5 Joint Deformation

The relation of average joint shear strain and joint shear stress are shown in Fig. 8. They were calculated from diagonal displacements (Δd_1 and Δd_2) which are the averaged displacement of eight displacement transducers for two direction (45 and 135 degrees) respectively. Shear strain of the specimen S3 is larger than that of Specimen S4 when joint shear stress exceeds around 3 MPa. The

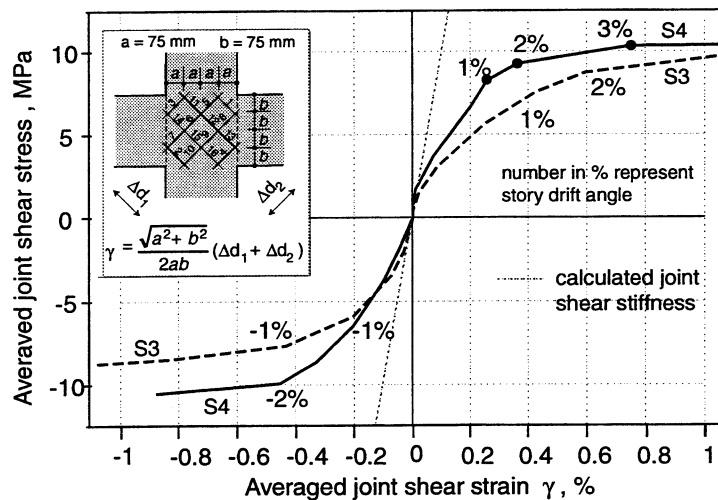


Figure 8: Joint shear strain

difference in joint shear strain increased as story drift increased. At 2% story drift, the joint shear strain in specimen S3 is around 70% larger than that of specimen S4. It reveals that the shear stress-strain relation was significantly affected by the new reinforcing detail of joint.

3.6 Total Anchorage Resistance in Beam Reinforcing Bars

The relation of anchorage resistance in beam bars and story drift angle is shown in Fig. 9. The anchorage resistance is defined here as difference of total forces in longitudinal beam bars at two sections, i. e. at sections at two opposite column faces. This resisting force is caused by the bond action and anchoring plate action. The force in beam bars was calculated based on the data of strain gauge on the bars. The anchorage resistance in the specimen S4 is quite larger

than that of the specimen S3. Maximum anchorage resistance of the specimen S4 was about 25% larger than that of S3 in the later cycles. The anchorage plate was especially effective to keep the stress in compression reinforcement in compression for specimen S4 as shown in Fig. 10, which shows the distribution of stress along the longitudinal bars passing through joint for both specimens. The tensile stress in compressive reinforcement of the specimen S3 reached 30 MPa in tension at 3% story drift. On the contrary to that, the stress in compressive reinforcement of the specimen S4 was larger than 200 MPa in compression. Therefore, it is concluded that the improvement of story shear of S4 was attributed solely to the improvement of its anchorage resistance by additional anchorage plate but not to the improvement of joint shear strength. The joint

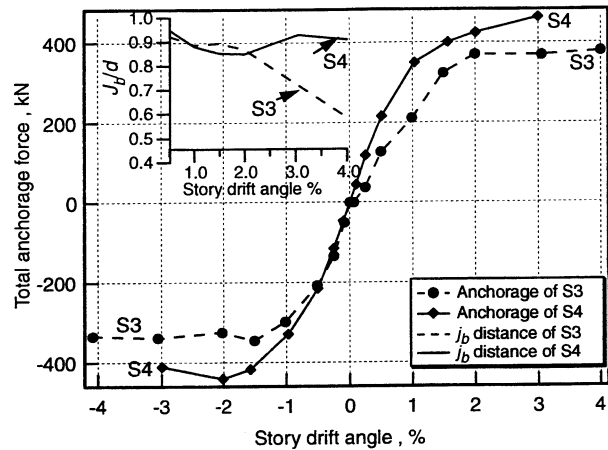


Figure 9: Total anchorage force in joint

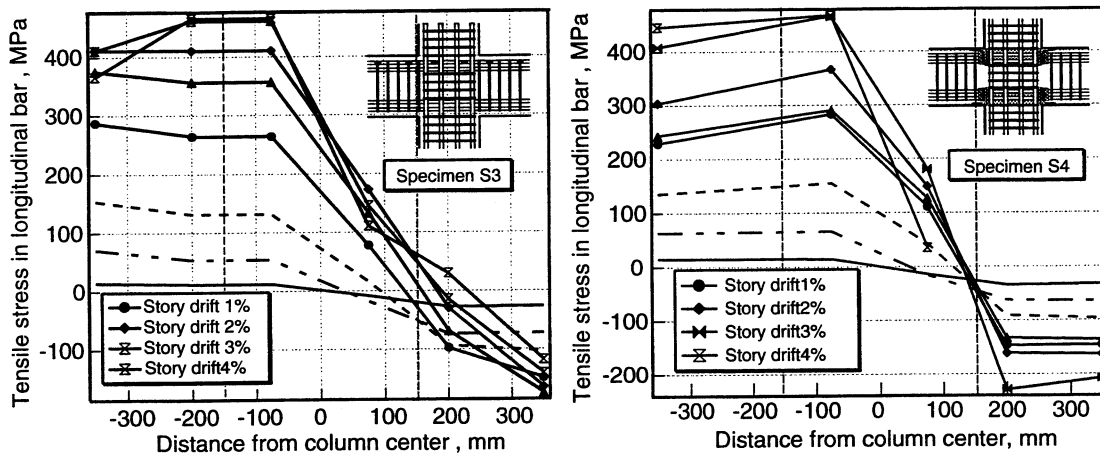


Figure 10: Observed stress in beam bars

shear deformation were reduced by the tie plates which confine the dilatation of beam-column connection.

4. CONCLUSIONS

A new joint reinforcing detail for beam-column joints was carried out. The detail was very effective to preclude joint shear failure. The comparison of the test results revealed that special reinforcing detail in joint led to (1) increasing the story shear 28% higher than conventional details (2) increasing energy dissipation (3) reducing the joint deformation and (4) converting the failure mode from joint failure to beam flexural yield. The enhancement in the story shear was attributed to the improved anchorage strength, while there seems to be no relation between joint shear stress and failure mode of beam column joint. The new detail may enable to design columns with smaller section and enable to utilize deformed bar with large diameter for interior beam-column joint. A preliminary model accounting for the strength enhancement of beam-column joints by this kind of anchorage plate and horizontal confining steel had been proposed by one of the authors⁴⁾. Further development of the mathematical models and design methodologies are essential to facilitate this innovative detail to be used in practice.

5. REFERENCES

- 1) ACI Committee 318: *Building Code Requirements for Structural concrete and Commentary*, ACI 318-95.
- 2) Architectural Institute of Japan: *AIJ Structural Design Guidelines for Reinforced Concrete Buildings (1991)*, Tokyo, 1991, (in Japanese).
- 3) Architectural Institute of Japan: *AIJ Structural Design Guidelines for Reinforced Concrete Buildings (1997)*, Tokyo, 1997. (in Japanese).
- 4) Hitoshi Shiohara: "New model for joint Shear failure of reinforcement concrete beam-column Joint," *Journal of the School of Engineering, The University of Tokyo*, Vol. XLV, 1998, pp. 15-40.

**The Second U.S.-Japan Workshop on Performance-Based Earthquake Engineering
Methodology for Reinforced Concrete Building Structures
11–13 September, 2000
Sapporo, Hokkaido, Japan**

RESOLUTIONS

Recent urban earthquakes have caused significant economic losses, injuries, and fatalities in both the United States and Japan. This was evident in the U.S. during the 1994 Northridge earthquake, and in Japan during the 1995 Hyogo-ken Nambu earthquake. These and other earthquakes such as the recent earthquake in Turkey and Taiwan point out the need for effective and practical methods for

- evaluating and rehabilitating existing hazardous buildings and
- designing new buildings for more reliable and improved performance.

While great progress previously has been made in engineering for earthquake resistance, suggested frameworks for performance-based earthquake engineering will accelerate progress by focusing efforts and bridging gaps. This will lead to a future of earthquake engineering that will include increased emphasis on quantitative measures of performance over qualitative measures, precision over approximation, reliability over uncertainty, and intelligent engineering and life-cycle cost design over minimum capital cost design.

Papers presented at the Second U.S.-Japan Workshop on Performance-Based Earthquake Engineering Methodology for Reinforced Concrete Building Structures demonstrate progress being made in performance-based earthquake engineering. The papers shall be reviewed and published as the proceedings of the workshop both on the U.S. side and the Japan side within a few months. Presentations in the plenary session and two working group sessions covered site effects and aleatory variability of earthquake ground motion, inelastic response of structures, performance of reinforced concrete components and structures, seismic assessment and design, performance-based design codes, design practice and examples, and future needs. Discussion of the presented papers enhanced understanding and advanced the state-of-the-art in performance-based earthquake engineering. Important outcomes of the Workshop include

- (a) better understanding of the present state of knowledge and practice of performance-based earthquake engineering in the U.S. and Japan, especially the requirements of

the recently revised Building Code of Japan and design practice being adopted in U.S.;

- (b) detailed understanding of seismic demands, especially the use of analysis methods for performance-based earthquake engineering of reinforced concrete buildings;
- (c) detailed understanding of seismic capacities of structures and members, especially reinforced concrete columns and beam-column joints;
- (d) identification of common areas of concern, areas of needed advancement, and areas that would benefit from joint study.

The topic of performance-based earthquake engineering is a particularly effective one for workshop discussion because it brings together and promotes a common focus of experts in ground motion, analysis, and design. Understanding of the work of individuals with different expertise was achieved in ways that would not be possible without meeting in this format.

The workshop was a successful continuation of progress made through over two decades of cooperative U.S.-Japan research in earthquake engineering. The success at this workshop suggests that the two countries will benefit from continued cooperation. Reasons for continued cooperation include

- (a) the two countries have a shared need to develop improved methods for seismic design and evaluation;
- (b) in both countries, there is a need for integrated analytical and experimental approaches, which is promoted in this meeting format; and
- (c) each side brings unique data, experience, knowledge, facilities, the sharing of which benefits all.

These discussions are best accomplished through face-to-face meetings of extended duration such as occur in a workshop format. Therefore, the following recommendations are offered:

- (1) Because of the rapid rate at which new information and applications are being achieved, the importance of advances to Japan and the U.S., and the success of the first and second workshops, the participants recommend that the Third U.S.-Japan Workshop on Performance-Based Earthquake Engineering Methodology for Reinforced Concrete Building Structures be organized by the U.S. side in about one year.

- (2) At future workshops, several topics for focused discussion should be considered. A reduced number of these should be the focus of the third workshop:
- (a) simplified and rigorous methods for predicting seismic demands:
 - (i) identification of damaging features of earthquakes including near- source effect, site effect, and aleatory variety;
 - (ii) continuation of the topic on inelastic displacement demands for SDF and MDF systems;
 - (iii) practical application of advanced analysis methods;
 - (iv) use of probabilistic bases for PBE incorporating uncertainty and variability;
 - (v) performance of strength-degrading structures;
 - (vi) seismic demands including life-cycle loss estimation,
 - (b) simplified and rigorous methods for predicting seismic capacities:
 - (i) definitions and measures of performance;
 - (ii) modeling of damage and definition of reparability;
 - (iii) hysteretic energy dissipation of members;
 - (iv) deformations at loss of lateral and gravity load capacity of members;
 - (v) continuation of the topic of residual gravity load capacity of members;
 - (vi) damage models including cumulative effects;
 - (vii) exchange of database on test results;
 - (viii) behavior of nonstructural components,
 - (c) design methodology to bring these together:
 - (i) validation of performance-based earthquake engineering methods;
 - (ii) assessment of system performance to be carried out based on component performance;
 - (iii) evaluation of moderate damage for assessment of damage repair cost;
 - (iv) development of performance-derived design criteria.
- (3) At the third workshop, the following format should be considered:
- (a) focus on three or four topics, emphasizing presentation of papers on those topics coupled with working group sessions to examine topics in greater detail; and
 - (b) participation of professional engineers, representatives of code-writing organizations, representatives of national organizations responsible for construction, etc.
- (4) Cooperative activities between individual participants from the U.S. and Japan are encouraged to address problems of mutual concern. Efforts should be undertaken to

facilitate exchange of personnel, including students, faculty, and professional researchers and practitioners, as well as of information on technical issues and applications. Funding agencies are encouraged to support these activities.